Study Report

APOLLO APPLICATIONS PROGRAM
LUNAR SURFACE MISSION PLANNING

Volume 2
SUPPLEMENTARY AND DETAILED STUDIES

November 1, 1967

Prepared by MILITARY ANALYSIS CENTER
Bell Telephone Laboratories — Wash

on behalf of Bellcomm, Incorporated

FOREWORD

This volume, "Supplementary and Detailed Studies," of the final study report on the AAP Lunar Surface Mission Planning presents the detailed analyses of the system and its operation. These analyses served as inputs to Volume 1, "Mission Analysis." Detailed analysis is not provided here for all facets of the system study, because some sections of Volume 1 do not require such a detailed treatment. Thus, no attempt has been made to make Volume 2 complete in itself. Some sections of this volume are specifically referenced in Volume 1, but sections providing background material of a general nature are not.

The text in this volume is not necessarily limited to direct or general support of Volume 1. Related information that was gathered and analyses made during the study are also included. This may be of use to system planners if changes are to be made in the system.

M. J. Evans

TABLE OF CONTENTS

Section I
CONFIGURATIONS — CAPABILITIES AND RISKS W. C. Meyer

Section II
ACCESSIBILITY R. A. Steigerwalt

Section III
TRAJECTORY CONSIDERATIONS C. D. DeJong

Section IV
LM LANDING D. C. Swanay

Section V
LSSM MOBILITY I. S. Yavelberg

Section VI
MAN'S CAPABILITIES E. P. Koslow and J. W. Fort

Section VII
METEOROID HAZARD A. A. Lundstrom

Section VIII
SOLAR FLARE HAZARD D. C. Swanay

Section IX
VISIBILITY W. C. Meyer

Section X
LUNAR CHARACTERISTICS D. E. Morgan

Section XI
LSR STRATEGY AND COST COMPARISONS D. C. Swanay

X68-84331

SECTION I. COMPARISONS OF CONFIGURATIONS WITH RESPECT TO CAPABILITIES AND RISKS

By W. C. Meyer

1. INTRODUCTION

The primary constraint for the Apollo Applications Program (AAP) extended lunar surface mission is the schedule of flights for the early 1970's using systems left over from Apollo. This focuses attention upon the characteristics of the basic Apollo systems and configurations and upon minor modifications which may be included to extend capabilities. Two important interrelated capabilities are payload and stay-time. The primary purpose of this section is to present the background data upon which the interpretations and conclusions in Volume 1 are based. To accomplish this, the capabilities for the various configurations are presented in conjunction with a detailed breakdown of elements determining the relationship between payload and stay-time. The cost figures for the various configurations are included. In addition, a qualitative measure of the risks associated with the operational characteristics of the various configurations is given. Interpretation of the data in this section is held to a minimum.

2. CANDIDATE CONFIGURATIONS

In view of the primary constraint stated above, the modifications are limited to the Lunar Module (LM) and must be derived from the basic Apollo LM. The candidate configurations considered herein are those covered in References 1 and 2*. They are briefly described below.

Lunar Module (LM)	The basic Apollo Lunar Module.
Shelter (S)	A 1-way vehicle modified for unmanned landing. It retains the basic LM structure and provides stay-time housing up to 14 days for the astronauts. It may remain in quiescent storage on the lunar surface for up to 90 days prior to occupancy by the astronauts who arrive by Taxi.

---

*References are listed at the end of the section.

Taxi (T)	The 2-way delivery vehicle in the Shelter/Taxi Dual-Vehicle Missions (DVM). It delivers two astronauts to the Moon's surface in the vicinity of the Shelter and returns them from the Moon's surface. The Taxi is the basic LM modified for up to 14-day quiescent storage during Shelter occupancy by the men.
Lunar Payload Module (LPM)	A 1-way vehicle with the standard LM ascent structure retained but the ascent engine and fuel tanks and the life support systems removed. It cannot house the men, but it provides increased payload delivery to the Moon and is used in DVM combinations with a 2-way vehicle which includes the housing.
Lunar Truck Module (LTM)	A 1-way vehicle with the entire standard LM ascent structure removed and the descent guidance and control systems relocated to the descent stage. The ascent stage is replaced with structure specifically accommodating the payload. This vehicle can be used similarly to the LPM, but provides greater payload capability.
Lunar Truck Module Shelter (LTMS)	The same as the LTM except part of the added payload capability is given over to a special shelter for housing.

The basic LM and each of the above derivations can also exist in an augmented version. Augmentation increases the descent propulsion and allows the vehicle to land a heavier payload. Tanks for fuel and oxidizer are increased, and the landing structure is strengthened. The augmented versions of the above-listed vehicles are referred to by preceding the name with the word "augmented" and prefixing the letter "A" to the abbreviation.

Dependent LM (DLM)	A 2-way vehicle and the final LM derivative considered. Used in DVM combinations, it depends upon the 1-way vehicle for the additional expendables required to extend the stay-time beyond the nominal 1-1/2 days of basic Apollo. It is contemplated that these expendables would be transported from the 1-way vehicle to the DLM and the oxygen and water tanks would be connected into the system via existing Ground Support Equipment (GSE) fittings.

3. PAYLOAD AND COSTS

The payload and stay-time characteristics of these LM derivatives along with cost figures are listed in Table I-1. These data derive from References 1 through 4.

Table I-1

PAYLOADS, COSTS, AND STAY-TIMES FOR LM DERIVATIVES

LM Derivatives	Manned Stay-Time (days)	Payload (lbs) to Earth	Payload (lbs) to Moon	Cost ($ million) Recurring	Cost ($ million) Non-Recurring
Non-Augmented					
LM	1-1/2	80	250	–	–
S	14	–	3,000	19	127
T	1/4	0	250	18	37
LPM	–	–	8,000	1.5	6
LTM	–	–	10,800	19	77
LTMS	14	–	9,000	30	220
DLM	1-1/2	250	–	1.5	3
Augmented					
ALM3	3	250	1,120	5	91
ALM5	5	250	925	5	91
ALM12	12	250	250	30	120
AS	14	–	5,100	23*	†
AT	1/4	250	2,000	22*	†
ALPM	–	–	10,000	5.5*	†
ALTM	–	–	12,800	23*	†
ALTM(S)	–	–	6,900	34*	†

---

*Basic augmentation cost of $4 million included.

†Basic augmentation cost of $75 million applied once to the Dual-Vehicle combination.

One division of AAP missions made in this study has been between those involving a single Saturn V launch and those involving two such launches. The Single-Vehicle Mission (SVM) uses an augmented LM which delivers the men to the Moon, houses them during their stay, and returns them from the Moon's surface. The

Table I-2

LM COMBINATIONS FOR SINGLE- AND DUAL-VEHICLE MISSIONS

LM Combinations	Single-Vehicle Mission SVM (2-Way LM)	Dual-Vehicle Mission DVM (1-Way LM/2-Way LM)		
	Housing in 2-Way LM	Housing in 2-Way LM		Housing in 1-Way LM
	Life Support in 2-Way LM	Life Support in 1-Way LM	Life Support in 2-Way LM	Life Support in 1-Way LM
Non-Augmented				
Lunar Module (2-day)	LM			
Lunar Payload Module/Dependent Lunar Module		LPM/DLM		
Lunar Truck Module/Dependent Lunar Module		LTM/DLM		
Shelter/Taxi				S/T
Lunar Truck Module (Shelter)/Taxi				LTM(S)/T
Augmented				
Augmented Lunar Module (4-day)	ALM 4			
Augmented Lunar Module (12-day)	ALM 12			
Augmented Lunar Payload Module/Augmented Lunar Module			ALPM/ALM	
Augmented Lunar Truck Module/Augmented Lunar Module			ALTM/ALM	
Augmented Shelter/Augmented Taxi				AS/AT
Augmented Lunar Truck Module (Shelter)/Augmented Taxi				ALTM(S)/AT

Dual-Vehicle Mission uses two of the LM derivatives that are referred to as the 1-way LM and 2-way LM. The 2-way LM both delivers the men to the moon and returns them from its surface. The 1-way LM is unmanned and performs only the descent function, delivering a relatively large payload to the Moon. Depending upon the particular combination of LM derivatives chosen for a DVM, the housing function may be performed in either LM. Table I-2 lists the LM combinations considered for AAP missions. Table I-3 gives payload and cost data for a DVM. The payloads to the Moon have been adjusted for a 12-day stay-time as taken from Figure I-1. The slopes of the lines in the figure are indicative of the rate at which various expendables must be supplied. The three different slopes are associated with the:

1. ALM (derived from payload and stay-time in Table I-1).
2. Shelter combinations (derived from data in References 5 and 6).
3. DLM combinations (derived from Shelter data and checks with results curve in Reference 2).

Table I-3

PAYLOADS AND COSTS FOR DUAL-VEHICLE MISSION FOR A 12-DAY STAY-TIME

LM Combinations (1-way LM/2-way LM)	Payload (lbs) to Earth	Payload (lbs) to Moon	Cost ($ millions) Recurring	Cost ($ millions) Non-Recurring
LPM/DLM	250	3,450	3	9
LTM/DLM	250	6,250	20.5	80
S/T	250	3,100	37	164
LTMS/T	250	5,050	48	257
ALPM/ALM	250	10,200	35.5	126
ALTM/ALM	250	13,200	53	197
AS/AT	250	7,250	45	239
ALTM(S)/AT	250	9,050	56	332

The individual items making up these rates are detailed in Table I-4. Figures I-2 through I-5 relate to the Shelter design and show some of the interrelation among the expendables which must be supplied. Table I-5 presents mission costs and capabilities derived from the data of Table I-3. The payloads reflect the additional micro-meteroid shielding required for the indicated stay-times. (See Section VII for details on shielding).

The cost figures which are for five missions, assume a $200-million cost for each Saturn V launch and includes "expected" costs (see Section XI).

Table I-4

USAGE RATES OF EXPENDABLE ITEMS INCLUDED IN PAYLOADS TO THE MOON

	Shelter (lbs/day)	Dependent LM (lbs/day)
WATER		
Usage		
Charge PLSS (6.8 lbs/3-hr EVA)	20.4	20.4
Metabolic, Hygiene, etc (9 lbs/man/day)	18.0	18.0
Thermal Control	8.0	100.0
Recovery		
Metabolic (0.125 lb/cabin manhours)	- 4.88	- 4.88
Fuel Cells, Manned Phase (16.45 lbs/day)	-16.45	—
Fuel Cells, PLSS Battery Recharge (0.267 lbs/EVA)	- 0.80	—
Total	24.27	133.52
Penalties		
Tankage (0.0943 lb/lbs H_2O)	2.29	12.59
Packaging (20 lbs/tank = (20/322) lb/lbs H_2O = 0.06211 lb/lbs H_2O)	—	8.29
Total (with penalties)	26.56	154.40
EXPENDABLES		
Usage		
Food (1.5 + 0.8 package) lbs/man/day)	4.6	4.6
Constant-Wear Garment (0.5 lb/man/day)	1.0	1.0
LiOH, PLSS (4.5 lbs/EVA)	13.5	13.5
LiOH, Cabin (7.6 lbs/day)	7.6	7.6
Total	26.7	26.7
OXYGEN (GOX) AND HYDROGEN (H_2)		
GOX Usage		
Environmental Control System		
Cabin Leakage (0.2 lb/hr)	4.8	4.8
Metabolic (0.0833 lb/cabin manhours)	3.25	3.25
Cabin Repressurizations (4/day)	7.2	27.6
PLSS Recharge (0.91 lb/3-hr EVA)	2.73	2.73
Electrical Power System		
Fuel Cells, Manned Phase (201.07 lbs/13.75 day)	14.6233	
Fuel Cells, PLSS Battery Recharge (9.244 lbs/39 EVA · 3 EVA/day)	0.711	—
Total	33.314	38.38

Table I-4 (continued)

	Shelter (lbs/day)	Dependent LM (lbs/day)
GOX Penalties		
Tankage (S, 1.1 lb/lb GOX; LM, 1.06 lb/lb GOX)	36.645	40.68
Packaging (20 lbs/tank = (20/45.2) lb/lb GOX = 0.4425 lb/lb GOX)	–	16.98
Total (with penalties)	69.96	96.04
H_2 Usage		
Electrical Power System		
Fuel Cells, Manned Phase (25.13 lbs/13.75 days)	1.828	–
Fuel Cells, PLSS Battery Recharge (1.1556 lbs/39 EVA · 3 EVA/day)	0.0889	–
Total	1.917	–
H_2 Penalties		
Tankage (16.765 lbs/lbs H_2)	32.135	–
Total (with penalties)	34.052	–
USAGE WITHOUT PENALTIES		
Water	24.27	133.52
Expendables	26.70	26.70
GOX, ECS	17.98	38.38
GOX, EPS	15.33	–
H_2, EPS	1.92	–
Total	86.20	198.60
USAGE WITH PENALTIES		
Water	26.56	154.40
Expendables	26.70	26.70
GOX, ECS	37.76	96.04
GOX, EPS	32.20	–
H_2, EPS	34.05	–
Total	157.27	277.14

Table I-5

CAPABILITIES AND COSTS FOR SINGLE- AND DUAL-VEHICLE MISSIONS

LM Combinations	Stay-Time (days)	Single-Vehicle Mission SVM (2-Way LM)			Dual-Vehicle Mission DVM (1-Way LM/2-Way LM)								
		Housing in 2-Way LM			Housing in 2-Way LM						Housing in 1-Way LM		
		Life Support in 2-Way LM			Life Support in 1-Way LM			Life Support in 2-Way LM			Life Support in 1-Way LM		
		Payload (lbs)		Cost for 5 Missions in $ billions	Payload (lbs)		Cost for 5 Missions in $ billions	Payload (lbs)		Cost for 5 Missions in $ billions	Payload (lbs)		Cost for 5 Missions in $ billions
		To Earth	To Moon		To Earth	To Moon		To Earth	To Moon		To Earth	To Moon	
Non-Augmented													
LM	1-1/2	230	250	1.1									
LPM/DLM	12				70	3300	2.3						
LTM/DLM	12				70	6100	2.5						
S/T	12										180	3000	2.6
LTM(S)/T	12										180	5000	2.8
Augmented													
ALM4	4	170	1000	1.2									
ALM12	12	70	100	1.4									
ALPM/ALM	12							70	10,000	2.6			
ALTM/ALM	12							70	12,800	2.8			
AS/AT	12										180	7200	2.8
ALTM(S)/AT	12										180	9000	2.9

4. SURFACE OPERATIONS

For Dual-Vehicle Missions, surface operations will be somewhat affected by the division of the housing and life support functions between the two vehicles. When both the housing and life support are provided in the 1-way LM (in this case, Shelter), surface operations must include a period to check out the Shelter prior to occupation and, later, a period to check out the Taxi before the return to Earth. When the housing is provided in the 2-way LM, normal usage of the payload delivered by the 1-way LM requires additional traffic between the two vehicles. When the 2-way LM is the DLM, this additional traffic includes transporting items such as the water and oxygen supply tanks essential to life support. These tanks must be connected into the operating system of the DLM as needed.

5. RISKS

Just as there are differences in surface operations among the candidate configurations, there are also differences in risks involved. However, comparisons of these risks are difficult to make. For instance, the DVMs requiring two launch vehicles have lower mission success probabilities than SVMs. However, the SVMs do not have the same capabilities, and, to achieve the same payoff (e.g. payload and stay-time on the Moon), more missions are required which increases the risk per unit of payoff. Similarly, short missions are less hazardous than long ones, but the total risk to achieve a given stay-time is quite likely to be greater for the more numerous short missions.

Three LM combinations are qualitatively compared in regard to mission failure probabilities for four general types of failure. It is assumed that all the LMs in which men are housed are designed to give the same crew safety level during the 12-day manned phase. The effect of operations alone on the probability of mission failure is then assessed. The failure probabilities are not known quantitatively, but a qualitative comparison among the three general DVM combinations is made (see Table I-6).

The first type of failure noted is the ascent capability of the 2-way LM such as a propellant tank leak. The probability of this type of failure, P_A, is the same for each of the three DVM combinations.

Probability of failure of the life-support equipment is divided between those cases which occur independent of whether the equipment is operating or not (P_N) and those cases which occur as a consequence of its operation (P_O). In the first case, the DVMs using the DLM or the ALM primarily involve only one life-support system and will each have a probability of P_N. However the Shelter/Taxi has a separate life-support system for each of the two LMs; therefore, the probability is $2P_N$. In the second case, the DVM using the DLM requires the transport of water and oxygen supplies from the 1-way LM to the 2-way DLM for use by the life-support equipment there. This transport procedure adds an element of failure probability (P_O'), thus giving a total of $P_O + P_O'$ due to operation of its life-support system. The DVMs with the 2-way ALM with housing and the Shelter/Taxi each have P_O for mission failure probabilities due to life-support malfunction arising from operation of that equipment.

Table I-6

MISSION FAILURE PROBABILITIES FOR DUAL-VEHICLE MISSIONS

Type of Failure	Housing in 2-way LM (DLM) Life Support Expendables in 1-way LM (LPM or LTM)	Housing and Life Support Expendables in 2-way LM (ALM)	Housing and Life Support Expendables in 1-way LM (S)
Ascent Capability	P_A	P_A	$\left.\begin{matrix}(S) & 0\\ (T) & P_A\end{matrix}\right\} = P_A$
Life Support Equipment Except Due to Operation	P_N	P_N	$\left.\begin{matrix}(S) & P_N\\ (T) & P_N\end{matrix}\right\} = 2P_N$
Life Support Equipment Due to Operation	$P_O + P_O'$	P_O	$\left.\begin{matrix}(S) & P_O\\ (T) & 0\end{matrix}\right\} = P_O$
Crew Injury	$P_I + P_I'$	P_I	P_I
Sum of Failure Probabilities	$P_{SUM} + P_O' + P_I'$	P_{SUM}	$P_{SUM} + P_N$

The probability of mission failure due to crew injury is higher by P_I' for the DVM using the 2-way DLM because of the added risk of transporting the water and oxygen supplies to it. This is a total of $P_I + P_I'$ compared to P_I for the other two configurations.

The risks to crew safety are a function of the contingency action when one of the failures noted in the table occurs. In the case of the Shelter/Taxi, such action entails the astronauts' return from the Shelter to the Taxi plus the sequence of bringing the Taxi up to the ready-condition for the ascent. In general, for each type of failure, the contingency actions required when operating from the three DVM combinations differ only in this additional return sequence required for the S/T.

In Table I-6 the sum of the failure probabilities P_A, P_N, P_O, and P_I is denoted as P_{SUM}. The lowest sum by an undetermined amount is associated with the DVM combination employing the ALM. If this is considered along with the contingency actions noted above, this DVM combination would be preferred. This qualitative comparison is of limited usefulness. Differences based upon payload capabilities are considered more significant and lead to the choices within the general category of Shelter/Taxi as discussed in Volume 1 of this report.

REFERENCES

1. "Augmented Lunar Module, Lunar Shelter, Lunar Taxi," NASA Committee Study Report, November 16, 1966.
2. Waldo, J. E. "Dependent LM and Lunar Payload Module Briefing Charts, Proposed Concept," November 21, 1966 Bellcomm, Inc. Briefing at Bell Telephone Laboratories, Whippany, N. J., December 19, 1966.
3. Waldo, J. E. Presentation Vu-Graphs for Lunar Surface Exploration, Bellcomm, Inc., November 23, 1966.
4. Apollo Applications Program Preliminary Definition Study of Utilization of LM Engineering Study of 3-day Augmented LM During October 1966 Final Report, Grumman Aircraft Engineering Corporation, November 15, 1966.
5. Apollo Extension System Phase B Final Report, V, "Shelter Design Analysis Summary," Grumman Aircraft Engineering Corporation (CONFIDENTIAL).
6. Apollo Extension System Phase B Final Report, VI, "Taxi Design Analysis Summary," Grumman Aircraft Engineering Corporation (CONFIDENTIAL).

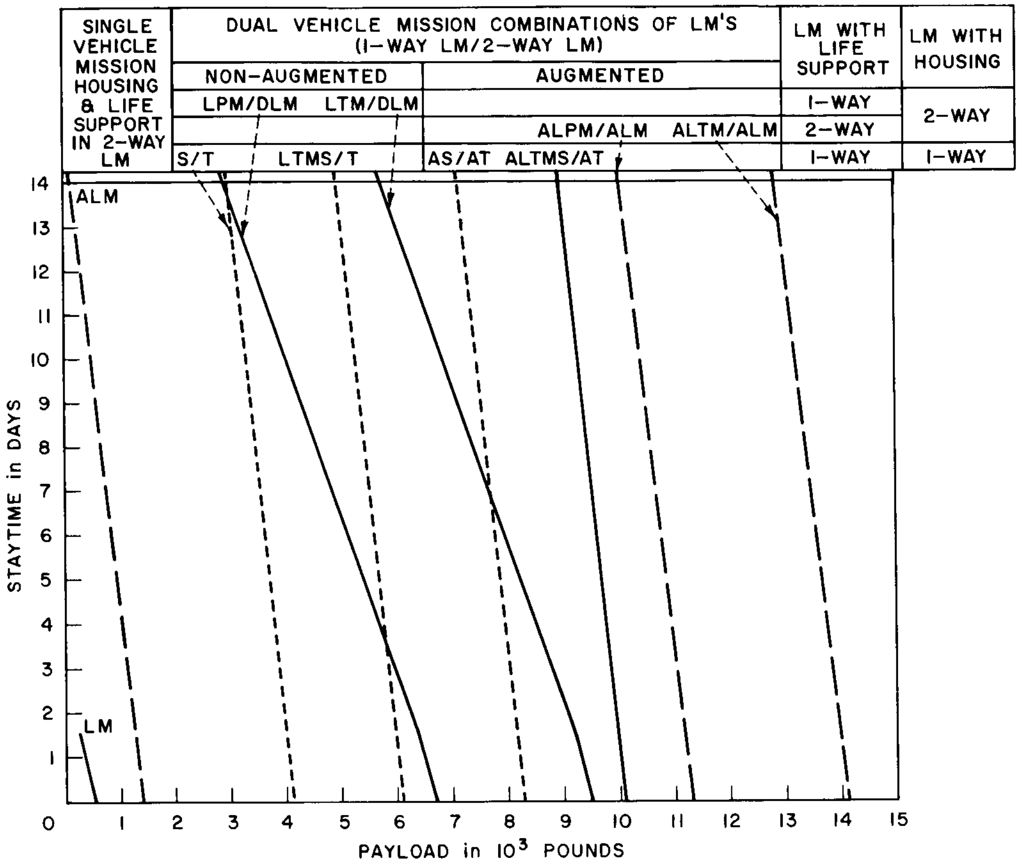

Figure I-1. Stay-Time versus Payload for SVMs and DVMs

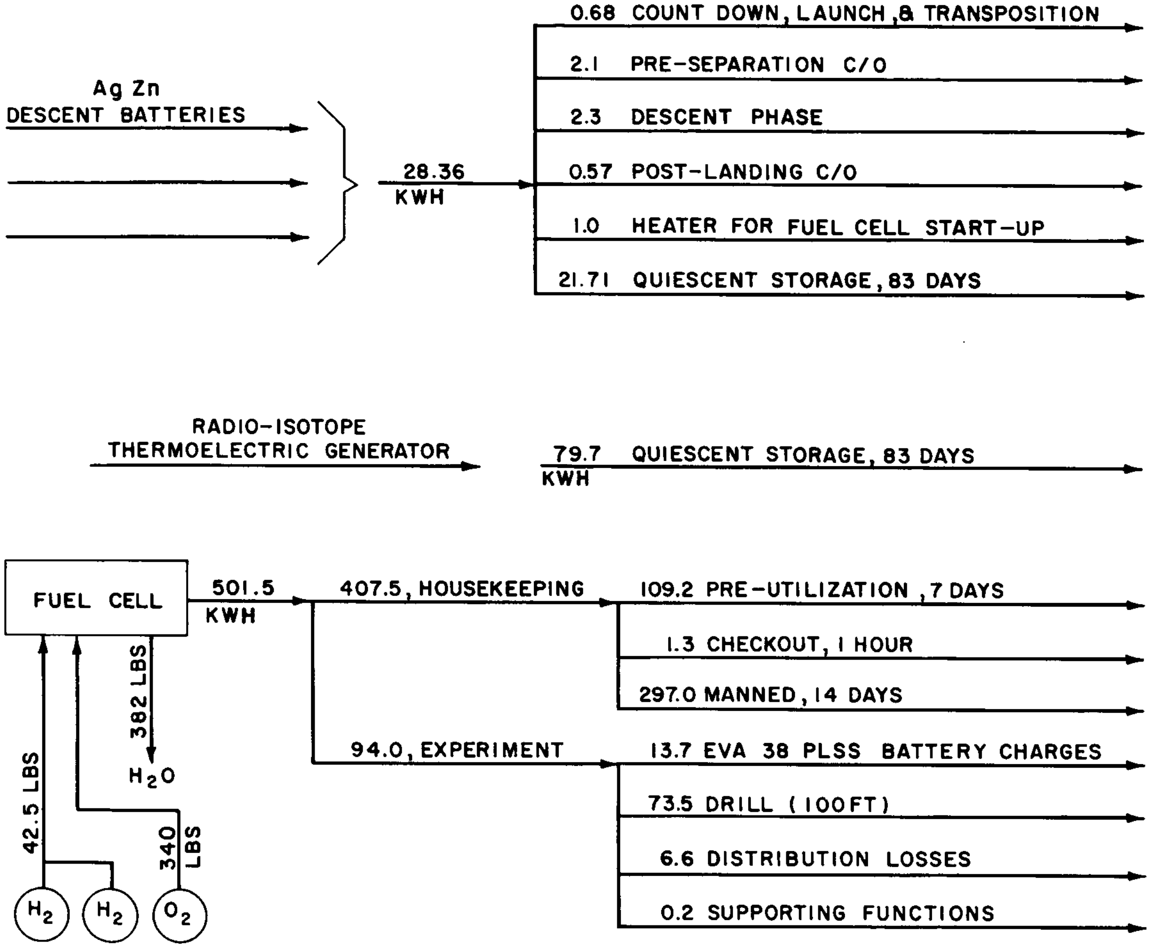
0.68 COUNT DOWN, LAUNCH, & TRANSPOSITION
2.1 PRE-SEPARATION C/O
Ag Zn
DESCENT BATTERIES
2.3 DESCENT PHASE
28.36
KWH
0.57 POST-LANDING C/O
1.0 HEATER FOR FUEL CELL START-UP
21.71 QUIESCENT STORAGE, 83 DAYS
RADIO-ISOTOPE
THERMOELECTRIC GENERATOR
79.7
KWH
QUIESCENT STORAGE, 83 DAYS
FUEL CELL
501.5
KWH
407.5, HOUSEKEEPING
109.2 PRE-UTILIZATION, 7 DAYS
1.3 CHECKOUT, 1 HOUR
297.0 MANNED, 14 DAYS
382 LBS
H₂O
42.5 LBS
94.0, EXPERIMENT
13.7 EVA 38 PLSS BATTERY CHARGES
73.5 DRILL (100FT)
340 LBS
6.6 DISTRIBUTION LOSSES
0.2 SUPPORTING FUNCTIONS
H₂
H₂
O₂

Figure I-2. Electrical Power Allocation for Shelter

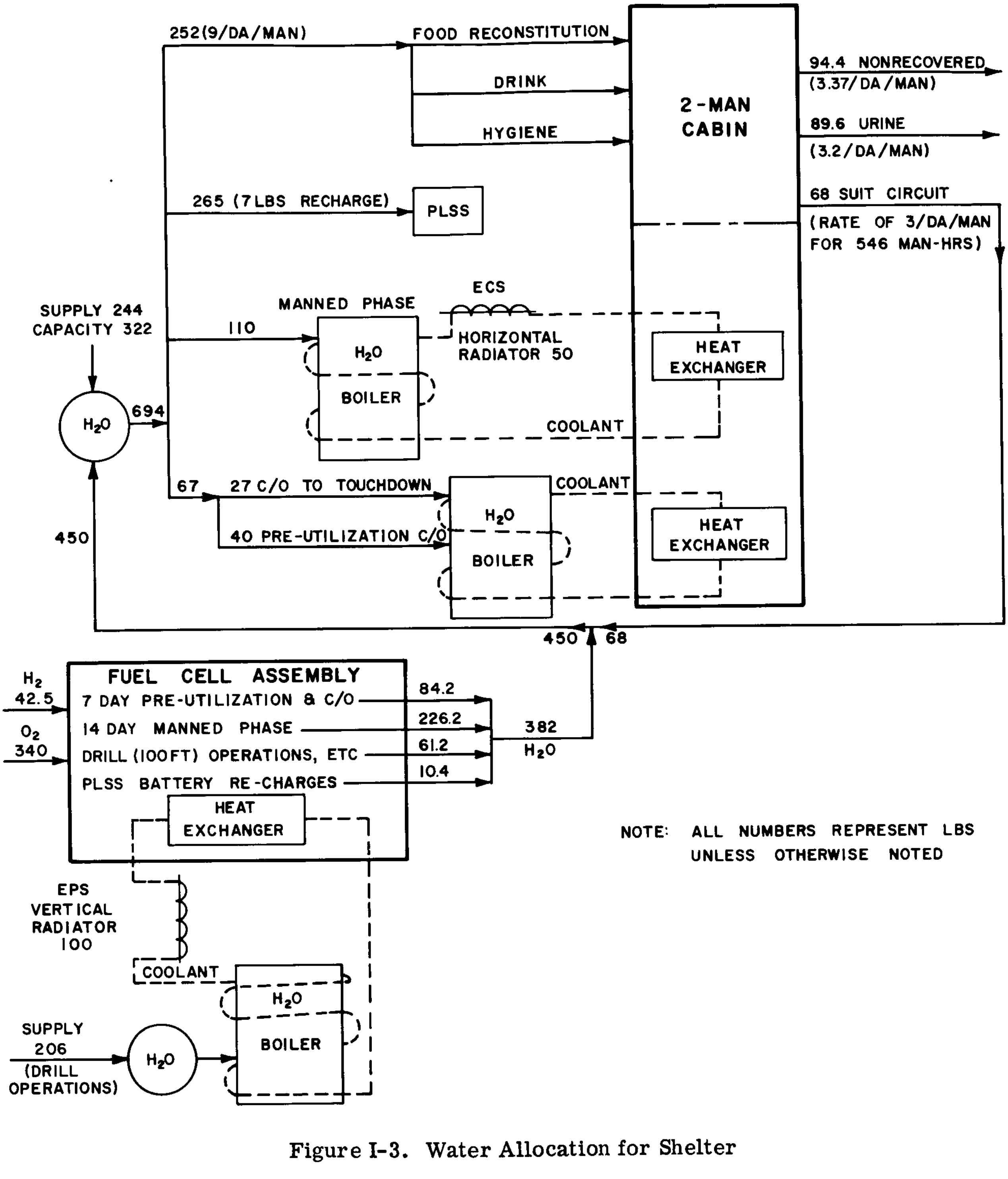
252(9/DA/MAN)
FOOD RECONSTITUTION
DRINK
HYGIENE
2-MAN CABIN
94.4 NONRECOVERED (3.37/DA/MAN)
89.6 URINE (3.2/DA/MAN)
68 SUIT CIRCUIT (RATE OF 3/DA/MAN FOR 546 MAN-HRS)
265 (7LBS RECHARGE)
PLSS
ECS
MANNED PHASE
SUPPLY 244
CAPACITY 322
110
H_2O
BOILER
HORIZONTAL RADIATOR 50
HEAT EXCHANGER
COOLANT
694
H_2O
67
27 C/O TO TOUCHDOWN
40 PRE-UTILIZATION C/O
COOLANT
H_2O
BOILER
HEAT EXCHANGER
450
450
68
H_2 42.5
O_2 340
FUEL CELL ASSEMBLY
7 DAY PRE-UTILIZATION & C/O
14 DAY MANNED PHASE
DRILL (100FT) OPERATIONS, ETC
PLSS BATTERY RE-CHARGES
84.2
226.2
61.2
10.4
382 H_2O
HEAT EXCHANGER
EPS VERTICAL RADIATOR 100
COOLANT
H_2O
BOILER
SUPPLY 206 (DRILL OPERATIONS)
H_2O
NOTE: ALL NUMBERS REPRESENT LBS UNLESS OTHERWISE NOTED

Figure I-3. Water Allocation for Shelter

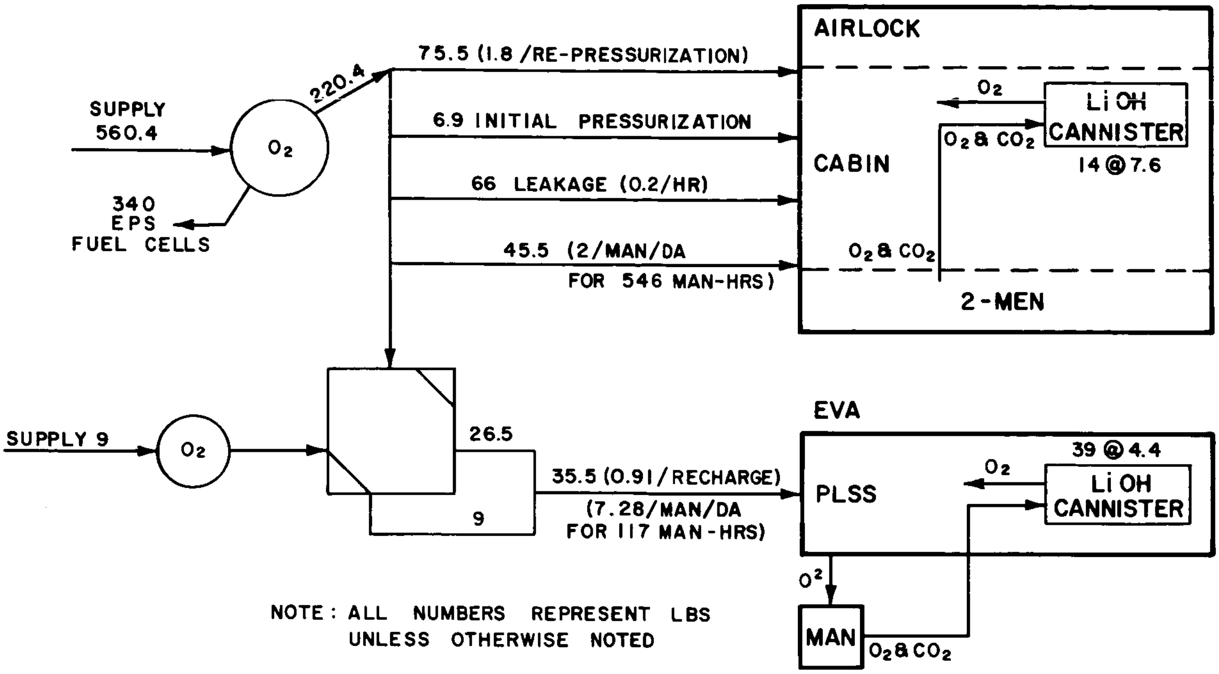
SUPPLY 560.4
O₂
340 EPS FUEL CELLS
220.4
75.5 (1.8 /RE-PRESSURIZATION)
6.9 INITIAL PRESSURIZATION
66 LEAKAGE (0.2/HR)
45.5 (2/MAN/DA FOR 546 MAN-HRS)
AIRLOCK
CABIN
O₂
O₂ & CO₂
LiOH CANNISTER
14 @ 7.6
O₂ & CO₂
2-MEN
SUPPLY 9
O₂
26.5
9
35.5 (0.91/RECHARGE)
(7.28/MAN/DA FOR 117 MAN-HRS)
EVA
PLSS
39 @ 4.4
O₂
LiOH CANNISTER
O²
MAN
O₂ & CO₂

NOTE: ALL NUMBERS REPRESENT LBS UNLESS OTHERWISE NOTED

Figure I-4. Oxygen Allocation for Shelter

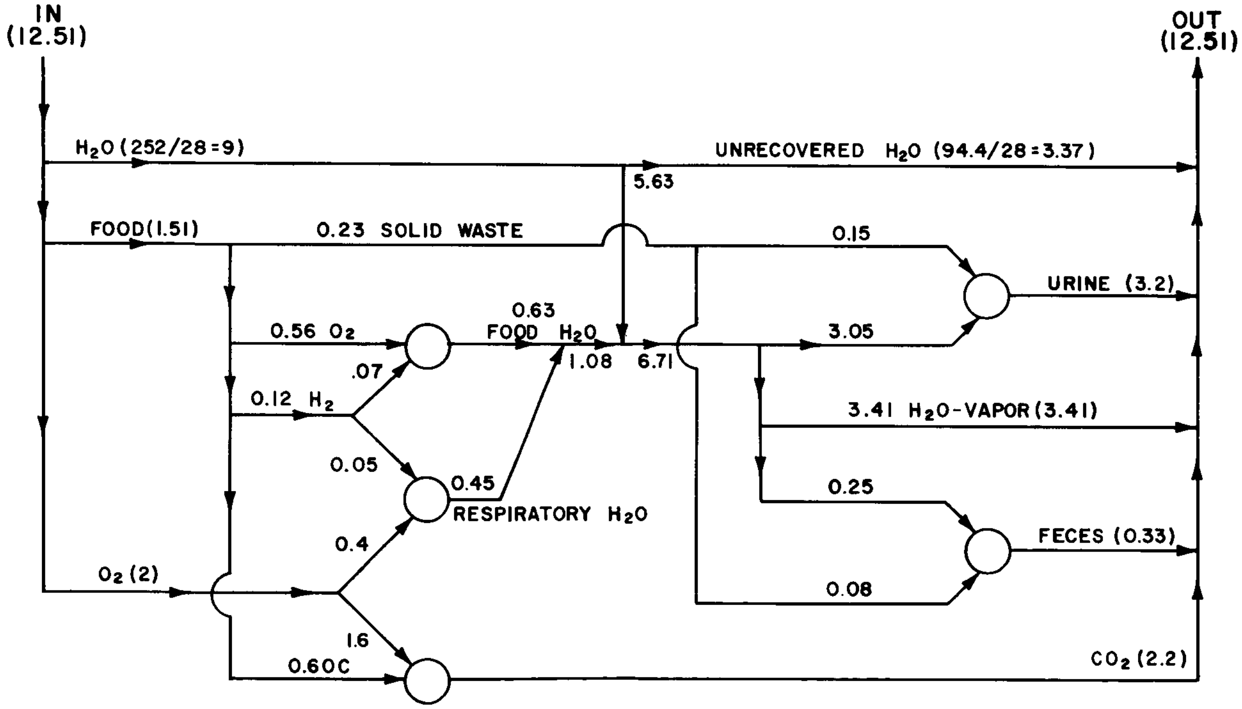
IN (12.51)
OUT (12.51)
H₂O (252/28=9)
UNRECOVERED H₂O (94.4/28=3.37)
5.63
FOOD (1.51)
0.23 SOLID WASTE
0.15
URINE (3.2)
0.56 O₂
0.63 FOOD H₂O
1.08
6.71
3.05
.07
0.12 H₂
3.41 H₂O-VAPOR (3.41)
0.05
0.45
RESPIRATORY H₂O
0.25
FECES (0.33)
0.4
O₂ (2)
0.08
1.6
0.60C
CO₂ (2.2)

NOTE: ALL NUMBERS REPRESENT LBS/MAN/DAY UNLESS OTHERWISE NOTED

Figure I-5. Daily Mass and Water Balance for One Man

X68-84332

SECTION II. EFFECTS OF LUNAR STAY-TIME ON ACCESSIBILITY

by R. A. Steigerwalt

1. INTRODUCTION

For the Appolo Application Program (AAP), extended-stay lunar surface missions have been proposed for exploration, sample gathering, and experimentation to increase data on the Moon and Earth-Moon system. Two representative stay-times of 5 days and 12 days are considered. The Apollo type mission requires a lunar orbit rendezvous (LOR), the effect of which is shown by Figures II-1 and -2. The Lunar Module (LM) must descend from the lunar parking orbit (LPO), remain on the lunar surface for some interval of time, and finally ascend and rendezvous with the CSM in the parking orbit. With reference to Figure II-1, the inclination i of the parking orbit is defined as

$$i = \varphi + \delta$$

where

φ is the latitude of the desired landing site.

δ is the minimum (in absolute value) angle required for a given stay-time, assuming inplane descent and ascent at points A and B, respectively.

In this section, i is positive for a retrograde orbit that allows sites in northern latitudes on the sub-Earth face of the Moon and negative for one that allows sites in southern latitudes on the sub-Earth face of the Moon. Similarly, δ is positive for sites in northern latitudes and negative for those in southern latitudes. The descent is made to point A, and after the moon has rotated the site to point B relative to the fixed LOR, the ascent and rendezvous of the LM with the CSM can be made. Because of possible hazards, such as solar flares and life-support equipment malfunction, the additional constraint of continuous abort to the CSM from the lunar surface is imposed. Therefore the maximum required plane change angle, $|\delta|$, must be within the capability of the CSM or the LM ascent engine. Since the capability for abort plane change must be provided, stay-time at a given site can be increased by allowing the moon to rotate further to point C before ascent is made. That is, with a plane change capability $|\delta|$, ascent and LOR can be achieved anywhere in the site

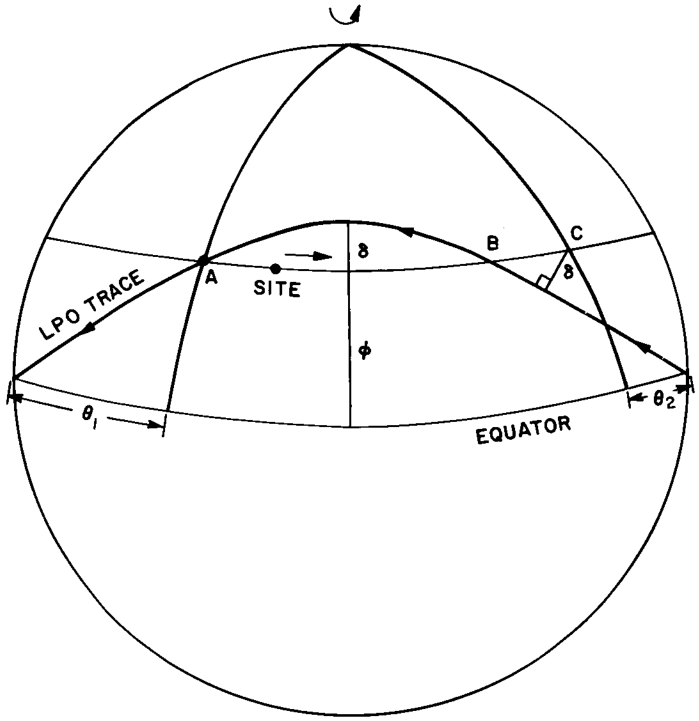
LPO TRACE
A
SITE
δ
B
C
δ
φ
θ₁
θ₂
EQUATOR

Figure II-1.
LPO Geometry Looking
Perpendicular to Line of Nodes

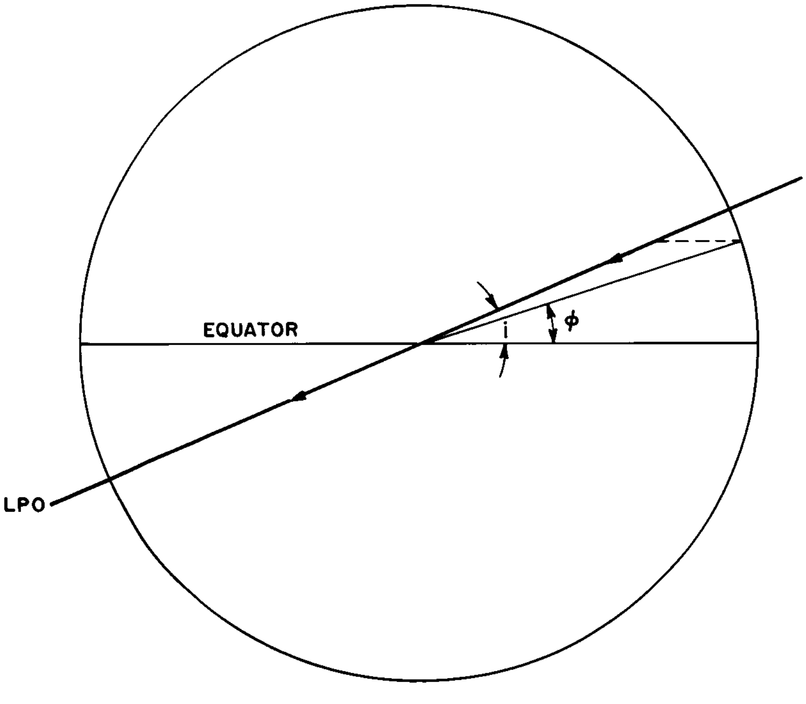
EQUATOR
i
φ
LPO

Figure II-2.
LPO Geometry Looking
Parallel to Line of Nodes

rotation between A and C. The geometrical relations used in this study are given in Reference 1.*

With parameters defined in Figure II-1, the stay-time at a latitude φ for a plane change δ on ascent is

$$\tau = \frac{180 - \theta_1 - \theta_2}{\omega}$$

where ω is the moon's sidereal rate of rotation (13.2 degrees/day).

A descent plane change is not considered since any additional capability of the LM is reserved for payload. Also, to maximize return payload by the LM, the plane change required for ascent is accomplished by the CSM.

Figure II-3 shows the $|\delta|$ required for various stay-times as a function of latitude of the desired landing site. Figure II-4 shows the plane change ΔV requirements as a function of latitude for various stay-times. Determining the accessible regions of the lunar surface then involves finding the loci of boundary points such that $\Delta V_1 + \Delta V_2 + \Delta V_3$ is equal to the ΔV capability of the Service Propulsion System (SPS), where:

ΔV_1 is the velocity required for translunar midcourse corrections and deboost into LPO.

ΔV_2 is the velocity required for CSM plane change for LOR and for providing an emergency LM rescue.

ΔV_3 is the velocity required for transearth injection (maximum required during the stay) and transearth midcourse corrections.

Each of the two midcourse corrections (translunar and transearth) is allowed 150 fps; and 600 fps is allowed for LM rescue from an intermediate orbit by the CSM. While the plane change velocity requirement is completely specified by stay-time and site latitude, a wide variation exists in both the ΔV_1 and ΔV_3 requirements. This is due to the large range of translunar and transearth trajectories available and the Earth-Moon-LPO geometrical variations with date.

Figure II-5 shows the periselene velocity as a function of flight time for typical translunar trajectories in the Earth-Moon orbital plane. Trajectories with long flight times are desirable in order to lower deboost velocity requirements. It is not possible, however, to obtain free-return trajectories with the long flight times. A reasonable substitute for the free-return constraint is the requirement that the LM descent engine be capable of supplying abort velocity in the event of SM failure to deboost.

---

*The references are listed at the end of the section.

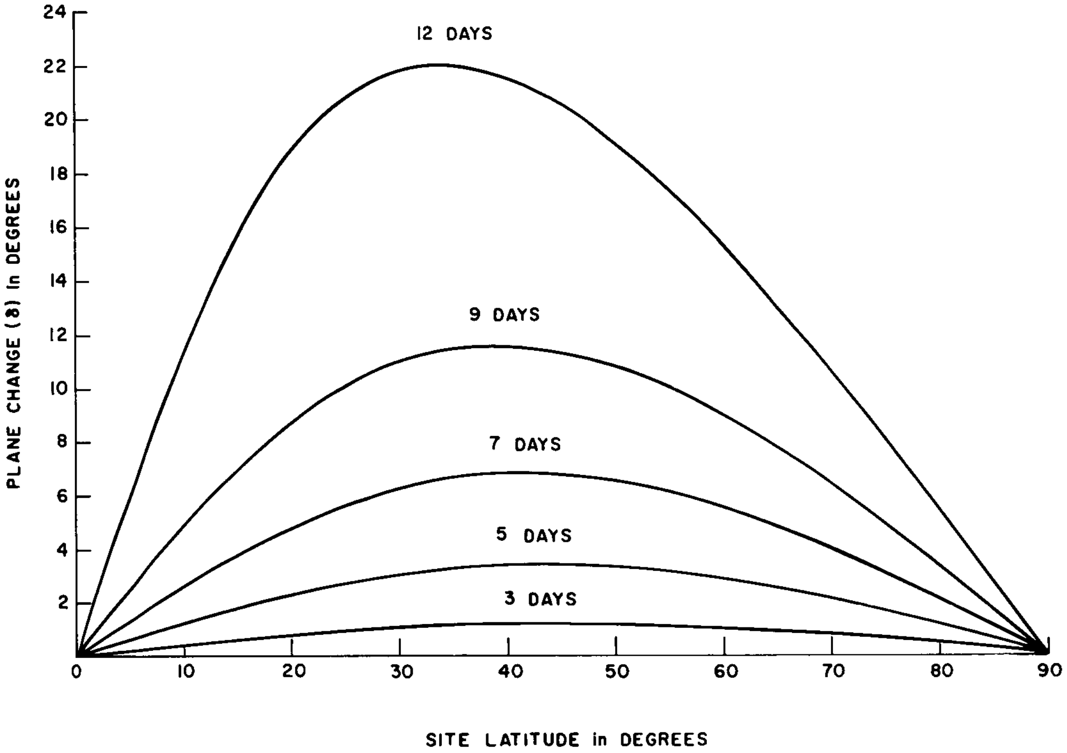

Figure II-3. Plane Change Angle versus Site Latitude for Various Stay-Times

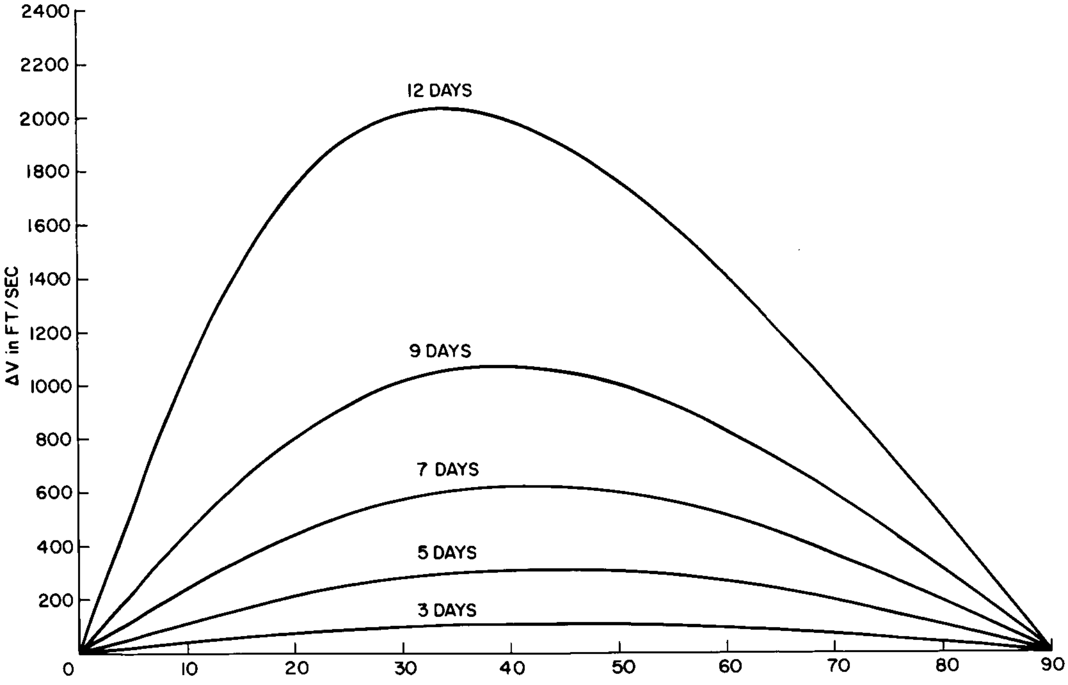

Figure II-4. Plane Change Velocity versus Site Latitude for Various Stay-Times

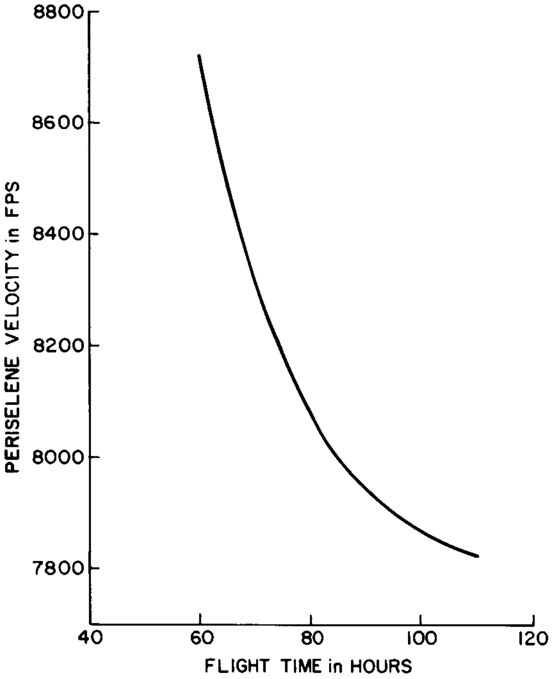

Figure II-5. Periselene Velocity versus Flight Time for Typical Translunar Trajectories

The following conditions were imposed for this study:

1. The trajectories are generated by the patched conic technique.
2. Double impulse is used for deboost into LPO and transearth injection.
3. A LM to CSM abort opportunity during each CSM orbit and CSM abort to earth each day (continuous abort) is provided.
4. The maximum orbital waiting time before descent to the surface is 3 days.
5. The maximum transearth flight time is 5 days.

The following CSM-LM characteristics are assumed:

SM Thrust	20,000 lbs
SM Weight Rate	63.9 lbs/sec (I_{sp}=313)
SM Fuel Weight	40,500 lbs
CSM Dry Weight + Crew + Unused Fuel	23,700 lbs
LM Weight	32,000 lbs
Adapter Weight	3,800 lbs
TL Injection Weight	100,000 lbs
Useful Injected Weight	96,200 lbs
Weight Loss at LM Descent (LM + 2 crew)	32,500 lbs
Weight Gain at TE Injection (300-lb payload + 2 crew)	800 lbs

Since the configuration cannot provide complete coverage of the lunar surface with the continuous abort constraint, the following investigation discussed here determines the bounds of accessibility. First, the perturbations on the LPO are examined.

2. PERTURBATION EFFECTS ON LPO FOR EXTENDED STAY-TIMES

The perturbations in order of increasing effect are caused by the Sun, the Earth, and the Moon's asphericity. For the extended stay, it is necessary to determine:

1. If these effects are significant.
2. If these effects can be advantageously utilized.

2.1 Sun Effects

The ratio of the gravitational attraction of the Sun on the satellite to the gravitational attraction of the Earth on the satellite can be approximated by

$$\frac{M_{\odot}}{M_{\oplus}}\left(\frac{r_{\oplus}}{r_{\odot\oplus}}\right)^3 \approx 0.00565$$

where $M_{\odot}$ is the Sun's mass, $M_{\oplus}$ is the Earth's mass, $r_{\oplus}$ is the Earth-Moon distance, and $r_{\odot\oplus}$ is the Earth-Sun distance. Thus, the effect of the Sun on the satellite's orbit is less than 0.6 percent of the Earth's effect.

2.2 Earth Effects

From the approximation of the Earth's effect on a lunar satellite by a potential function in selenographic coordinates (Reference 2), the ratio of the effect of the Moon's oblateness to the Earth potential yields the results shown in Table II-1.

Table II-1

Relative Effects of Earth Perturbation

Altitude (Lunar Radii)	J_{20}/Earth Perturbation	J_{22}/Earth Perturbation
0	84.7	15.0
1	10.6	1.9
2	3.1	0.6
3	1.3	0.2
4	0.7	0.1

The Earth's perturbation and the lunar J_{22} term are equal at a satellite altitude of 1460 nmi. An altitude of 3290 nmi is required for unity ratio of the J_{20} term and Earth perturbation. For close lunar orbits the effects can be neglected and since the effect of the Sun, as shown above, is less than that of Earth the Sun's perturbation can also be neglected.

2.3 Lunar Asphericity Effects

With retention of only the most significant terms, the lunar gravitational potential is represented by the following function

$$U = \frac{\mu_m}{r}\left[\frac{J_{20}}{3}\left(\frac{r_m}{r}\right)^2 (1-3\sin^2\Phi) + J_{22}\left(\frac{r_m}{r}\right)^2 \cos^2\Phi \cos 2\theta\right]$$

where

μ_m = gravitation constant times the Moon's mass.
r_m = the Moon's radius.
r = the satellite radius.
Φ = selenographic latitude.
θ = selenographic longitude.

The most significant effect for a retrograde orbit is a secular eastward change of the line of nodes caused by the J_{20} term. The magnitude decreases with inclination according to the equation of Reference 3.

$$\frac{d\Omega}{dt} = - \left[\frac{3J_{20} \cos i}{2\left(\frac{a}{r_0}\right)^2 \left(1-e^2\right)^2} \right] \left(\frac{\mu_m}{a^3} \right)^{1/2}$$

For an 80-nmi circular parking orbit the rate of change varies from -1.12 degree/ day for $i = 3$ degrees to 0 degree/day for $i = 90$ degrees. For a 12-day stay-time, this amounts to -13.4 degrees or an increase of 1 day of stay-time at $i = 3$ degrees. However, at 30° latitude ($i = 33$ degrees), the maximum stay-time is 5 days. At $i = 33$ degrees, $d\Omega/dt = 0.94$ degree to give an increase (0.94×5) of only 1/3 of a day. Thus, percentage increase for cases where an advantageous effect could be utilized is so small that this effect is neglected in the remaining portion of this investigation.

Lunar asphericity also causes periodic variations in other orbital elements of the LPO. The effect of these variations is much smaller than the effect caused by rotation of the line of nodes as discussed above.

3. THE LUNAR PARKING ORBIT PHASE OF OPERATIONS

Since the LPO phase can be treated analytically, it is treated first and then the TL and TE portions are tied in to determine the accessible longitudes for a given site latitude. For a given stay-time and for continuous abort, the site latitude (φ) determines the plane change angle (δ). Since $i = \varphi + \delta$, the inclination of the LPO is known. A solution for the inclination of the LPO after plane change and LM rendezvous is necessary.

The angle θ_1 between the LPO ascending node for the southern latitudes (descending for northern) and site longitude is also completely determined by site latitude and stay time. For a given site, the deboost maneuver must result in an LPO with specified inclination and ascending node at time of descent such that for sites in southern latitudes

$$\Omega_A = \lambda - \theta_1$$

and for sites in northern latitudes

$$\Omega_A = \lambda - \theta_1 + 180$$

where

Ω_A = the ascending node, and
λ = the site longitude.

An inplane LM descent is assumed. Figure II-6 shows θ_1 as a function of stay-time. Figure II-7 shows LPO inclination on arrival as a function of site latitude for various stay-times.

At the completion of the lunar stay, the CSM will perform the plane change necessary to allow an inplane LM ascent and rendezvous from point C of Figure II-1. This plane change will cause a new LPO inclination and in addition shift the line of nodes eastward. The inclination increases as illustrated in Figure II-8. The change in ascending node, Figure II-9, can generally be neglected for the long stay-times because the continuous abort to Earth constraint will cause the ascending node at departure to fall near a minimum TE velocity. It can be neglected as well for short stays because it is small.

After the requirements of the LPO have been determined (i.e., Arrival inclination and ascending node, plane change velocity, and departure inclination), the TL and TE segments to maximize the accessible area can be selected, beginning with the transearth requirements.

Maximizing accessible area for a given stay-time means minimizing the maximum transearth injection velocity for a given site over the time interval from deboost into the LPO to transearth injection and then determining which sites are within the SM capability. Because of large variations in trajectories, and hence in ΔV, it is impossible to specify completely the accessible regions for all combinations of stay times and dates. It is desirable, however, to determine trends and methods of predicting limits in accessibility and launch dates for sites within these limits.

To begin, consider Figure II-10 which gives the transearth injection velocity requirements as a function of ascending node for an 80-nmi LPO of inclination 45 degrees on August 14, 1970. The upper curve is for single-impulse injection and the lower curve for double impulse. The transearth flight time is 116 hours to a site near Hawaii. The velocity was calculated for intervals of ascending node of 10 degrees (this caused the discontinuities in the curves). It is evident that to gain coverage off the lunar equator a double-impulse transearth injection maneuver must be employed. Assume the velocity requirements of Figure II-10 are valid for all dates. Then for a 12-day stay in which the ascending node shifts by 160 degrees, 4200 fps is the minimum transearth injection velocity that must be provided to insure a continuous abort capability. If stay-time is reduced, the minimum transearth velocity requirement is reduced. For a TE velocity provision of 3000 fps, the stay-time is reduced to 2 days. In each of the above extreme cases, the site longitudes are fixed by the TE velocity provided.

The characteristics of Figure II-10 are, however, representative of only one day during the month. Therefore the stay-time and velocity relationships worked out above on the basis that the curve of Figure II-10 holds for all dates is illustrative only. Detailed mission planning will require full consideration of a sequence of daily requirements.

Maximizing accessible area requires effective utilization of the shifts in velocity minimums and maximums throughout the lunar rotation. For example, consider a 12-day stay at a site at 0° longitude. From Figure II-6 θ_1 is 27 degrees and, therefore, the ascending node on arrival must be -27 (or 333) degrees. If an arrival date of April 21, 1971, is chosen, the maximum latitude can be attained. Figure II-11 indicates a requirement of about 3200 fps for an LPO with 25-degree inclination for transearth injection on April 21. Four days later on April 25, 1971, the velocity required is about 3000 fps (Figure II-12). On April 29, 1971 (Figure II-13), the velocity is 3400 fps. At the end of the stay on May 3, 1971, the required velocity is about 3200 fps (Figure II-14). Thus, by utilization of the shift in velocity requirements with time, a maximum of 3400 fps TE velocity would be required at any time during the 12-day stay.

From the foregoing discussion, it is evident from trajectory considerations that the timing of lunar missions is extremely important in maximizing the accessible lunar surface area. Figures II-15 and -16 cover the extremes of transearth injection velocities for one month. Figure II-15 shows the characteristic when the angle ($\Delta\Omega$) between velocity minimums (measured across the 180° line) is at its maximum and Figure II-16 when the angle is at its minimum. Figure II-17 gives the variation in $\Delta\Omega$ versus day of the year for an LPO inclination of 45 degrees and for the period July 23, 1970, to October 17, 1970. $\Delta\Omega$ is cyclic with the sidereal period of 27.3 days. The minimum for $\Delta\Omega$ corresponds to a minimum of the maximums of the velocity near the ascending node longitude of 180° and the maximum for $\Delta\Omega$ corresponds to a minimum of the maximums of velocity near ascending node longitude of 0° (Figures II-15 through -16). It was noted from such curves that the maximum to minimum excursion of $\Delta\Omega$ is a measure of the range of variation of the local maximums of velocities.

Figure II-18 shows the plot of $\Delta\Omega$ as a function of the year for 1978 for an LPO inclination of 45 degrees. As before, the curve has a monthly period; however the maximum to minimum excursion is substantially less due to the smaller range of lunar declination over the month. This indicates that the local maximums will not vary over as wide a range in 1978 (the extremes are shown in Figures II-19 and -20) as in 1970. Hence, some sites accessible in 1970 will not be accessible in 1978. Since 1978 is a year in which variation in declination of the moon through the month is a minimum, this suggests that maximum accessibility will occur during

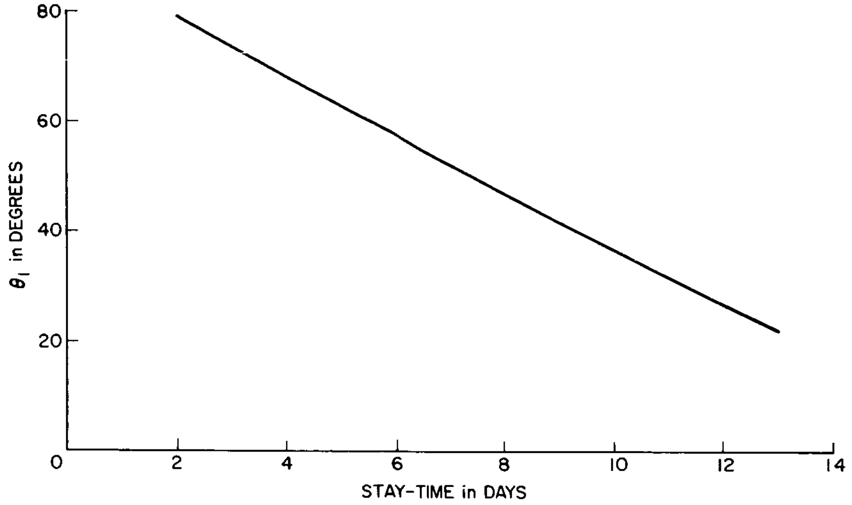

Figure II-6. Angle between Site Longitude and LPO Ascending Node versus Stay-Time

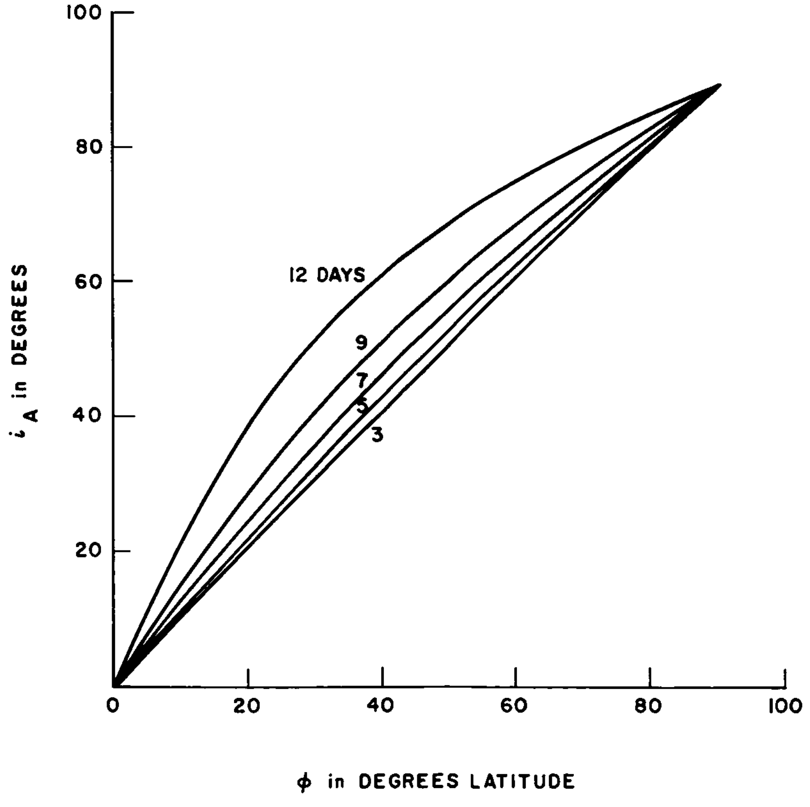

Figure II-7. Arrival Inclination versus Site Latitude for Various Stay-Times

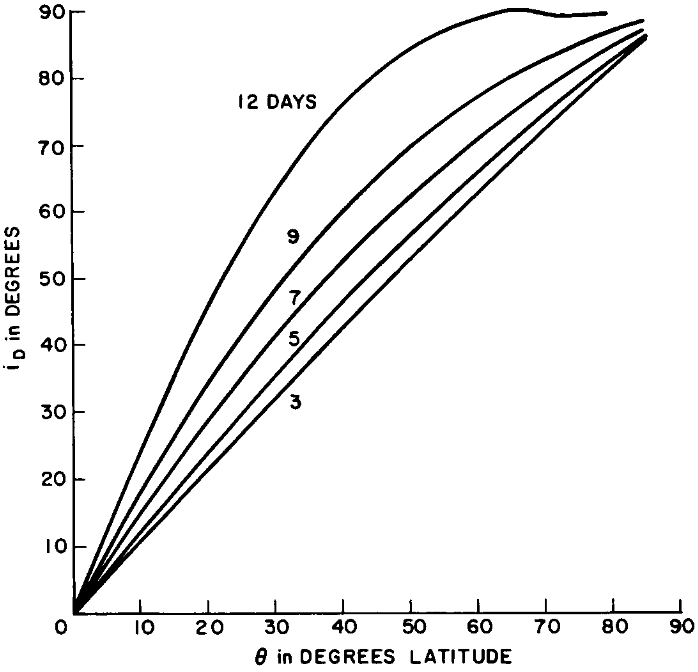

Figure II-8. Departure Inclination versus Site Latitude for Various Stay-Times

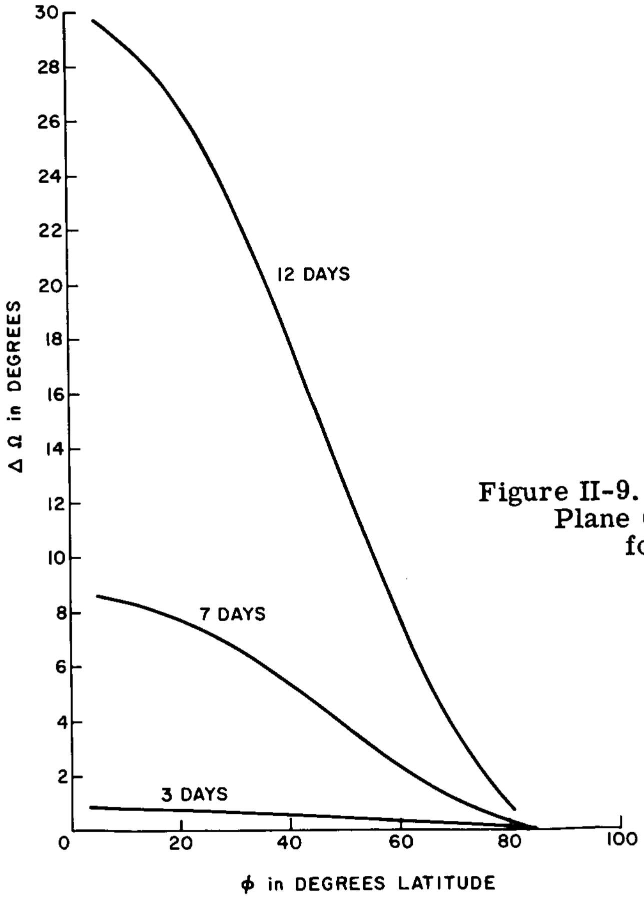

Figure II-9. Change in Ascending Node After Plane Change versus Site Latitude for Various Stay-Times

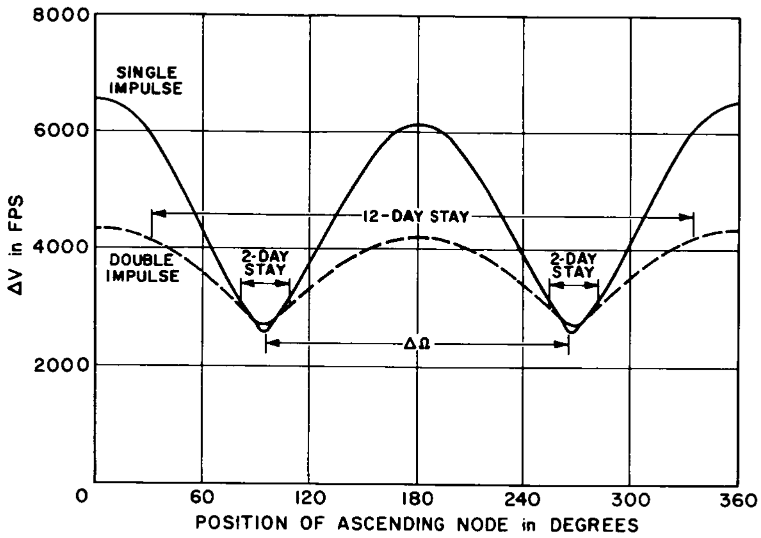

Figure II-10. Required TE Injection Velocity on August 14, 1970 for LPO with 45-Degree Inclination

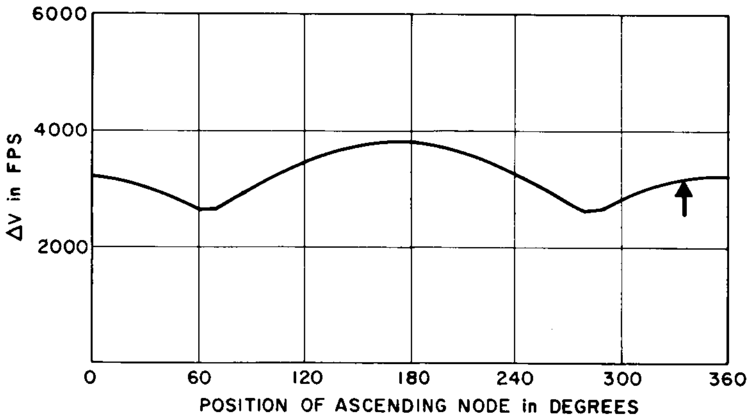

Figure II-11. Required TE Injection Velocity on April 21, 1971 for LPO with 25-Degree Inclination

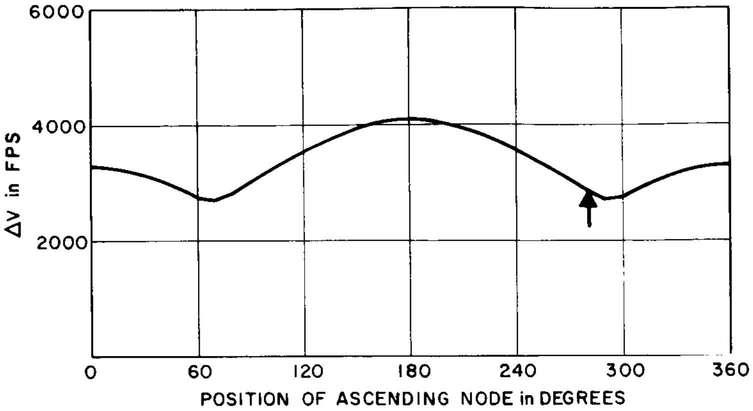

Figure II-12. Required TE Injection Velocity on April 25, 1971 for LPO with 25-Degree Inclination

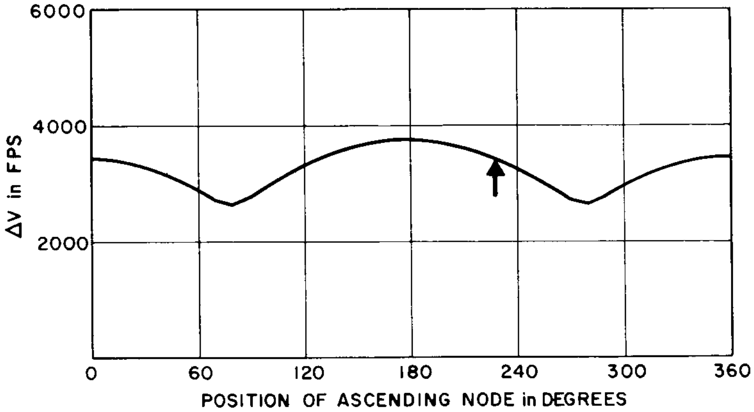

Figure II-13. Required TE Injection Velocity on April 29, 1971 for LPO with 25-Degree Inclination

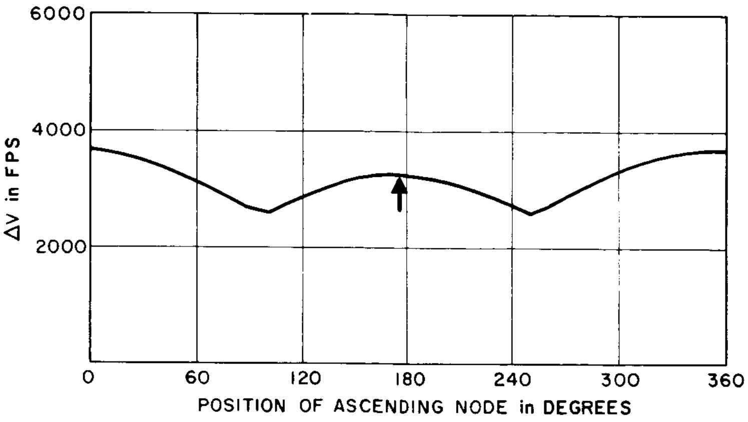

Figure II-14. Required TE Injection Velocity on May 3, 1971 for LPO with 25-Degree Inclination

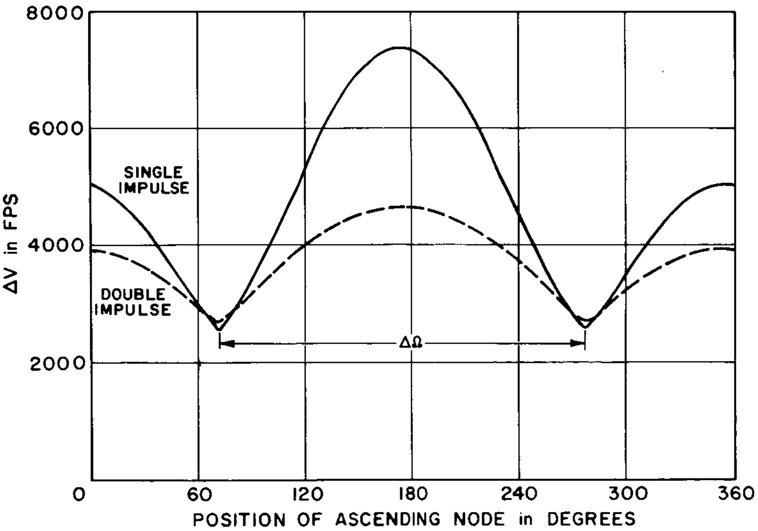

Figure II-15. Required TE Injection Velocity on August 21, 1970 for LPO with 45-Degree Inclination

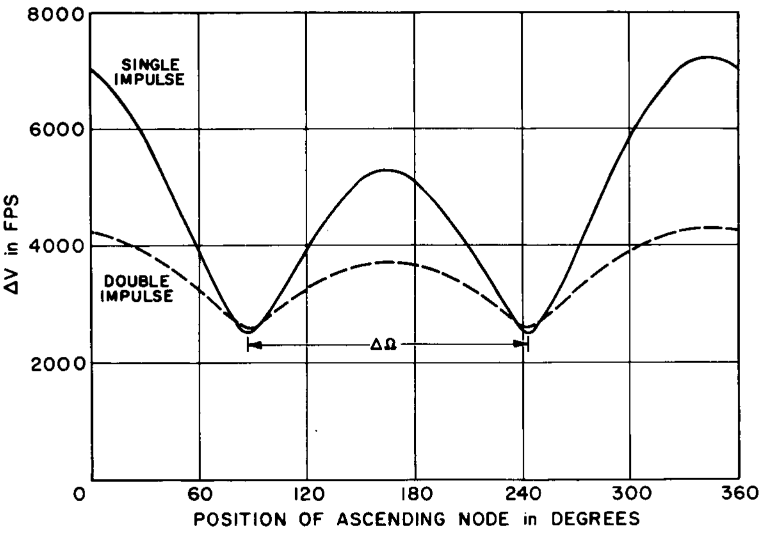

Figure II-16. Required TE Injection Velocity on September 2, 1970 for LPO with 45-Degree Inclination

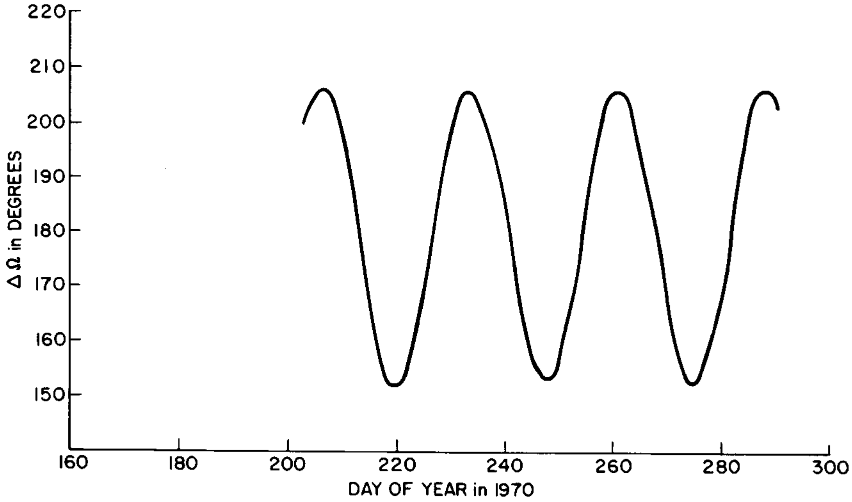

Figure II-17. Δ Ω for 1970

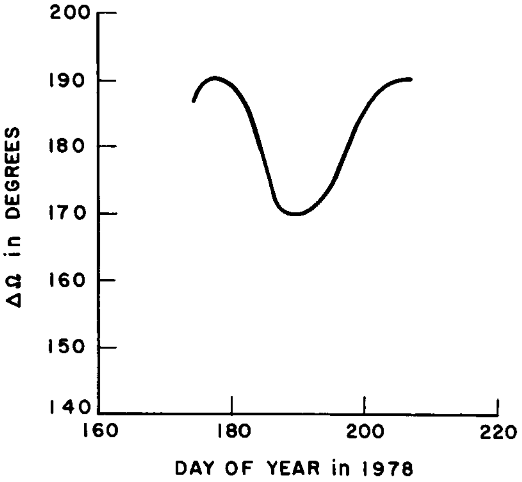

Figure II-18. Δ Ω for 1978

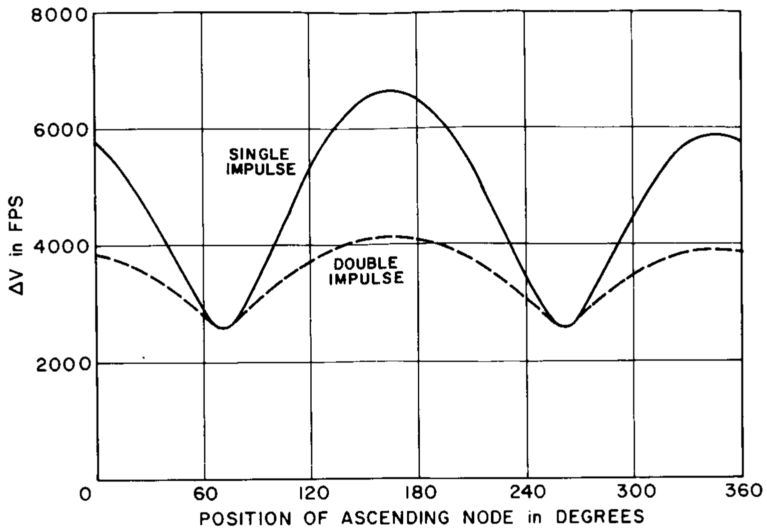

Figure II-19. Required TE Injection Velocity on July 5, 1978 for LPO with 45-Degree Inclination

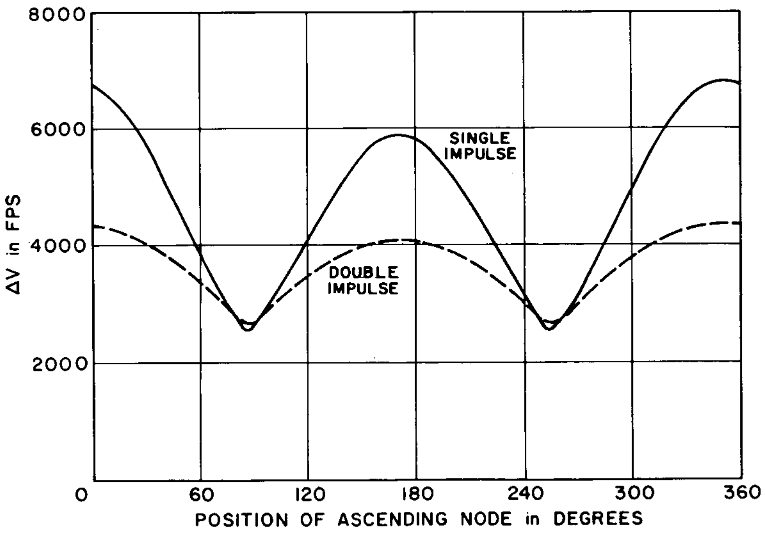

Figure II-20. Required TE Injection Velocity on July 19, 1978 for LPO with 45-Degree Inclination

the years of greatest variation in declination. Therefore to obtain an idea of maximum accessibility, and in consideration of the time schedule for the AAP, the year 1971 was selected for further study.

Stay-times of 5 days and 12 days are considered. For a given latitude and stay time, the arrival and departure inclinations and plane change velocity are determined. ΔV_2 can then be specified. A search is then conducted to determine the ascending nodes (and hence site longitudes) within the SPS capability. The transearth velocity requirement will be the maximum velocity occurring over a range of ascending nodes defined by

$$\Omega_A \text{ to } \Omega_A - 13.2\ (\tau+T_W)$$

where

Ω_A = the ascending node on arrival.

τ = the surface stay-time in days.

T_W = the orbital waiting time (in days) on arrival.

This maximum velocity plus an allowance of 150 fps for TE midcourse corrections will be denoted by ΔV_3.

4. DETERMINATION OF ALLOWABLE DEBOOST VELOCITIES

From the transearth velocity requirements and the CSM characteristics, the weight prior to transearth injection W_3 can be calculated from

$$W_3 = W_f e^{\left(\frac{\Delta V_3}{32.174 I_{sp}}\right)}$$

where

W_f = the known final weight of the CSM including crew, return payload, and unusable propellant.

ΔV_3 = the required transearth injection velocity plus a midcourse allowance.

I_{sp} = the specific impulse of the SM engine.

When the weight prior to transearth injection has been determined, the weight W_2 can be determined from

$$W_2 = \left(W_3 - \Delta W_2\right) e^{\left(\frac{\Delta V_2}{32.174 I_{sp}}\right)}$$

where

ΔW_2 = the weight of two astronauts and return payload, and

ΔV_2 = the sum of velocities for plane change and LM rescue.

Velocity ΔV_1 allowed for deboost from the translunar trajectory can then be computed from

$$\Delta V_1 = 32.174 I_{sp} \ln\left(\frac{W_1}{W_2+\Delta W_1}\right) - V_m$$

where

W_1 = the translunar injected weight,
ΔW_1= the weight of the LM and crew, and
ΔV_m = a midcourse correction allowance.

5. DETERMINATION OF POSSIBLE ASCENDING NODES ON ARRIVAL

When the maximum allowable deboost velocity has been found, the allowable ascending nodes on arrival can be found from curves of deboost velocity versus ascending node. These curves also vary with date and display the same characteristics as the transearth injection velocity curves. Figure II-21 shows the deboost velocity characteristic for a translunar flight time of 110 hours and LPO inclination of 45 degrees with launch on August 2, 1970. Again the upper curve represents a single-impulse deboost, and the lower curve a double-impulse deboost. A wider variation in ascending node than indicated on Figure II-21 can be obtained for a given deboost velocity by varying translunar flight time. Figures II-22 and -23 for flight times of 95 and 80 hours, respectively, for an LPO inclination of 45 degrees and launch on August 2, 1970, illustrate this. A comparison of Figures II-21, -22, and -23 show that for a 110-hour flight time the ranges of ascending nodes available for a maximum allotment of 3000 fps for deboost are 70 to 110 degrees and 247 to 285 degrees. With flight times down to 80 hours, these ranges for the same velocity allotment increased to 70 to 125 degrees and 247 to 303 degrees.

6. ACCESSIBILITY FOR 1971 FROM TRAJECTORY CONSIDERATIONS

An investigation of accessibility was conducted for the month of April 1971. Since, for sites not accessible every day during the month, accessibility is repeated at 27.3-day intervals, determination of monthly accessibility is sufficient to cover the entire year. Figure II-24, transearth $\Delta\Omega$ versus day of the year for 1971, indicates that for long stay-times maximum latitude sites are obtained when the ascending node falls near 180 degrees on April 11 and 0 degrees on April 24.

All TE trajectories for this study are constrained to a particular landing site near Hawaii. This simplifies the recovery procedure by utilization of the same return site for normal as well as abort conditions. The trajectories are constrained to a maximum flight time of 120 hours. These constraints determine the transearth flight time which, during April 1971 , varies as shown in Figure II-25. For the

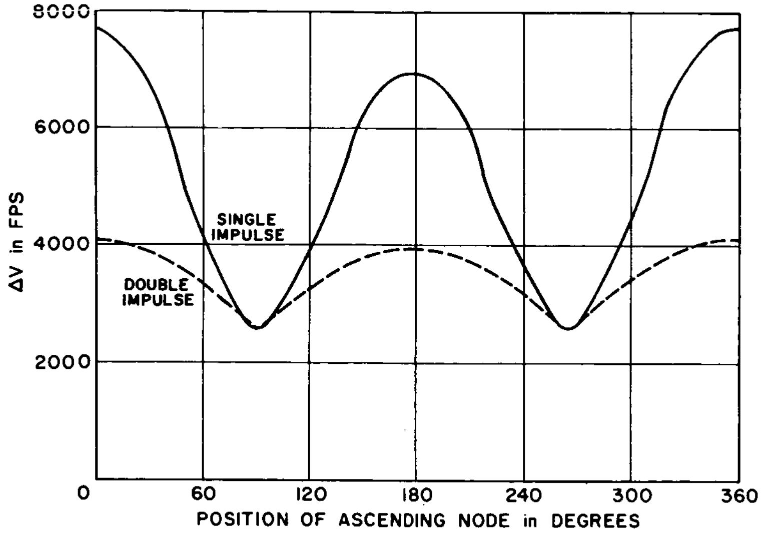

Figure II-21. Required TE Deboost Velocity on August 2, 1970 for LPO with 45-Degree Inclination, 110-Hour Flight Time

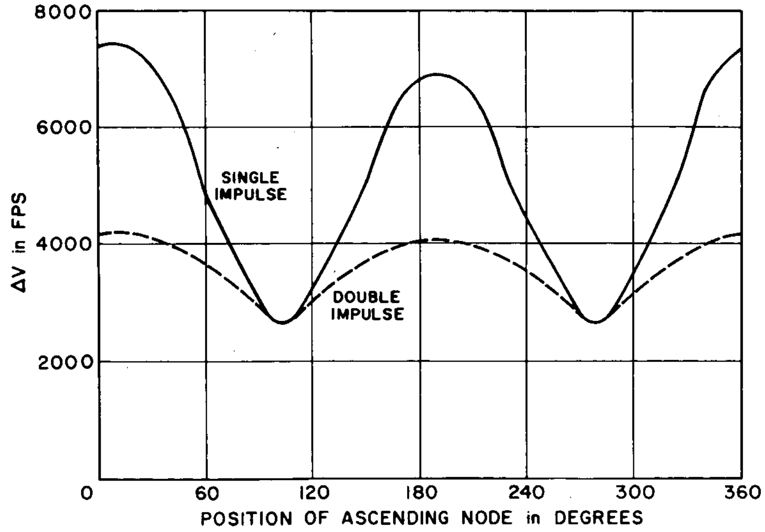

Figure II-22. Required TE Deboost Velocity on August 2, 1970 for LPO with 45-Degree Inclination, 95-Hour Flight Time

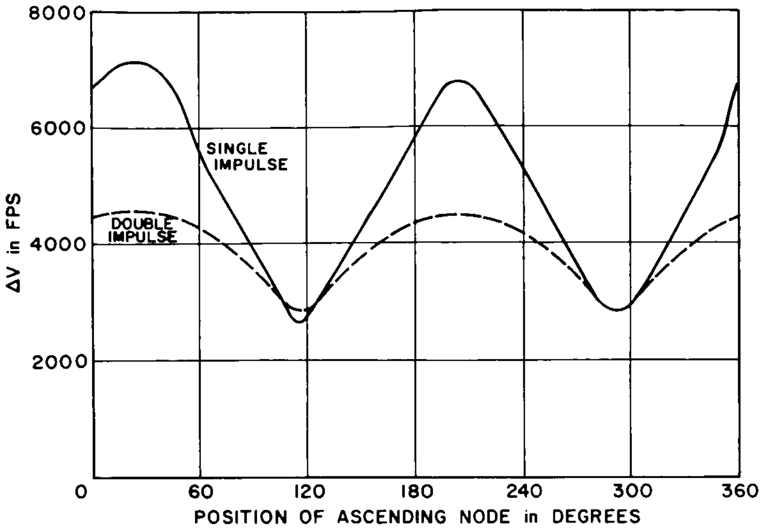

Figure II-23. Required TE Deboost Velocity on August 2, 1970 for LPO with 45-Degree Inclination, 80-Hour Flight Time

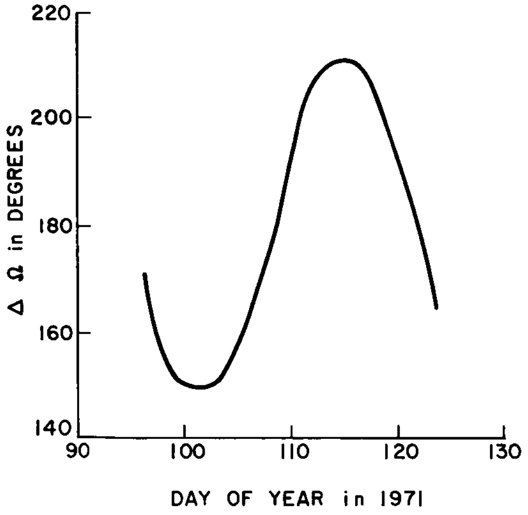

Figure II-24. Angular Difference Between Minimums of TE Injection Velocity

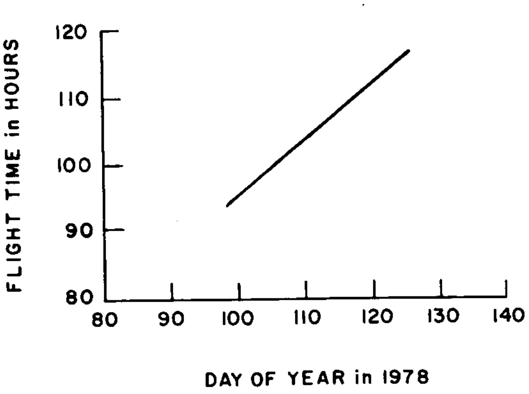

Figure II-25. TE Flight Time versus Day of Year for 1978

entire year, this will appear as a periodic sawtooth. Since returns to a given site can occur at intervals of 24 hours, some variation in velocity versus ascending node characteristics can be obtained in this manner. However, flight times cannot be reduced much below 80 hours since the required velocities will increase rapidly for times below this value.

Figure II-26 is a map of the accessible area for the month of April 1971 for stay-times of 5 and 12 days. Although the actual mission schedule and vehicle weights are themselves not precisely defined, the map has a primary value because of the conclusions that can be derived from its shape. These are as follows:

1. The maximum northern and southern latitudes attainable are about 30°N and 30°S respectively for a stay of 5 days. For a 5-day stay, θ_1 is 63 degrees and since the location of ascending nodes for transearth and translunar velocities to achieve 30°S is at 295°E, the site longitude is fixed at 2°W for the 30°S latitude. For 30°N, the site longitude is 17°W. In general for the short stays, the maximum latitudes attainable will occur in a region about longitude 0 because of the large value of θ_1 associated with short stays.
2. For a 5-day stay, latitudes between 20°N and 20°S are accessible for all longitudes at some time during the month if up to 3 days orbital waiting time prior to descent is allowed. To achieve this area, the shift in velocities required during the month are utilized; therefore, mission timing is important in attaining a given date.
3. For a 12-day stay, the small value of θ_1 has shifted the maximum attainable latitude locations from the center of the moon to regions near the limb.
4. For a 12-day stay, latitudes within 5°N and 5°S are attainable for all longitudes at some time during the month.

7. OTHER CONSIDERATIONS

The foregoing discussion has considered only constraints imposed by the spacecraft configuration. Other constraints further affect the accessible area of Figure II-26.

Required lighting conditions on the lunar surface at LM descent in conjunction with the trajectory considerations can severely limit launch opportunities to particular sites. A lighting constraint for LM descent is a sun elevation angle between 7 and 20 degrees. For latitudes within ± 25° of the equator, this angle can be approximated by the central angle in the lunar equatorial plane measured from the dawn terminator to the site meridian of longitude. Since lighting is determined by the synodic month of period 29.5 days (12.2 degrees per day), the lighting constraint allows only 1 day per synodic month for descent to a given longitude within the latitude range of 25°N to 25°S. Site accessibility from trajectory constraints for those sites relying on favorable trajectories will occur at 1-year intervals.

Both Single-Vehicle Missions (SVM) and Dual-Vehicle Missions (DVM) have been proposed for lunar exploration. For a DVM to be successful, both vehicles must land at the same site within a specified time period (of duration, < 1 year), and the sites must be located within the region always accessible. If they are not located within this region, and if there is a delay in launching the second vehicle after the first has already landed, the next favorable launch period will not occur until a year later. For the SVM with a specified time for mission completion, the possibility of launch delay forces a selection of alternate sites for a given mission if the higher latitudes of Figure II-26 are to be attained.

A second major consideration, communications to earth, restricts site longitudes to the interval 45°W to 45°E. Figure II-27 shows the area always accessible during the month of April 1971 from trajectory considerations alone. Communications constraints further reduce this to those longitudes within 45°W and 45°E. Finally, since this area will remain essentially fixed throughout the year the lighting constraint will allow one launch per month to a particular site within this region.

CONCLUSIONS

The study has indicated the salient points in determining lunar surface accessibility for a given spacecraft configuration under the assumption of a continuous abort constraint from surface to CSM and CSM to Earth. In particular, it has shown that for long stays a significant departure from the equator is not possible but that for short stays latitudes of 30°N and 30°S can be attained near 0° longitude. To achieve the higher latitudes, departure from free-return trajectories must be allowed. A propulsion system redundancy can be used as a substitute for the free-return constraint. If SM fuel can be jettisoned, approximately 4500 fps can be obtained from the LM descent and RCS engines (using propellant from ascent stage tanks). If SM fuel is not jettisoned, only 2500 fps is available.

Abort precedures in the event of SM failure to perform the deboost maneuver must be considered. Since a double-impulse deboost was assumed with the first impulse applied near MSI entrance, corrective action could be taken at least by MSI exit if an early detection of this failure is made.

Trajectories with flight times as long as 110 hours may be required for a mission to a particular site. Since the minimum ΔV for abort at MSI exit for a 110-hour trajectory is 3400 fps, a SM fuel jettison system is required if trajectories with 110-hour flight times are used. If the fuel jettison capability is not

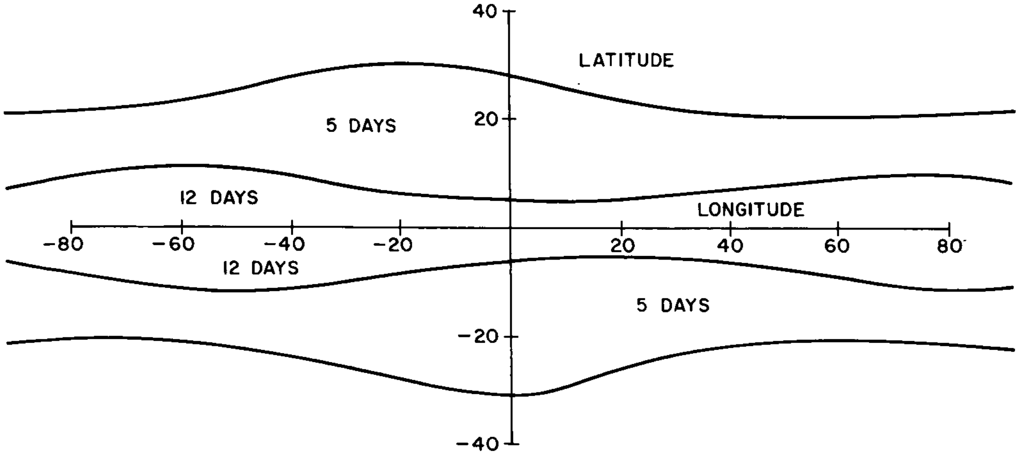

Figure II-26. Accessible Area for April 1971 with Consideration of Spacecraft Constraints

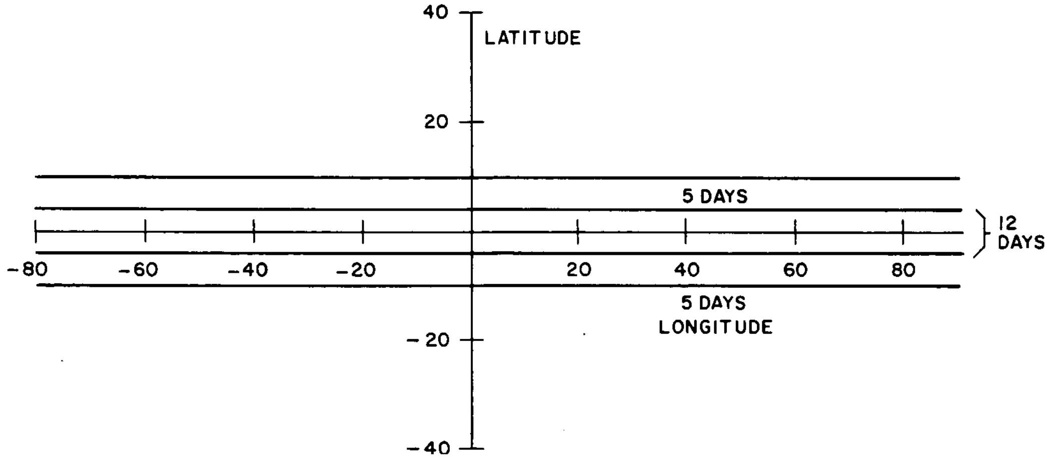

Figure II-27. Accessible Area for April 1971 with Consideration of All Constraints

provided, either accessible sites are severely limited or the abort requirement must be dropped.

Expected weights for a Taxi mission are given in paragraph 1. The total injected weight assuming a full SM fuel load for this mission equals the current estimated S-IVB stack limit. Since the accessibility of Figure II-26 is based on a maximum fuel load and since the most effective plan is the use of augmented LMs for short stays, then the stack limit must be increased by the amount of increase caused by augumentation to make development worthwhile.

REFERENCES

1. Enderson, Jr., L. W. A Study of Lunar Landing Sites and Associated Stay Times, NASA TN D-2795, May 1965.
2. Lunar Flight Handbook, Volume II, Parts 1, 2, and 3, NASA.
3. Blitzer, L. Perturbative Effects on Lunar Satellite Orbits, Space Technology Laboratories, Inc. 8408-6022-RV-000, July 19, 1963.
4. Bellcomm Apollo Simulation Program Operations and Maintenance Manuals.

X68-84333

SECTION III. TRANSLUNAR AND TRANSEARTH TRAJECTORY CONSIDERATIONS FOR THE AAP

by C. D. DeJong

1. INTRODUCTION

Mission planning for the Apollo Applications Program (AAP) requires a knowledge of the bounds on the performance that can be extracted from the Apollo system. An important measure of system performance is lunar surface accessibility, consistent with constraints on crew safety. This measure depends heavily on the characteristics of AAP Translunar/Transearth (TL/TE) trajectories.

Earth-Moon trajectories have been studied extensively for the Apollo mission.* However, AAP TL/TE trajectories are affected by two significant factors which are different from Apollo:

1. Accessibility — If possible, AAP shall have the capability to explore any site on the moon.
2. Stay-time — The stay on the surface may be as much as 2 weeks.

To meet these needs, the following trajectory and operational differences were investigated:

1. Free return — The translunar trajectory for the AAP mission may not be of the free-return class.
2. Surface stay-time — The return from the Moon may have to come anytime during the planned stay-time.
3. Double-impulse burns — The deboost into lunar orbit and transearth injection maneuvers may each consist of two separate burns for AAP.
4. Orbital waiting times — AAP mission plans may allow pre-descent and post-ascent orbital wating times.
5. Lunar orbit — The lunar parking orbit used for AAP may differ from that used for Apollo by not requiring some of the following Apollo constraints:
   (a) 80-nmi altitude
   (b) Circular orbits
   (c) Retrograde orbits

---

*References are listed at the end of the section.

2. SUMMARY

The characteristics of the possible trajectory differences between AAP and Apollo have been investigated. Associated trends and trade-offs have been generated by defining a reference mission and perturbing various mission parameters. A patched-conic model of the Earth-Moon system was used.

It is clearly desirable to relax the free-return constraint because of the increased mission flexibility and trajectory optimization that this allows. Variation in translunar trajectory inclination (measured at the Moon) will permit an in-plane deboost to a lunar orbit of any desired inclination, and raising the translunar flight time above the value required for free return can provide up to 3100 lbs more weight into lunar orbit.

The resulting abort velocity requirements increase significantly as the mission parameters move away from the values required for free return. Since the free-return trajectory itself is a safety back-up in the event of a Service Propulsion System (SPS) failure, an alternate back-up must be provided. The LM descent engine can provide this back-up. Its abort capabilities depend on certain hardware modifications, particularly a provision for jettisoning unused SPS fuel, which can raise the ΔV available for abort from 1800 fps to more than 3200 fps. The effect on accessibility of this alternate constraint, assuming the CSM hardware modifications, is to allow lunar orbits with inclinations up to approximately 60 degrees. For highly inclined orbits, fast flight times are necessary to satisfy the alternate constraint, while the more economical low-energy trajectories may be used only for low-inclination lunar orbits.

The long-duration surface stay-times considered for AAP are significant because of the resulting geometrical Earth-Moon-lunar orbit relationships. High-inclination parking orbits require prohibitively large plane changes at certain times in the mission.

Establishment of a desired lunar parking orbit (LPO) from a translunar trajectory involves trade-offs among time of flight, plane change, and orbital waiting times. The trade-offs are presented in terms of curves showing ΔV deboost (primarily a function of time of flight and plane change) against ascending node of the lunar orbit (primarily a function of the orbital waiting time). A double-impulse maneuver may be used to reduce the plane change required and also the orbital waiting time. It is shown to be most effective for large plane changes and long flight times.

The corresponding trade-offs for transearth injection are also presented.

A consequence of the long stay-times is that nominal LM ascent must occur near local sunset (after a 2-week stay-time); thus, the nominal Earth touchdown point will be either in darkness or shortly before darkness, rather than in daylight as planned for basic Apollo.

Small changes in the LPO altitude and eccentricity do not significantly affect TL/TE trajectories. Therefore, if they prove advantageous in orbital rendezvous studies (Sec II of this volume), they can be used.

It is possible that the use of direct orbits instead of retrograde orbits would allow more efficient use of some of the propulsion systems, but the resulting abort requirements are so large that direct orbits cannot be used.

3. GENERATION OF TRAJECTORIES

The trajectories used in this study were generated by a modified version of the Bellcomm Apollo Simulation Program (Reference 3).

The patched-conic model of the Earth-Moon system was utilized, together with a true lunar ephemeris. The model assumes two domains of influence in Earth-Moon space:

1. A sphere centered at the Moon within which a spherical Moon is the principal gravitational force and the Earth's attraction is neglected.
2. The region outside of the Moon's sphere of influence (MSI) where it is assumed that a spherical Earth is the principal gravitational force and the Moon's attraction is neglected. The boundary of the MSI is defined as the surface where the ratio of the perturbation of the Moon to the central force of the Earth (geocentric coordinates) is equal to the ratio of the perturbation of the Earth to the central force of the Moon (selenocentric coordinates). This locus of points is approximated by a sphere centered at the moon whose radius is approximately one tenth of the Earth-Moon distance.

Thus, trajectories in Earth-Moon space are approximated by conic sections patched at the boundary of the MSI. The geocentric conic is generally an ellipse of ecentricity near 1; the selenocentric conic is invariably a hyperbola. The two conics are patched together at the MSI by a coordinate transformation that accounts for the Moon's orbital motion. It should be noted that the origin of the coordinate system used within the MSI (selenocentric coordinates) is moving under the influence of the Earth's gravitational force, so that the error of the two-body approximation within this region is approximately the vector difference of the Earth's gravitational force at the Moon and at the spacecraft. This enables the patched-conic model to be used to generate approximate trends and trade-offs with a computing speed advatage of several orders of magnitude over precision simulation. The accuracy of the patched-conic model is discussed in Reference 2.

It was further assumed for this study that velocity changes are impulsive. It is shown in Reference 4 that this assumption will lead to only slight underestimates of ΔV.

It was desired to isolate the effects of various mission parameters as much as possible. Thus, a reference mission was established, and perturbations were made to one or more parameters at a time as desired. The parameter values chosen for the reference mission were:

Date of Launch — August 2, 1970

This date was chosen since the Earth-Moon declination is near 0 degrees, thus eliminating any bias due to Earth-Moon geometry. The Earth-Moon distance is approximately 64 Earth radii, near the maximum value. In addition, it is a reasonable date for the areas of the Moon near longitude 0° when sun angles are considered, assuming some orbital waiting times are allowed.

Launch Azimuth — 90 Degrees

The launch azimuth can be varied to obtain a continuous launch window. For this study, it was fixed to take maximum advantage of the Earth's rotation.

Translunar injection — Atlantic (inject south)

An Atlantic injection has a performance advantage over Pacific injection for the reference date.

Translunar trajectory — Non-free Return

The translunar trajectory was not constrained to be of the free-return class to allow mission flexibility.

Translunar Flight Time — 80 Hours

An 80-hour flight time is near the middle of the range of flight times under consideration for AAP, so it provides a convenient reference point.

Lunar Orbit Inclination — 6.7 Degrees

This is approximately the inclination of the Moon's equator to the Earth-Moon plane. Thus, trajectories will be essentially in this plane.

Ascending Node of Lunar Orbit

The value is chosen by the targeting program so that deboost is in-plane, eliminating an undesirable bias.

Radius of Lunar Orbit — 80 NMI

This is the value adopted for Apollo.

Transearth Trajectory Inclination — Unconstrained

Since the transfer angle from transearth injection to re-entry is 170 to 180 degrees, then re-entry will be in the immediate vicinity of the antipode. This ensures that Earth landing will be in a temperate zone.

Return Flight Time — < 120 Hours

In general, 120 hours is the most economical return flight time for a direct return when the Earth-Moon distance is near its maximum value.

Mission parameters not specified above were assigned Apollo values (e.g., the desired re-entry angle is -6.4 degrees at an altitude of 400,000 feet).

In addition, a standard spacecraft model was adopted so that weight differences and ΔV capabilities could be computed. The assumed weights in Earth lbs were:

TL Injection	102,000
LM separation	32,750
CSM main engine fuel	41,000
LM descent fuel	17,360
LM ascent fuel	4,960
LM RCS fuel	510

The TL injection weight was chosen so that the fuel requirements could be taken as upper bounds.

4. RELAXING THE FREE-RETURN CONSTRAINT

4.1 Free Return/Non-Free Return Trajectory Characteristics

For the Apollo mission, the translunar trajectory is constrained to be of the free-return class. A free-return trajectory is defined to be a circumlunar trajectory that is constrained to return safely to the earth without a major thrusting event. It must be symmetrical with respect to the rotating plane formed by a plane perpendicular to the Earth-Moon plane, passing through the centers of the earth and the Moon. Thus, the velocity vector of the spacecraft at periselene must be directed nearly opposite to the Moon's velocity vector. This implies that the velocity vector at periselene must be approximately in the Earth-Moon plane. The turning effect of the Moon on the spacecraft trajectory depends on the velocity magnitude and the periselene distance, which requires that for a given periselene distance the velocity magnitude must be near some fixed value.

Hence, the free-return constraint severely limits both the inclination and the energy (or equivalently, the flight time) of the nominal translunar trajectory. The limitations may be inferred from Figure III-1. This figure was generated by

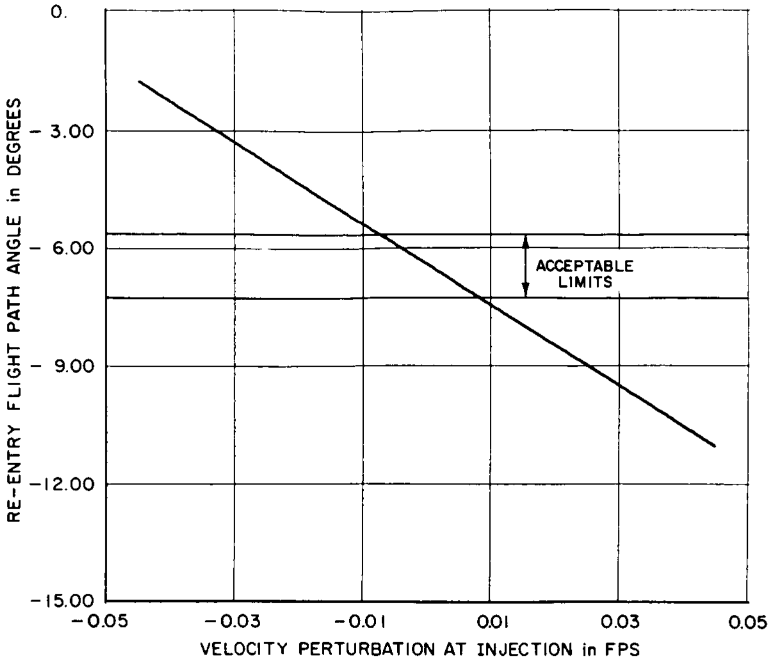

Figure III-1. Injection Sensitivities of Free-Return TL Trajectory

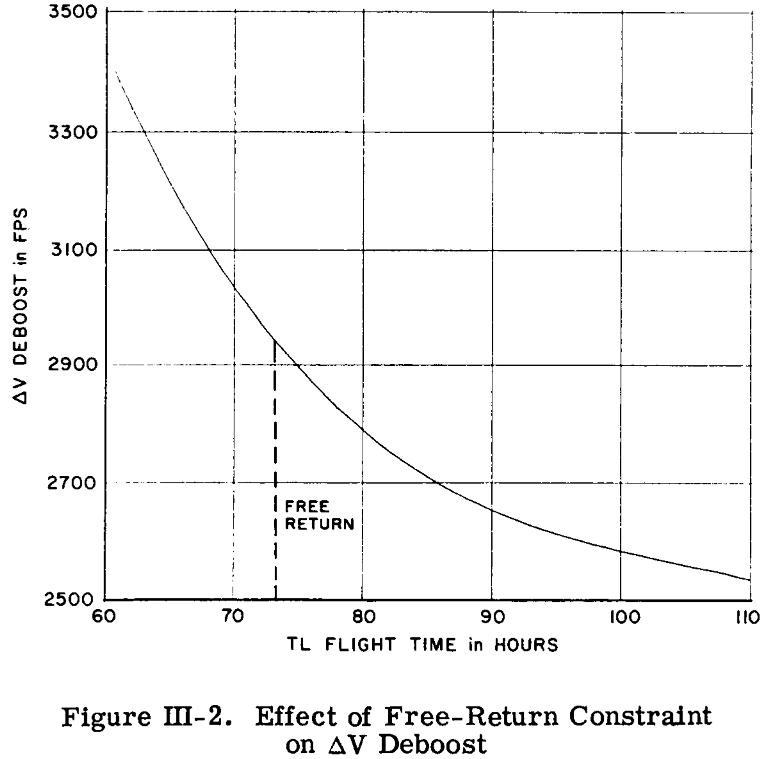

Figure III-2. Effect of Free-Return Constraint on ΔV Deboost

precision simulation, i.e. by numerical integration of the appropriate differential equations, rather than by the use of patched conics as done elsewhere in this study. A nominal free-return trajectory, targeted to re-enter at -6.4 degrees, was perturbed in each component of the translunar injection velocity vector, thus perturbing the translunar inclination, flight path angle, and velocity magnitude. The resultant re-entry angle was noted. It would appear that such a high sensitivity would not allow free return from a trajectory perturbed by guidance errors. However, the small midcourse corrections necessary for a safe return are not "a major thrusting event."

If this constraint can be relaxed for AAP, the parameters of inclination and flight time become available for mission flexibility and optimization. Variation in translunar inclination (measured at the Moon with respect to the lunar equator) can provide mission flexibility by allowing a lunar orbit with any desired inclination to be established without a plane change at deboost. Clearly, this is also the optimum procedure (in terms of ΔV cost) for establishing a lunar orbit of a specified inclination. However, it should be pointed out that for a given flight time, the ascending node of the established lunar orbit is not arbitrary. It varies primarily as a function of flight time and inclination for a particular Earth-Moon geometrical configuration. This will be discussed in paragraph 6.

Flight time can be varied for mission flexibility as mentioned above, but more significant is the change in fuel requirements. For an in-plane deboost into lunar orbit, the longer flight times require considerably less ΔV. (See Figure III-2). In addition, a smaller translunar injection velocity is required for the lower energy trajectory, as illustrated by Figure III-3. Thus a longer flight time permits injecting more weight into translunar flight while requiring less fuel for deboost into lunar orbit. The difference of weight into lunar orbit (caused by fuel savings at deboost alone) is shown in Figure III-4, where the weights are referenced to an 80-hour trajectory. The free-return flight time for this particular configuration is 73.12 hours. Raising the flight time from 73.12 hours to 110 hours allows approximately 3100 lbs more weight to be put into lunar orbit as either payload or fuel. As CSM fuel, the 3100 lbs can provide approximately 700 fps if the LM is not attached. This can be useful for parking orbit plane changes, for example. The extra 3100 lbs can not necessarily be landed on the lunar surface since landed payload is LM-restricted.

There are practical limits on the variation of flight time for translunar trajectories. Trajectories below 60 hours have excessive fuel requirements whereas trajectories above 110 hours are no longer direct flights to the moon, i.e., lunar encounter is post-apogee.

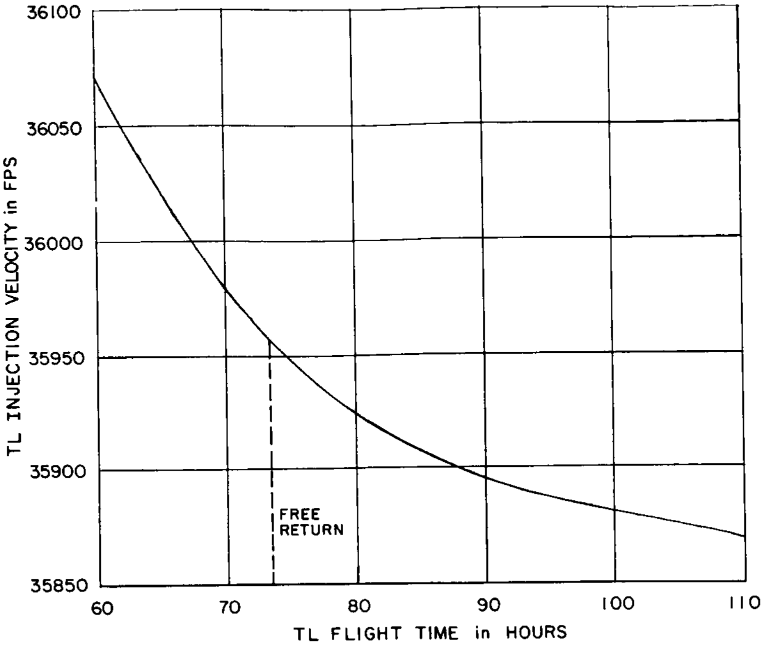

Figure III-3. Effect of Free-Return Constraint on TL Injection Velocity

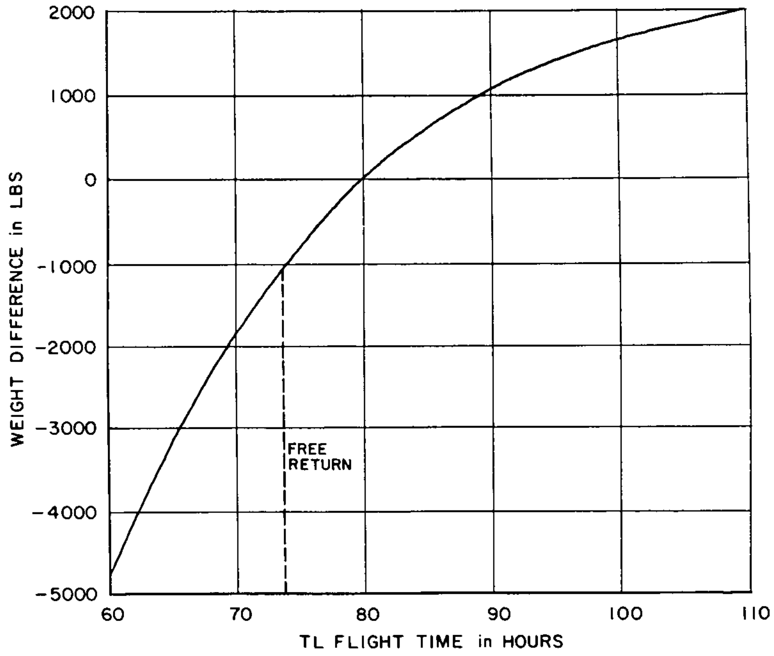

Figure III-4. Effect of Free-Return Constraint on Weight into Lunar Orbit

A less-obvious advantage of releasing the free-return constraint is the lowering of ΔV requirements for a direct abort to Earth from a translunar trajectory that has not yet entered the MSI (see Figure III-5). This is due simply to the fact that the non-free-return trajectories of interest are lower-energy trajectories than the free-return trajectories.

Clearly it is desirable to relax the free-return constraint for AAP. It is, however, a safety constraint. In the event of failure to deboost into lunar orbit, a spacecraft on a free-return trajectory will re-enter the Earth's atmosphere at an acceptable flight path angle without a major thrusting event. Thus, the following questions must be answered before this constraint can be relaxed:

1. What is the cost of replacing the abort capability provided by the free-return constraint?
2. What LM systems are available as back-ups to the CSM main propulsion system?
3. Under what conditions is the cost within the capabilities of the available LM backup systems?
4. What is a reasonable alternate constraint, and what is its effect?

The first question is difficult to answer because of the large number of variables in an AAP mission. The approach taken in this study is to define a reference mission (as described earlier) and then perturb various parameters through a reasonable range of values and note the effect on the abort characteristics. In no way does this provide an exhaustive answer to the question, but rather a reduction of the problem to a more manageable and more easily understood form. Furthermore, it can give insight concerning possible ways to lower abort requirements.

The problem of what type of abort to consider arises. An abort from a circumlunar trajectory can be one of two general types, circumlunar or direct. Aborts can be further subdivided according to landing areas, for example primary recovery area, contingency recovery area, water landing, or unrestricted. In addition, aborts can be time-critical or fuel-critical. However, the abort capability provided by the free-return constraint ensures only a safe re-entry angle with no constraint on landing site or time of flight. Thus for comparison, the cost of providing the abort capability should be based on the same type of abort, namely a fuel-critical abort to an unrestricted landing site. Most curves presented in this study are based on this type.

Some curves show also the cost associated with aborts to a particular landing site, i.e., Hawaii. These curves must be interpreted with care. For a particular abort situation, both types of aborts depend primarily on Earth-Moon geometry which is a slowly varying function of time. However, an abort to a particular landing site depends also on the inertial position of the landing site which is rotating

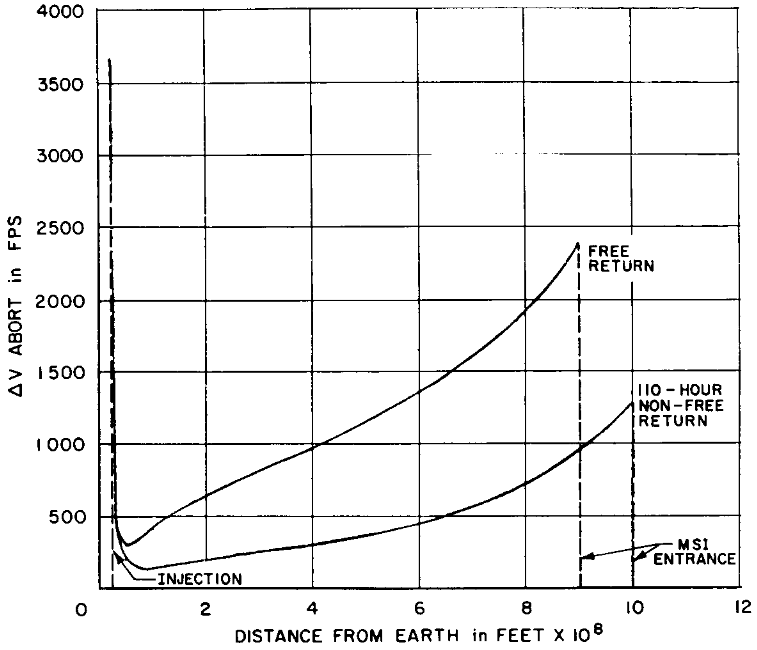

Figure III-5. Direct Abort from TL Trajectory before MSI Entrance

with the earth, and thus is a rapidly varying function of time. Hence two nearly identical abort situations 12 hours apart will have approximately the same abort requirements to an unrestricted site, but significantly different abort requirements to a particular landing site. The result is that abort curves to an unrestricted landing site can be interpreted to show trends and approximate magnitudes, whereas abort curves to a particular landing site can indicate approximate magnitudes only.

The calculation of ΔV required for abort is discussed in detail in the appendix to this section. The method used depends on the type of abort. For those to unrestricted landing sites, there are three components of the abort velocity (magnitude, flight path azimuth, and flight path angle) but only one constraint on the abort trajectory (re-entry angle), leaving 2 degrees of freedom available for optimization. For an abort to a particular landing site, there are three constraints on the abort trajectory (re-entry angle, landing site latitude and longitude), but a limited amount of optimization is still possible by varying the time of flight, i.e., varying the inertial position of the landing site which in effect varies the constraints. Double-impulse aborts were not considered.

Question 1 can be asked at various meaninful places along the trajectory. In this study, it is answered at the following places:

1. Pre-MSI Entrance — An abort executed before the spacecraft has entered the MSI will be a direct return to the earth. Abort requirements for a free-return and a 110-hour trajectory are shown in Figure III-5 as a function of distance from Earth. In all other cases, the pre-MSI abort requirements are given for two particular points; namely, translunar injection and a point midway between injection and MSI entrance. The abort at injection could occur for a number of reasons while an abort at the midway point could occur, for example, if the SM failed to ignite for a midcouse correction.
2. MSI Entrance — An abort executed near the entrance to the MSI will result in a circumlunar trajectory. It could occur here if the SM failed to ignite for a midcouse correction or perhaps for the first burn of a planned two-impulse deboost into lunar orbit.
3. Periselene — An abort executed at periselene also results in a circumlunar trajectory. It could occur if an abort was made immediately following failure of SM ignition for the deboost maneuver.
4. MSI Exit — By an abort at MSI exit is meant an abort from a circumlunar trajectory at its place of exit from the MSI if deboost into lunar orbit did not occur.

5. Post-MSI Exit — This is an abort from a circumlunar trajectory after it has passed through from the MSI if deboost into lunar orbit did not occur. Figure III-6c shows that abort requirements rise sharply as the spacecraft gets closer to the earth. For this reason, post-MSI exit abort requirements are not computed for the other trajectories considered.

4.2 Abort Costs

These costs for the reference mission are shown in Figures III-6a, b, and c for aborts occuring before MSI entrance, within the MSI, and after MSI exit, respectively. The abort costs for particular places of interest are tabulated below.

Place of Abort	ΔV in fps (unrestriced site)	ΔV in fps (particular site)
TL Injection	4713	not computed
Midway	927	not computed
MSI Entrance	73	422
Periselene	252	434
MSI Exit	742	947

Consider the effect of changing the day of month of the mission, holding all other parameters constant. This is equivalent to changing the lunar distance and declination through a set of consistent values. The range of dates considered here cover Earth-Moon distances from 64 to 56 Earth radii (i.e., from the maximum to the minimum) and cover declinations from 5 degrees down to -28 degrees (minimum value) and backup to -10 degrees. The change in declination introduces discontinuities in some of the trajectory parameters. When the declination is decreasing, the most economical procedure for translunar injection is to inject south (Atlantic) while a northerly (Pacific) injection is most economical when the declination is increasing. This results in a discontinuity for lunar arrival on August 12, 1970, when the declination changes from increasing to decreasing. The discontinuity is most apparent on the abort curves for a particular Earth landing site, since it produces a discontinuity in the time of launch.

Because the resulting changes in Earth-Moon geometry are reasonably large, a change in the date of the mission has significant effects on the achieved trajectory. Figure III-7 shows a decrease in translunar injection velocity; Figure III-8 shows a similar decrease in ΔV deboost, with the resulting difference in terms of weight into lunar orbit given in Figure III-9. Note that the weight difference can be more than 600 lbs for the same mission configuration flow at different dates.

As the date changes, the differences in ΔV abort are not large for aborts at TL injection and midway between injection and MSI entrance (Figures III-10 and -11).

However, the differences are significantly large for aborts within the MSI (Figures III-12 through III-14). The upper curves show ΔV abort to a specified landing site, and the lower curves are for unrestricted aborts.

Figure III-12, aborts from MSI entrance, has an additional discontinuity on the landing site abort curve. This occurs when periselene of the minimum-ΔV abort trajectory drops below a safety limit, taken here to be 40 nmi above the lunar surface. In general, the minimum-ΔV abort trajectory is a faster trajectory than the original trajectory, which has a periselene of 80 nmi because of inplane deboost. Since speeding up the trajectory has the effect of lowering periselene when approximately the same sweep angle is desired (the angle between the asymtotes of the lunar hyperbola), a considerably faster trajectory may violate the periselene constraint. In this study, the periselene constraint is violated only by MSI entrance aborts to a specified landing site because the difference between the two types of aborts is primarily time of flight to allow the Earth landing site to rotate to the correct position. The violation is handled simply by incrementing the flight time by 24 hours — the time for the landing site to again rotate to the desired position. Hence the discontinuity is a discontinuity in flight time.

It should be pointed out that the change in Earth-Moon distance causes a large change in the translunar trajectory energy for an 80-hour flight time. An 80-hour trajectory flown when the Earth-Moon distance is near its minimum value has the equivalent energy of a 110-hour trajectory flown when the Earth-Moon distance is near its maximum value. This must be considered when the abort curves are interpreted, as the abort cost depends on the energy rather than the flight time.

There is interest in determining the abort costs for translunar trajectories with periselene below the nominal 80-nmi parking orbit radius, in case lower orbits are used or the optimum deboost point is not at periselene. The range considered is 20 up to 100 nmi. Values above 100 nmi cannot be used due to LM restrictions.

The portion of the translunar trajectory that is not near the moon is not significantly changed. Injection velocity varies about 1 fps, while abort costs both at injection and midway between injection and MSI entrance vary about 2 fps. The trajectory variation at deboost (performed in-plane) is larger, covering a range of 75 fps, resulting in a weight difference of up to 500 lbs (Figures III-15 and -16). For aborts within the MSI, the abort costs generally increase as the spacecraft swings around the Moon as shown in Figures III-17 through -19. As noted before, the upper curve is for an abort to a particular landing site and the lower curve for an unrestricted abort.

Consider next the change in abort costs resulting when translunar flight time (or equivalently, translunar injection energy) is varied, with other mission parameters held constant. It was shown earlier (Figures III-2 through -4) that a major result of relaxing the free-return constraint is to allow optimization by allowing variation in the time of flight. The values considered here range from 60 to 110 hours; the free-return flight time for this mission configuration is 73.12 hours.

As implied earlier by Figure III-5, the abort requirements at translunar injection and midway between injection and MSI entrance (Figures III-20 and -21) are somewhat lower for the lower energy trajectories. However, this is not the case for aborts initiated within the MSI, shown in Figures III-22 through -24. In this region, the cost is small for the trajectories whose energies are near the free return value, and increases as the energy moves away from this value. Note again that the abort cost for the circumlunar aborts increases as the spacecraft travels around the Moon.

There is a discontinuity apparent on the unrestricted abort curves in Figures III-22 through -24. This is because the re-entry direction for the minimum ΔV abort trajectory jumps from retrograde to direct near a flight time of 70 hours as the flight time is increasing. However, it must be noted that although the abort trajectory resulting in the minimum-ΔV maneuver re-enters in a retrograde direction under certain conditions, retrograde returns cannot be allowed because of the excessive re-entry (relative) velocities encountered. The discontinuity does not appear on the curves for specified landing sites since those abort trajectories are constrained to have direct reentry. The discontinuity shown in Figure III-22 is due to the periselene constraint.

Another result of relaxing the free-return constraint is the mission flexibility provided by variation in translunar trajectory inclination. Fixing the other mission parameters and varying the translunar trajectory inclination, measured at the Moon, are equivalent to varying the inclination of the lunar orbit since deboost is inplane. The investigated range of values is from -90 degrees to +90 degrees, i.e., all possible retrograde orbits. Direct lunar orbits were not considered for reasons to be discussed later.

The velocity requirements at translunar injection and at deboost do not change significantly. The variation in injection velocity is less than 7 fps, while the deboost velocity variation is less than 10 fps. Similarly, the abort requirements at injection and midway between injection and MSI entrance show little variation. However, aborts in the vicinity of the Moon, i.e., circumlunar aborts, show considerable variation (Figures III-25 through -27). Here the abort cost is smallest for trajectories with an inclination of near -7 degrees (close to the inclination of the free-return trajectory with this mission configuration). The cost increases as the inclination moves away from this value. Note the discontinuity in Figure III-25 caused by the periselene constraint. Note also that the abort cost within the MSI for high-inclination orbits is larger at periselene than at MSI exit, rather than increasing as the spacecraft moves away from the Moon. This is because a large plane change is required for an abort from a high-inclination orbit since the angle between the Moon's velocity vector and the spacecraft's velocity vector at periselene is large, and plane changes are best done where the velocity vector is small, i.e., at MSI entrance or exit.

Figure III-2 indicated that the most economical translunar flight time for the range considered is 110 hours for an inplane deboost. Thus, to know the abort requirements for the reference mission flown with a 110-hour flight time at various inclinations would be useful. These requirements are shown in Figures III-28 through -30 for aborts within the MSI. Aborts to a particular landing site are not shown. Note that these curves are similar in shape to the corresponding curves presented for an 80-hour flight time (Figures III-25 through -27) except that the overall requirements for the 110-hour trajectories are somewhat higher, as was implied by Figure III-22 through -24 which showed the effects of raising the flight time. However, the differences between the corresponding curves are large for low-inclination orbits, but much smaller for high inclination orbits.

The curves presented so far have shown how abort costs vary with respect to one, or possibly two, mission parameters. These curves may also indicate how a mission may be altered to lower the abort cost. To illustrate: Figures III-22 through -24 indicate that this cost is a minimum for a trajectory whose translunar flight time is near the value required for free return. This would imply that the abort requirements for the reference mission flown at 73.12 hours at various inclinations would be somewhat lower than the corresponding curves representing 80 hours and 110 hours. That this is the case is substantiated by Figures III-31 through -33. Note again that the shape of the curves is similar.

The other parameters considered cannot, as a rule, be varied as much as flight time. The date of the mission for a particular month depends on the sun angles desired at the lunar landing site upon arrival, as well as other variables, and can be varied only slightly by changing the pre-descent waiting period in lunar orbit. The radius of the lunar orbit may be varied consistent with LM restrictions, but it is too small to be effective when the resulting change in LM operations is considered. The lunar orbit inclination is generally dictated by orbit-landing site geometry and desired stay time and cannot be varied greatly.

It has been shown that the abort costs increase as a translunar trajectory changes its inclination and/or flight time away from the values required for a free-return trajectory. Furthermore, the abort cost is highly dependent on where the abort is initiated. For circumlunar aborts, it is lowest at MSI entrance and then at MSI exit when large plane changes are required; otherwise it is lowest at the places furthest from Earth (measured along the trajectory from re-entry).

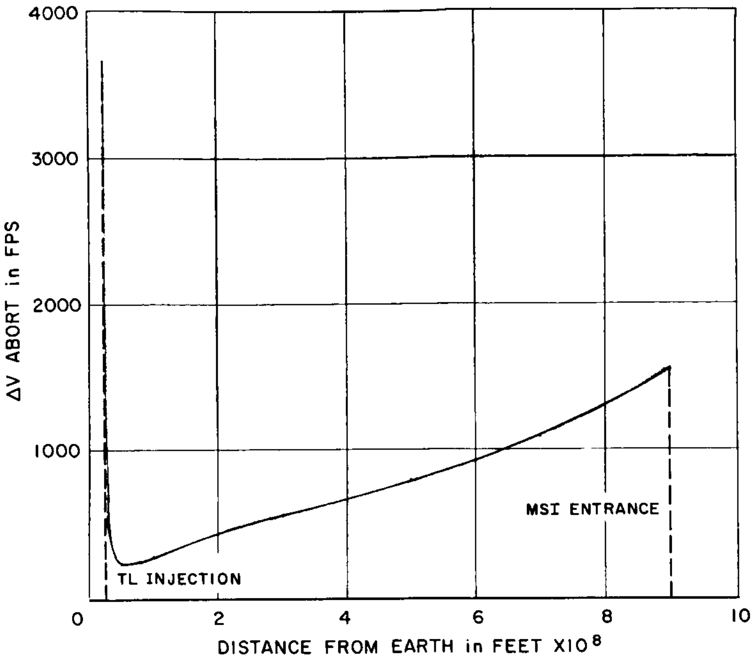

Figure III-6a. Abort from 80-Hour TL Trajectory before MSI Entrance

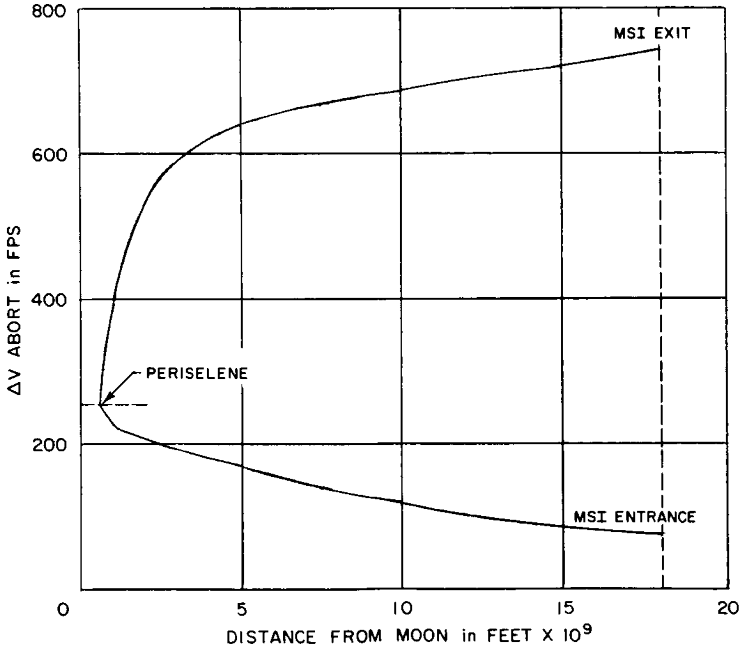

Figure III-6b. Abort from 80-Hour TL Trajectory within MSI

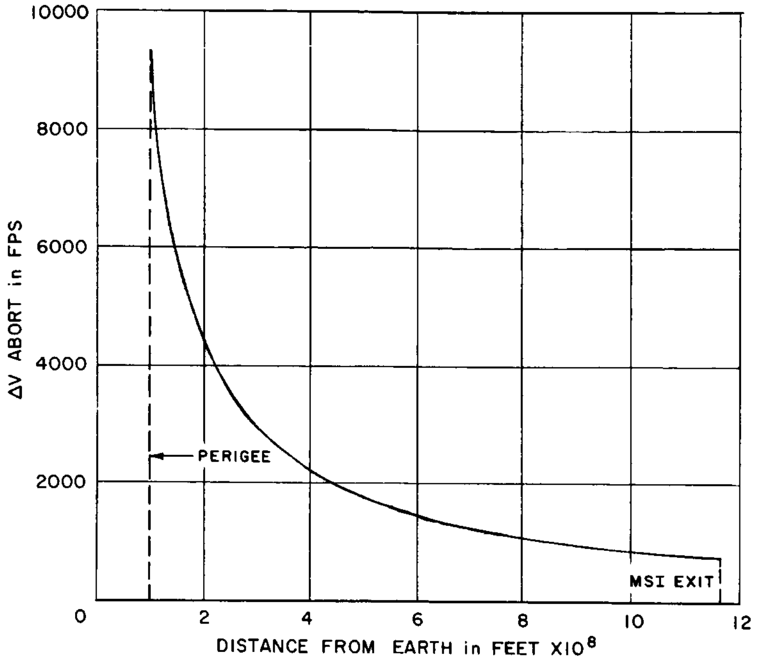

Figure III-6c. Abort from Extended 80-Hour TL Trajectory after MSI Exit

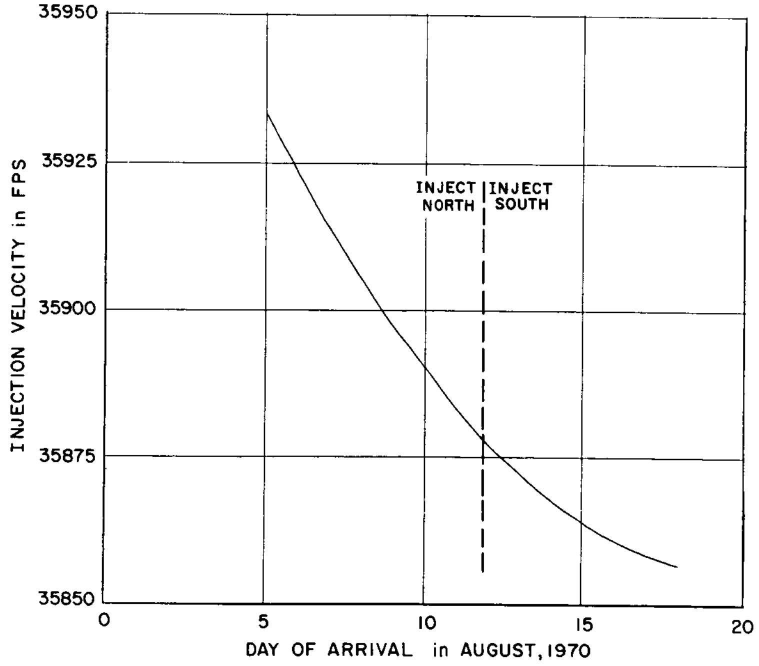

Figure III-7. Effect of Lunar Distance and Declination on TL Injection Velocity

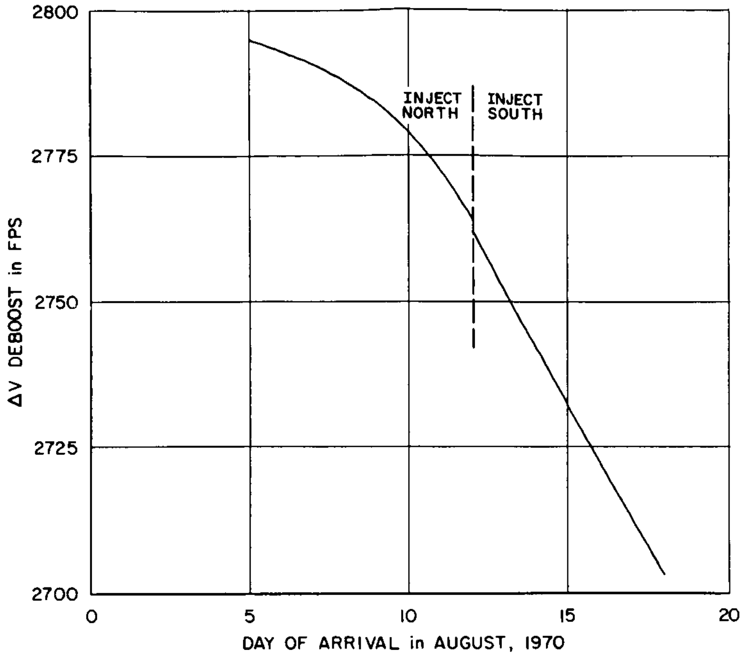

Figure III-8. Effect of Lunar Distance and Declination on ΔV Deboost

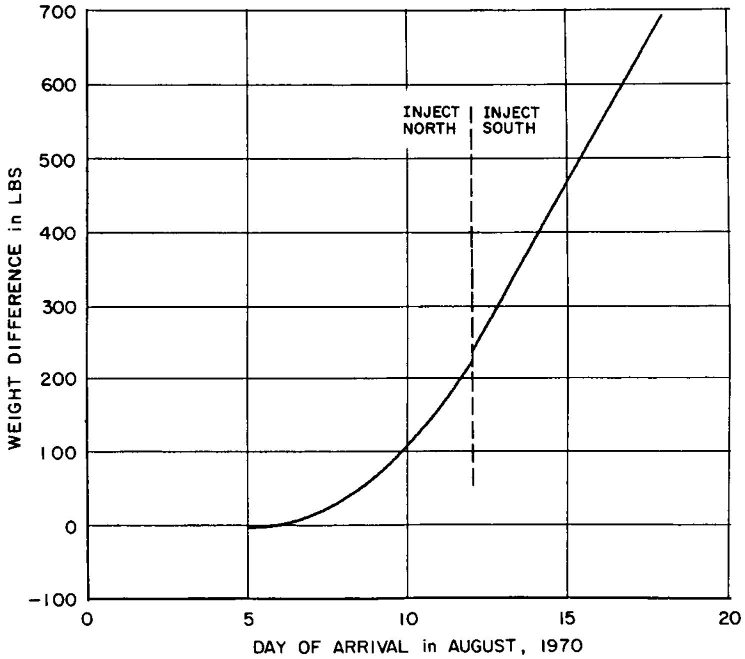

Figure III-9. Effect of Lunar Distance and Declination on Weight into Lunar Orbit

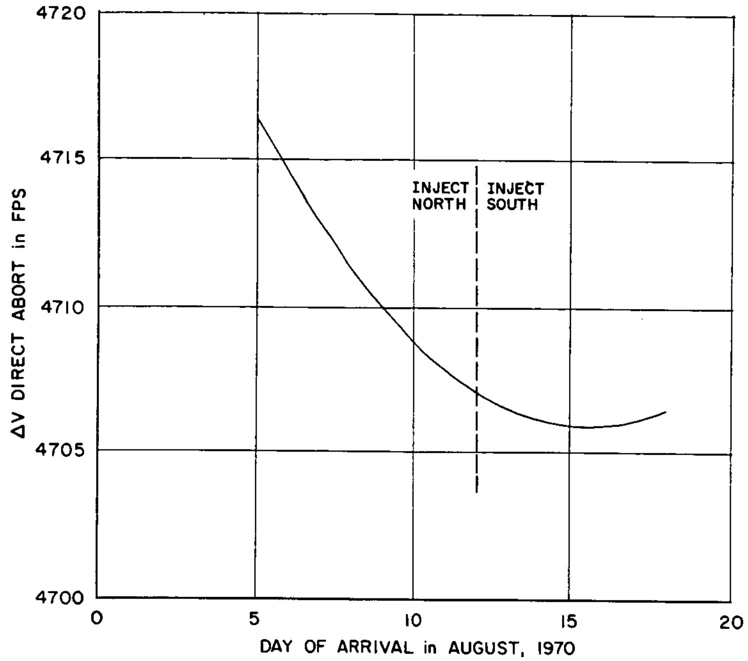

Figure III-10. Effect of Lunar Distance and Declination on Direct Aborts at TL Injection

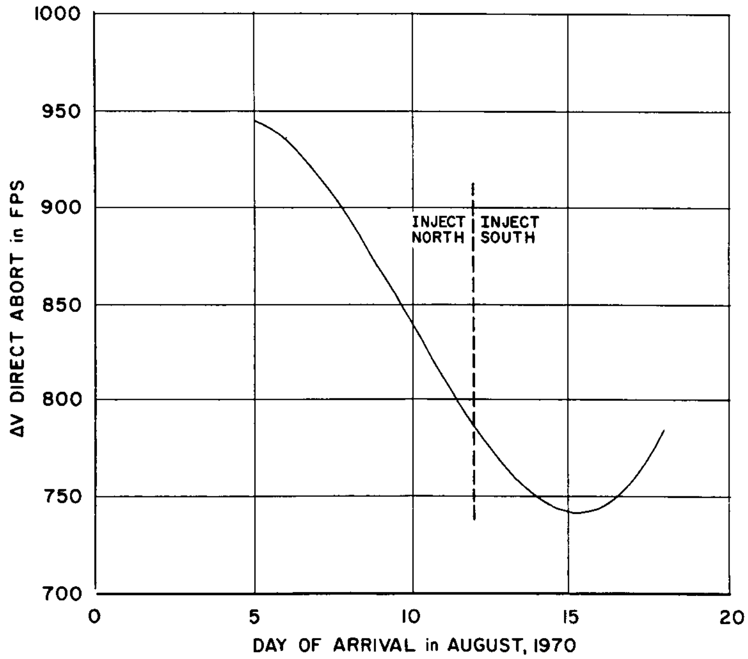

Figure III-11. Effect of Lunar Distance and Declination on Direct Aborts at Midway

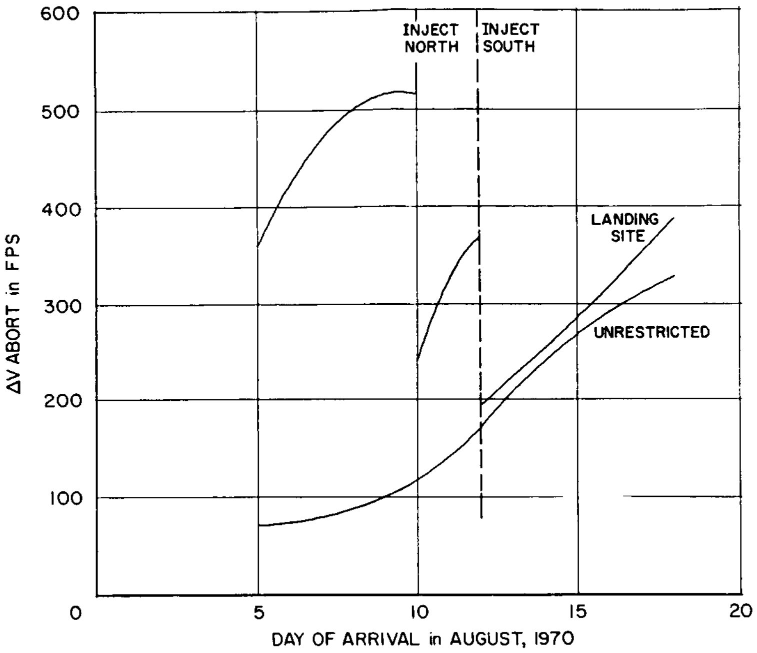

Figure III-12. Effect of Lunar Distance and Declination on MSI Entrance Aborts

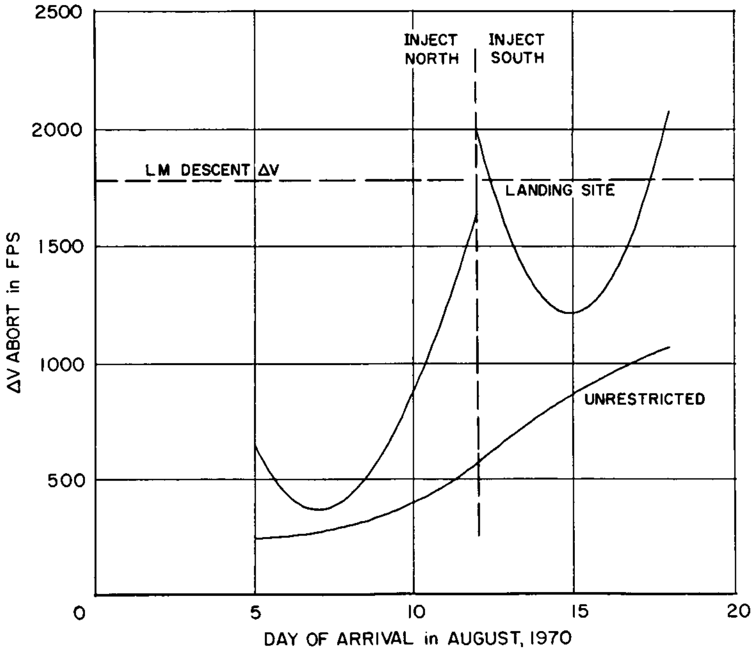

Figure III-13. Effect of Lunar Distance and Declination on Periselene Aborts

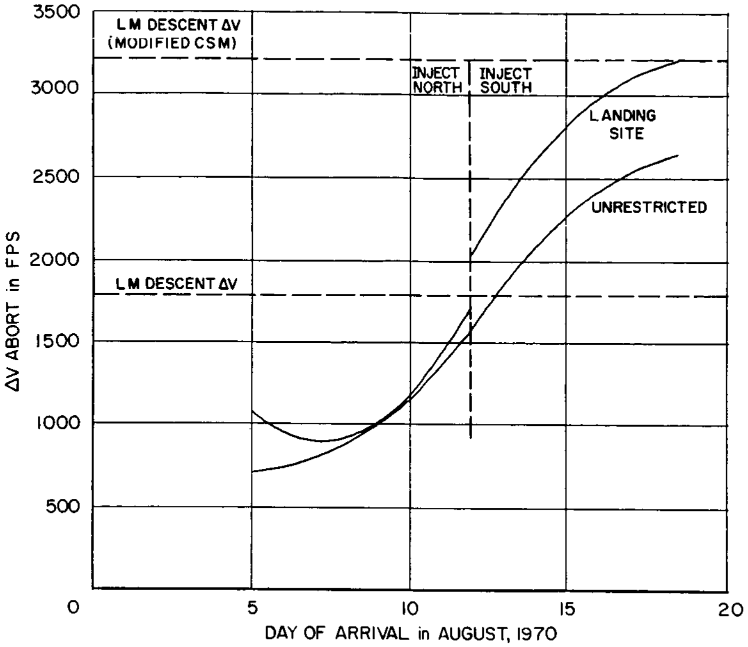

Figure III-14. Effect of Lunar Distance and Declination on MSI Exit Aborts

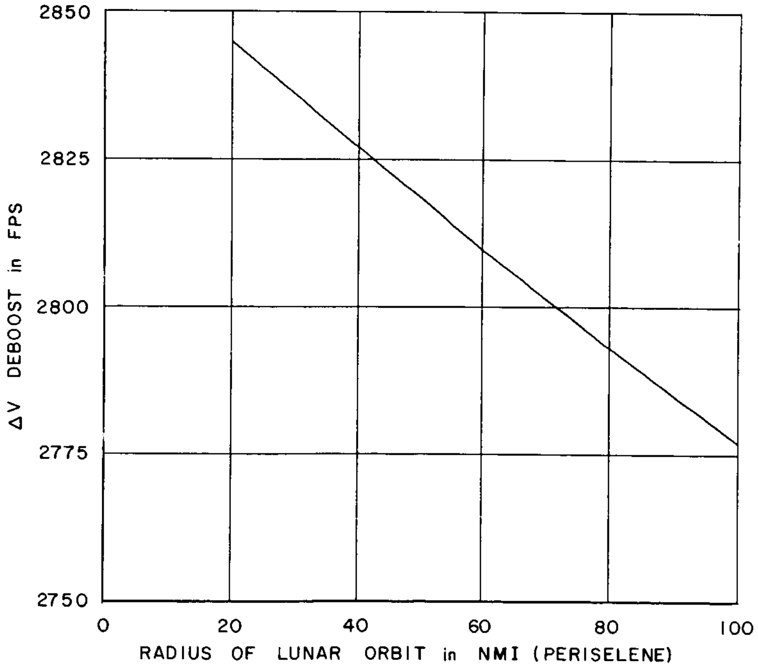

Figure III-15. Effect of Lunar Orbit Radius on ΔV Deboost

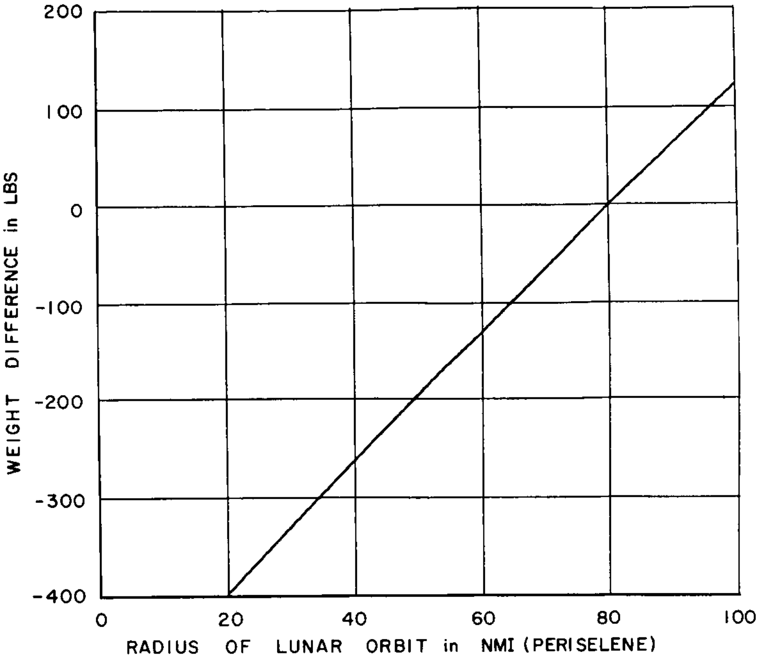

Figure III-16. Effect of Lunar Orbit Radius on Weight into Lunar Orbit

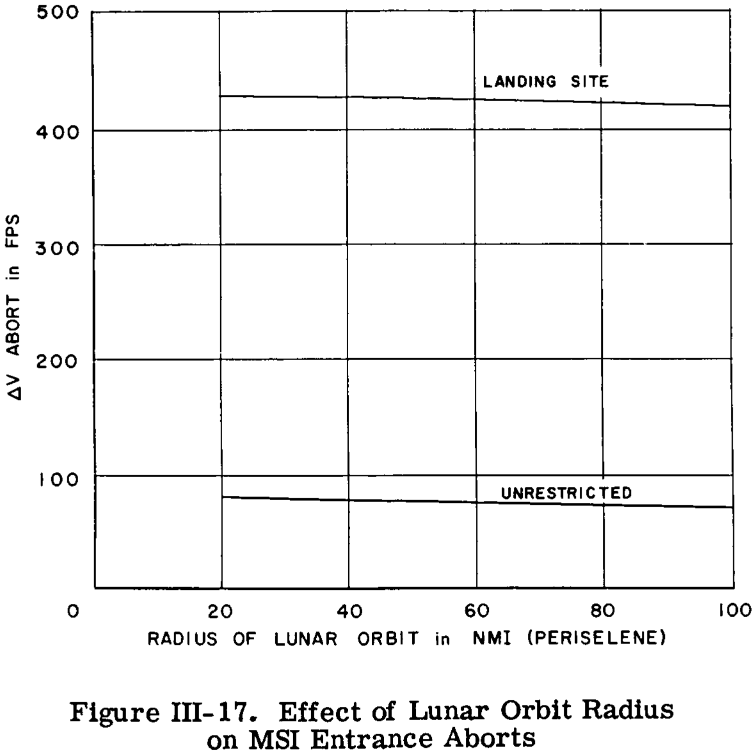

Figure III-17. Effect of Lunar Orbit Radius on MSI Entrance Aborts

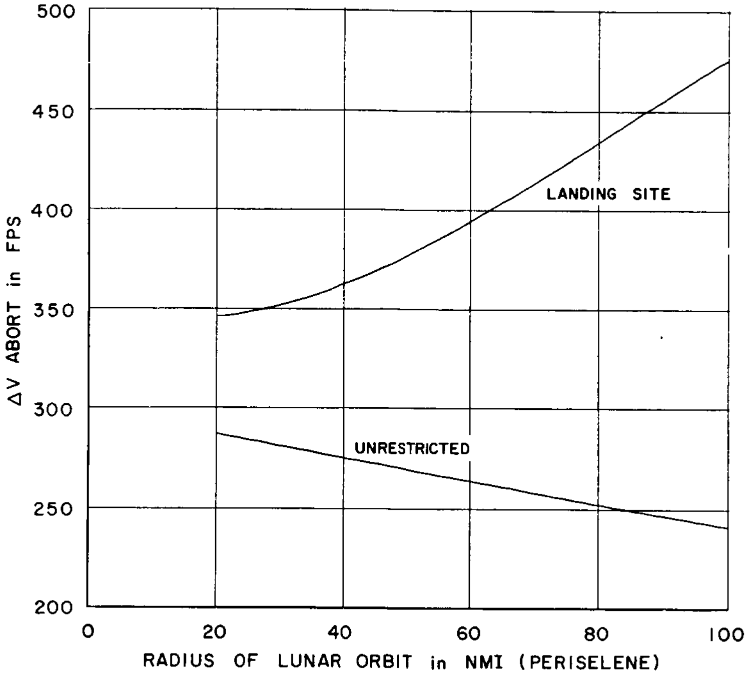

Figure III-18. Effect of Lunar Orbit Radius on Periselene Orbits

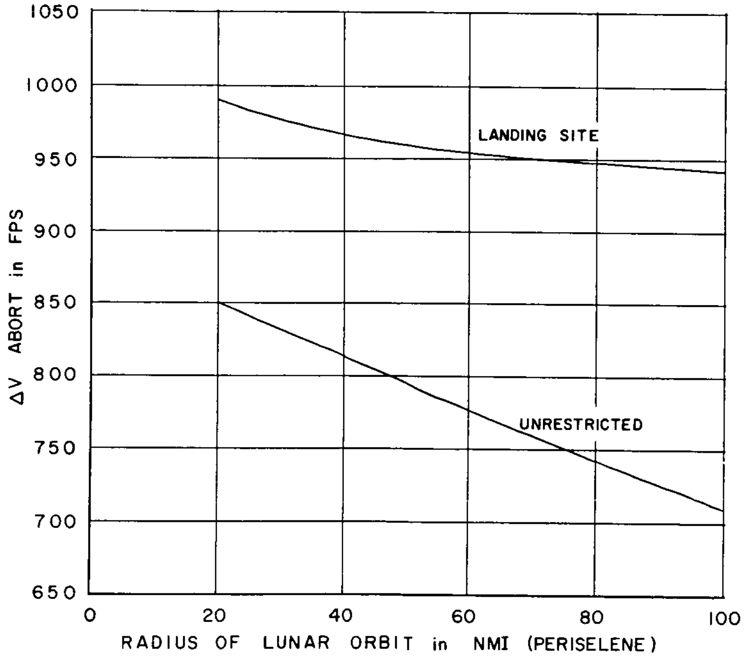

Figure III-19. Effect of Lunar Orbit Radius on MSI Exit Aborts

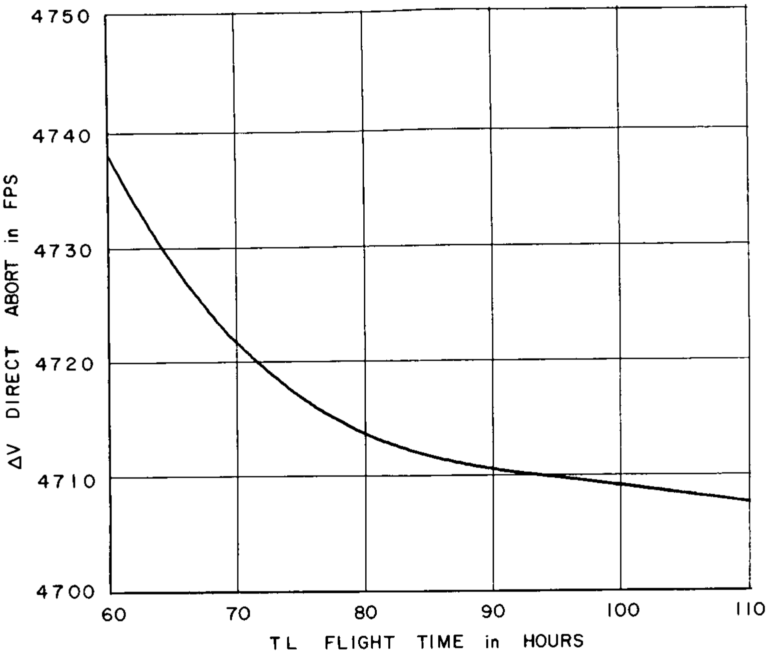

Figure III-20. Effect of TL Flight Time on Direct Aborts at TL Injection

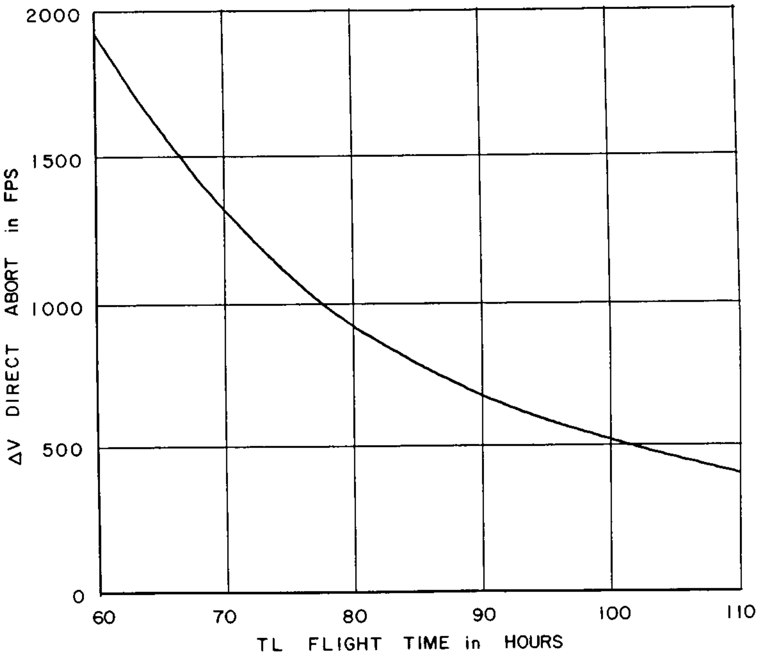

Figure III-21. Effect of TL Flight Time on Direct Aborts at Midway

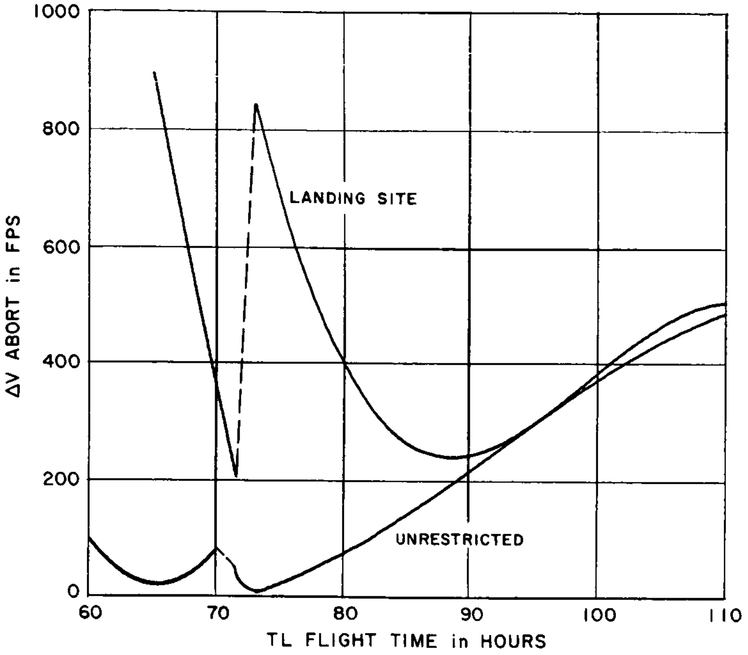

Figure III-22. Effect of TL Flight Time on MSI Entrance Aborts

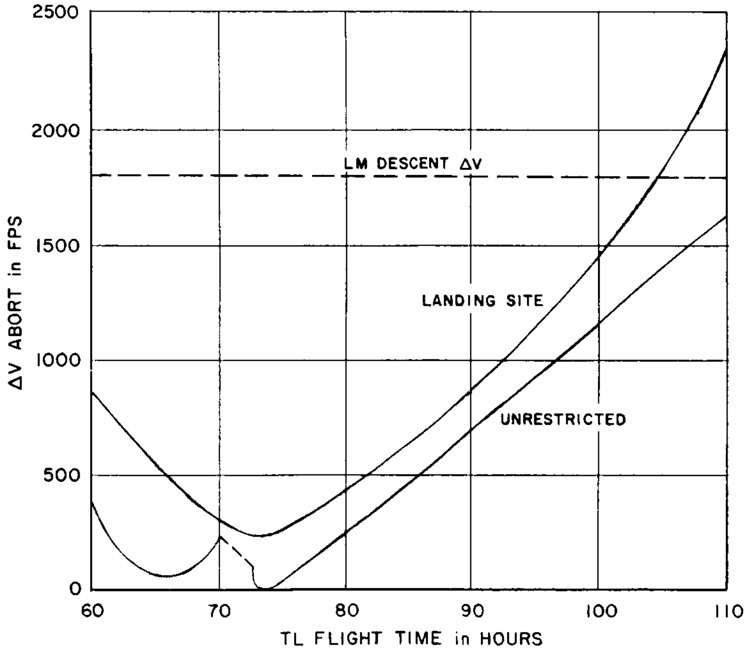

Figure III-23. Effect of TL Flight Time on Periselene Aborts

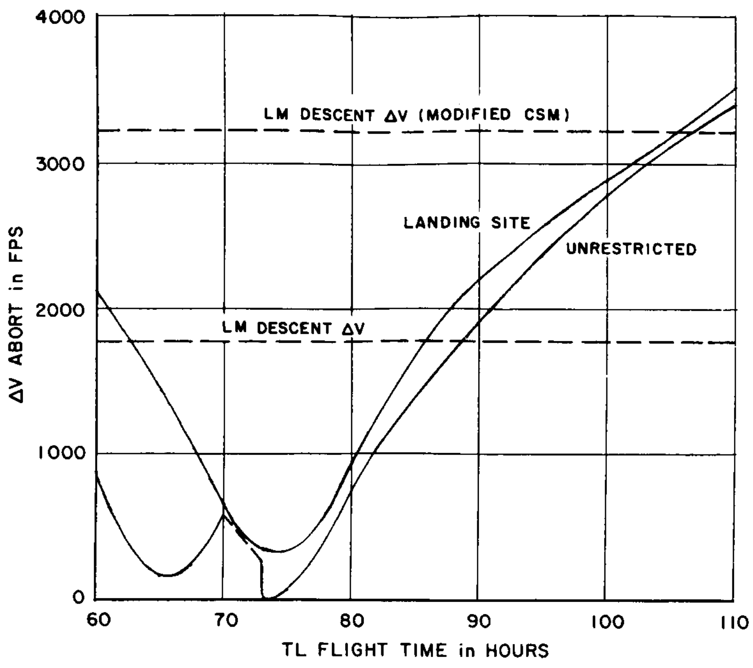

Figure III-24. Effect of TL Flight Time on MSI Exit Aborts

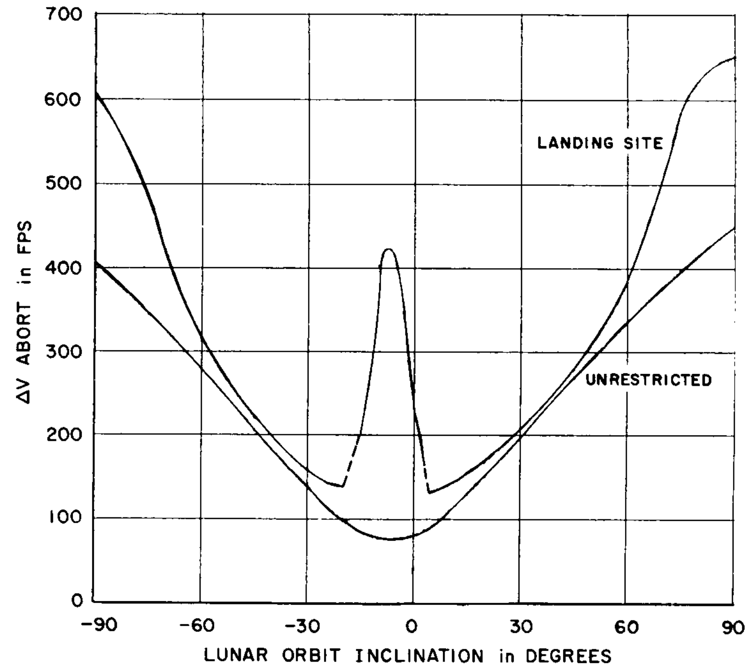

Figure III-25. Effect of Lunar Orbit Inclination on MSI Entrance Orbits, 80-Hour TL Trajectory

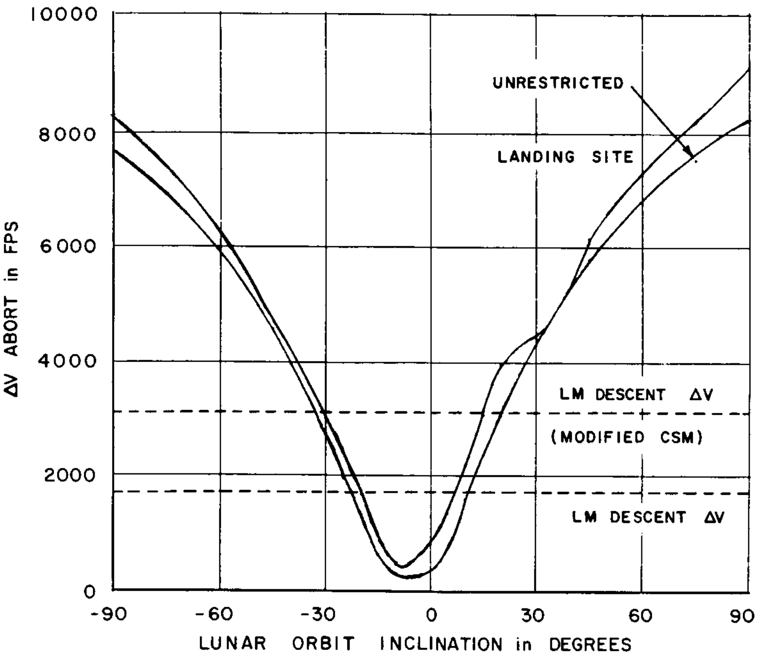

Figure III-26. Effect of Lunar Orbit Inclination on Periselene Aborts, 80-Hour TL Trajectory

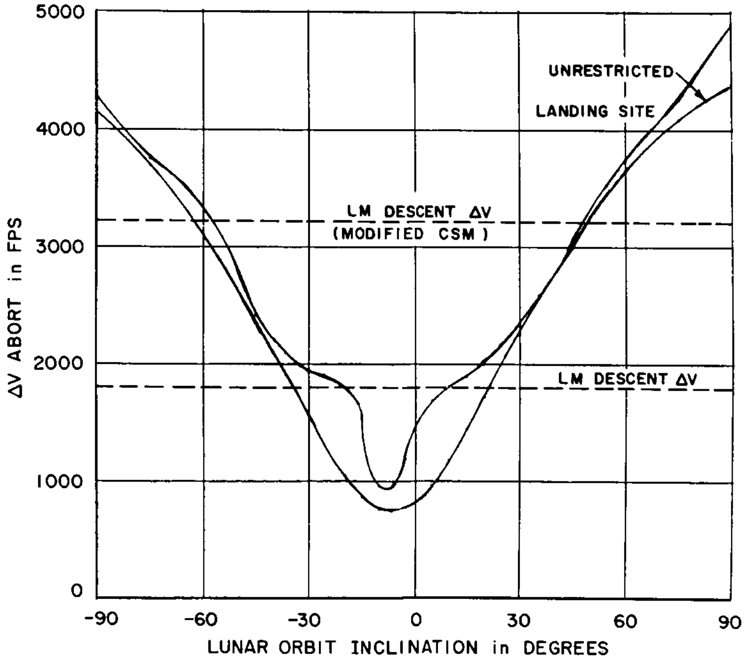

Figure III-27. Effect of Lunar Orbit Inclination on MSI Exit Aborts, 80-Hour TL Trajectory

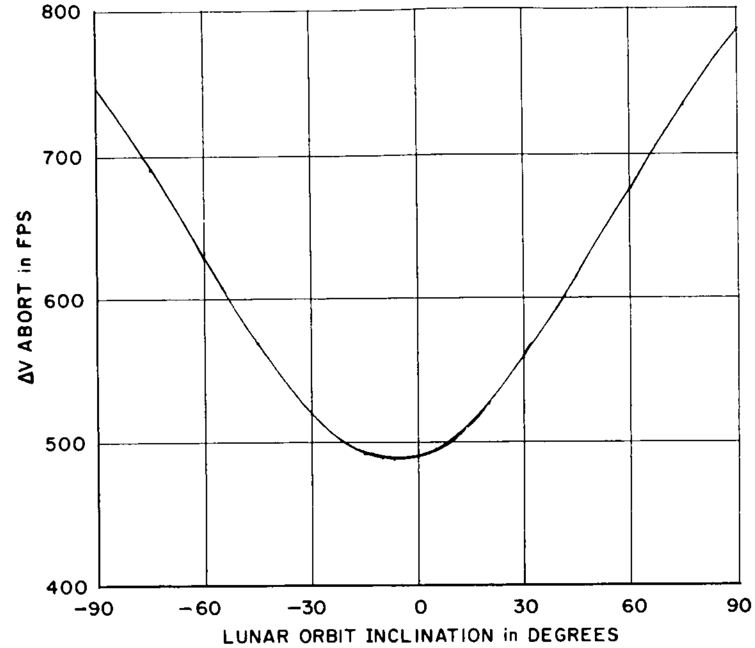

Figure III-28. Effect of Lunar Orbit Inclination on MSI Entrance Aborts, 110-Hour TL Trajectory

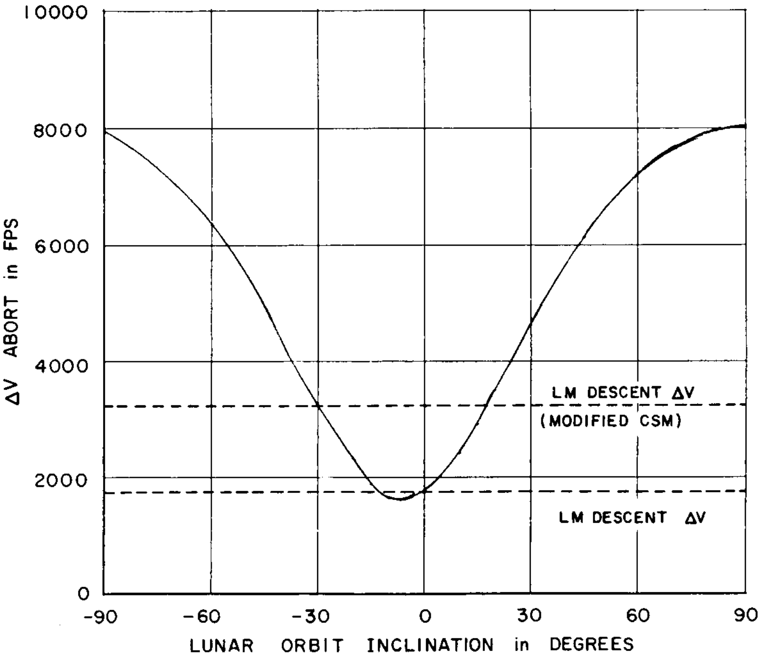

Figure III-29. Effect of Lunar Orbit Inclination on Periselene Aborts, 110-Hour TL Trajectory

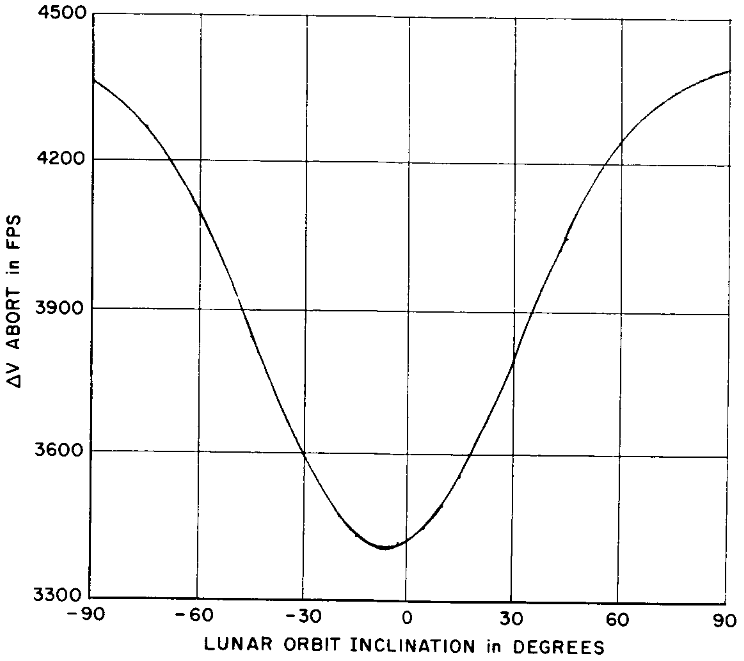

Figure III-30. Effect of Lunar Orbit Inclination on MSI Exit Aborts, 110-Hour TL Trajectory

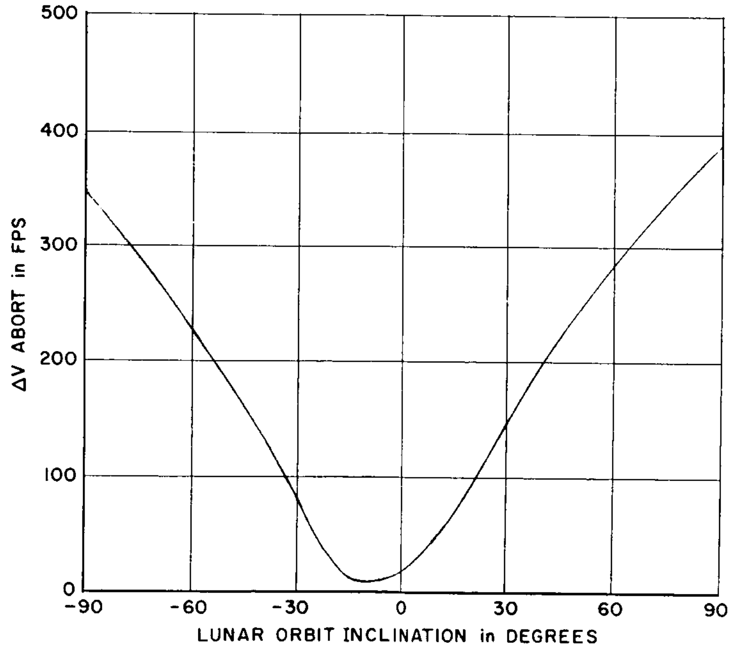

Figure III-31. Effect of Lunar Orbit Inclination on MSI Entrance Aborts, 73.1-Hour TL Trajectory

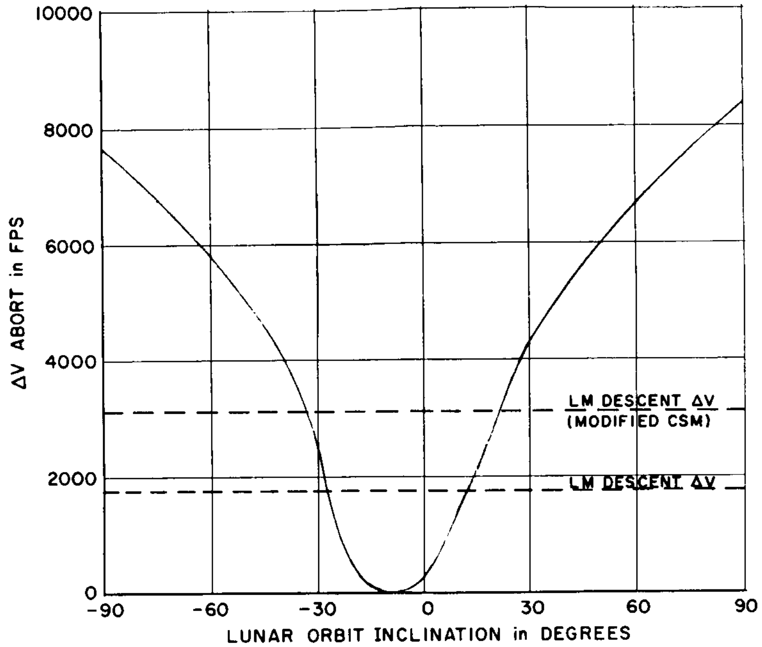

Figure III-32. Effect of Lunar Orbit Inclination on Periselene Aborts, 73.1-Hour TL Trajectory

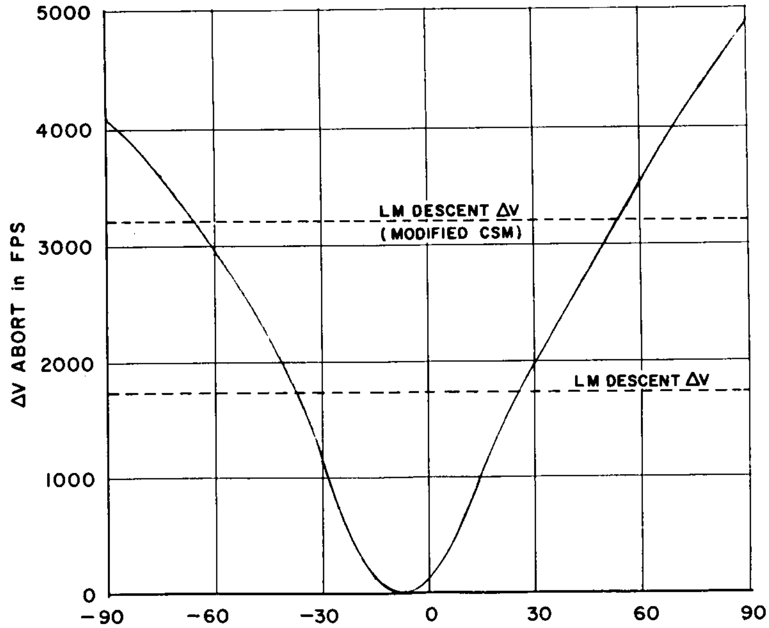

Figure III-33. Effect of Lunar Orbit Inclination on MSI Exit Aborts, 73.1-Hour TL Trajectory

4.3 Alternative to the Free-Return Constraint

There are three LM propulsion systems — the descent stage, ascent stage and the reaction control system (RCS). Of these, the LM descent stage and LM RCS are feasible backups for the CSM main propulsion system. The LM ascent engine is not feasible due to control problems. A detailed discussion of the feasibility of the available LM systems is in Reference 5.

The ΔV capabilities available from the backup systems, using the spacecraft model assumed earlier, are as follows:

LM Descent, 1798 fps
LM RCS (using ascent fuel), 488 fps
Combined, 2383 fps

The performance obtained can be enhanced considerably, as noted below, if provisions are made for jettisoning the remaining SM fuel:

LM Descent, 3233 fps
LM RCS (using ascent fuel), 828 fps
Combined, 4406 fps

For comparison purposes, the ΔV capability of the SM main engine is 5178 fps with the LM attached or 9028 fps without it.

The LM RCS capabilities assume that the RCS engines can be operated for approximately 3100 seconds while the rated burning time for 0.997 probability is only 1000 seconds. (However, it has been estimated that the RCS engines can operate for at least 2000 seconds without difficulty, and can probably operate the full 3100 seconds.) This implies that if SM propulsion were not available, an abort to an unrestricted landing site would be initiated by the descent stage and the necessary midcourse corrections carried out by the LM RCS and/or the CSM RCS. The remaining LM RCS propulsion could then be used to adjust the time of flight so that a desired landing area could be reached.

Thus, a reasonable alternate to replace the free-return constraint is that the translunar trajectory be such that the available LM backup systems can return the spacecraft safely to Earth in the event of SM failure to deboost into lunar orbit. This alternate constraint allows greater variation in translunar trajectory inclination and flight time for optimization and flexibility while providing for the possiblity of SM failure.

Clearly, its effect is that of a cutoff function at the point where the abort requirements exceed the capabilities of the LM descent stage. The abort cost must be based on an abort position that is reached after the nominal deboost position, since it may not be known until deboost that the SM has failed. Thus, for a single-impulse deboost, the abort position must be after periselene, for example, at MSI exit. For a double-impulse deboost, the abort position may be any place after the first scheduled impulse, i.e., after MSI entrance. (The possibility of completing the first burn but not the second burn was not considered.) It should be pointed out here that the preburn portions of the single- and double-impulse translunar trajectories are nearly identical so that their abort requirements are similar. Hence, the data presented can be interpreted as being applicable to either case with a reasonable amount of accuracy.

The effect of the alternate constraint on lunar surface accessibility in terms of attainable lunar orbits depends on whether or not certain hardware modifications can be made. For maximum accessibility, provisions would have to be made for jettisoning the remaining SM fuel and for the utilization of LM ascent fuel by the LM RCS engines. Assuming that this can be done, lunar orbits with inclinations from -65 to 55 degrees can be reached while the acceptable range is limited to about -35 to 30 degrees if the hardware modifications cannot be made (see Figure III-33).

The amount of allowable optimization possible by varying the flight time is also affected. For highly inclined orbits, fast flight times are necessary to keep the abort requirements below the LM descent stage capabilities. Low-energy trajectories may be used only for low-inclination lunar orbits. For example, from Figure III-29, it is evident that a 110-hour translunar trajectory can reach only orbits of between -30 and 15 degrees inclination if the hardware modifications are made, but practically no orbits if the modifications are not made.

In general, the range of permissible lunar orbits depends on many mission variables. The spacecraft configuration affects the capabilities of the LM backup systems, and the abort cost is a function of many variables as discussed earlier. A crucial factor in the abort cost is the amount of ΔV available for deboost, effectively limiting the allowable flight time.

4.4 Other Abort Considerations

The aforegoing discussion has been concerned primarily with aborts to unrestricted landing sites from trajectories failing to deboost into lunar orbit. An exception to this has been the case of a direct abort from translunar trajectories that have not yet entered the MSI. However, the problem of a burn being only partially completed at, for example, translunar injection or deboost has not been examined. Neither has the problem of a time-critical abort that could arise (e.g., the failure of a crucial life-support system). These problems have been studied extensively for the Apollo mission which will use a free-return translunar trajectory, and the results of these studies can be used as guidelines for determining non-free-return characteristics. Since these latter trajectories are in general of a lower energy, the results of the studies concerning partial burns can be taken as upper bounds. The velocity increments required to speed up a transearth trajectory are similar for both types of trajectories.

5. EFFECT OF STAY-TIME ON TL AND TE TRAJECTORIES

The AAP mission may be on the lunar surface for periods up to two weeks, requiring a total mission time (from launch to re-entry) up to 28 days. This is significant when the resulting changes in Earth-Moon-lunar orbit geometry are considered. The changes do not affect the TL trajectory or any of the possible aborts from it. However, the parking orbit is fixed in inertial space (neglecting the Moon's orbital motion), and the moon rotates underneath it at the rate of 13.2 degrees per day. As the stay-time increases, the angular distance from the landing site to the orbit plane increases to some maximum value and then decreases to zero. For non-equatorial orbits, this changing geometry makes continuous abort from the surface difficult because of the costly plane changes required for rendezvous at certain times. The problem of aborting from lunar surface to the orbiting CSM is discussed in Section II. It is mentioned here to point out that the ΔV available for transearth injection varies as a particular mission progresses.

As the lunar orbit-Moon geometrical relationship varies, the Moon-Earth relationship varies. Therefore, the set of TE trajectories available in one mission must cover a wide variety of lunar orbit-Earth relationships if continuous abort from the lunar orbit to Earth is to be provided. The selenocentric velocity vector of the TE trajectory at injection must be directed nearly opposite the Moon's velocity vector so that the resultant vector enables the spacecraft to return to the earth. Thus, prohibitively large plane changes may be necessary during the mission such as when the node of a high inclination orbit is near the Earth-Moon line. This is a motivation for considering orbital waiting times and multiple impulse trajectories.

Another result of the long surface stay-times planned for AAP is the change in Earth lighting conditions at touchdown. Consider an AAP nominal surface stay-time at a lunar landing site on the 0° longitude line. The sun elevation angle at the landing site during descent is constrained by visibility considerations to be from 7 to 20 degrees, but the sun elevation angle at LM ascent is constrained only to be positive to ensure daytime operations. Figure III-34 indicates that for a mission to have a 2-week stay-time and satisfy the ascent and descent lighting constraints, LM ascent (and TE injection) must occur near the time of sunset at the lunar landing site. Since the transfer angle from transearth injection to re-entry is generally between 170 to 180 degrees, re-entry is going to be in the immediate vicinity of the antipode. The resulting geometrical relationships are shown in Figure III-35. Note that the nominal Earth landing point is near local sunset. Although

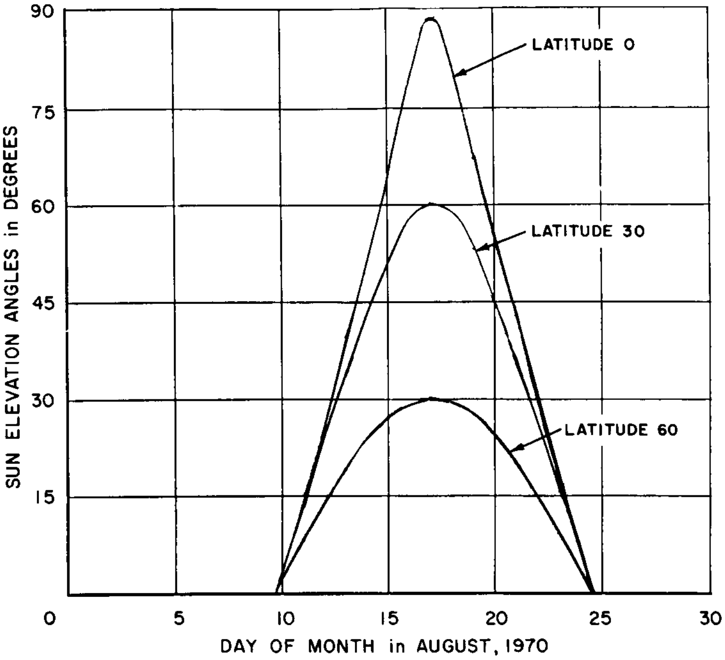

Figure III-34. Sun Elevation Angles at 0° Longitude

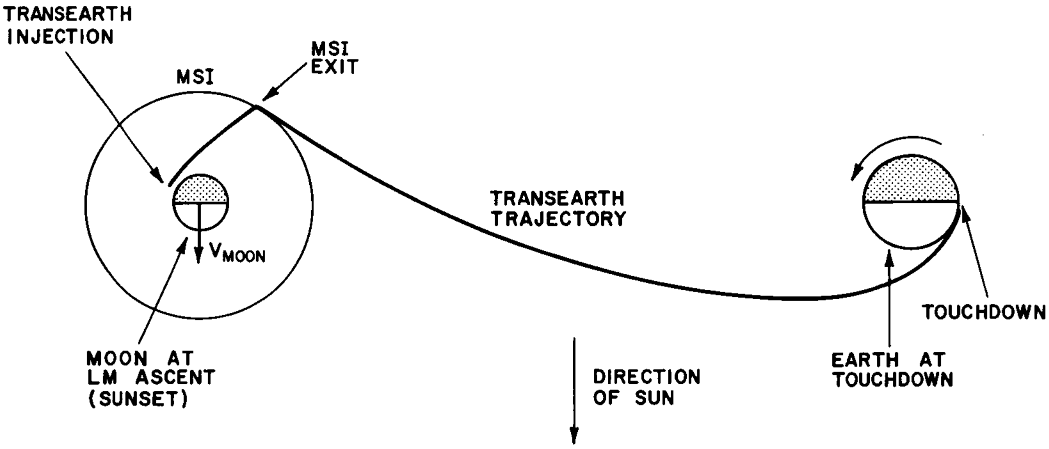
TRANSEARTH INJECTION
MSI
MSI EXIT
TRANSEARTH TRAJECTORY
V_{MOON}
MOON AT LM ASCENT (SUNSET)
DIRECTION OF SUN
EARTH AT TOUCHDOWN
TOUCHDOWN

Figure III-35. Lighting Conditions for TE Trajectory

the geometrical relationships are changed slightly if the lunar landing site is not at 0 degrees longitude, the nominal touchdown point is still near sunset.

Thus, planning for AAP recovery should take into account that the nominal earth landing for a 14-day mission will be either in darkness or shortly before while Apollo nominal touchdown will occur in the early daylight hours because of the much shorter surface stay-times. (It is noted, however, that some Apollo abort trajectories may involve nighttime recovery and that there is no Apollo constraint on lighting conditions at touchdown).

6. ORBITAL WAITING TIME AND DOUBLE IMPULSE

For a given lunar landing site and a moderately long surface stay-time, the requirement of continuous abort will generally dictate the inclination of the parking orbit. Thus, a translunar trajectory must be chosen that will establish the required orbit in the best possible way. If the free-return constraint is relaxed, a trajectory can be chosen to establish the desired orbit without a plane change at deboost. However, a no-plane-change deboost fixes the node of the parking orbit to the value of the node of the trajectory. For a given flight time, there are two possible positions for the node, one corresponding to a translunar trajectory with positive inclination and the other with negative inclination. The relationship between these two nodes, with respect to various inclination orbits (a constant flight time being assumed) can be seen by considering the locus of deboost points generated by the reference mission flown with various inclinations (Figure III-36). The resulting nodes are plotted in Figure III-37 as a function of inclination. Generally, the node required for the orbit to pass over the given landing site will not be one of the two available nodes. Thus, there is a similar desire for translunar considerations to move the node of either (or both) the parking orbit or the translunar trajectory.

For both the TL and TE cases, the desired effect can be obtained in similar ways because of symmetry. The following discussion will consider primarily only translunar trajectories, but unless otherwise noted, the remarks apply to both cases.

There are essentially three methods of establishing the desired node of the lunar parking orbit:

1. Varying time of flight.
2. Executing a plane charge.
3. Utilizing orbital waiting times.

Varying the time of flight will move the node of the translunar trajectory. Consider Figures III-36 and -38 which show the loci of deboost points for 80-hour and 110-hour flight times, respectively, for the reference mission flown at inclinations ranging from -90 degrees to 90 degrees. There is a shift in longitude toward the trailing edge of the moon for the slower trajectory. The magnitude of the shift is in the order of 30 degrees; thus, its effect is clearly limited.

There are other constraints on a large variation in flight time for the purpose of moving the node of the established orbit. The lower limit is bounded by the substantial increase in velocity requirements at deboost and translunar injection as flight time is lowered, and the upper limit is bounded by the requirements for aborting from a non-free-return trajectory.

Transearth trajectories allow a somewhat greater variation. The upper bound is set by the only requirement that the return flight is a direct flight, i.e., the transearth trajectory may not pass through apogee of the return ellipse, while the lower bound is set by the amount of fuel remaining in the SM. Also, it should be pointed out that the shift of the node is toward the leading edge of the moon as the transearth trajectory flight time decreases due to symmetry. This condition may be used in the selecting of a desirable flight time for a given set of conditions.

A second method of establishing the desired lunar orbit is by means of a plane change. The plane change may be made after the lunar parking orbit has been established without a plane change at deboost, but it is more economical to incorporate the plane change at deboost since the translunar trajectory may then be altered somewhat for optimization. The ΔV required for deboost for a given flight time depends only on the angle between the velocity vector on the translunar trajectory and that on the parking orbit at the point of intersection of the orbits because the two velocity magnitudes are constant. The intersection angle is determined by both the flight path angle difference and the angle between the planes of the two orbits. If there is no plane change at deboost, the intersection angle is zero at periselene and hence the optimum deboost point is at periselene. However, if a plane change is desired at deboost, moving the deboost point away from periselene reduces the required plane change so that even though the flight path angle difference is increased, the total intersection angle is decreased. Note that if deboost is not at periselene, the periselene radius of the translunar trajectory must then be depressed below the radius of the lunar orbit.

A plane change to move the node of the established orbit is quite expensive for high-inclination orbits. In fact, it rapidly becomes prohibitive as the inclination increases. Using a double-impulse deboost can decrease the cost of a plane change. Most of the change is made by an impulse at MSI entrance, where the spacecraft velocity is small, and the velocity magnitude is changed slightly. The deboost maneuver is then completed by a second impulse at the parking orbit and is nearly inplane. There are two reasons for the considerable saving in ΔV deboost. First, most of the plane change is made when the velocity vector is small, and second, the

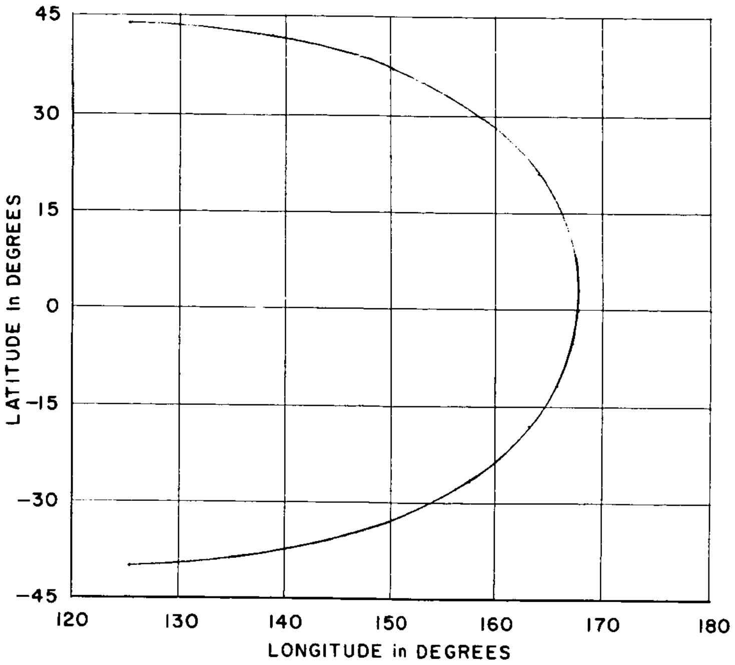

Figure III-36. Locus of Deboost Points for 80-Hour TL Trajectory

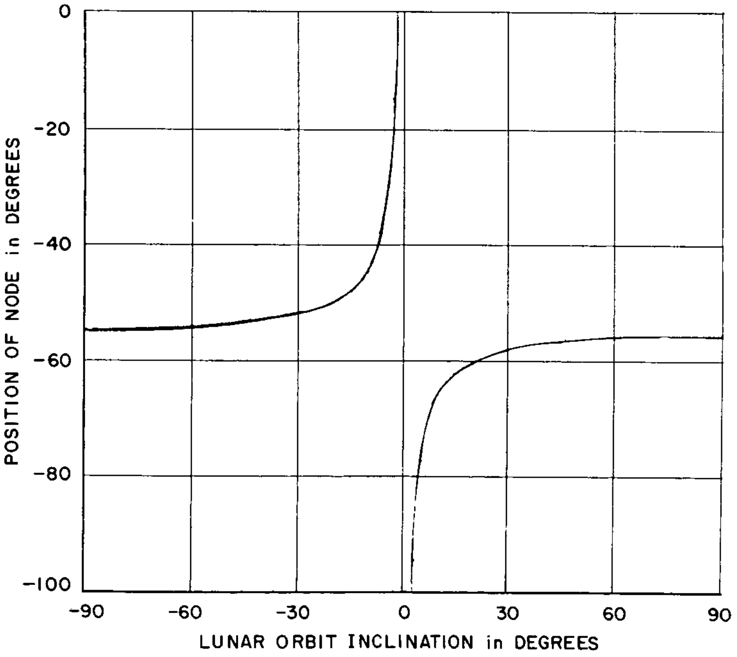

Figure III-37. Node Positions for 80-Hour Trajectory, No Plane Change at Deboost

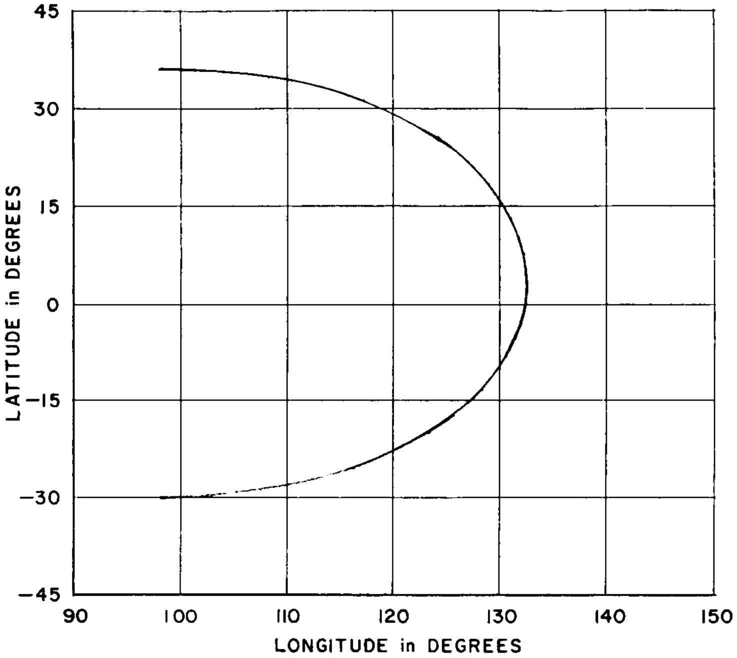

Figure III-38. Locus of Deboost Points for 110-Hour TL Trajectory

total change executed is reduced considerably. For example, the reference mission flown to a 30-degree inclination lunar orbit with ascending node at longitude 0 requires a plane change of > 33 degrees for a single-impulse deboost, but a total plane change of < 29 degrees for a double-impulse deboost. The ΔV required is thereby reduced from 4827 to 4014 fps, for a ΔV saving of more than 800 fps. In general, the ΔV saving increases as the plane change increases. For small plane changes, little or no savings will occur, and the double impulse reduces to a single impulse. The double impulse is discussed in detail in Reference 6.

The most economical way to move the node of the parking orbit is simply to wait for the moon to rotate underneath the orbit. However, a drawback to the exclusive use of orbital waiting times is that the slow rotation of the moon (13.2 degrees/day) can disproportionately increase total mission time. Another drawback affecting only transearth operations is that it may not always be possible to wait in orbit, especially if a time-critical abort is necessary.

In practice, any one of the three methods presented for obtaining the desired node is too limited to be used effectively by itself. Trade-offs consistent with the mission objectives and spacecraft capabilities must be made. For example, it may be desirable to incorporate orbital waiting times to permit relaxing somewhat the launch window constraint of lunar landing site sun angles, since predescent orbital waiting time can be adjusted to vary the time of landing.

The trade-offs available can be seen from consideration of Figures III-39 and -40. Those concerning the translunar trajectory can be inferred from Figure III-39, which shows the ΔV deboost necessary to establish a specified ascending node for the reference mission flown at various inclinations and flight times. Figure III-40 shows the corresponding curves for transearth operations, for which the date of return was taken to be approximately 7 days after deboost, i.e., August 13, 1970. In both figures, the upper curve represents the single-impulse maneuver and the lower represents the double-impulse maneuver.

Several conclusions, most of which have already been discussed, can be drawn from the curves.

1. In every case, there are two ascending nodes that can be obtained without a plane change, i.e., with minimum ΔV.
2. The location of the no-plane-change ascending nodes shifts as the flight time changes.
3. The plane change (and thus ΔV) required for a given ascending node generally increases as the inclination of the lunar orbit increases.
4. The maximum plane change required occurs when the ascending node is in the vicinity of the Earth-Moon line.

5. The double-impulse maneuver results in greater savings when the plane change is large.
6. In general, ΔV requirements for deboost decrease as flight time is increased.
7. The double-impulse manuever results in greater savings as the flight time is increased.

The possible trade-offs vary for each combination of inclination and ascending node. One example, however, can serve to illustrate possible types. Assume that a 30-degree parking orbit with its ascending node at longitude 0° is desired. The trade-offs possible are summarized in Figure III-41, where ΔV deboost represents the results of combinations of flight time and the consequent plane change. Again, the lower curve represents the double-impulse maneuver. It is interesting to note that for the single-impulse curve it is more expensive to have an orbital waiting time up to 3 days than to have none at all.

7. EFFECT OF CHANGING LUNAR PARKING ORBIT

The lunar parking orbit used for AAP may differ from that used for Apollo in several ways that may affect TL and TE trajectories.

One possible difference is the altitude of the lunar orbit, constrained to be 80 nmi for Apollo. The changes in the translunar trajectory and the associated abort costs, which have been discussed, appear to be small. Similarly, the changes in the transearth trajectory are small. For example, Figure III-42 shows that the transearth trajectory variation at injection covers a range of about 75 fps, the same range as the variation in deboost. Thus the altitude of the lunar orbit can be based on LM restrictions or operational considerations, such as CSM-LM communication time, without affecting TL and TE operations significantly.

Another possible change for the AAP parking orbit is that it may be direct rather than retrograde. A translunar trajectory resulting in a direct orbit will decrease the velocity requirements at injection and deboost under some conditions, but the ΔV saving is small. To illustrate: The reference mission flown to a direct parking orbit will require 13 fps less at translunar injection, but about 17 fps less at deboost. This difference is negligible; however, the difference in the abort requirements is not. If the spacecraft fails to deboost into a direct parking orbit, the resulting velocity at MSI exit is hyperbolic with respect to the Earth. This is because the velocity vector at periselene is in the general direction of the Moon's velocity vector, and the resultant vector sum (which is the velocity vector of the spacecraft with respect to the Earth) becomes quite large. The resulting abort requirements are 3584 fps at perigee of the hyperbola (which occurs slightly inside the Moon's orbit), compared to 742 fps for the reference mission at MSI exit. Since there does not appear to be any significant gain to be realized by a direct orbit and since the abort requirements are much higher, there does not seem to be any motivation for considering direct lunar orbits for AAP.

It is possible that the AAP parking orbit may not be constrained to be circular. Elliptical parking orbits may be desirable if, for example, large plane changes are necessary while in lunar orbit so that the ΔV required can be reduced by making the plane changes near aposelene. There can be so many combinations of aposelene, periselene, inclination, and node of the desired elliptical orbits that a general discussion of elliptical orbits would be difficult.

However, it is possible to relate the results presented earlier to elliptical orbits. If deboost into an elliptical orbit is performed inplane, at either periselene or aposelene, the translunar trajectory is identical to the corresponding translunar trajectory that results in a circular orbit with the same node and inclination, and whose radius is equal to the radius of the insertion point of the ellipse. Thus, approximate abort requirements for non-free-return trajectories terminating in elliptical orbits can be determined from the abort data presented earlier. Deboost ΔV can be computed in this case by simply subtracting the difference between elliptical velocity and circular velocity at the radius of the deboost maneuver from the ΔV required for deboost to a circular orbit with this radius.

If a large plane change is made at deboost, the translunar trajectory for an elliptical parking orbit cannot easily be related to a translunar trajectory for circular orbits. This is because the optimization procedure used for deboost into circular orbits depends on the magnitude of the radius vector being constant. For small plane changes, or for elliptical orbits with small eccentricities, a constant magnitude can be assumed in obtaining a rough approximation of the translunar trajectory characteristics. As it seems unlikely at this time that highly elliptic orbits can be used for AAP because of LM restrictions, they are not considered further in this study.

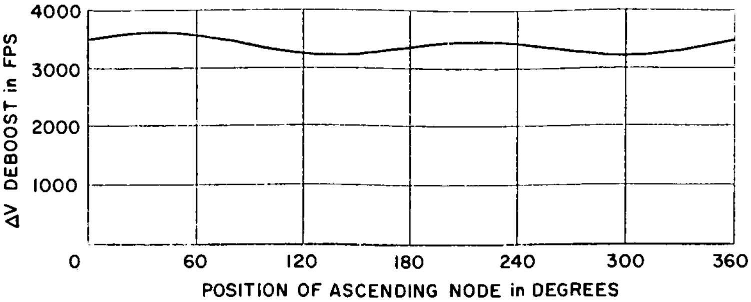

Inclination, 10 Degrees
TL Flight Time, 65 Hours

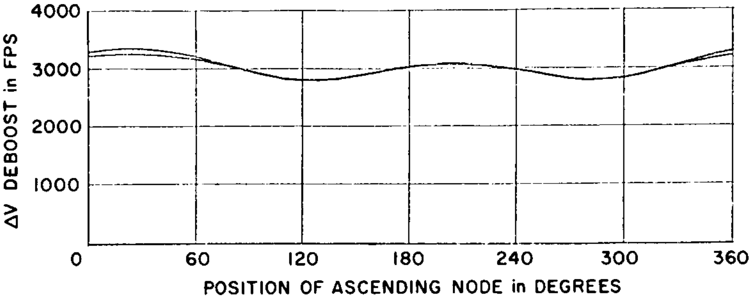

Inclination, 10 Degrees
TL Flight Time, 80 Hours

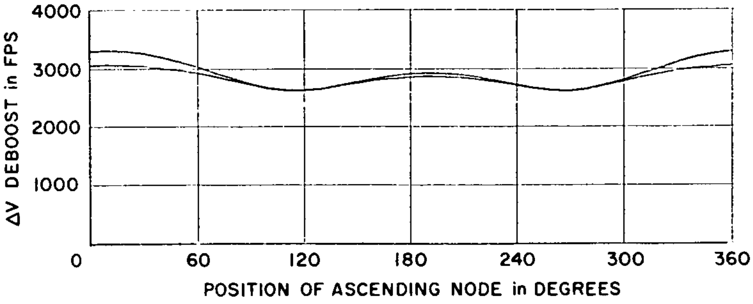

Inclination, 10 Degrees
TL Flight Time, 95 Hours

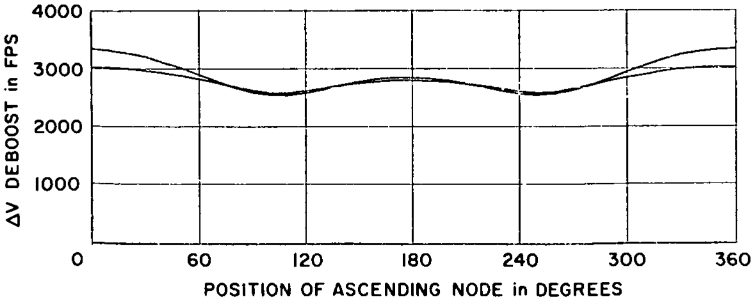

Inclination, 10 Degrees
TL Flight Time, 110 Hours

Figure III-39. Effect of Lunar Orbit Inclination and TL Flight Time on ΔV Deboost

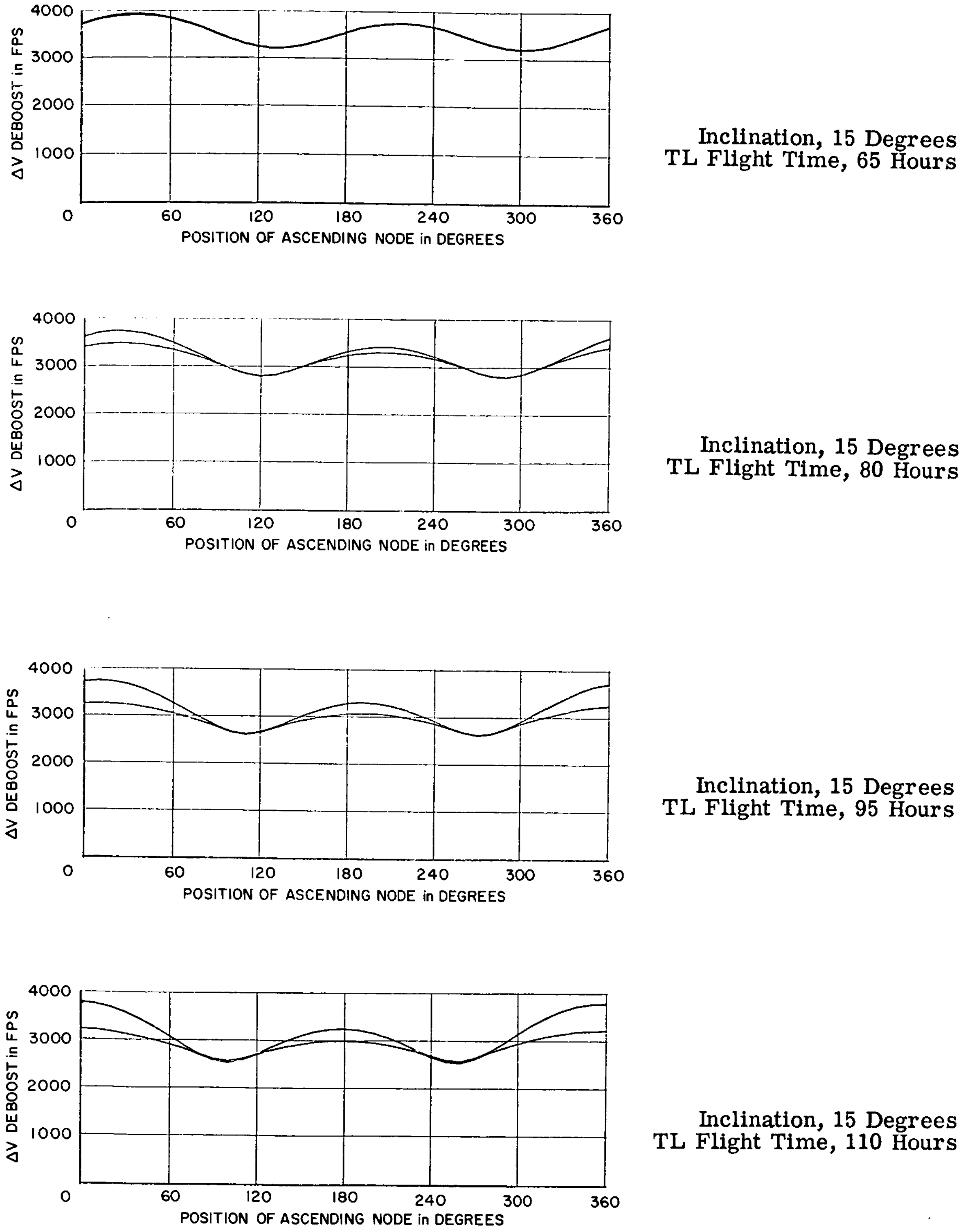

Inclination, 15 Degrees
TL Flight Time, 65 Hours

Inclination, 15 Degrees
TL Flight Time, 80 Hours

Inclination, 15 Degrees
TL Flight Time, 95 Hours

Inclination, 15 Degrees
TL Flight Time, 110 Hours

Figure III-39. Effect of Lunar Orbit Inclination and TL Flight Time on ΔV Deboost

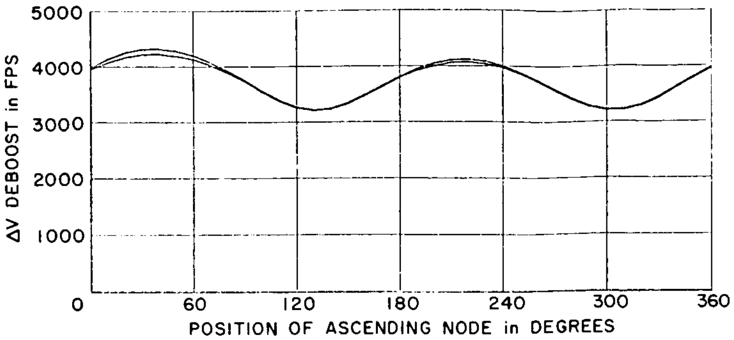

Inclination, 20 Degrees
TL Flight Time, 65 Hours

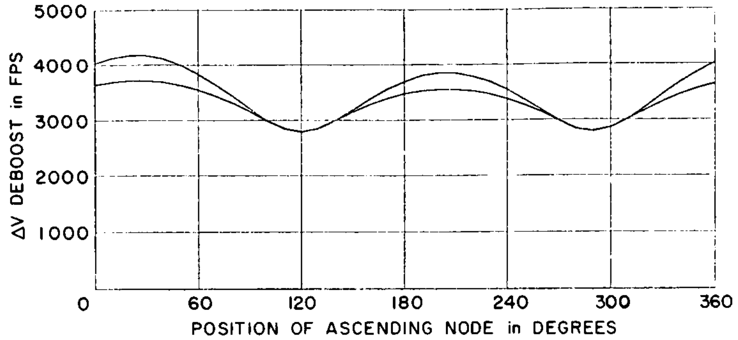

Inclination, 20 Degrees
TL Flight Time, 80 Hours

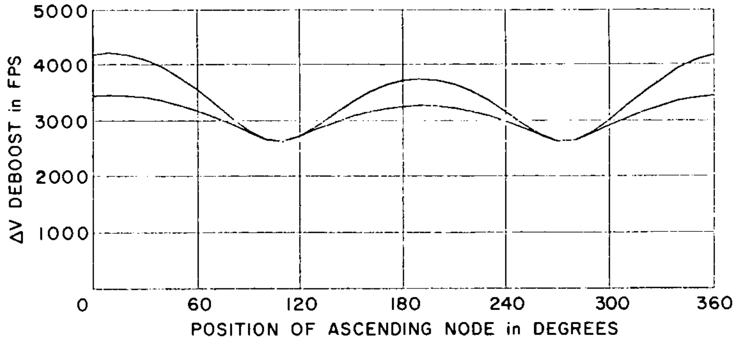

Inclination, 20 Degrees
TL Flight Time, 95 Hours

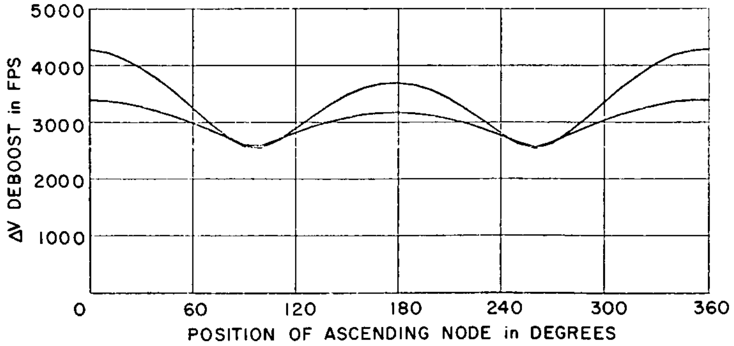

Inclination, 20 Degrees
TL Flight Time, 110 Hours

Figure III-39. Effect of Lunar Orbit Inclination and TL Flight Time on ΔV Deboost

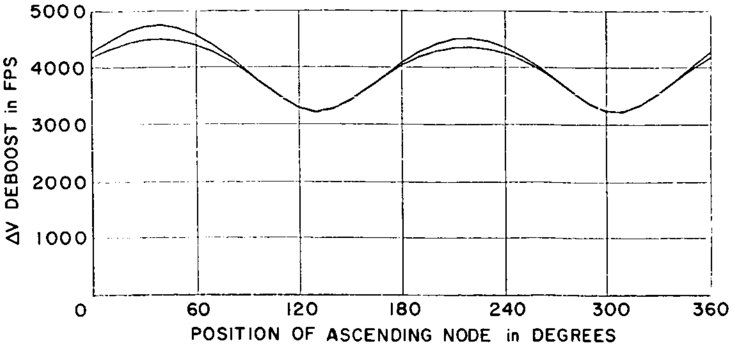

Inclination, 25 Degrees
TL Flight Time, 65 Hours

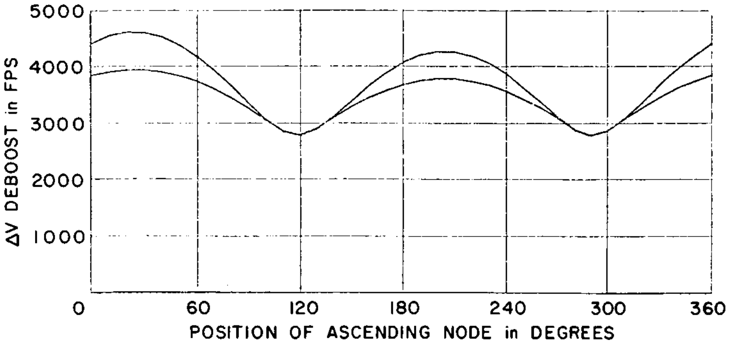

Inclination, 25 Degrees
TL Flight Time, 80 Hours

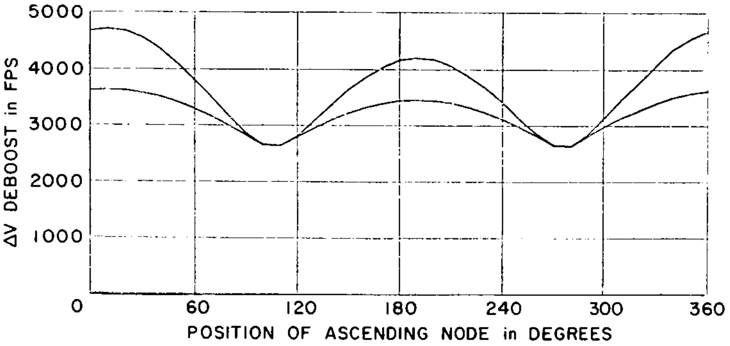

Inclination, 25 Degrees
TL Flight Time, 95 Hours

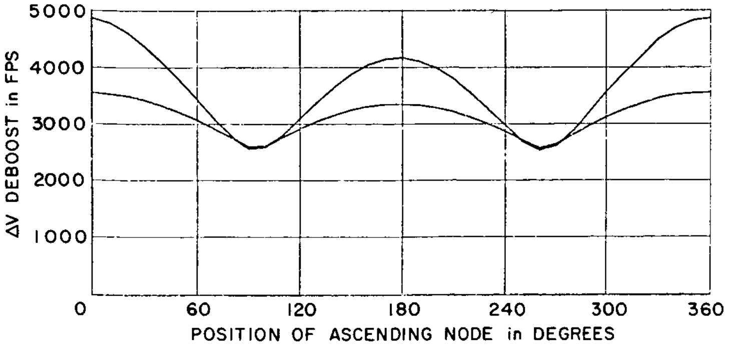

Inclination, 25 Degrees
TL Flight Time, 110 Hours

Figure III-39. Effect of Lunar Orbit Inclination and
TL Flight Time on ΔV Deboost

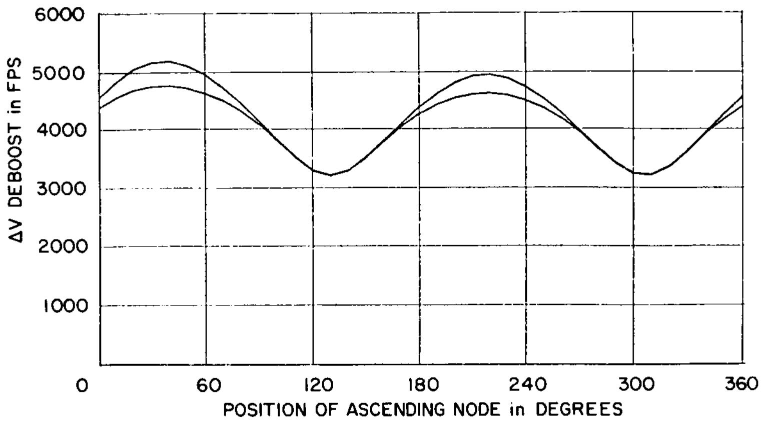

Inclination, 30 Degrees
TL Flight Time, 65 Hours

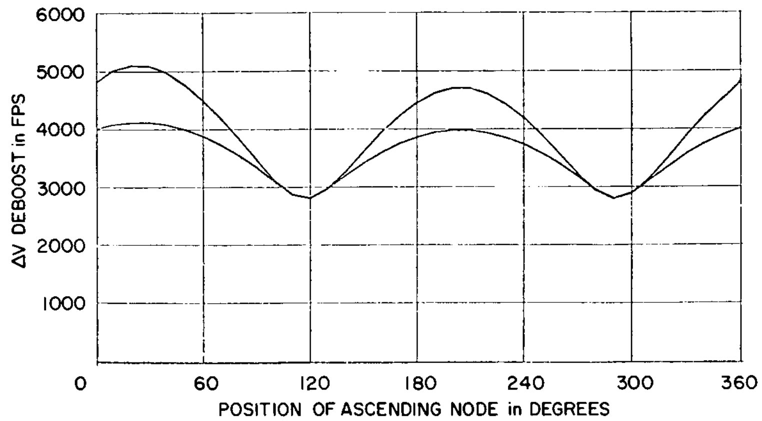

Inclination, 30 Degrees
TL Flight Time, 80 Hours

Figure III-39. Effect of Lunar Orbit Inclination and TL Flight Time on ΔV Deboost

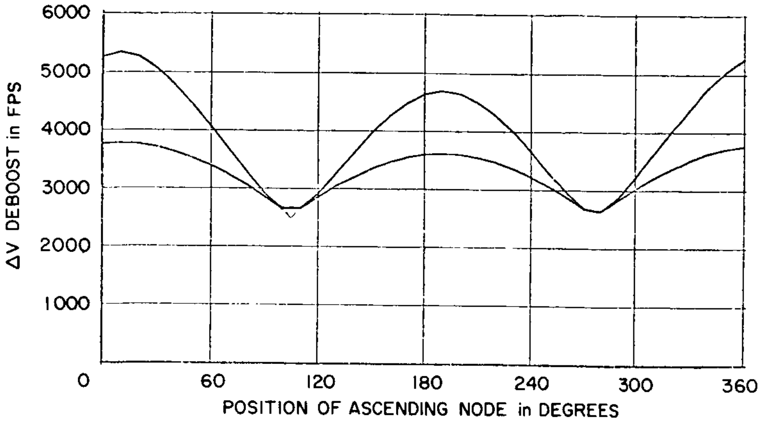

Inclination, 30 Degrees
TL Flight Time, 95 Hours

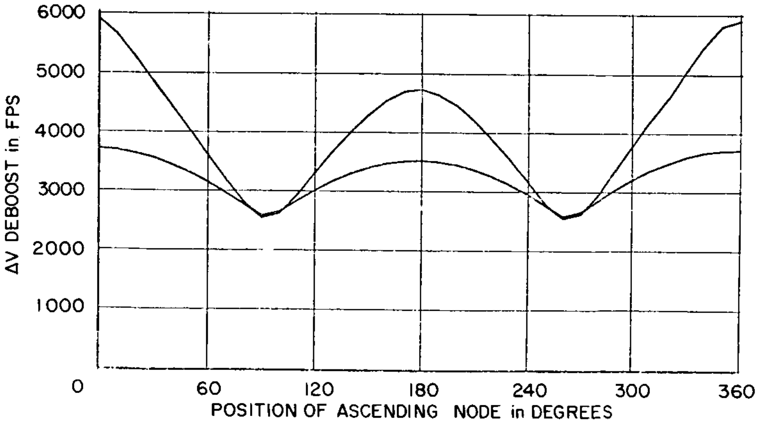

Inclination, 30 Degrees
TL Flight Time, 110 Hours

Figure III-39. Effect of Lunar Orbit Inclination and TL Flight Time on ΔV Deboost

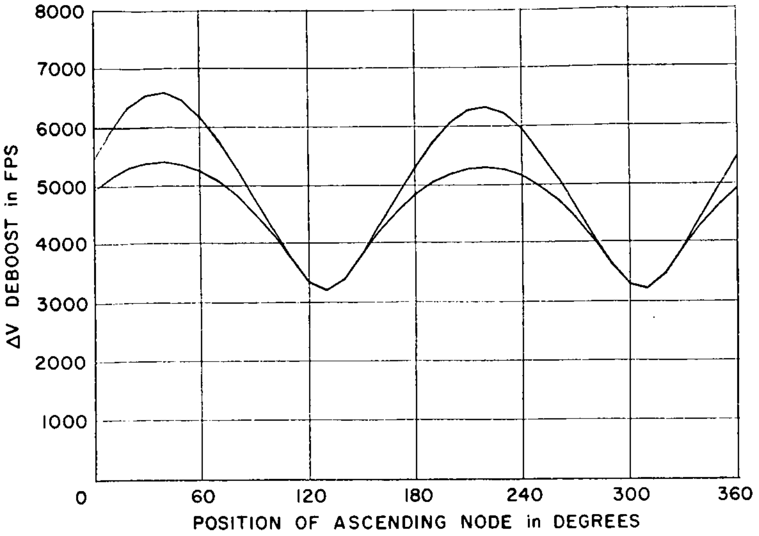

Inclination, 45 Degrees
TL Flight Time, 65 Hours

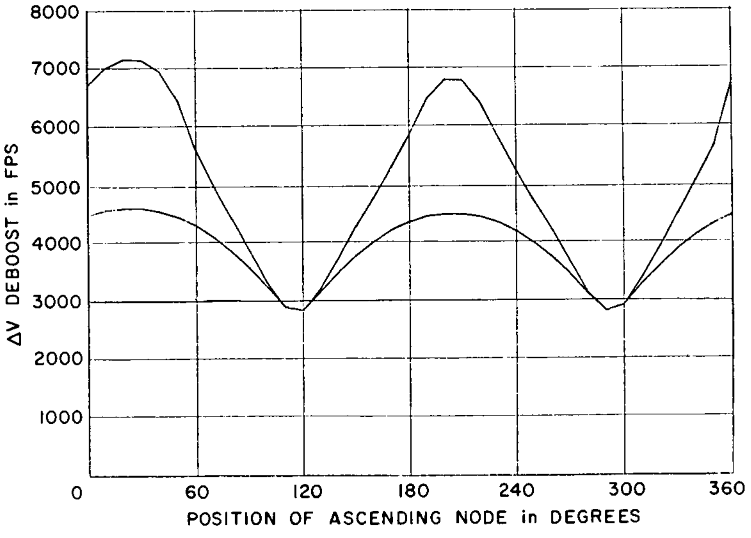

Inclination, 45 Degrees
TL Flight Time, 80 Hours

Figure III-39. Effect of Lunar Orbit Inclination and TL Flight Time on ΔV Deboost

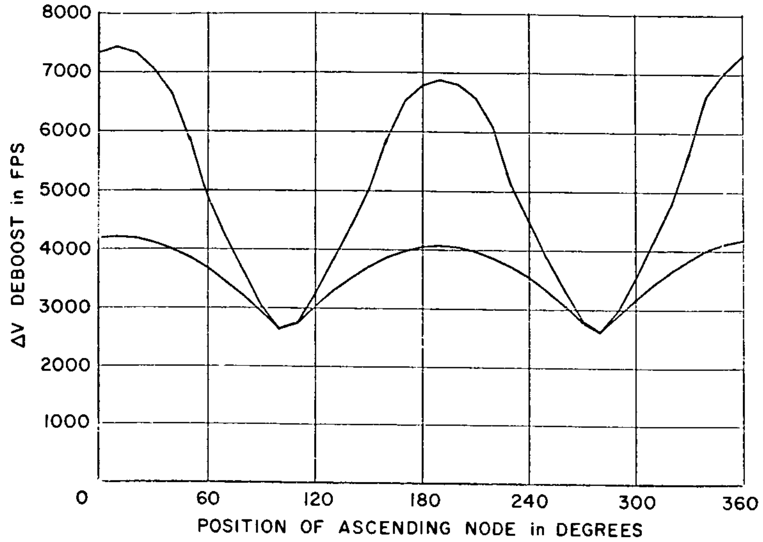

Inclination, 45 Degrees
TL Flight Time, 95 Hours

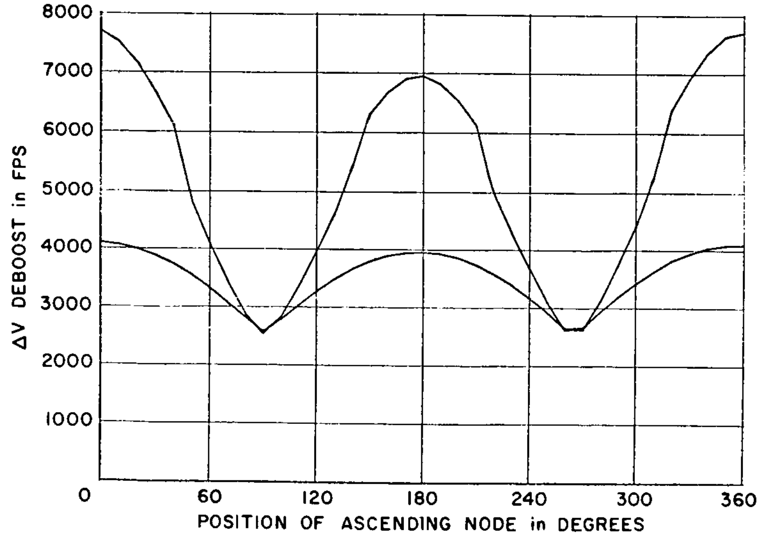

Inclination, 45 Degrees
TL Flight Time, 110 Hours

Figure III-39. Effect of Lunar Orbit Inclination and TL Flight Time on ΔV Deboost

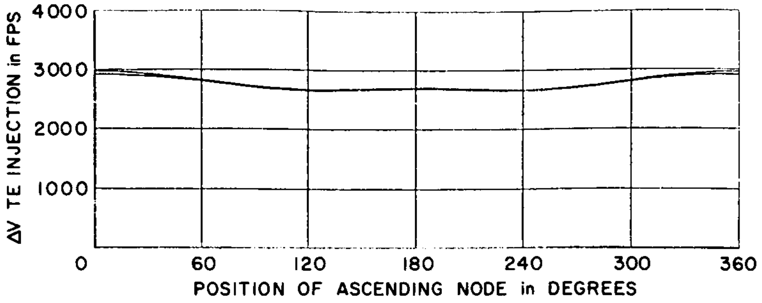

Inclination, 5 Degrees
TE Flight Time, 116 Hours

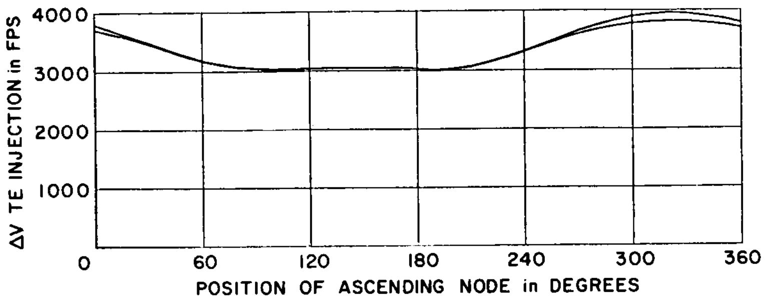

Inclination, 10 Degrees
TE Flight Time, 68 Hours

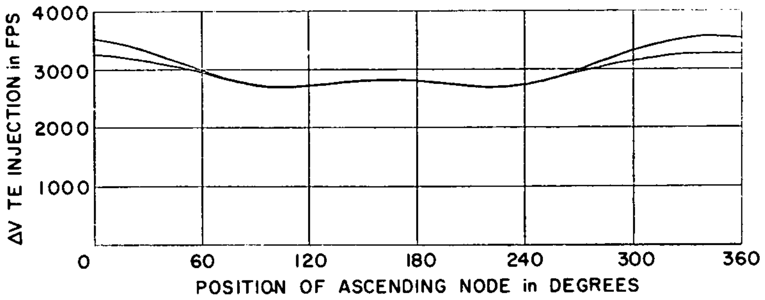

Inclination, 10 Degrees
TE Flight Time, 92 Hours

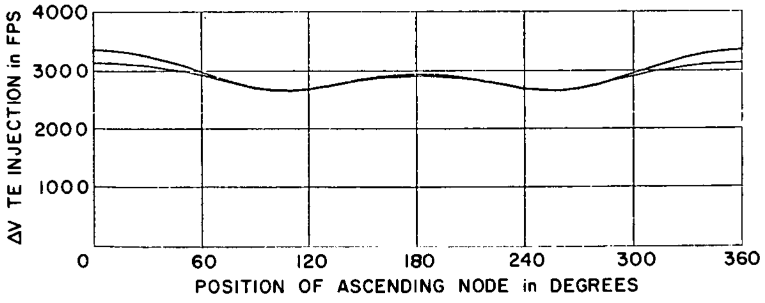

Inclination, 10 Degrees
TE Flight Time, 116 Hours

Figure III-40. Effect of Lunar Orbit Inclination and TE Flight Time on ΔV TE Injection

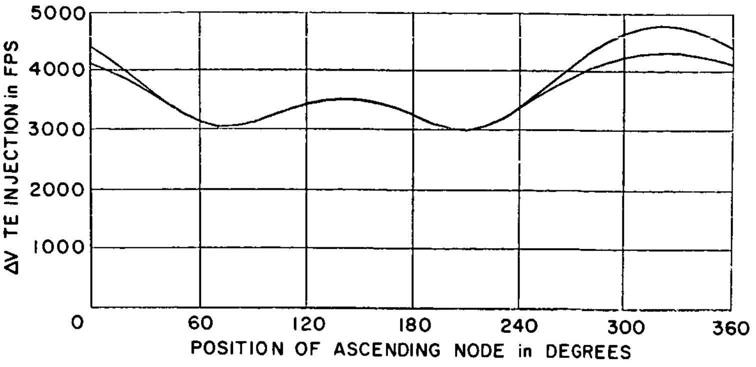

Inclination, 20 Degrees
TE Flight Time, 68 Hours

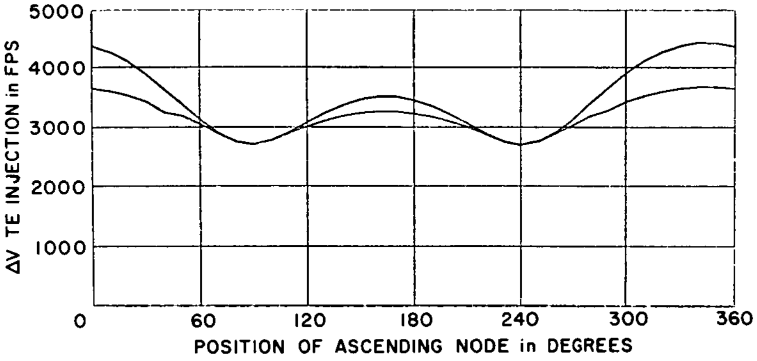

Inclination, 20 Degrees
TE Flight Time, 92 Hours

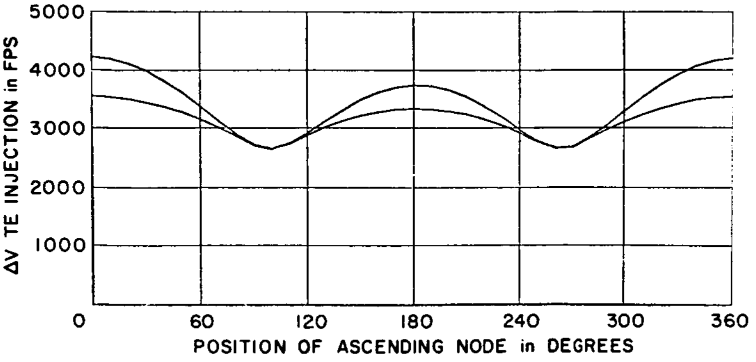

Inclination, 20 Degrees
TE Flight Time, 116 Hours

Figure III-40. Effect of Lunar Orbit Inclination and
TE Flight Time on ΔV TE Injection

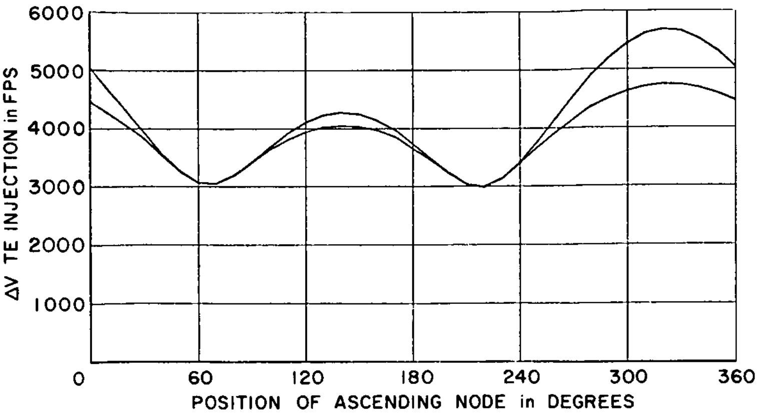

Inclination, 30 Degrees
TE Flight Time, 68 Hours

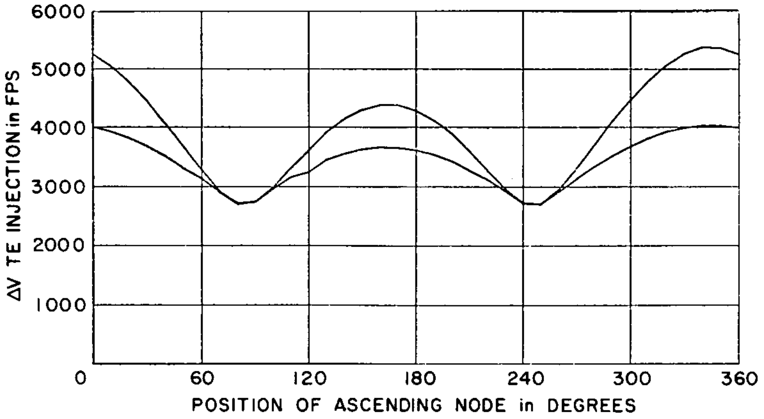

Inclination, 30 Degrees
TE Flight Time, 92 Hours

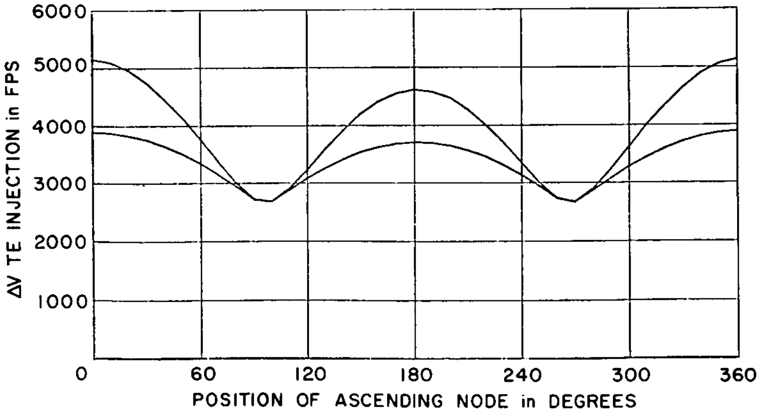

Inclination, 30 Degrees
TE Flight Time, 116 Hours

Figure III-40. Effect of Lunar Orbit Inclination and TE Flight Time on ΔV TE Injection

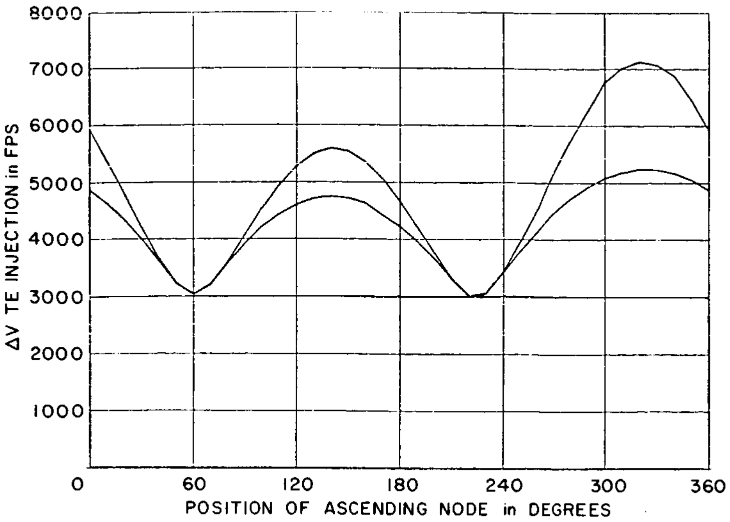

Inclination, 45 Degrees
TE Flight Time, 68 Hours

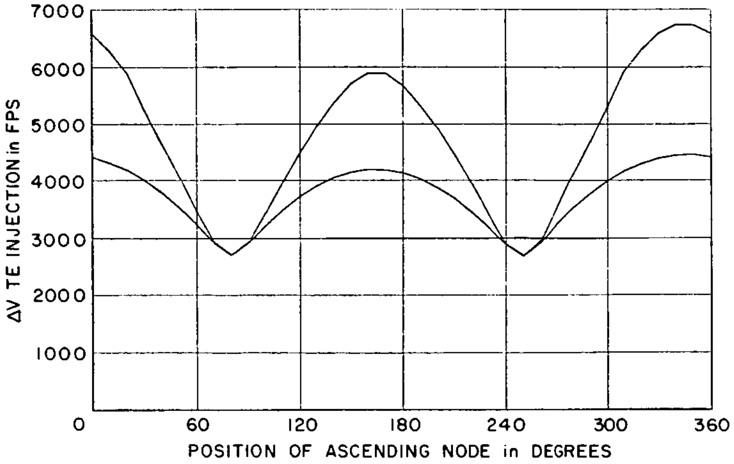

Inclination, 45 Degrees
TE Flight Time, 92 Hours

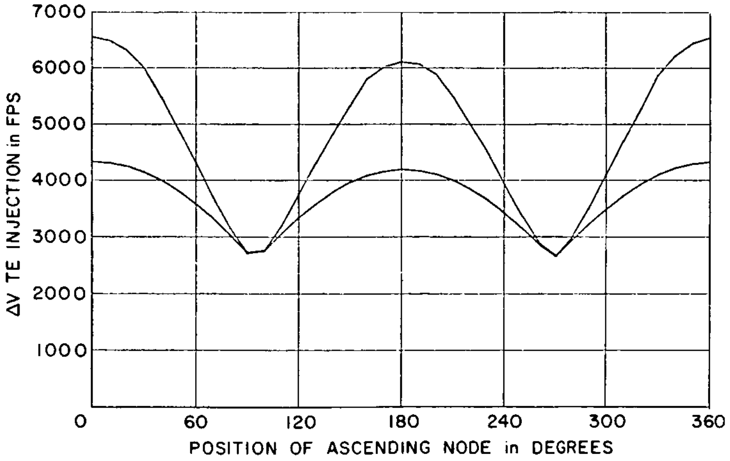

Inclination, 45 Degrees
TE Flight Time, 116 Hours

Figure III-40. Effect of Lunar Orbit Inclination and TE Flight Time on ΔV TE Injection

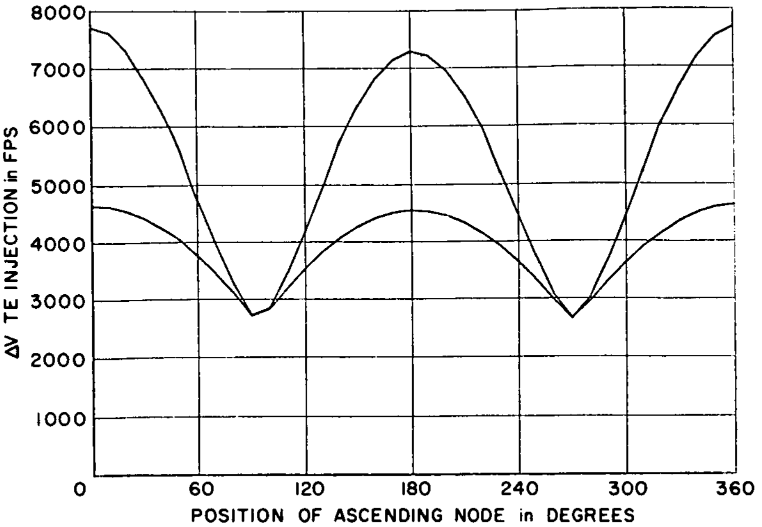

Inclination, 60 Degrees
TE Flight Time, 116 Hours

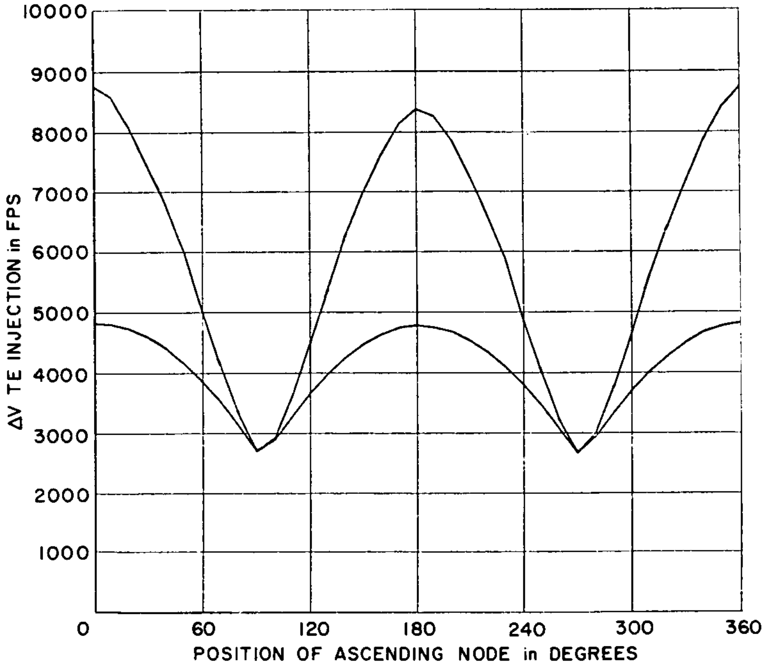

Inclination, 75 Degrees
TE Flight Time, 116 Hours

Figure III-40. Effect of Lunar Orbit Inclination and TE Flight Time on ΔV TE Injection

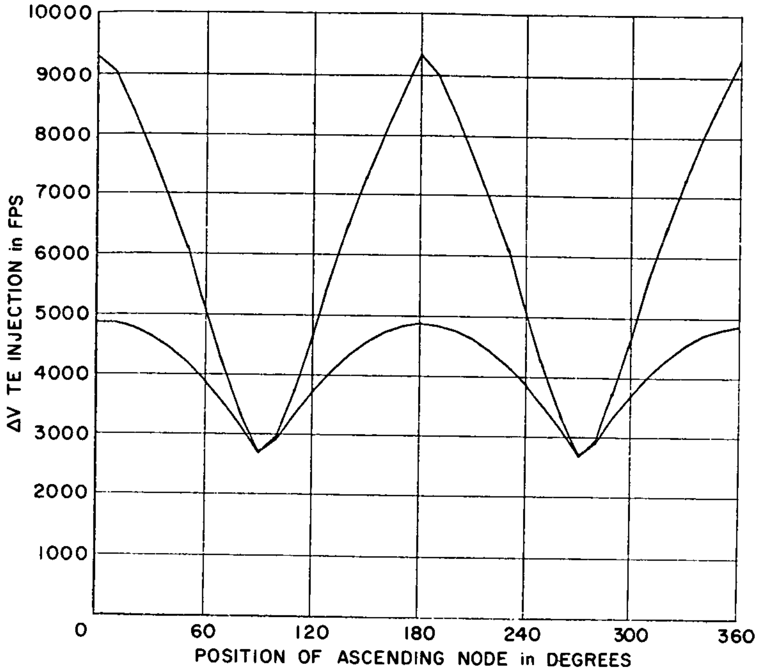

Inclination, 90 Degrees
TE Flight Time, 116 Hours

Figure III-40. Effect of Lunar Orbit Inclination and TE Flight Time on ΔV TE Injection

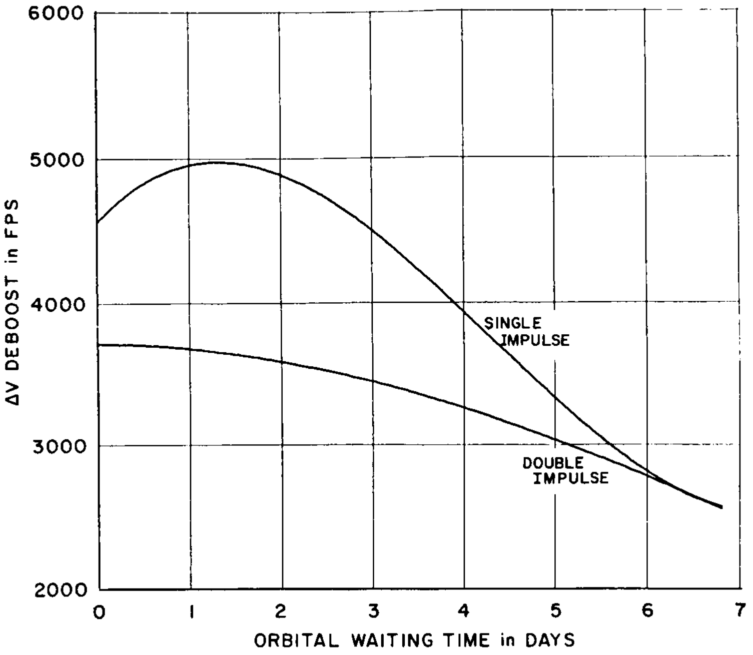

Figure III-41. Effect of Orbital Waiting Time on ΔV Deboost

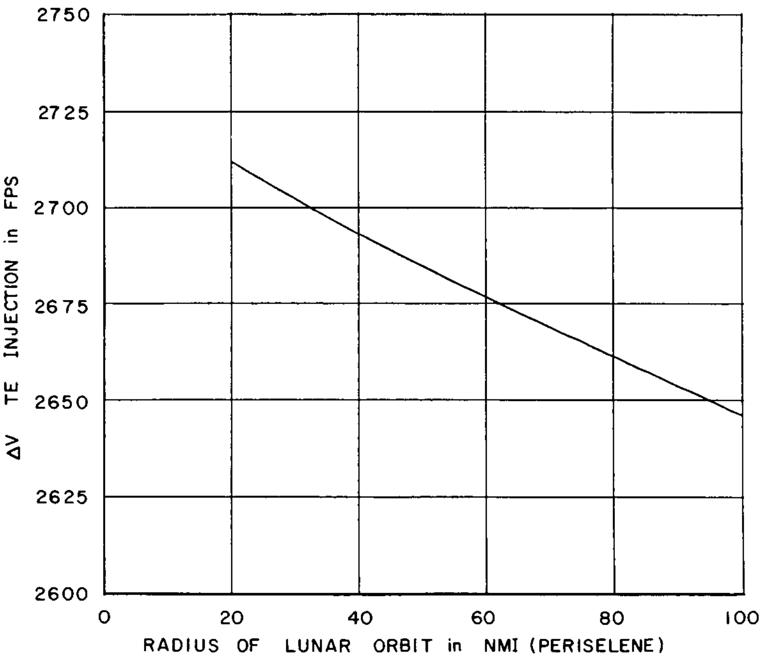

Figure III-42. Effect of Lunar Orbit Radius on TE Injection

Appendix

CALCULATION OF ΔV ABORT

The type of abort primarily considered in this study is a fuel-critical abort to an unrestricted landing site, constrained only to re-enter the earth's atmosphere with a flight path angle of -6.4 degrees. In some instances, fuel-critical aborts to a particular landing site (Hawaii) were also considered.

The method of computing the minimum ΔV abort is different for unrestricted and restricted landing sites, and each is discussed. The position of the abort, i.e., whether or not the abort trajectory passes through the MSI, also affects the method of computation, and each of these is covered. Thus, there are four categories to consider.

Cislunar Aborts — Unrestricted Landing Site

The problem of a cislunar abort can be stated as follows:

> Given the position and velocity of a spacecraft in cislunar space, find the minimum ΔV required to return the spacecraft at a safe re-entry angle to the earth.

Assume that the abort trajectory does not pass through the MSI, i.e., the spacecraft is under the influence of the Earth alone.

Let E = energy
H = angular momentum
R = position
V = velocity
α = flight path azimuth
β = flight path angle
μ_E = Earth's gravitational constant

The subscripts T and A denote the trajectory immediately before and after the abort maneuver, respectively, and the subscript R denotes the abort trajectory at re-entry. The geometry is shown in Figure III-43.

Assume that $V_A > V_T$, $\beta_A > \beta_T$, and $\alpha_A > \alpha_T$. From Figure III-44,

$$(\Delta V)^2 = V_A^2 - 2V_A V_T \cos\gamma + V_T^2 \tag{1}$$

where,

$$\cos\gamma = \cos(\alpha_A - \alpha_T)\cos(\beta_A - \beta_T) \tag{2}$$

Equation (1) is also true for $V_A \le V_T$, $\beta_A \le \beta_T$, and $\alpha_A \le \alpha_T$.

Of the three unknowns, V_A, β_A, and α_A, the first two can be related by considering the conservation of energy and the conservation of angular momentum of the abort trajectory. Conservation of angular momentum yields

$$V_A = V_R \frac{R_R \cos \beta_R}{R_A \cos \beta_A} \tag{3}$$

V_R can be found from the conservation of energy expression

$$V_R^2 = V_A^2 + 2\mu_E \left(\frac{1}{R_R} - \frac{1}{R_A}\right) \tag{4}$$

Combining (3) and (4) yields

$$V_A^2 = \frac{C_1 C_2}{\cos^2 \beta_A - C_2} \tag{5}$$

where

$$C_1 = 2\mu_E \left(\frac{1}{R_R} - \frac{1}{R_A}\right) \tag{6}$$

$$C_2 = \frac{R_R^2}{R_A^2} \cos^2 \beta_R \tag{7}$$

Note that since $R_R < R_A$, $C_1 > 0$ and $0 < C_2 < 1$.

Thus, $(\Delta V)^2$ has been reduced to a function of two variables, β_A and α_A. Minimizing $(\Delta V)^2$ will minimize ΔV. This requires that the following relationships hold:

$$\frac{\partial (\Delta V)^2}{\partial \alpha_A} = 0 \tag{8}$$

$$\frac{\partial (\Delta V)^2}{\partial \beta_A} = 0 \tag{9}$$

From (1) and (2),

$$\frac{\partial (\Delta V)^2}{\partial \alpha_A} = 2 V_A V_T \sin (\alpha_A - \alpha_T) \cos (\beta_A - \beta_T) \tag{10}$$

Equation (8) is clearly satisfied if $\alpha_A = \alpha_T$, which implies that the optimum abort trajectory will be in the plane of the pre-abort trajectory, i.e., the abort maneuver will not include a plane change. Under this condition, (1) can be rewritten

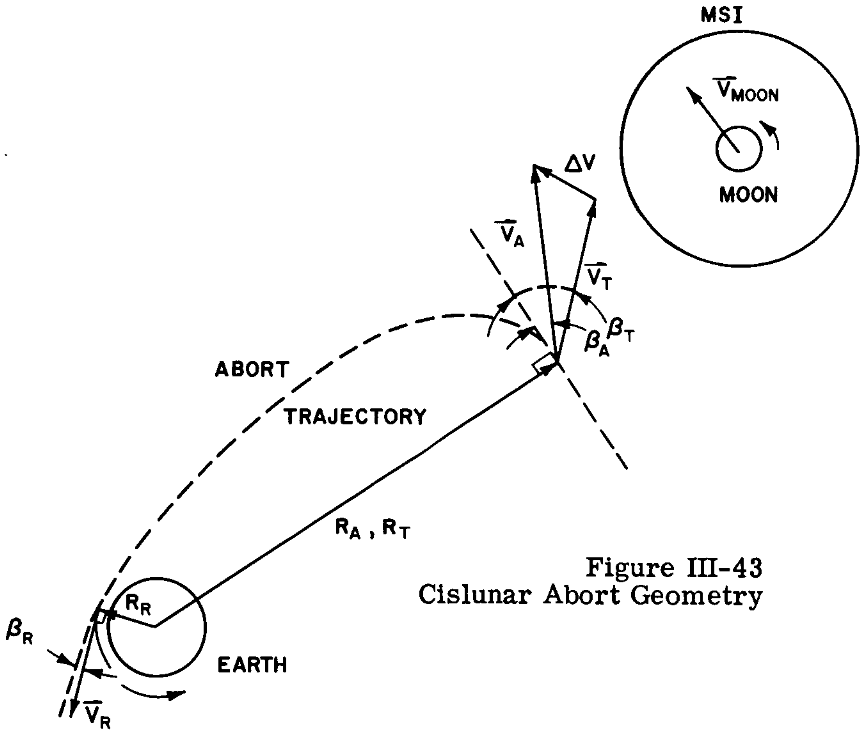
MSI
$\overline{V}_{MOON}$
MOON
ΔV
$\overline{V}_A$
$\overline{V}_T$
β_T
β_A
ABORT
TRAJECTORY
R_A, R_T
R_R
EARTH
β_R
$\overline{V}_R$

Figure III-43
Cislunar Abort Geometry

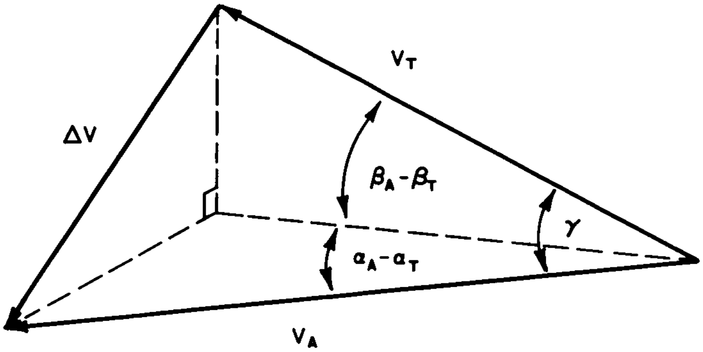
V_T
ΔV
$\beta_A - \beta_T$
γ
$\alpha_A - \alpha_T$
V_A

Figure III-44. Cislunar Abort Velocity Vectors

$$(\Delta V)^2 = V_A^2 - 2V_A V_T \cos\left(\beta_A - \beta_T\right) + V_T^2 \qquad (11)$$

Substituting (5) into (11) yields

$$(\Delta V)^2 = \left[\frac{C_1C_2}{\cos^2\beta_A - C_2}\right] - 2\left[\frac{C_1C_2}{\cos^2\beta_A - C_2}\right]^{1/2} V_T \cos\left(\beta_A - \beta_T\right) + V_T^2 \qquad (12)$$

Equation (12) can be minimized by solving for β_A such that (9) is satisfied. Equations (9) and (12) produce

$$\begin{aligned}\frac{\partial(\Delta V)^2}{\partial\beta_A} = 0 = C_1C_2 &\left[\frac{2\cos\beta_A \sin\beta_A}{\left(\cos^2\beta_A - C_2\right)^2}\right] \\ &-2\left[C_1C_2\left(\cos^2\beta_A - C_2\right)\right]^{1/2}\left[\frac{\cos\beta_A \sin\beta_A}{\left(\cos^2\beta_A - C_2\right)^2}\right] V_T \cos\left(\beta_A - \beta_T\right) \\ &+2\left[\frac{C_1C_2}{\cos^2\beta_A - C_2}\right]^{1/2} V_T \sin\left(\beta_A - \beta_T\right)\end{aligned}$$

which reduces to

$$\begin{aligned}0 = &\frac{\left(C_1C_2\right)^{1/2}}{V_T}\cos\beta_A \sin\beta_A \\ &- \left(\cos^2\beta_A - C_2\right)^{1/2}\cos\beta_A \sin\beta_A \cos\left(\beta_A - \beta_T\right) \\ &+ \left(\cos^2\beta_A - C_2\right)^{3/2}\sin\left(\beta_A - \beta_T\right) \qquad (13)\end{aligned}$$

To solve (13) for β_A, it is necessary to isolate a zero and proceed numerically. Since $\beta_T > 0$,

$$\left.\frac{\partial(\Delta V)^2}{\partial\beta_A}\right|_{\beta_A = 0} = \left(1 - C_2\right)^{3/2}\sin\left(-\beta_T\right) < 0 \qquad (14)$$

and

$$\lim_{\beta_A \to \beta'} \frac{\partial(\Delta V)^2}{\partial\beta_A} = \frac{\left(C_1C_2\right)^{1/2}}{V_T}\cos\beta' \sin\beta' > 0 \qquad (15)$$

where

$$\beta' = \cos^{-1}\left(C_2^{1/2}\right).$$

Thus a zero of (13) exists in the interval (0, β') and can be found numerically.

A test of this method was made by computing the ΔV abort needed by a free-return trajectory and a non-free-return trajectory at MSI exit. Figure III-45 shows a plot of ΔV vs. β_A, where the lower curve represents the free-return values. For the free-return trajectory, the computed ΔV abort was 4.9 fps. The ideal minimum of 0 fps could not be attained since the pre-abort trajectory would not have re-entered at exactly -6.4 degrees, but at -6.4036 degrees. The computed ΔV abort for the non-free return was 1654 fps.

Circumlunar Aborts — Unrestricted Landing Site

The problem examined here can be stated as follows:

> Given a time, position, and velocity in the vicinity of the moon (i.e., within the MSI), compute the minimum ΔV necessary to abort to a safe reentry angle, i.e., -6.4 degrees.

The resulting trajectory consists of two parts: a Moon-centered hyperbola and an Earth-centered ellipse, joined at the MSI. Since the MSI is moving in space, the patching of the two conic sections is most easily done by iteration.

The procedure (Figure III-46) is as follows: Estimate the time and position at MSI exit. Compute the required geocentric velocity at MSI exit to return at a safe re-entry angle assuming that its flight path azimuth and magnitude are given. Compute the selenocentric velocity necessary at the abort position to achieve the required MSI exit velocity, find the resulting position and time at MSI exit, and compare these to the estimated position and time. If they are within tolerances, then the required abort velocity at the abort position has been found for a given MSI exit velocity and flight path angle. Otherwise, the resulting position and time become new estimates. The process is repeated until the patching of the two conics is complete (i.e., the resulting position and time agree with their estimated values).

The first estimate of time and position at MSI exit is not critical, but a good estimate speeds convergence. Experience has shown that a good estimate will result if the given position, velocity and time (from which the abort is made) are simulated to MSI exit.

The required geocentric velocity at MSI exit can easily be computed provided its magnitude and flight path azimuth are given.

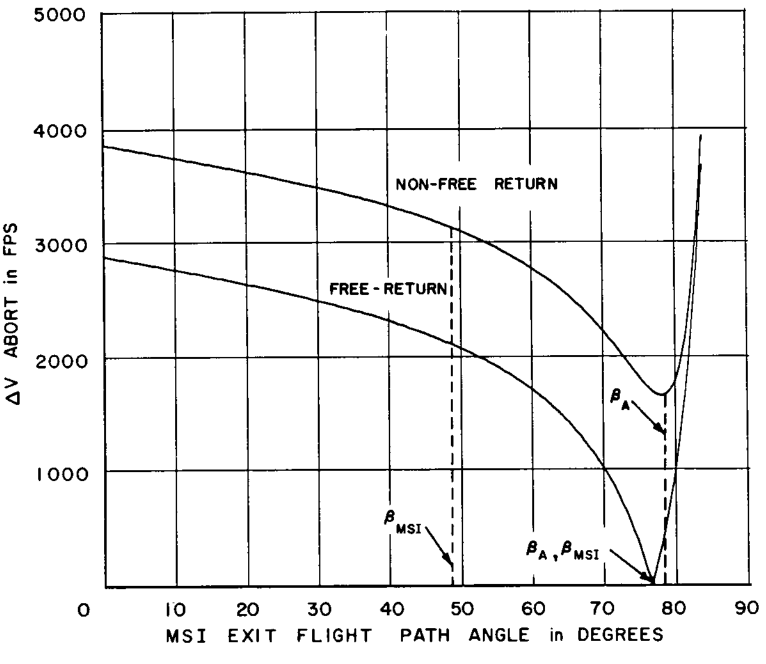

Figure III-45. Effect of MSI Exit Flight Path Angle on MS1 Exit Abort

Let V = velocity
R = position
β = flight path angle

The subscript M denotes conditions at MSI exit, and the subscript R denotes re-entry conditions. See Figure III-47. Equating energy and momentum at MSI exit and re-entry produces:

$$\frac{1}{2} V_M^2 - \frac{\mu_E}{R_M} = \frac{1}{2} V_R^2 - \frac{\mu_E}{V_R} \tag{16}$$

and

$$R_M V_M \cos \beta_M = R_R V_R \cos \beta_R \tag{17}$$

Combining (16) and (17) and solving for β_M gives

$$\cos \beta_M = \frac{R_R \cos \beta_R}{R_M V_M} \left[V_M^2 + 2\mu_E \left(\frac{1}{R_R} - \frac{1}{R_M} \right) \right]^{1/2} \tag{18}$$

Thus, the tangential and radial components of V_M can be computed as follows:

$$V_{M_t} = V_M \cos \beta_M \tag{19}$$

$$V_{M_r} = V_M \sin \beta_M \tag{20}$$

Finally, the geocentric velocity vector can be obtained as

$$\overline{V}_M = V_{M_r} \overline{r} + V_{M_t} \overline{t} \tag{21}$$

where $\overline{r}$ = unit radial vector $= \dfrac{\vec{R}_M}{|R_M|}$

$\overline{t}$ = unit vector perpendicular to $\overline{R}_M$ in the direction specified by the given flight path azimuth.

The selenocentric velocity necessary at the abort position to achieve the required MSI exit velocity (converted to a selenocentric velocity at the estimated time) is computed by iteration. Let the subscript A represent conditions immediately after abort.

From conservation of energy, the magnitude of V_A can be computed:

$$V_A = \left[V_M^2 + 2\mu_M \left(\frac{1}{R_A} - \frac{1}{R_M} \right) \right]^{1/2} \tag{22}$$

where μ_M = Moon's gravitational constant.

Furthermore, V_A must be in the plane defined by $\overline{V}_M$ and $\overline{R}_A$, whose unit angular momentum vector is

$$\overline{h} = \frac{\overline{R}_A \times \overline{V}_M}{\left|\overline{R}_A \times \overline{V}_M\right|} \tag{23}$$

The flight path angle β_A remains to be found. Two cases can occur depending on the angle η between $\overline{R}_A$ and $\overline{V}_M$, measured in the direction of the given velocity (before the abort).

If η is $<$ 180 degrees, the following expression can be derived (see Reference 3).

$$\sin\left(\eta + \beta_A\right) = \frac{1}{V_A}\left[V_M - \frac{\mu_M}{R_M V_M} + \frac{\mu_M}{R_A V_A \cos\beta_A}\right] \tag{24}$$

This expression cannot be solved in closed form and must be solved by iteration.

If η is $>$ 180 degrees, Equation (24) can be solved, but the resulting $\overline{V}_A$ obtained requires a large ΔV impulse. A much better value of β_A can be obtained by initially taking β_A as the flight path angle required for conservation of angular momentum, on the assumption that the resulting position at MSI exit is going to be the estimated position $\overline{R}_M$. Thus

$$\cos\beta_{A_0} = \frac{R_M V_M \cos\beta_M}{R_A V_A} \tag{25}$$

By the use of β_{A_0}, $\overline{V}_A$ can be found and the resulting $\overline{V}'_M$ (and $\overline{R}'_M$) computed. In general, $\overline{V}'_M$ is not equal to $\overline{V}_M$ and a correction based on the size of the error

$$\epsilon\left(\beta_A\right) = \left|\overline{V}'_M - \overline{V}_M\right| \tag{26}$$

is made to β_A:

$$\beta_{A_{k+1}} = \beta_{A_k} - \frac{\epsilon\left(\beta_{A_k}\right)}{\epsilon'\left(\beta_{A_k}\right)} \tag{27}$$

where the derivative is approximated by the first difference.

In either case when β_A is found, V_A is fully specified, and the resulting V_M and R_M can be found with standard conic section techniques. Thus, the overall result of this procedure is to compute a ΔV for a given MSI exit velocity and flight path azimuth, and the problem of minimizing ΔV abort has been reduced to the

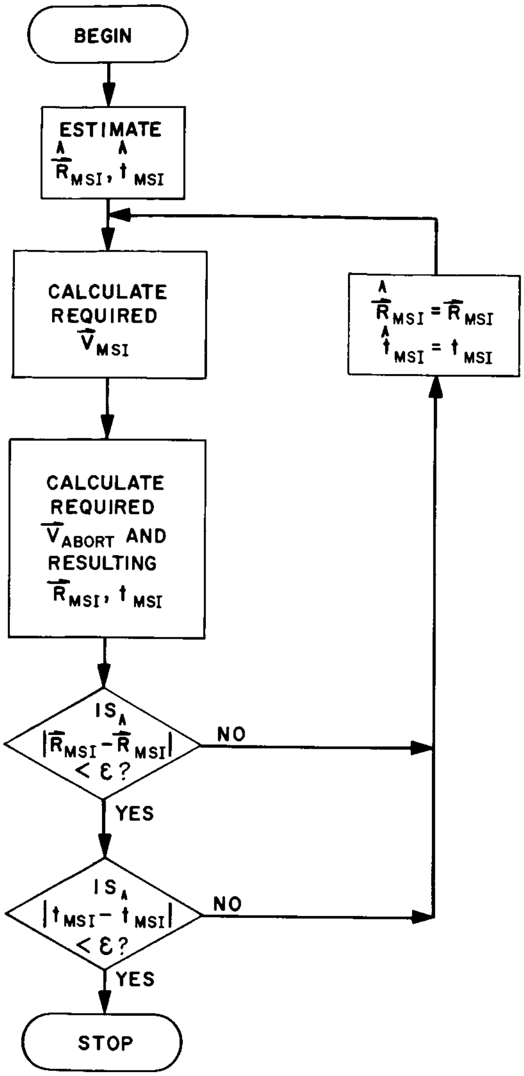
BEGIN
ESTIMATE $\hat{\bar{R}}_{MSI}, \hat{t}_{MSI}$
CALCULATE REQUIRED $\bar{V}_{MSI}$
CALCULATE REQUIRED $\bar{V}_{ABORT}$ AND RESULTING $\bar{R}_{MSI}, t_{MSI}$
IS $|\bar{R}_{MSI} - \hat{\bar{R}}_{MSI}| < \varepsilon$?
NO
YES
IS $|t_{MSI} - \hat{t}_{MSI}| < \varepsilon$?
NO
YES
STOP
$\hat{\bar{R}}_{MSI} = \bar{R}_{MSI}$
$\hat{t}_{MSI} = t_{MSI}$

Figure III-46
Circumlunar Abort Logic

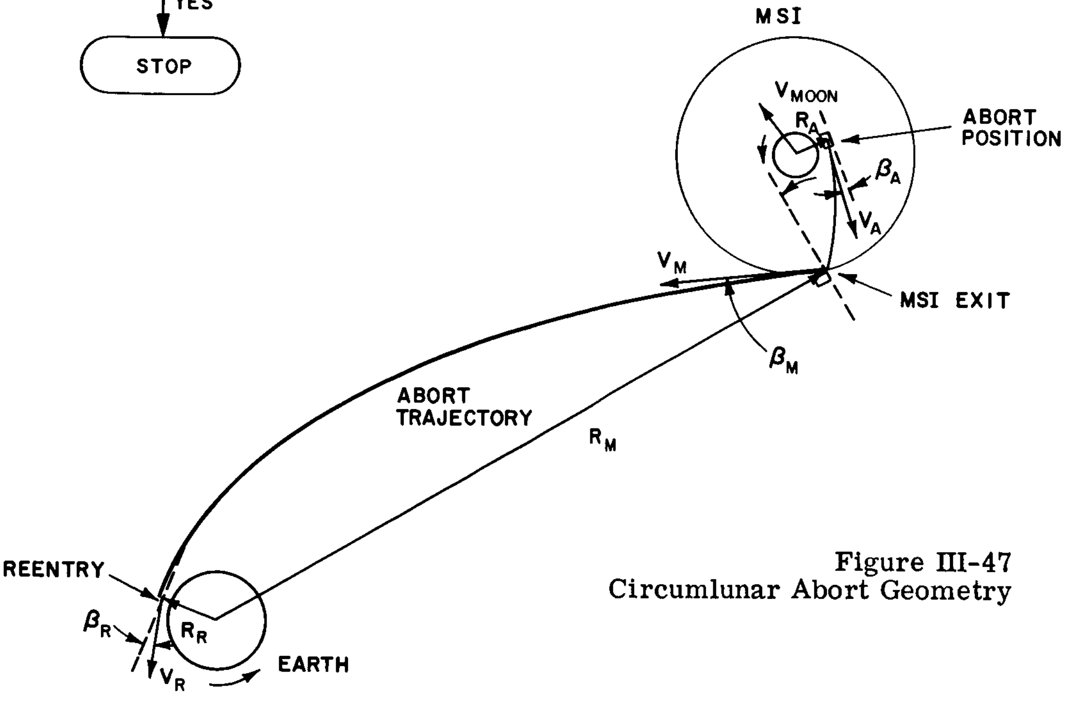
MSI
V_{MOON}
R_A
ABORT POSITION
β_A
V_A
V_M
MSI EXIT
β_M
ABORT TRAJECTORY
R_M
REENTRY
β_R
R_R
V_R
EARTH

Figure III-47
Circumlunar Abort Geometry

minimization of a function of two variables. This is most easily solved by a straightforward search.

Assume initially that the minimum ΔV abort will be inplane, and fix the MSI exit flight path azimuth accordingly. Search for the MSI exit velocity magnitude that requires the minimum ΔV (Figure III-48). When this optimum velocity magnitude is found under the inplane assumption, fix its value and search for the optimum flight path azimuth (Figure III-49). The resulting ΔV is the minimum ΔV required for abort.

A test of this method of computing ΔV abort was made by applying it to a free-return trajectory and comparing the resulting ΔV aborts to the ideal minimum of 0 fps. However, the trajectory did not return exactly to -6.4 degrees, but to -6.4036 degrees and, hence, the minimum ΔV abort was slightly more than 0 fps. The computed ΔV required at periselene was 7.1 fps and 11 fps at MSI entrance.

Cislunar Aborts — Specified Landing Site

The abort trajectory to an unspecified landing site must satisfy one constraint, namely re-entry angle. However, there are three components of the abort velocity (magnitude, flight path azimuth, and flight path angle) and thus two degrees of freedom are available for optimization. An abort to a specified landing site places two additional constraints on the abort trajectory, Earth landing site latitude and longitude, but a limited amount of optimization is still possible by varying the time of flight to vary the inertial position of the Earth landing site.

The method used is very similar to that derived in Reference 3 and thus many details are omitted. In addition to previous notations, there are

ϕ = Earth landing site latitude
λ = Earth landing site longitude
δ = declination
RA = right ascension

The re-entry angle constraint can be related to the flight path angle β_T by assuming, for the moment, that V_T is known. From Equation (18),

$$\cos \beta_T = \frac{R_R \cos \beta_R}{R_T V_T} \left[V_T^2 + 2\mu_E \left(\frac{1}{R_R} - \frac{1}{R_T} \right) \right]^{1/2} \tag{28}$$

It is shown in Reference 3 that the latitude constraint on the landing site determines the flight path azimuth α_T which is

$$\cos \alpha_T = \frac{\sin \phi - \sin \delta_A \cos \Delta f}{\cos \delta_A \sin \Delta f} \tag{29}$$

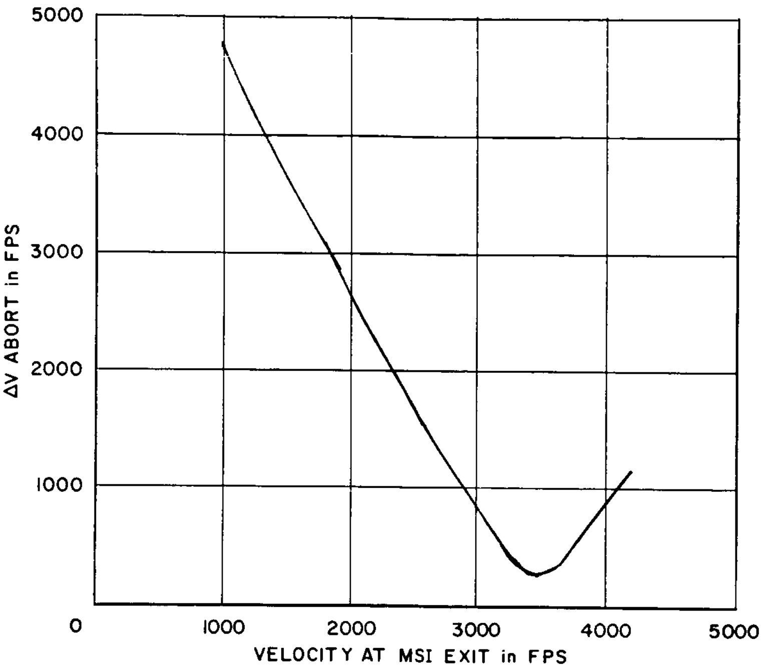

Figure III-48. Effect of MSI Exit Velocity on Periselene Abort, Inplane Abort

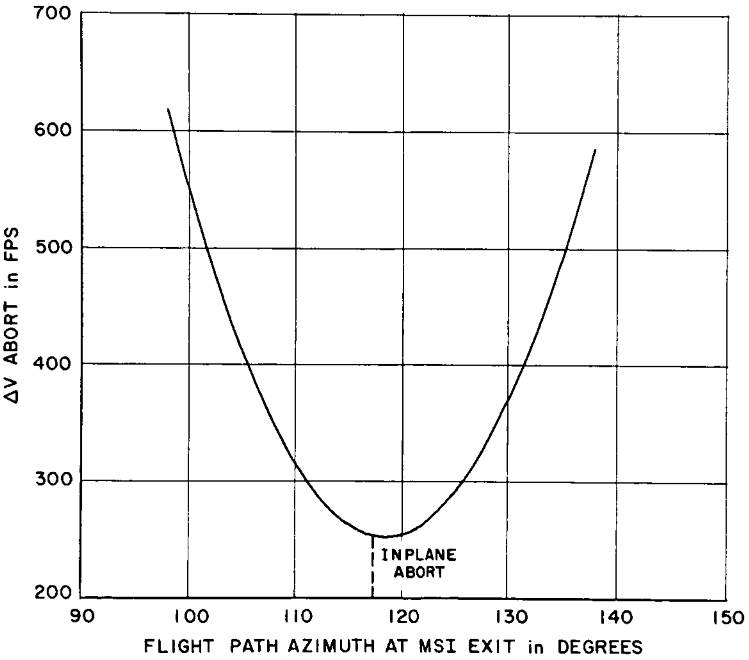

Figure III-49. Effect of MSI Exit Flight Path Azimuth on Periselene Abort, Constant MSI Exit Velocity

where Δf is the total flight arc from the abort position to Earth landing. The declination of the abort position may be found from

$$\cos \delta_A = \frac{\left(R_{A_X}^2 + R_{A_Y}^2\right)^{1/2}}{\left|R_A\right|} \tag{30}$$

and

$$\sin \delta_A = \frac{R_{A_Z}}{\left|R_A\right|} \tag{31}$$

The positive α_T satisfying (29) is used for direct returns and the negative α_T used for retrograde returns.

V_T remains to be determined from the Earth landing site longitudfrom the earth landing of RA at landing and the time of landing. At landing,

$$RA = RA_T + \Delta\lambda \tag{32}$$

where

$$RA_T = \tan^{-1}\left[\frac{R_{T_Y}}{R_{T_X}}\right] \tag{33}$$

and Δλ is given by

$$\cos \Delta\lambda = \frac{\cos \Delta f - \sin \delta_A \sin \phi}{\cos \delta_A \cos \phi} \tag{34}$$

and

$$\sin \Delta\lambda = \frac{\sin \Delta f \sin \alpha_T}{\cos \phi} \tag{35}$$

where α_T is given by (29).

The resulting landing site longitude is determined by referencing RA at landing to that of Greenwich at the time of landing. Generally, the resulting λ is not the desired landing site and a correction to V_T is needed. The correction, computed by assuming that the error is due to an error in landing time,

$$V_{T_{k+1}} = V_{T_k} - \frac{\epsilon\left(V_{T_k}\right)}{\epsilon'\left(V_{T_k}\right)} \tag{36}$$

where $\epsilon\left(V_{T_k}\right)$ is the error in landing time and the derivative is approximated by the first difference.

Note that a change in V_T results in a change in β_T [Equation (28)] and α_T (implicitly, from a change in Δf). Hence, the solution involves iteration. When the iteration has converged, i.e., the landing site longitude error is small, the velocity vector can be obtained as in Equation (21)

$$\overline{V}_T = V_{T_r}\,\overline{r} + V_{T_t}\,\overline{t} \qquad (37)$$

The time of flight from abort to Earth landing can now be adjusted by 24-hour increments to provide for a limited amount of optimization. The adjustment made becomes an adjustment in V_T according to Equation (34).

Circumlunar Aborts — Specified Landing Site

A circumlunar abort to a specified landing site is computed by using the general scheme developed for a circumlunar abort to an unrestricted landing site, which consisted of the patching together of two conics at the MSI. The difference for an abort to a specified landing site is that the required geocentric velocity vector at MSI exit is computed for a given landing site according to the equations presented in the last section. The remaining logic is unchanged. Refer to Figure III-46.

REFERENCES

1. Herbaugh, J. A., Lakamp, L. L., and Penzo, P. A., Some Trajectory Considerations for the Apollo Mission, TRW Report No. 9883.5-22, October 10, 1964.
2. Penzo, P. A., An Analysis of Free Return Circumlunar Trajectories, TRW, AIAA Paper No. 63-404, August 1963.
3. Amman, R. J., "Mission Analysis and Open-Loop Trajectory Targeting Theory for the Bellcomm Apollo Simulation Program," Bell Telephone Laboratories, Inc., MM66-4264-2, January 10, 1966.
4. Robins, H. M., An Analytic Study of the Impulsive Approximation, IBM Electronics System Center, AIAA Paper No. 66-12, January 24, 1966.
5. Rimer, M., and Treffersen, D., "Use of LEM Propulsion Systems as Backup to Service Module Propulsion System," AMPTF, Report No. LED-540-8, June 27, 1964.
6. Gunther, P., "Optimum Two-Impulse Deboost into Lunar Orbit," Bellcomm, Inc., TM-65-1011-9, March 31, 1965.

X68-84334

SECTION IV. LM LANDING

by D. C. Swanay

1. INTRODUCTION

The requirements on the AAP LM landing, whether manned or unmanned, are:

1. Retargeting the guidance system to bring the LM to the desired landing area. Landing point errors due to guidance inaccuracies can be on the order of several thousand feet for an uncorrected descent. Errors of this magnitude could seriously degrade the scientific return of a mission designed to carry out a detailed study of a particular feature.
2. After the desired landing area is reached, retargeting the guidance system to bring the LM to a hazard free landing point. This is necessary to attain a high probability of safe landing.
3. Once hover is reached, correcting position and velocity errors arising from inertial platform and landing radar errors. This operation is necessary to allow landings in relatively hazardous areas.
4. Aligning the inertial platform prior to initiation of the powered descent. This will be seen to be particularly important in the case of the unmanned landing.
5. Acquiring the Earth-based S-band antenna with the LM steerable S-band antenna.

Since the LM was designed to take full advantage of man's capabilities, these requirements can be met in a fairly straightforward fashion on the manned LM landing. The unmanned landing presents a more difficult problem. An unmanned LM landing system has been studied which provides a high probability of a safe, accurate LM landing by superposing remote command inputs on Primary Guidance and Navigation System (PGNCS) inputs. Most of the study effort has dealt with a system in which a controller located on Earth generates the remote commands based upon TV information transmitted from the LM. Some improvement in unmanned landing capability with a TV system could probably be attained by locating the controller in the orbiting CSM, rather than back on Earth. However, this alternative was not studied due to the uncertainties associated with location of a large scale TV display in the CSM.

An alternate system which updates the PGNCS with Rendezvous Radar information also appears feasible. However, this system requires the manned LM to land first, followed in a few hours by the unmanned LM. This delivery mode is not compatible with the strategy recommended in Section XI of this volume and will be discussed only briefly at the end of this report.

2. TV UNMANNED LANDING SYSTEM

Several constraints were placed on the study of a TV Command Landing System. They were designed to avoid creating more problems than were answered by the study. In particular, it was desired to avoid placing difficult new requirements on trajectory shaping, guidance, and landing site selection. Modifications to Apollo hardware and operational procedures were kept to a minimum and as simple as possible. These constraints were:

1. A descent trajectory similar to those planned for Apollo.
2. Uprange landing site redesignation capability limits similar to Apollo.
3. TV camera located near the Apollo pilot's position with similar line-of-sight restrictions.
4. TV camera driven by guidance system to the point at which guidance expects to land.
5. Landing system not to require landing sites near unusual landmarks.

It is realized that the unmanned landing problem could be made less severe by loosening these constraints. For example, TV viewing geometry could be improved by placing the camera outside the LM cabin and reshaping the descent trajectory. However, this study demonstrates the general feasibility of the unmanned landing in the more difficult case postulated above and, hence, also for the less-difficult problem obtained by loosening the constraints. The background work performed in support of the TV design specification is described in general terms, so that a new design could be attained by simple modifications of existing work should the problem be eased by lifting one or more of the above constraints. Before getting into the specification of the TV system, we must consider the capability requirements for landing point redesignation to correct PGNCS errors.

2.1 Trajectory Requirements

The AAP requirement for landing at a particular site in the presence of guidance system errors leads to requirements on landing site redesignation capability at High Gate. We required that the LM be able to reach the desired site for any guidance landing point in the guidance error ellipse at the 0.997 probability level.

An AAP descent trajectory similar to the trajectories studied for Apollo with a High Gate flight path angle of about 15 degrees is assumed. High Gate altitude and

ΔV required for the desired level of position error correction are determined. The guidance system can be taking the LM to a landing site position P_p, which is significantly different from the guidance aim point P_a, because of errors in lunar orbit navigation, descent orbit injection, powered descent, and landing site location in guidance coordinates. Reference 1* indicates that the guidance landing error ellipse has a major axis of 22,000 feet and a minor axis of 16,800 feet at the 0.997 probability level. P_a is biased uprange of the desired landing site P_d, by an amount B. Figure IV-1 gives the locus of possible landing sites P_p at which guidance could land the LM if the above errors were not corrected. Three extreme cases of guidance landing site position error are denoted by P_{p1}, P_{p2}, and P_{p3}. Consideration of these extreme cases leads to a determination of the redesignation capability required. To land the LM at P_d when the guidance system is taking it to P_{p2}, a crossrange redesignation capability of 8400 feet must be provided at High Gate. If the LM is going to P_{p3}, an uprange redesignation capability of 11,000 -B is required. If the LM is going to P_{p1}, a downrange redesignation capability of 11,000 + B is required. Uprange capability is limited by constraints on propulsion system performance and line-of-sight angle. The propulsion system cannot be operated at throttle settings above 60 percent of maximum thrust once the engine is throttled down. When the line of sight is within 25 degrees of the LM longitudinal axis, vision will be blocked by the LM window bottom and a landing pad. In determining uprange redesignation capability, we assume a requirement to maintain the line of sight 30 degrees above the longitudinal axis (5 degrees above the window bottom) when the guidance system is taking the LM to the uprange extremity (P_{p1}) of the position error ellipse. Other events causing guidance perturbations could occur in such a combination as to use up the 5-degree line-of-sight margin and cause a loss of landing site visibility during the approach. However, since a guidance landing at P_{p1} already represents a low-probability (0.003) perturbation, the probability of the combined event which would use up the 5-degree visibility margin is so low as to have no effect on capability requirements. It is assumed that the line-of-sight limit is reached at approximately the same time as the thrust limit and sets the uprange capability. Redesignation footprint data presented in Figures 35 and 36 of Reference 2 give maximum uprange capability as a function of High Gate altitude. In the computation of uprange capability, it was assumed that 10 seconds following High Gate would be required for controller determination of position errors, issuance of corrective commands, and transmission of commands. An altitude descent rate of 100 feet/second was assumed at High Gate and thus the commands did not begin to affect the LM until it was 1000 feet below High Gate altitude. This initial altitude was then used in calculations of redesignation capability and cost.

---

*References are listed at the end of the section.

Data presented in Figures 32, 35 and 36 of Reference 2 allow computation of the cost of the required position error correction capability. The cost is presented in terms of ΔV above that required for a nominal, unbiased LM descent trajectory with a High Gate altitude of 6100 feet. Since an uprange bias must be provided, a nominal LM descent would have a ΔV cost above that of a nominal, unbiased trajectory with a 6100-foot High Gate. This cost has two components – that of changing High Gate altitude and that of correcting the required uprange bias. The ΔV required for LM descent increases as High Gate altitude increases. On the other hand, the size of the bias required for correction of extreme uprange errors decreases as High Gate altitude increases (since uprange redesignation capability increases) and the ΔV cost of a given correction also decreases as High Gate altitude increases. Combination of these two effects gives a ΔV cost for a nominal trajectory, with the required bias, which is virtually independent of High Gate altitude, as shown in Figure IV-2. The figure also shows the ΔV cost of reaching P_d, for any P_p in the position error ellipse, as a function of High Gate altitude. This cost is determined by the downrange position correction requirement of 11,000 feet excluding bias for case P_{p1}, since the ΔV required to change the LM landing site from P_{p1} to P_d gives a LM redesignation capability footprint whose width is greater than the 16,800-foot width of the position error ellipse. The total ΔV required above a nominal, unbiased LM descent from a 6100-foot High Gate is then the sum of the position error correction velocity and the requirement for the nominal trajectory with the necessary uprange bias. Figure IV-2 shows that the total ΔV cost decreases monotonically as High Gate altitude increases. A High Gate altitude of 10,000 feet was chosen for landing system design purposes since this trajectory permits attainment of all of the landing objectives while allowing use of the information developed for Apollo descent trajectories. The maximum uprange redesignation capability for this trajectory is 5400 feet. Choice of the minimum bias B then places the guidance aimpoint 5600 feet uprange of the desired landing point.

The final portion of the AAP LM descent trajectory is assumed to be identical to the sample LM descent trajectory presented in Reference 3. LM altitude (H) and LM elevation at the nominal landing site (E_{LM}) are shown over the last 80 seconds before hover in Figures IV-3 and -4. LM surface range (R) and slant range (D) from the nominal landing site are then obtained from the relations:

$$R = H/\tan E_{LM}$$

$$D = \sqrt{R^2 + H^2}$$

It is assumed that the Low Gate guidance target is at the hover point, allowing use of the LPD right up to the landing site. This is consistent with current LM descent planning reported in Reference 4.

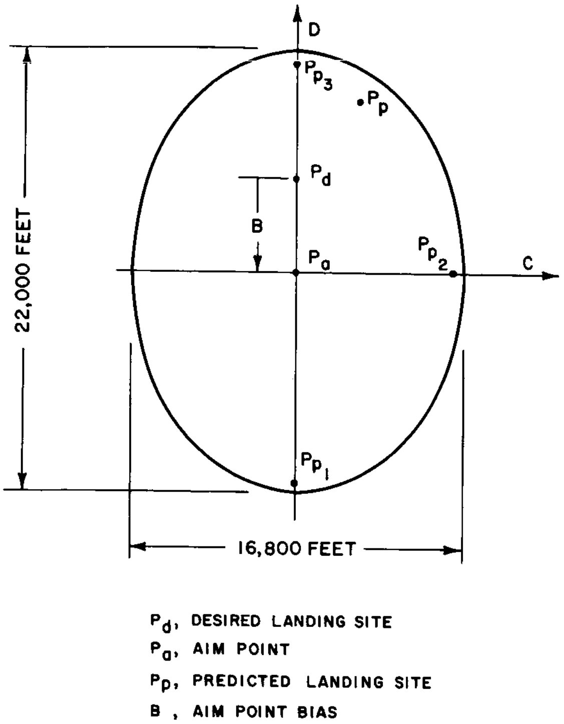
D
P_{p_3}
P_p
P_d
B
P_a
P_{p_2}
C
P_{p_1}
22,000 FEET
16,800 FEET
P_d, DESIRED LANDING SITE
P_a, AIM POINT
P_p, PREDICTED LANDING SITE
B , AIM POINT BIAS

Figure IV-1. Landing Error Ellipse

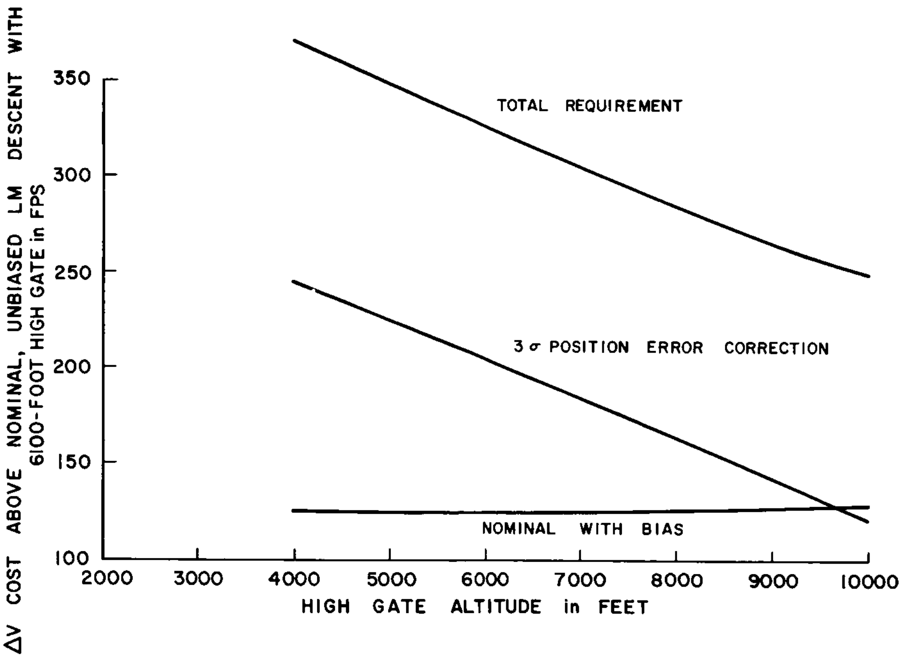

Figure IV-2. ΔV Cost of Position Error Correction over the Entire 3σ Ellipse Flight Path Angle ≃ 15 Degrees at High Gate

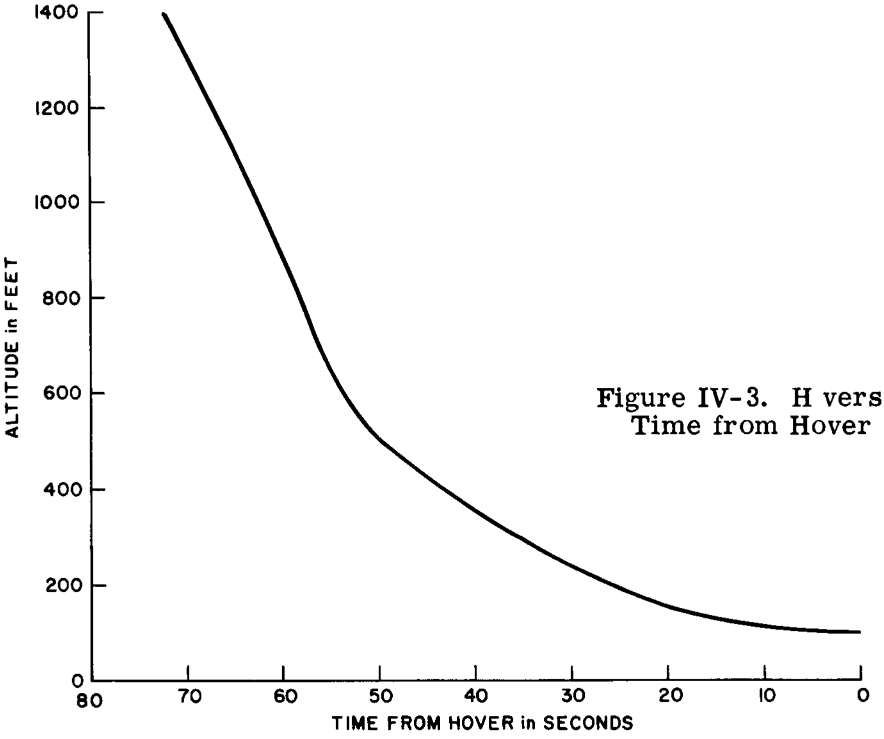

Figure IV-3. H versus Time from Hover

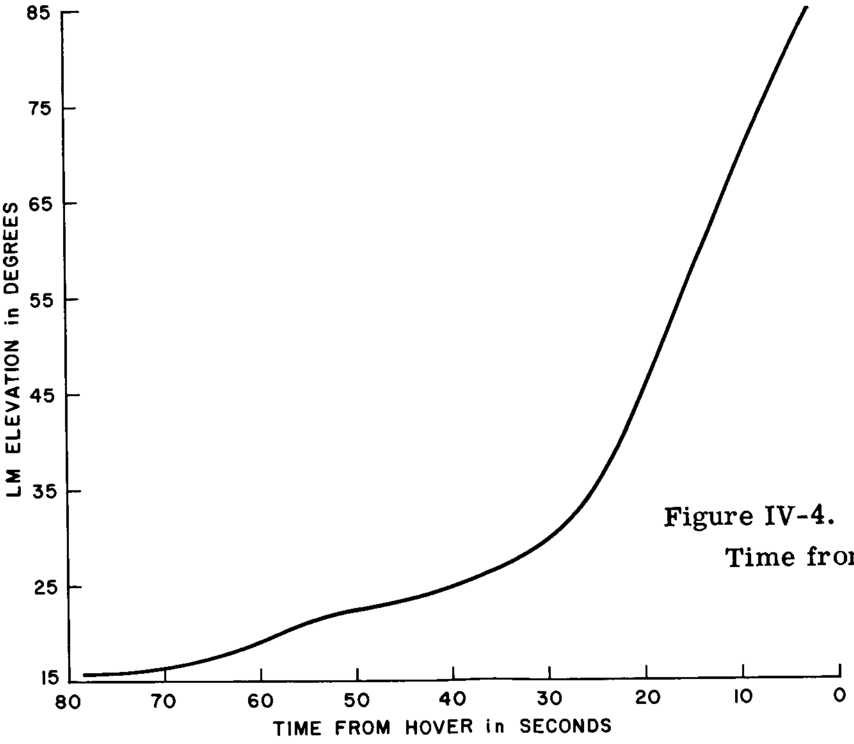

Figure IV-4. E_{LM} versus Time from Hover

2.2 Selection of TV System Parameters

The specification of TV system parameters can be divided into four steps:

1. Select a TV camera field of view which will give a scan area large enough to meet the requirements for correcting guidance system position errors and selecting a safe landing site.
2. Determine the number of lines per TV scan necessary to give the vertical resolution required for reliable perception of hazards and landmarks.
3. Select a TV frame rate which is high enough to allow object correlation from one TV frame to the next, while low enough to maintain an attainable bandwidth.
4. Determine the video frequency bandwidth required to give horizontal resolution equal to the vertical resolution.

2.2.1 TV Field of View

Position error correction – The controller gets his first view of the landing area at High Gate, approximately 2 minutes before hover. At this point the controller must ascertain where the guidance system is landing the LM relative to the desired landing site from the landmarks appearing in his TV display. He then retargets the guidance system to bring the guidance landing site to the desired landing site by using the Apollo landing point designation system. It is desirable to perform these operations as soon as possible since redesignation capability decreases and the fuel cost of a given maneuver increases as the LM descends.

The geometry of the TV field of view is shown in Figures IV-5a and -5b. It is assumed that the TV camera is driven continuously to point at the current guidance landing site P_p. An elevation field-of-view angle θ gives an along-track scan length, ℓ, in the surface plane. This is divided into uprange and downrange components, u and d. Referring to Figure IV-5, we can relate the field-of-view angles to the surface scan lengths:

$$u = S/\sin E_{LM}$$

where

$$\frac{S}{H/\sin\left(E_{LM} + \theta/2\right)} = \sin \theta/2$$

Thus,

$$u = \frac{H \sin \theta/2}{\sin E_{LM} \sin\left(E_{LM} + \theta/2\right)} \qquad (1)$$

Now, using the law of sines:

$$\frac{d}{\sin \theta/2} = \frac{D}{\sin\left(E_{LM} - \theta/2\right)}$$

Thus,

$$d = \frac{H \sin \theta/2}{\sin E_{LM} \sin\left(E_{LM} - \theta/2\right)} \tag{2}$$

$$\ell = u + d \tag{3}$$

An azimuth field of view, ψ, gives a cross-track scan length, w, in the surface plane. Neglecting the variation of pattern width as slant range varies along the scan length, we get a pattern of average width:

$$w = 2D \tan \psi/2 \tag{4}$$

L, the downrange distance at which landmarks can be perceived, is also shown on Figure IV-5a. As the controller looks downrange, his ability to perceive landmarks diminishes since his line-of-sight angle β approaches the sun elevation angle E_S. The controller's ability to distinguish landmarks is poor when $\beta - E_S$ is small, for two reasons. First, small values of $\beta - E_S$ lead to the "wash-out" phenomenon of lunar visibility, i.e., sloping surfaces reflect the same amount of light as the surrounding horizontal surface and, thus, cannot be distinguished. Second, the visible portion of landmark shadows decreases as β approaches E_S due to line-of-sight blocking by the surface casting the shadow. In fact, no shadows at all are visible when $\beta - E_S \leq 0$.

The elevation field-of-view, θ, was chosen on the basis of providing as much landmark information as possible to the controller while minimizing the bandwidth required. The ability to see the landmark craters is a function of sun elevation angle, line-of-sight angle and crater size. As the location of a given crater moves lower in the field of view, the line-of-sight angle to the crater increases and a greater portion of its shadow can be seen. Thus, to ease the requirements on sun angle and landmark crater size, it is desirable to have u as large as possible. However, the desire to minimize the bandwidth implies that no useless information should be transmitted which, in our case, would happen when any portion of the TV beam is below the LM window bottom. When the maximum uprange redesignation is required (guidance taking the LM to P_{p3} in Figure IV-1), the line of sight is close to the window bottom, being only 5 degrees above it after the maneuver is completed. This worst case represents the minimum angular separation between line-of-sight and window bottom for landing points in the position error ellipse. Thus, if the elevation field of view is chosen to have a half-angle ($\theta/2$) of 5 degrees, the maximum uprange scan length possible without transmitting useless information (the window bottom) will be attained for the worst case.

A sun elevation angle of 10 degrees is assumed for our sample mission. Then, at High Gate on the sample trajectory (E_{LM} = 15 degrees), no landmark shadows would be visible at the downrange extremity of the TV scan. Landmark crater visibility would be poor over most of the downrange portion of the scan. Thus, to be conservative, L = 0 was chosen for the visibility limit of Figure IV-5a.

To correct for navigation system errors, the controller must first recognize the location of P_p relative to P_d. He is required to do this by looking at landmark crater patterns. Since an L = 0 has been set, the TV scan must be made wide enough so that the scan area uprange of P_p at High Gate is sufficiently large to allow the controller to quickly determine the location of P_p relative to P_d by looking at landmarks uprange of P_p.

An experiment was performed to determine the scan area required to enable a trained controller to determine this relative location by a quick examination of crater patterns at High Gate. The scan area required was determined as a function of the size of the smallest crater visible to the controller. This minimum visible size depends on the resolution of the TV system. Figure IV-6 illustrates the situation the controller must deal with at High Gate. The dashed ellipse represents the area over which the controller must be able to recognize crater patterns. This area is generated by moving that portion of the TV scan used by the controller for landmark recognition (since we have taken L = 0, the usable portion of the scan is the area uprange of P_p of area u x w) along with the locus of possible camera aim points. Since the camera is pointed at the current guidance landing site, this locus is just the position error ellipse. A crater distribution typical of that presented to the controller for pattern recognition is shown in Figure IV-6. Computer-generated maps of randomly placed craters of diameter greater than the minimum visible value were used as a basis for the pattern recognition experiment. This was consistent with the requirement that no unusual landmarks need be at or near the desired landing site. A crater density typical of maria areas was used. A mask representing usable scan area presented to the controller was placed over the crater map. To be conservative, it was assumed that the controller's action would be based on information in the scan area available to him 10 seconds after High Gate. The length u of the usable area was determined from Figure IV-7, which relates the scan lengths on the surface 10 seconds after High Gate to the angular field of view, according to Equations (1), (2), (3), and (4). An elevation field of view θ = 10 degrees gives an u = 9000 feet. The w was varied by the experimenter to obtain an area (u x w) containing enough visible craters to allow pattern recognition regardless of the field of view location. The experiment was repeated for a range of minimum visible crater sizes, for several different crater maps, and for several different experimenters. The averaged results are presented in Figure IV-8. The cross-hatched area represents the combinations of minimum visible crater size and field of view for which it is reasonable to expect that a controller could be trained to recognize crater patterns regardless of the location of his field of view. The field

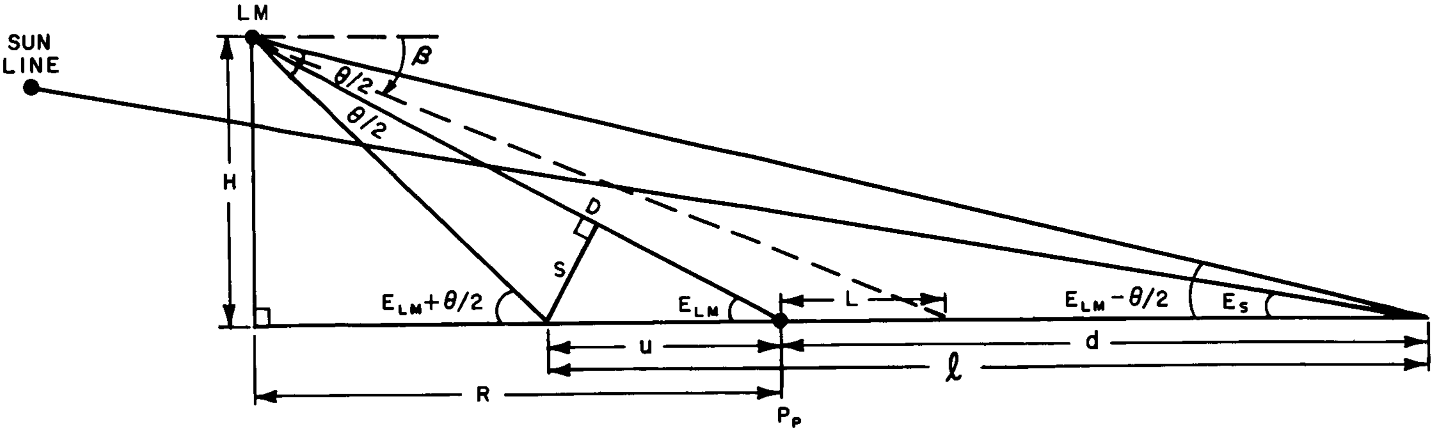
LM
SUN
LINE
β
θ/2
θ/2
H
D
S
$E_{LM}+\theta/2$
E_{LM}
L
$E_{LM}-\theta/2$
E_S
u
d
ℓ
R
P_P

Figure IV-5a. TV Field-of-View Geometry in Along-Track (H-R) Plane

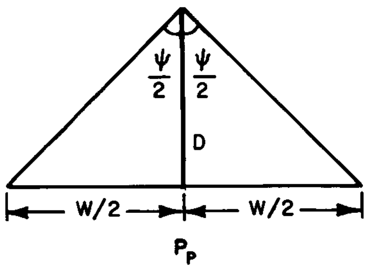
ψ/2
ψ/2
D
W/2
W/2
P_P

Figure IV-5b. TV Field-of-View Geometry in Cross-Track Plane

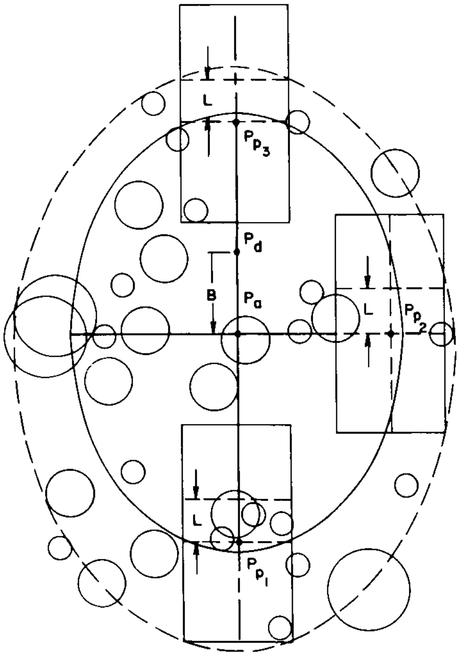
L
P_{P_3}
P_d
B
P_a
L
P_{P_2}
L
P_{P_1}

Figure IV-6. Field of View on Error Ellipse

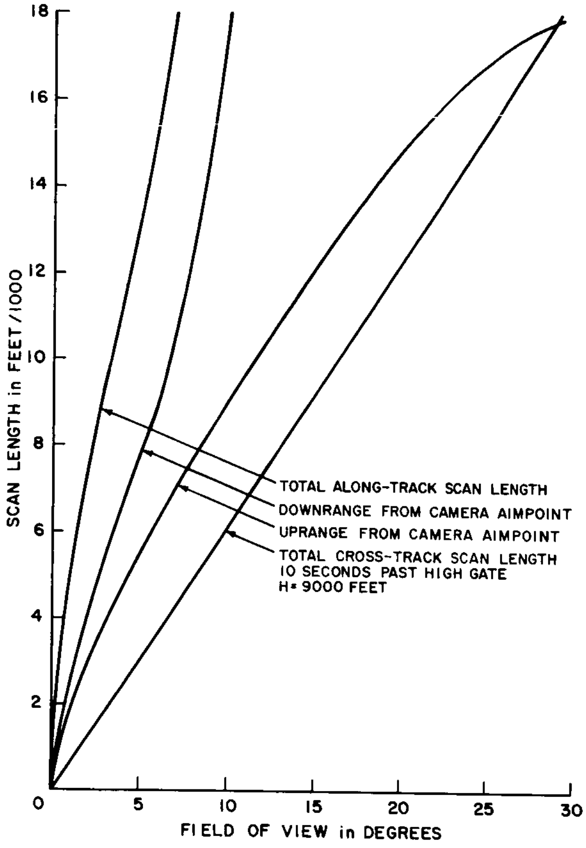

Figure IV-7. Scan Length versus Field of View 10 Seconds Past High Gate

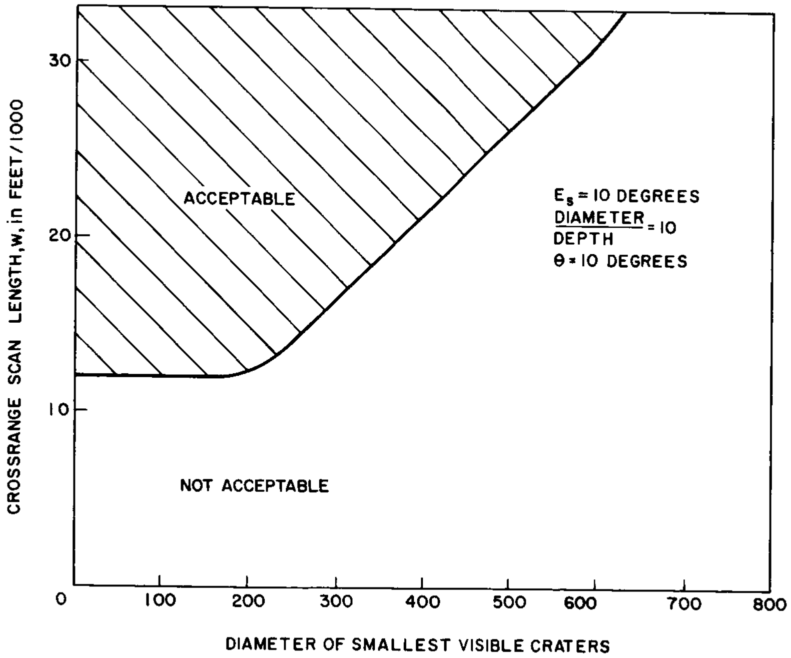

Figure IV-8. Crossrange Scan Required for Landmark Pattern Recognition

of view required generally decreases as the minimum visible crater size decreases and more pattern information becomes available. However, for minimum visible crater diameters below 200 meters, the controller could not be expected to quickly recognize the location of the TV camera aimpoint (which is identical to the current guidance landing site) in a smaller field of view because there are too many possible patterns to memorize. Thus, he would ignore the smaller craters and look only for patterns made up of the larger craters. Figure IV-8 then indicates that the minimum acceptable value of w is 12,000 feet. From Figure IV-7 it is seen that this corresponds to an azimuth field of view of 20 degrees. Use of the minimum value of w to specify ψ assumes that TV system resolution is such that the minimum visible crater size is 200 meters or smaller. This assumption will be verified later.

The assumption of a high degree of controller skill in landmark recognition was implicit in the criterion for acceptable scan area used in the experiment. It was assumed that sufficient area for pattern recognition was provided as soon as all possibility of pattern ambiguity was removed. In this case, pattern ambiguity means that similar patterns could be presented to the controller for two different locations of the TV camera aimpoint in the error ellipse. It is reasonable to expect that a controller could be trained to perform the pattern-recognition task very well. A model of the landing area can be constructed, based on Lunar Orbiter information, as soon as the desired landing site is selected and the controller can be trained and tested under the same conditions of lunar visibility and TV system resolution to be encountered during the flight.

It should be noted that the controller's ability to order crossrange redesignations to the right might be impaired by blockage of the landing site by the right side of the window. This problem could be resolved either by moving the camera centerline left of the design eye point or by providing a crossrange bias. The most-conservative estimate of the size of the bias gives a crossrange requirement still within the capability provided by the ΔV of 250 feet/second allotted for position error correction.

To summarize, a TV camera field of view of 10 degrees in elevation by 20 degrees in azimuth provides sufficient scan area to meet the AAP requirements on position error correction at High Gate.

Safe landing site selection — The camera field of view must also give a scan area large enough to ensure a high probability that a safe landing area will be included in the scan when all landing hazards become visible. All landing hazards must be visible to the controller 50 seconds before hover. The choice of 50 seconds was based on a consideration of bandwidth required as a function of time from hover. (This tradeoff is developed later in this discussion.) Figure IV-9 relates surface scan length to TV camera field of view 50 seconds before hover. It is seen that

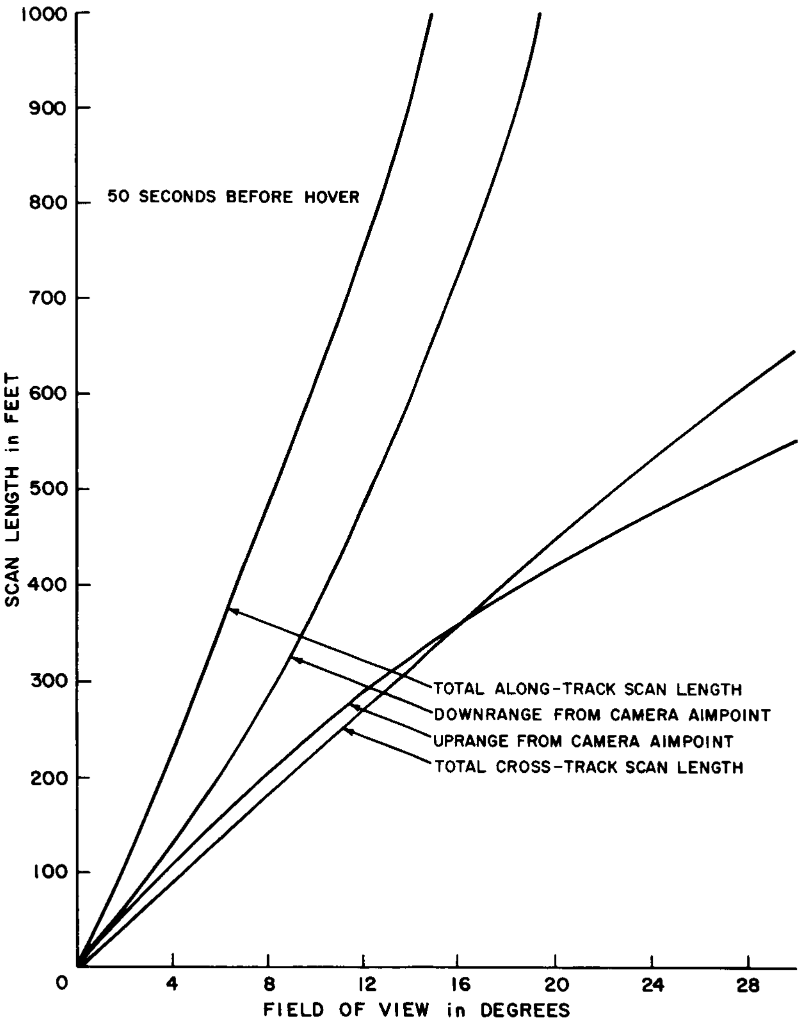

Figure IV-9. Scan Length versus Field of View 50 Seconds before Hover

the 10- by 20-degree field of view required for position error correction gives a 620- by 460-foot scan pattern.

A 0.99 probability that at least one safe landing site is included in the scan area will be required. The scan area size required to attain this probability is a function of LM landing uncertainty footprint size and the hazard density. First, we determine p, the probability that a circle of diameter D is hazard-free. This was done experimentally by using the computer-generated maps of randomly placed craters. The crater locations were chosen according to a uniform probability distribution which agrees well with observations. Two crater-size distributions were used. One was based on Ranger 7 observations made in Mare Cognitum and is referred to as the "smooth" hazard density case. The other was based on Ranger 9 observations in the crater Alphonsus and is referred to as the "intermediate" hazard density case.

To find p as a function of footprint diameter D, the crater diameters in the distribution were all increased by D and a 1-km^2 surface generated. Any point on the surface not covered by an "increased-size" crater then represented a point on which a landing footprint of diameter D could be centered without impinging on a hazard, i.e., the center point of a hazard-free landing site. Under the assumption of a uniform probability distribution, the ratio of non-covered area to total area on our map was then equivalent to the probability that an arbitrarily placed landing footprint of diameter D was hazard-free. This was the desired probability p.

The ratio of non-covered area to total area was found by mechanically measuring the non-covered area on the map. This procedure was carried out for both the smooth and the intermediate cases. For illustration, Figure IV-10 presents a 200- by 200-meter segment of the map, with increased-size craters corresponding to a 60-foot footprint diameter and the smooth hazard density case. Figure IV-11 gives the probability p as a function of D for the two hazard densities considered.

The probability that there are no hazard-free landing sites in the scan area A is equal to the probability q that there are no hazard-free circles of diameter D in the same area. To simplify the determination of this probability, the D-diameter circles are replaced with squares of side D. This simplification results in a somewhat conservative determination of required scan area. Now q becomes the probability that there are no hazard-free squares of side D in the scan area. This probability is equal to the one that we cannot find a hazard-free square of side D in any subdivision of the scan area into squares of this size. An arbitrary subdivision of the scan area A into squares is shown in Figure IV-12. In any subdivision, the number of squares is A/D^2. To find the probability that the subdivision contains no hazard-free squares, let us assume that the hazard-free probability for any square

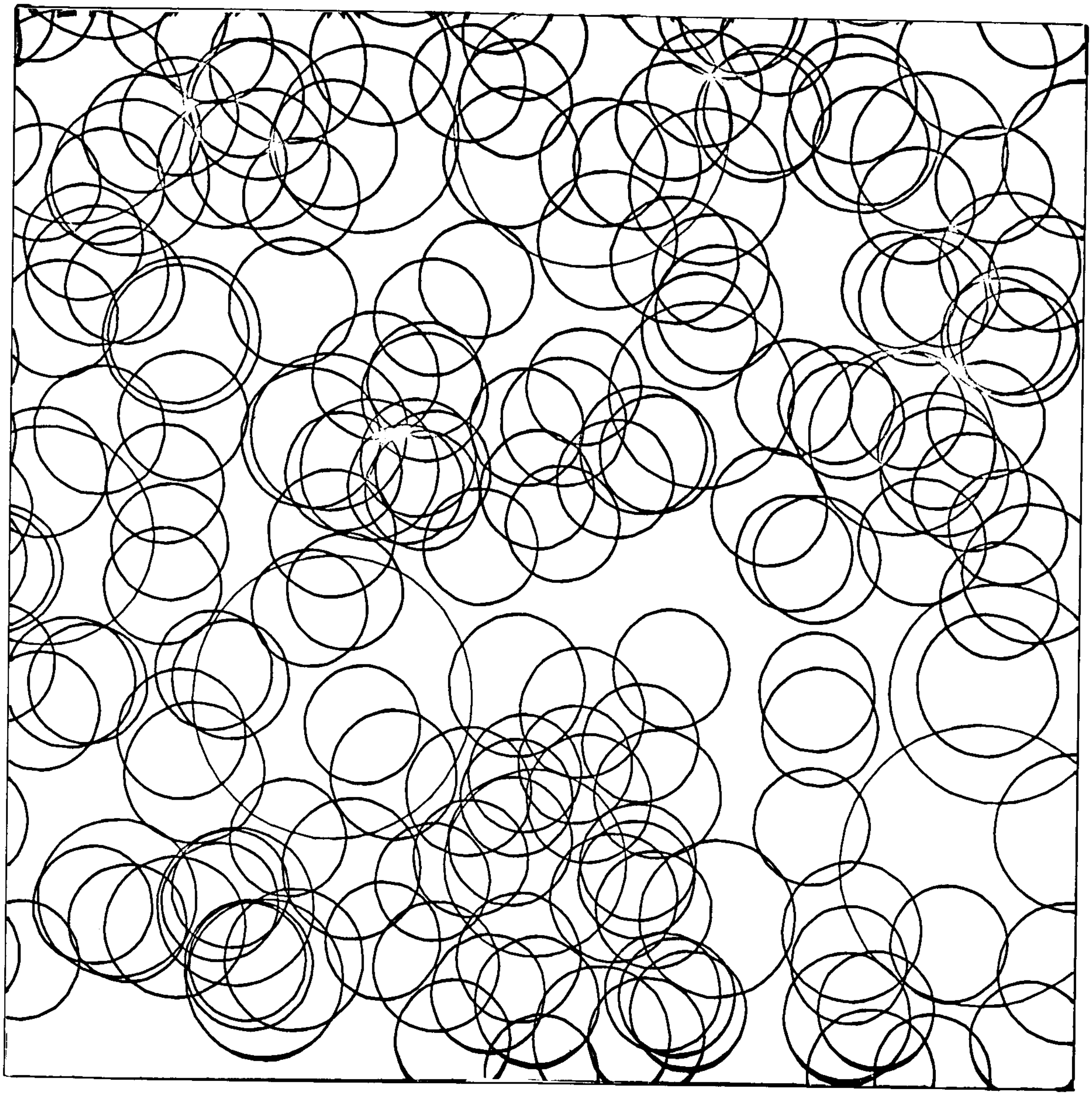

Figure IV-10. Computer-Generated Crater Map, Diameters Increased by 60 Feet

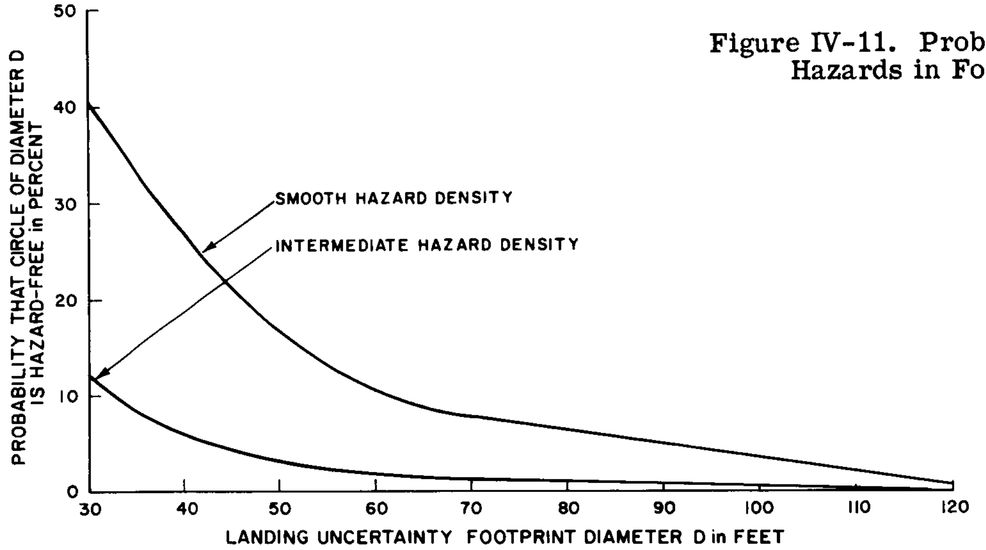

Figure IV-11. Probability of No Hazards in Footprint

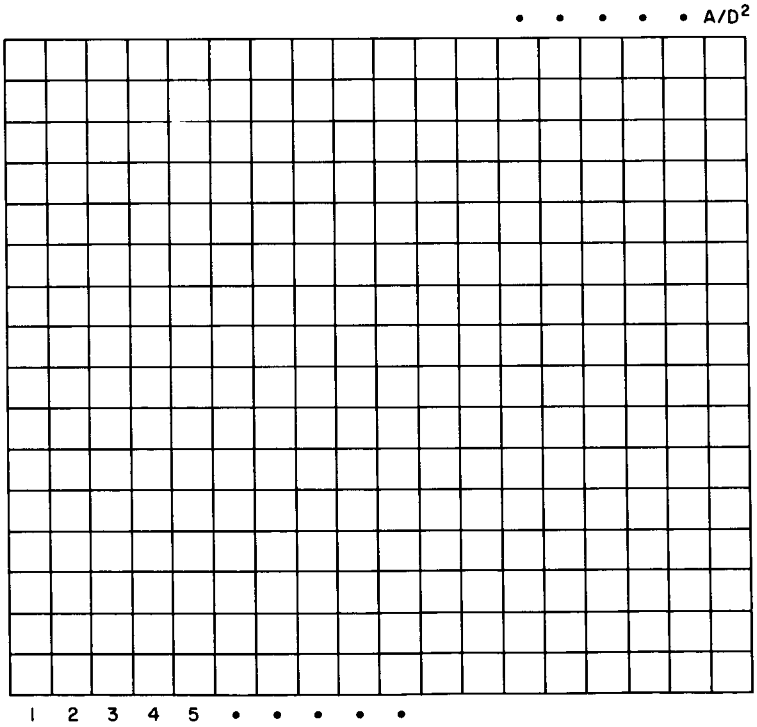

Figure IV-12. Subdivision of Scan Area into Squares of Side D

in a subdivision is independent of and identically distributed with the hazard-free probabilities of all other squares in the subdivision. That is, for all i, j, k, and l:

$$P(i-j\text{th square is hazard-free}) = P(k-l\text{th square is hazard-free}) = p$$

and the events

$$E_{ij} = (i-j\text{th square is hazard-free}) \text{ and}$$

$$E_{kl} = (k-l\text{th square is hazard-free}) \text{ are independent.}$$

Both of these assumptions are good as long as most landing hazards in the area are of smaller dimension than the footprint diameter D. This will generally be the case. For example, it is shown later that the landing uncertainty footprint is on the order of 60 feet in diameter at the 0.997 probability level. Crater frequency estimates, based on observations made by Ranger 7 in Mare Cognitum, indicate that an average of two craters of diameter > 60 feet would be expected in a 620- by 460-foot area in that region.

On the basis of the above assumptions,

$$\begin{aligned} P(\text{no hazard-free sites in subdivision}) = {} & P(\text{square 1 has hazards}) \cdot \\ & P(\text{square 2 has hazards}) \cdot \\ & P(\text{square } A/D^2 \text{ has hazards}) = (1-p)^{A/D^2} \end{aligned}$$

Since the subdivision used was arbitrary, the probability that there are no hazard-free sites in any subdivision is still $(1-p)^{A/D^2}$. This is the desired probability

$$q = (1-p)^{A/D_2} \tag{5}$$

We can now require that P(at least one hazard-free landing site in the area) = 0.99, or equivalently that q = 0.01, and solve Equation (5) for A:

$$A = \frac{D^2 \operatorname{Log}_{10}(0.01)}{\operatorname{Log}_{10}(1-p)} \text{ or}$$

$$A = \frac{-2D^2}{\operatorname{Log}_{10}(1-p)} \tag{6}$$

Then the scan area required to provide a 0.99 probability that at least one safe landing site is included in the scan is given as a function of footprint diameter D and hazard distribution by Equation (6) where p is given as a function of D and hazard distribution in Figure IV-11. The required scan area is presented in Figure IV-13. For an unmanned landing in a smooth hazard density region with a landing uncertainty footprint diameter of 60 feet, a scan area of 150,000 square feet is required.

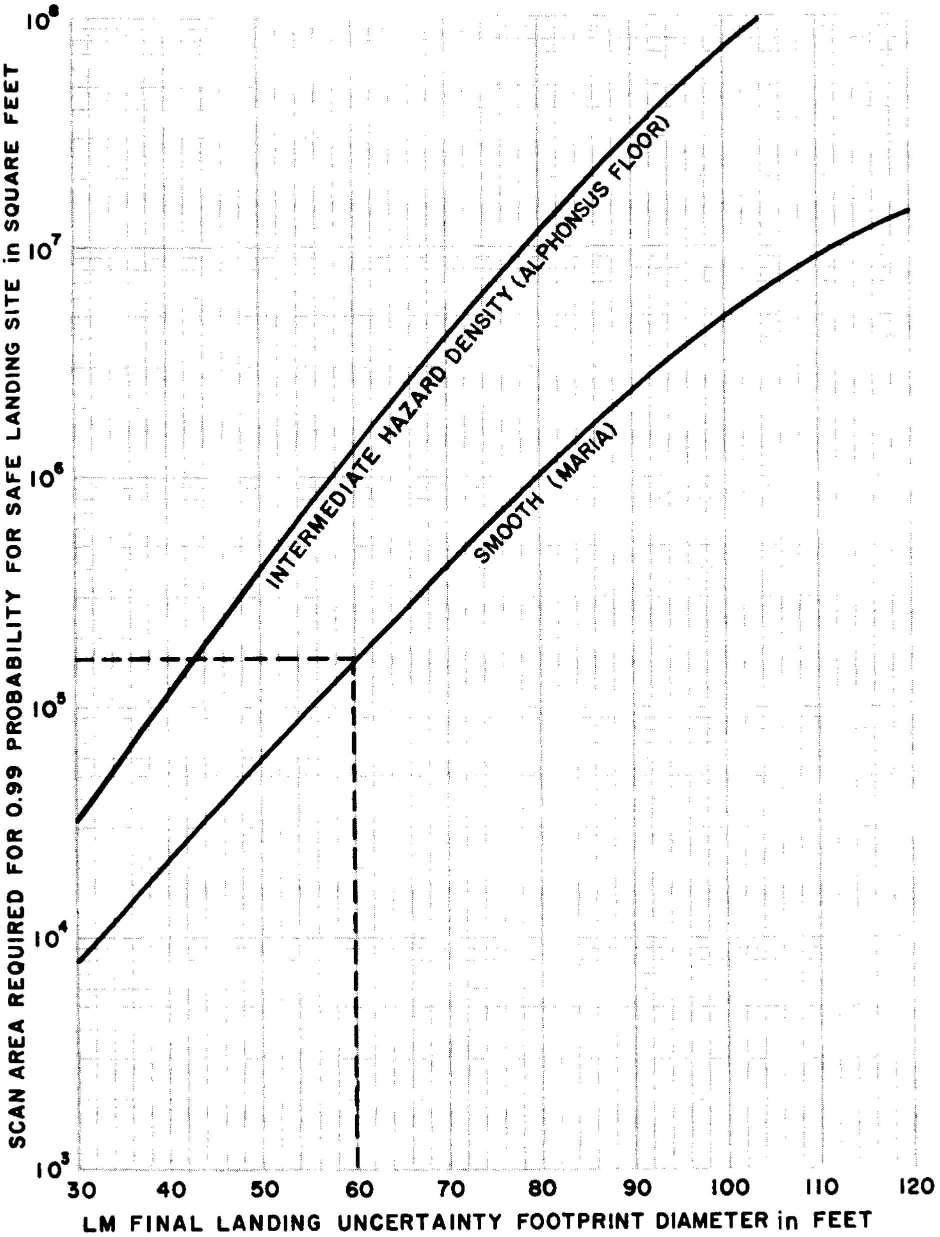

Figure IV-13. Search Area for LM Landing

This scan area must be provided 50 seconds before hover. As noted above, the 10- by 20-degree field of view required for position error correction yields a 620- by 460-foot area (285,000 square feet) 50 seconds before hover. Therefore, this field of view satisfies our requirements on both safe landing site selection and position error correction.

At the time this work was performed, little information was available on the distribution of rocks which would pose a hazard for the LM landing (heights > 50 cm), so rocks were not included in the computer-generated maps used in determining the scan area. However, it can be shown that the addition of a reasonable rock distribution does not place severe new requirements on the TV system design. A moderately dense rock distribution was postulated for work done in Section X. This distribution was based on data from the Ranger series and the first Surveyor, and calls for 1090 rocks of heights > 50 cm distributed uniformly over an area of $1 \times 10^6 m^2$. For an example, assume a landing uncertainty footprint of 60-foot diameter and a landing in a smooth hazard density area. Figure IV-11 then gives $p = 0.105$ when only craters are considered. This is equivalent to the statement that 10.5 percent of the reference area ($1 \times 10^6 m^2$) or $1.05 \times 10^5 m^2$ is hazard-free. Under the assumption of a uniform distribution, $0.105 \times 1090 = 114$ hazardous rocks will be in the hazard-free area. Now we reduce the hazard-free area by the amount ΔA that is covered by the 114 hazardous rocks with diameter increased by the landing footprint uncertainty. Subtracting the entire amount ΔA from the hazard-free area involves the conservative assumption that the 60-foot (18.2 meter) diameter circles associated with the rocks do not intersect each other.

$$\Delta A = \frac{114 \pi (18.2)^2}{4} = 2.94 \times 10^4$$

Now the reduced free area A' is given by:

$$A' = A - \Delta A = (1.05 - 0.294) \times 10^5 = 7.6 \times 10^4 m^2$$

This leads to a reduced value for p:

$$p' = \frac{7.6 \times 10^4}{10^6} = 0.0764$$

That is, 7.6 percent of the reference area is hazard-free when both craters and rocks are considered. Recomputing Equation (5), we find that a scan area of 212,000 square feet is required to attain a 0.99 probability of finding a safe landing site in a smooth hazard density area with rocks included and a landing uncertainty footprint of 60 feet. The 10- by 20-degree field of view required for position error correction gives a scan area of 285,000 square feet 50 seconds before hover, and thus satisfies our increased requirement for safe landing site selection.

A high probability of finding at least one hazard-free landing site can be provided by giving the controller enough scan area, as was demonstrated above. However, a successful lunar surface rendezvous (LSR) mission requires the existence of a safe landing site for the manned LM close to the site of the unmanned landing. It can be shown that the probability that at least two hazard-free landing sites are located in the scan area is almost identical to the probability that at least one hazard-free landing site is located in the scan area for high probability levels and relatively small footprint sizes. This conclusion holds under the conservative assumption that the landing uncertainty footprint of the manned LM is the same as that of the unmanned LM. The probability P ($\geq$ 1) that at least one hazard-free landing site is located in the scan area is related to the probability P ($\geq$ 2) that at least two hazard-free landing sites are located in the scan area by the equation $P(\geq 1) = P(1) + P(\geq 2)$, where P (1) is the probability that exactly one hazard-free landing site is located in the scan area. The decrease in probability brought about by requiring that at least two rather than one site be located in the scan area is then given for an arbitrary subdivision by

$$P(\geq 1) - P(\geq 2) = P(1) = p\,(1 - p)^{A/D^2 - 1}\left(A/D^2\right) \qquad (7)$$

Returning to the example of an unmanned landing in a region of smooth hazard density with a 60-foot-diameter landing uncertainty footprint, we recall that a 10- by 20-degree field of view gave a scan area of 285,000 square feet 50 seconds before hover. Thus, $A/D^2 = 79$. Evaluation of Equation (7) with $p = 0.1051$ then shows a decrease in probability of $1.5\text{x}10^{-3}$ when we require at least two hazard free sites in the scan area. An obvious conclusion which follows from this result is that the controller can concern himself exclusively with locating a hazard-free landing site for the unmanned LM, with no requirement that he locate or verify a second one.

A final point pertinent to consideration of TV field of view should be mentioned here. We have provided a scan area 50 seconds before hover that guarantees a high probability of at least one hazard-free landing site being located in the scan. However, this need not mean that the controller will be able to easily find that site in his scan. Figure IV-14 is a computer-generated map of a typical 200 x 200m area in a smooth region. This area is of roughly the same dimensions as the TV scan 50 seconds before hover. Only craters of a size sufficient to be LM landing hazards are shown. TV system resolution will be set so that the smallest size LM landing hazard can just be reliably perceived 50 seconds before hover. The LM 30-foot-diameter physical landing footprint and the 60-foot-diameter landing uncertainty footprint are shown on the map. There will be distortion of the perspective of Figure IV-14, caused by the low elevation (about 22 degrees) of the TV camera viewpoint 50 seconds before hover. In addition, the controller's major visual cues will

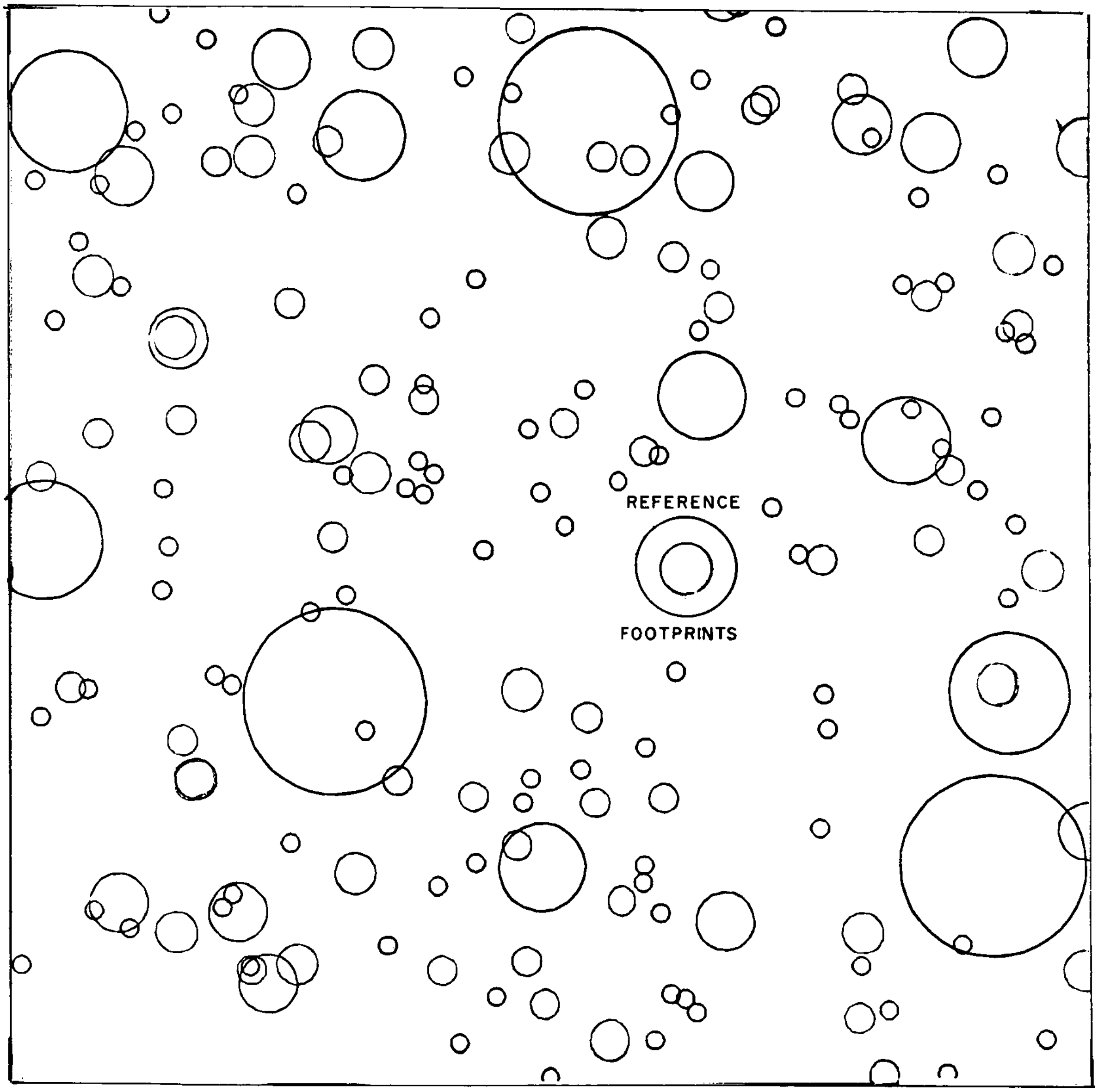
REFERENCE
FOOTPRINTS

Figure IV-14. Computer-Generated Crater Map

be in the form of shadows of visible length equal to a quarter of the actual crater diameter. Even allowing for these anomalies, Figure IV-14 seems to indicate that it is reasonable to assume that the controller will have no difficulty in finding a hazard free landing site in such an area.

Due to the decrease in scan area as the range to the landing site decreases, the TV camera field of view must be switched to 30- by 50-degrees about 25 seconds before hover, in order to provide sufficient TV information at hover. The considerations involved in the choice of hover field of view will be developed later.

In summary, a 10- by 20-degree field of view, switched to a 30- by 50-degree field of view about 25 seconds before hover, satisfies the AAP requirements on both safe landing site selection and position error correction.

2.2.2 Number of TV Scan Lines. TV resolution in the horizontal plane of the lunar surface varies along the scan length ℓ since the TV camera is at an elevation $E_{LM} < 90$ degrees relative to its aimpoint. A derivation of equations expressing this effect follows. Figure IV-15 illustrates the geometry of the situation, with ρ_1 the resolution at the center of the scan in the plane perpendicular to the center line of the TV beam; λ_1 the resolution at the center of the scan in the horizontal plane; and ρ_2, λ_2 and ρ_3, λ_3 the corresponding quantities at the downrange and uprange extremities of the scan, respectively. $\rho_1 \doteq \lambda_1 \sin E_{LM}$ at the center of the scan. Now, since $\theta/2$ is small (5 degrees), $D_1 \doteq D$ and $\rho_2 \doteq \rho_1$ are good approximations. Also, AB and A'B' are almost parallel, and the triangles ABC and A'B'C are thus similar to a good approximation. In addition, since λ_2 and ρ_2' are both very small compared to $H/\sin\left(E_{LM} - \theta/2\right)$,

$$\left[H/\sin\left(E_{LM} - \theta/2\right)\right] - \left(\lambda_2^2 - \rho_2'^2\right)^{1/2} \doteq H/\sin\left(E_{LM} - \theta/2\right)$$

is a good approximation. Thus,

$$\frac{\rho_2'}{H/\sin\left(E_{LM} - \theta/2\right)} \doteq \frac{\rho_2}{D_1} \doteq \frac{\rho_1}{D}$$

or

$$\rho_2' \doteq \rho_1 \frac{\sin E_{LM}}{\sin\left(E_{LM} - \theta/2\right)}$$

since $D = H/\sin E_{LM}$. Now,

$$\lambda_2 = \rho_2'/\sin\left(E_{LM} - \theta/2\right) \doteq \rho_1 \sin E_{LM}/\sin^2\left(E_{LM} - \theta/2\right)$$

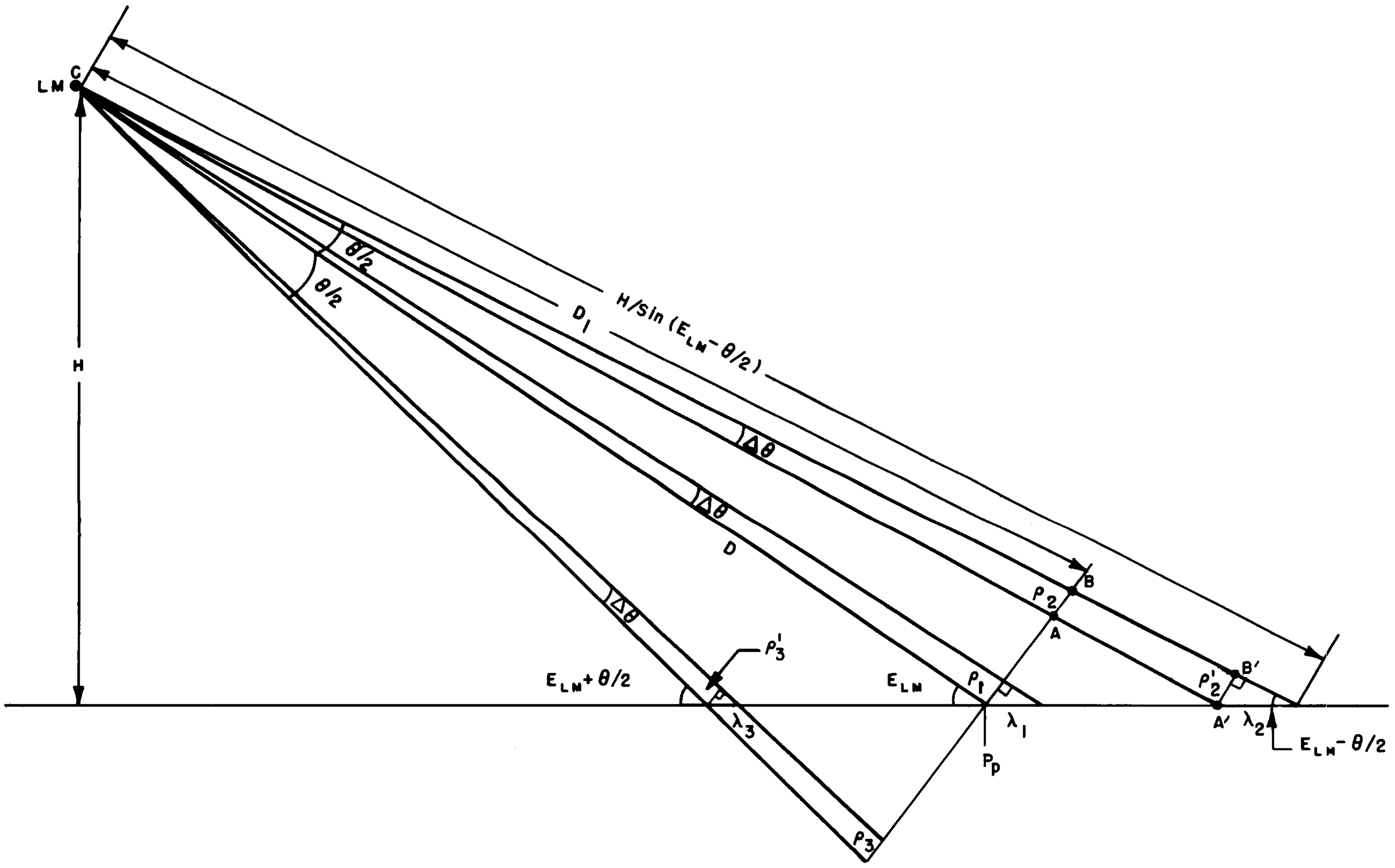
LM
C
H
θ/2
θ/2
D1
H/Sin (ELM - θ/2)
Δθ
Δθ
D
Δθ
B
ρ2
A
ρ'3
ELM + θ/2
ELM
ρ1
λ1
Pp
λ3
ρ3
ρ'2
B'
A'
λ2
ELM - θ/2

Figure IV-15. TV Resolution Geometry

Thus, the ratio of horizontal resolution at the downrange extremities of the scan to horizontal resolution at the center of the scan is given by:

$$\lambda_2/\lambda_1 \doteq \left[\sin E_{LM}/\sin\left(E_{LM} - \theta/2\right)\right]^2$$

This ratio is presented as a function of time before hover in Figure IV-16. It is seen that for an elevation field of view of 10 degrees, horizontal resolution at the downrange extremities of the scan for a given number of scan lines is 62 percent less than at the center of the scan, 50 seconds before hover. Similarly, the ratio of horizontal resolution at the uprange extremities of the scan to horizontal resolution at the center of the scan is given by:

$$\lambda_3/\lambda_1 \doteq \left[\sin E_{LM}/\sin\left(E_{LM} + \theta/2\right)\right]^2$$

When the TV scan beam is sweeping over a scene containing horizontal detail lines, the vertical resolution depends on the position of the detail relative to the scanning lines. This effect is illustrated in Figure IV-17 where a pattern containing horizontal lines of alternate black and white elements is to be televised. If the relative position of image and scanning lines is such that the center of the transmitting scanning beam travels along the center of a row of black and white elements, the vertical resolution is perfect, all elements being resolved. If the scanning beam falls half on one horizontal row and half on the row above or below, the pattern is reproduced as a uniform grey and resolution is zero. Experimental investigation of the vertical resolution obtained with a given number of scan lines when scenes from nature are scanned, has resulted in a determination of the ratio k between the number of "effective" scan lines N' and the total number of scan lines N. A value of k = 0.7 has attained considerable acceptance as a good average and was used in this study.

The vertical resolution at the center of the scan in the plane perpendicular to the camera pointing line is then obtained by dividing the vertical dimension of the scan by the effective number of scan lines. By reference to Figure IV-15,

$$\rho_1 = \frac{2D \tan(\theta/2)}{kN}$$

The vertical resolution at the center of the scan in the surface plane is then given by:

$$\lambda_1 = \rho_1/\sin E_{LM} = \frac{2D}{\sin E_{LM}} \frac{\tan \theta/2}{kN} \tag{8}$$

Figure IV-18 shows the total number of scan lines required 50 seconds before hover to obtain a given resolution at the center of the scan in the surface plane.

In order to determine the number of scan lines needed, it was necessary to find the vertical resolution at the center of the scan in the surface plane which would

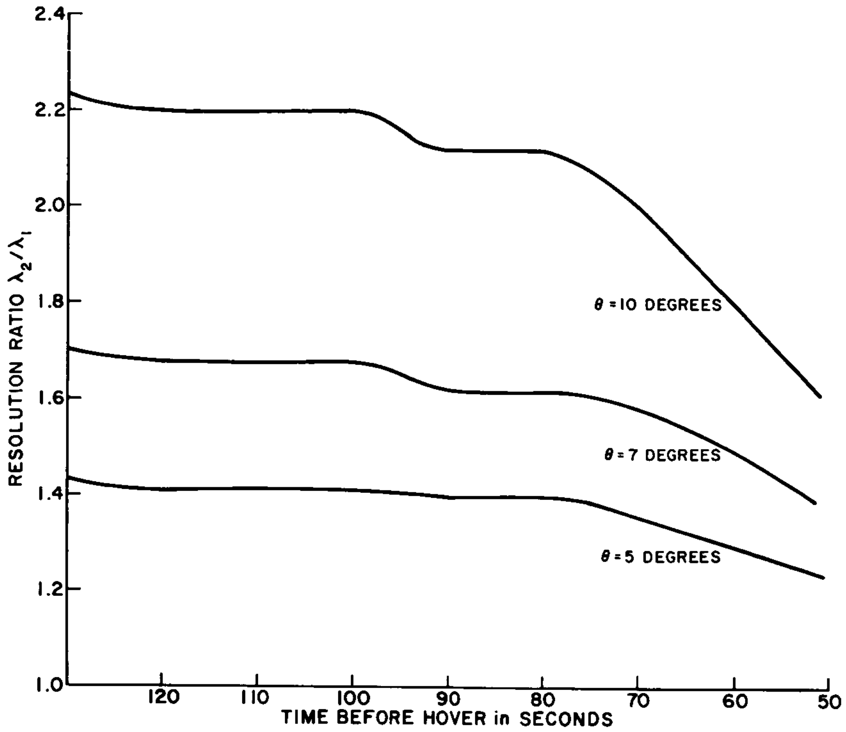

Figure IV-16. Leading Edge Resolution Degradation versus Time before Hover

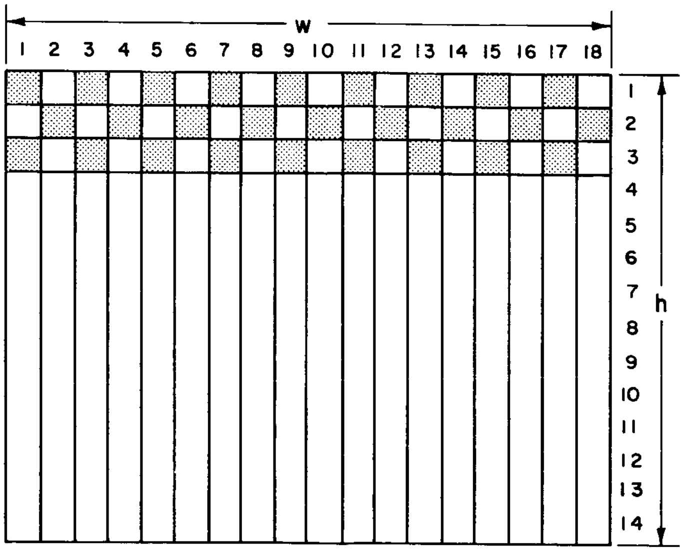
w
1 2 3 4 5 6 7 8 9 10 11 12 13 14 15 16 17 18
1
2
3
4
5
6
7
8
9
10
11
12
13
14
h

Figure IV-17. TV Resolution Pattern

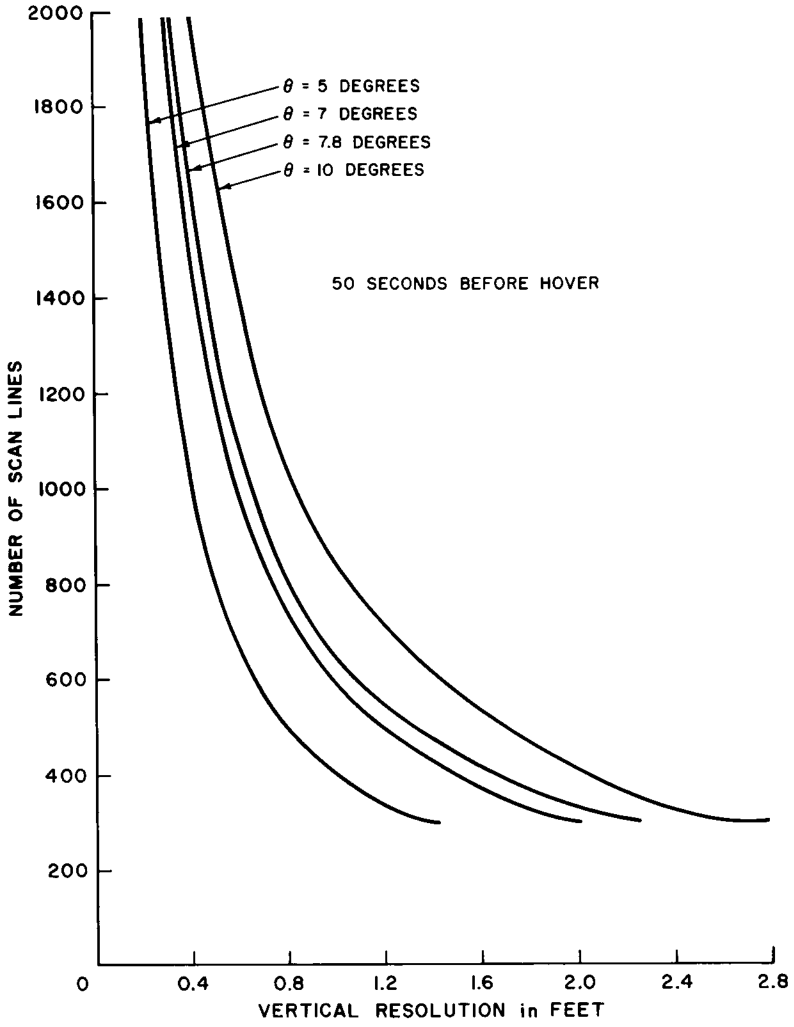

Figure IV-18. Vertical Resolution versus Number of Scan Lines

allow perception of all LM landing hazards in the scan area 50 seconds before hover. It was assumed that perception of the landing hazards will be based entirely on shadow cues. This was somewhat conservative but not unrealistic, since a low frame rate, single-camera system with a rapidly decreasing scan area could not be expected to give significant perceptual information based on motion parallax, binocular parallax, or size comparison with a reference object. The smallest features classed as LM landing hazards were 50-cm-high rocks (diameter/height ≈ 3), 3m-diameter primary craters (diameter/depth ≈ 4), and 5m-diameter secondary craters (diameter/depth ≈ 7). These definitions of minimum-size hazards were based on considerations of LM impalement and tip-over. Thus, the first step in determining the number of scan lines necessary was an evaluation of the shadow characteristics of the minimum size LM landing hazards.

The visible shadow length presented to the TV scan was evaluated for three different rock shapes (rectangular, conical, and elliptical) and three different crater shapes (rectangular, conical, and circular). Visible shadow lengths were also computed for small variations in diameter/height or diameter/depth ratios. Visible shadow length did not vary significantly for small departures from the assumed ratios. The rounded contours of the elliptical rocks and circular craters gave smaller visible shadow lengths than the rectangular or conical shapes. Thus, results will only be presented for elliptical rocks and circular craters.

Figure IV-19 illustrates the shadowing situation for an elliptical rock of height h and diameter/height ratio k. L is the visible shadow length presented to the TV scan when the viewing angle is E_{LM}. In the XY coordinate system the equation of the ellipse is

$$\frac{X^2}{k^2h^2/4} + \frac{Y^2}{h^2} = 1$$

The equation of the sun line AB is

$$Y = -\left(\tan E_S\right)X + K_o$$

where K_o is constant. The sun line and the rock intersect at the point c on the ellipse having a slope of -tan E_S. Differentiating along the ellipse:

$$\frac{2X\,dX}{k^2h^2/4} + \frac{2Y\,dY}{h^2} = 0$$

$$dY/dX = -4X/k^2Y = -\tan E_S \text{ at the point of intersection, c.}$$

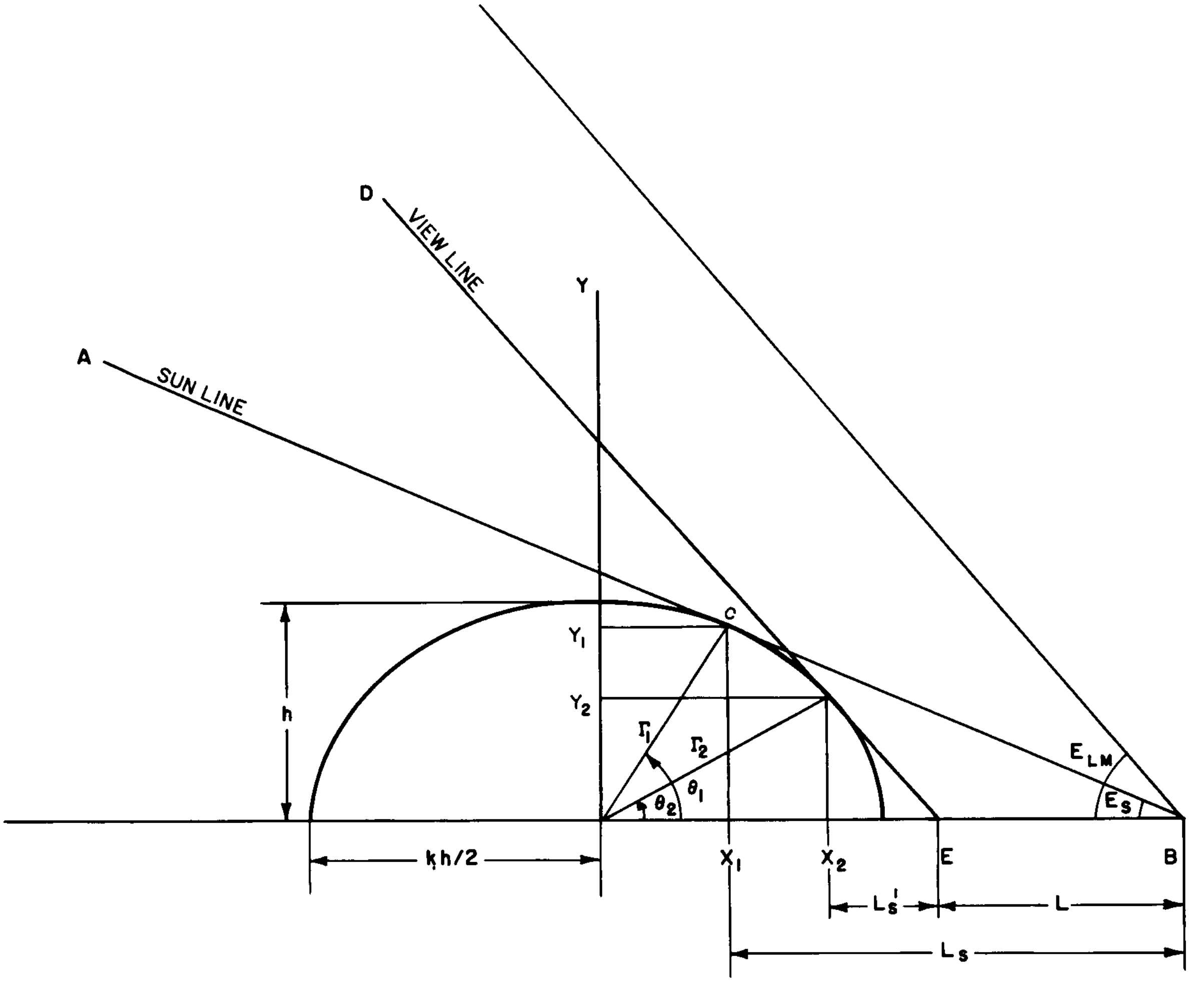
D
VIEW LINE
A
SUN LINE
Y
C
Y_1
Y_2
h
Γ_1
Γ_2
θ_1
θ_2
E_{LM}
E_S
$k_1 h/2$
X_1
X_2
E
B
L_s'
L
L_s

Figure IV-19. Visible Shadow Length for Elliptical Rocks

Thus, at c,

$$Y_1 = 4\ X_1/k^2 \tan E_s$$

$$\tan \theta_1 = Y_1/X_1 = 4/k^2 \tan E_s$$

Now we know θ_1, $\sin \theta_1$, and $\cos \theta_1$ once k and E_s are specified. In polar coordinates, the intersection point on the ellipse can be expressed as

$$\Gamma_1 = \frac{h}{\sqrt{1 - \left(1-4/k^2\right) \cos^2 \theta_1}}$$

So knowing Γ_1, we can find X_1, Y_1, and L_s:

$$X_1 = \Gamma_1 \cos \theta_1$$
$$Y_1 = \Gamma_1 \sin \theta_1$$
$$L_s = Y_1/\tan E_s$$

Following the same procedure with the limiting viewing line DE and the view angle E_{LM}, gives X_2, Y_2 and L_s'. Then, we have the visible shadow length L:

$$L = L_s - L_s' - \left(X_2 - X_1\right) \tag{9}$$

Figure IV-20 shows the shadowing geometry for a circular crater. L is the visible shadow length for a viewing angle of E_{LM}. Specification of the diameter D and diameter/depth ratio k, determines the circle:

$$\frac{D/2}{\Gamma - (D/k)} = \tan \theta/2$$

$$D/2 = \Gamma \sin \theta/2$$

Solution of these two equations for the two unknowns, Γ and θ gives:

$$\theta = 2 \sin^{-1} \frac{2(2/k)}{1 + (2/k)^2}$$

$$\Gamma = \frac{1 + (2/k)^2}{8/k} D = aD$$

where a is introduced for convenience.

To find L_s, we first get the equations of the circle and the sun line AB in XY coordinates:

$$X^2 + Y^2 = a^2 D^2$$

$$Y = -\left(\tan E_s\right) X + \left(a - 1/k - 1/2 \tan E_s\right) D$$

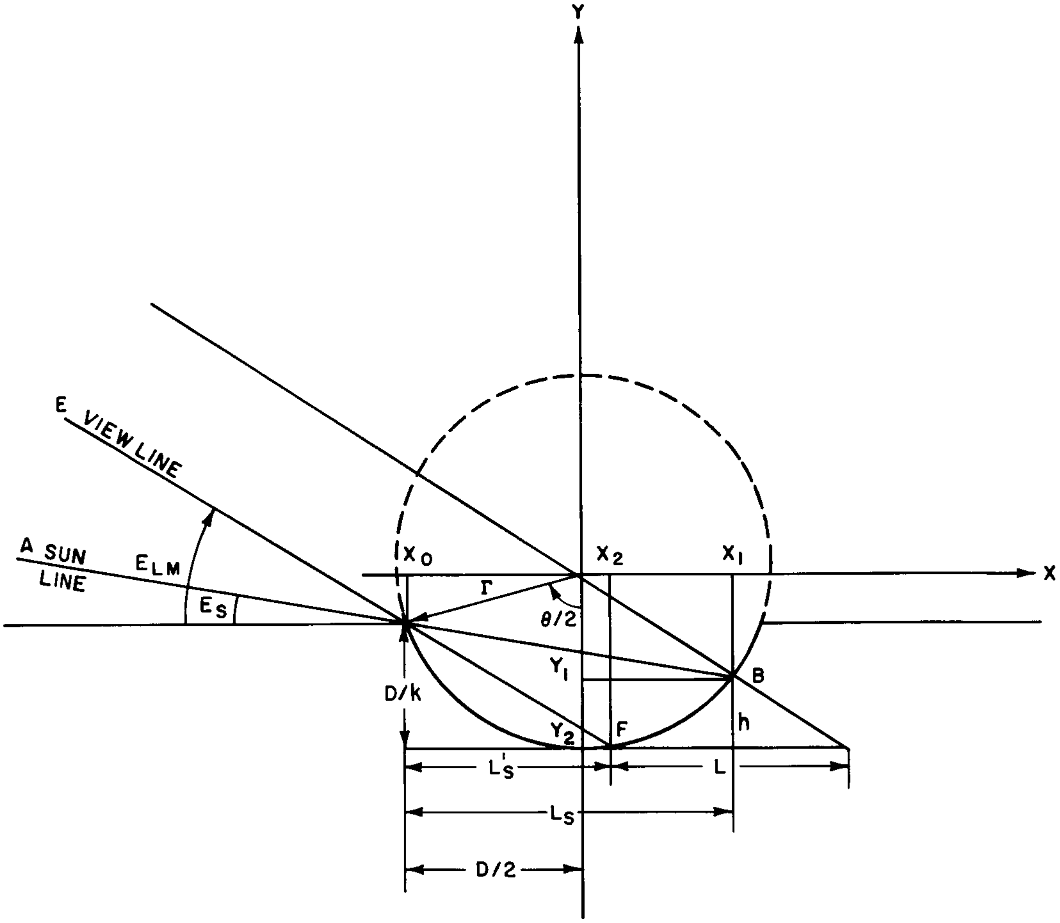
Y
X
E VIEW LINE
A SUN LINE
E_{LM}
E_S
X₀
X₂
X₁
Γ
θ/2
Y₁
B
D/k
Y₂
F
h
L'_S
L
L_S
D/2

Figure IV-20. Visible Shadow Lengths for Circular Craters

These equations are solved for X_o and X_1, the X coordinates of the two points of intersection of the sun line and the circle. Then L_s is determined from $L_s = X_1 - X_o$ with a solution of the form: $L_s = bD$. By following the same procedure with the limiting viewing line EF and the view angle E_{LM}, a solution for L'_s is found: $L'_s = cD$.

To solve for L:

$$X_1 = L_s - D/2 = (b - 1/2)\,D$$

$$Y_1^2 = a^2 D^2 - (b - 1/2)^2 D^2$$

$$Y_1 = -D\sqrt{a^2 - (b - 1/2)^2}$$

$$X_2 = L'_s - D/2 = (c - 1/2)\,D$$

$$Y_2^2 = a^2 D^2 - (c - 1/2)^2 D^2$$

$$Y_2 = -D\sqrt{a^2 - (c - 1/2)^2}$$

$$h = Y_1 - Y_2 = D\left(\sqrt{a^2 - (c - 1/2)^2} - \sqrt{a^2 - (b - 1/2)^2}\right)$$

$$\frac{h}{L - \left(L_s - L'_s\right)} = \tan E_{LM}$$

$$L = L_s - L'_s + h/\tan E_{LM}$$

$$L = D\left[b - c + \frac{\left(\sqrt{a^2 - (c - 1/2)^2} - \sqrt{a^2 - (b - 1/2)^2}\right)}{\tan E_{LM}}\right] \qquad (10)$$

Equations (9) and (10) were evaluated to obtain the visible shadow lengths for the minimum-size LM landing hazards defined above. It was assumed that the sun elevation angle was 10 degrees for the sample mission. The results are shown in Figure IV-21. It is seen that 3m primary craters place the most stringent requirements on TV system resolution. To guarantee that the controller can see all landing hazards in the scan area 50 seconds before hover, shadows of length 4 feet must be reliably resolved anywhere in the scan area. Reliable resolution is provided by requiring that three TV scan lines intersect the 4-foot shadow. This requirement is conservative enough to guarantee perception over a wide range of display system/ controller configurations. As one example, if a 6- by 6-foot display screen similar to the Eidophor display system at NASA MSC were used, with the controller located 10 feet from the display, then three scan lines in a 1000-line display would subtend approximately 6 minutes of arc at the controller's eye. A high-contrast image, such as a black shadow in a gray surrounding, can be perceived if it subtends an arc as small as 1 minute at the eye. The requirement for three TV scan lines to intersect the 4-foot shadow means that the scan lines must not be separated by more than 4/3 feet in the surface plane for any point in the scan area. In particular, Figure IV-16 indicates that the vertical resolution in the surface plane at the center of the scan must be $\lambda_1 = (4/3)/1.62 = 0.82$ foot to meet this requirement at the uprange boundary of the scan area 50 seconds before hover, with an elevation field of view of 10 degrees. Referring to Figure IV-18, we see that 1025 TV scan lines are required for $\lambda_1 = 0.82$ foot, 50 seconds before hover.

Finally, it was necessary to verify that 1025 lines gave sufficient resolution in the 10 seconds following High Gate to allow landmark recognition. The choice of an azimuth field of view of 20 degrees was based on the assumption that the controller could reliably perceive 200m-diameter craters in the uprange portion of the scan area. Figure IV-22 shows High Gate resolution in the surface plane at the center of the TV scan. It is seen that a 1025-line scan gives resolution $\lambda_1 = 36.7$ feet. Since landmark pattern recognition is to be based on information in the uprange portion of the scan, this value represents the poorest resolution in the required scan area and thus was used to determine landmark perception capability. It was again required that three scan lines intersect the viewed object for perception. This meant that the controller had the ability to perceive shadows of length 110 feet or greater at High Gate. Large craters tend to have a higher diameter/depth ratio then the small craters which are landing hazards. Assuming a diameter/depth ratio of 10 and a sun elevation angle of 10 degrees, evaluation of Equation (10) indicated that the visible shadow length would be approximately one quarter of the diameter of the crater. This meant that craters of diameter greater than 453 feet (138 meters) would have visible shadow lengths in excess of 110 feet and could thus be perceived. Thus, our assumption that the controller could perceive craters 200m in diameter was justified.

In summary, it was demonstrated that a vertical resolution of 1025 TV scan lines per frame met the AAP requirements on both landing hazard detection and landmark pattern recognition for position error correction.

2.2.3 TV Frame Rate. Experiments were performed to determine the minimum frame rate required to allow the controller to easily correlate viewed objects from one frame to the next. A movie film of the pilot's view on a simulated LM landing trajectory similar to the TV system design trajectory had been produced for NASA MSC by Eastman Kodak. Copies of this film were obtained and altered to simulate the controller's view at low frame rates. Figure IV-23 illustrates how the 24-frame/second film was altered to present the controller's view at 1 frame/second.

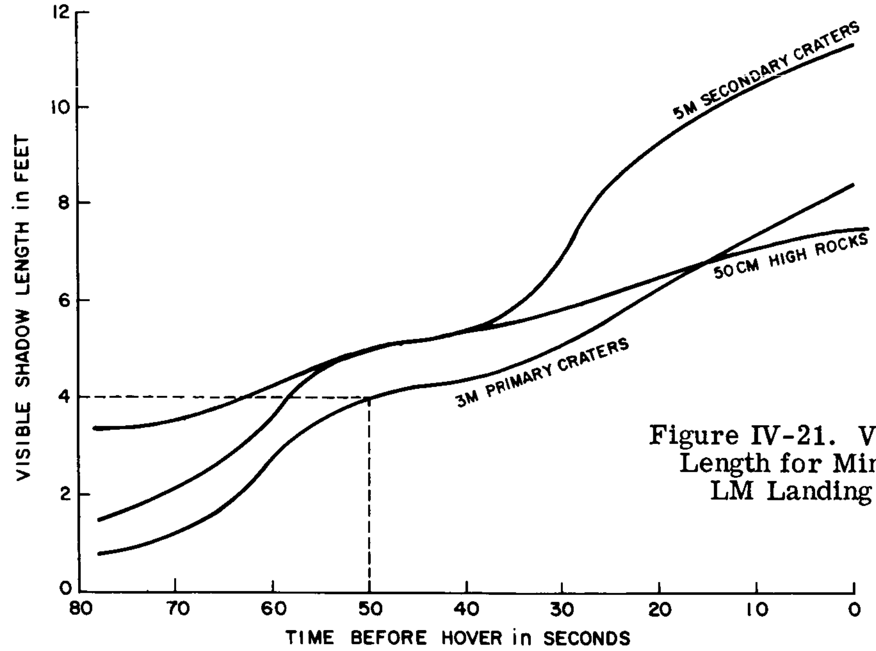

Figure IV-21. Visible Shadow Length for Minimum-Size LM Landing Hazards

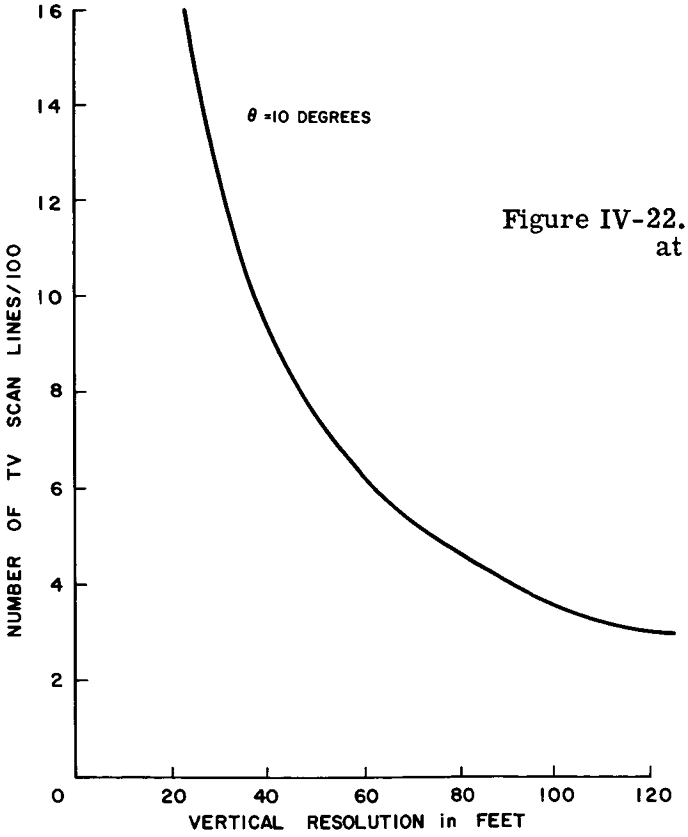

Figure IV-22. Vertical Resolution at High Gate

Films with frame rates of 1/2, 1 and 2 frames/second were generated and shown to eight subjects. Some were able to easily follow a given crater from one frame to the next at 1/2 frame/second. All were able to easily correlate from one frame to the next at 1 frame/second. At 2 frames/second, some subjects noted a distinctly unpleasant interaction between frame rate and their sequential information processing rate. A similar effect was noted in an investigation of low frame rate TV systems for Picturephone application (Reference 5). The theory advanced to explain this phenomenon stated that the visual information was processed as a sequence of "still" pictures, or snapshots, at rates below 2 frames/second. At rates above 6 to 10 frames/second, the information was processed continuously, as a movie film is viewed. The information processing mechanism appeared to be in transition between sequential and continuous processing for rates between 2 and 6 frames/second. This transition caused most observers to report unfavorable reactions for these rates. Since rates of 6 frames/second or more place exceedingly severe requirements on LM Earth bandwidth growth capability, these rates were not investigated in the LM descent controller view experiment. That led to a choice of a very low frame rate system with sequential rather than continuous information processing by the controller. Since all subjects were able to correlate easily at 1 frame per second, this frame rate is recommended for the TV system.

The experiment described above indicated that 1 frame/second should be a satisfactory information rate for the controller. However, two requirements on the TV system were implicit in the design of the experiment. First, since selected frames were taken from the high-frame-rate (24 frames/second) Kodak film and repeated a given number of times, to simulate low frame rates, the experiment assumed no motion distortion (blurring) of the image. However, the maximum LM guidance rate is 10 degrees/second, and this rate combined with a TV scan spread over a 1-second interval would produce unacceptable motion distortion. This consideration leads to a requirement for a wide bandwidth store and transmit device in the LM which would permit a fast TV scan coupled with transmission at 1 frame/second. Second, the films generated to simulate low frame rates provide a smooth transition with no "blackout" or after-image from one frame to the next, i.e., frame 1 to frame 25 in Figure IV-23. To avoid noticeable blackout periods or after-images in the TV display from one frame to the next at 1 frame/second, it would be necessary to record each frame and display it repetitively at a high rate on a low-retention screen for 1 second. For example, the Eidophor display system used at NASA MSC has a memory time of 0.033 second, so the TV frame from the LM would have to be recorded and repetitively displayed at 30 frames/second until the next TV frame was ready for display, 1 second later.

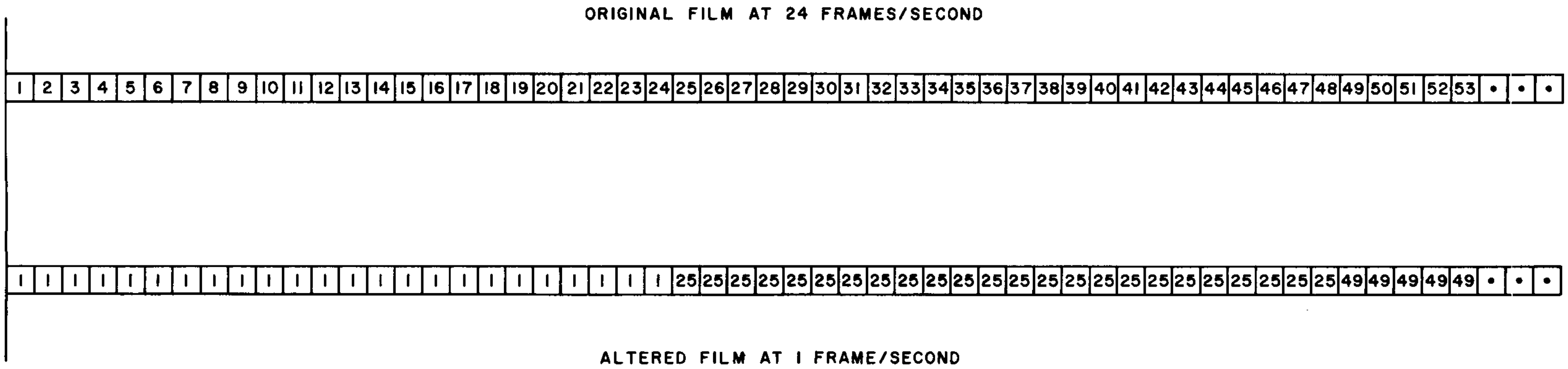
ORIGINAL FILM AT 24 FRAMES/SECOND
1 2 3 4 5 6 7 8 9 10 11 12 13 14 15 16 17 18 19 20 21 22 23 24 25 26 27 28 29 30 31 32 33 34 35 36 37 38 39 40 41 42 43 44 45 46 47 48 49 50 51 52 53 • • •
1 1 1 1 1 1 1 1 1 1 1 1 1 1 1 1 1 1 1 1 1 1 1 1 25 25 25 25 25 25 25 25 25 25 25 25 25 25 25 25 25 25 25 25 25 25 25 25 49 49 49 49 49 • • •
ALTERED FILM AT 1 FRAME/SECOND

Figure IV-23. Simulation of One Frame/Second Rate

In summary, experiments indicated that a TV frame rate of one frame/second should satisfy the controller's information requirements if store and transmit devices are provided for the LM and the TV display system on Earth.

2.2.4 Video Bandwidth. The video bandwidth necessary to give horizontal resolution equal to the vertical resolution was determined. Vertical resolution is the ability of the TV system to reproduce abrupt changes in tonal value occurring along a line at right angles to the scanning lines. That is, the vertical resolution measures the sharpness of reproduction of horizontal lines in the image. The horizontal resolution of a TV system is its ability to reproduce abrupt changes in tonal value occurring along the scanning lines. That is, horizontal resolution measures the sharpness of reproduction of the vertical lines in the image.

Vertical resolution is different in nature from the horizontal resolution. Vertical resolution can only be increased by providing more lines, while horizontal resolution increases as the video frequency is raised. Reference 6 derives the relation between maximum video frequency required for equal resolution and number of TV scan lines. In the interest of completeness, that derivation is reproduced here.

The video signal is generated by repeatedly scanning the elements composing an image of the scene; the beam moves over them in a series of lines and the output at any element represents the tonal value of that element. The video signal contains two strongly marked frequencies; the first equal to the number of fields transmitted/second, and the second equal to the number of lines scanned/second. The second component is known as the line frequency and is equal to NP where N is the number of lines composing the picture and P is the number of pictures transmitted per second.

In addition to these two alternating components, the video signal has a dc component and high-frequency components (harmonics of the field and line frequencies) corresponding to detail in the picture. The upper frequency limit depends on the picture frequency, the number of lines composing the picture, and the shape of the picture and can be assessed in the manner discussed below.

An element of a television picture may be defined as an area, assumed to be square, with a maximum dimension equal to h/N where h is the height of the picture and N is the number of lines composing it. The assumption that the elements are square is equivalent to assuming that the horizontal definition of the television system is equal to the vertical definition. However, the reproduced picture is made up of horizontal lines, and the vertical definition differs in nature from the horizontal definition as explained above. Figure IV-17 illustrates a picture composed of alternate black and white square elements. The scanning beam at the transmitter usually has dimensions approximately equal to those of an element and the finest detail which can then be transmitted has the size of an element; this is the detail which exists when a white element is next to a black one. Thus if Figure IV-17 has N horizontal rows of elements, this diagram represents the finest detail which can be transmitted when the scanning beam has dimensions approximating those of an element.

The video signal does not consist of an uninterrupted succession of picture signals generated by scanning rows of elements. At the end of each line, a line-sync signal is introduced which is contained within the period of blanking level known as the line-blanking period. This period has a duration T_{lb} appreciable compared with the period H of one line (H = 1/line frequency). Moreover at the end of each field, a field-sync signal is introduced which is also contained within a period of blanking level known as the field-blanking period. This period has a duration which is an appreciable fraction of the field period (1/field frequency) and has the effect of suppressing a number of lines N_{fb}. The number of lines seen in the reproduced picture (known as active lines) is thus $(N - N_{fb})$.

If Figure IV-17 represents the reproduced picture, there are $(N - N_{fb})$ horizontal rows of elements and the vertical dimension of each element is $H/(N - N_{fb})$. The ratio of width to height of the received picture is known as the aspect ratio a, and if we assume the elements to be square, there are $a(N - N_{fb})$ elements in each row. During the scanning of each line, the video signal rises when the scanning beam traverses a white element and falls when it traverses a black element. One rise followed by a fall constitutes one cycle of alternation in the video signal since the positive half of one cycle corresponds to a white element and the negative half to a black element. The number of cycles corresponding to one line is thus $a(N - N_{fb})/2$, and these are generated in the camera in a period $H - T_{lb}$. Thus, the frequency corresponding to detail of the size of an element is given by

$$f = \frac{a\left(N - N_{fb}\right)}{2\left(H - T_{lb}\right)} \tag{11}$$

The video signal corresponding to a picture composed of alternate black and white elements is, of course, a square wave with a frequency given by Equation 11. If such a picture were scanned in a camera with an electron beam of negligibly small dimensions, the camera output would have a square waveform. Such a signal has components at frequencies f, 2f, 3f, etc., up to an infinite frequency. If, as in practice, the scanning beam has dimensions comparable with those of an element, as assumed above, the upper frequency components are greatly attenuated and the camera output tends to be sinusoidal in form and with a frequency given by Equation 11. This frequency, the fundamental component of the square wave corresponding to a picture of alternate black and white elements, is generally regarded as the upper frequency limit in video frequency amplifiers.

Although N_{fb} and T_{lb} are appreciable compared to N and H in general, because of the special nature of our TV system (in particular the low frame rate) it seems reasonable to assume that line and field synchronization can be provided so that N_{fb} and T_{lb} are negligible compared to N and H. Under this assumption, Equation (11) becomes

$$f = a\,N^2 P/2 \qquad (12)$$

Equation (12) is evaluated in Figure IV-24 for various values of N and P. For our TV system, N = 1025 lines, P = 1 frame per second and a, the ratio of width to height of received picture, is given by:

$$a = \frac{2D \tan \psi/2}{2D \tan \theta/2} = 1.99$$

for a 10- by 20-degree field of view. Then, the maximum video frequency which must be transmitted in order to provide horizontal resolution equal to vertical resolution is 1.0 MHz.

The present bandwidth of the LM-Earth S-band link is assumed to be 0.7 MHz. Thus, the bandwidth requirements for video transmission plus whatever telemetry is desired exceed the current capabilities of the communication system. Bandwidth growth is possible in two directions. The most straightforward approach to increasing the bandwidth would apparently be the use of the 210-foot-diameter antenna at Goldstone during the LM descent. This would provide a 7-dB increase in system gain over the 85-foot antenna currently in use. The resultant 5-fold increase would bring the LM-Earth bandwidth up to 3.5 MHz, which would easily satisfy unmanned LM landing requirements. The associated constraint on mission timing — that LM-Goldstone line of sight should exist during the LM descent — does not appear to be severe. The second approach to increasing LM bandwidth involves hardware modifications to the LM transmitter. LM transmitter power could be doubled by parallel operation of two of the 20-watt traveling wave tube (TWT) power amplifiers used in the present LM transmitter. The resultant doubling of LM-Earth bandwidth would provide 1.4 MHz, which should be adequate for unmanned LM landing requirements.

In summary, the video bandwidth required to meet AAP requirements is 1 MHz. Sufficient bandwidth could be provided through use of Goldstone's 210-foot antenna or by parallel operation of two 20-watt TWT's in the LM transmitter.

2.3 TV Design Sensitivities

The required video bandwidth is very sensitive to the choice of a time at which the controller must be able to perceive all LM landing hazards in the scan area.

This is caused by the strong interaction of hazard perception capability with LM elevation (E_{LM}) and range (D) to the landing site. Required bandwidth increases as the time at which all LM landing hazards must be perceived is moved away from hover. Three factors contribute to this increase. First, the minimum shadow length which must be perceived decreases as the time interval before hover is increased. This effect is shown in Figure IV-21. Second, the resolution degradation factor (λ_2/λ_1) at the downrange boundary of the scan area increases with an increase in time interval before hover, as shown in Figure IV-16. Third, the number of TV scan lines necessary to attain a given resolution increases as the time interval before hover increases. This can be seen by noting the effect of a decrease in E_{LM} and an increase in D (associated with an increase in the time interval before hover) on N in Equation (10). Since bandwidth varies as N^2 in Equation (12), a rapid increase in required bandwidth results from an increase in the time interval before hover. TV designs were computed for several values of the time at which all LM landing hazards in the scan area must be perceived by the controller. Figure IV-25 gives the resulting bandwidth requirements as a function of time before hover for the sample descent trajectory used. It is seen that a choice of "all hazards visible" time greater than 55 or 60 seconds before hover places an impossible bandwidth requirement on the communications system. On the other hand, it is desirable to leave as much time as possible for steering to the chosen safe landing site. A trade-off between these two factors led to a choice of 50 seconds before hover as the time at which all LM landing hazards should be made visible to the controller.

The TV design is also sensitive to the hazard density of the landing area. For example, if it is desired to land an unmanned LM in an area of intermediate hazard density such as the floor of Alphonsus, the requirement for a 0.99 probability of a safe landing site in the scan area sets the field of view. In this case, Figure IV-13 indicates a requirement for a scan area of 1.2 million square feet when the landing uncertainty footprint is 60 feet in diameter. A 25- by 30-degree field of view then meets the requirements on both position error correction and safe landing site selection. Perception of all LM landing hazards 50 seconds before hover then requires 7750 TV scan lines/frame. This makes necessary a video bandwidth of 36 MHz. Thus, an unmanned LM landing in a region of intermediate hazard density, such as the floor of Alphonsus, is not feasible due to the excessive requirement on video bandwidth.

Finally, the sensitivity of TV design bandwidth to sun elevation angle should be noted. The visible shadow length of LM landing hazards decreases with an increase in sun elevation angle. This means that more TV scan lines, and thus more video bandwidth, must be provided to insure perception of all LM landing hazards in the scan area 50 seconds before hover. The video bandwidth requirements as a

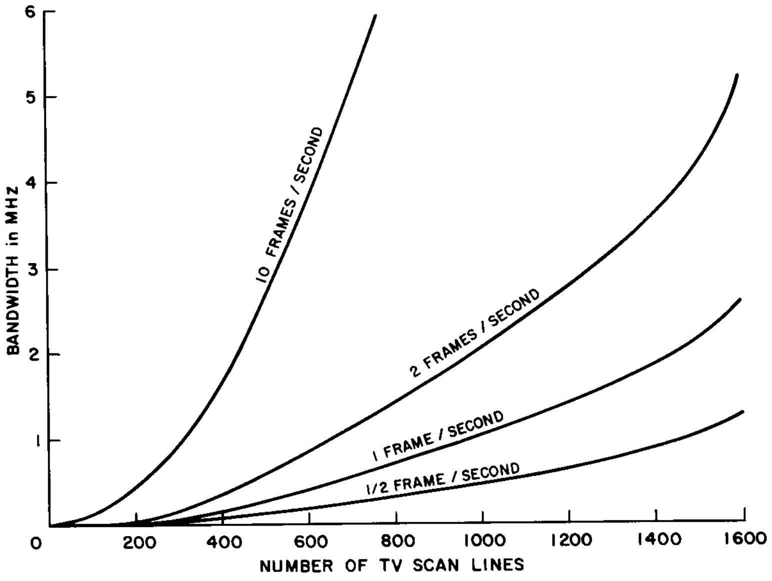

Figure IV-24. Video Bandwidth Required for Horizontal Resolution Equal to Vertical Resolution

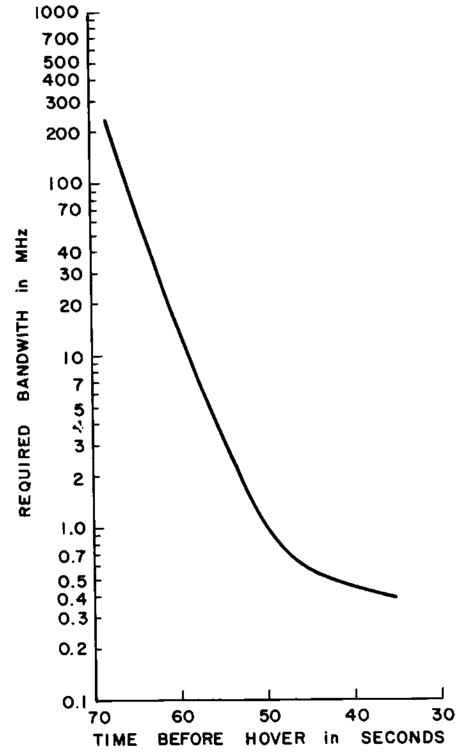

Figure IV-25. Required Bandwidth versus Time when all LM Landing Hazards must be Perceived

function of sun elevation angle are presented in Figure IV-26. Sun elevation angles above about 13 degrees place excessive bandwidth demands on the communication system.

The above results are all conservative in that perception of landing hazards is assumed to be based entirely on shadow information. The video bandwidth required may be reduced, depending on the additional amount of information provided by the contrast between the horizontal surround and the sloping surfaces of the rocks and craters. Nonetheless, it is reasonable to conclude that unmanned LM landings will necessarily be limited to relatively smooth regions with sun elevation angle at landing around 10 degrees.

2.4 Hover Error Correction Maneuver

Errors in the landing radar velocity measurement leave the LM with residual velocity when the guidance system thinks hover has been achieved. If this velocity error is allowed to go uncorrected, unacceptably large position errors are accumulated between the last controller target redesignation command and touchdown. An estimate of the landing radar errors is presented in Figure 10 of Reference 2. This indicates downrange and crossrange hover velocity errors of 1.5 fps (3 sigma). The circle containing 99.7 percent of all horizontal hover velocity errors then has a radius of 1.7 fps. If a velocity error of 1.7 fps at hover were not corrected, a radial position error of 42 feet would accumulate during the 25 seconds required for descent to touchdown from the hover altitude of 100 feet. Adding the 15-foot radius of the LM landing gear footprint to this position uncertainty yields a total LM landing uncertainty footprint 115 feet in diameter. From Figure IV-13, it is seen that a footprint of this size would require a scan area of about 10,000,000 square feet for a 0.99 probability of finding a safe landing site in a region of smooth hazard density. This scan area is not attainable due to limitations on video bandwidth. Thus, high probabilities of safe landing cannot be provided unless hover velocity error correction is performed before descent to touchdown. However, the controller located on Earth probably cannot take over direct attitude control and "fly the LM in" by continuously correcting errors as a LM pilot would do, since the Earth-Moon transmission time delay would probably cause an unsatisfactory Earth-LM control-loop response. This means that the controller must measure the position and velocity errors based on TV observations and then command an open-loop LM attitude maneuver to correct the errors.

Errors in the inertial platform attitude reference cause an acceleration error with the associated velocity and position errors integrating over the time interval from guidance termination to touchdown. Most of these errors will accumulate after the error measurement for the open-loop maneuver, so the only way to minimize the position error resulting from the attitude error is to make the time interval from guidance termination to touchdown as small as possible.

A simple strategy for sequential correction of hover velocity and position errors caused by landing radar errors is now presented. This is not intended as a recommended strategy but rather as a demonstration of the feasibility of hover error correction and as a basis for rough error estimates. More efficient error correction schemes are possible and desirable. The strategy can be divided into six phases, with a total time interval of 35 to 47 seconds from guidance termination to touchdown, depending on the size of the errors to be corrected.

Phase 1 begins when the guidance system thinks it has reached its hover target point, and ends 10 seconds later. During this time the controller has five tasks to perform. He selects a reference object (crater or rock), marks its initial position on the screen, selects the desired landing site, marks its position on the screen, and marks the location of the reference object at the end of the 10-second period.

Phase 2 occupies the 5 seconds following Phase 1 and is used for computation of the magnitude and direction of the velocity and position errors measured in Phase 1 and for issuing corrective commands. If the reference object moves ΔP_V feet during Phase 1, then the magnitude of the error velocity vector $\overline{\Delta V}$ is $\Delta P_V/10$ fps. The error position vector $\overline{\Delta P}$ is found by suitably updating the position dispersion to the desired landing site with the known velocity. Equations will be developed below for translating the position measurements made on the TV screen during Phase 1 into measurements of actual LM motion over the lunar surface. With the aid of a small computer and suitable interface equipment, it seems reasonable that all of the functions of Phase 2 could be automated in a straightforward fashion, making possible the small time interval allotted.

The LM is rolled to the proper orientation for velocity error correction during Phase 3. Since the attitude maneuver to correct the velocity error can be either positive or negative pitch or yaw (pilot roll), proper orientation can be achieved with a roll of 45 degrees or less. Assuming that the roll will be performed at the maximum automatic rate of 10 degrees per second, Phase 3 will take less than 4.5 seconds.

The velocity error $|\overline{\Delta V}|$ is corrected by an attitude maneuver during Phase 4. The attitude maneuver consists of a pitch (or yaw) at maximum rate to an attitude determined by the size of the velocity error, followed immediately by a pitch (or yaw) at maximum rate $(\dot{\theta})$ back to vertical attitude. The geometry of the maneuver is shown in Figure IV-27. The acceleration A_X in the direction opposite to that of the velocity error is given by:

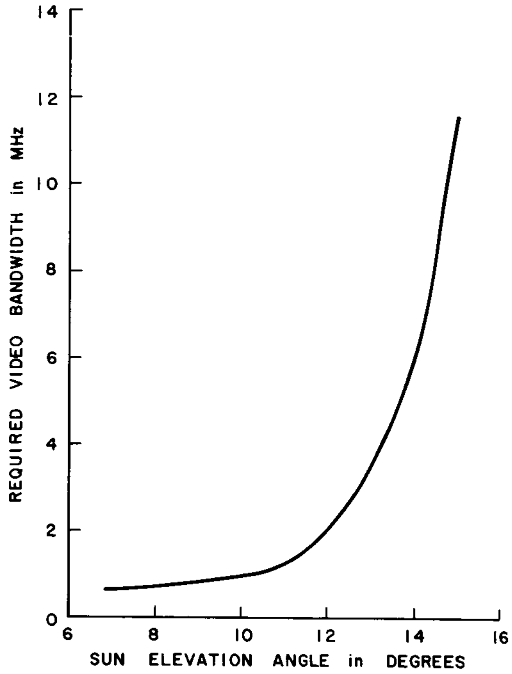

Figure IV-26.
Required Video Bandwidth
versus Sun Elevation Angle

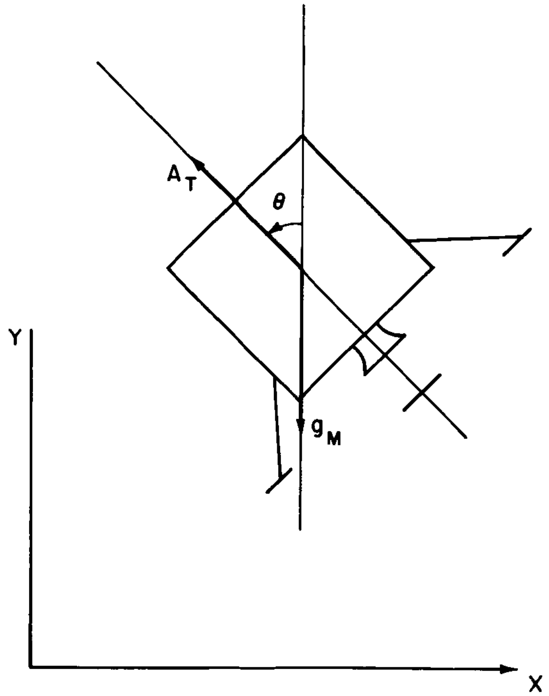
A_T
θ
g_M
Y
X

Figure IV-27.
LM Attitude Maneuver

$$A_X = \begin{cases} A_T \sin \dot{\theta}\, t & \text{when } 0 \le t \le \theta_{max}/\dot{\theta} \\ A_T \sin\left(2\theta_{m\bar{a}x}\ \dot{\theta}t\right) & \text{when } \theta_{max}/\dot{\theta} \le t \le 2\theta_{max}/\dot{\theta} \end{cases}$$

Then, integrating over the entire maneuver, the velocity change is given by:

$$V_X = \frac{2\,A_T}{\dot{\theta}}\left(1 - \cos \theta_{max}\right)$$

Thus to correct a velocity error $\Delta V = |\overline{\Delta V}|$, we order a maximum attitude dispersion of

$$\theta_{max} = \cos^{-1}\left(1 + \frac{\Delta V \dot{\theta}}{2A_T}\right) \qquad (13)$$

Integrating once more, we see that the position accumulated during this maneuver is

$$P_X = \left(\frac{V_X}{2}\ \frac{\theta_{max}}{\dot{\theta}}\right) + \frac{2\,A_T}{\dot{\theta}}\left(\theta_{max} - \sin \theta_{max}\right) \qquad (14)$$

Now at the 0.997 probability level, the magnitude of the velocity error is bounded by $\Delta V = 1.7$ fps. It is assumed that $A_T = g_M$ at hover with negligible orders from guidance to maintain constant altitude and $\dot{\theta} = 10$ degrees/second. Then, evaluation of Equation (13) indicates an attitude change of 14 degrees off the vertical to correct 1.7 fps. This maximum velocity correction maneuver takes 2.8 seconds. From Equation (14), we see that a negligible position change of 2 feet is accumulated during the maneuver.

During Phase 5, the LM is rolled to the proper orientation for the position correction maneuver. By the considerations of Phase 3, a roll of < 45 degrees is required, with a maximum time of 4.5 seconds for this phase.

Position error correction and descent to touchdown are accomplished during Phase 6. The two functions were combined to minimize the time interval over which position errors could build up from reference attitude errors. The position error correction maneuver consists of an attitude change to some maximum attitude off vertical, determined by the magnitude of the position error, followed by an immediate return to vertical. Immediately, the mirror image attitude maneuver is performed, bringing the total velocity change for the maneuver to zero. From Figure IV-27, the acceleration profile in the direction of the position error is:

$$A_X = \begin{cases} A_T \sin \dot{\theta}t & \text{when } 0 \le t \le \theta_{max}/\dot{\theta} \\ A_T \sin\left(2\theta_{max} - \dot{\theta}t\right) & \text{when } \theta_{max}/\dot{\theta} \le t \le 2\ \theta_{max}/\dot{\theta} \\ A_T \sin\left(2\theta_{max} - \dot{\theta}t\right) & \text{when } 2\theta_{max}/\dot{\theta} \le t \le 3\theta_{max}/\dot{\theta} \\ A_T \sin\left(\dot{\theta}t - 4\ \theta_{max}\right) & \text{when } 3\theta_{max}/\dot{\theta} \le t \le 4\theta_{max}/\dot{\theta} \end{cases}$$

Integrating twice, we get a position change over the entire maneuver of:

$$P_X = 0 + \frac{AT}{\dot{\theta}^2}\left(\theta_{max} - \sin\theta_{max}\right)$$

$$+ \frac{V_X}{2}\,\frac{\theta_{max}}{\theta} + \frac{A_T}{\dot{\theta}^2}\left(\theta_{max} - \sin\theta_{max}\right)$$

$$+ V_X\,\frac{\theta_{max}}{\dot{\theta}} - \frac{AT}{\dot{\theta}^2}\left(\theta_{max} - \sin\theta_{max}\right)$$

$$+ \frac{V_X}{2}\,\frac{\theta_{max}}{\dot{\theta}} - \frac{A_T}{\dot{\theta}^2}\left(\theta_{max} - \sin\theta_{max}\right)$$

or

$$P_X = 2V_X\,\theta_{max}/\dot{\theta} \tag{15}$$

where V_X is as defined above. Evaluation of Equation (15) gives the relation between position error and maximum attitude θ_{max}, as shown in Figure IV-28.

Before the maximum position error correction maneuver size can be determined, a LM hover point bias must be specified to insure that the desired landing site will be visible above the window bottom at hover. To find the required bias size, it is assumed that the controller issues his last LPD command at 25 seconds before hover and that there is zero position error at that time. As a worst case for landing site visibility (0.997 probability level), assume that radar errors impart a downrange velocity error of 1.7 fps to the LM, causing the desired landing site to move down toward the window bottom. This velocity error integrated over the 25 seconds to hover gives a position error of 43 feet at hover. In addition, the line of sight to the desired landing site must be more than 25 degrees above the vertical at hover to avoid blocking by the window bottom. The situation is illustrated in Figure IV-29. An uprange LM hover point bias of 90 feet must be provided to insure that the desired landing site remains above the window bottom in the "worst case" situation postulated. An elevation field of view θ and TV camera pointing angle E, consistent with this situation, were found by simultaneous solution of the two equations:

$$E + \theta/2 = 65 \text{ degrees} \tag{16}$$

$$\frac{H \sin\theta/2}{\sin E}\left[\frac{1}{\sin(E + \theta/2)} + \frac{1}{\sin(E - \theta/2)}\right] = 2\ (25 \text{ sec})\ (1.7 \text{ fps}) \tag{17}$$

Equation (16) requires the bottom of the TV beam to graze the window bottom. Equation (17) insures that the desired landing site will remain in the along-track scan for all along-track velocity errors in the 0.997 probability circle. Solution of these two equations gives $\theta = 30$ degrees, $E = 50$ degrees. Similarly, solution of the crosstrack scan length equation:

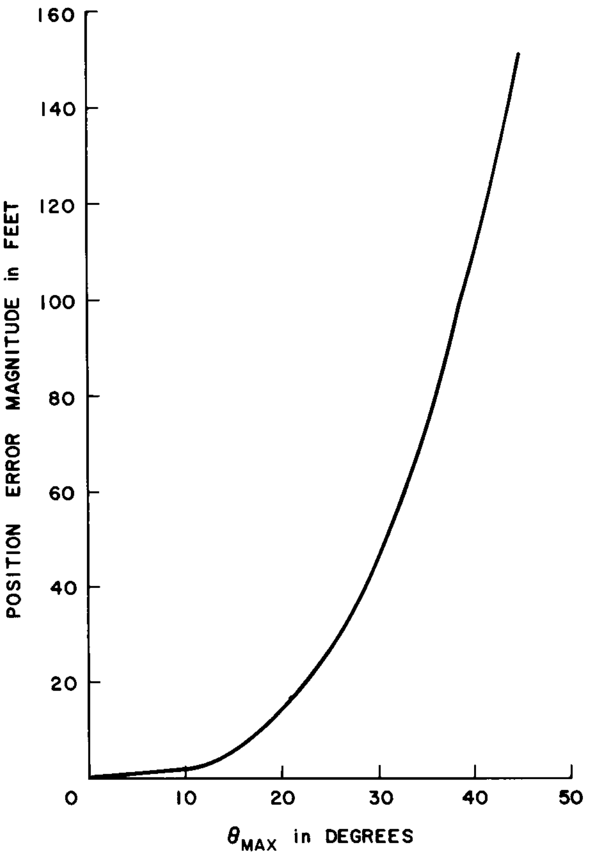

Figure IV-28. Position Error Magnitude versus θ_{max}

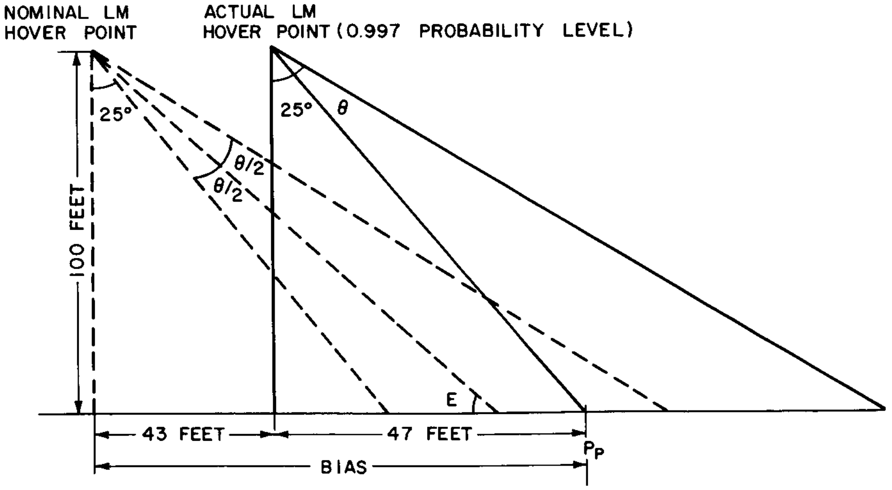
NOMINAL LM HOVER POINT
ACTUAL LM HOVER POINT (0.997 PROBABILITY LEVEL)
25°
25°
θ
θ/2
θ/2
100 FEET
E
43 FEET
47 FEET
BIAS
P_P

Figure IV-29. LM Hover Point Bias

$$2H \tan \psi/2 = 2\ (25\ \text{sec.})\ (1.7\ \text{fps})$$

gives an azimuth field of view of ψ = 50 degrees which insures that the desired landing site will remain in the crosstrack scan for all crosstrack velocity errors in the 0.997 probability circle. The switch from the 10- by 20-degree to the 30- by 50-degree TV field of view should take place about 25 seconds before hover to give the controller time to orient himself.

Returning to the position error correction maneuver, we have a required bias of 90 feet so that, from Figure IV-28, there is a 37-degree attitude maneuver in the nominal case. Performance of this maneuver at 10 degrees/second requires $4\theta_{max}/\dot{\theta}$, or about 15 seconds. If we have an uprange velocity error of 1.7 fps integrating over the time interval from 25 seconds before hover to its correction 18 seconds after hover, a total downrange position change of 90 + 73 = 163 feet is necessary, requiring a 46-degree attitude maneuver taking about 18 seconds. This sets the upper bound on maneuver duration. The lower bound is set by a velocity error of the same magnitude and opposite direction. Then, a position change of 90 - 82 = 8 feet is necessary, requiring a 17-degree attitude maneuver taking about 7 seconds. If guidance establishes a 5-fps descent rate just prior to initiation of the position correction maneuver, at the conclusion of the maneuver when zero translational velocity is achieved, the LM will be at an altitude of 65 feet for the minimum maneuver, 25 feet for the nominal maneuver, and 10 feet for the maximum maneuver. On the assumption that guidance can control initial altitude as well as it can be measured (6.5 feet at the 0.997 level), a simple combination maneuver of this type should be satisfactory.

Figure IV-30 summarizes the functions and time intervals associated with the six phases of the hover maneuver.

2.5 Hover Maneuver Errors

The two major components of touchdown point errors after completion of the hover maneuver are assumed to be:

1. Error in the measurement of LM position change over the lunar surface by measurement of position change on the TV display screen.
2. Inertial platform errors giving errors in the attitude reference between correction of observed errors and touchdown.

It is assumed that the LM can execute the commanded attitude changes with sufficient accuracy so that the errors in the hover maneuver arise almost entirely from errors in the position and velocity measurements which determine the attitude changes to be made.

2.5.1 Measurement Equations. Before an estimate can be made of the accuracy with which LM position and velocity can be measured by TV display screen measurements, we must develop the equations which would be used. Referring to Figure IV-31, we can develop the relations between small changes in viewing angle α and small changes in along-track surface length $L_E(\alpha)$. Using the viewing geometry equation:

$$L_E(\alpha) = \frac{H}{\sin E} \frac{\sin \alpha}{\sin(E - \alpha)}$$

we can find the differential of along-track surface length with respect to view angle.

$$\frac{dL_E}{d\alpha} = \lim_{\Delta\alpha \to 0} \frac{L_E(\alpha + \Delta\alpha) - L_E(\alpha)}{\Delta\alpha} = \frac{H}{\sin E} \frac{\cos \alpha + \sin \alpha \cot (E - \alpha)}{\sin (E - \alpha)}$$

$$dL_E = \frac{H}{\sin E} \frac{\cos \alpha + \sin \alpha \cot (E - \alpha)}{\sin (E - \alpha)} d\alpha \tag{18}$$

where positive values of α give view lines in the downrange portion of the TV scan.

Now, to relate changes in scan angle α to changes in TV display screen vertical length measurement n, we assume a 6- by 6-foot display with a constant angular displacement/linear displacement scale factor. Then, in the along-track dimension with the hover field of view:

$$\frac{\Delta\alpha}{30^\circ} = \frac{\Delta n}{6 \text{ ft}}$$

$$d\alpha = 5 \, dn \text{ degrees/feet.}$$

Finally, to relate along track displacement dL_E to vertical displacement dn on the display screen:

$$\frac{dL_E}{dn} = \left(\frac{dL_E}{d\alpha} \frac{\text{ft}}{\text{rad}}\right) \left(\frac{1}{57.2} \frac{\text{rad}}{\text{deg}}\right) \left(\frac{d\alpha}{dn} \frac{\text{deg}}{\text{ft}}\right)$$

Assuming hover conditions:

$$dL_E = 11.44 \frac{\cos \alpha + \sin \alpha \cot (50^\circ - \alpha)}{\sin (50^\circ - \alpha)} dn$$

or, since $\alpha = 5n$ for a 6-foot display:

$$dL_E = 11.44 \frac{\cos 5n + \sin 5n \cot (50^\circ - 5n)}{\sin (50^\circ - 5n)} dn$$

where the origin of the display screen coordinate (n = 0) corresponds to the TV camera pointing direction on the surface ($L_E = 0$), and positive vertical displacements on the display screen correspond to downrange displacements on the lunar surface.

$\Delta T_1 = 10$	$\Delta T_2 = 5$	$0 \leq \Delta T_3 \leq 4.5$	$0 \leq \Delta T_4 \leq 2.8$	$0 \leq \Delta T_5 \leq 4.5$	$\Delta T_6 = 20$
PHASE 1	PHASE 2	PHASE 3	PHASE 4	PHASE 5	PHASE 6
SELECT, MARK, AND TRACK	COMPUTE AND ISSUE COMMANDS	ROLL FOR VELOCITY CORRECTION	VELOCITY CORRECTION	ROLL FOR POSITION CORRECTION	POSITION CORRECTION AND DESCENT

Figure IV-30. Hover Maneuver Time Line

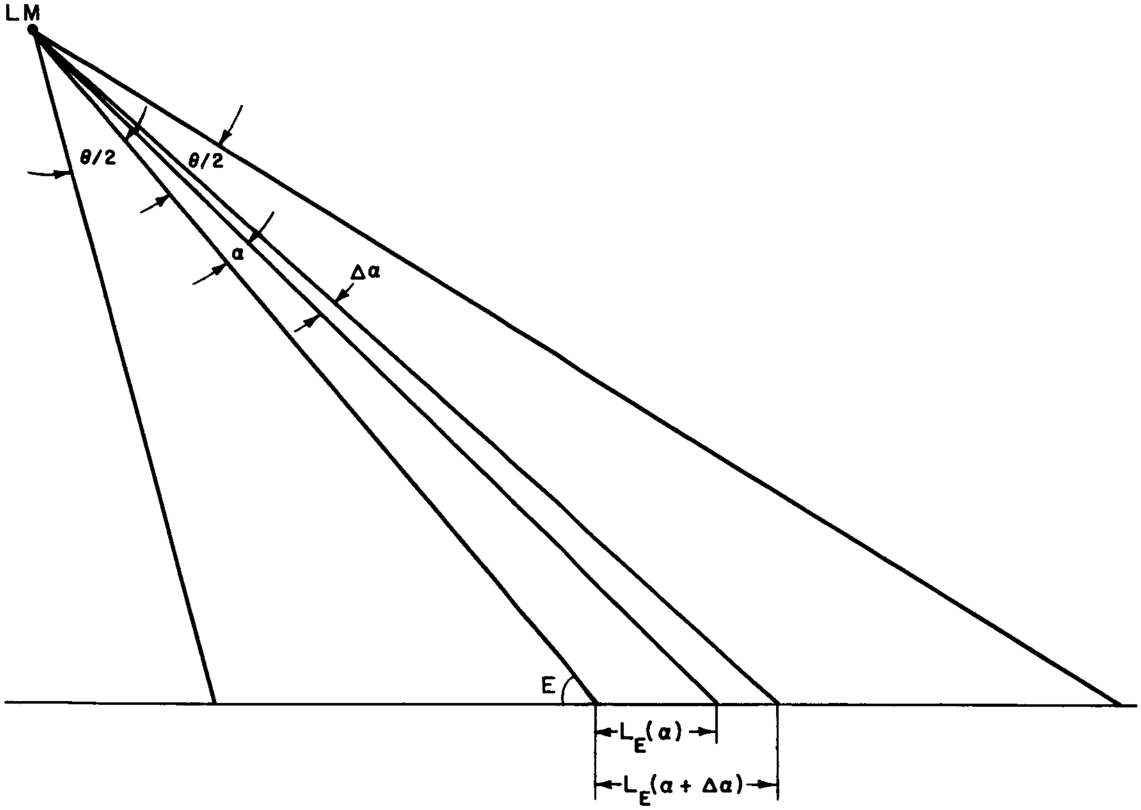
LM
$\theta/2$
$\theta/2$
α
$\Delta\alpha$
E
$L_E(\alpha)$
$L_E(\alpha + \Delta\alpha)$

Figure IV-31. Relationship between Viewing Angle and Along-Track Surface Scan Length

We can relate crosstrack displacement dL_A on the surface to horizontal displacement dm on the display screen, by setting E = 90 degrees in the above development:

$$dL_A = H \left(1 + \mathrm{Tan}^2 \alpha\right) d\alpha \tag{19}$$

$\Delta\alpha/50° = \Delta m/6$ ft for a 6-foot-wide display screen with the hover field of view. Then,

$$d\alpha = 8.33 \text{ dm}$$

$$dL_A = 14.6 \left(1 + \tan^2 8.33 \text{ m}\right) dm$$

Since dL_E/dn and dL_A/dm serve as scale factors relating lunar surface displacement to display screen displacement, we introduce the notation:

$$SF_E\ (n) \triangleq \frac{dL_E}{dn}$$

$$SF_A\ (m) \triangleq \frac{dL_A}{dm}$$

Referring to Figure IV-32, we can find the crosstrack distance $d_c(P_1, P_2)$ between two points P_1 and P_2 on the lunar surface by measuring their horizontal coordinates on the display screen:

$$d_c\left(P_1, P_2\right) = \lim_{\Delta m \to o} \sum_{m_1}^{m_2} SF_A\left(m_i\right) \Delta m = \int_{m_1}^{m_2} SF_A(m) dm \tag{20}$$

Similarly, we can find the along-track distance $d_a(P_1, P_2)$ between P_1 and P_2 by measuring their vertical coordinates on the display screen:

$$d_a\left(P_1, P_2\right) = \int_{n_1}^{n_2} SF_E\ (n)\ dn \tag{21}$$

Then, with $\overline{P_1 P_2}$ representing the motion of our reference object over a 10-second measurement period, the velocity error vector is specified by:

$$|\overline{\Delta V}| = \frac{1}{10} |\overline{P_1 P_2}| = \frac{1}{10} \left[d_c\ \left(P_1, P_2\right) \sqrt{+}\ d_a\ \left(P_1, P_2\right)\right]$$

where the notation $\sqrt{+}$ implies the root-sum-square operation. The orientation of the velocity error vector is given by:

$$< \overline{\Delta V} = \tan^{-1} \frac{d_a\left(P_1, P_2\right)}{d_c\left(P_1, P_2\right)}$$

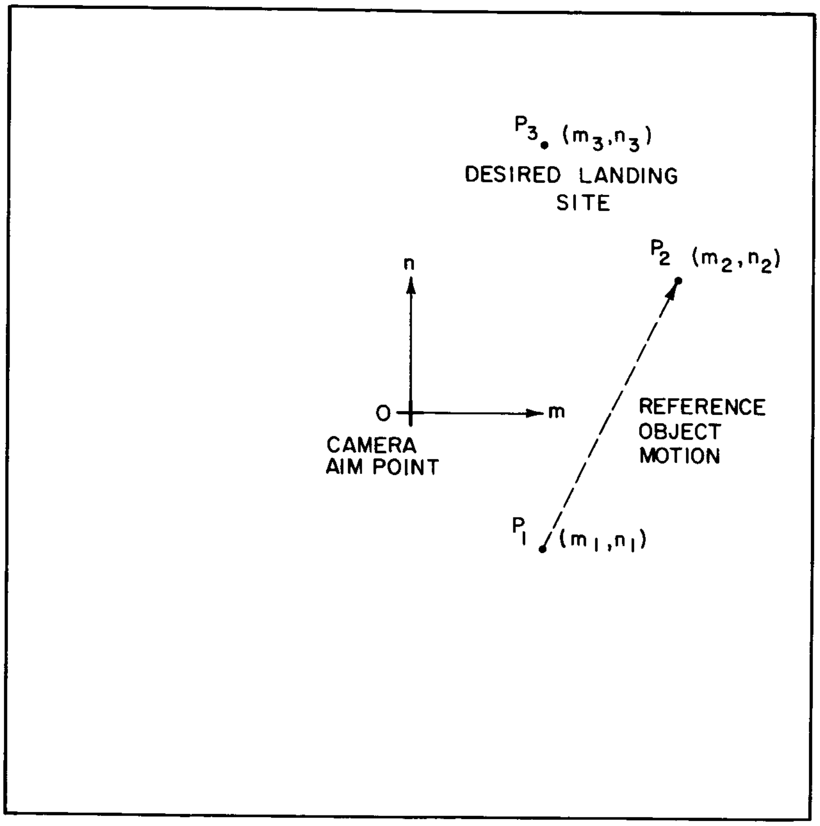
P_3 (m_3, n_3)
DESIRED LANDING SITE
P_2 (m_2, n_2)
n
O
m
CAMERA AIM POINT
REFERENCE OBJECT MOTION
P_1 (m_1, n_1)

Figure IV-32. TV Display Measurements

Similarly, we can get the position error vector $\overline{\Delta P'}$ from TV camera aimpoint to desired landing site:

$$d_c\left(O, P_3\right) = \int_0^{m_3} SF_A(m)\, dm \tag{22}$$

$$d_a\left(O, P_3\right) = \int_0^{n_3} SF_E(n)\, dn \tag{23}$$

$$|\overline{\Delta P'}| = |\overline{OP_3}| = d_c\left(O, P_3\right) \sqrt{+}\, d_a\left(O, P_3\right)$$

$$<\overline{\Delta P'} = \tan^{-1} \frac{d_a\left(O, P_3\right)}{d_c\left(O, P_3\right)}$$

Assuming that LM roll attitude is held constant after hover, so that the TV camera elevation coordinate corresponds to the along track surface coordinate, the vector $\overline{\Delta P_{LM}}$ from LM subpoint to camera aimpoint is oriented in the along track direction and, from Figure IV-29, has magnitude

$$|\overline{\Delta P_{LM}}| = d_a\ (LM, O) = H \tan\left(25° + \theta/2\right) = H \tan 40°$$

Then, the position error vector $\overline{\Delta P}$ from LM subpoint to desired landing site is the sum of these two vectors:

$$\overline{\Delta P} = \overline{\Delta P'} + \overline{\Delta P_{LM}}$$

2.3.2 Error Analysis. Now that the measurement equations are specified, we can proceed with the error analysis. All error components are assumed to be normally distributed with zero mean. The 1-sigma values of the along track and cross track components of touchdown point error, σ_a and σ_c, are determined by the errors in position, velocity, and acceleration in each direction. The position errors, σ_{P_a} and σ_{P_c}, arise from the limitations on our ability to measure the displacement from LM subpoint to the desired landing site. The velocity errors, σ_{V_a} and σ_{V_c} are determined by the accuracy with which we can measure LM hover velocity error. The thrust acceleration errors, $a_T\sigma_\theta$ and $a_T\sigma_\psi$ are caused by errors in the pitch and yaw attitude reference. The total errors are then given by:

$$\sigma_a = \sigma_{P_a} \sqrt{+}\, \sigma_{V_a}\, \Delta t_1 \sqrt{+}\, \frac{1}{2} a_T \sigma_\theta\, \Delta t_2^2 \tag{24}$$

$$\sigma_c = \sigma_{P_c} \sqrt{+}\, \sigma_{V_c}\, \Delta t_1 \sqrt{+}\, \frac{1}{2} a_T \sigma_\psi\, \Delta t_2^2 \tag{25}$$

where

Δt_1 is the time elapsed between hover velocity error correction and touchdown.

Δt_2 is the time interval over which acceleration errors can integrate uncorrected (i.e., end of measurement period to touchdown).

From Figure IV-30, $\Delta t_1 \leq 24.5$ seconds and $\Delta t_2 \leq 36.8$ seconds. To be conservative, we use the maximum values. The thrust acceleration a_T is assumed to have magnitude $a_T = g_m$ from hover to touchdown.

The along-track position error σ_{P_a} has two components:

1. σ_1, error in our estimate of the distance from LM subpoint to TV camera aimpoint
2. σ_2, error in our measurement of the along-track distance between camera aimpoint and desired landing site.

Since the TV camera pointing direction is fixed at 40 degrees above the vertical at hover, the error σ_1 is determined by the hover altitude error σ_H. Since the distance estimate is given by:

$$d_a\ (LM, O) = H \tan 40°$$

$$\sigma_1 = \sigma_H \tan 40° \tag{26}$$

We assume that guidance controls hover altitude and that altitude can be controlled to the accuracy with which it can be measured. Then σ_H is just the altitude measurement accuracy of the landing radar when it is operated 100 feet above the surface.

To compute the error σ_2, Equation (23) is rewritten as:

$$d_a \left(O, P_3\right) = \widetilde{SF}_E \left(O, n_3\right) n_3$$

$$\widetilde{SF}_E \left(O, n_3\right) = \frac{1}{n_3} \int_O^{n_3} SF_E(n)\, dn$$

is the integral average of the scale factor over the range of interest defined in Figure IV-32. $\widetilde{SF}_E\ (O, n_3)$ could be found by explicit integration, but for simplicity, the approximation

$$\widetilde{SF}_E \left(O, n_3\right) \doteq \frac{SF_E(O) + SF_E\left(n_3\right)}{2}$$

was made. Then the measurement error is given by:

$$\sigma_2 = \sigma_{\widetilde{SF}_E \left(O, n_3\right)} n_3 \sqrt{+}\ \widetilde{SF}_E \left(O, n_3\right) \sigma_{n_3} \tag{27}$$

Errors in the scale factor (and hence in the average scale factor) are assumed to be of two main types — sweep circuitry errors and hover altitude errors. The sweep circuit error would appear as a fraction k of the total scale factor. Altitude variations would cause a scale factor error of size

$$\frac{\partial \widetilde{SF}_E\left(O, n_3\right)}{\partial H}\,\sigma H.$$

Referring to Equation (18), we see that:

$$\frac{\partial \widetilde{SF}_E\left(O, n_3\right)}{\partial H} = \frac{\widetilde{SF}_E\left(O, n_3\right)}{H}$$

Thus, we have

$$\sigma_{\widetilde{SF}_E\left(O, n_3\right)} = k\,\widetilde{SF}_E\left(O, n_3\right) \sqrt{+}\, \frac{\widetilde{SF}_E\left(O, n_3\right)}{H}\,\sigma_H \tag{28}$$

Next, we assume that the error in our measurement of either TV display coordinate (m, n) is normally distributed with mean zero and variance σ_m^2, so that $\sigma_{n_3} = \sigma_m$. Thus, from Equations (27) and (28) we have:

$$\sigma_2 = \left[k\,\widetilde{SF}_E\left(O, n_3\right) \sqrt{+}\, \frac{\widetilde{SF}_E\left(O, n_3\right)}{H}\,\sigma_H\right] n_3 \sqrt{+}\, \widetilde{SF}_E\left(O, n_3\right)\sigma_m \tag{29}$$

Now σ_1 is caused by hover altitude errors and would tend to be correlated with that component of σ_2 caused by altitude errors. To be conservative, we combine those errors by addition rather than root-sum-square, and get:

$$\sigma_{P_a} = k\,\widetilde{SF}_E\left(O, n_3\right) n_3 \sqrt{+} \left[\frac{SF_E\left(O, n_3\right)}{H}\, n_3 + \tan 40^\circ\right]\sigma_H \sqrt{+}\; \widetilde{SF}_E\left(O, n_3\right)\sigma_m \tag{30}$$

The cross track position error σ_{P_c} is found by the same procedure as above, except that there is no crossrange component in the position vector from LM subpoint to camera aimpoint, under the assumption that LM roll attitude is controlled. The above considerations then lead to a one sigma value for crossrange position error of:

$$\sigma_{P_c} = \left[k\,\widetilde{SF}_A\left(O, m_3\right) \sqrt{+}\, \frac{\widetilde{SF}_A\left(O, m_3\right)}{H}\,\sigma_H\right] m_3 \sqrt{+}\, \widetilde{SF}_A\left(O, m_3\right)\sigma_m \tag{31}$$

where

$$\widetilde{SF}_A \left(O, m_3\right) = \frac{SF_A (O) + SF_A \left(m_3\right)}{2}$$

Similar procedures lead to estimates of the accuracy with which we can measure the hover velocity error, given a 10-second period to track the position displacement of a reference object. Assuming that a precise time reference can be provided, the along-track velocity measurement error σ_{V_a} is solely determined by the error in our measurement of the along-track position displacement of the reference object over the 10 second period:

$$\sigma_{V_a} = \frac{1}{10} \sigma_{D_a}$$

The error in measurement of position displacement between two points is found by the same considerations as above, except that there is no need to measure the distance from LM subpoint to camera aimpoint. From the notation of Figure IV-32, the appropriate measurement equation, Equation (21), is thus rewritten as:

$$d_a \left(P_1, P_2\right) = \widetilde{SF}_E \left(n_1, n_2\right) \left(n_2 - n_1\right)$$

where

$$\widetilde{SF}_E \left(n_1, n_2\right) \doteq \frac{SF_E \left(n_1\right) + SF_E \left(n_2\right)}{2}$$

Following the previous development, we end up with:

$$\sigma_{V_a} = \frac{1}{10} \left\{ \left[k\, \widetilde{SF}_E \left(n_1, n_2\right) \sqrt{+}\, \frac{\widetilde{SF}_E \left(n_1, n_2\right)}{H} \sigma_H \right] \left(n_2 - n_1\right) \sqrt{+}\, \widetilde{SF}_E \left(n_1, n_2\right) \sqrt{2}\, \sigma_m \right\} \qquad (32)$$

where the 1-sigma value for the error in measuring the distance between the two points on the TV display screen is computed by using the relationship for the difference of two normally distributed random variables:

$$\sigma_{n_2 - n_1} = \sigma_m \sqrt{+}\, \sigma_m = \sqrt{2}\, \sigma_m$$

In the crossrange direction, we get a similar result:

$$\sigma_{V_c} = \frac{1}{10}\left\{\left[k\,\widetilde{SF}_A\left(m_1, m_2\right) \sqrt{\;}^{+} \frac{\widetilde{SF}_A\left(m_1, m_2\right)}{H}\,\sigma_H\right]\left(m_2 - m_1\right) \sqrt{\;}^{+} \widetilde{SF}_A\left(m_1, m_2\right)\sqrt{2}\,\sigma_m\right\} \tag{33}$$

The thrust acceleration errors in the along-track and cross-track directions are caused by pitch and yaw attitude errors at hover. These attitude errors consist of initial platform alignment errors and integrated gyro drift. It is assumed that an automatic star tracker is provided which has the capability to align the LM inertial platform just prior to the powered landing maneuver, thus minimizing the effects of the integrated gyro drifts, $\sigma_{\theta_{GD}}$ and $\sigma_{\psi_{GD}}$. It is further assumed that this tracker can align the platform with errors equivalent to those of the LM pilot, σ_{θ_I} and σ_{ψ_I}. We then have:

$$\sigma_\theta = \sigma_{\theta I} \sqrt{\;}^{+} \sigma_{\theta_{GD}} \tag{34}$$

$$\sigma_\psi = \sigma_{\psi I} \sqrt{\;}^{+} \sigma_{\psi_{GD}} \tag{35}$$

Finally, to compute the total along-track position error σ_a, we combine the results of Equations (30), (32) and (34) as indicated by Equation (24). To get the total cross-track position error σ_c, we combine the results of Equations (31), (33) and (35) according to Equation (25).

It can be seen from the form of the error equations that the numerical results depend on the error models for the landing radar, inertial platform, TV sweep circuitry and display screen measurement. However, the results also depend on the location of the desired landing site relative to the camera aimpoint and the location of the reference object and direction of its motion, since the scale factors and measurement coordinates appear in the error equations. The approach taken is to postulate the worst cases which can reasonably be expected for position and velocity measurement, compute the individual errors in each coordinate (along track and cross track), and then use the upper bound error in each coordinate in computing the total error.

The assumed landing radar error model is that postulated in Figure 10 of Reference 2. The 3σ velocity errors in both directions are 1.5 fps so that 99.7 percent of all velocity errors will be contained in a circle of radius 1.7 fps. The altitude measurement accuracy at a hover altitude of 100 feet is $\sigma_H = 2.2$ feet. The inertial platform error model is given in Figure 6B of Reference 2. This postulates an initial alignment error of $\sigma_{\theta I} = \sigma_{\psi I} = 0.06$ degree. The gyro drift is 0.03 degree/ hour in both pitch and yaw. Since we assume an automatic star tracker alignment of the inertial platform just prior to initiation of the powered descent, the gyro drift will have integrated over only about one-sixth of an hour at hover. The accumulated attitude error at hover will be $\sigma_{\theta GD} = \sigma_{\psi GD} = 0.005$ degree. Thus, $\sigma_\theta = \sigma_\psi = 0.06$ degree. It seems reasonable to assume that sweep circuits can be produced with a 1σ error of 1 percent of the scale factor, $k = 0.01$. If this accuracy can be attained, then sweep circuit errors will have a negligible effect on total error. Finally, it is assumed that a reasonable value for the accuracy with which a point on the TV display screen can be measured in display coordinates is 0.5 inch at the 3σ level. This gives $\sigma_m = 0.0139$ feet.

Three cases were considered to get an upper bound on the position errors, σ_{P_a} and σ_{P_c}. In each case, the controller was not allowed to issue any further landing point redesignation commands after the TV camera field of view was switched at 25 seconds before hover. It was assumed that the LM was directed to the desired hover point (biased uprange from the desired landing point for landing point visibility) with zero error at this time and that the maximum velocity error of 1.7 fps integrated over the 25-second interval ending at hover. Cases 1, 2 and 3 correspond to uprange, downrange, and crossrange velocity error directions, respectively. Figure IV-33 illustrates for each case the position of P_N, the nominal location, and P_A, the actual location, of the desired landing point on the display screen. Position displacements are shown to scale for a 6- by 6-foot display. The position error equations were evaluated for each case, with the following results:

Case 1 $\sigma_{P_a} = 2.9$ feet $\sigma_{P_c} = 0.3$ feet

Case 2 $\sigma_{P_a} = 2.7$ feet $\sigma_{P_c} = 0.3$ feet

Case 3 $\sigma_{P_a} = 1.9$ feet $\sigma_{P_c} = 1.0$ feet

To be conservative, we select the maximum values for use in the total error equation:

$$\sigma_{P_a} = 2.9 \text{ feet} \tag{36}$$

$$\sigma_{P_c} = 1.0 \text{ feet} \tag{37}$$

The velocity measurement errors, σ_{V_a} and σ_{V_c}, were found by considering three cases corresponding to the maximum velocity error of 1.7 fps with either downrange, uprange, or crossrange orientation. In each case, the reference object

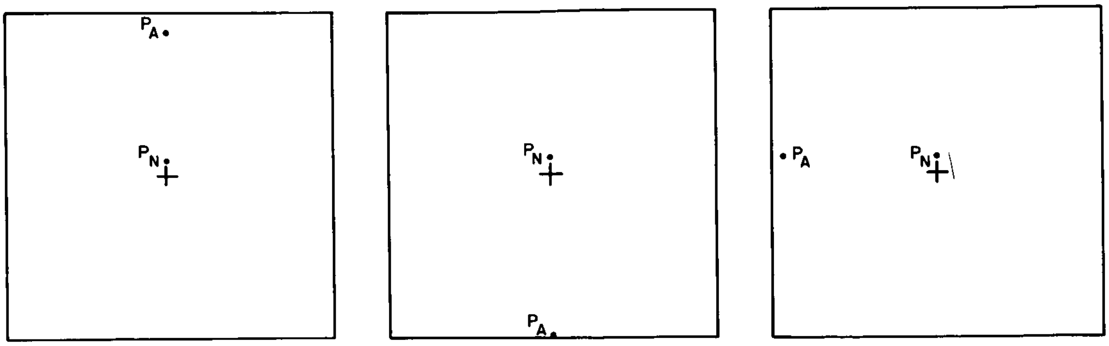

CASE 1

1.7 FPS UPRANGE FOR
25 SECONDS BEFORE HOVER

CASE 2

1.7 FPS DOWNRANGE FOR
25 SECONDS BEFORE HOVER

CASE 3

1.7 FPS CROSSRANGE FOR
25 SECONDS BEFORE HOVER

Figure IV-33. Hover Position Error Display

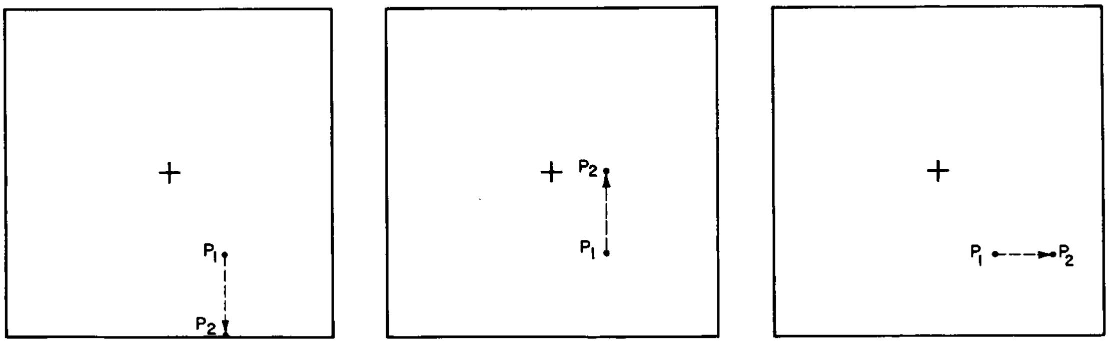

CASE 1

1.7 FPS DOWNRANGE
FOR 10 SECONDS

CASE 2

1.7 FPS UPRANGE
FOR 10 SECONDS

CASE 3

1.7 FPS CROSSRANGE
FOR 10 SECONDS

Figure IV-34. Hover Velocity Error Display

initial point was assumed to be at display screen coordinates of (-1.5, 1) feet. Computations with the velocity measurement error equations indicate that best accuracy can be attained by choosing the reference object such that its motion during the 10-second tracking period will be through minimum scale factor regions on the display screen. The initial point specified above represents a conservative choice in that the controller should always be able to do at least this well with the number of possible reference objects expected to be visible to him at this point. The three cases considered are illustrated in Figure IV-34. Reference object motion is shown to scale for a 6- by 6-foot screen. The velocity error equations then yield:

Case 1	$\sigma_{V_a} = 0.04$ fps	$\sigma_{V_c} = 0.03$ fps
Case 2	$\sigma_{V_a} = 0.05$ fps	$\sigma_{V_c} = 0.03$ fps
Case 3	$\sigma_{V_a} = 0.02$ fps	$\sigma_{V_c} = 0.05$ fps

Thus, for use in the total error equation, we choose:

$$\sigma_{V_a} = 0.05 \text{ fps} \tag{38}$$

$$\sigma_{V_c} = 0.05 \text{ fps} \tag{39}$$

The attitude errors, σ_θ and σ_ψ followed directly from the postulated inertial platform error model:

$$\sigma_\theta = 0.06 \text{ degrees} \tag{40}$$

$$\sigma_\psi = 0.06 \text{ degrees} \tag{41}$$

The total along-track position error σ_a was then found using the results of Equations (36), (38) and (40) in Equation (24). Similarly, using the results of Equations (37), (39) and (41) in Equation (25), the total cross-track position error σ_c was found.

$$\sigma_a = 2.9 \sqrt{}^{+} (0.05)\ (24.5) \sqrt{}^{+} \frac{1}{2}\ (5.0)\ \frac{(0.06)}{57.2} \left(36.8\right)^2 = 4.6 \text{ feet}$$

$$\sigma_c = 1.0 \sqrt{}^{+} (0.05)\ (24.5) \sqrt{}^{+} \frac{1}{2}\ (5.0)\ \frac{(0.06)}{57.2} \left(36.8\right)^2 = 3.7 \text{ feet}$$

The joint distribution of the independent, normally distributed errors in along-track and crosstrack touchdown position is chi-square with two degrees of freedom. Using the values for σ_a and σ_c with the chi-square density law, the contour on the lunar surface containing 99.7 percent of all touchdown points is an ellipse centered at the nominal touchdown point with a semi-major axis of 15.8 feet along track and a semi-minor axis of 12.8 feet crosstrack. This elliptical touchdown error footprint is approximated by a circular footprint of radius 15 feet. When the 15-foot radius of the

LM landing gear is added to the uncertainty in touchdown point, a circular total landing uncertainty footprint of diameter 60 feet is obtained.

2.6 Fuel Budget

The ΔV required for the assumed descent trajectory appears to be within the DPS capability. Table IV-1 presents the fuel budget in terms of ΔV required. This fuel budget is a modification of the one presented in Reference 3 for a preliminary Apollo reference trajectory with 6100-foot High Gate. The mean requirement (see Figure IV-2) for 130 fps during the final approach phase (High Gate to 50 seconds before hover) represents the cost of raising High Gate altitude from 6100 feet to 10,000 feet plus the downrange redesignation through the bias distance of 5600 on a nominal descent. The 120-fps, 3σ allowance during this phase provides a redesignation capability sufficient to permit attainment of the desired landing point for any guidance landing point in the ellipse containing 99.7 percent of all guidance landing points. The mean requirement for 175 fps during the landing phase (50 seconds before hover to touchdown) represents the 35-second hover maneuver required to remove the hover point bias. The 3σ allowance of 60 fps is the cost of the additional 12 seconds of hover time needed to correct position and velocity error at the 99.7 percent probability level. The other items in the fuel budget are identical with Reference 3 and are explained there.

Table IV-1

FUEL BUDGET

Mission Phase	Design Reference	Flexibility Mean	Flexibility 3σ	Contingency
Hohman Transfer	97	13		
Braking	5362	15	20	
Final Approach	672	130	120	
Landing	450	175	60	30
Totals	6581	333	136	30
		7080		

The total ΔV cost is 7080 fps as compared to 7046 fps for the trajectory of Reference 3. From a vehicle weight breakdown associated with that trajectory, it appears that the DPS fuel tanks were off-loaded by 470 lbs. The small additional ΔV required for the unmanned descent can be attained by either loading up the fuel tanks or by lowering CSM orbit altitude. For example, if an extra 470 lbs of fuel could be loaded into the DPS tanks, an additional ΔV of 210 fps would be available. Alternatively, if CSM orbit altitude were lowered to 40 nmi, Reference 7 indicates that a

ΔV savings of 100 fps would result. In any case, it appears that sufficient ΔV can be provided for correcting both High Gate and hover errors.

2.7 S-Band Steerable Antenna Pointing

Since the S-band communication link will be used to transmit the television picture to the LM controller and to send the controller's commands back to the LM, the success of the landing, and thus the mission, depends on maintenance of a reliable S-band link between the LM and the controller. For this reason, an X-Y scanner for the steerable antenna is required for the initial acquisition operation and for reacquisition if lock is lost for any reason.

Due to the critical nature of the S-band communications link, a desirable requirement is that S-band lock-on be achieved and verified prior to the LM DPS ignition. However, the structural interference problems associated with the present LM steerable S-band antenna location makes it impossible to meet this requirement for many landing sites in the accessible region.

The structural interference problem can be solved in either of two ways:

1. Move the S-band steerable antenna to the rendezvous radar mount. The rendezvous radar is not needed since the unmanned LM is left on the lunar surface.
2. Perform the LM descent with a yaw (pilot roll) angle allowing a yaw angle offset in the antenna pointing direction that is sufficient to clear the structural interference.

Reference 8 discusses this problem in detail and shows that a yaw angle solution to the problem is possible for all landing sites in the region accessible to Apollo.

2.8 Switching Operations

Switching operations such as DPS engine-on signal will be performed automatically by the LM Mission Programmer (LMP). The main elements of the LMP are the LM Guidance Computer, the Digital Command Assembly, the Programmer Reader Assembly and the Programmer Coupler Assembly. The LMP was designed to perform switching operations during unmanned LM maneuvers in Earth orbit, but it has the inherent capability of performing all the switching operations required in the unmanned LM landing system. Reference 9 discusses this particular application of the LMP.

2.9 Summary of TV Unmanned LM Landing System

It has been shown that a high probability of a safe, accurate LM landing can be achieved through use of an Earth-based controller superposing commands on LM guidance commands. These remote command inputs are based on TV information transmitted from the LM. The major modifications to Apollo equipment and procedures are:

1. Addition of TV system.
2. Use of automatic star tracker for inertial platform alignment.
3. Provision of X-Y scanner for the steerable S-band antenna.
4. Application of LM Mission Programmer to switching operations.
5. Improvement of bandwidth through use of the 210-foot Goldstone antenna during the descent, or parallel operation of two of the 20-watt traveling wave tube power amplifiers used in the Apollo LM transmitter.

3. RENDEZVOUS RADAR UNMANNED LM LANDING SYSTEM

3.1 System Operation

This LM landing system configuration depends on landing the manned LM first. The unmanned LM lands a few hours later, aided by the rendezvous radar on the landed LM.

The astronauts in the manned LM select a landing site during the approach phase of their descent under the constraint of also finding a second acceptable landing site within a suitable distance of the first site. Since the men will necessarily have a very high probability of finding a safe landing site, the probability that a safe site for the unmanned landing is located nearby will also be very high, if the unmanned landing footprint is reasonably small, as was shown in the development of the TV system. Thus, locating two safe landing sites should not present a difficult problem for the LM pilot. Just prior to its descent from hover, the manned LM must roll 180 degrees about its thrust axis. This places the unmanned LM descent trajectory entirely within the gimbal limits of the rendezvous radar. After touchdown and checkout, an astronaut leaves the LM and places a radar beacon at the second hazard-free site. The rendezvous radar on the manned LM is then pointed at the beacon and the radar range and angle are recorded. Landing point offset coordinates are then computed and transmitted for input to the unmanned LM guidance system.

A rendezvous radar beacon is required on the unmanned LM. After initiation of the unmanned LM descent, the rendezvous radar on the manned LM tracks the beacon on the unmanned LM. The LM guidance computer (LGC) in the manned LM converts the radar range, range rate, angle, and angle rate measurements into position and velocity vectors in the guidance coordinate system. Position and velocity updates are then transmitted to the LGC in the unmanned LM for use in the computation of guidance acceleration commands.

There would be no reason to fly a descent trajectory of Apollo type when the rendezvous radar is used in the unmanned landing system. In this case, a more nearly fuel-optimum descent trajectory could be used. For example, a direct powered descent from a CSM orbit altitude of 20 nmi would result in a ΔV savings of about 1000 fps over an Apollo descent trajectory. With this descent trajectory, the LM would rise above the radar horizon at the landing site about 30 seconds before ignition of the DPS. Approximately 200 seconds of tracking at radar elevation angles above 5 degrees would be available.

With these tracking conditions, it is reasonable to expect that the accuracy with which guidance can bring the LM to the desired landing site is approximately equal to the accuracy with which the rendezvous radar can measure position as the LM approaches hover. Referring to the rendezvous radar error model of Reference 10, the one sigma position measurement errors at a radar slant range of 10,000 feet are 30 feet along track and 24 feet cross track. Thus, it seems reasonable to expect that the guidance position error footprint at hover should be roughly a circle about the nominal hover point with radius 100 feet at the 0.997 probability level. In addition, radar range rate measurement errors will leave the LM with an along-track hover velocity error of about 1 fps at the same probability level. The hover position and velocity errors must be removed prior to touch-down to reduce the size of the final landing uncertainty footprint and ease the requirements on the size of the safe landing area which the astronauts must locate during their descent. It should be possible to perform hover position and velocity error correction without requiring the astronauts to take over direct control of the unmanned LM. This could be done by providing a radar measurement period after hover during which smoothed estimates of the position and velocity errors are computed in the LGC of the manned LM. Using these estimates of the errors, attitude maneuvers to correct them, such as those developed for the TV landing system, could be computed and transmitted to the LGC of the unmanned LM for execution.

The relatively short transmission ranges between the unmanned LM and the manned LM during the unmanned LM descent would allow high data-transmission rates over an S-band link between the two LM's if the omnidirectional S-band antenna on the unmanned LM was used in conjunction with the steerable antenna on the manned LM. Thus, it should be possible to eliminate the requirement for automatic scanning of the steerable S-band antenna on the unmanned LM in the case of a rendezvous radar landing system. The automatic star tracker for inertial platform alignment and the LMP for switching operations would be required by the rendezvous radar landing system.

The primary difficulty in implementation of the rendezvous radar landing system appears to be its requirement for simultaneous operation of two Apollo systems.

At this point, the Ground Operational Support System (GOSS) appears capable of supporting two missions simultaneously as long as critical events (launches, injections, deboosts, landings) do not occur simultaneously. The major problem involves the effects of delays in launching the second system after the first system is on its way to the Moon.

The manned LM must not be committed to a landing until the unmanned LM is in the proper lunar orbit and verified to be ready for Lunar Surface Rendezvous (LSR) operations. To accomplish LSR at a particular landing site, a waiting period in lunar orbit must be a part of the nominal mission plan. This waiting time is chosen so that the second launch vehicle has enough launch opportunities available to guarantee the desired probability of launch. The first vehicle launch date and lunar orbit are chosen so that the orbit track will pass over the desired landing site at the end of the preplanned waiting period with acceptable lunar lighting conditions for the landings. Even if the second vehicle is launched on the first attempt, both systems will have to wait out the specified time in lunar orbit, before the landing operations to the desired site can begin. Section XI considers the effects of second system launch probability and LM reliability on the probability of successful LSR when the simultaneous landing strategy is used. These considerations allow computation of the expected cost penalty associated with the nearly simultaneous landings required by the rendezvous radar unmanned landing system.

3.2 Summary of Rendezvous Radar Unmanned LM Landing System

It appears that a high probability of a safe, accurate unmanned LM landing can be achieved by landing the manned LM first and using its rendezvous radar to update guidance during the unmanned LM descent. The major modifications to Apollo equipment and procedures are:

1. Simultaneous operation of two Apollo systems.
2. Addition of rendezvous radar beacon on unmanned LM.
3. Provision of data link between LGC on landed LM and LGC on unmanned LM.
4. Use of automatic star tracker.
5. Application of LMP for switching.

The radar landing system can be compared with the TV landing system in general terms by noting that the radar landing system will require relatively simple equipment design and modification and relatively complex modifications to Apollo operational procedures. On the other hand, the TV landing system will require relatively complex equipment design and modification and relatively simple modifications to Apollo operational procedures.

REFERENCES

1. Byrne, C. J. "Potential Lunar Landing Capability of Apollo", Case 340, Bellcomm, Inc., August 9, 1967.
2. Cheatham, D. C. and Bennet, F. V. "Apollo Lunar Module Landing Strategy", NASA MSC, Paper presented at Apollo Lunar Landing Mission Symposium, June 25-27, 1966.
3. Bennett, F. V. and Steele, D. E. "Preliminary LEM Powered Descent Trajectory for Flight AS-504A", NASA MSC, MSC Internal Note 66-EG-10, March 18, 1966.
4. Bush, G. L. "LM Descent Guidance Review" MIT/IL, Case 310, Bellcomm, Inc., May 23, 1967.
5. Baldwin, M. W. and Averbach, E. "Film Experiments Related to Picturephone Viewing", Bell Telephone Laboratories, MM57-134-17, June 11, 1957.
6. Amos and Birkinshaw, *Television Engineering*
7. Nathan, A. "Mapping of Hohman Descent Orbit Characteristics" GAEC, LM Engineering Memorandum, LM0-550-96, October 1, 1963.
8. Merritt, A. C. "LM-Earth S-Band Communications for Powered Descent and Ascent Phases of the Lunar Mission," Bellcomm, Inc., May 15, 1967.
9. Levidow, W. "LM Mission Programmer Control of an Unmanned LM Lunar Landing", Case 310, Bellcomm, Inc., July 11, 1966.
10. Apollo Navigation Working Group "*Apollo Missions and Navigation Systems Characteristics*," NASA GSF and NASA MSC, Technical Report No. 7-AN-1.2, January 17, 1967.

Y68-84335

SECTION V. LSSM MOBILITY

by I. S. Yavelberg

1. INTRODUCTION

In AAP surface missions, the ability of the astronauts to traverse significant distances from the LM is essential for achieving major scientific and technological contributions. Mobility aids will permit the astronaut to:

1. Visit, photograph, map, and obtain samples from many specific points of interest.
2. Provide separation for emplaced experiments.
3. Cover large areas with surface and subsurface measurements.
4. Test lunar surface mobility aids for future operations.

One vehicle for extending surface mobility in AAP is a Local Scientific Survey Module (LSSM) (see Reference 1).* Two basic LSSM configurations are presently under consideration: a six-wheeled, semiflexible vehicle (Figure V-1) and a four-wheeled vehicle with foldout suspension arms (Figure V-2). While they differ considerably in appearance, their capabilities are similar, and are treated as such in this study. The LSSM is battery-powered, weighs about 1000 lbs (unloaded), and depends on the astronaut backpack's Portable Life Support System (PLSS) for life-support capability.

Principal constraints on LSSM design are the specification of the payload weight and volume and the interface allowances of the Saturn V and the Apollo/LM Spacecraft. An LSSM design is required which, in the face of expected lunar surface characteristics, will provide the capability of carrying out the basic mission objectives as outlined above. Available documentation of surface mission planning uses LSSM capabilities that do not include significant environmental effects such as topographical hazard avoidance and visibility limitations. It is the purpose of this study to assist in evaluating LSSM performance under typical lunar surface conditions and to predict the regions where it can operate effectively.

---

*References are listed at the end of the section.

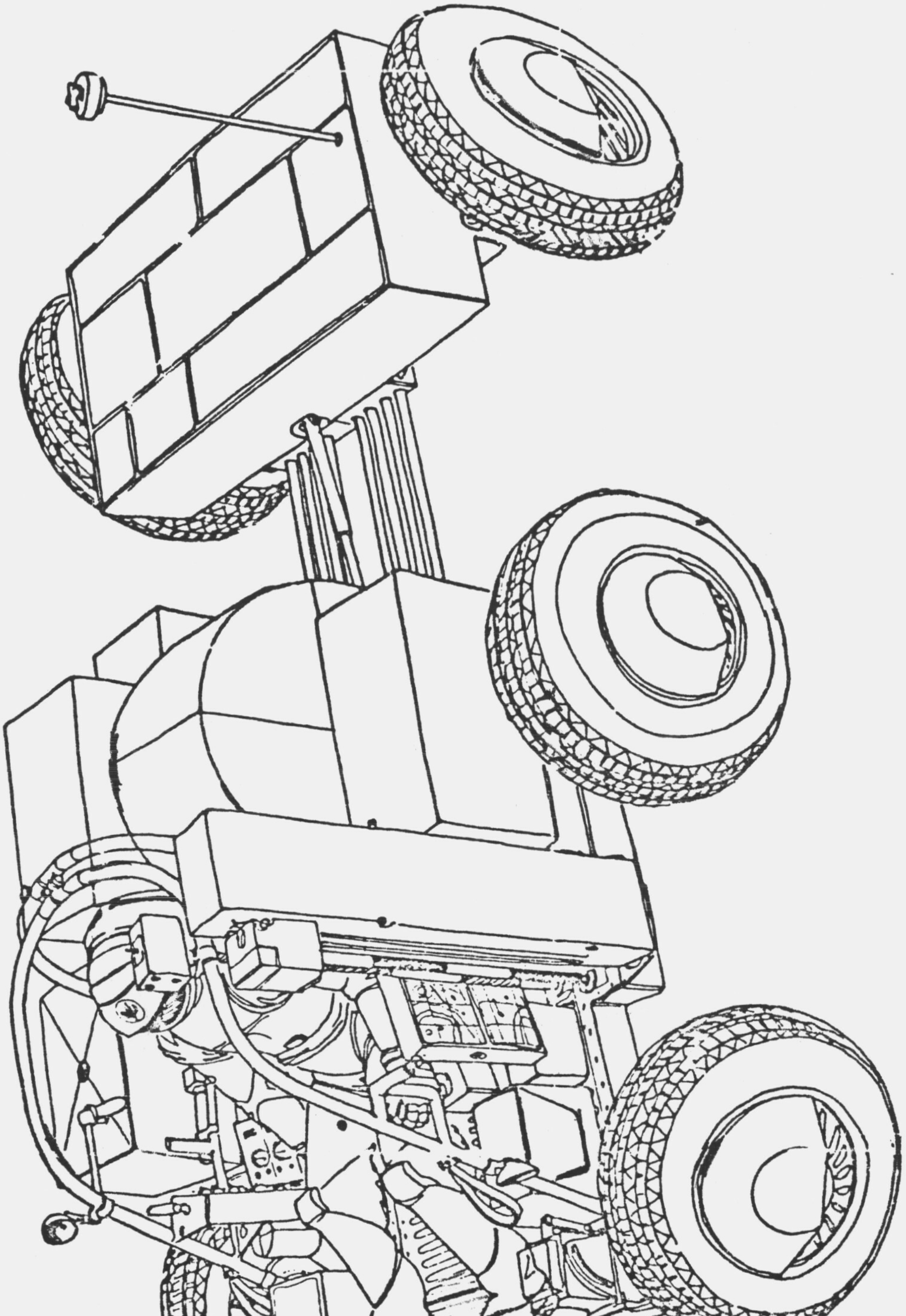

Figure V-1. General View of Baseline LSSM (Reference 1)

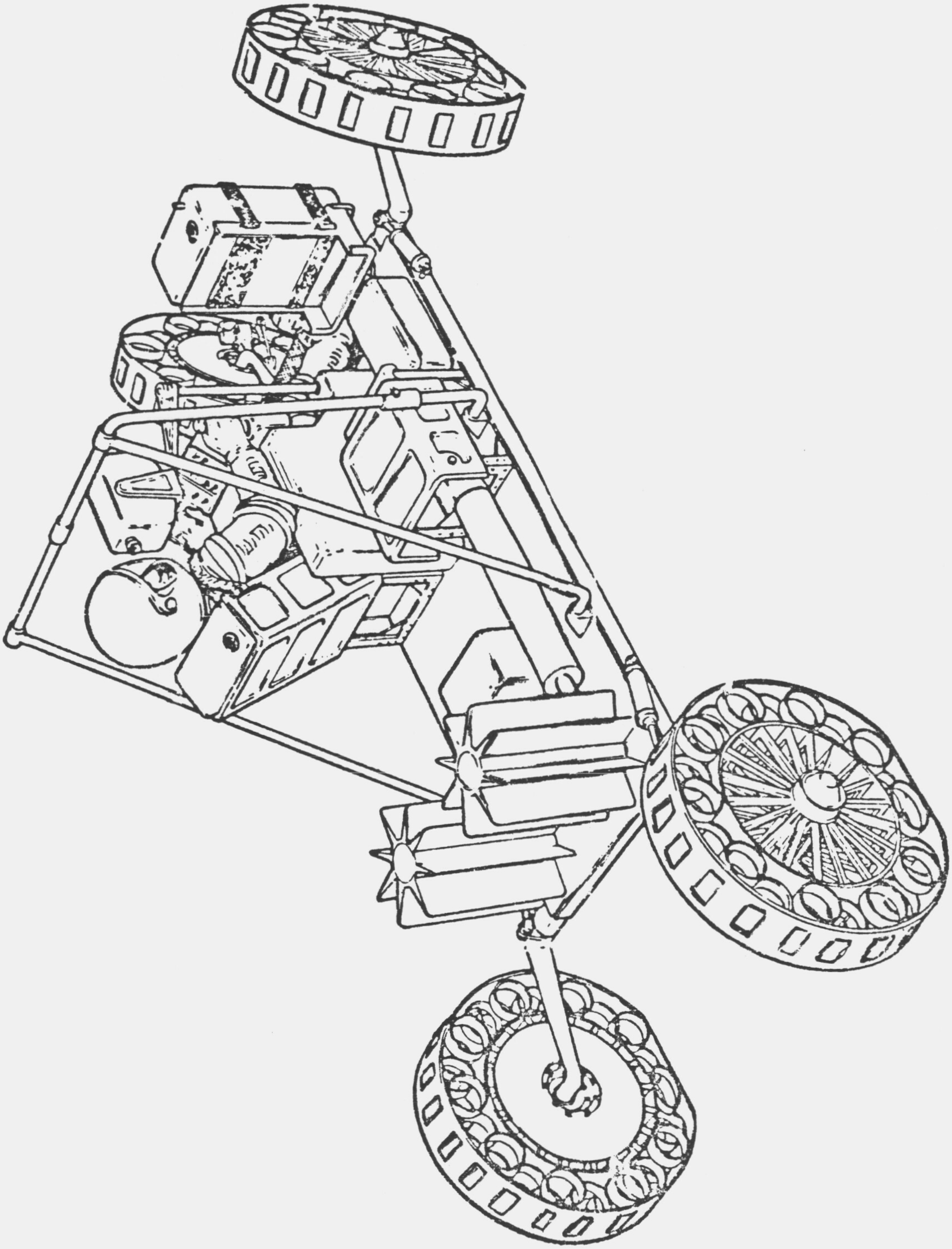

Figure V-2. LSSM Baseline Configuration (Reference 1)

2. APPROACH

For both scientific and technological reasons, it will be desirable to traverse lunar areas with significantly different surface characteristics. A measure of the effectiveness of an LSSM in traversing such areas will be useful in mission planning and in evaluating vehicle design.

It was estimated that a 1000-lb LSSM will be able to travel over nonhazardous lunar terrain under ideal conditions at some average speed and energy. Then, the effects of hazard avoidance and astronaut visibility on traverses were evaluated by taking the following steps:

1. Determination of the limitations of a vehicle of typical design.
2. Definition of craters and rocks as obstacles and hazards when their dimensions exceed LSSM capabilities (clearance, track width, etc.).
3. Generation by computer of surface maps with crater and rock densities typical of lunar areas.
4. Definition of traverse constraints dependent on vehicle and visibility limitations.
5. Simulation of traverses by tracing across the surface maps.

The quantitative results presented in this study are approximate because of the simplifying assumptions used (described in more detail in paragraph 4.2).

3. SUMMARY AND CONCLUSIONS

3.1 Mobility versus Hazards

From simulated traverses, it is concluded that the 1000-lb LSSM can, in most regions of the maria, provide the mobility necessary to perform the scientific tasks outlined for AAP surface missions. This concension is based on the conclusion that the LSSM will have sufficient time, energy, and life-support margins.

As the hazard density increases above that typical of the maria, mobility is adversely affected. Lunar regions of intermediate hazard density, such as the rougher maria and interiors of some large craters, approach the capability limit for the vehicle. The resultant time and energy penalties make the feasibility of surface missions in those areas marginal.

It is concluded that the LSSM cannot effectively negotiate, for the most part, the terrain of the continents because of the increased roughness. At best, only short penetration from relatively smooth areas into these regions will be possible.

3.2 Time and Energy Penalties

A summary of the time and energy penalties for representative lunar surfaces under different conditions is shown in Table V-1. These predicted quantitative

Table V-1

TIME AND ENERGY PENALTIES

Crater Distribution	Rock Distribution*	Visibility	Percentage Increase Required Over Minimum Time	Percentage Increase Required Over Minimum Energy
Light (maria)	Light	Good	6	5
		Poor	70	40
	Heavy	Good	17	12
		Poor	85	55
Intermediate (Interior of Alphonsus)	Light	Good	45	25
		Poor	100	60
	Heavy	Good	75	50
		Poor	145	95
Heavy (continents)	Light	Good	Traverse Impossible	

---

*For rock distribution, heavy is defined to be the density found in sample areas near Surveyor I; light is 1/10 the heavy density.

results are derived from repeated simulated traverses, and the records of all events affecting the time required and vehicle energy expended. These predicted penalties are so variable, depending on the surface and visibility assumptions, that they must be considered in surface mission planning.

To determine if the results are sensitive to small variations and to determine if changes can be made that significantly improve performance, sensitivities of time and energy penalties to vehicle parameters were obtained. Table V-2 gives these sensitivities based on good visibility traverses. Variations of 30 percent from the baseline (current best estimate) values in the vehicle's obstacle and hazard definition, allowable path width, or turn radius have a negligible effect on the penalties until the terrain becomes intermediately rough.

A 30-percent variation on the driver's visual height has negligible effect on the penalties under all visibility conditions.

Mobility effectiveness in poor visibility traverses might be improved through the use of visibility aids. Four such aids (Table V-3) are: maps showing hazards, marked traverse paths, a periscope, and a shadow illuminator. They are evaluated in detail in paragraph 4.4.3. As noted in the table, only low-resolution hazard maps and marked traverse paths are recommended.

Table V-2

EFFECT OF PARAMETRIC VARIATIONS ON TIME/ENERGY PENALTIES

Parametric Variations (±30 percent)	Percentage Increase in Penalties	
	Hazard Density	
	Light	Intermediate
Obstacle and Hazard Definition	1	6
Vehicle Turn Radius	<1	2
Traverse Path Width	1	5
Driver Visual Height	<1	<1

Table V-3

EFFECT OF VISIBILITY AIDS ON TIME/ENERGY PENALTIES

Visibility Aids	Decrease in Penalties	Comments
Maps		
High Resolution (>1m)	—	Operationally not feasible
Low Resolution (>30m)	10-15 percent in rougher terrain	Practical aid
Marked Traverse Paths	Up to 70 percent	Practical aid
Optical Periscope	Large for low elevation in angles	Operationally difficult
Shadow Illuminator	Small	
Sun Reflector		Operationally not feasible
Headlamp		Excessive power requirements

3.3 Effects on Traverse Planning

The study results indicate that hazard density and driver visibility are important variables in planning surface traverses. LM landing sites near specific points of interest should be selected to minimize the visibility problem, and daily mission planning should reflect changing visibility.

Estimated LSSM speed in combination with the astronaut's walk-back capability will limit the operational radius. Total locomotion energy required per sortie can then be fixed, based on the estimates of Table V-1. Because of the safety requirements on traverse time and operating radius, the estimated total locomotion energy available per sortie, 3.0 kWh, does not appear to be a pacing item. Figure V-3 reflects the effect of these safety constraints on traverse planning for a limited sample of environmental conditions. In the curves, scientific time at the remote site is fixed at 2 hours. LSSM and astronaut speeds are based on this study and a corresponding astronaut walking mobility study discussed in Section VI. It is evident in some cases that LSSM speed limits remote site distance and in other cases the astronaut walk-back capability is the pacing item. The large variations in distance capability (5 to 8 km) illustrate the importance of considering degradations to LSSM capability in site selection and traverse planning.

3.4 Smaller LSSM

A scaled down version of the LSSM from 1000 to 500 lbs may be desirable for certain missions (Reference 3). For this vehicle it is estimated that the baseline energy requirement will be halved and the baseline average speed decreased by about 30 percent. The computer-generated surfaces were again traversed with adjusted estimates of obstacle definition, path width, turn radius, and driver height. The results indicate that the 500-lb vehicle can traverse the same terrain as the 1000-lb vehicle. In addition, there are similar energy/time penalties for the smaller vehicle. However, the decreased baseline average speed (3.5 km/hr) allows less-useful scientific time on the traverses and/or would cut down operational radius capability. Also, useful payload weight would be less for the smaller LSSM. Figure V-4 illustrates the traverse limitations of the 500-lb vehicle. For a scientific time of 2 hours, the operating radius is between 3.5 to 4.5 km.

3.5 Sample Mission Plans

As stated in paragraph 3.1, the degradation in LSSM performance due to the avoidance of surface hazards should not prevent the vehicle from providing the necessary mobility to the astronauts. Careful LM landing site selection as well as optimum traverse planning should permit successful surface AAP missions using the LSSM as a mobility aid.

On the basis of the mobility restrictions estimation in this study (as well as other system constraints discussed elsewhere), two representative mission plans were generated — one using the 1000-lb LSSM in a Dual-Vehicle (LM) 12-day mission and one using the 500-lb LSSM in a single-vehicle Augmented LM 4-day mission. The missions, primarily with respect to daily traverse planning, are outlined in Volume 1 of this report (Reference 3).

Figure V-3. Operating Radius of 1000-LB LSSM

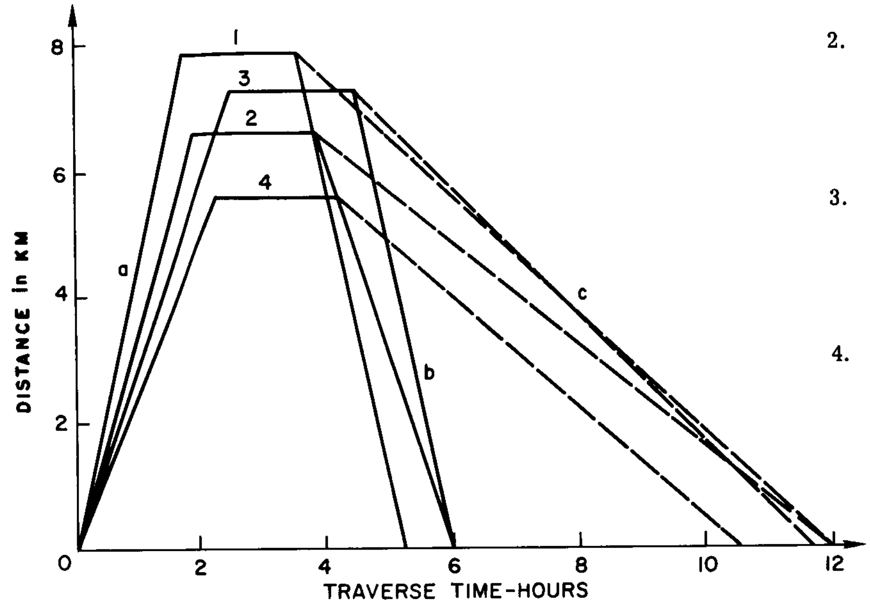

— LSSM Path
a. Forward Traverse
b. Return Traverse
--- c. Astronaut Walk-Back Path

1. a. Maria, Good Visibility (4.75 km/hr)
   b. Maria, Poor Visibility, Marked Path (0.95 km/hr)

2. a. Intermediate, Good Visibility (3.5 km/hr)
   b. Intermediate, Poor Visibility, Marked Path (3.5 km/hr)
   c. Intermediate, Poor Visibility, Marked Path (0.80 km/hr)

3. a. Maria, Poor Visibility (3.0 km/hr)
   b. Maria, Good Visibility (4.75 km/hr)
   c. Maria, Good Visibility (0.98 km/hr)

4. a. Intermediate, Poor Visibility (2.5 km/hr)
   b. Intermediate, Good Visibility (3.5 km/hr)
   c. Intermediate, Good Visibility (0.88 km/hr)

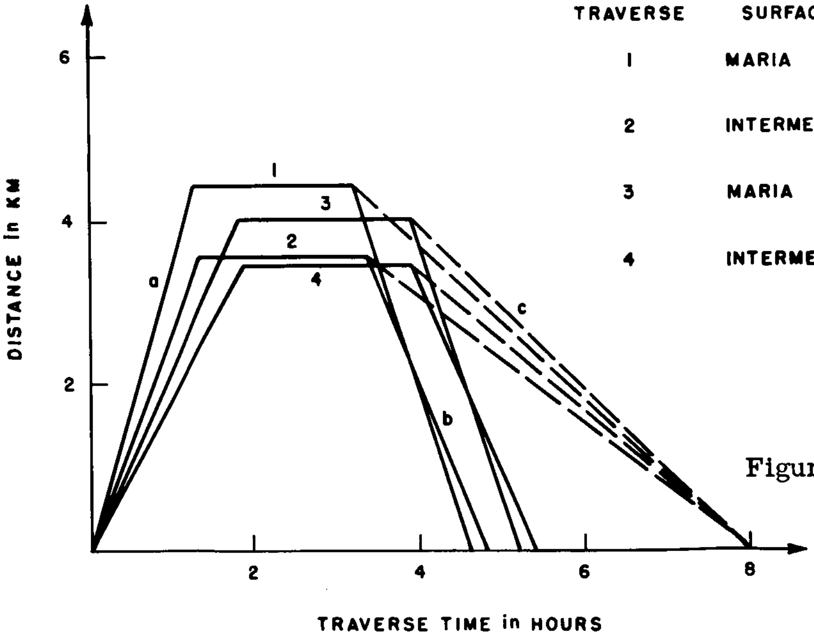

TRAVERSE	SURFACE	VISIBILITY
1	MARIA	a, = GOOD
		b,c = POOR
2	INTERMEDIATE	a, = GOOD
		b,c = POOR
3	MARIA	a, = POOR
		b,c = GOOD
4	INTERMEDIATE	a, = POOR
		b,c = GOOD

Figure V-4. Operating Radius of 500-LB LSSM

4. DETAILED MOBILITY STUDY

4.1 Step-by-Step Procedure

A brief outline of the procedure used to estimate LSSM mobility effectiveness was given in paragraph 2. A more detailed expansion follows.

Step 1: Select a vehicle description,,and from this estimate a set of vehicle capabilities.

Step 2: From the vehicle capabilities, establish mobility parameters such as path width, speed, minimum turn radius, and energy and power requirements.

Step 3: Convert the vehicle capabilities to dimension limitations of craters and rocks, thereby defining obstacles and hazards.

Step 4: Select the type of lunar surface area to be traversed (a given hazard density).

Step 5: With the crater and rock-size frequency distributions for the lunar area in question, generate a sample surface map showing only those craters and rocks equal to or exceeding those defined in Step 3.

Step 6: Choose random traverse starting points and objectives on the generated surface map.

Step 7: Simulate the visibility degradation by exposing only that part of the surface that the astronaut will be able to visually evaluate (a function of the sun's elevation angle, azimuth angle, etc.). This is approximated by an overlay that is moved along the path.

Step 8: Decide what, if any, mobility aids are to be used, and simulate their use.

Step 9: Attempt to traverse, i.e., mark a safe path, across the surface, recording all quantitative and qualitative measures of mobility effectiveness. Repeat this with other surface samples, visibility assumptions, and aids until statistical estimates can be made of all parameters affecting total time and energy penalties.

Step 10: Change the lunar surface area to be investigated, and repeat the experiment. This will establish mobility effectiveness for varying lunar roughness.

Step 11: Change the vehicle description, and repeat the experiment.

The assumptions and techniques used in each of the above steps are described in subsequent paragraphs.

4.2 Limitations of Results

Quantitative results are approximate because of the simplifying assumptions made in the study. Among the most notable of these are:

1. Computer-generated surface representations show only craters and rocks as potential hazards, thus, ignoring all other surface features (ridges, rilles, domes, faults, hummocks, etc.).
2. The craters and rocks are distributed randomly and independently; there is, of course, some correlation between the locations of these hazards.
3. The sample surfaces are two-dimensional; the three-dimensional effects are accounted for by very general traverse rules.
4. Astronaut driving capabilities are only partially simulated. The visibility assumptions alone (Section IX) are based on simplified modeling of the complex phenomena. Navigational problems are not included. Also, vehicle dynamics are not considered to contribute to the fatigue of the astronauts (This assumption follows the results of studies described in References 4 and 5).

The time and energy penalties derived from results of the sample traverses are based on a series of assumptions and approximations outlined in detail in paragraph 4.4. The major contributor to time and energy penalties, however, is increased path length which converts to the penalties in a straightforward manner.

4.3 Mobility

4.3.1 Parameters Affecting Mobility. A working (baseline) set of mobility parameters for the 1000-lb LSSM is given below. The numbers are the best available estimates (References 2, 6, 7).

1. Sortie time	6 hrs
2. Average speed on compacted, level soil with expected microscopic slope and roughness characteristics but with no vehicular obstacles, hazards, or astronaut visibility problems	5 km/hr
3. Vehicle length	5.0 meters
4. Vehicle width	2.5 meters
5. Slope negotiability	35 degrees
6. Obstacle crossing (straddle)	
Height (chassis clearance)	0.5 meter
Width (chassis clearance)	2 meters
7. Obstacle crossing (under wheels)	0.5 meter
8. Height of Driver's eyes above ground	2.5 meters
9. Locomotion energy available per sortie	3.0 kWh
10. Average locomotion energy required for speed given above in item 2.	0.1 kWh/km

It is to be determined if these capabilities are sufficient to provide the necessary mobility over varying surface conditions.

4.3.2 Application to Lunar Surface Characteristics. The list of LSSM capabilities can be related to lunar surface terrain features. Because astronaut safety is of prime concern, vehicle movement should be confined to paths somewhat more restrictive than those theoretically negotiable by the LSSM itself. For example, crevices in the surface may imply unsafe bearing strength and regardless of the vehicle's crevice capability, it should be avoided for fear of collapse. Therefore, for a meaningful evaluation of lunar surface mobility, both apparent and potential hazards need be defined. Apparent hazards are basically a function of vehicle capability and potential hazards a function of astronaut terrain evaluation.

LSSM obstacle negotiability limits the dimensions of traversable lunar terrain features, the most obvious of which are craters and rocks. Craters represent a slope (tipping or sliding) and/or protuberance (carriage damage) hazard to the LSSM. Ranger photographs (References 8 and 9), reveal craters of the size which affect AAP mission mobility. These can be divided into two classes, primary and secondary. Primary craters are characterized by their sharp outlines, steep slopes, and usually raised rim. It is generally accepted that primary craters are formed by impact at high velocities. Secondary craters have soft outlines, negligible rim, and more gradual slopes than primaries. Their diameter-to-depth ratios are generally larger and they are much more abundant on all parts of the lunar surface. So-called secondary craters are attributed to both secondary impact and internal collapse phenomena. It is clear that the hazard dimensions of primary and secondary craters would differ significantly for a given set of vehicle capabilities.

Rocks on the lunar surface will be hazards if their dimensions are greater than the prospective vehicle's capability limitations, for example, the chassis clearance capability. On a traverse, an astronaut would tend to avoid rocks which could not be cleared by the vehicle body between the wheels. Thus, rock size frequency distribution, vehicle wheel base, and chassis height represent mobility tradeoff variables.

Mobility effectiveness becomes significantly more complicated when, in addition to hazards, certain-size craters or rocks are considered negotiable, but at a somewhat reduced speed and/or increased power. For example, craters of diameter greater than D_2 are classified as hazards and, therefore, must be bypassed by the LSSM (this assumes a certain diameter (D) to depth (d) ratio). In this case, speed and power are not affected, only distance traveled. Craters of diameters less than D_1 are classified as non-obstacles and non-hazards. The vehicle wheels can pass directly over craters with diameter $D_1 < D < D_2$, but with some effect on vehicle speed and power. The same kind of classification is applied to rocks on the lunar surface, where the limiting dimensions here are height H and width W. The baseline values in meters for the 1000-lb LSSM are:

	D_1	D_2	
Primary Craters	1	3	$\left(\frac{D}{d} \approx \frac{4}{1}\right)$
Secondary Craters	3	3	$\left(\frac{D}{d} \approx \frac{7}{1}\right)$
	H_1	H_2	
Rocks	0.20	0.50	$\left(\frac{H}{W} \approx \frac{1}{3}\right)$

4.3.3 Surface Simulation. To evaluate LSSM mobility, a representation of the surface for specific areas of interest is necessary. For final mission planning, these surfaces will be recorded in high-resolution photographs of the areas to be traversed. Mobility would be evaluated by laying out traverse paths on these to satisfy explicit mission requirements. Thus, each surface terrain characteristic (including craters, rocks, rilles, ridges, domes, cracks, etc.) could be individually evaluated with respect to its classification as a mobility hazard, either apparent or potential. However, it is helpful in early mission planning to estimate mobility effectiveness in a more general, less costly, and perhaps less tedious sense. To accomplish this, a computer program was written which draws hazard and obstacle maps typical of particular areas on the lunar surface. The following paragraph describes the input and output of this program and its application to this mobility study. A complete description of the FORTRAN, storage requirements, running time, etc., can be found in Reference 10.

From the Ranger, Surveyor, and Lunar Orbiter Programs, statistical descriptions of certain areas on the lunar surface has been established by various photographic interpretation techniques (References 8, 9, 11 and 12). These statistics are limited to crater and rock size distributions for a few areas of the Moon (see Figures V-5 through V-9). Studies of terrestrial impact craters (Reference 6) have led to the hypothesis that the distribution of lunar rocks and secondary craters is not random over a region, but clustered in "ejecta" form about large primary craters. Energy and mass considerations could be used to simulate this effect. However, in areas of dimension necessary to study LSSM mobility, ejecta effects from very large craters located outside the study area can be considered to be nearly randomly distributed in the study area. For simplicity of programming, it has been assumed that all rocks and craters are distributed randomly. For this study, crater and rock distributions are approximated using the following functions (see Figures V-5 through V-9).

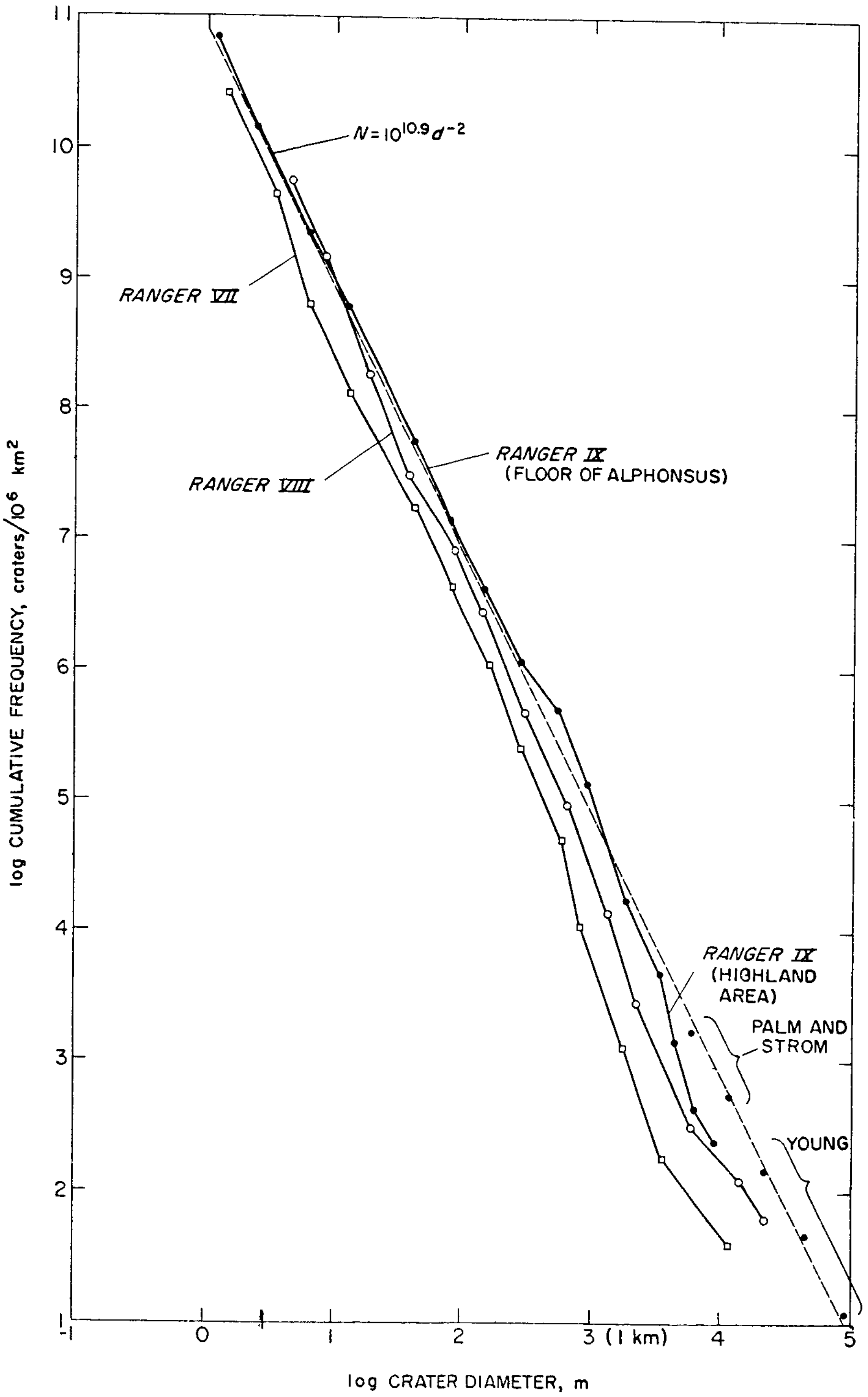

Figure V-5. Comparative Data of Crater Distribution in Ranger VII, VIII, and IX Impact Areas (Reference 9)

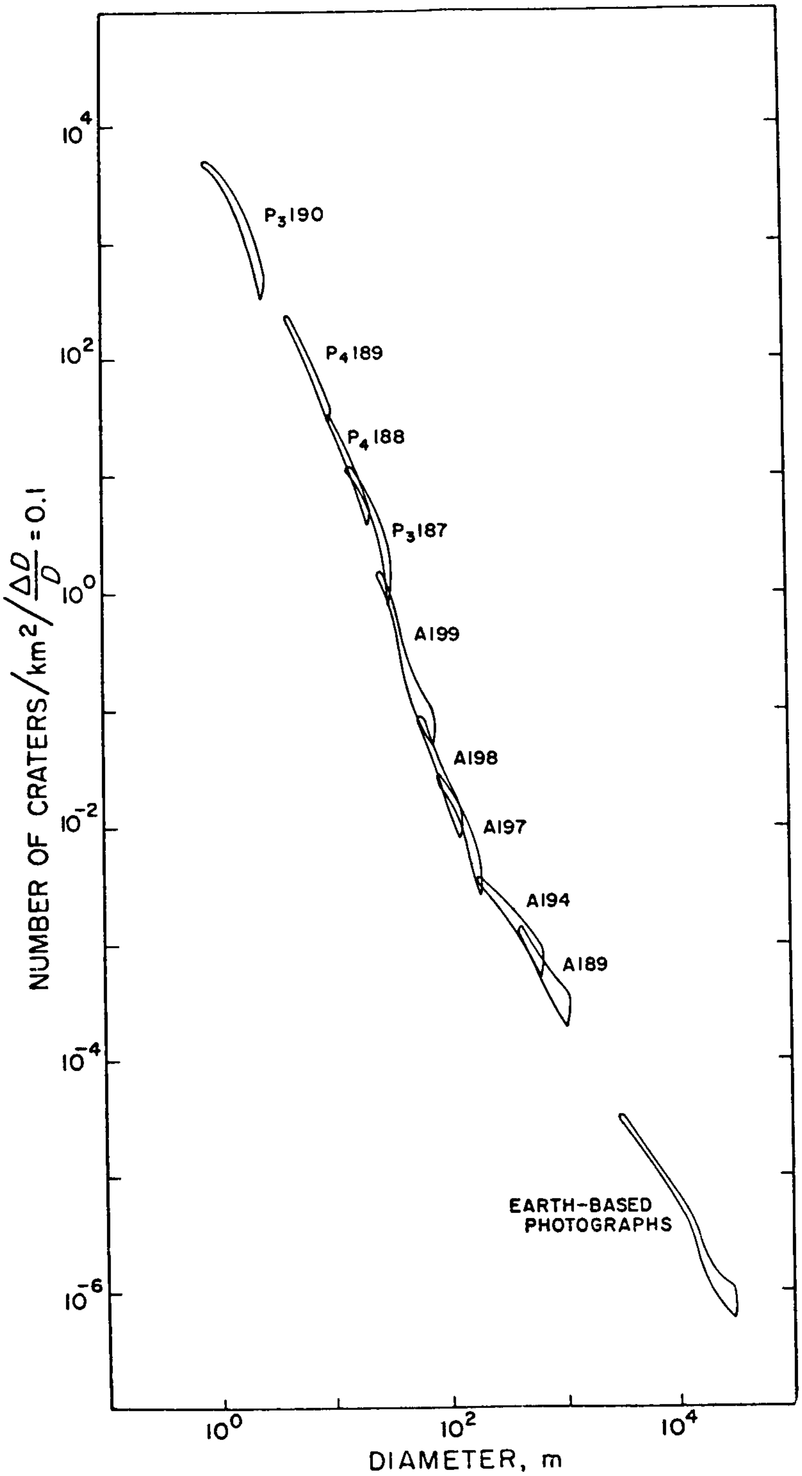

Figure V-6. Size-Frequency Distribution of Sharp Craters in Ranger VII Impact Area (Reference 9) (Width of segments represent the uncertainty in the actual position.)

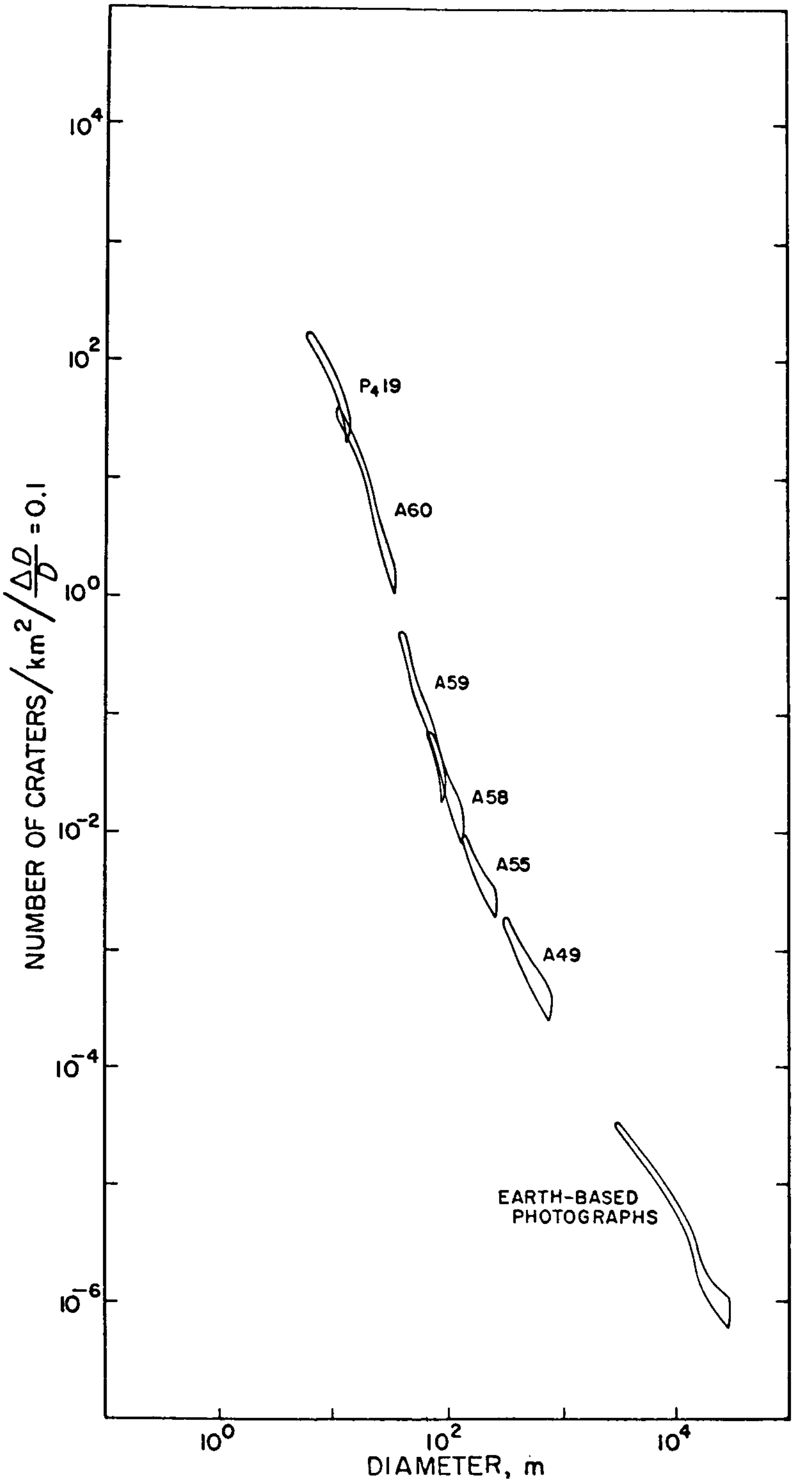

Figure V-7. Size-Frequency Distribution of Sharp Craters in Ranger VIII Impact Area (Reference 9) (Width of segments represent the uncertainty in the actual position.)

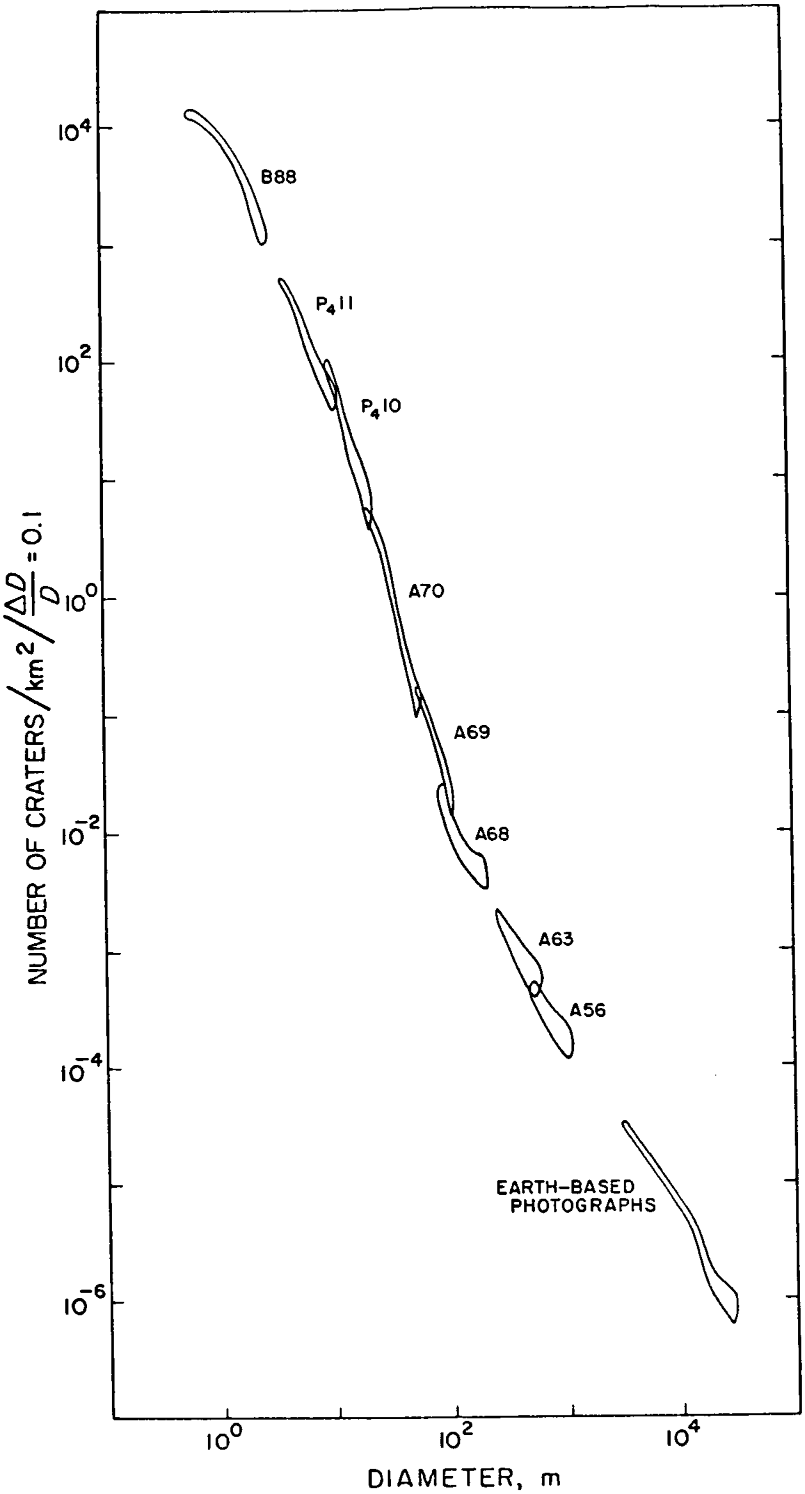

Figure V-8. Size-Frequency Distribution of Sharp Craters in Ranger IX Impact Area (Reference 9) (Width of segments represent the uncertainty in the actual position.)

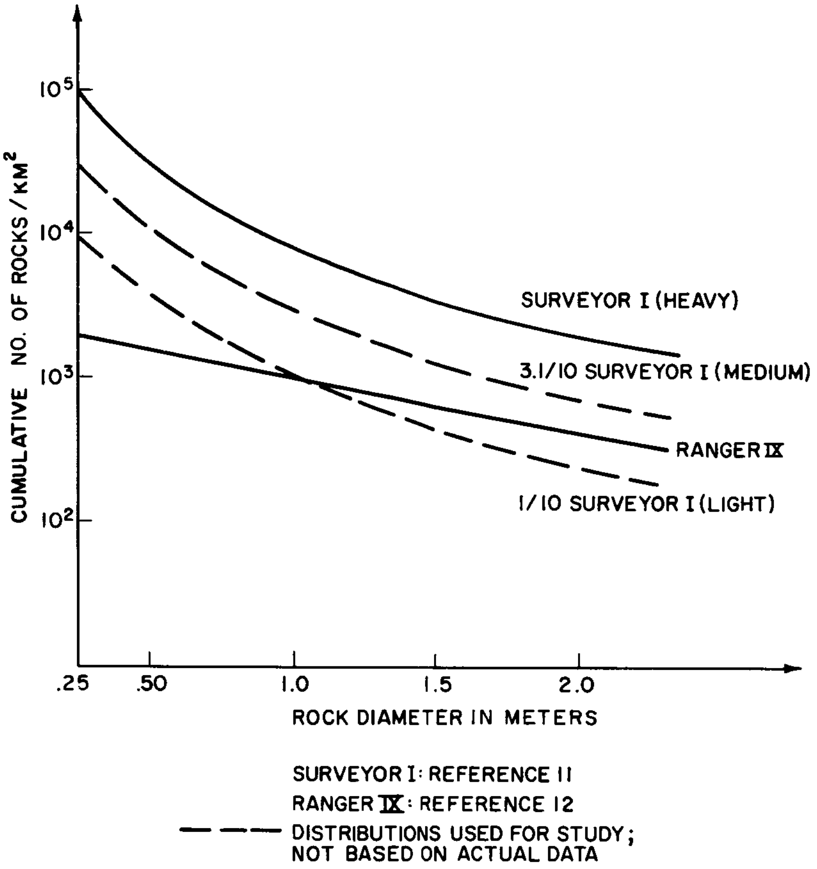

Figure V-9. Cumulative Distribution of Rocks on the Lunar Surface

Crater Cumulative Distribution $f_c(N) = 10^{A_i} D^{-2}$

Maria	$A_1 = 4.6$
Intermediate or Crater Interior	$A_2 = 4.9$
Continents	$A_3 = 5.1$

Rock Cumulative Distribution $f_R(N) = 10^{C_i} D^{-1.77}$

Light	$C_1 = 3.0$
Medium	$C_2 = 3.3$
Heavy	$C_3 = 4.0$

These distributions are randomly sampled via the computer program to generate simulated two-dimensional surface areas. Figure V-10 is an example of the expanded microfilm output of the program. It represents a maria with medium rock density, with craters and rocks represented by the open and closed circles respectively. Only those which represent either obstacles or hazards to the LSSM are plotted.

4.4 Traverse Simulation

4.4.1 Ideal Conditions. Given a surface map and a fixed set of vehicle capabilities, a measure of the traverse capability is obtained. As a basis for comparison, traverses are performed under optimum conditions, i.e., the entire surface available for path selection under perfect visibility conditions. This provides an estimate of the minimum time and energy penalties that can be expected for a particular surface and vehicle definition. All mobility parameters which have an effect on these penalties are recorded. Sufficient random traverses are made to calculate reasonable statistical estimates. Table V-4 is the worksheet used to record the values for the above estimates. The effect of each mobility parameter listed in the table on energy and time can then be calculated.

In this study, the average vehicle speed and average energy requirement for the 1000-lb LSSM (2000 lbs loaded) were assumed to be 5 km/hr and 0.1 kWh/km, respectively, for the following defined conditions: A lunar terrain with expected slope and roughness characteristics, but no obstacles or hazards, under good visibility conditions. The above values were taken from Reference 2.

Quantitative energy and time penalties associated with each mobility parameter are functions of many factors (1/6g, soil properties, dynamic effects, etc.).

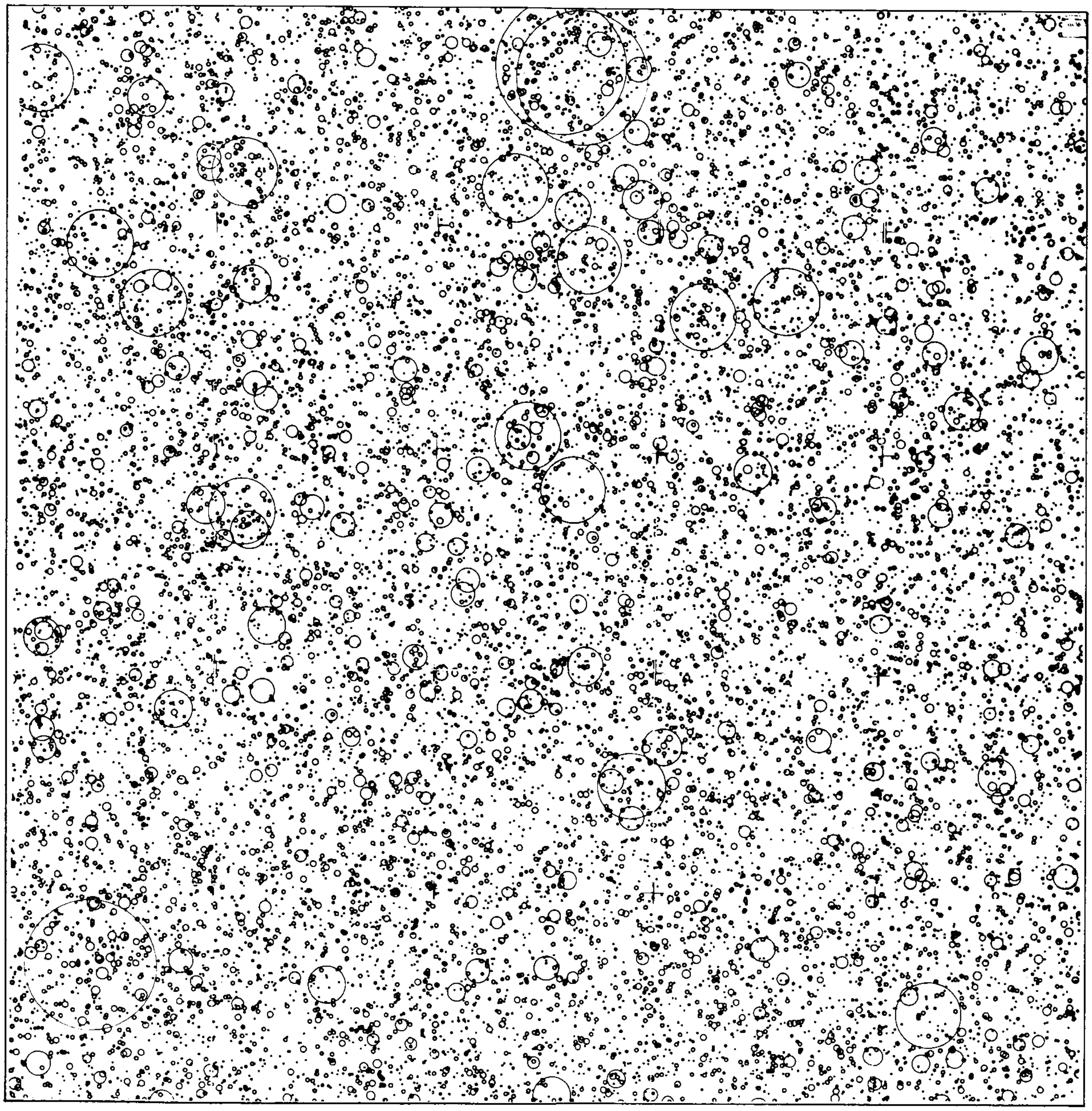

Figure V-10. Sample Lunar Surface Having a Medium Rock Density

Table V-4

MOBILITY STUDY WORKSHEET

SAMPLE AREA:

Random Sample No:

ASSUMPTIONS

Vehicle:

Visibility:

Mobility Aids:

	Traverses	Percent Traverse Distance Over Minimum	Percent of Traverse Distance where Turn Radius, $r_c < 1.1\ r_c$ min	Number of Decisions Per km which Result in Traversing in Reverse	Number of 1-2m Primary Craters under Wheel/km	Number of 2-3m Primary Craters under Wheel/km	Number of 0.2-0.33m High Rocks under Wheel/km	Number of 0.33-0.5m High Rocks under Wheel/km
TRIAL 1	A							
	B							
	C							
	D							
	E							
	F							
	G							
	H							
	I							
TRIAL 2	A							
	B							
	C							
	D							
	E							
	F							
	G							
	H							
	I							
TRIAL 3	A							
	B							
	C							
	D							
	E							
	F							
	G							
	H							
	I							

No attempt is made to incorporate all these factors independently; instead, gross estimates are made based on the most important factors. Major assumptions are:

a. Obstacle crossing is assumed to cost primarily the potential energy required to lift the vehicle and the time required to slow down to a safe crossing speed, cross, and then resume normal speed.
b. When the vehicle is turning within 10 percent of its turn radius capability ($r_{c\ min}$), its speed will be halved.
c. No time is allotted for path selection; however, whenever the vehicle is required to backtrack, approximate time penalties are assumed.

Table V-5 summarizes the time and energy penalty calculations for each mobility parameter, along with additional quantitative assumptions. These penalties are presented in the form of "Percent Increase Over Minimum" to allow for fluctuations in the basic speed and energy assumptions associated with somewhat varying microscopic lunar surface estimates. The relative energy and time penalties estimated in this study should not vary significantly for reasonably small changes in baseline assumptions.

For each random sample surface, several traverses are performed, shown by rows A through I in Table V-4. Different trials are performed over the same A-I traverses to give an ensemble variation. Figure V-11 is an example of 9 LSSM traverses on a random surface map. Figure V-12 depicts, in actual size, a portion of one sample traverse in Figure IV-11. Also illustrated are the rules used in path selection.

Figures V-13 through V-19 illustrate the sensitivies of the parameters to varying lunar surface definitions. From these curves, energy and time penalties can be estimated. These are shown in Figures V-20 and V-21. Differences in the curves are attributed to the factors noted. An example of the breakdown of energy and time penalties derived from each traverse parameter is shown in Figures V-22 and V-23.

Variations in results due to different drivers selecting the paths (ensemble) were an order of magnitude less than sensitivities to surface variations. This is illustrated in Figure V-24 for the parameter "total distance". The deviations between trials on a given surface are seen to be small compared to the distance sensitivities themselves. This indicates that not much depends on individual choice during a traverse. The deviations are somewhat larger as the surface becomes rougher.

4.4.2 Effect of Limited Visibility. A computer program has been written (Reference 5) which generates qualitative (good, fair, poor) visibility patterns which are used to overlay the sample surfaces in the form of a LSSM-locked

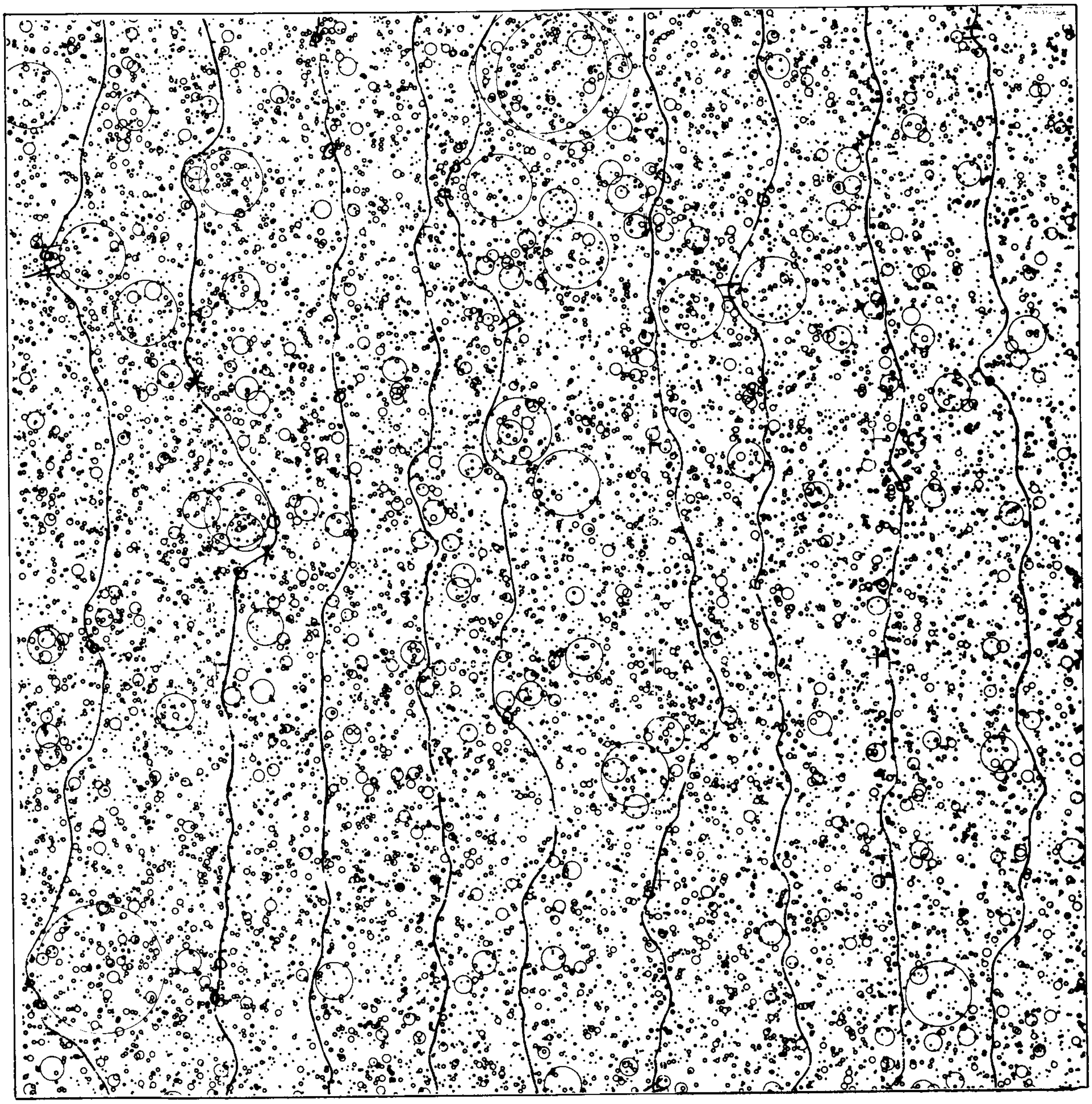

Figure V-11. Sample Lunar Surface with Traverses

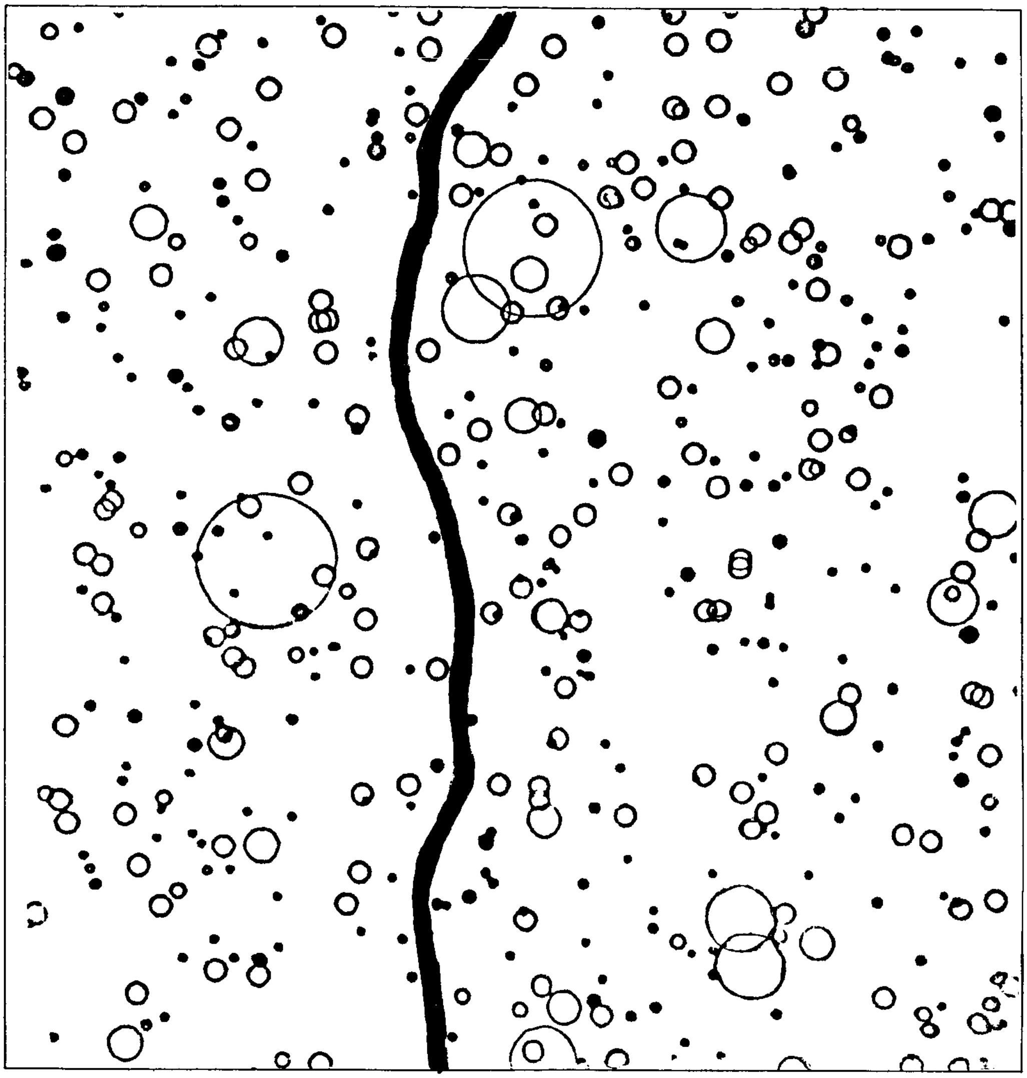

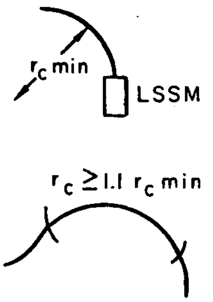

CRATERS

Diameter	Remarks
○ 1-2m	Obstacle under wheel
○ 2-3m	Obstacle under wheel
○ > 3m	Hazard

ROCKS

Height	Remarks
● 0.2-.33m	Obstacle under wheel
● 0.33-0.5m	Obstacle under wheel
● >0.5m	Hazard

Figure V-12. Example of Traverse

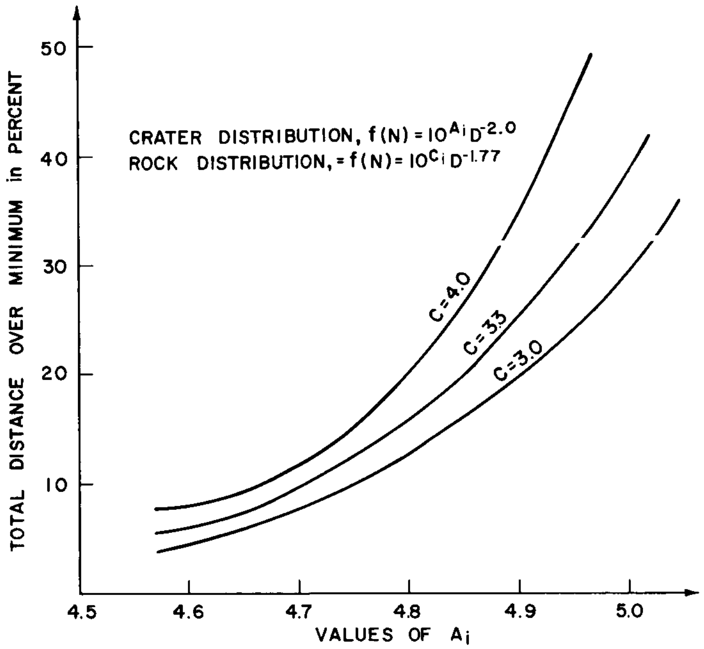

Figure V-13. Percentage of Total Distance Traveled Over the Minimum versus Crater Distribution

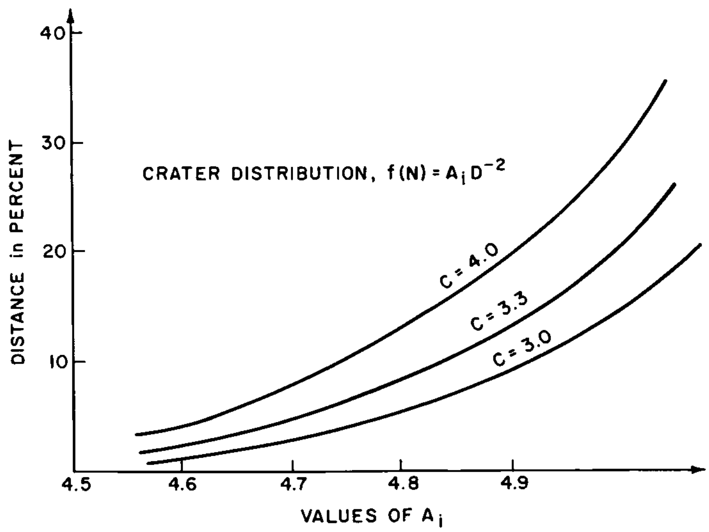

Figure V-14. Percentage of Distance where $r_c \leq 1.1\, r_{c\,min}$ versus Crater Distribution

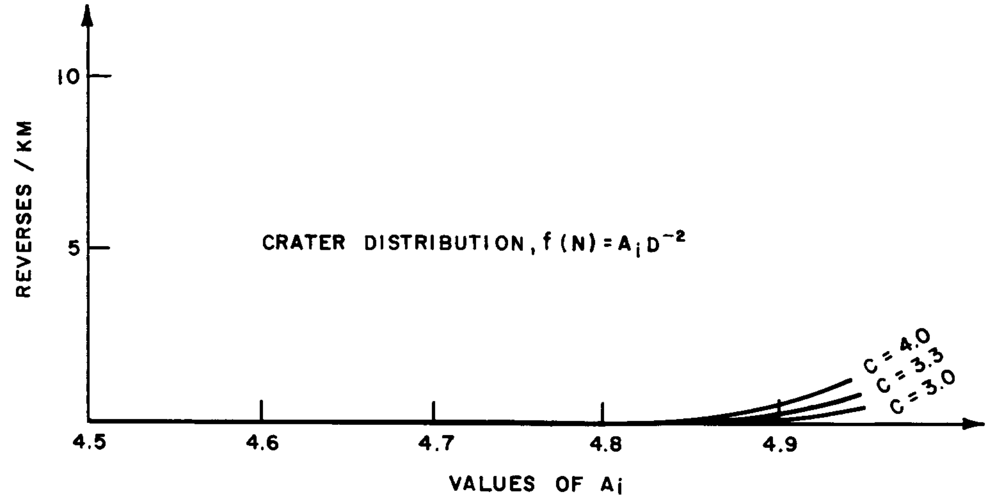

Figure V-15. Number of Reverses/KM versus Crater Distribution

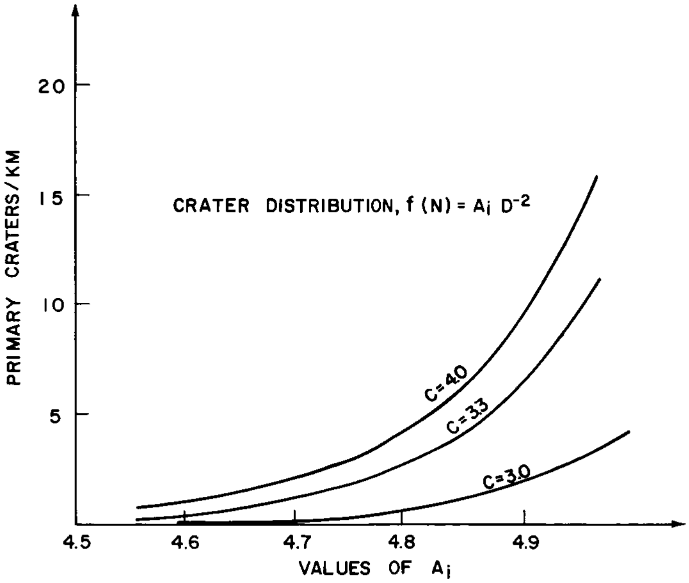

Figure V-16. Number of 1-2M Primary Craters/KM under Wheels versus Crater Distribution

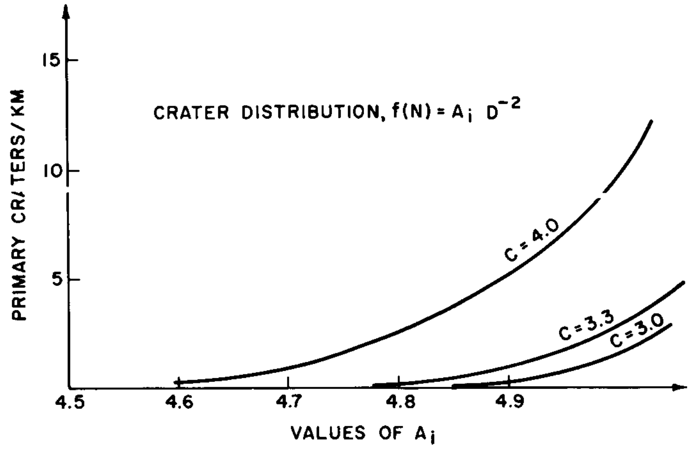

Figure V-17. Number of 2-3M Primary Craters/KM under Wheels versus Crater Distribution

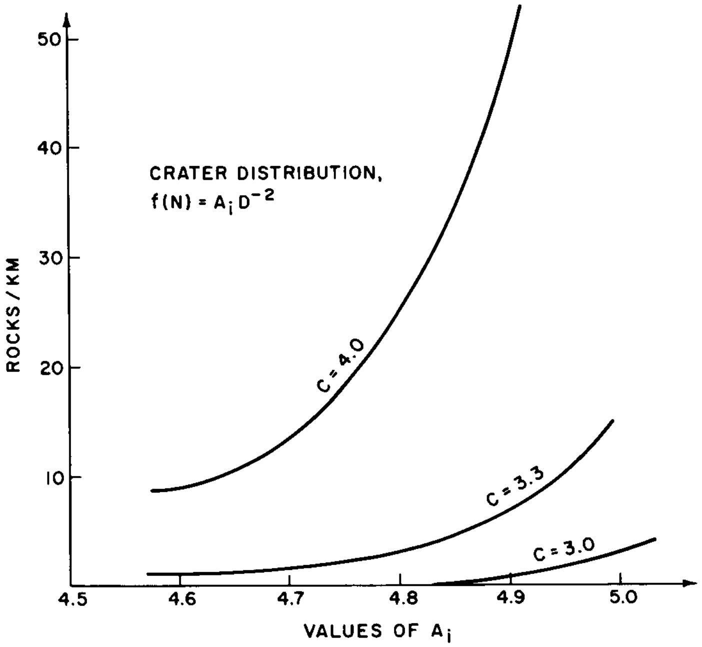

Figure V-18. Number of 0.2-0.33M High Rocks/KM under Wheels versus Crater Distribution

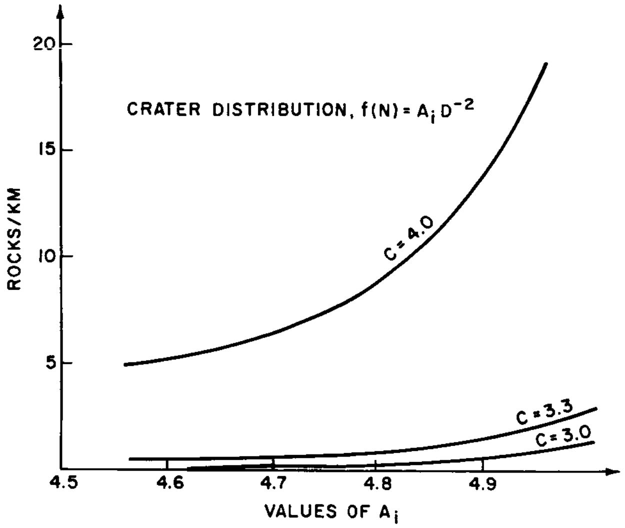

Figure V-19. Number of 0.33-0.5M Rocks/KM under Wheels versus Crater Distribution

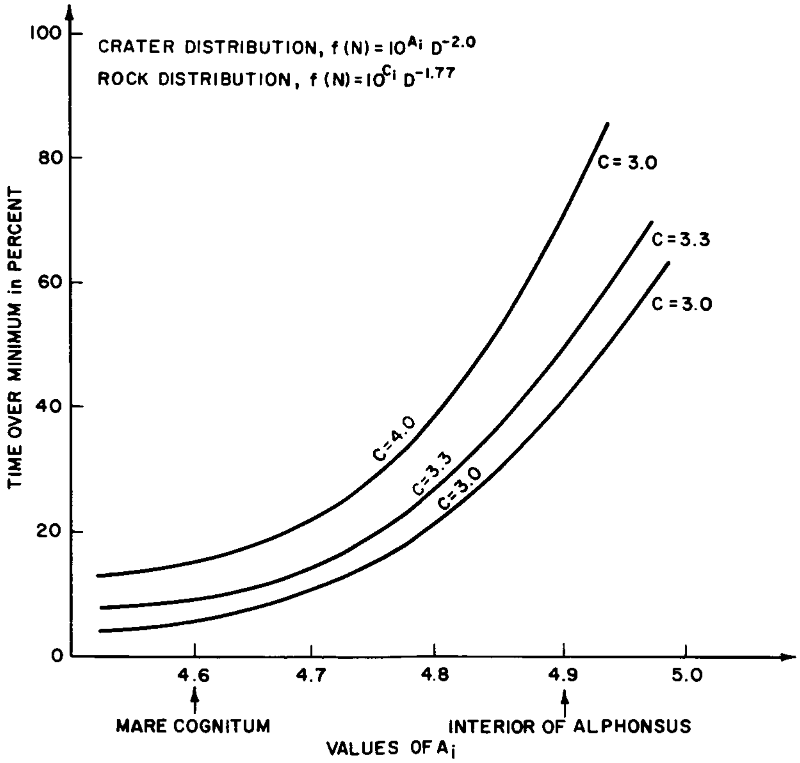

Figure V-20. Percentage of Time over Minimum versus Crater Distribution for Baseline Configurations

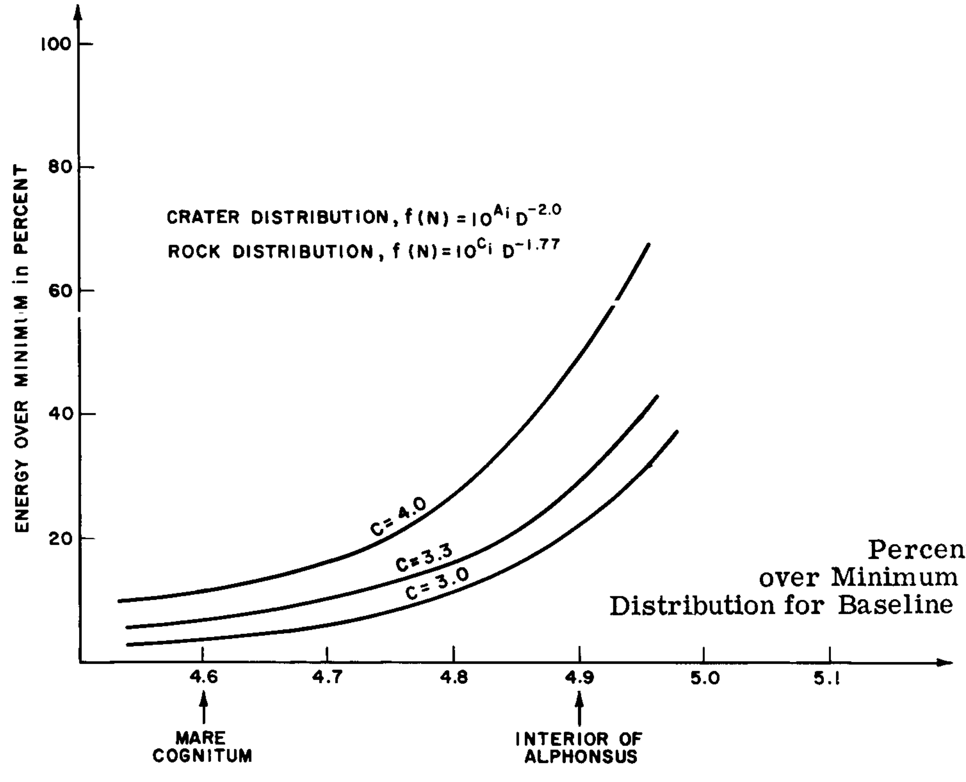

Figure V-21.
Percentage of Energy
over Minimum versus Crater
Distribution for Baseline Configurations

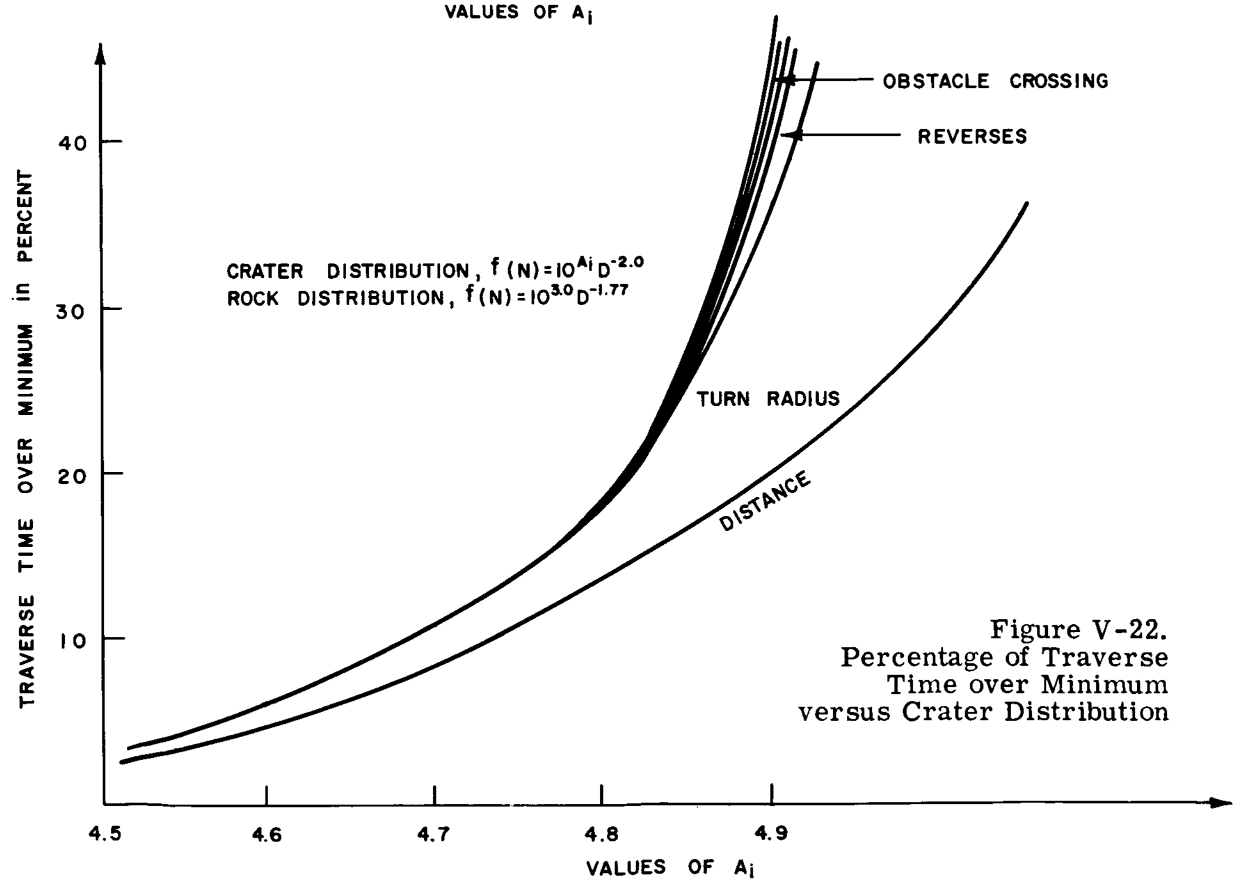

Figure V-22.
Percentage of Traverse
Time over Minimum
versus Crater Distribution

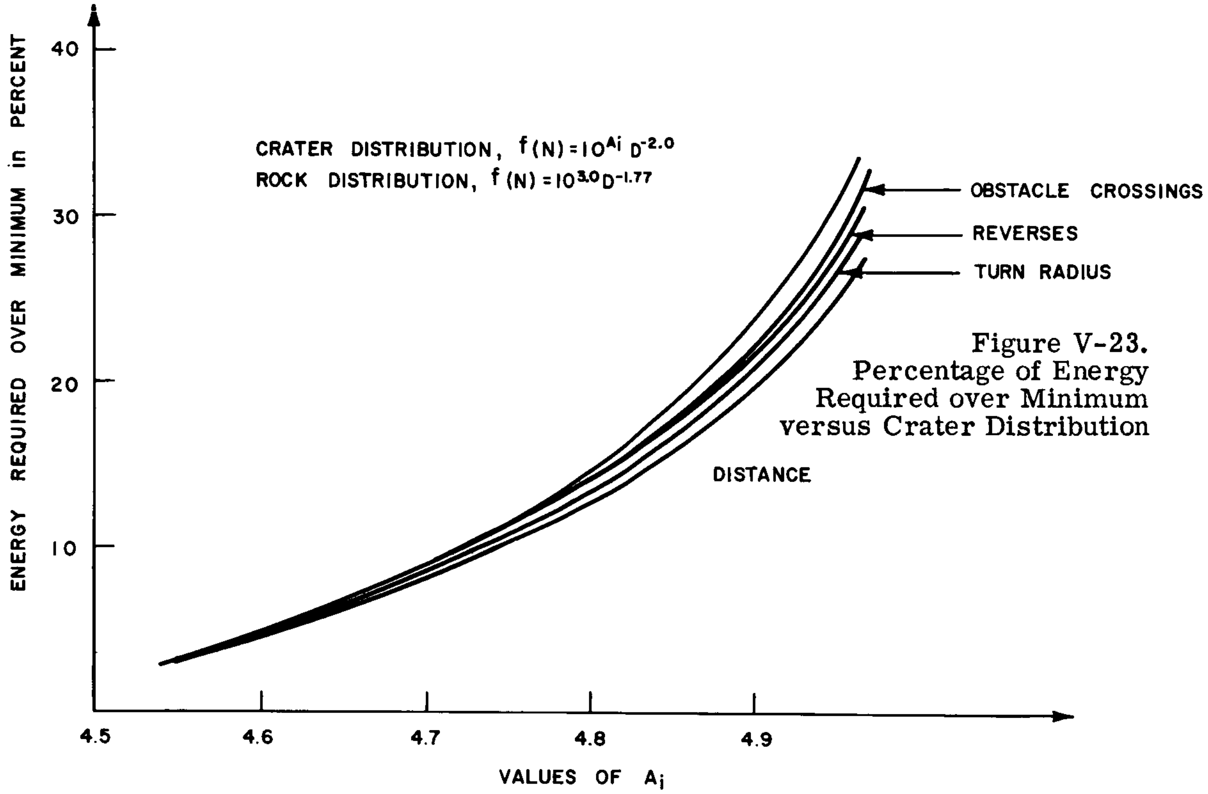

Figure V-23.
Percentage of Energy
Required over Minimum
versus Crater Distribution

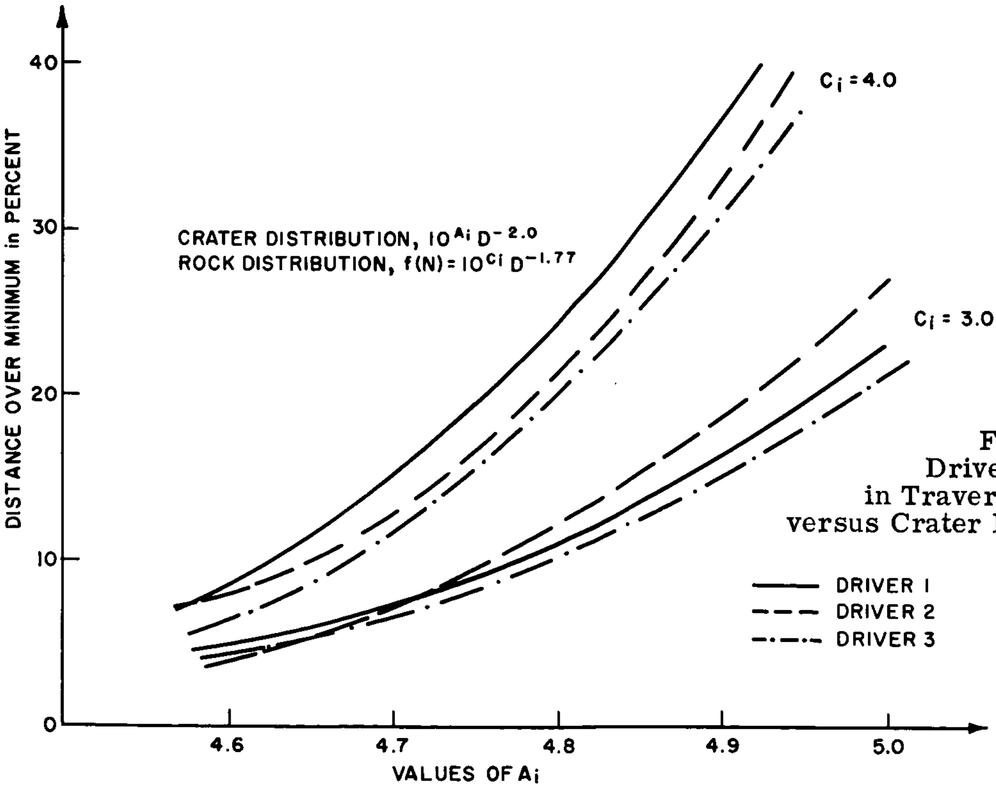

Figure V-24.
Driver Variation
in Traverse Distance
versus Crater Distribution

template. These visibility templates approximate the path selection capability of the driver under varying solar angle conditions, line-of-sight direction, and range. One such template is shown in Figure V-25. In the figure, E_0 is the solar elevation angle, and A_0 is the angle between the driver's line-of-sight and the projection of the sun's rays on the surface. The maximum good viewing range is limited to 100 m in all directions.

The arrow in Figure V-25 represents the case where the sun is directly behind the LSSM at an elevation of 30 degrees. Here, the driver would find it extremely difficult to head directly forward, even if vehicle shadow effects are ignored. Speed would have to be decreased to prevent over-running unseen hazards. In addition, allowances would have to be made for the vehicle's turn radius capability. That is, hazard detection range must allow for avoidance maneuvers. This phenomenon is shown in Figure V-26.

To avoid driving in a poor-visibility direction, the driver would be forced to use a "tacking" technique. The surface maps were traversed using visibility templates for various solar positions. Figure V-27 illustrates one set of traverses where the tacking technique was employed. Figures V-28 through V-34 illustrate the effect of visibility on the mobility parameters. From these curves, energy and time penalties can be calculated using Table V-5. These are shown in Figures V-35 and V-36.

Because of the large sensitivities of energy and time penalties to solar position, the time of lunar day should play an important role in sortie planning as well as path selection during any one traverse. Lunar base location is also important. An example of how these factors influence LSSM time and energy penalties follows.

> Assume an AAP lunar surface mission begins on August 12, 1970 at a base site at latitude 0°, longitude 0° in a maria-like region. On August 12, a traverse is desired to a point of interest located due west of the base site. The LSSM driver's visibility capability can be estimated by first referring to Figures V-37 and V-38 to obtain values for the solar elevation and azimuth angles (about 30° and 90° respectively). In a westerly direction, E_0 is still 30° and A_0 is 0° (-90° +90°). This falls in the "poor" visibility traverse category (Figure V-25), and time and energy estimates can be based on the predicted crater and rock distribution from the corresponding curves (Figures V-35 and V-36). The time and energy penalties are 75 and 40 percent respectively.

4.4.3 Visibility Aids. For AAP mission planning, the following two questions are of interest: Will visibility aids reduce traverse time and energy penalties? And to what extent can they be employed before becoming impractical?

Table V-5

TIME/ENERGY PENALTIES DERIVED FROM TRAVERSE MOBILITY PARAMETERS

Mobility Parameter	Energy Penalty (percent)	Time Penalty (percent)
1. X – Percent traverse distance over minimum. Both energy and time are directly proportional to traverse distance.	X	X
2. Y – Percent traverse distance where $r_{c\ min} < r_c < 1.1\ r_{c\ min}$ assuming speed when $r_c < 1.1\ r_{c\ min} \approx \frac{A}{2}$ km/hr. Percent time penalty $\approx \left[\frac{1-X/100}{A} + \frac{X/100}{A/2} - \frac{1}{A}\right]\frac{100}{1/A}$	None	Y
3. Z – Number of decisions/km resulting in traversing in reverse, where ΔE = Energy cost/decision $\approx (2)\ \frac{m(A)^2}{2}\ (3.8 \times 10^{-7})$ $\approx 4.0 \times 10^{-4}$ kWh Δt = Time cost/decision $\approx$ 0.003 hours	0.4Z	1.5Z
4. $N_{1,2}$ – Number of 1-2m craters/km under wheels. ΔE = Energy penalty/crossing $\approx (2)\ \frac{m}{2}\ g\Delta H$ $\approx 4.0 \times 10^{-4}(.5)$ kWh Δt = Time cost/decision $\approx$ 0.007 hr Percent time penalty $\approx \left[X\right]\left[\frac{100}{1/A}\right]\left[0.007\right]$	0.2 $N_{1,2}$	0.35 $N_{1,2}$
5. $N_{2,3}$ – Number of 2-3m craters/km under wheels. $\Delta E \approx 4.0 \times 10^{-4}(0.75)$ kWh $\Delta t \approx$ 0.001 hr	0.3 $N_{2,3}$	0.5 $N_{2,3}$
6. $M_{.2,.33}$ – Number of 0.2-0.33 meter high rocks/km under wheels. $\Delta E \approx 4.0 \times 10^{-4}(.33)$ kWh $\Delta t \approx$ 0.0007 hr	$0.14M_{0.2,0.33}$	$0.35M_{0.2,0.33}$
7. $M_{.33,.5}$ – Number of 0.33-0.5m high rocks/km under wheels. $\Delta E \approx 4.0 \times 10^{-4}(0.5)$ kWH $\Delta t \approx$ 0.001 hr	$0.2M_{0.33,0.5}$	$0.5M_{0.33,0.5}$

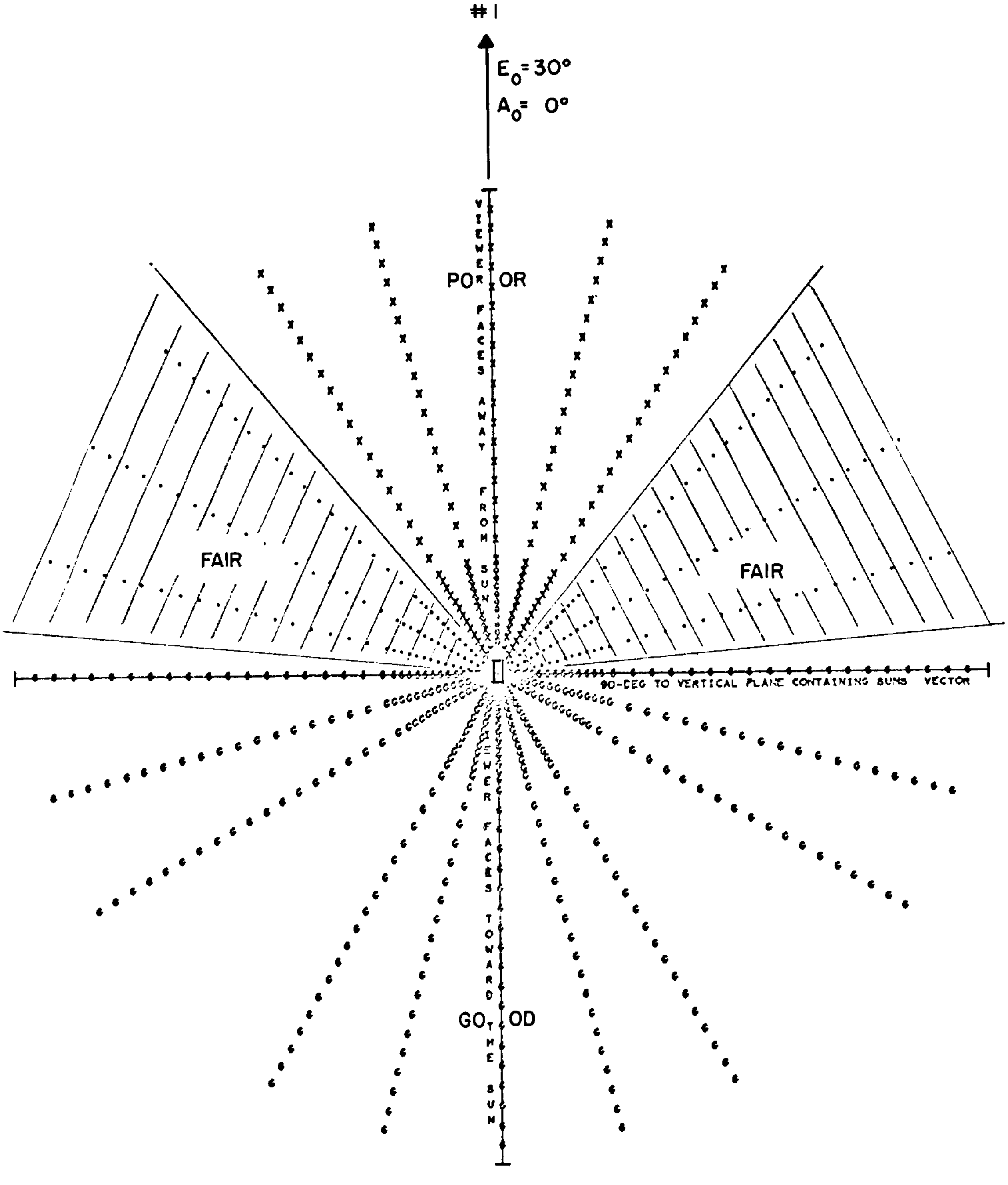
#1
E_0= 30°
A_0= 0°
POOR
VIEWER FACES AWAY FROM SUN
FAIR
FAIR
90-DEG TO VERTICAL PLANE CONTAINING SUNS VECTOR
VIEWER FACES TOWARD THE SUN
GOOD

Figure V-25. Visibility Conditions
Sun Elevation Angle of 30 Degrees
View Out to 100 Meters
Observer's Height, 2.5 Meters

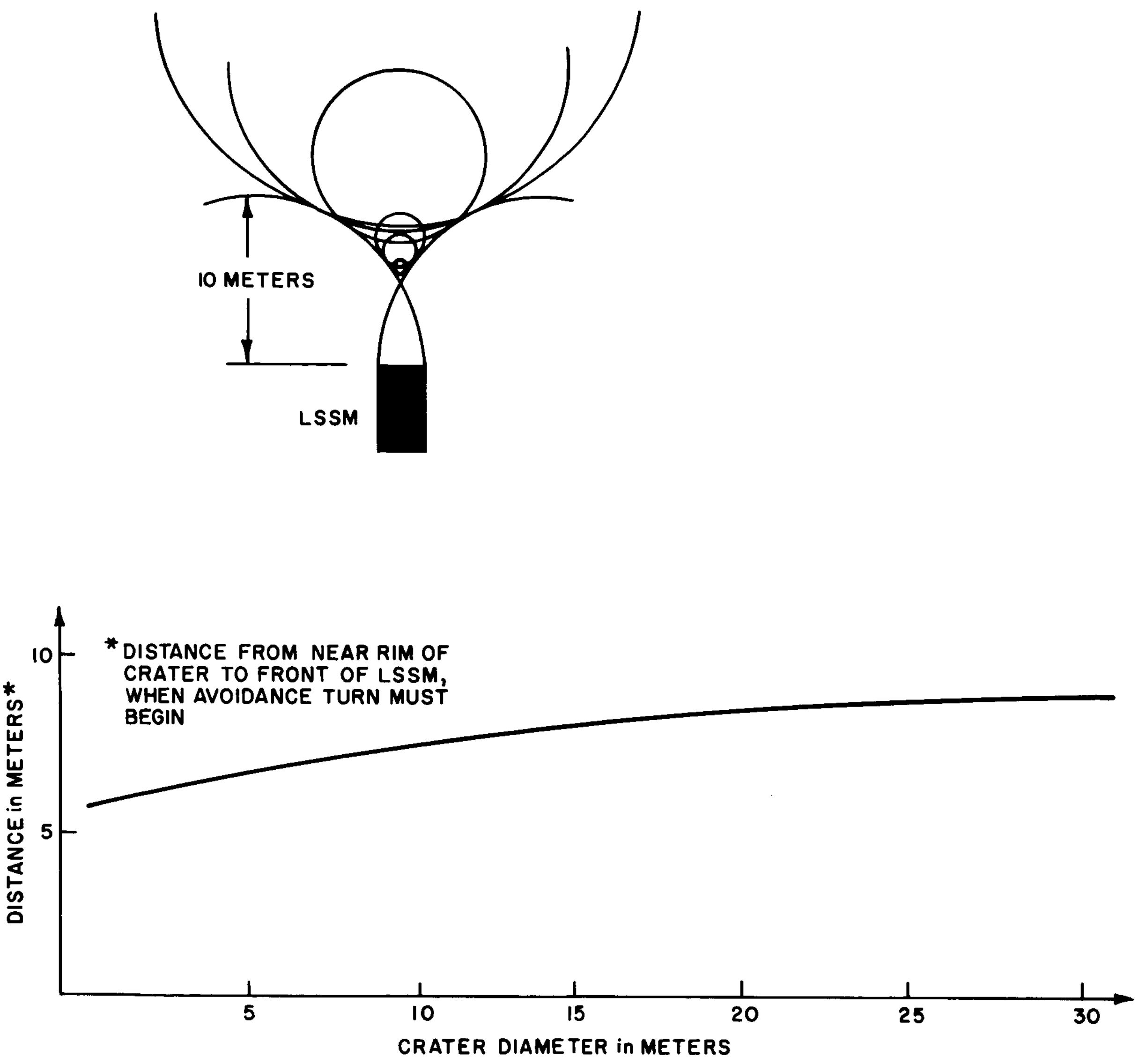

Figure V-26. Hazard Detection Range

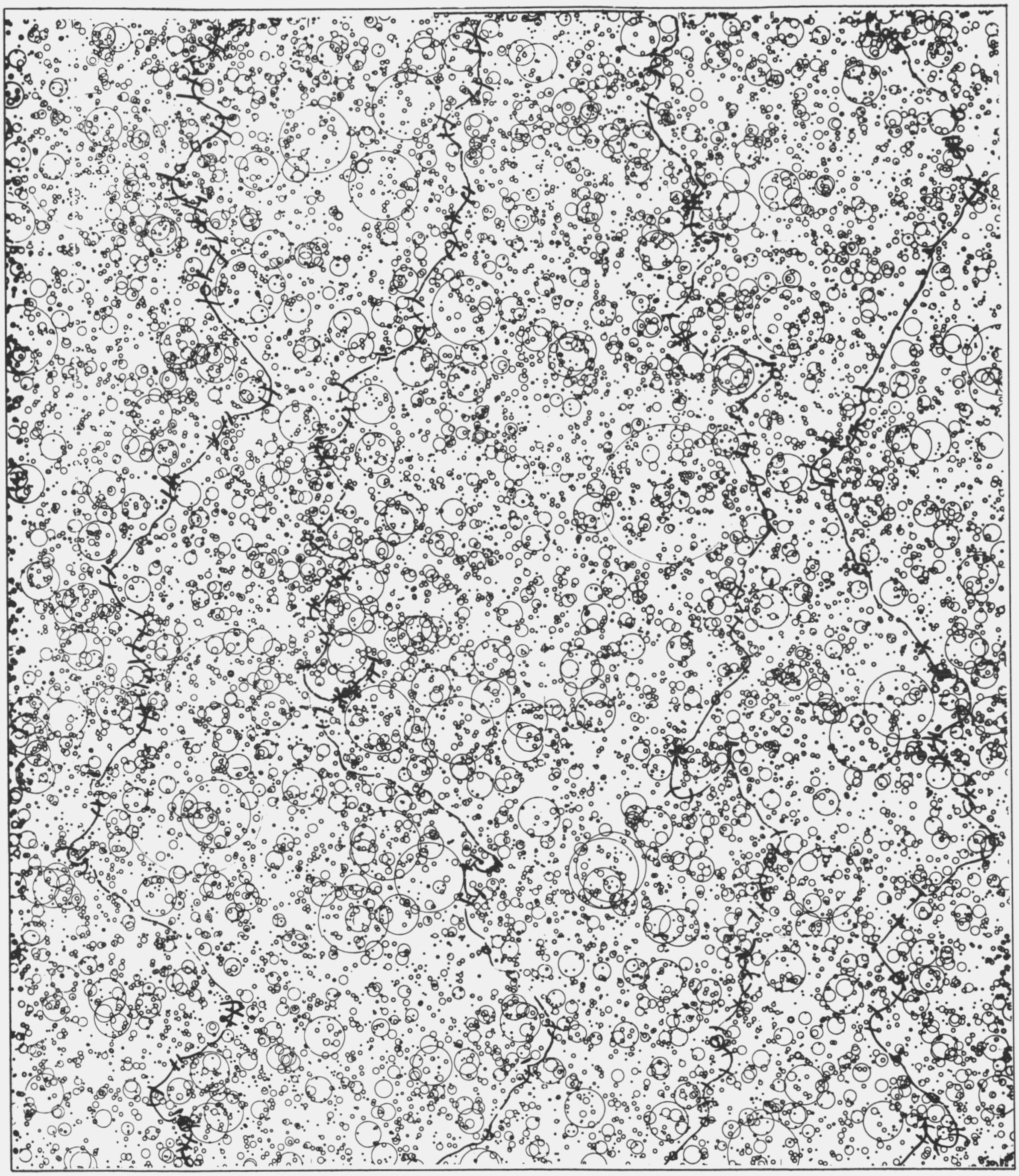

Figure V-27. Sample Lunar Surface with Traverses, Poor Visibility Conditions

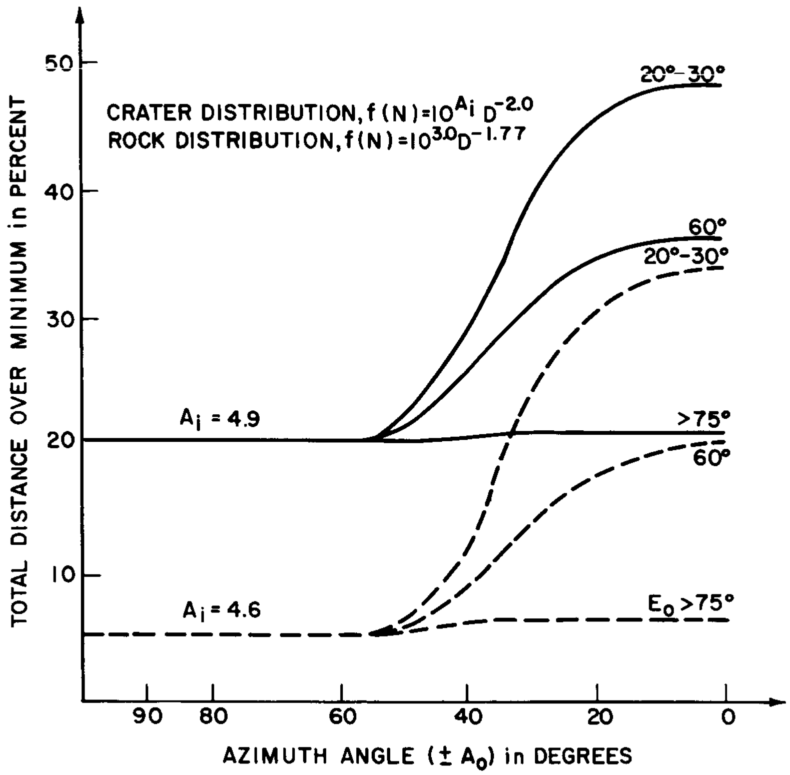

Figure V-28. Percentage of Total Traverse Distance over Minimum Azimuth Angle

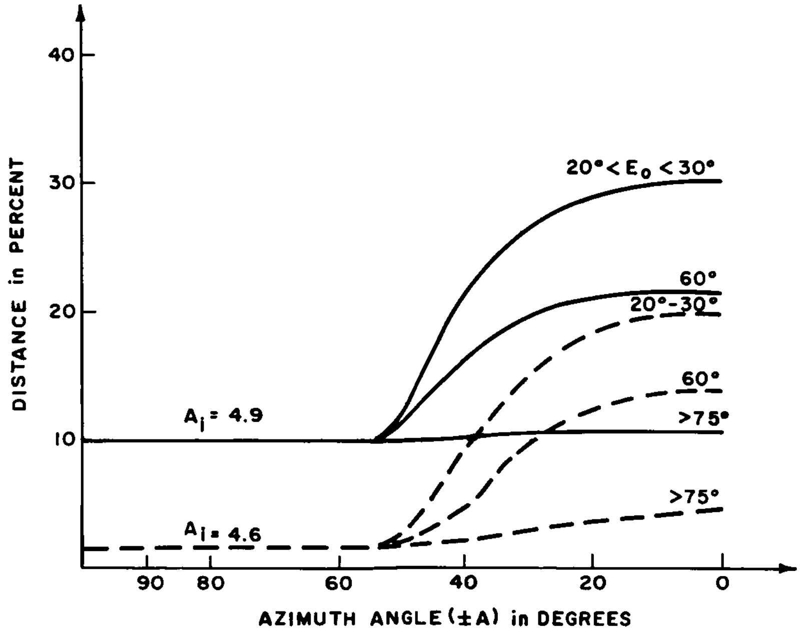

Figure V-29. Percentage of Distance where $r_c \leq 1.1\ r_{c\ min}$ versus Azimuth Angle

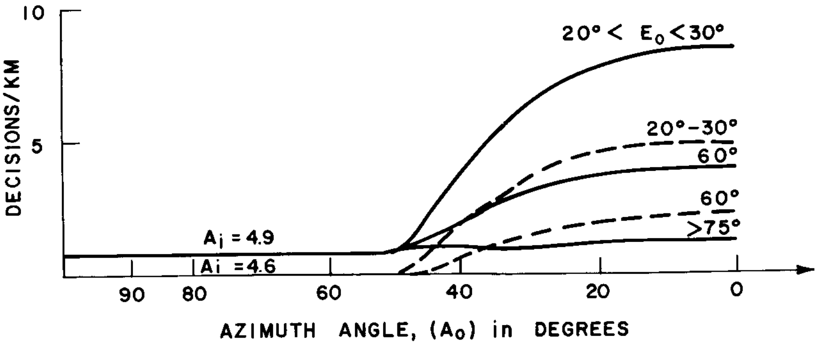

Figure V-30. Number of Reverse Decisions/KM Resulting in Reverse Traveling versus Azimuth Angle

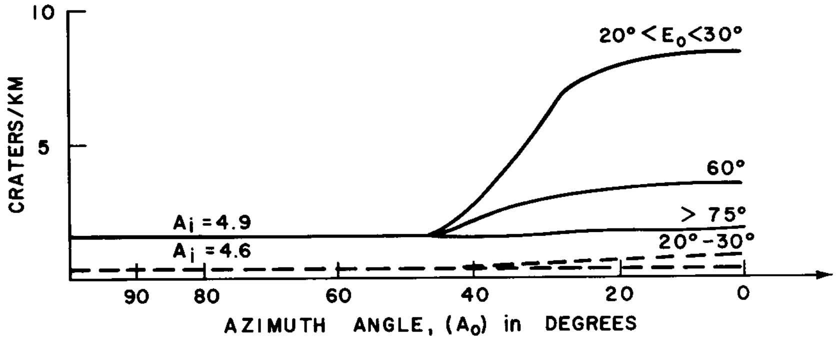

Figure V-31. Number of 1-2M Primary Craters/KM under Wheels versus Azimuth Angle

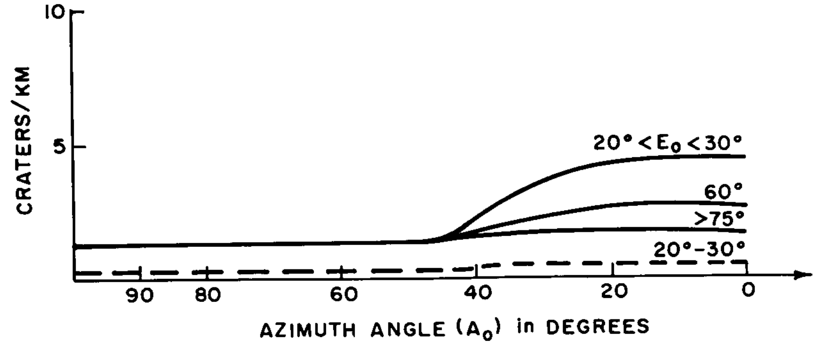

Figure V-32. Number of 2-3M Primary Craters/KM under Wheeld versus Azimuth Angle

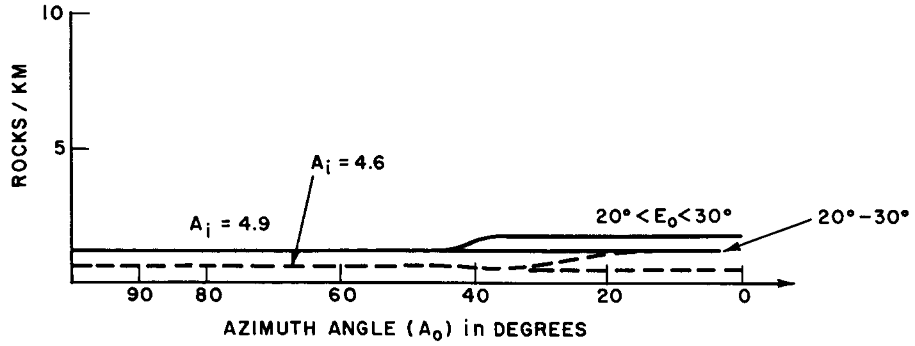

Figure V-33. Number of 0.2-0.33M High Rocks/KM under Wheels versus Azimuth Angle

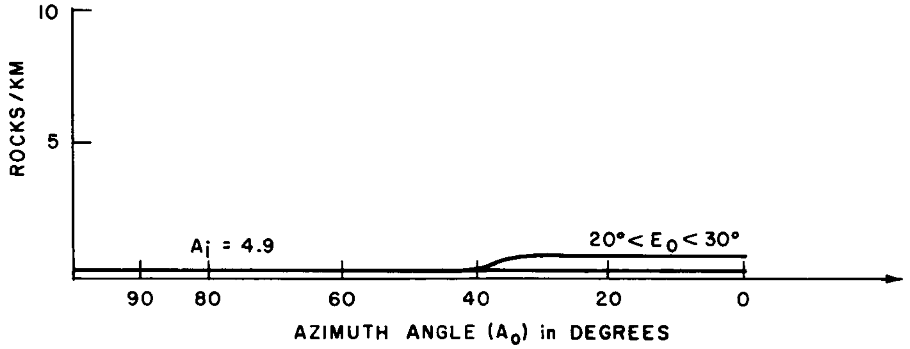

Figure V-34. Number of 0.33-0.5M High Rocks/KM under Wheels versus Azimuth Angle

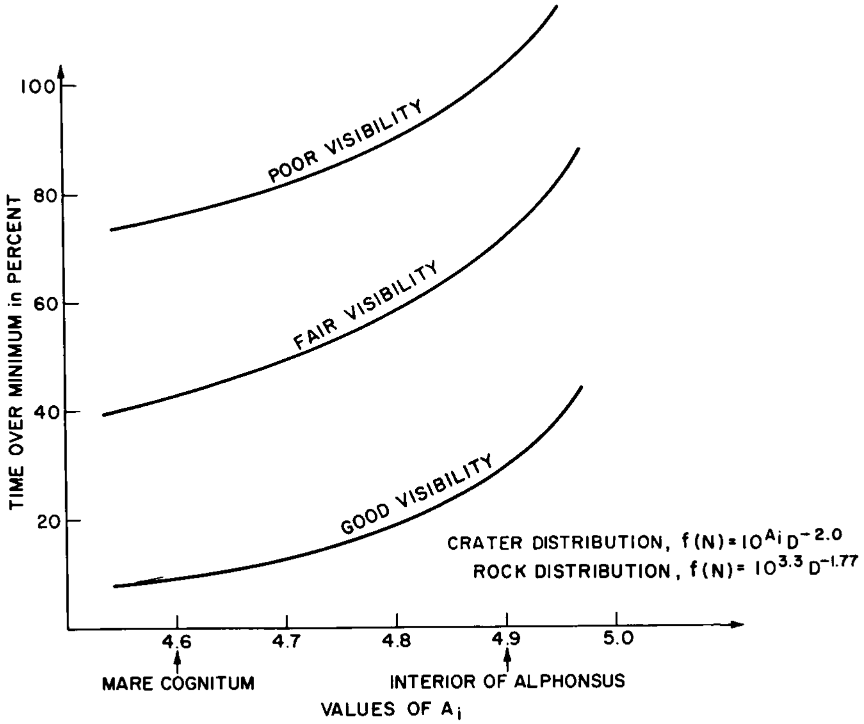

Figure V-35. Percentage of Time over Minimum versus Crater Distribution

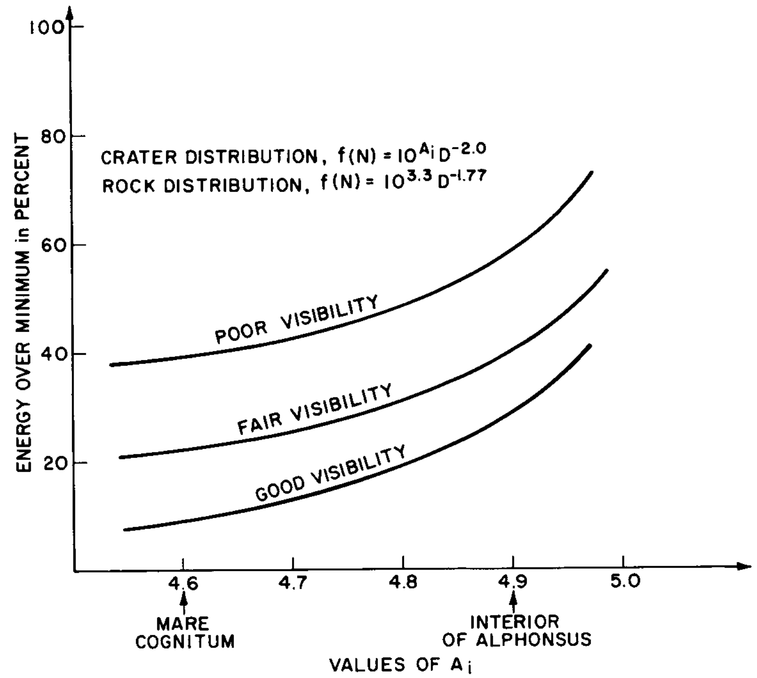

Figure V-36. Percentage of Energy over Minimum versus Crater Distribution

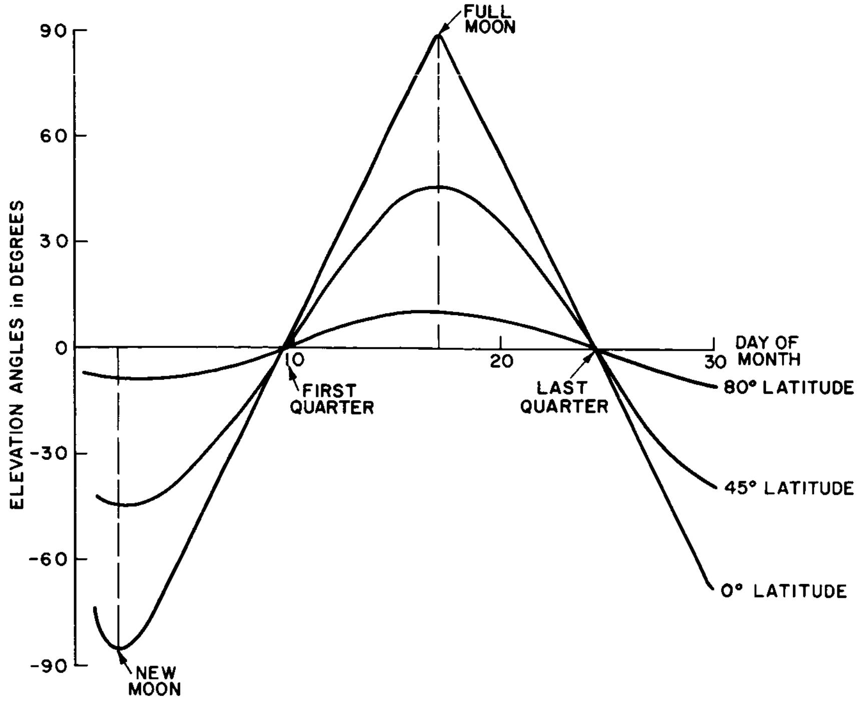

Figure V-37. Elevation Angles for August 1970 at 0° Longitude

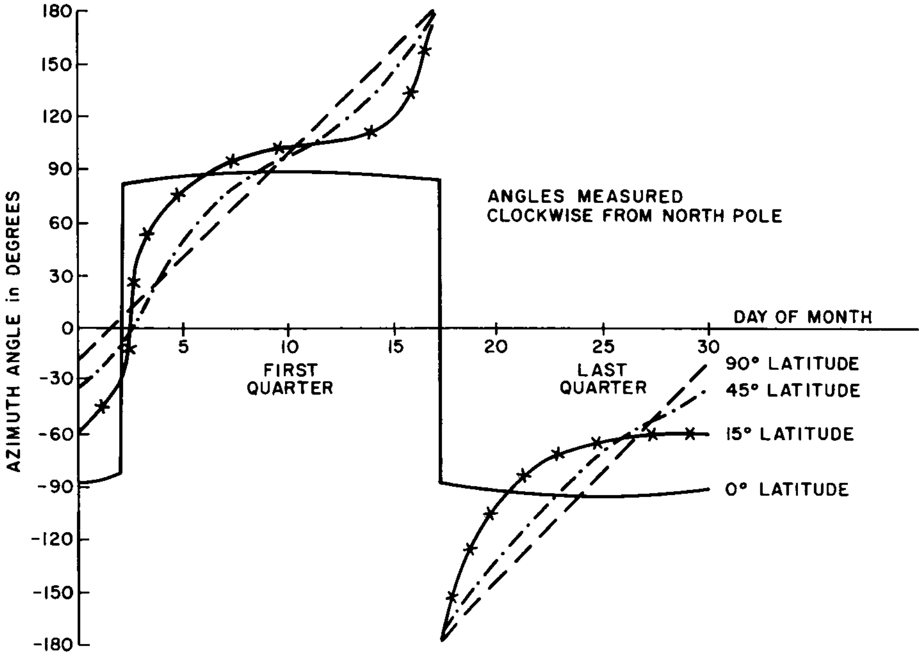

Figure V-38. Azimuth Angles for August 1970 at 0° Longitude

Surface maps — High-resolution maps showing all mobility hazards, with preselected meter-by-meter traverse paths for use by the LSSM driver, seem unrealistic. Most important, following a traverse path on a high-resolution map would be tedious and time-consuming; especially for a single astronaut. The time required to correlate the terrain with the map could be better spent selecting an optimum path extemporaneously.

A lower-resolution map (>30m features) appears more practical. Tentative preplanned traverses can be laid out, avoiding major surface obstructions, but leaving fine-path selection to the driver. These maps would provide useful directional information by indicating major landmarks.

To determine the effect of maps on time and energy penalties, the following experiment was performed. Dual traverse simulations were made with identical start and finish points and the same traverse rules except for visibility. In one case, in addition to the visibility templates, all craters >30m were exposed, while in the other, only visibility templates were used. Results indicated that mapping provides little benefit from a time/energy penalty standpoint until the surface becomes rough and visibility poor. Here, the total exposed surface occasionally prevented poor path selection which sometimes resulted in backtracking.

Traverse path marking — Because of line-of-sight limitations, driver path selection difficulty, and other potential visibility problems, it would be advantageous to mark the vehicle's path. This would cut down the energy/time penalties in the return direction when the driver's visibility may be the same or worse. (See Figure V-25) To illustrate the value in path marking, consider the time/energy penalties estimated in Table V-1. In the case of traversing a "smooth" region, assume the forward path was chosen with good visibility. Here, the expected time and energy penalties are 6 and 5 percent respectively. Suppose the return path is under poor visibility, then by following a marked path, up to 60 percent in time and 35 percent in energy can be saved. Also, the marked path remains for possible future traverses (which may occur under poor visibility conditions).

In addition, in case of vehicle breakdown, the driver's walk-back capability would be enhanced by return path marking. This is analyzed in detail in Section VI.

Shadow illuminator — A light directed into the vehicle shadow would assist the driver when the vehicle is moving away from the sun, especially at low sun elevation angles. During a "tacking" traverse, a shadow illuminator would allow safer and surer turning at the end of each tack decreasing time penalties associated with this maneuver. In addition, because of the darkness of all shadowed areas on the lunar surface, an illuminator would provide a useful general purpose exploration aid.

Two possible light sources were considered: a battery-powered headlamp and a sun reflector. A directional headlamp is more practical from an operational standpoint, but its energy requirements are large — on the order of the mobility requirement of the vehicle itself. A sun reflector has no energy requirement but appears to be difficult to design and operate. To be very useful the reflecting surface would have to automatically fix on the sun during the vehicle's continuous irregular traverse path.

While a shadow-eliminator would be helpful under poor visibility conditions, it does not appear necessary for acceptable LSSM mobility performance.

Optical periscope — Under good visibility conditions, variations in the visual height of the LSSM driver has negligible effect on traverse path selection and time/energy penalties. However, distance to the horizon is enhanced or degraded as shown in Figure V-39. The driver has a natural horizon capability of about 2.5 km (in relatively flat terrain); increasing his effective height by 10m extends the horizon to almost 7 km.

Under poor visibility conditions, driver visual height is one input in determining (qualitatively) how well surface features can be detected in a given direction and distance. Small variations, which might reflect LSSM design differences (30 percent), appear to have small effect. This was determined by generating new visibility templates varying only viewing height. The question then arises; Would further increasing visual height through the use of some type of optical periscope improve the driver's visibility significantly ?

An examination was made of the effect of increased visual height by generating new visibility templates. Figure V-25 illustrates the potential visibility problem traveling away from the sun. The "poor" region is a result of "washout," a lack of contrast in the reflecting surface. As described in an earlier section, to avoid driving in this poor visibility direction, a tacking traverse may be required. However, by greatly increasing the visual height of the driver, visibility can be improved. This phenomenon is represented in Figure V-40 for the case of $E_0 = 30°$, $A_0 = 0°$. The LSSM driver can see fairly well (except for the terrain masked by the vehicle shadow) up to about 2.4m ahead. If an average vehicle speed of 5 km/hr is assumed, this is about 1.5 seconds lead time. If the driver needs a minimum of 10m (7 sec) of good visibility to avoid tacking, an optical periscope of height 4.2m would be necessary. Figure V-41 illustrates this effect from a top view. The required periscope height for a 10m good visibility range is a function of solar elevation angle. This is shown in Figure V-42.

While theoretically an effective instrument, the periscope has several operational difficulties:

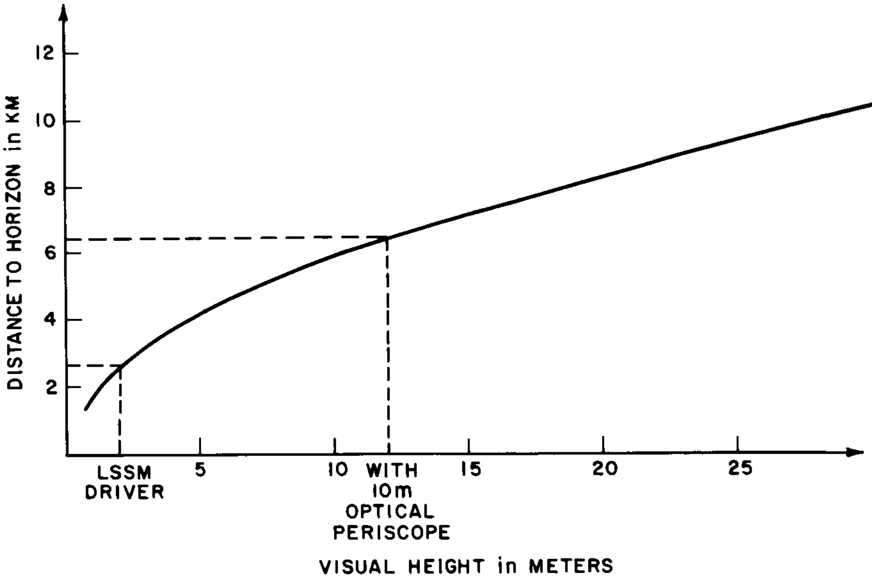

Figure V-39. Distance to Horizon versus Visual Height

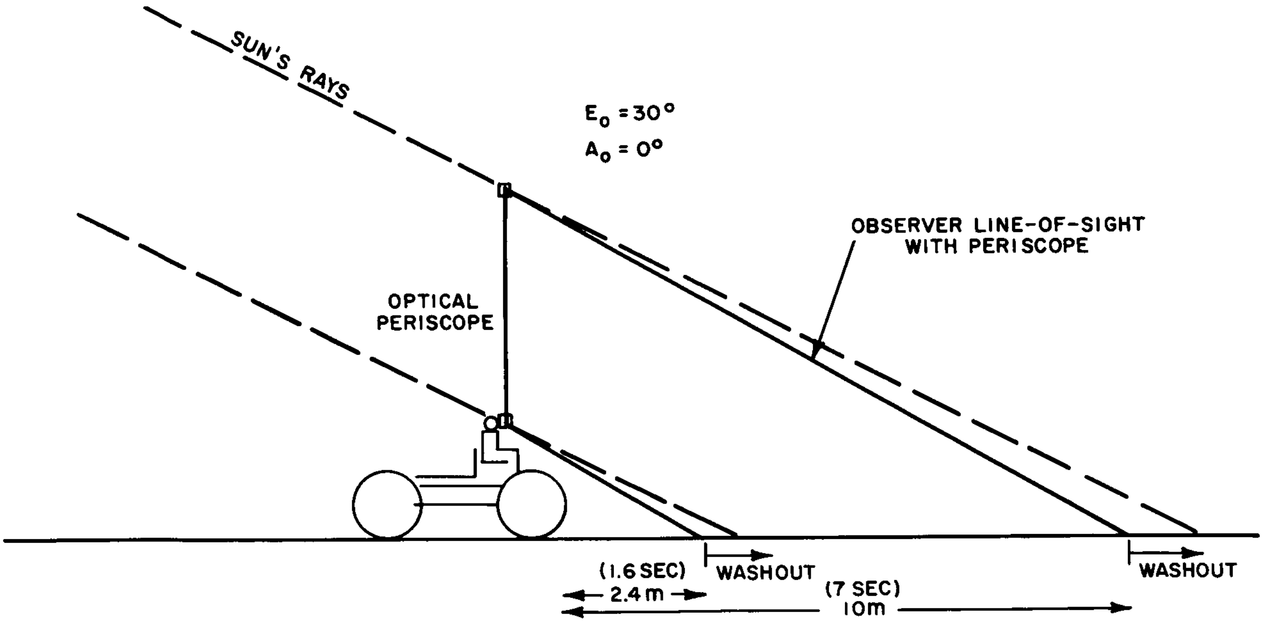
SUN'S RAYS
$E_0 = 30°$
$A_0 = 0°$
OBSERVER LINE-OF-SIGHT WITH PERISCOPE
OPTICAL PERISCOPE
(1.6 SEC)
2.4 m
WASHOUT
(7 SEC)
10m
WASHOUT

Figure V-40. Optical Periscope

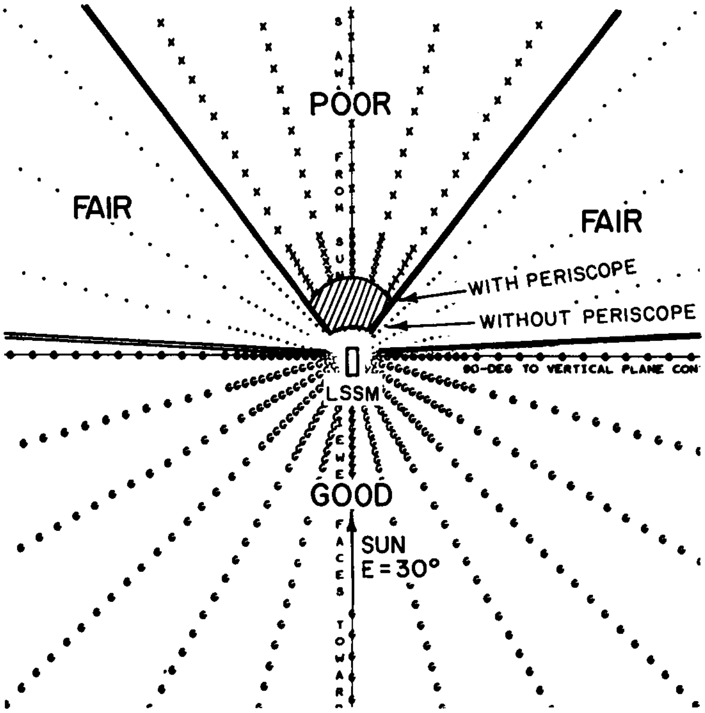
SAW
POOR
FROM SUN
FAIR
FAIR
WITH PERISCOPE
WITHOUT PERISCOPE
90-DEG TO VERTICAL PLANE CON
LSSM
EWE
GOOD
FACES TOWAR
SUN
E = 30°

Figure V-41. Visibility Range
with Optical Periscope

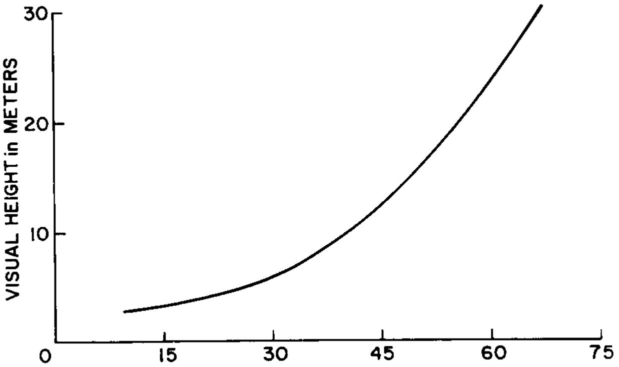

Figure V-42. Required Visual Height versus
Solar Elevation Angle
10M Good Visibility
A_0 = 0 Degrees

1. The higher the visual height, the farther away the surface features appear in the immediate forward path.
2. A raise in the center of gravity of the vehicle will degrade vehicle stability.
3. The hazardous nature of the terrain will allow little opportunity while the vehicle is in motion for the driver to divert his attention from his forward proximity. Thus, to operate a periscope, a stop-and-go procedure might be required. However, this would be too costly in time penalties.
4. The field-of-view using this instrument would be considerably less than that of an unaided LSSM driver.

In summary, it appears some visual aid may be derived from an optical periscope. However, operational problems and difficulties in design exist. Well-planned daily traverses, using maps and marked paths when practical, should reduce much of the visibility problem, thus reducing the profit of a periscope.

4.4.4 Vehicular Sensitivities

General — The preceding paragraphs described mobility sensitivities with the vehicle and obstacle definition held fixed at their "baseline" values. There are two reasons for determining the sensitivities of time and energy penalties to variations in the major parameters affecting mobility. First, since the baseline values may be inaccurate, the traverse results are of value only if they are relatively insensitive to the assumptions. Second, it is of interest to determine if small design changes can significantly improve mobility. Independently, path width and turn radius were varied ±30 percent, and traverses were made over the same sample surfaces. The effect only became noticable in the rougher terrain. Similarly, mobility parameters were insensitive to 30-percent variations in obstacle dimensions until the terrain became rough. Figure V-43 shows the effect of these variations on time penalties. A more practical experiment should be to decrease the vehicle size (thereby improving path width and turn radius) combined with a corresponding decrease in obstacle dimension definition. This is basically what was done in evaluating the smaller LSSM described below.

Smaller LSSM — A 500-lb LSSM has been suggested for ALM short-duration missions (Reference 3). It is of interest to estimate the time/energy penalties associated with this smaller vehicle. For simplicity, a scaled-down version of the 1000-lb LSSM is considered. Dimensionally, this would convert to new vehicular characteristics and hazard definition, the more important of which are listed below:

	1000-lb LSSM	500-lb LSSM
Average speed with optimum conditions	5 km/hr	3.5 km/hr
Vehicle length	5.0m	3.5m
Vehicle width	2.5m	1.75m
Height of driver's eyes	2.5m	1.75m
Average energy with optimum conditions	0.1 kWh/km	0.05 kWh/km
Turn radius	10m	7m
Hazardous crater diameter	3m	2m
Hazardous rock height	0.5m	0.35m

In the same manner that was used to estimate the 1000-lb LSSM capabilities, sample surfaces were traversed by the simulated smaller vehicle as described above. The results can be summarized as follows (See Figure V-44):

1. The time/energy penalties associated with the maria were similar to that of the larger vehicle. Moreover, the traverse paths were almost indistinguishable.
2. As the sample surfaces became rougher, the time/energy penalties continued to be similar to the larger vehicle even though the traverse paths themselves were quite different. This reflected the phenomena of the increased vehicle maneuverability (path width, turn radius) balancing the effect of the smaller-dimensioned hazards.

Thus, it appears that a 500-lb LSSM can negotiate the same terrain as the 1000-lb LSSM, with similar percentage penalties over their respective baseline estimates of speed and energy.

5. APPLICATION TO MISSION PLANNING

A safe operating radius is a function of LSSM mobility, required scientific time, payload weight, and astronaut walk-back capability. For illustrative purposes, assume total mission time is limited to 6 hours, total scientific time at the "remote site" is fixed at 2 hours, payload requirements limit the number of PLSS's to three, and the astronaut has the option of returning in a marked forward path. The quantitative estimates of vehicle and walking speeds (functions of terrain and visibility) then limit remote-site capability. Figure V-3 shows this effect for the 1000-lb LSSM. From the curves, it is seen that the distance capability varies from 5 to 8 km, depending on environmental conditions. Traverse 1 is limited in operating radius by the life support capability of three PLSS's (12 hours in a contingency situation). Traverses 3 and 4 are limited by LSSM speed. Traverse 2 has remote site capability at the limits of both constraints.

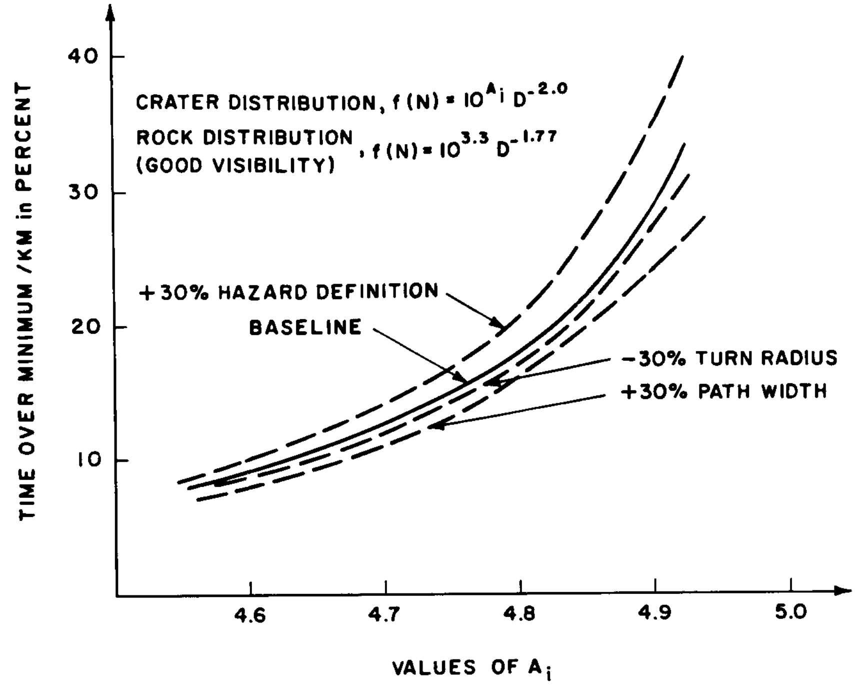

Figure V-43. Percentage of Time Over Minimum/KM versus Crater Distribution for 30-Percent Variations in Vehicle Turn Radius, Vehicle Path Width, and Hazard Definition

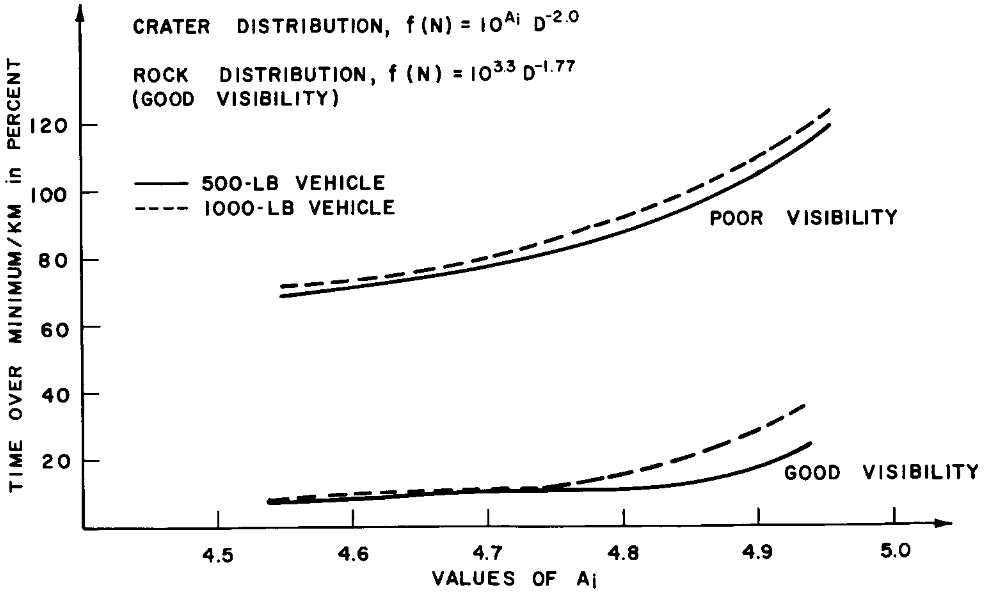

Figure V-44. Percentage of Time over Minimum/KM versus Crater Distribution

Figure V-4 has corresponding curves for the 500-lb LSSM. For this vehicle, payload constraints limit the number of PLSS's to two. Visibility degradations are assumed similar to those of the larger LSSM. The distance capability varies from 3.5 to 4.5 km.

While these results are somewhat more restrictive than vehicle capabilities generally assumed in available NASA literature, useful surface missions can still be formulated with all traverses within the operating radius of the LSSM.

Daily traverse planning should reflect the importance of varying sun angles on visibility. For example, at sites near the equator, north-south traverses will always be more desirable than east-west traverses, so landing sites should be generally north or south of interesting features. Also planning should make optimum use of marked paths for recurrent use.

To illustrate the mobility capabilities of the LSSM (as well as other system constraints) two sample mission plans were generated — one using the 500-lb vehicle on a augmented LM 4-day mission and one using the 1000-lb vehicle on a Dual LM 12-day mission. Figures V-45 and V-46 depict the LSSM traverses planned for these two representative missions. The 4-day mission landing site is southeast of the Central Peak in the Crater Alphonsus (intermediate hazard density) and the 12-day site is south of Hypatia Rille I in Southern Mare Tranquillitatis (smooth hazard density). By the use of estimates of scientific requirements, LSSM traverse missions were laid out — within the mobility limitations of this study. A detailed description of these traverses (time schedules, payloads, scientific activities, etc.) can be found in Reference 3.

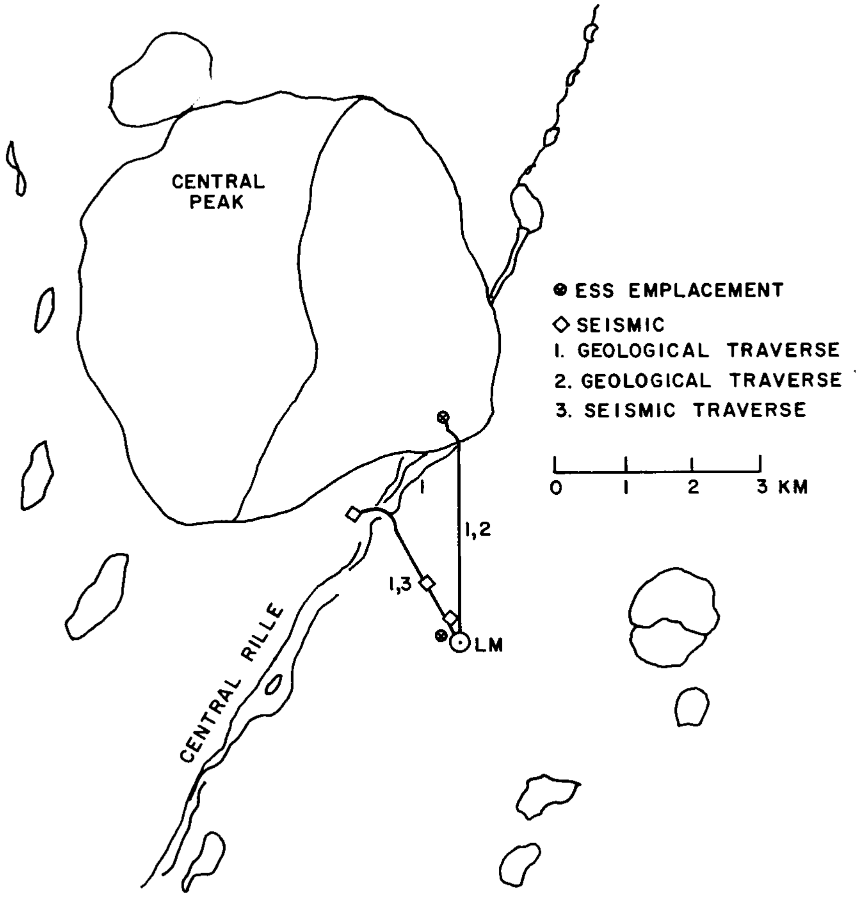
CENTRAL PEAK
⊗ ESS EMPLACEMENT
◇ SEISMIC
1. GEOLOGICAL TRAVERSE
2. GEOLOGICAL TRAVERSE
3. SEISMIC TRAVERSE
0 1 2 3 KM
1
1,2
1,3
LM
CENTRAL RILLE

Figure V-45. Site of 4-Day Mission
to the Central Peak in Crater Alphonsus

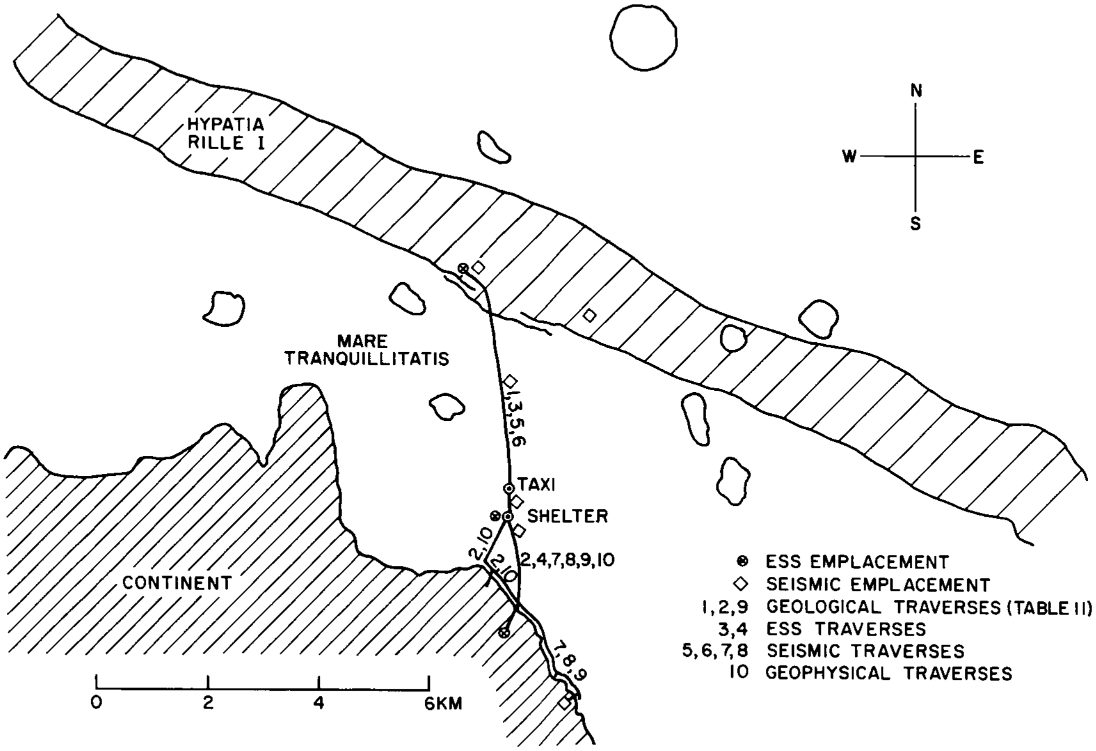
HYPATIA RILLE I
MARE TRANQUILLITATIS
CONTINENT
N
W
E
S
TAXI
SHELTER
1,3,5,6
2,4,7,8,9,10
2,10
7,8,9
⊗ ESS EMPLACEMENT
◇ SEISMIC EMPLACEMENT
1,2,9 GEOLOGICAL TRAVERSES (TABLE II)
3,4 ESS TRAVERSES
5,6,7,8 SEISMIC TRAVERSES
10 GEOPHYSICAL TRAVERSES
0
2
4
6KM

Figure V-46. Site of 12-Day Mission to Hypatia Rille I in Southern Mare Tranquillitatis

REFERENCES

1. The Local Scientific Survey Module, Appendix For Flight Handbook, NASA, December 13, 1966.
2. Typical SAA 14-Day 2-Man Lunar Exploration Missions, MSFC August 4, 1966.
3. Apollo Applications Program, Lunar Surface Mission Planning, — Bell Telephone Laboratories.
4. Styler, E. F. and Merchant, D. H. "Dynamic Analysis of a Lunar Surface Vehicle, Space Division, the Boeing Company, Seattle, Washington.
5. Carr, J. H. and Romano, S. "A Mobile Lunar Laboratory System," Advances in the Astronautical Sciences, 20, Part II, General Motors Corp., Santa Barbara, California, 3 May 1965.
6. Baldwin, R. B. "Measure of the Moon".
7. LSSM For Apollo Applications Program, Interim Report, BSR 1427, NASA Hqs., October 1966.
8. Ranger VII, Part II, Technical Report No. 32-700, Jet Propulsion Laboratories, Pasadena, California, February 10, 1965.
9. Ranger VIII and IX, Part II, Technical Report No. 32-800, Jet Propulsion Laboratories, Pasadena, California, March 15, 1966.
10. Fort, J. W. "Sample Surface Generation Program," Bell Telephone Laboratories, To be published.
11. Surveyor I, A Preliminary Report, NASA Washington, August 5, 1966.
12. Lunar Photo Study, Eastman Kodak Company, Apparatus and Optical Division, October 1965.
13. Oliver, J. R., and Valentine, R. E. Engineering Lunar Model Obstacles (ELMO), J. F. Kennedy Space Center, NASA, March 8, 1965.
14. Mason, R. L., McCombs, W. M., and Cranbit, D. C. Engineering Lunar Model Survey (ELMS), Launch Operations Center, NASA.

X68-84336

SECTION VI. MAN'S CAPABILITIES

BIO-ENERGETIC CONSIDERATIONS IN LUNAR SURFACE MISSION PLANNING FOR AAP

by E. P. Koslow

The following discussion is the result of a study made at the beginning of the BTL AAP study. It reflects the state of knowledge in mid-1966 rather than the state of knowledge at the time of this report. Because of the inadequacies noted in the following paragraphs, the estimate of locomotion, contained in Volume 1, was made by a conservative interpretation of the simulated data of energy expenditure and a conservative estimate of PLSS capability.

The term "mission", as used in this discussion, refers to surface missions, i.e., a given set of astronaut activities in a given period of time, rather than the overall (launch to recovery) mission.

INTRODUCTION AND SUMMARY

The goal of the Apollo Program is to take man to the Moon and back safely. The Apollo Applications Program (AAP) presumes that this goal has been achieved and concentrates its efforts on having man perform meaningful work. For lunar surface missions, this work is to increase knowledge about the Moon and to advance the state of lunar technology. Two areas of study have evolved which will aid AAP in this endeavor:

1. Bio-energetic studies are being conducted to establish the physical capabilities of a man on the Moon.
2. Daily work excursions on the lunar surface are being planned by geologists and other scientists.

Needless to say, information from both these areas of study is vital to AAP planning; however, to successfully accomplish the single goal that man do work on the Moon, these two areas must be intertwined. That is, lunar mission plans must reflect the results of the latest bio-energetic studies, and studies of man's physical capabilities on the Moon should be oriented by what geologists and other scientists would like him to do there.

The purpose of this paper is to review the state of the art in both lunar bioenergetic studies and lunar surface mission plans to show that the endeavors of each of these areas does not reflect the current knowledge or lack of it in the other area. Suggestions to improve this situation will be made not so much in an attempt to solve this problem but more to promote "thinking with the other area in mind" by those people directly involved in the research studies.

Some conclusions that can be drawn from this study are:

1. Present long-range planning of AAP missions should not depend critically on predicted astronaut work capabilities because of incomplete knowledge of these capabilities.
2. Detailed mission planning should be flexible to account for variations in astronaut and equipment performances.
3. For long-duration missions, training and testing astronauts on the lunar surface early in the mission may be useful to provide data for planning the later phases of the mission.

2. LUNAR WORKING CONDITIONS

Mission plans are being designed in which an astronaut leaves his lunar shelter, travels some distance on the lunar surface either on foot or on a lunar surface roving vehicle, performs some scientific work activities, and then returns to the shelter. Because the Moon's total atmosphere is less than 10^{-11} torr and temperatures vary from -250°F to +250°F, the man on the Moon will be constrained in carrying out these mission plans by the necessity of wearing a spacesuit and carrying a Portable Life Support System (PLSS).

It is expected in planning lunar surface missions that the lunar landing site selected will be representative of large areas of the Moon and well-suited for conducting on foot and on a roving vehicle investigations directed at answering specific lunar questions (Reference 1).* Unmanned lunar landings and orbital flights should provide information to help in landing site selection. In addition, information concerning specific lunar "soil" and hazard conditions will be gleaned from these flight results. Some data in these latter areas of concern has already been accumulated.

The results of Surveyor I indicate that certain characteristics of the lunar surface (where it landed) are much like that of a newly plowed field, i.e. a porous sintered structure with low traction. Lunar Orbiter pictures lead one to feel that some areas will be negotiable on foot, but many others appear too rough. However, even in relatively smooth-looking areas, appearances can be deceiving. Without more knowledge of the slope, texture, bearing strength, and shear strength of the surface, the lunar worker may encounter truly hazardous conditions.

---

*References are listed at the end of this part of the section.

Other hazardous conditions exist which affect mission planning. Cosmic radiation and meteoroid particles pelt the lunar surface intermittently and would treat a surface worker similarly. Visual protection is necessary to cope with light rays directly from the Sun and also reflections of the Sun's rays (Reference 2). And finally, lighting conditions on the Moon are such that contrasts in illumination from reflection off irregular surfaces and from shadows vary greatly, resulting in severe visibility problems, both in acuity and depth perception. (See Section IX of this volume and Reference 3.)

3. EFFECTS OF THE TRIP TO THE MOON

Poor working conditions on the lunar surface are not the only disagreeable factors with which the lunar workman may have to contend. Bio-energetic studies of recent Earth orbital flights in space have indicated that the trip to the Moon may prove physiologically deconditioning to man. In passing through a period of weightlessness during his journey to the Moon, an astronaut will experience many effects which include bone deminearalization, body fluid level shifts, blood content changes, a decrease in the ability to transport oxygen (Reference 4), and general muscle weakening. In addition, basic cellular changes may be involved although no positive evidence of this has yet been found (Reference 5).

It is encouraging to note that the preceding effects are being very closely monitored in current space flights and much will be done to stop the degeneration of the body in a reduced gravity environment by means of a strictly controlled diet, exercise and, possibly, special garments (Reference 5). However, these known effects may not be completely counteracted, and unexpected physiologically damaging events may take place in an AAP flight which were not considered *a priori*. Thus, the astronaut on the lunar surface may not be as physically capable a worker as he had been on Earth because of the effects of his trip. Perhaps his stay on the Moon will allow him to overcome some of these effects. Whether or not this is the case, it is essential that lunar surface mission plans as well as bio-energetic studies consider the effects of the journey as they affect a man's peak physical performance with respect to lunar surface stay-time.

4. BIO-ENERGETIC STUDIES TO DETERMINE PHYSICAL WORK CAPACITY

In order to understand more fully the physical work capacity of a lunar surface worker, some insight into the state of the art in the study of energy expenditure on Earth is essential.

4.1 General Knowledge of Energy Expenditure on Earth

The expenditure of human energy can be monitored by one of the following methods:

1. Directly measuring work output.
2. Directly measuring heat output.
3. Measuring total caloric intake and subtracting the stored amount.
4. Measuring the turnover of fuels in the body.
5. Measuring carbon dioxide production, an index of fuel oxidation.
6. Measuring oxygen consumption.

Method 6 is generally considered to be the best (Reference 6); however, it must be cautioned that these measurements are extremely difficult to perform accurately. Also variations in energy expenditure are considerable from person to person and from time to time in the same person. Body size, training, day-to-day physiological differences within the same person, and changes in operating conditions do account for much of this variation, but even after attempting to account for all these variables, measurements under the most controlled conditions have differed by as much as 15 percent. Furthermore, oxygen consumption is not synomynous with useful work. Part of it is used for fixation energy and friction loss, and some is merely wasted (Reference 7). The efficiency with which external work is produced, which is the ultimate concern of most workers, varies by as much as 20 percent in doing common tasks and 35 percent in cycling and walking on an inclined treadmill (Reference 6). Such uncertainty in Earth-based measurements leads to pessimism concerning the accuracy of predictions of energy expenditure on the Moon and mission planning based strictly on such measurements.

4.2 Energy Expenditure on the Lunar Surface

As mentioned earlier, the lunar surface worker will be wearing a pressurized spacesuit and carrying a PLSS. His spacesuit will most probably be a hard suit of aluminum (Reference 8) weighing 60 to 80 lbs. Mobility restrictions of this spacesuit will impair the astronauts performance. Physical effort is needed to bend and flex this spacesuit, and complex compound movements such as bending and crouching are exceedingly difficult. Furthermore, refinements in the suit are still being made in the helmet, boots, and gloves — areas exceedingly important in the calculation of physical work capacity (Reference 5). The rechargeable PLSS will be worn on the lunar surface as a back-pack, an unbalancing means of carrying a load (Reference 4).

To learn more about man's physical capabilities on the Moon, three interacting approaches are being employed: simulation, current experience in Earth orbital spaceflight EVA, and purely analytical studies.

Simulation in general as it applies to a reduced gravity environment can mean one of two things:

1. Earth conditions are being simulated (on the moon or in space) to aid performance in the reduced gravity environment.
2. The reduced gravity environment is being simulated on Earth so that performance under this condition will be better understood.

To date, simulation of a 1g environment for use on the moon by means of a lower body negative pressure chamber or other devices doesn't seem to be likely for AAP missions, especially in view of the aforementioned difficulty of working in the usual spacesuit. Therefore, only those means of simulating a 1/6g environment on Earth will be discussed.

Theoretically all gravity situations between 1 and 0g can be simulated exactly* using an airplane flying in a near-Keplerian trajectory. Figure IV-1 illustrates the forces acting on a test subject during such a flight. Two problems arising in using this method of simulation are that the flight time for weightlessness and also 1/6g is less than one minute and that slight perturbations may disturb the accuracy of the technique sufficiently to distort the result. This particular means of simulation has been used extensively in studying weightlessness and, in view of recent EVA experience in weightlessness, the usefulness of this kind of simulation as other than a check on other methods is questionable.

Until very recently the most popular means of simulating lunar gravity involved sling supports from an overhead trolley system suspending men over inclined walkways (see Figure VI-2). The suspension system carried 5/6 the weight of the test subjects while they walked, ran, performed vertical and broad jumps, etc. Typical optimistic results from such tests are shown in Figure VI-3 wherein it can be seen that walking on the moon in a pressurized spacesuit will be no more difficult than walking on Earth in an unpressurized spacesuit.

With this type of device, much needed work in developing locomotive gaits efficient in lunar gravity, though possibly not "natural" on Earth, has been undertaken. For example, it has been found that loping rather than walking is a comfortable locomotive gait in simulated lunar gravity. Further exploration into the area of lunar locomotive gaits is desirable; however, such exploration as it applies to mission planning should be tempered by some of the hazardous lunar conditions mentioned earlier. For instance, difficulty with visibility would make loping on the Moon rather dangerous.

The harness-type of simulator has a number of limitations which tend to make it an inaccurate estimator of both energy expenditure and locomotive gaits.

---

*All other simulation techniques discussed will simulate lunar gravity, a body force, by means of a surface force.

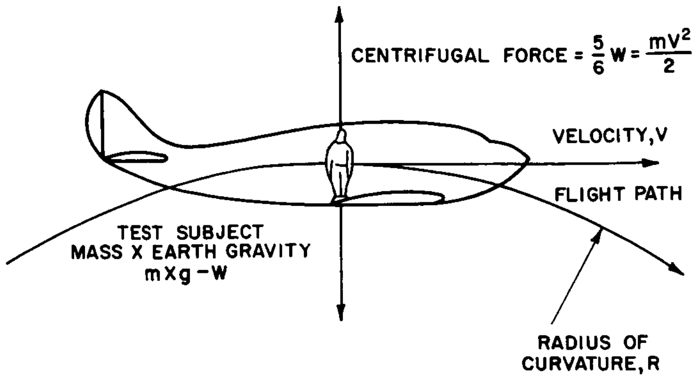
CENTRIFUGAL FORCE = $\frac{5}{6}$W = $\frac{mV^2}{2}$
VELOCITY,V
FLIGHT PATH
TEST SUBJECT
MASS X EARTH GRAVITY
mXg -W
RADIUS OF
CURVATURE, R

Figure VI-1. Forces Acting on a Test Subject during a Flight in Near-Keplerian Trajectory

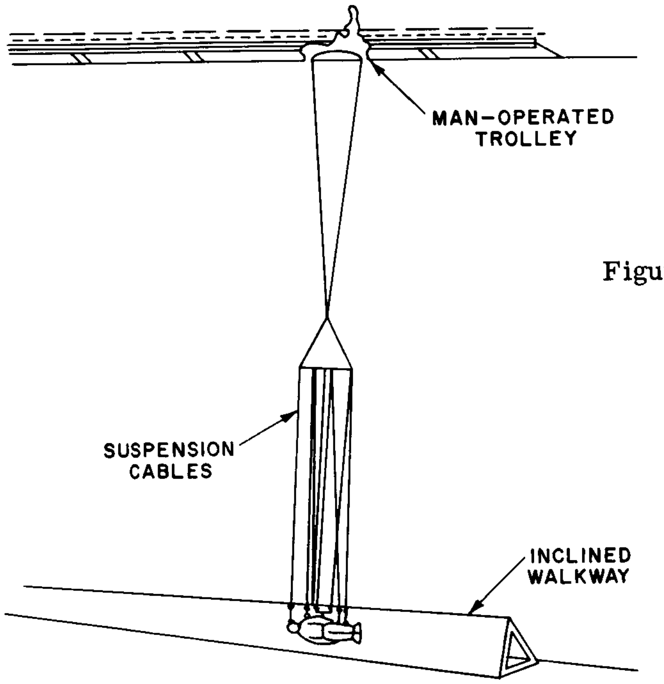
MAN-OPERATED
TROLLEY
SUSPENSION
CABLES
INCLINED
WALKWAY

Figure VI-2. Suspension System Simulating Effect of Lunar Gravity

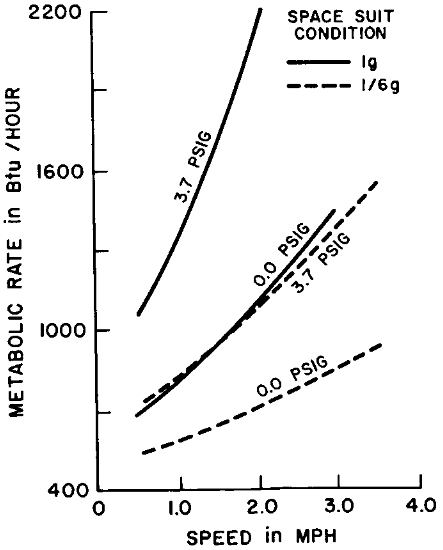

Figure VI-3. Comparisons of Walking under 1g and Simulated 1/6g Conditions in Pressurized and Non-Pressurized Spacesuits

First, it restricts body motions to planar motions in the fore-and-aft direction (Reference 8). Second, the test subject should be suspended at the center of gravity of each limb, etc. and, since each is within his body he cannot be. Furthermore, during locomotion his center of gravity changes. Thus, the harness setup is unbalancing. There are other limitations to the application of this technique. Their effects on mission planning are less clear although thought to be "negligible" in the literature. One such limitation is the fact that the body's internal organs still get the full effects of Earth's gravity.

Another means for simulating a reduced gravity environment which could be adapted for use in studies of lunar gravity effects involves the immersion of a test subject in some liquid of proper density to produce the desired buoyant forces. However, results from this simulation scheme can be misleading for the viscous forces of the liquid that develop as the subject moves about can be excessive. In addition, inherent in buoyancy simulation of reduced gravity is the problem that buoyancy depends upon the center of gravity of the displaced fluid whereas reduced gravity depends upon the center of gravity of the test subject.

The most recent simulator system which may yield a better understanding of lunar locomotion has been developed by Martin Company's Denver Division. (Reference 9) This system involves a servo-driven, 6-degree-of-freedom moving base controlled by analog computers. Test subjects are mounted on a 3-degree-of-freedom gimballed head, supported by the 3-degree-of-freedom translation carriage. A load cell array measures all forces and moments generated by astronaut movements and relays this information to an analog computer which solves the equations of relative motion associated with the test subject and the work area. The solution of these equations activates command voltages which drive the moving base and gimbal system to simulate proper reduced 0g reactions on the test subject.

At present, this simulation method is being used for 0g calculations and is said to have given results more in line with actual EVA experience than have other simulations. That is, it took much more time to perform the same kinds of tasks simulated by other means. There does not appear to be any mathematical limitation to adapting this technique for lunar gravity simulations and the energy expenditure results from a 6-degree-of-freedom simulation should prove more realistic than all lesser degree-of-freedom simulations for the efficiency of work decreases as the number of degrees of freedom increases (Reference 7).

What are the implications on mission planning of the second approach to learning about lunar work capacity — current space flight experience ? Recent EVA maneuvers have proved exhausting to the extent that such maneuvers had to be abruptly curtailed. In Gemini 11, Astronaut Richard Gordon terminated his scheduled EVA tasks because of high-level fatigue and perspiration. It has been estimated that, in the Gemini Program, astronauts expended energy at peak rates in excess of 3000 Btu/hour and average rates in excess of 2000 Btu/hour during the performance of relatively simple tasks (Reference 10). On Earth, an expenditure of 2000 Btu/hour, signifies that "heavy work" is being done and 3000 Btu/hour "unduly heavy work" (Reference 6). Such results do not seem encouraging, especially since they were not anticipated by the previously discussed method of approach to understanding man's physical capabilities on the Moon, namely by simulation of anticipated conditions.

The last means to learning more about man's physical work capacity on the Moon is via analytical studies. Such studies involve analyzing quantitatively the mechanics of locomotion at 1g and extrapolating to 1/6g to obtain changes in the mechanics of motion. In this way percentages of total energy used against gravity in walking and running have been computed (see Table VI-1). Noting such facts as the percentage of total energy used to work against gravity was only 12 at a high walking speed and 18 at a medium walking speed, one may compute an optimal walking speed for use in the reduced gravity environment. Going one step further, it is possible by consideration of the utilization of various muscle groups to calculate efficient lunar walking gaits, subject, of course, to the aforementioned lunar surface condition restrictions.

Table VI-1

ENERGY USED IN WORKING AGAINST GRAVITY

(Reference 7)

Walking Speed	Percentage of Total Energy Used
Low	13
Medium	18
High	12

At this point it should perhaps be re-emphasized that all three approaches to learning more about man's physical capabilities on the lunar surface, namely: simulation of lunar conditions, EVA experience in orbital space flights, and analytical studies of the mechanics of lunar locomotion, are essential to the success of AAP mission planning. Each approach not only contributes some knowledge of energy expenditure estimates, but also serves as a check on the other.

5. LUNAR SURFACE MISSION PLANS

Because of the curiosity of geologists and other scientists (see Table VI-2 for "Questions on the Moon Formulated by the National Academy of Sciences"), the number of tasks that a lunar surface worker in AAP could be asked to perform is quite large. Two types of activities are found in the proposed tasks, traverse activities and shelter site activities. Traverse activities involve geological observations, photography, sample taking, instrument surveys, satellite ESS installation, and active seismic surveys. Shelter site activities include installing a central ESS, drilling a 3m hole for a thermal flux measurement probe, sample examination and preparation, local walking traverses, and local mapping. A sample mission plan including both types of activities published August 4, 1966 by Manned Space Flight Center, based on the present maximum single mission duration time of 3 hours (for PLSS considerations), can be seen in Table VI-3. These particular mission plans are scheduled at specific times, and time allotments for various tasks are calculate to 1/100 of an hour. This exactness is rather surprising in view of the fact that variations in energy expenditure measurements of simple Earth activities were noted earlier to be as high as 15 percent, with variability in efficiency as much as 35 percent.

Some evolution in mission planning reflecting recent EVA difficulties has taken place since the planning shown in Table VI-3. An attempt has been made to eliminate the unrealistic exact-time scheduling of mission planning. Furthermore, time estimates for performing various tasks no longer go beyond the first decimal place and are specified by an upper and lower time limit for the tasks. Table VI-4 illustrates one of the more recent task time estimates and Figure VI-4 is a sample mission plan reflecting this new type of variable schedule thinking. However, in view of energy expenditure uncertainty, mission planning is still not as realistic as it should be. It is hoped that criticism will initiate further development.

6. CRITICISMS OF THE BIO-ENERGETIC/MISSION PLAN INTERFACE

On the basis of lunar mission plans and bio-energetic studies, there appears to be a need for better communication between these two areas of study.

It has been shown that the peak working ability of an astronaut because he has just passed through a state of weightlessness may not occur in the early part of his lunar stay. Other factors may very well cause variations in his ability while on the lunar surface. Yet all mission plans, except the very first mission, appear to be of nearly equal physical difficulty. Furthermore, the adjustment to working under actual lunar conditions (for example, learning to drive the roving vehicle) which may involve considerable time has not been taken into account by mission

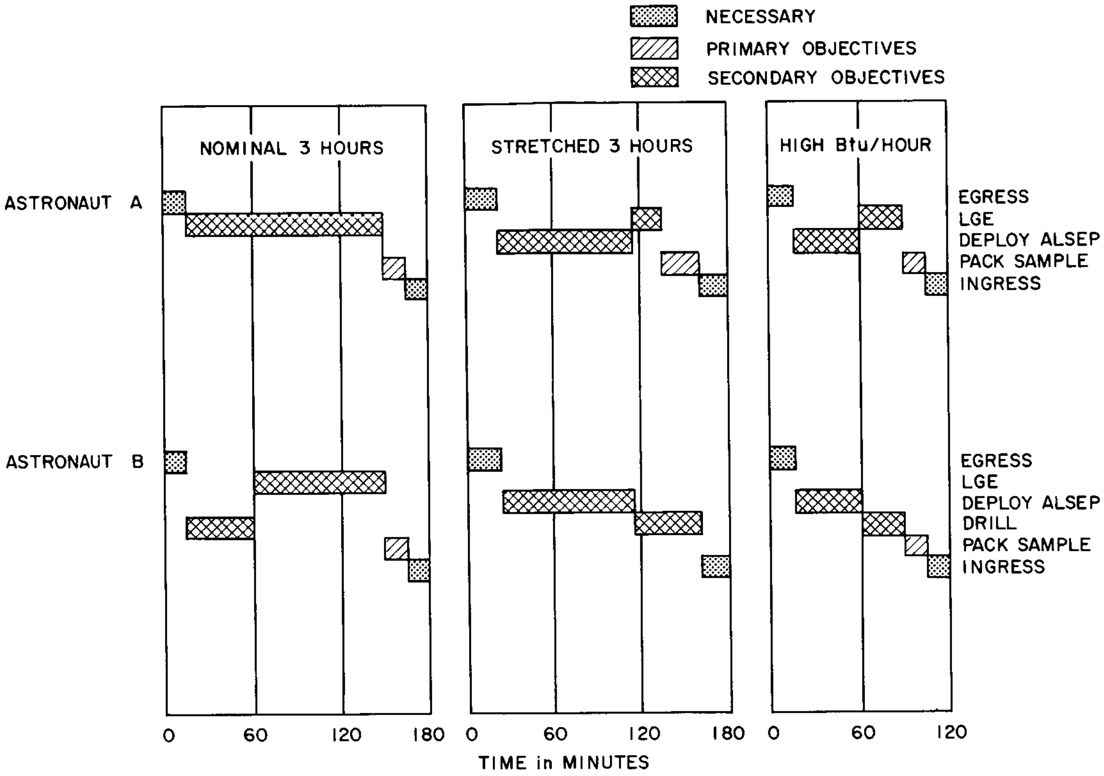

Figure VI-4. Sample Mission Plan

Table VI-2

QUESTIONS ON THE MOON FORMULATED BY THE NATIONAL ACADEMY OF SCIENCES

(Reference 1)

1. Is the internal structure of the Moon radially symmetrical like the Earth, and if so, is it differentiated ? Specifically, does it have a core and does it have a crust ?

2. (a) What is the geometric shape of the Moon ? How does the shape depart from fluid equilibrium ? (b) Is there a fundamental difference in morphology and history between the sub-Earth and averted faces on the Moon ?

3. What is the present internal energy regime of the Moon ? Specifically, (a) what is the present heat flow at the lunar surface and (b) what are the sources of this heat ? (c) Is the Moon seismically active, and (d) is there active volcanism ? (e) Does the Moon have an internally produced magnetic field ?

4. What is the average composition of the rocks at the surface of the Moon and how does the composition vary from place to place ? Are volcanic rocks present on the surface of the Moon ?

5. What the are principle processes responsible for the present relief of the lunar surface ?

6. What is the present tectonic pattern on the Moon and distribution of tectonic activity ?

7. What are the dominant processes of erosion, transport, and deposition of material on the lunar surface ?

8. What volatile substances are present on or near the surface of the Moon or in a transitory lunar atmosphere ?

9. Is there evidence for organic or proto-organic materials on or near the lunar surface ? Are living organisms present beneath the surface ?

10. What is the age of the Moon ? What is the range of age of the stratigraphic units on the lunar surface and what is the age of the oldest exposed material ? Is a primordial surface exposed ?

11. What is the history of dynamical interaction between the Earth and the Moon ?

12. (a) What is the thermal history of the Moon ? (b) What has been the distribution of tectonic and possible volcanic activity in time ?

13. What has been the flux of solid objects striking the lunar surface in the past and how has it varied with time ?

14. What has been the flux of cosmic radiation and high-energy solar radiation over the history of the Moon ?

15. What past magnetic fields may be recorded in the rocks at the Moon's surface ?

Table VI-3

MOLTKE B TIME BUDGET
NO. 1 LOCAL DRILLING AND NO. 1 ACTIVE SEISMIC TRAVERSES

(Reference 11)

Tenth Day; No. 1 Active Seismic Traverse

Astronaut B	Incremental Time (hours)	Cumulative Time (hours)
1. Drive 8 km	1.07	1.07
2. Set up drill	0.25	1.32
3. Drill 3m hole	2.50	3.82
4. Set up gravimeter during drilling operations; take reading upon completion.	—	3.82
5. Recover core.	0.25	4.07
6. Install explosive and detonator.	0.25	4.32
7. Drive back 3.5 km.	0.53	4.85
8. Set up single geophone recorder.	0.08	4.93
9. Continue back 4.5 km.	0.53	5.46
10. Gravimeter readings (6 at 1 km intervals on return leg).	0.50	5.96
Astronaut A		
1. Detonate remote charge (No. 1 long seismic experiment).	0.08	0.08
2. Drive 1/2 km to 1.5m hole and turn on detonator radio.	0.07	0.15
3. Return to shelter.	0.07	0.22
4. Detonate near charge (No. 1 short seismic experiment).	0.08	0.30
5. Pick up 12 geophone units and cable	0.50	0.80

Table VI-4

CREW TASK TIME ESTIMATES
(Reference 13)

Tasks	Man-Hours
Egress-Ingress	0.5 — 1 per excursion
Acclimitization	0.5
S-band Antenna Erection	0.25 — 0.5
Engineering Tasks	0.5 — 1
Reconnaissance TV and Photographs	0.5 — 1
Grab Sampling	0.25
ALSEP Deployment	1.5 — 3
Initial Geologic Exploration	2
Drill Operation	0.25 — 1
Geologic Exploration	>2
Miscellaneous (includes sample packing)	0.5 — 1 per excursion
Mission Totals	
Single-Excursion	9 — 14
Two-Excursion	10 — 16
Three-Excursion	11 — 18

planners. Should this adjustment indeed prove time-consuming, alternating driving missions between the two astronauts may not be practical. Why spend time training two astronauts to drive?

The difficulty of working in the spacesuit has been discussed earlier, especially the difficulty in bending and crouching. Coupling this problem with the lack of knowledge about lunar "soil" conditions leads to concern about an astronaut being able to get up after falling. Should this turn out to be extremely difficult and costly energy-wise, it would be better to find out near the LM and in sight of the other astronaut. In fact, the procedure would be the better way to learn about the astronaut's ability to perform a number of tasks. Perhaps practice sessions early in the lunar stay would be in order. Whether or not a practice session is planned, similar tasks should be classified and, at any given site, alternate mission plans should be designed which exclude or minimize the performance of activities that may prove costly in terms of energy expenditure. That is, mission plans should appear in flowchart form wherein different paths represent the degree of difficulty of particular activities. For instance, one mission path might be used if it were difficult to climb but easy to dig; another might be better in the situation where digging is difficult, but climbing is relatively easy. Also included in a flowchart mission plan should be paths for contingencies arising from the unavailability of any hardware used in carrying out an objective, e.g. the surface roving vehicle being disabled.

Thus far, mission plans have been criticized for bio-energetic considerations. It is also possible to criticize the work of lunar bio-energetists as overlooking the desires of geologists and other scientists. Perhaps the most costly oversight is the fact that few simulations to gain insight into lunar energy expenditure, if any, involve decision-making. Geologists expect the lunar workman to select samples from the lunar surface, to seek out different lunar geological features, to make various types of measurements. In brief, the astronaut will be asked to do a variety of tasks which will involve his subjective judgment. Such judgment takes time. Yet current lunar simulations do not include decision-making tasks, only completely specified ones.

Other decision-making problems which are often not included in the simulations are those involved in locomotion. Not enough lunar simulations include lunar surface and visibility conditions. Energy expenditures calculated from treadmill conditions rather than changing surface conditions ignore time used in judging and, thus, will prove too conservative.

7. CONCLUSIONS

Lunar surface mission planning is not, in any sense, an easy job. Very little is known about actual lunar surface conditions, and much that is known is not encouraging. Many hazardous conditions may exist, including poor visibility. Furthermore, there is so much variability involved in estimating human energy expenditure on Earth that current predictions of lunar working capacity are, at best, first approximations.

It is hoped that the state of knowledge will be improved by Apollo and pre-Apollo flights as well as by better simulations of lunar conditions on Earth. However, since overall AAP planning is presently concerned with lunar mission planning as it affects other AAP considerations, at least preliminary surface mission planning must be done now. Such planning, though it be preliminary, should not proceed in spite of the lack of knowledge that exists in the area of work capacity, rather it should proceed taking into account this lack of knowledge by constructing mission plans with built-in variability to encompass this lack.

REFERENCES

1. "Space Research, Directions for the Future, Part One, Planetary and Lunar Exploration," Report of a Study by the Space Science Board, National Academy of Sciences, Woods Hale, Massachusetts, December 1965.
2. Kincaide, W. C. "Space Suit for the Moon", Mechanical Engineering, 49-53, November 1965.
3. Hamza, V. and Rodin, H. W. "Lighting and Approach Angle Considerations for Manned Lunar Landings", Bellcomm, Inc., TM-65-1012-13, December 7, 1965.
4. Kontaratos, A. N. "Astronaut Performance During the Apollo Lunar Era", Bellcomm, Inc., TM-66-1011-3, July 27, 1966.
5. Aviation Week and Space Technology, pp. 54-129, August 15, 1966.
6. Webb, P., M.D. ed., Bioastronautics Data Book, NASA SP-3006, Scientific and Technical Information Division, Washington, D. C., 1964.
7. Roth, E. M., M.D. Bio-Energetics of Space Suits for Lunar Exploration, Scientific and Technical Division, NASA, Washington, D. C., 1966.
8. Spady, A. A., Jr. and Kraskow, W. D. Exploratory Study of Man's Self-Locomotion Capabilities with a Space Suit in Lunar Gravity", Langley Research Center, Langley Station, Hampton, Va., NASA TN D-2641, 1966.
9. Technology Week, pp. 37-38, October 10, 1966.
10. Discussion with A. N. Kontaratos, Bellcomm, Inc., Washington, D. C., October, 1966.
11. "Typical SAA 14-Day 2-Man Lunar Exploration Missions" Manned Space Flight Center, Houston, Texas, August 4, 1966.
12. Society of Automotive Engineers Journal, 71, p. 48.
13. Hinners, N. W. "Lunar Surface Stay Time for AS-504A-Case 340", Bellcomm, Inc., August 9, 1966.

SECTION VI. MAN'S CAPABILITIES

EFFECTS OF VISIBILITY AND TOPOGRAPHY ON LUNAR WALKING

by J. W. Fort

1. INTRODUCTION

In the planning of Apollo Applications Program (AAP) missions, data on the effects of the lunar environment are desirable if planning is to be realistic. Much of the data will be obtained in the Apollo program, but since preliminary planning for AAP must be done in advance of the first Apollo flights, the effects must be estimated.

One area in which data is lacking is man's capability to walk on the lunar surface. This section covers a study on walking as affected by visibility limitations and topographical hazards. There are, of course, other important effects such as those caused by spacesuit constraints and energy consumption rate in the 1/6g environment, but these are beyond the scope of this study.

2. SUMMARY AND RECOMMENDATIONS FOR MISSION PLANNING

In traveling between two points on the lunar surface, the astronaut must pick his way around craters and move in directions of favorable visibility. Since a slight misstep could be serious, it is likely he will avoid rocks and craters of dimensions down to 0.5 meter. The increased distance traversed over the straight-line distance between the two points was evaluated for various sun angles and for crater hazard densities typical of maria, moderately rough surfaces (such as the interior of Alphonsus), and the rough surface of the continents.

For smooth and moderately rough surfaces, it is shown that the greatest increase in path length for walking occurs when the sun is at or near 45 degrees of elevation and zero degrees of azimuth, i.e., the sun at the astronaut's back. Azimuth angles >35 degrees give good results regardless of elevation angle whereas elevation angles >60 degrees or <25 degrees are generally good regardless of azimuth. Large variations in path length as a function of hazard densities and sun angles require that these factors be taken into account in estimating astronaut walking capabilities.

For the rough surfaces (e.g. the continents), simulated traverses between two given points are often found to be impossible. Penetration into these areas, without aiming for a given point, appears possible provided adequate time is allowed and the path is marked so the astronaut can be sure of finding his way out.

The operating radius of the Local Scientific Survey Module (LSSM) is limited by the astronaut's walk-back range in the event of LSSM failure. A comparison of walking and LSSM traverse data in Section V shows that when the astronaut must walk back, the following rules tend to minimize his return path length:

1. Follow the LSSM track if the visibility was good going out on the LSSM.
2. Pick his own way back if the visibility was poor going out on the LSSM. This choice assumes that a means of direction-finding is provided to the astronaut.

If rule 1 is followed, the astronaut will have a return path which was picked when the visibility was good. When rule 2 is followed, the astronaut can pick a good path because his visibility would be good.

The time available for walk-back is determined by the amount of life support the astronaut can carry. Then, path length, walk-back velocity, and PLSS operating time limit determine the maximum LSSM operating radius.

3. SURFACE MAPS

Primary aids used in the study were typical lunar surface maps which were generated by computer. The hazard densities represented by these maps were determined from Ranger and Earth-based photographs (Reference 1)*. According to these data, the hazard distribution for lunar surfaces are described reasonably well by

$$N = 10^A D^B$$

where

N is the number of hazards of diameter greater than D.

A is a constant which depends on the size area for which N is defined and the lunar locality considered.

B is a constant which depends on the lunar locality considered.

For an area of $10^6 m^2$, a reasonable representation of the floor of Alphonsus is obtained with $A = 4.9$ and $B = -2$; on the maria, $A = 4.9$ and $B = -2$; and on the continents, $A = 5.1$ and $B = -2$. In generating the models, the computer employed a uniform random number generator to locate each hazard and then plotted it as a circle (Reference 2). Examples of maps for the three densities appear as Figures VI-5a, -5b, and -5c.

---

*References are listed at the end of this part of the section.

4. VISIBILITY TEMPLATE

Another tool used in the study was a set of visibility templates made from computer-generated visibility charts (Reference 3). These are based on a photometric function developed from studies in lunar visibility (Section IX of this volume). An astronaut (considered to have an eye level of 5 feet) will be confronted with varying degrees of contrast as he views objects at different points on the lunar surface. Figure VI-6 is an example of a chart showing good, fair, and poor areas of contrast. For a given sun elevation angle one chart can represent all sun azimuth angles. The viewer is represented as being in the center of the plot and the sun shining in the direction from the bottom towards the top of the chart. A template was made from a chart by cutting away that area in which contrast was good or fair, leaving the poor area. Though sufficient for the study, this was a simplification of the true situation of continuous gradation in contrast. Figure VI-7 shows the chart of Figure VI-6 in template form.

5. DESIGN OF THE EXPERIMENT

An experiment to simulate the path a walking astronaut would follow on the lunar surface was performed using previously described surface maps and visibility templates. The first step was to place a transparent plastic overlay on a map followed by a template oriented to give the desired sun azimuth angle. Walking between chosen end points was then simulated by picking the best apparent route through the hazards with only the limited visibility allowed by the template. This route was marked on the overlay with a grease pencil and then measured with an opisometer.

The entire process was then repeated changing either the elevation angle of the sun, azimuth angle of the sun, or the hazard density of the surface. A map with the overlay and the marked traverse is depicted in Figure VI-8.

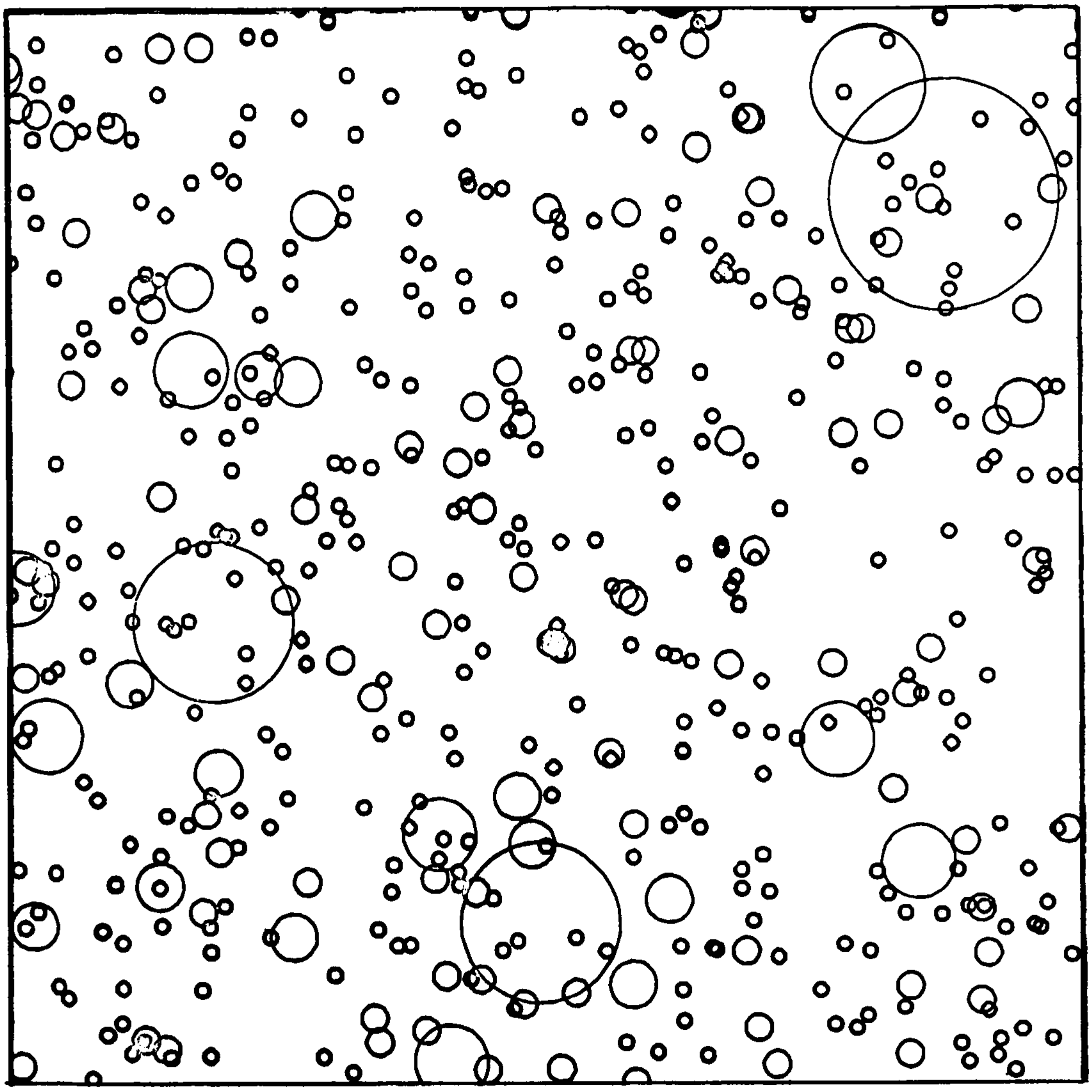

Figure VI-5a. Maria Crater Map

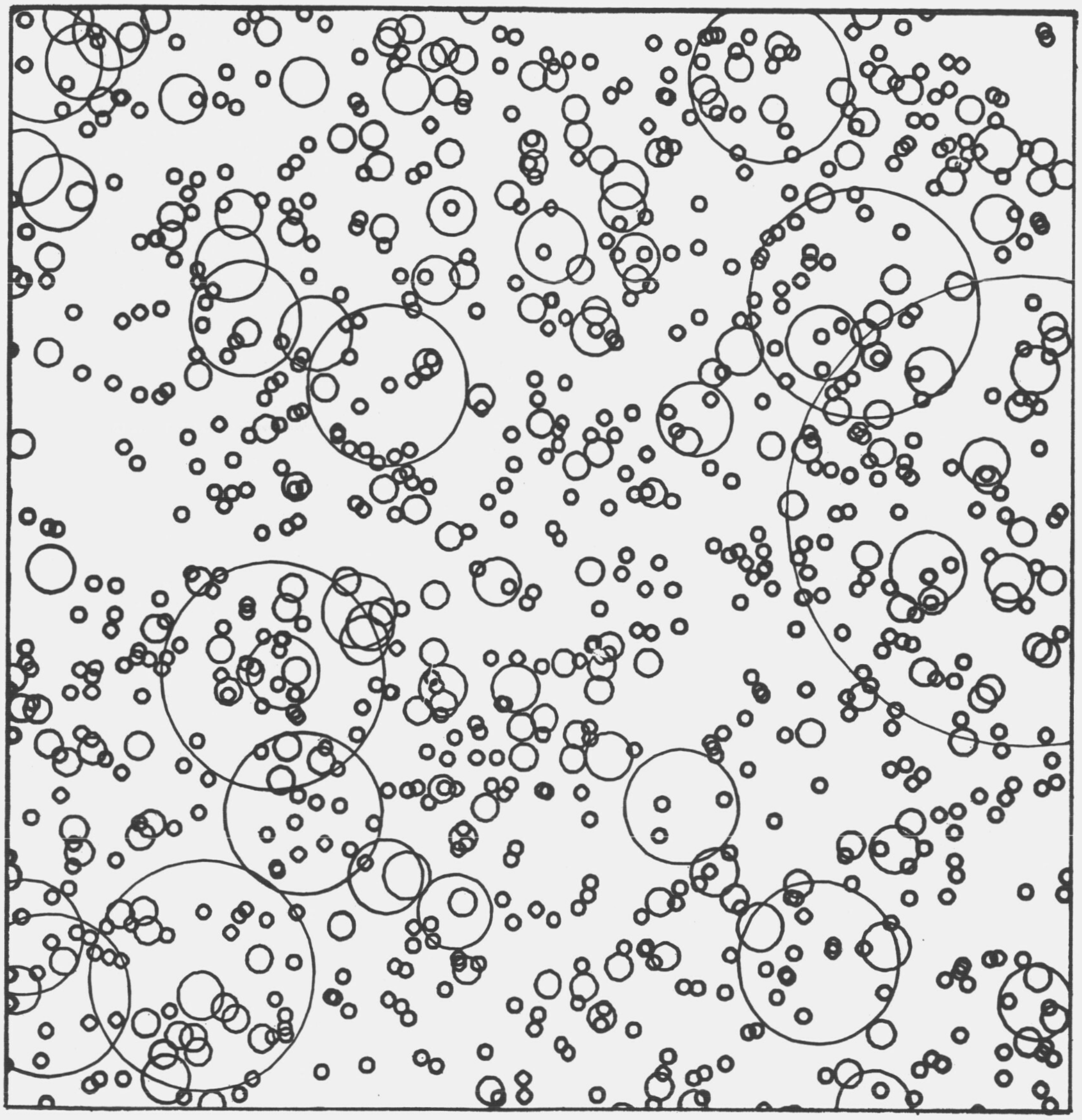

Figure VI-5b. Moderately Rough Crater Map

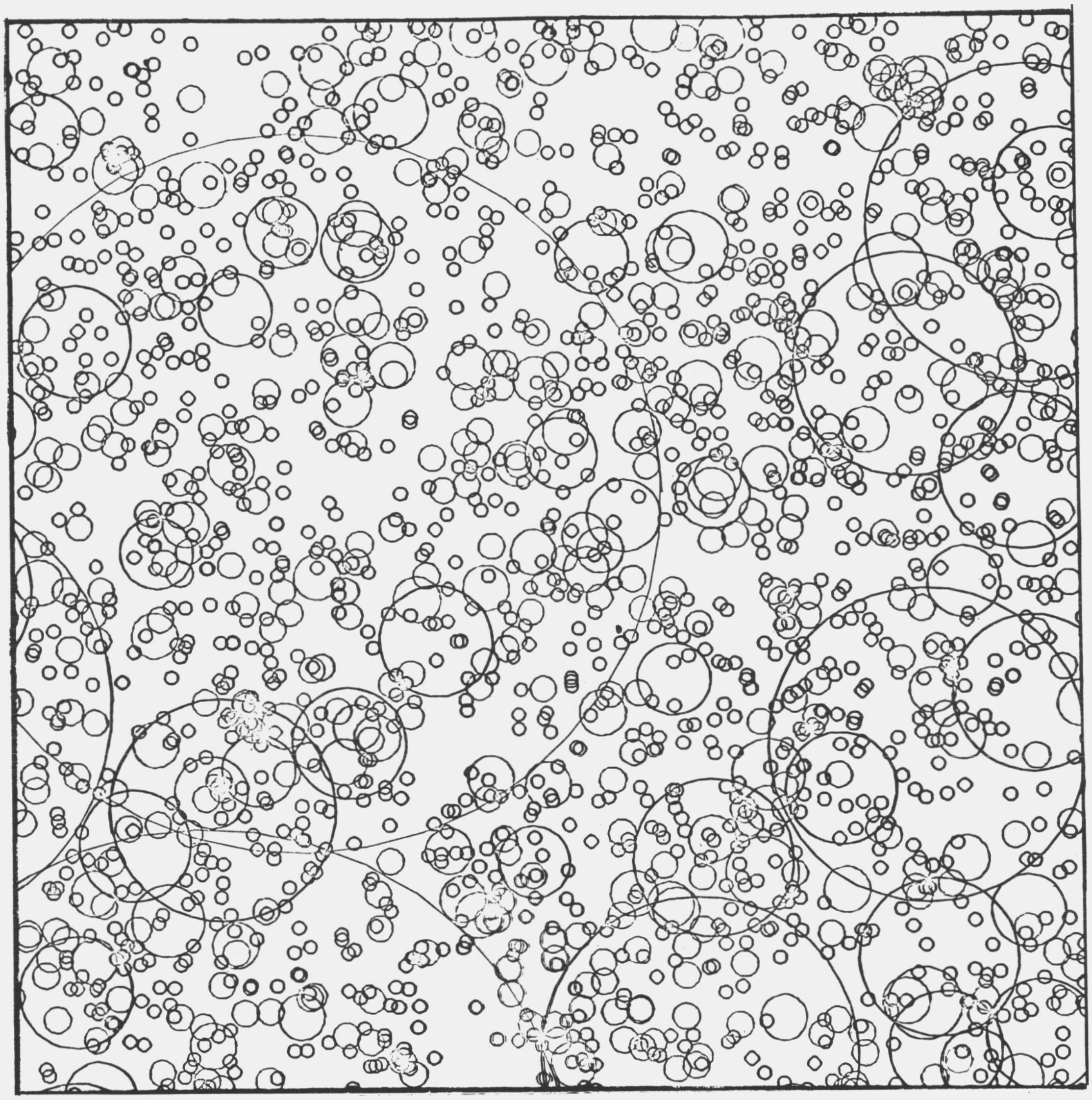

Figure VI-5c. Rough Crater Map

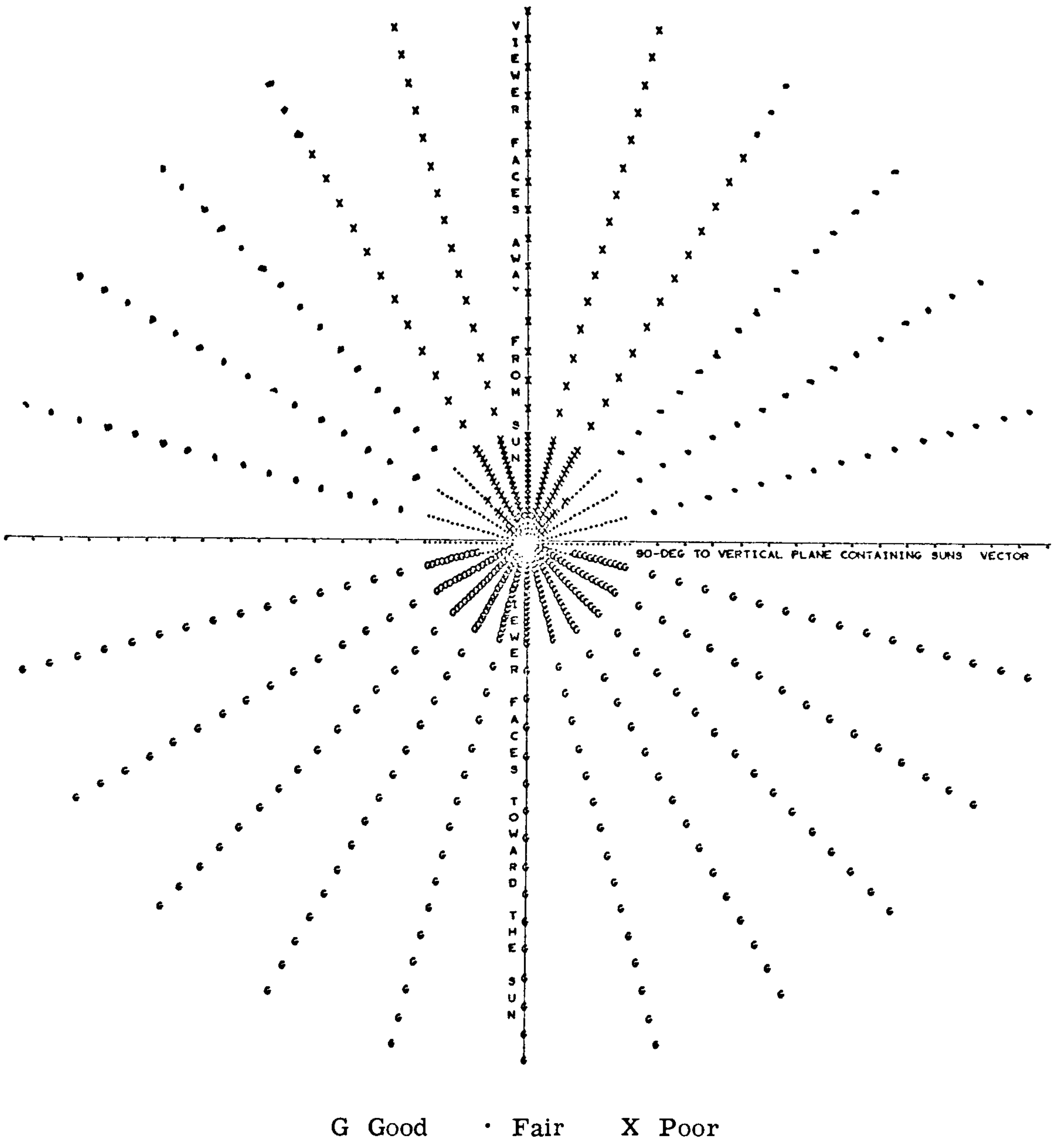

Figure VI-6. Chart of Good, Fair, and Poor Areas of Contrast for 45-Degree Sun Elevation Angle Observer's Height, 5 Feet

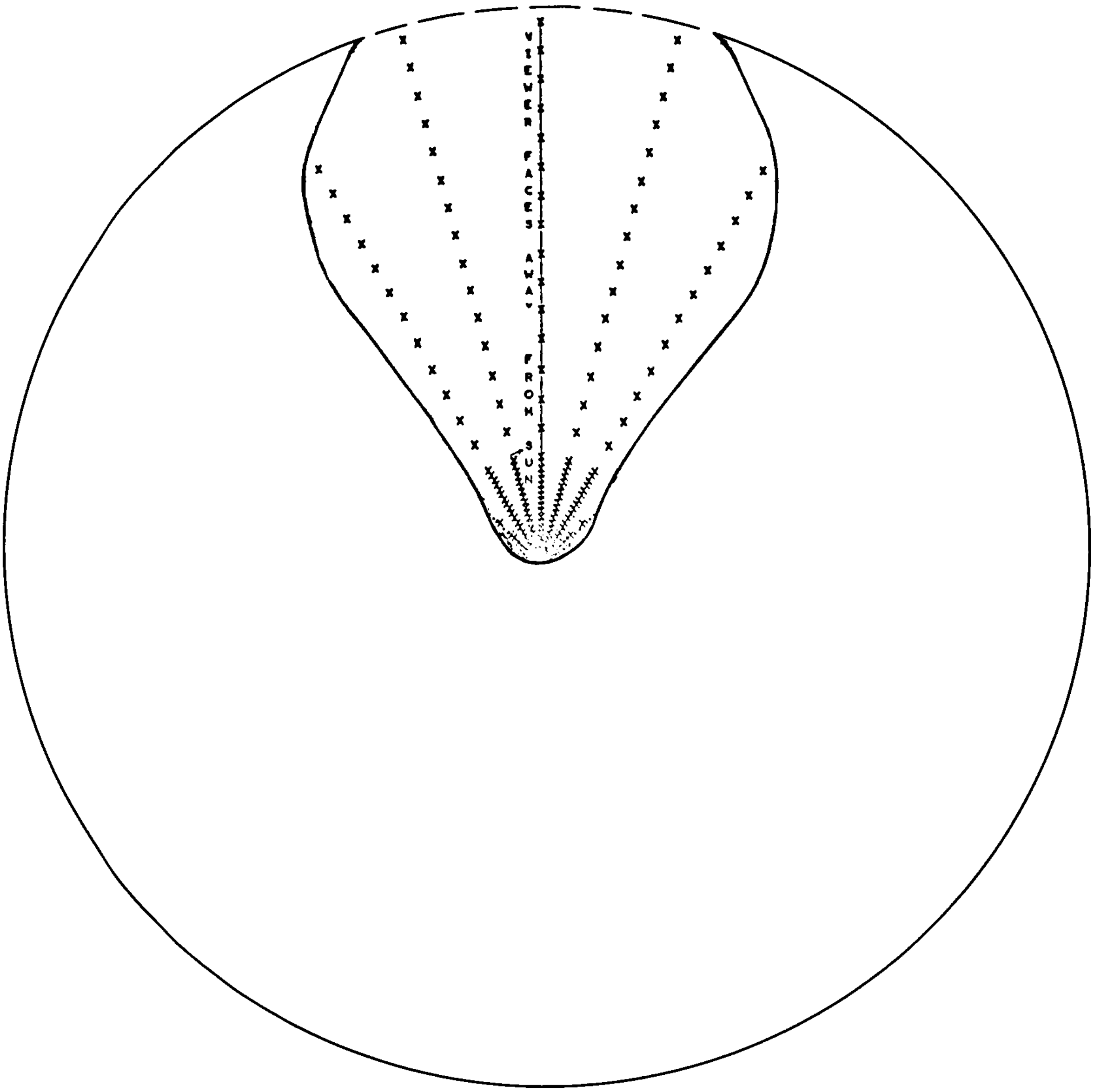
VIEWER FACES AWAY FROM SUN

Figure VI-7. Visibility Template for 45-Degree Sun Elevation Angle Observer's Height, 5 Feet

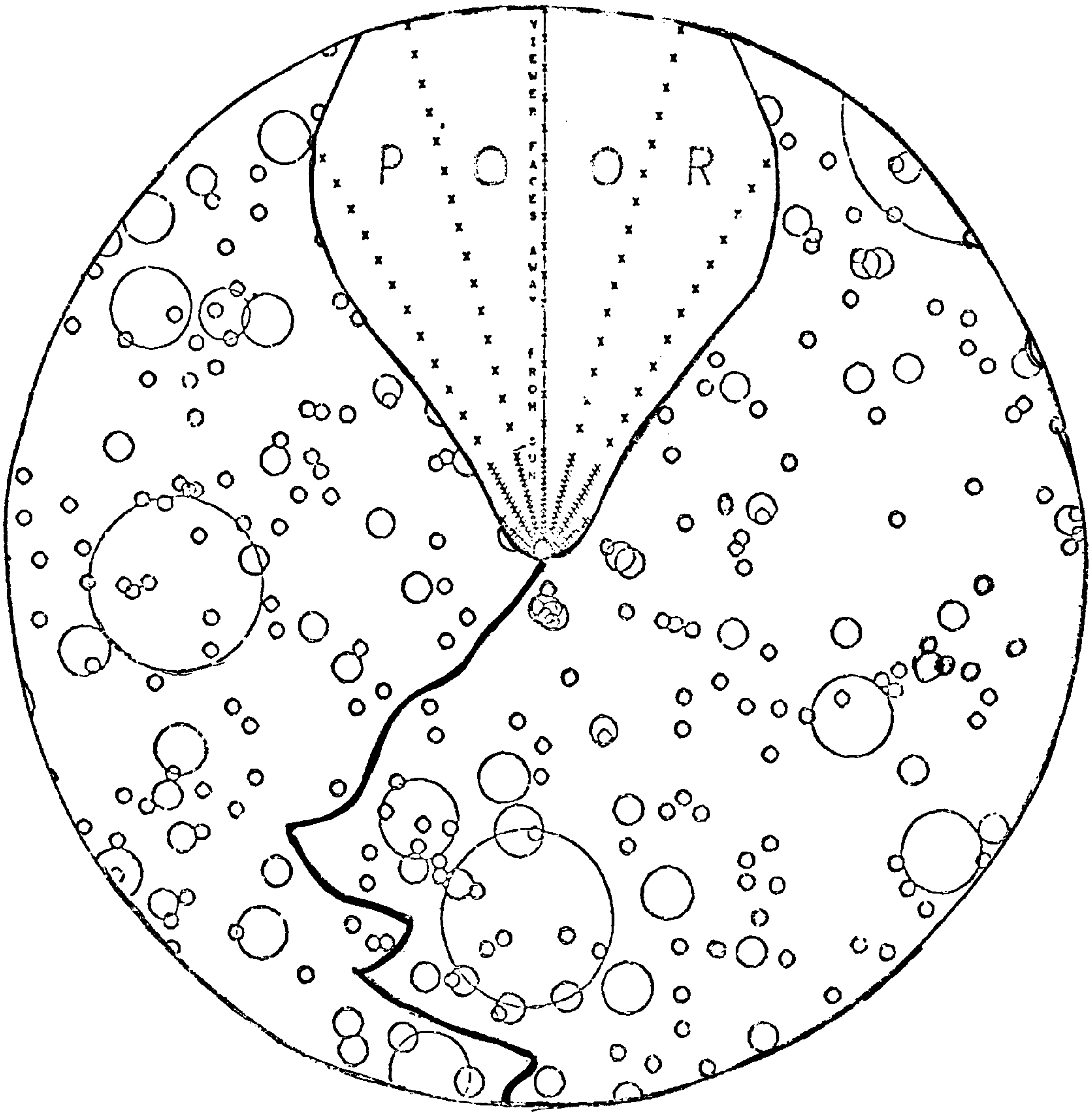
P O O R
VIEWER FACES AWAY FROM SUN

Figure VI-8. Simulated Lunar Surface with Marked Traverse
for 45-Degree Sun Elevation Angle
Observer's Height, 5 Feet

6. ASSUMPTIONS

Given here are certain assumptions of which anyone, making use of the results of this study, should be aware. For the most part, however, it is felt that the results, if used for system planning, are not highly dependent on these assumptions. They are:

1. Contrast, as defined in Section IX in this volume, is the major factor affecting visibility, and all other factors are negligible or can easily be reduced to a negligible level. For example, glare can be sufficiently reduced by shading the eyes.
2. A 10-degree tilt of the surface toward the observer is representative for detecting the sides of rocks and craters.
3. Effects of hazard density and visibility conditions on walking are independent of other effects and can be studied separately.
4. A hazard for a walking astronaut is defined as any crater having diameter >0.5 meter. This selection is based on the somewhat-intuitive reasoning that an unexpected stepdown of 5 inches or more is serious for an astronaut walking in a restrictive spacesuit that might preclude, or make difficult, his seeing exactly where he places his feet.
5. Rocks are considered a part of the crater distribution. Since they number so few, no consequential effect on the results will occur.

7. RESULTS

7.1 Effect of Visibility

Results, measured as a percentage increase in total walking distance over the straight-line distance to an objective, are plotted in Figure VI-9 as a function of azimuth angle with elevation as a parameter. As indicated by the plot, the worst effect occurs at a sun elevation angle of 45 degrees and an azimuth angle of 0 degrees, i.e. the sun directly at the astronaut's back. Azimuth angles >35 degrees in magnitude gave fairly good results regardless of elevation angle whereas, generally, an elevation angle >60 degrees or < 25 degrees did not present a great problem regardless of azimuth.

7.2 Effect of Hazards

Comparing Figure VI-9 curves, derived from models which are representative of Alphonsus and the Maria, one can see that the increase difference between the two surfaces ranges between 10 and 20 percent. Because the hazards were so dense for the continents, it was impossible in most cases to walk from one randomly

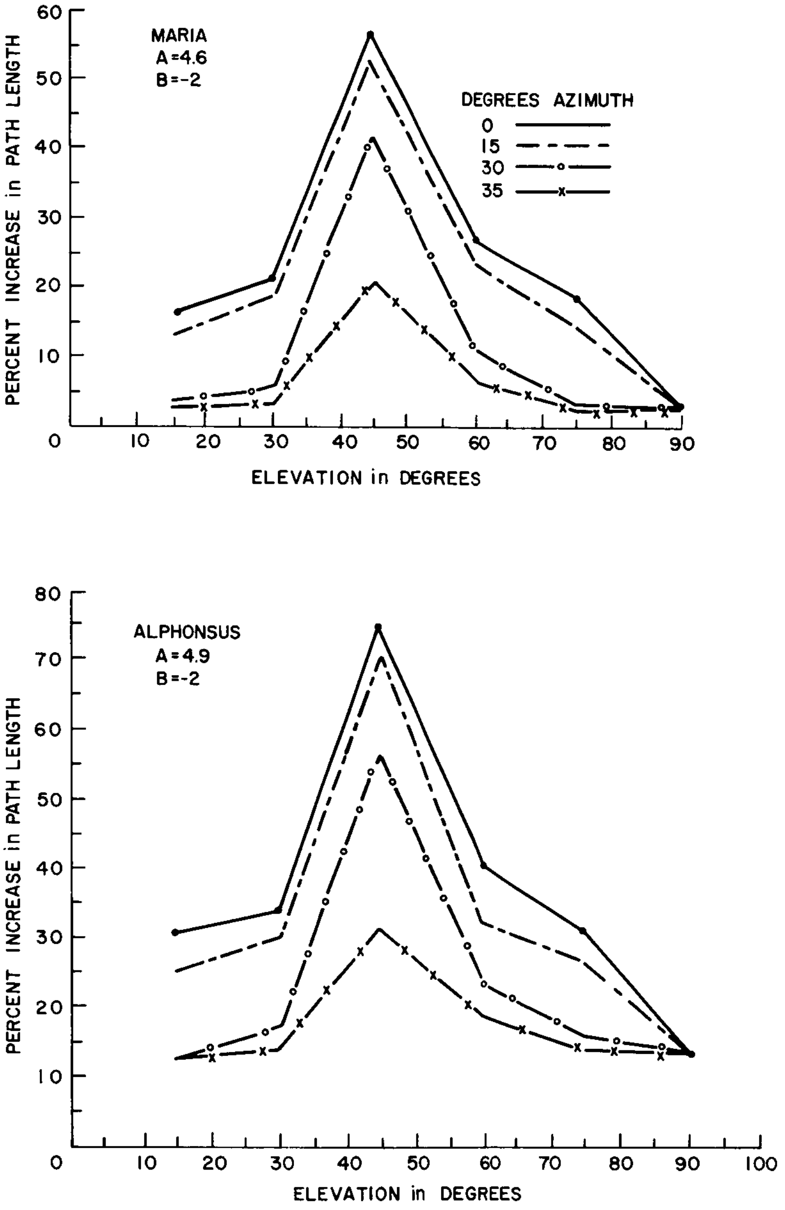

$N = 10^A D^B$

N = NO. OF HAZARDS WITH DIAMETER > D

A = CONSTANT DEPENDENT ON AREA AND LOCALITY CONSIDERED

B = CONSTANT DEPENDENT ON LOCALITY CONSIDERED

Figure VI-9. Effect of Surface Hazards and Visibility on Path Length

chosen point to another. It seems likely, for a surface with a hazard density as great or greater than this, that it would be futile to attempt any planned surface traverse. But on the assumption that an LM landing near such an area, could be accomplished, random penetration seems possible provided a return trail is marked and adequate time is allowed for the return trip.

REFERENCES

1. Ranger VIII and IX, Part II, Technical Report No. 32-800, Jet Propulsion Laboratories, Pasadena, California, March 15, 1966.
2. Fort, J. W. "Computer Program for Generating Typical Maps of the Lunar Surface," MF7-4165-2, Bell Telephone Laboratories, December 5, 1967.
3. Meyer, W. C. "Program for Computing Lunar Surface Contrast," MF7-4165-3, Bell Telephone Laboratories, December 5, 1967.

X68-84337

SECTION VII. METEOROID HAZARD

by A. A. Lundstrom

The Apollo Applications Program (AAP) includes missions for lunar surface explorations of up to 12 days. This section concerns the meteoroid shielding for the Lunar Module (LM) for these long stay-times and the effect on payload return from the Moon.

The 12-day stay may be accomplished by landing two LMs at the same site. One vehicle, the 1-way LM, has descent capability only, lands unmanned, and primarily carries payload to the Moon in place of the astronauts, the ascent engine, and its propellant. The other vehicle, the 2-way LM, carries two astronauts to and from the Moon and returns payload from the Moon. Provision can be made for the astronauts to be housed on the lunar surface in either LM. The meteoroid shielding required for each of these alternatives is evaluated. It is shown that a significant gain in payload from the Moon is available if the 1-way LM is used for astronaut housing.

A 4-day lunar surface stay is possible if only one 2-way LM is landed at the exploration site. The effect of meteoroid shielding on return payload from the Moon is evaluated for this case also.

1. CHARACTERISTICS OF METEOROIDS

Meteoroids are relatively small solid objects in interplanetary space which are distributed in the size range of 10^{-4} cm to a few meters in diameter. They are considerably larger than an atom or molecule and considerably smaller than the nucleus of a comet (Reference 1).* When a meteoroid enters the earth's atmosphere, it produces the phenomena of a meteor. A meteorite is a meteor that has reached the surface of the earth without being completely vaporized.

The heaviest particles are iron and stone which range in mass from 10^2 gms to greater than 10^{10} gms. It is believed they are derived from the asteroidal belt. These occur so infrequently that they are not expected to be a significant hazard during the AAP missions.

---

*References are listed at the end of this section.

The particles between 10^{-12} gms and 10^{2} gms are of unknown material but are believed to be derived from comets and have been identified as cometary meteoroids. They have sufficient mass and abundance to be a hazard to the AAP space vehicles and crew.

The meteoroids with masses of 10^{-12} gms and less have been described as interplanetary dust or micrometeoroids. Although they have maximum abundance, their mass is so small that they constitute no significant hazard to the spaceship and crew.

Cometary meteoroids travel in orbits about the sun which are usually within ±30 degrees of the plane of the ecliptic. They are divided between sporadic, stream, and swarm occurrences.

Sporadic occurrences are a background of activity maintained by a large number of minor streams as well as by single particles which as a result of planetary perturbations are pursuing isolated paths in space (Reference 2). Sporadic meteoroids move in interplanetary orbits and are not from interstellar space as was commonly believed at one time. The total number of sporadic meteoroids that enter the earth's atmosphere during a year exceed the total of those from streams and swarms.

Sporadic activity is higher after midnight than before and is higher during the second part of the year than the first. They reach a broad maximum during June, July, and August when the rate may be as much as a factor of 2 greater than the average. The least prolific months are February, March, and April when the rate may be depressed by a factor of two (Reference 1).

The major meteoroid streams (identified here as streams) bring into the atmosphere over the year a mass that is 1/4 to 1/3 of that brought in by sporadics. In this case, the meteoroids are more or less uniformly distributed over their orbits as continuous streams which intersect the earth's orbit at predicted times during the year. Streams are manifest as meteor showers which are observed by radar and at night by optics. These are observed to have rates of particle appearances which are 1.5 to 7 times the average for sporadics. Each stream is characterized by a duration that is somewhere between 0.5 to 45 days. There are at least 25 predictable showers from major streams which are scattered over all months of the year with the exception of February and September (Reference 3). Figure VII-1 includes plots that show the boundaries of the meteor rates and major shower occurrences from these streams. From meteor to meteor within a shower, the velocity is constant. However, from shower to shower there is a wide range in velocities (10 to 70 km/sec).

Some cometary meteoroids are localized as swarms within their orbits to give a density per hour as great as 1000 times the average sporadic flux and with

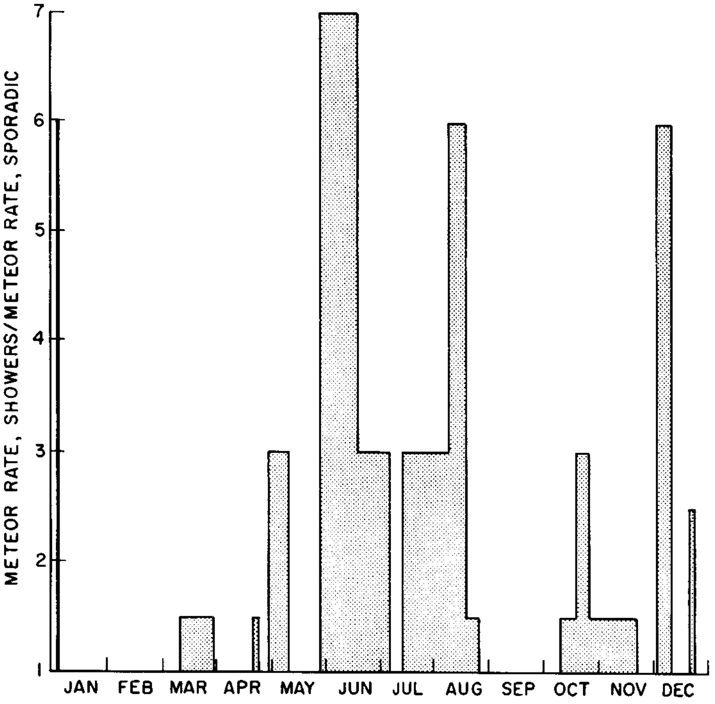

Figure VII-1. Boundaries of Meteor Rates and Duration of Major Shower Occurrences

durations of 1 to 5 hours (Reference 3). In this case, depending on the relation of the period of the earth's orbit and the period of the cometary meteoroid's orbit, it is usual to have many years between appearances. The entry of a meteoroid swarm into the earth's atmosphere is manifest as a meteor storm. These storms occur three or four times a century, and can never be predicted with certainty. Astronomers have been caught almost unaware by several storms during the last century. As of 1964, the Giacobinids in 1946 is the only storm to have been observed by modern methods (Reference 1).

The impact of meteoroids (primaries) on the lunar surface gives rise to ejecta (secondaries) which is an added hazard to the astronaut and his equipment. Based on laboratory measurements and analysis, Gault-Shoemaker and Moore (Reference 4) have constructed a model of secondary flux. The work indicates that secondaries are 10^3 to 10^5 times as numerous as that of primaries and have an average velocity that is 10^{-2} times that of the primaries.

2. MODELS FOR SHIELDING DESIGN

2.1 Limitations

There have been and will continue to be many studies on the phenomena and on the hazard of meteoroids. Unfortunately, unknowns beset all of this work. There does not yet exist a thoroughly verified relationship for determining particle mass and density from photo recordings of luminescence and velocity of meteor appearances. Cometary meteoroids are usually entirely consumed on entry into the Earth's atmosphere; therefore, there are no remnants to analyze. In the same way, there does not exist a verified relation to determine particle mass and density from radar observations of ionization intensity and velocity.

Present direct satellite measurements are statistically significant only for cumulative flux levels three orders of magnitude higher than are of interest to AAP. The detectors used do not have a fully satisfactory means for determining the mass and velocity levels. Meteoroid velocities are distributed from 10 to 70 km/sec and for these velocities it is beyond laboratory technology to make impact penetration tests with representative masses. Currently, meteoroid penetration analysis is based on theory and on extrapolation from laboratory measurements made at 10 km/sec and below.

2.2 Models Used

2.2.1 Sporadics. In a recent study by J. S. Dohnanyi of Bellcomm (Reference 5), the relation between particle flux and shield penetration is refined for sporadic cometary meteoroids. This is based on an analysis of photographic observations of meteors which when combined with radar and satellite measurements reveal a reasonably consistent relationship. A recent change to the Natural Environment and Physical Standards for the Apollo Program reflects these results and is used here (Reference 6).

2.2.2 Streams. The Natural Environment and Physical Standards states that "For Apollo applications, cumulative fluxes of $\geq 10^{-11}\,m^{-2}\,sec^{-1}$ are of interest. Except for the possibility of the Leonids, however, the meteoroid showers are not known to contribute significantly to this flux range; this contribution is considered to be included in the sporadic meteoroid model given." The lack of a fully quantitative model and the significantly higher flux for streams than for sporadics and the abundance of these streams in the period from early May through mid-August suggests that the AAP lunar surface mission be scheduled to avoid this period (as well as the Leonids in November). The enhancement of sporadic flux during this period adds support to the suggestion.

2.2.3 Swarms. It is assumed here that swarm occurrences coinciding with missions are random. This is pessimistic because there is some predictability of swarms which thus provides a degree of avoidance by mission scheduling. Appendix A shows that the low probability of occurrence of swarms more than compensates for the high flux during the occurrences. As a result, the probability of penetration from swarms is very much lower than that due to sporadics.

3. SHIELDING

3.1 Secondary versus Primary Shielding

For the longer exposures of the AAP mission, the LM shielding for primaries can be a relatively lightweight bumper shielding. However, the bumper concept does not give a weight advantage for secondaries because of their relatively low velocities. For the most part, the weight of shielding (bumper plus backup sheets) is determined by the secondaries. The proper proportioning of the thickness and separation of the two sheets is determined by the primaries. The effectiveness against primaries is so high, that crew safety and mission success probabilities of no penetration is essentially due, for AAP extended lunar surface missions, to exposure to secondaries.

For the purpose of this report, the extra meteoroid shielding required for the AAP lunar surface mission is approximated by using the formula for secondaries in Reference 6. The results of a detailed shielding calculation by Grumman for the 14-day Taxi LM is used as the base of reference for shielding weight calculations (Reference 7).

The LM shielding varies over its surface as determined by structural and other requirements. However, uniform shielding was assumed to establish a measure of the cost of the additional meteoroid shielding required for the AAP-LM configurations considered.

3.2 Spacesuit Shielding

The 12-day AAP stay time on the lunar surface will have a spacesuit meteoroid exposure times flux that is approximately eight times that for the 1.5-day stay-time of Apollo. Therefore, the weight of suit (and meteoroid cape) is about twice ($8^{1/3} = 2$) that just required for Apollo (see Appendix B). This assumes that the same probability of crew safety achieved for Apollo is acceptable for AAP.

If the suit and cape used for Apollo does not have sufficient margin for the longer exposure required by AAP, its meteoroid shielding will have to be increased.

3.3 2-Way LM Shielding

The mission configurations considered in this report will require various lunar ejecta exposure times for each type of LM to be used. These exposure times establish the shielding required in each case.

Detailed meteoroid shielding calculations for the Taxi made by Grumman (Reference 7) are used as a basis for estimating the shielding required for the 2-way LM. The details are given in Appendix C. The calculations were adjusted for the 8/15/66 change to the NASA Standard (Reference 6) relating to meteoroids. Further, they were adjusted to bring the crew safety probability for meteoroids from 0.9955 to 0.9982. The latter value was used by Grumman for the meteoroid shielding calculations on the Shelter (Reference 8).

For crew safety during the long surface stay-time, the 2-way LM without housing requires additional meteoroid shielding for the ascent engine fuel and oxidizer tanks. The 2-way LM with housing needs additional shielding for the pressurized cabin as well.

The shielding weight was estimated for the 2-way LM with no housing (Taxi) and for the 2-way LM with housing (dependent or independent LMs). For these two basic types of LMs, the shielding weight increase as a function of lunar surface stay time is shown by the plot of Figure VII-2. For example, the 12-day stay with the 2-way LM having no housing will require about 90 lbs more shielding. The same stay with the 2-way LM having housing will require about 210 lbs.

The effect of these shielding increases on the return payload (including container weight) is shown by Figure VII-3. For the 12-day stay-time, the 2-way LM without housing can carry about 180 lbs, but the 2-way LM with housing can only carry about 70 lbs. For a 4-day stay time, the 2-way LM with housing (ALM4) can carry 170 lbs to Earth.

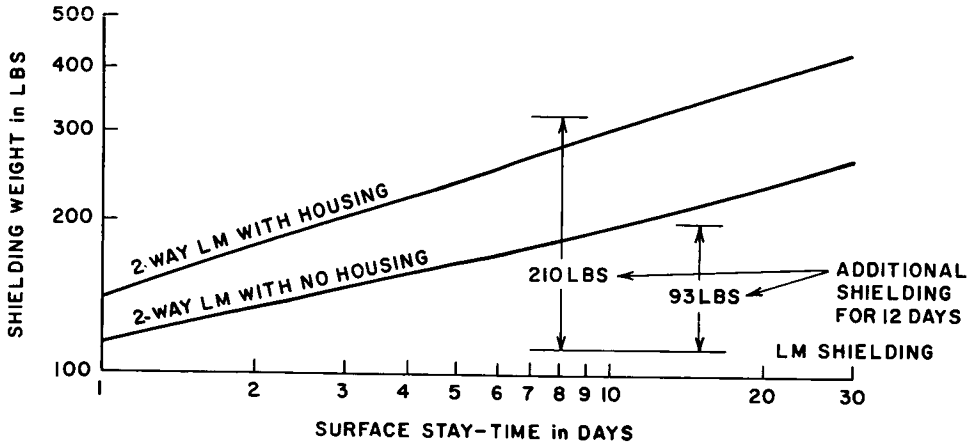

Figure VII-2. Estimate of Meteoroid Shielding for 2-Way LM versus Lunar Surface Stay-Time

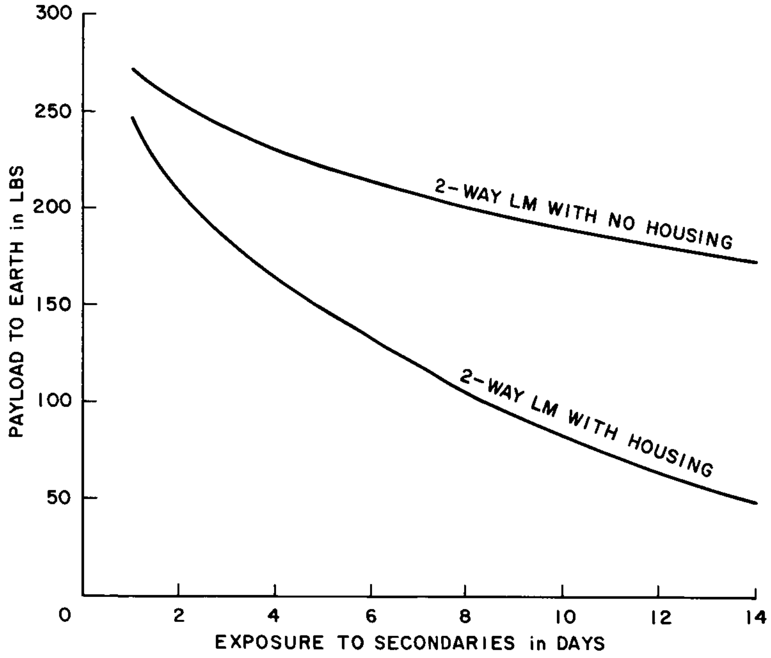

Figure VII-3. Estimate of Payload to Earth versus Lunar Surface Stay-Time

3.4 1-Way LM Shielding

The 1-way LMs are not required to have ascent capability and are limited only in their payload capacity to the Moon. Since this capacity is a magnitude or more times the weight of meteoroid shielding required, the shielding of this LM has little or no effect on system planning.

4. SUMMARY

It is expected that the added shielding weight required for the 2-way LMs with housing imposes an unacceptably high penalty on payload to Earth. The 2-way LMs without housing are less seriously limited. (See Figure VII-3.)

The suggestion is made that meteoroid streams be avoided by mission scheduling until their characteristics can be sufficiently determined to permit an acceptable evaluation of the hazard.

To the extent of their predictability, mission scheduling should also avoid swarms. However, the low probability of occurrence reduces this hazard to insignificance.

Because of the considerable increase in EVA, a significant increase in spacesuit weight over that just required for Apollo is expected.

Appendix A

PROBABILITIES OF SWARM OCCURRENCES

Where N is the number of penetrating lunar ejecta impacts per unit area and unit time,

$$N_1 = \frac{\left(-\ln P_1\right)}{At_1} \qquad (1)$$

$$N_2 = KN_1 = \frac{\left(-\ln P_2\right)}{At_2} \qquad (2)$$

in which

Subscript 1 holds for sporadic-generated lunar ejecta.

Subscript 2 holds for swarm-generated lunar ejecta.

K = ratio between rate of meteoroid arrival from a swarm and from sporadic.

A = area exposed.

P_1 = probability of no penetration from secondaries due to sporadic.

P_2 = probability of no penetration from secondaries due to swarms.

t_1 = duration of exposure from secondaries due to sporadics = duration of mission on lunar surface.

t_2 = duration of secondaries due to swarms = 1 to 5 hours per occurrence.

then

$$\frac{\ln P_2}{\ln P_1} \frac{t_1}{t_2} = K$$

and

$$P_2 = \epsilon^{-K \frac{t_2}{t_1} \left(-\ln P_1\right)} \qquad (3)$$

Since there is about one swarm per 25 years, the probability, p, of the random coincidence of a swarm in a mission interval of t_3 in days is approximately

$$p = \frac{10^{-4}}{4} t_3 \qquad (4)$$

Combining Equations (3) and (4) gives

$$P_3 = \left[1 - \left(1 - P_2\right)p\right] = 1 - \frac{10^{-4}}{4}\frac{Kt_2t_3}{t_1}\left(-\ln P_1\right)\left[\frac{1 - \epsilon^{\frac{-Kt_2\left(-\ln P_1\right)}{t_1}}}{\frac{K\,t_2\left(-\ln P_1\right)}{t_1}}\right]$$

in which

P_3 = probability of no penetration from swarms.

$t_3 = t_1$.

Since the bracketed term on the far right is always less than unity,

$$P_3 > \left[1 - \frac{10^{-4}}{4} K\,t_2\left(-\ln P_1\right)\right]$$

The swarm may have a meteoroid occurrence rate that is 1000 times that for the average rate of sporadics. The interval for the swarm may be as long as 1/5 of a day. Then

$$P_3 > \left[1 - 0.005\left(-\ln P_1\right)\right]$$

when

$P_1 > 0.99$,

then approximately

$$\left(1 - P_3\right) < 0.005\left(1 - P_1\right) \tag{5}$$

Therefore, the probability $(1 - P_3)$ of penetration from swarms is very much lower than the probability $(1 - P_1)$ of penetration from sporadic flux.

Appendix B

AMES (SUMMER 1959) PENETRATION CRITERION

The penetration thickness of a single or multisheet shield to secondaries is proportional to particle velocity and mass, as follows:

$$T \alpha \left(v^2 M\right)^{1/3}$$

where

T = penetration thickness.
v = velocity of the impinging particle.
M = mass of the impinging particle.

Appendix C

METEOROID SHIELDING OF THE LM ASCENT STAGE FOR AAP

The weights of shieldings required for 2-way LMs with housing and for 2-way LMs without housing (i.e., Taxi) are estimated as a function of lunar surface stay-time. The shielding area of the LM ascent stage is approximately:

Cabin	14 m^2	
Tanks	20 m^2	
Total	34 m^2	(1)

The significant crew safety shielding areas on the ascent stages of the two types of vehicle are:

2-Way LM With Housing	2-Way LM Without Housing	
34 m^2	20 m^2	(2)

The tanks include fuel and oxidizers for ascent propellant. Therefore, their shielding is a crew safety item whether the LM is manned or unmanned during the lunar surface stay. The cabin shielding has crew safety significance only when manned as in the case of ascent-housing. It is assumed that successful ascent with a nonpressurized cabin is possible if necessary. When unmanned, cabin shielding may affect mission success but not crew safety.

Bumper shielding is assumed; therefore, secondary, rather than the primary, exposure controls the shielding weight. For purposes of simplification, and for weight estimates sufficiently accurate for configuration recommendation, uniform shieldings over the tank areas and over the cabin area are assumed. The LM ascent stage referenced in the Taxi study by Grumman (Reference 7) is used as the point of departure.

The referenced LM is assumed to be aluminum with a uniform shielding of 0.15 gms/cm^2 which gives the following shielding weights:

Cabin Shielding	46 lbs	
Tank Shielding	66 lbs	
Total	112 lbs	(3)

The Taxi study was completed before the 8/15/66 change to the Natural Environment Standard for primaries and secondaries was in effect; therefore, the old standards were used in that study. The old standard for secondaries was:

$$M_o = \left[10^{14.52} N\right]^{-1/1.34} \qquad (4)$$

The new standard is:

$$M_n = \left[10^{12.91} N\right]^{-1} \qquad (5)$$

where:

N = number of impacts/m^2/sec from ejecta particles exceeding mass M.
M_o = old standard for mass of ejecta particles in kgms.
M_n = new standard for mass of ejecta particles in kgms.
Ejecta density = 2.5×10^3 kgm/m^3.
Ejecta velocity = 0.2 km/sec.

The thickness of shielding and therefore the weight of shielding for a given area is proportional to the mass of the ejecta M to the 1/3 power (see Appendix B). Therefore, from Equations (4) and (5) and for a given N

$$\frac{W_n}{W_o} = \left(\frac{M_n}{M_o}\right)^{1/3} = \frac{0.2035}{N^{0.08458}} \qquad (6)$$

where

W_n = weight of shielding with the new standards.
W_o = weight of shielding with the old standards.

Next let (Reference 9)

$$N = \frac{\delta}{At} \qquad (7)$$

where

A = area of shielding being considered in m^2.
t = time of exposure to secondaries in seconds.
δ = probability of penetration in A during t.

Combining (6) and (7) gives

$$W_n = \frac{0.2035\, W_o}{\left(\frac{\delta}{At}\right)^{0.08458}} \qquad (8)$$

This relationship is plotted as Figure VII-4.

The Taxi study (Reference 6) gives the results of shielding calculation as follows:

Lunar Surface Stay-Time	14 days	
Crew Safety (Secondaries)	0.9955	
Added Weight to LM	25 lbs	
Payload Return (with container)	250 lbs	
Meteoroid Standard	old	(9)

Since the Taxi will be manned for only a fraction of a day, the probability of cabin puncture during that time is not significant. If a cabin puncture occurs while unmanned, it does not affect crew safety since LM ascent and rendezvous with the CSM is assumed to be feasible if the cabin is not pressurized. However, there must be adequate shielding of the fuel, oxidizer, and helium tanks to insure the ascent of the Taxi. To show the approximate shielding weight penalties for various configurations, we assume that crew safety probability is due entirely to secondary particle exposure of these tanks during the 14-day stay-time.

For tank shielding, from (1), (3), and (9)

$t = 14$ days.

$A = 20\ m^2$.

$\delta = 1 - 0.9955 = 4.5 \times 10^{-3}$.

$W_o = 66 + 25 = 91$ lbs (Taxi tank shielding).

$\frac{\delta}{At} = 1.86 \times 10^{-10}$.

Then from (8),

$$W_n = 124 \text{ lbs} \tag{10}$$

for Taxi Tank Shielding for the new meteoroid standard.

From this, for a Taxi crew safety of 0.9955, the shielding increase should be (124 - 66) or 58 lbs instead of 25 lbs. However, it is noted that the crew safety for the Shelter (Reference 8) was calculated by Grumman to be 0.9982. To be compatible, the Taxi tank shielding should be increased from 0.9955 to 0.9982.

From Appendix B and Equations (5) and (7) it is concluded that the shielding thickness and therefore the weight is inversely proportional to δ to the 1/3 power:

$$W_1 = W_n \left(\frac{\delta_n}{\delta_1}\right)^{1/3} \tag{11}$$

and with

W_n = 124 lbs.
$\delta_n = 1 - 0.9955 = 4.5 \times 10^{-3}$.
$\delta_1 = 1 - 0.9982 = 1.8 \times 10^{-3}$.

it is found that

$$W_1 = 167 \text{ lbs} \tag{12}$$

for Taxi tank shielding for the new standard and for crew safety = 0.9982.

In this case, the shielding increase should be (167 - 66) or 101 lbs for a 14-day stay-time.

As pointed out elsewhere in this report, the maximum feasible stay-time on the lunar surface is 12 days. From Appendix B, (5), and (7), the shielding weight is proportional to the lunar surface exposure time to the 1/3 power. Thus,

$$W_2 = W_1 \left(\frac{t_2}{t_1} \right)^{1/3} \tag{13}$$

for W_1 = 167 lbs.
t_2 = 12 days.
t_1 = 14 days.

Therefore,

$$W_2 = 159 \text{ lbs.} \tag{14}$$

This is the Taxi tankage shielding weight for a crew safety of 0.9982, lunar stay-time of 12 days on the basis of the new standards. The LM increase in meteoroid shielding for the Taxi and the above conditions is (159 - 66) or about 93 lbs. From (3), the total shielding weight for the Taxi then becomes

Cabin Shielding	46 lbs	
Tank Shielding	159 lbs	
Total	205 lbs	(15)

The total weight was calculated and plotted for the Taxi (2-way LM without housing) for various lunar surface stay-times on Figure VII-2.

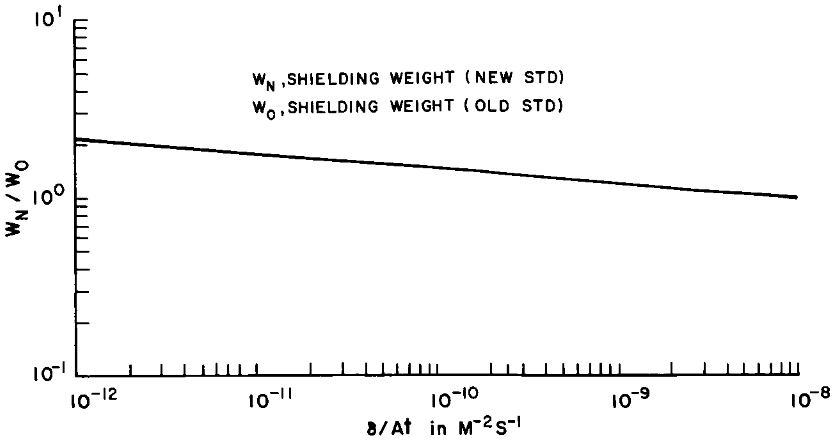

Figure VII-4. Ratio of Shielding Weight Between New and Old Natural Environment Standards for Lunar Ejecta (Secondaries)

Now the tabulated values in (9) become as follows:

Lunar Surface Stay-Time	12 days
Crew Safety (Secondaries)	0.9982
Added Weight to LM	93 lbs
Payload Return (with container)	182 lbs
Meteoroid Standard	new

(16)

Note that Payload Return including container = 250 - (93 - 25) = 182 lbs.

The return payload (including container) for the 2-way LM without housing is plotted as a function of lunar stay-time in Figure VII-3.

Now consider the 2-way LM with housing which is manned for the entire lunar surface stay-time. In this case, shielding must be added to the cabin as well as the tanks for the lunar surface stay-time. A cabin puncture during "shirt-sleeve" manning is likely to be fatal.

From Appendix B, (5) and (7), the shielding thickness (new meteoroid standard) is proportional to the area to the 1/3 power. Therefore, the shielding weight is proportional to the area to the 4/3 power.

$$\frac{W_3}{W_2} = \frac{A_3}{A_2}\left(\frac{A_3}{A_2}\right)^{1/3} = \left(\frac{A_3}{A_2}\right)^{4/3} \qquad (17)$$

Now, from (14), (1), and (3)

W_2 = 159 lbs (tank shielding).
A_2 = 20 m^2.
A_3 = 34 m^2 (cabin plus tank shielding area).
0.9982 = crew safety.
t = 12 days.
W_3 = shielding weight for ascent stage of 2-way LM with housing.

Therefore,

$$W_3 = 2.02\,W_2 = 322 \text{ lbs} \qquad (18)$$

The added shielding weight would be (322 - 112) or 210 lbs. The tabulation comparable to that for (15) is

Lunar Surface Stay-Time	12 days
Crew Safety (Secondaries)	0.9982
Added Weight to LM	210 lbs
Payload Return (with container)	65 lbs
Meteoroid Standard	new

(19)

For the 12-day lunar stay, the useful return payload by the 2-way LM with housing is less than 40 percent of that possible with the 2-way LM without housing because of the heavier meteoroid shielding required. The effect of stay-time on the shieldings and payloads for the 2-way LM with housing are also shown by Figures VII-2 and -3.

REFERENCES

1. Hawkins, Meteors, Comets, and Meteorites, McGraw-Hill.
2. Lowell, Meteor Astronomy, Oxford Press, 1954.
3. Orrok, O. T. The Meteoroid Environment of Project Apollo, (2nd Edition), Revised February 20, 1964, NASA Abstract N66-12857.
4. Gault, Shoemaker, and Moore, Spray Ejected from the Lunar Surface by Meteoroid Impact, Ames Research Center, NASA, Moffett Field, California, D-1767, April 1963.
5. Dohnanyi, J. S. Model Distribution of Photographic Meteors, Bellcomm, TR66-340-1, March 29, 1966.
6. Natural Environment and Physical Standards for the Apollo Program, M-D E 8020.008B, SE 015-001-1, Modified August 15, 1966.
7. Apollo Extension System Phase B Final Report, VI, "Taxi Design Analysis Summary," Grumman Aircraft Engineering Corporation, December 8, 1965 (CONFIDENTIAL).
8. Apollo Extension System Phase B, V, "Shelter Design Analysis Summary," Grumman Aircraft Engineering Corporation, December 8, 1965 (CONFIDENTIAL).
9. Maiden, C. J. "Meteoroid Impact," Space Exploration, Engineering and Science Extension Series, University of California, p. 236.

X68-84338

SECTION VIII. SOLAR PARTICLE HAZARD FOR AN EXTENDED LUNAR STAY MISSION

by D. C. Swanay

1. INTRODUCTION

This report represents an analysis of the impact of the solar particle hazard on mission planning for an AAP extended lunar stay mission. The mission under consideration is designed to place two men on the Moon for a period of 12 days. Several of these missions are planned, with the first occurring in the early 1970's. The next maximum of the 11-year solar cycle will occur in 1970. Thus, the first extended lunar stay missions will occur during a period of relatively intense solar particle activity. This makes it necessary to examine mission planning in the light of this hazard.

This section addresses itself to three areas of interest to the mission planner:

1. What is the probability that a 12-day lunar stay mission would be terminated prematurely due to a solar particle event? How would this probability of premature termination be affected by the Solar Particle Alert Network (SPAN), currently under development?
2. Can abort procedures be devised which will enable the astronauts to return to Earth before accumulating a serious radiation dose in the event of a major solar particle event?
3. Is it feasible to add shielding to the LM so that the astronauts could wait out a major solar particle event in the LM on the lunar surface, returning to work after the event has subsided?

The answers given to these questions are based on the results of computations using data from the last maximum portion of the solar cycle — 1956 to 1961. Thus, when these results are projected to predict the solar particle environment from 1967 to 1972, the assumption is implicit that the next maximum portion of the solar cycle will be like the last one. This assumption should be questioned and examined as data on the next solar cycle becomes available.

The data available from solar particle measurements during the last solar maximum is not adequate for a precise determination of quantities of interest.

Sensor limitations make radiation dose calculations uncertain to a factor of two. In addition, there is an uncertainty of 50 percent or more in the current estimates of human biological response to radiation exposure. The most conservative approach to mission planning would be to assume worst-case values for the uncertain parameters and then plan for enough radiation protection to ensure the desired crew safety probabilities. However, the magnitude of the uncertainties, in combination with the limitations on AAP system capabilities, make this approach impossible. The approach taken is to base mission planning on the best estimates of the solar particle environment and human response to radiation. Insurance against underestimates of the environment and human response to it is provided through abort procedures.

The solar particle environment model is based on Webber's description of the events of the last solar maximum (Reference 1).* The maximum allowable radiation dose used in mission planning is based on a NASA determination of human response to radiation (Reference 2).

Radiation can cause two principal types of injury to the astronauts: "deep-dose" effects on the blood-forming organs and gastro-intestinal track, and "shallow-dose" effects on the skin. The maximum allowable skin dose will virtually always be attained before the maximum allowable deep dose (measured at a depth of 4 or 5 cm) in the lightly shielded LM. This consideration holds to an even greater extent under spacesuit shielding. This predominance of the skin dose is due to the fact that large numbers of relatively low-energy particles are able to penetrate the light shielding and contribute to the skin dose, but most of them are stopped by the 4 or 5 cm of tissue between the skin and the point at which the deep dose is measured. For example, the soft (peak characteristic rigidity of 70 Mv), high-flux event of July 14, 1959, gave a peak skin-dose rate of 130 rads/hour under spacesuit shielding, but the peak deep-dose rate was only 0.7 rads/hour. Thus, the maximum allowable crew radiation dose is placed at 400 rads skin dose (Reference 2). This is an estimate of the skin dose which would produce erythema (skin reddening) in 10 percent of the population.

We now consider the three areas of interest defined above: probability of premature termination, solar particle abort procedure, and feasibility of shielding the LM so the astronauts can wait out a major particle event on the lunar surface.

2. PROBABILITY OF PREMATURE MISSION TERMINATION

A mission is defined to be prematurely terminated if the astronauts are required to cancel their lunar surface stay entirely, or if they are forced to return to the CM sooner than 12 days after touchdown. The probability of premature mission termination is calculated by assuming a uniform probability distribution for solar particle event occurrences. It is assumed that each day in the 6-year solar maximum period represents a possible lift-off day for a 12-day mission with the exception of those days on which a solar particle event occurs. Thus, associated with each isolated event large enough to cause an abort, there are 12 possible 12-day missions that would be terminated prematurely. After suitable correction for the bunching effect (large events tend to occur in groups of two or three separated by only a few days), the desired probability is simply the ratio of total number of prematurely terminated missions to total number of possible missions in the time span considered.

---

*References are listed at end of the section.

Radiation damage to the crew could be minimized by a strategy calling for mission termination as soon as a buildup of energetic particles indicates that an event is occurring. In this case, each of the events in the 6-year time span would be a source of prematurely terminated missions. Then, the probability of a 12-day mission terminating prematurely due to solar particle activity is 0.18. Under the 11-year periodicity of solar activity, this leads to a prediction that approximately one out of every five 12-day lunar missions would terminate prematurely due to solar particle activity in the period from 1967 through 1972. This abort probability is unacceptably high, and could be reduced by either using an abort strategy based on SPAN event size predictions or by scheduling the mission during the period of minimum solar activity in the middle of the 1970's.

First, consider the effect on abort probability of utilization of SPAN, described in Reference 3. SPAN is a network of radio and optical solar telescopes which is designed to give a prediction of event size at or shortly before initiation of the event. The radio telescopes observe the Type IV centimetric radio bursts which are associated with almost all solar particle events. The optical telescopes observe the optical flares associated with solar particle events in order to reduce the high false alarm rate which appears to be inherent in the radio measurements. The prediction is based on an analysis of the Type IV radio signature accompanying the event. At this point, it is not possible to define the probability distribution of SPAN prediction errors. However, there is a possibility of achieving predictions accurate to ±50 percent of true dose if 4 hours of particle energy spectrum measurements are available after onset. Assuming that the 4-hour measurement period can be provided, we can use the bounds on SPAN prediction error to get an upper bound on the abort probability. A solar particle event giving the maximum allowable skin dose of 400 rads would have a SPAN predicted dose of between 200 and 600 rads, corresponding to maximum under- and overpredictions. In order to guard against underprediction, the abort strategy would call for an abort whenever the SPAN prediction was greater than 200 rads. Now, to get the upper bound on abort probability, we note that an event giving a true dose under 133 rads would not cause a SPAN prediction over 200 rads (and thus an abort) even in the case of maximum overprediction. The upper bound on abort probability for a 12-day mission is then just the probability of encountering a flare giving a dose above 133 rads. Figure VIII-1 gives the probability of exceeding a given radiation dose on a 12-day mission when the crew waits out the event in the LM. The curves were generated as follows: The skin dose which would have been received by the crew in the LM was computed for each flare in the environmental model. The method used to compute radiation doses under nonuniform LM shielding is described in the Appendix. The resulting data were used to form the probability distribution for total dose received if an event occurs. This dose probability was then multiplied by the probability of an event occurring on a 12-day mission (about 0.2 for the peak years) which gives the probability distribution for dose received on a 12-day mission. Curve A gives the dose received under the Apollo LM shielding configuration specified in Figure VIII-2. Curve B gives the dose received when Apollo LM shielding is upgraded through the use of onboard water as described later in this section. Looking at the 133-rad dose level, we see that the upper bound on abort probability is 0.06 when the astronauts are protected by Apollo LM shielding and 0.03 when the upgraded shielding is used. In either case, an abort strategy based on the SPAN prediction significantly reduces the abort probability.

Premature termination of a 12-day mission would have a varying effect on mission success, depending on how early in the mission the abort occurred. Under the assumption of a uniform event occurrence probability, an average of 6 days would be lost on missions terminated prematurely. When the averaging is performed over all 12-day missions, including those which are not aborted, the expected value of days lost per mission due to solar particle activity is 1.2 days per mission when SPAN is not used, 0.4 day per mission when SPAN is used with Apollo LM shielding, and 0.2 day per mission when SPAN is used with the upgraded LM shielding.

The probability of premature mission termination could also be reduced by scheduling the mission in the period of minimum solar activity. If we consider the time period of 1972 through 1977, then we can get a rough idea of the decline in solar particle activity over this period by measuring the decrease in sunspot activity as a function of time from solar maximum. Using the averaged sunspot activity curve on page 241 of Reference 4, we arrive at the rough estimate that solar particle activity should be down by a factor of four in the 1972-1977 period, as compared with the 1967-1972 period. Assume that the particle events in both 5-year periods are identically distributed in intensity and that event frequency is down by a factor of four during the minimum period. This leads to a rough prediction that the abort

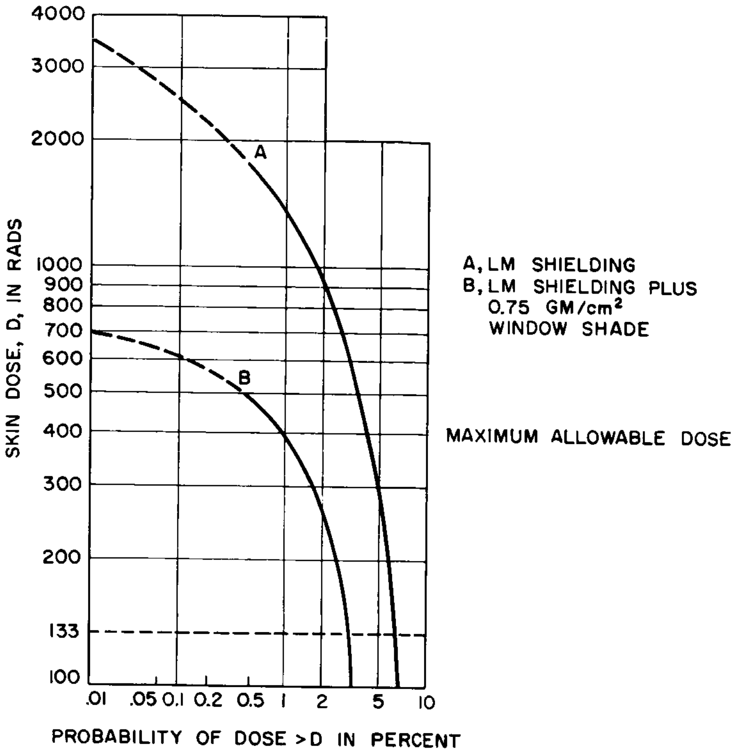

Figure VIII-1. Probability of Exceeding Given Dose for 12-Day Stay-Time

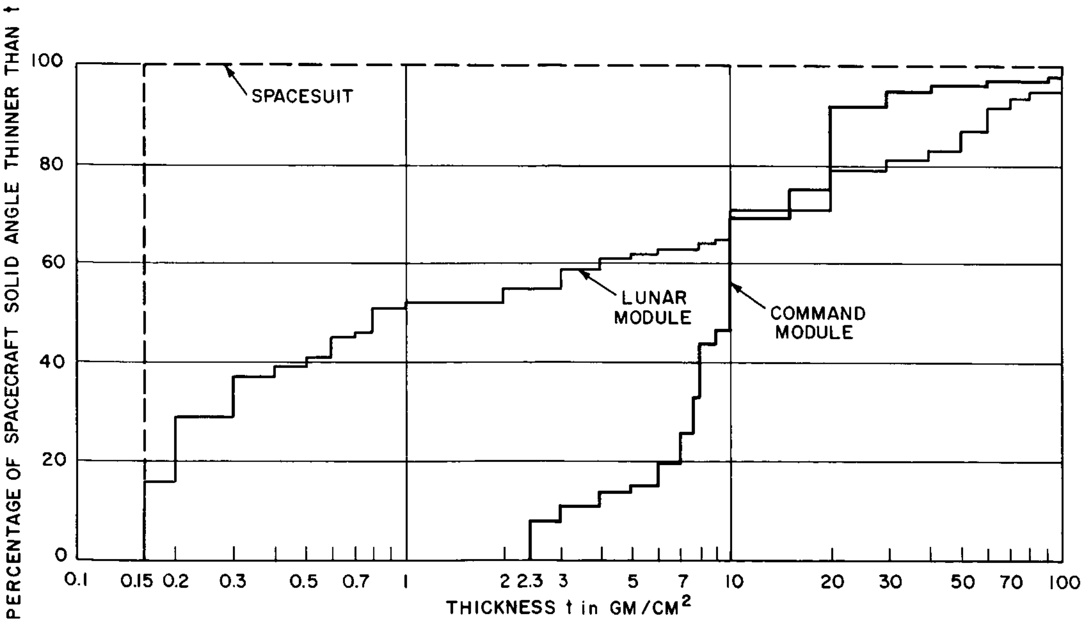

Figure VIII-2. Radiation Shielding for Spacesuit, CM, and LM

probability for a 2-week lunar stay mission in the period 1972 through 1977 would be 0.05 if no warning system is used and 0.02 if SPAN is used with Apollo LM shielding.

3. ABORT PROCEDURE AND CREW ABORT DOSE

To be conservative, assume that the SPAN prediction is made at onset of the event with no advance warning and that the astronauts initiate abort procedures coincident with the rapid buildup of energetic particles associated with the onset of a solar particle event. We want to determine the probability that the astronauts will receive a dose above the maximum allowable dose before they reach Earth. First, it is necessary to find the time interval from particle onset to astronaut entry into the CSM during an abort. This total time interval, the expected value of abort time, can be broken into six components, two of which are random variables. These components are:

1. Traverse return time — The mission plan in Volume 1 calls for a maximum of 6 hours traverse activity per 24-hour period. The traverse return time as a function of traverse time elapsed is given for a typical traverse in Figure VIII-3. It is assumed that the probability of flare occurrence is uniformly distributed in time. Then the expected value of traverse return time, given that a flare occurs during a traverse, is 1.3 hours and the probability that an event occurs during the 6 hours of traverse activity in each 24-hour period is 0.25. Thus, the expected value of traverse return time is 0.34 hour. Spacesuit shielding of 0.15 gm/cm^2 is assumed for the astronauts during traverse return.
2. Particle spectrum measurement period — Four hours were allotted to particle spectrum measurement for attaining the assumed bounds on SPAN prediction accuracy. These measurements can be performed concurrently with the astronauts' traverse return, so that the sum of the traverse return and particle measurement times is 4 hours, with the astronauts protected by Apollo LM shielding for an expected value of 3.67 out of the 4 hours.
3. Transfer to the 2-way LM — A time interval of 0.5 hour is assumed for transfer from the 1-way LM to the 2-way LM. The crew will be under spacesuit shielding during this period. Apollo LM shielding is assumed once the crew has reached the 2-way LM.
4. Ascent preparations — An ascent preparation time of 2 hours is assumed for the 2-way LM.
5. CSM orbit synchronization — Up to 2 hours can be required for CSM orbit synchronization once a state of launch readiness has been reached. The expected value for this time interval is 1 hour.

6. Ascent and docking — A total of 1.3 hours is assumed from lift-off to CSM entry. Crew shielding is modified to reflect the decrease in shadowing of incident radiation by the Moon due to the smaller central angle subtended by the Moon at an altitude of 80 nmi.

Thus, the expected time interval from particle onset to CSM entry is 8.8 hours, with the astronauts protected only by spacesuit shielding for 0.83 hour, by Apollo LM shielding for 6.67 hours, and by Apollo LM shielding with reduced lunar shadowing for 1.3 hours. Figure VIII-4 presents the abort dose probability curve for the 8.8-hour abort, given that a solar particle event requiring abort has occurred. The increase in intensity of the event, from onset to maximum, was assumed to be exponential as a function of time. The parameters specifying the time history of each event in our environmental model were taken from Reference 1. The dose data used to generate Figure VIII-4 includes the dose accumulated from CM entry to Earth return. Figure VIII-4 indicates that the probability of exceeding the maximum allowable dose during an abort is appreciably less than 0.001. Thus, the probability of serious radiation injury to the crew during a solar particle abort can be made acceptably low with simple abort procedures. In fact, as claimed above, a properly timed abort appears to offer enough safety margin to insure safe return of the crew, even in the face of the uncertainties in our knowledge of the radiation environment and human response to it.

4. INCREASED LM SHIELDING

If the astronauts followed the strategy of waiting out solar particle events in the LM and then returning to work, an unacceptably high probability of exceeding the maximum allowable skin dose would result unless LM shielding was increased. Dose probability curve A of Figure VIII-1 indicates that the probability of exceeding the maximum allowable skin dose on a 12-day mission is about 0.04 when a no-abort strategy is followed under Apollo LM shielding.

It would be highly desirable to upgrade the LM radiation shielding to a level such that the astronauts could remain in the LM and wait out a major solar particle event, returning to work on the surface once the radiation level is safe again. However, the weight penalty which must be paid in terms of payload is quite severe, if increased shielding is provided by adding thickness to the LM wall structure. Thus, the possibility of providing additional shielding for a small weight penalty by using onboard water in a highly localized shielding scheme is considered.

This latter shielding configuration acts as a radiation "window shade." The window shade configuration takes advantage of the fact that a large portion of the total dose in the LM comes through the 37 percent of solid angle having shielding less than or equal to 0.3 gm/cm^2. In fact, 70 percent of the total LM dose in the

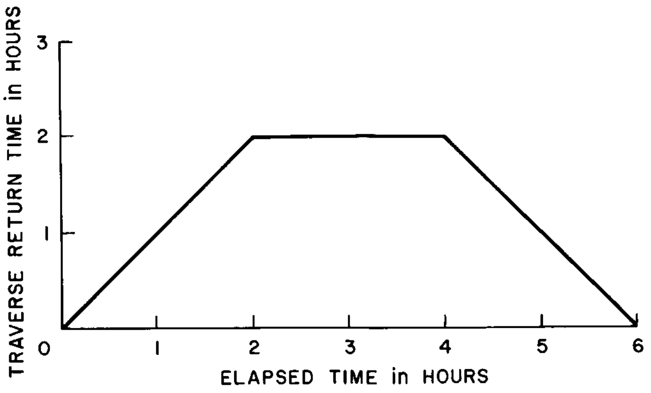

Figure VIII-3. Return Time on a Typical Traverse

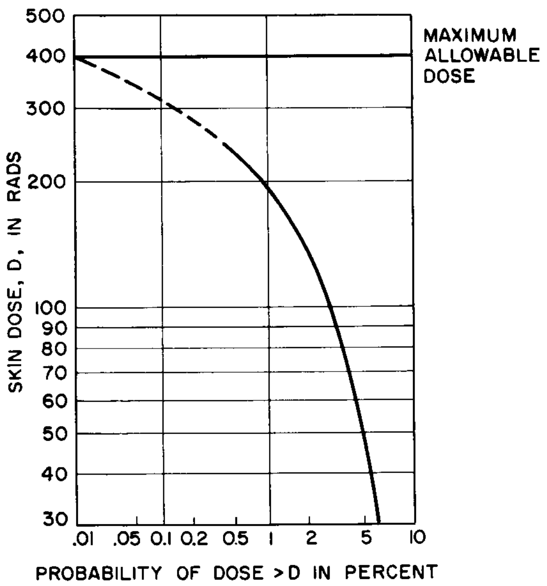

Figure VIII-4. Probability of Exceeding Given Dose during 8.8-Hour Abort

high-energy event of February 23, 1956, and 80 percent in the low-energy event of July 14, 1959, were due to radiation passing through this portion of the total solid angle. The shielding scheme requires the astronauts to take normal resting positions in their crew couches. A tubular framework is erected about each couch with thin, water-filled patches attached to the framework at positions corresponding to radiation "windows" in the LM structure. In this configuration, the astronauts would be free to take short exercise breaks, quickly react to emergency situations in the LM and perform personal hygiene and recreational tasks in their couches for the duration of the flare. It is important to limit the astronauts' operational freedom as little as possible, since a major solar particle event has a typical duration of 2 days or more. After the event is over, the water used for shielding is returned to normal storage and operations are resumed.

The weight penalty paid when this configuration is used consists of that water used for no other purpose than shielding, plus the tubular support frame and the containers which hold the shielding water on the frame. It might be necessary to modify fittings on the storage tank to allow the return of the shielding water to normal storage after the solar particle event is over. The capability for transferring water from normal storage to the shielding containers already exists, since the LM water supply has been pressurized and fitted with a long hose and nozzle to minimize the fire hazard.

Curve B of Figure VIII-1 shows the dose probability for a 12-day mission using this shielding configuration. The configuration used provides extra shielding of 0.75 gm/cm^2 of water for the critical areas. This curve was generated by appropriately increasing the shielding thickness of the 37 percent of LM solid angle shielded by less than 0.3 gm/cm^2, computing the modified no-abort doses for all of the events in the environmental model, and calculating the dose probability distribution as described above. The probability of exceeding the maximum allowable skin dose on a 12-day mission is about 0.01 when a no-abort strategy is followed under the window shade shielding.

The results of Figure VIII-1 seem to indicate that a strategy of waiting out solar particle events in the LM under window shade shielding might yield an acceptable dose probability curve for a 12-day mission. However, further operational modifications are required due to the apparent tendency of large solar particle events to occur in groups. During the last solar maximum period, a large event was followed in a few days by another large event about 50 percent of the time. Thus, the astronauts could wait out a single large event with an acceptably high probability of not exceeding the maximum allowable skin dose, but since 50 percent of the time a second large event would occur within the next few days, the additional skin dose accumulated during the abort procedure would yield a total skin dose above the maximum allowable dose. The desired overall probability of not exceeding the maximum allowable skin dose can be attained by defining an abort criterion on which to base a decision to either abort or go back to work at the conclusion of an event. The operating agency will set an acceptable probability level for crew radiation exposure. To provide an example of the development of an abort criterion, an exposure goal has been arbitrarily set requiring that the probability of exceeding a skin dose of 400 rads be less than or equal to 0.01. The abort criterion giving an overall probability of 0.01 that the crew receives a skin dose above 400 rads when two events occur can now be found.

We want to find a dose level, X rads, that satisfies the following probability equation:

$$\left(P_r\right)\left(P'_r\right)\left(P''_r\right) = 0.01$$

where

P_r = probability that skin dose from first event $\geq$ X rads on 12-day mission using window shade shielding.

P'_r = probability that second event occurs within a few days after the first event.

P''_r = probability that abort skin dose during second event $\geq$ 400 - X rads.

This equation can be solved for X, once the probability distributions are specified. The probability of obtaining a skin dose greater than X rads during the first event is given in Figure VIII-1. The probability of a second event occurring after a large event is assumed to be 0.5. The probability of getting a total abort skin dose of greater than 400 - X rads is based on Figure VIII-4, but the probability distribution must be modified to yield the abort dose probability given that a second large event occurs. It is necessary to get an abort dose probability distribution for large events since the apparent bunching tendency appears to hold only for large events (a large solar particle event being followed by a second large event about 50 percent of the time). An abort dose probability distribution for large events was calculated by arbitrarily defining a "large event" environmental model consisting of those events in the environmental model yielding more than 7×10^8 particles/cm^2 at energies above 30 Mev. The abort doses computed are for a modification of the 8.8-hour abort procedure defined above. If the crew waits out an event and a second event occurs, the indicated high level of solar particle activity would probably dictate an immediate abort, and the 4-hour spectrum measurement required for an accurate SPAN prediction would be eliminated. This gives an expected abort time of 5.1 hours. Figure VIII-5 gives the large event abort dose probabilities for the 5.1-hour abort. All of the components of the overall mission dose probability equation are now specified. Solution of the equation for X yields an abort criterion that gives the specified overall probability of not exceeding the maximum allowable skin dose in the presence of bunched solar particle events, i.e., an abort should be performed at the conclusion of any event giving a measured skin dose of more than 250 rads under window shade shielding.

If the astronaut skin dose exceeds the abort dose criterion while they are still waiting out an event under window shade shielding, it is important that abort procedures requiring significant extravehicular activity should not be initiated until radiation subsides to safe levels. Since a skin dose exceeding the abort criterion under window shade shielding would only be caused by a major event, such an event would probably give dangerously high dose rates under spacesuit shielding.

Thus, a set of solar particle abort rules can be developed if mission planning calls for an attempt to wait out major solar particle events under window shade shielding. The abort rules would be based on the abort criterion using SPAN dose predictions, the "post-event" abort criterion using actual dose measurements, and consideration of mission time remaining.

We can get an idea of the amount of water required by the 0.75 gm/cm^2 window shade configuration by assuming that the tubular frame surrounding each man is a sphere of diameter d. This simplifies the water requirement computations since a total water-shielding surface area of $0.37 \times 4\pi \times (d/2)^2$ would shield the vulnerable 37 percent of the total solid angle if the shielding patches are attached to the spherical frame. Thus, if each man has 0.75 gm/cm^2 water shielding patches on a 6-foot-diameter spherical frame, the total water requirement is 135 lbs. This estimate tends to be conservative since those shielding patches in positions which do not cause significant astronaut movement restrictions can be moved closer to the body with the resultant reduction in blanket segment area.

We next consider the interaction between mission planning and the weight cost of additional shielding. The net weight costs associated with the additional shielding are dependent on the operational configuration, as can be illustrated by considering two possible missions, one using a LM Shelter and one using a Dependent LM.

In the case of LM Shelter, it is assumed that:

1. Water is generated by fuel cell recovery and metabolic recovery during the lunar surface stay.
2. Thermal control is achieved with a system using a radiator.
3. There is a schedule requiring nine man-hours of extravehicular activity per day.
4. The solar particle event duration is 3 days.
5. All of the water remaining in the tank is available for shielding except for a 3-day supply for the thermal control system. Implicit in this assumption

is the requirement that water used for shielding remains uncontaminated and can be returned to the tank and used normally after the flare.

The time history of LM Shelter water usage (compiled from Reference 5) presented in Figure VIII-6 indicates that 100 percent of the water requirement for the window shade configuration (135 lbs H_2O) could be provided out of the nominal water supply for a solar particle event occurring in the first 7 days of the lunar stay. That is, no weight penalty is paid, other than that of the water containers and the support frame, for waiting out a solar particle event occurring in the first 7 days of the lunar stay. Past this point, a weight penalty must be paid, in the form of water not required for uses other than shielding, plus the associated tankage. The water weight penalty reaches a maximum of 65 lbs for an event occurring on the tehth day. There would be little value in waiting out an event occurring after the tenth day, since there would be little or no time left in the nominal lunar stay by the time it would be safe to resume operations.

A significant source of shielding material could be the astronauts' urine. It is estimated that 75 lbs of urine will be generated during a 12 day stay (Reference 5). If it is assumed that urine provides the same shielding level as water and that it can be used in the shielding system without contaminating the water, then 100 percent of the shielding requirements could be provided for an event occurring in the first 10 days of the mission.

Next, consider the Dependent LM configuration. It is assumed that:

1. Fuel cells are not used.
2. Thermal control is achieved with a system using a radiator.
3. The lunar stay is 12 days, with a schedule of 9 man-hours of extra-vehicular activity per day.

This configuration would then require three LM water tank refills (Reference 6). The three refill tanks are delivered on the Lunar Payload Module and transported to the Dependent LM by the astronauts, shortly after landing.

In this case, Figure VIII-6 shows that 100 percent of the water requirement for the window shade configuration could be provided out of the nominal water supply for a solar particle event occurring at any point in the mission. That is, no weight penalty would be paid, other than that of the shielding water containers and the support frame, for waiting out a solar particle event occurring during the Dependent LM mission. Finally, it should be noted that the considerations involved in waiting out a solar particle event place a restriction on Dependent LM resupply strategy. It would be desirable to have the capability to initiate Dependent LM tank refill from within the LM. But if it were necessary to go over to the Lunar Payload Module and bring back a new water tank each time a tank refill was required, or even if it were

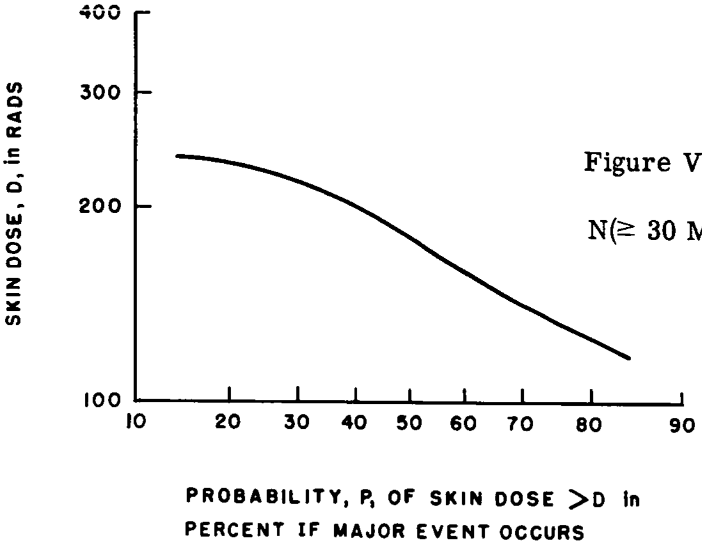

Figure VIII-5. Probability Distribution for Events with Flux $N(\geq 30\ \text{MEV}) \geq 7 \times 10^8\ \text{Particles/cm}^2$

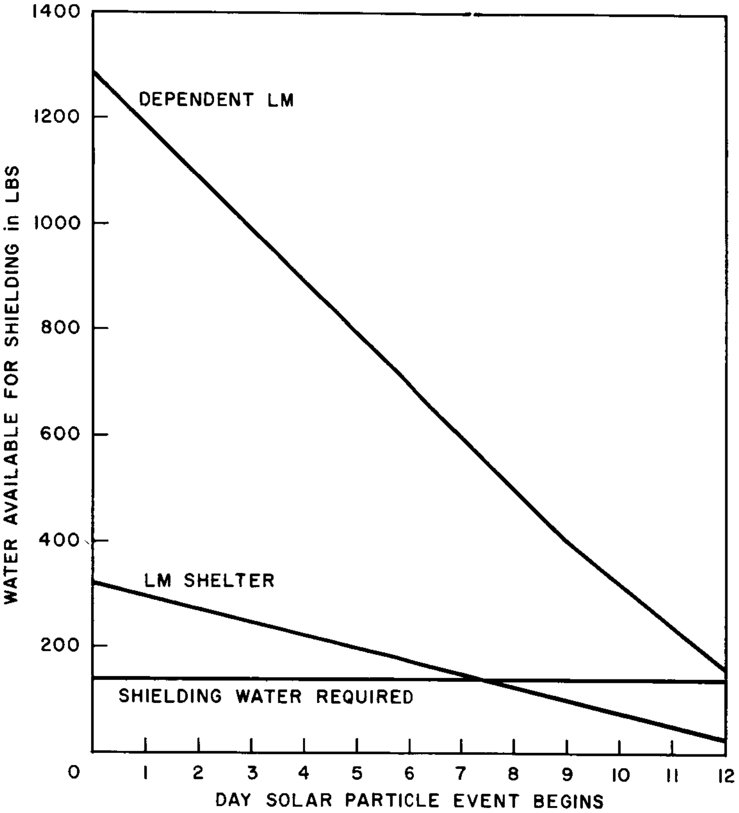

Figure VIII-6. Water Usage

necessary only to go outside the LM to make connections at the time of refill, the astronaut could accumulate a significant radiation dose if a major solar particle event was occurring at the time of refill.

5. SUMMARY

The quantitative results presented in this report are intended only to lend support to the qualitative conclusions presented. The uncertainties in the environmental model and in human response to radiation make it impossible to interpret the data as a precise numerical picture of the solar particle hazard. The major qualitative conclusions which emerge are:

1. The relatively high probability of solar particle activity during a 12-day lunar landing mission in the 1967-1972 period places a requirement on mission planning to minimize the effect of a solar particle abort on the mission goals. Significant reductions in abort probability could be realized by utilization of SPAN, or by scheduling the 12-day lunar landing mission during the period of declining solar activity in the middle of the next decade.
2. There appears to be no great problem in devising abort procedures that will enable the astronauts to return safely to earth if a major solar particle event occurs.
3. It might well be feasible to augment LM shielding with low weight cost, highly localized shielding using onboard water, enabling the astronauts to wait out a major solar particle event in the LM and then return to work.

APPENDIX

The purpose of this presentation was to provide qualitative answers to questions of interest to the mission planner. For this reason, the fullest possible use was made of the data analysis and dose calculations already performed by others, thereby eliminating time-consuming repetition of detail work. The main example of this was in the calculation of radiation doses in the LM.

Rather than develop a radiation dose calculation program which could calculate LM doses directly as described in Reference 7, data from this reference was used in conjunction with that supplied by R. H. Hilberg of Bellcomm, to arrive at LM dose rates indirectly. LM Peak dose rates were calculated as follows:

$$\dot{D}_{LM} = \dot{D}_{SS} \sum_{t_i} P_{LM}(t_i) D'(t_i)/D'_{SS}$$

where

$P_{LM}(t_i)$ = fraction of LM solid angle with shielding of t_i gm/cm^2. These values were taken from Figure VIII-2, supplied by R. H. Hilberg.

$D'(t_i)/D'_{SS}$ = ratio of dose under t_i gm/cm^2 shielding to dose under spacesuit shielding (0.15 gm/cm^2). These values were taken from Figure VIII-7 (Reference 7). A set of dose ratios for all t_i's was tabulated for several values of characteristic rigidity for both proton and alpha particle spectra.

$\dot{D}_{SS}$ = peak dose rate on the lunar surface under spacesuit shielding. These dose rates were taken from Reference 7.

Evaluation of the sum then gives equations of the form:

$$\dot{D}_{LM}{}^{k} = \dot{D}_{SS}{}^{k} F^{k}(R_o)$$

where

k = 1 refers to protons.

k = 2 refers to alpha particles.

$F^{k}(R_o)$ = the dose reduction factor between uniform 0.15 gm/cm^2 shielding and the shielding configuration under consideration.

The dose reduction factor as a function of characteristic rigidity is presented in Figure VIII-8 for LM shielding and for LM shielding augmented by a 0.75 gm/cm^2 water window shade.

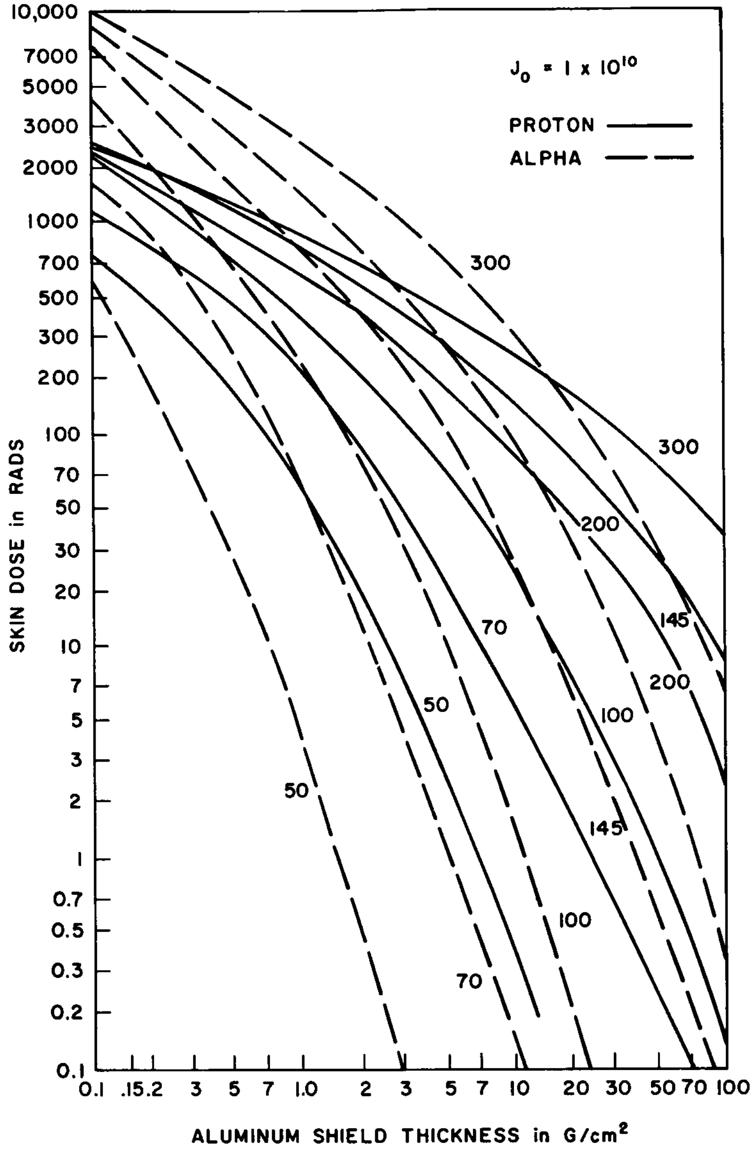

Figure VIII-7. Skin Dose as a Function of Shield Thickness for Various Values of Characteristic Rigidity, R_0

Thus, to get the peak LM proton dose rate for a particular event, the proton dose reduction factor is found from Figure VIII-8 based on the characteristic rigidity for that event, and multiplied by the peak proton dose rate under uniform 0.15 gm/cm^2 shielding for that event. The peak LM alpha dose rate is found in the same way. Then the peak LM total dose rate is given by:

$$\dot{D}_{LM} = \dot{D}^{1}_{LM} + \dot{D}^{2}_{LM}$$

The LM dose accumulated during any time interval after onset of particles is found from the peak dose rates by assuming exponential rise and decay times, t_R and t_D:

$$\dot{D}_{LM}(t) = \begin{cases} \dot{D}_{LM}\, e\left(\frac{t-t_P}{t_R}\right) & \text{for} \quad t \le t_P \\ D_{LM}\, e\left(\frac{t-t_P}{t_D}\right) & \text{for} \quad t_P \le t \end{cases}$$

where t_P is the time of peak dose rates. Then the dose accumulated in the LM between t_1 and t_2 is given by:

$$D_{LM}\left(t_1,t_2\right) = \int_{t_1}^{t_2} \dot{D}_{LM}(t)dt$$

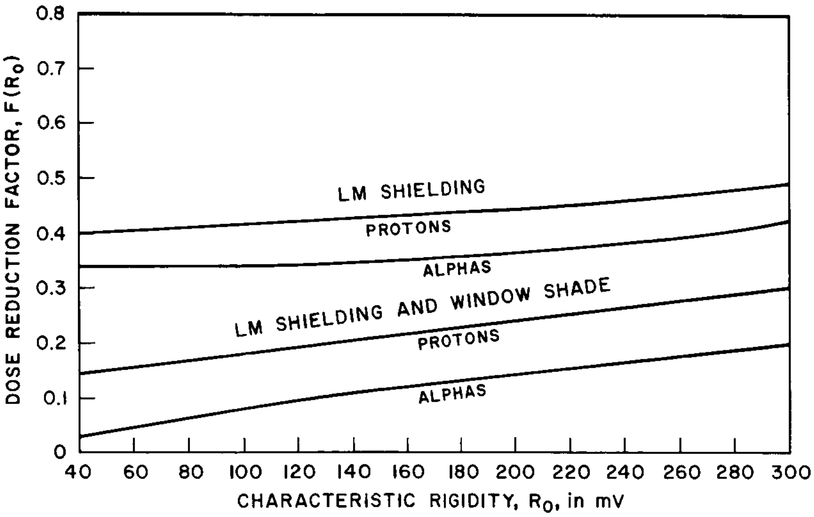

Figure VIII-8. Dose Reduction Factor as a Function of Characteristic Rigidity, R_o

REFERENCES

1. Webber, W. R. An Evaluation of the Radiation Hazard Due to Solar Particle Events, The Boeing Co., Report D2-90469.
2. Coons, D. Owen "Radiation Dose Levels for Apollo Crew Members," AS-503, Memorandum from DD/Medical Operations Office to FA/Technical Assistant for Apollo, March 1, 1967.
3. Baker, B. R. and Higgins, P. W. "The Apollo Space Radiation Warning System," NASA MSC, Presented to the Institute of Environmental Sciences, Philadelphia, Pa., April 13-15, 1964.
4. Bray, R. J. and Loughhead, R. E. Sunspots, John Wiley and Sons, Inc., 1965.
5. Apollo Extension System — LEM Phase B Final Report, V, "Shelter Design Analysis Summary," Grumman Aircraft Engineering Corp.
6. Waldo, J. E. Dependent LM and Lunar Payload Module Briefing Charts, Bellcomm, Inc.
7. Shipley, E. N. Radiation Dose Calculations, Bellcomm, Inc. TM64-1012-2.
8. Modisette, J. L., Vinson, T. M., and Hardy, A. C., Model Solar Proton Environments for Manned Spacecraft Design, NASA MSC. NASA TN D-2746.
9. Hilberg, R. H. Solar Cosmic Ray Events, Bellcomm, Inc. TR-65-340-1.

N68-84339

SECTION IX. VISIBILITY

by W. C. Meyer

1. INTRODUCTION

Difficulties in visibility on the Moon will be encountered because of lunar surface and incident light characteristics. On Earth, the light is so diffused by the atmosphere that the reflected light is substantially the same over a wide range of viewing angles and sun angles, and its surface reflects many color and intensity variations for different materials. Lunar conditions, however, lack these favorable characteristics. In this study, the visibility restrictions that limit man's effectiveness during lunar explorations are investigated. The results of introducing these restrictions into simulated mobility traverses on a computer-generated lunar surface are also described.

Visibility on the lunar surface is affected by:

1. Shadows cast by both the viewer and the objects being viewed.
2. The contrast in levels of light reflected from different surface materials.
3. The contrast in levels of light reflected from different surface slopes.
4. The size of the objects being viewed.
5. The presence of glare under certain viewing conditions.

A shadowed area, being almost completely devoid of light, provides maximum contrast against an illuminated background, but within the shadow itself nothing is visible. Shadows are most significant at the low sun angles early in the lunar day (during the landing phase) and very late in the lunar day (most likely after departure of the men from the lunar surface). Therefore, they will have little effect on the astronaut's ability to perform his tasks while on the surface.

Observations made from Earth, Orbiters, and Surveyors indicate that contrasts among different materials are probably not an important factor even for close observation. But contrast produced by different surface slopes is important to lunar visual perception, and its effect is the main subject of this discussion.

Under given lighting conditions, object size and contrast together determine an observer's ability to detect an object. Generally, for a fixed level of light, the relationship exists whereby the larger the object, the less the contrast that is necessary to detect it. However, a contrast threshold exists below which this relationship no longer holds, and the ability to detect an object is unimproved for targets of larger size. In this study the size of objects large enough to be a hazard to the astronaut (see Section V) is used to determine the lower limit of acceptable contrast.

The sun constitutes a glare source of tremendous magnitude when it appears in the field of view, either directly or in reflection from a surface such as the highly polished metallic surface of the Lunar Module. For purposes of this study, it is assumed that the adverse effects from glare are countered by the design of the spacesuit visor.

2. CONTRAST CALCULATIONS

The contrast of a surface slope may be calculated with respect to the horizontal background surface as follows (Reference 1)*:

$$C = \frac{L_S - L_B}{L_B}$$

where

C is the contrast.

L_S is the luminance of the sloping surface.

L_B is the luminance of the background surface.

The luminance values are determined from a photometric function developed from measurements of the lunar surface. This function relates reflectance from the lunar surface to two angles determined from the geometry of the viewing. The function used in this study is the so-called Lunar Reflectivity Model (References 1 and 2). A 10-degree sloping surface is used in the calculations since it appears reasonably within the range of surface slopes expected for raised crater rims, the walls of craters, the face of rocks, and other potential hazards on the lunar surface. However, the actual value of the slope is not too important in drawing the general conclusions which are significant in mission planning.

A study conducted by Bellcomm, Inc., (Reference 3) used contrast calculations based upon 10-degree slopes to investigate visibility of the lunar surface during the landing of LM. The results of the above study are in substantial agreement with two comprehensive analytical studies which accounted for both the geometric shadow and the area of the object being viewed (Reference 1).

Figure IX-1 shows the geometry for the special viewing conditions where the observer's line of sight, the sun's incidence vector, and the normal to the sloping surface all lie in the same plane. The two angles required for use on the photometric function are PHASE and TAU. PHASE is the angle between the observer's line of sight and the sun's incidence vector. TAU is the angle between the observer's line of sight and the normal to the surface being viewed. The sign of TAU is positive if the line of sight lies between the surface normal and the sun's incidence vector; otherwise TAU is negative. Figure 4 of Reference 2 shows the photometric function which gives a brightness factor (proportional to luminance) in terms of TAU and PHASE. A computer program designed to calculate contrast based upon this figure has tabled values of the brightness factor at the points of intersection of the constant PHASE curves with 19 values of TAU. Figure IX-2 shows the photometric function as generated from the table of this computer program.

---

*References are listed at the end of the section.

The brightness factor is determined from the table based upon calculations of TAU and PHASE both for the 10-degree slope and for the background, and the contrast is then calculated with the above equation. These contrast data can be organized and presented in several forms. Since sun position remains relatively fixed for the short periods that an observer spends in moving about on the lunar surface, it seems natural to organize the data for a fixed elevation angle of the sun, while varying the observer's viewing angle for different azimuths with respect to the sun's position. Both the computer program printouts and the various microfilm plots are presented in this basic form for a fixed sun elevation angle, presenting contrast versus viewing angle (or object distance) with azimuth as the parameter.

Before proceeding to a discussion of the data, the geometry of the physical situation shown in Figure IX-1 is presented in its more general form in Figure IX-3. The special condition of Figure IX-2, where the observer's line of sight and the sun's incidence vector are coplanar with the surface normal occurs only for azimuth 0 (sun behind observer) and 180 degrees (observer facing into sun). For the general case, PHASE is defined as the angle between the line-of-sight vector and the sun's incidence vector and is measured in the phase plane formed by these two vectors. The surface normal is projected into the phase plane and angle TAU is measured between this projection and the line-of-sight vector. The sign of TAU is positive only if the line of sight falls between the sun's incidence vector and the projection of the surface normal into the phase plane.

3. LUNAR SURFACE VISIBILITY

3.1 General Considerations

For one type of data presentation, contrasts were categorized in a qualitative manner as: Poor for values up to 0.02; Fair for values between 0.02 and 0.10; and Good for values greater than 0.10. Reference 3 provides some justification for such categories based upon evaluation of pictures taken of a lunar-surface model under different viewing conditions. In connection with the present study, a lunar-surface model was also produced. This model was made up of several different sized obstacles (craters, slopes, rocks, rilles), and it was dusted with cupric oxide to simulate

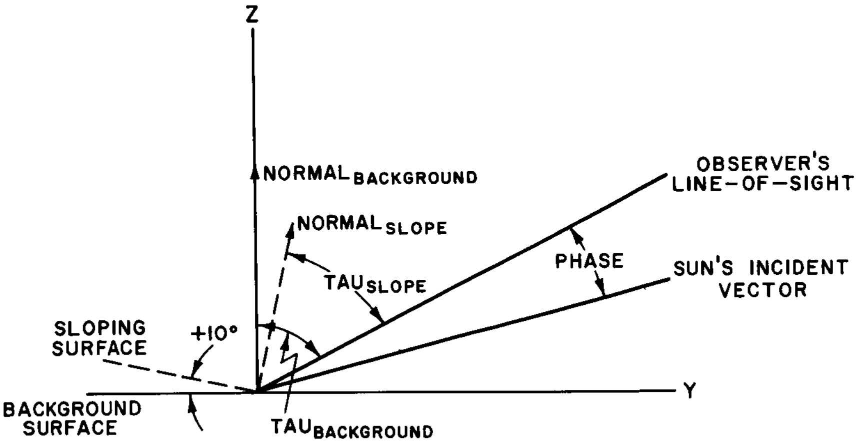
Z
NORMAL$_{BACKGROUND}$
NORMAL$_{SLOPE}$
OBSERVER'S LINE-OF-SIGHT
PHASE
SUN'S INCIDENT VECTOR
TAU$_{SLOPE}$
SLOPING SURFACE
+10°
Y
BACKGROUND SURFACE
TAU$_{BACKGROUND}$

Figure IX-1. Geometry for Inplane Viewing Conditions

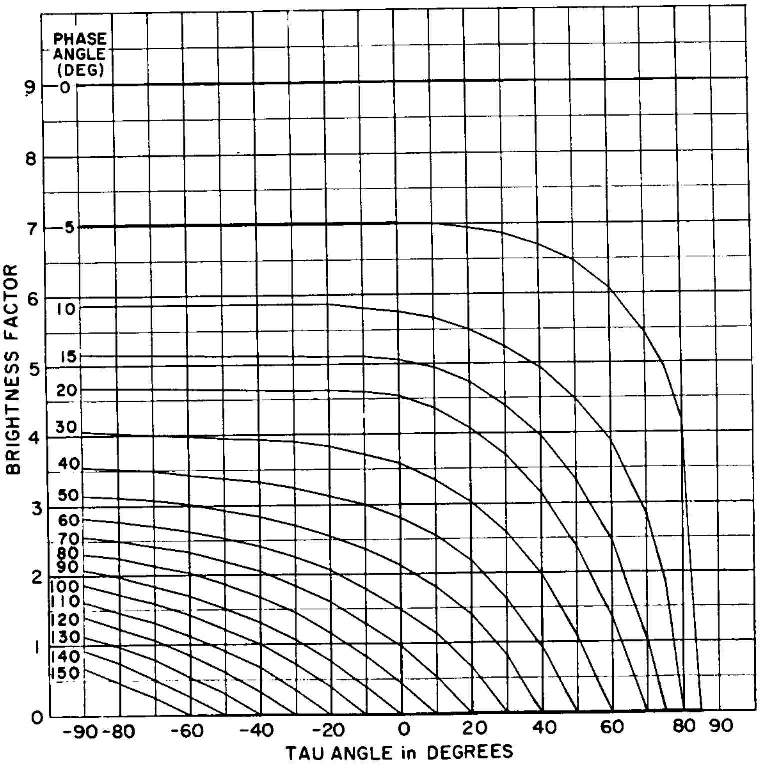

Figure IX-2. Photometric Function

the photometric function. Photographs taken of this model under different viewing conditions also generally corroborate the Poor-Fair-Good gradations presented in the various data plots.

Both the size of the object being viewed and the contrast between it and the background surface will determine whether or not the object can be seen. This is of particular interest for objects large enough to be a hazard to the mobility of the astronaut on the lunar surface. Visibility data referred to as the "Blackwell-Tiffany Data" (see References 1, 4 and 5) provide the relationship between contrast and object size at several fixed levels of lighting. Figure IX-4 relates these data to the size of hazardous objects as viewed from different distances. With reference first to the plot of angular subtense (object size) versus viewing contrast, it is noted that up to a point the larger the object size, the less the contrast needed to detect the object. However, detection of objects subtending arcs greater than about 30 minutes of arc require essentially the same minimum value of viewing contrast. Reference 3 gives a qualitative rating for the brightness levels in foot-Lamberts as follows: "1000 foot-Lamberts correspond to the brightness one experiences in full daylight; 100 foot-Lamberts, an overcast day; 10 foot-Lamberts, a very dark day; and 1 foot-Lambert corresponds approximately to twilight." Lighting conditions facing the astronaut during exploration will certainly be of the brightest variety, and from Figure IX-4, the contrast threshold will therefore be somewhat less than 0.003. The left-hand portion of the illustration plots the angular subtense of objects defined as hazards versus the distance of the viewer from the objects. The 6-foot viewing height corresponds to an astronaut walking and the 8-foot height corresponds to his riding. The area of the crater opening visible to the astronaut was converted to an equivalent circular area for the purpose of determining angular subtense. The rock was assumed to present a circular area to the viewer. Figure IX-4 shows these hazardous objects to be of the size associated with the minimum threshold contrast. Effectively, this means that, under laboratory conditions, 50-percent correct detection of hazardous objects can be attained at the minimum contrast of 0.003 under the brightest lighting conditions. To compensate for the poorer visibility performance which must be expected under field conditions outside of the laboratory, the contrast data must be modified by field factors. There is no general agreement upon all the various factors which ought to be included, much less their individual magnitudes. References 1 and 4 discuss field factors and include examples of their use. Individual items mentioned include the observer's knowledge of object location; uniformity of background; the time to expect its occurrence; observer's level of vigilance; the effects of training, glare, vibration; and a factor necessary to convert to higher than the 50-percent correct detection level. One contrast study using a crater model (Reference 1) used a total field factor of 18;

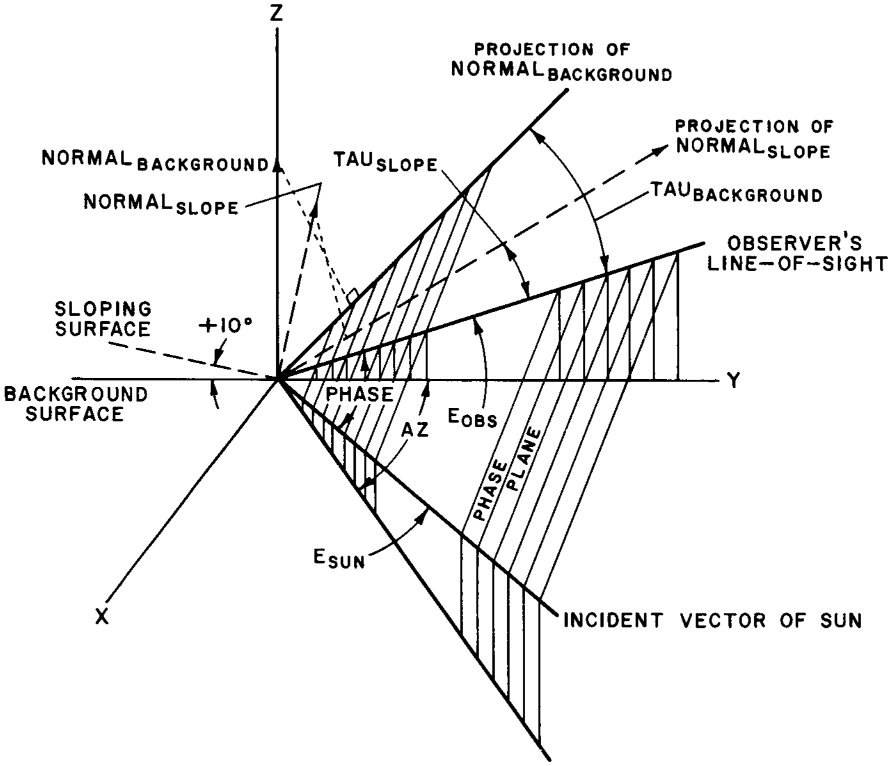
Z
PROJECTION OF NORMAL$_{BACKGROUND}$
PROJECTION OF NORMAL$_{SLOPE}$
NORMAL$_{BACKGROUND}$
TAU$_{SLOPE}$
NORMAL$_{SLOPE}$
TAU$_{BACKGROUND}$
OBSERVER'S LINE-OF-SIGHT
SLOPING SURFACE
+10°
BACKGROUND SURFACE
Y
PHASE
AZ
E$_{OBS}$
PHASE PLANE
E$_{SUN}$
X
INCIDENT VECTOR OF SUN

Figure IX-3. Geometry for General Viewing Conditions

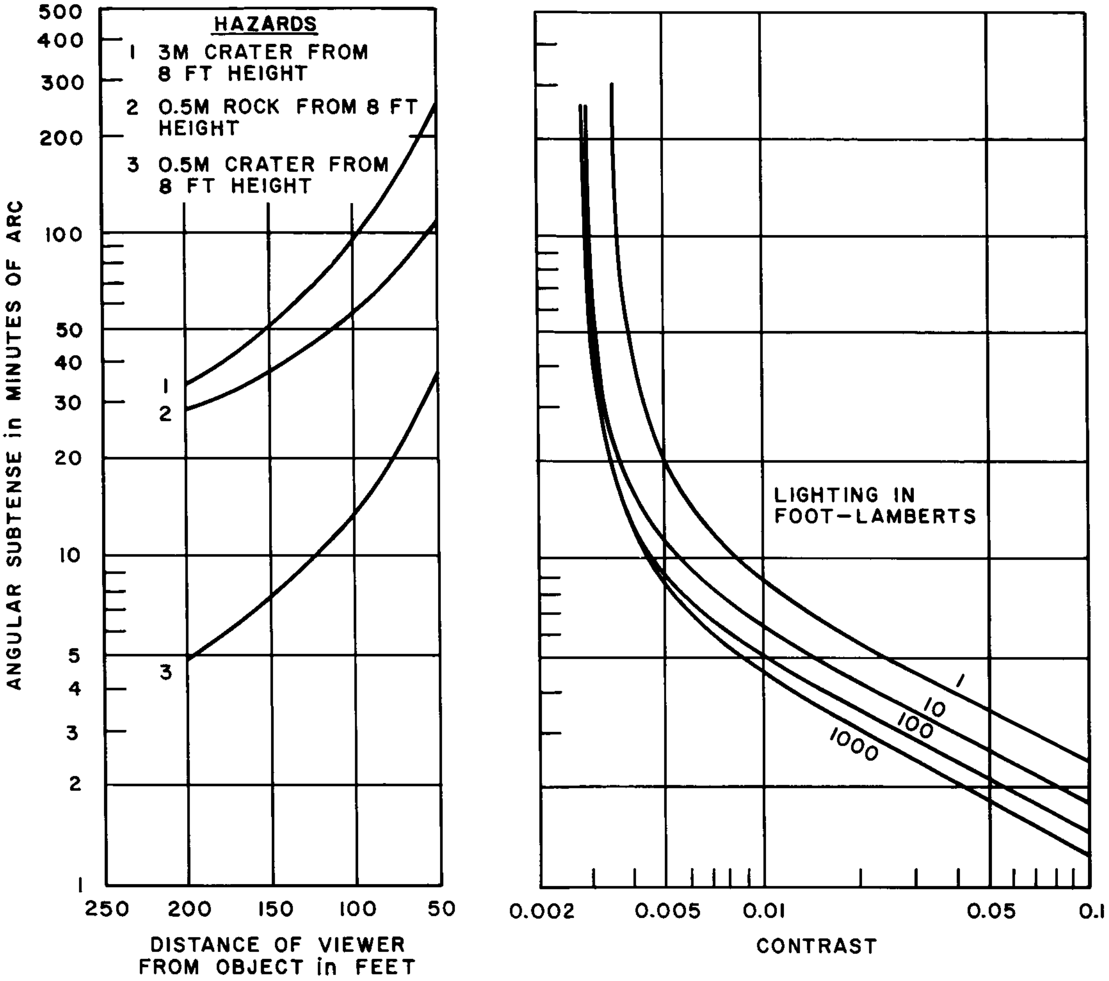

Figure IX-4. Contrast Developed from Hazards at a Given Distance

an example in Reference 4 uses one of 12. Both of these include a factor for converting the 50-percent level to at least 95. At the 50-percent level, this total factor would be in the order of 9 and 7 respectively for the two examples. If these factors are applied to the contrast of 0.003, the statement concerning hazardous conditions may be restated. Effectively, now under field conditions, 50-percent correct detection of hazardous objects can be attained at contrasts of 0.02 or 0.03 under the brightest lighting conditions. Thus, on the assumption that the field factors are representative, the selection of 0.02 as the boundary between Poor and Fair visibility at least seems reasonable.

3.2 Results of Contrast Calculations

Figures IX-5 through IX-7 are data plots produced on the computer as an aid in determining the effects of limited visibility upon traverses made over the computer-generated lunar surface described in Section V. For a fixed sun elevation angle the data are plotted along several azimuths out to a predetermined range with special characters (X, •, G) denoting contrast as being Poor, Fair, Good. These particular plots are for ranges out to 100 meters (328 feet). The observer is located at the center of the plot at a height of 8 feet, which is estimated to be his height while sitting in the lunar surface vehicle. These particular patterns were used as overlays on the computer-generated lunar surface maps for simulated LSSM (Local Scientific Survey Module) traverses. The Fair and Good regions were cut away and the opaque Poor region remained as a simulation of the poor visibility to be encountered in that particular section. In general, it is seen that with the viewer facing away from the sun, and with a sun angle of 15 degrees (Figure IX-5), contrasts are Poor for the angular sector of about ±40 degrees in azimuth. With the viewer facing into the sun (azimuth=180) the contrasts are Good for azimuths of 180 ± 105 degrees. With increasing sun elevation angles, the patterns are seen to change with both the Good and the Poor areas shrinking and changing over to Fair as the angles increase to 75 and 90 degrees.

In addition to the LSSM traverses, some walking traverses were also simulated on lunar surface maps generated with an expanded scale. A set of contrast patterns with a scale ranging to 23 meters (75 feet) is shown in Figures IX-8 through IX-10, which are simply expansions of the close-in region of the previous plots. Figure IX-9 (30-degree sun elevation) is also marked at three points which correspond to the approximate viewing conditions under which three photographs (Figures IX-11 through IX-13) of the lunar-surface model were taken. These pictures, which are only in sharp focus just in front of the large crater, generally corroborate the gradations of Poor-Fair-Good on Figure IX-9. In each of the remaining groups of figures, the 30-degree sun elevation plot is also marked at the three points corresponding to the three photographs.

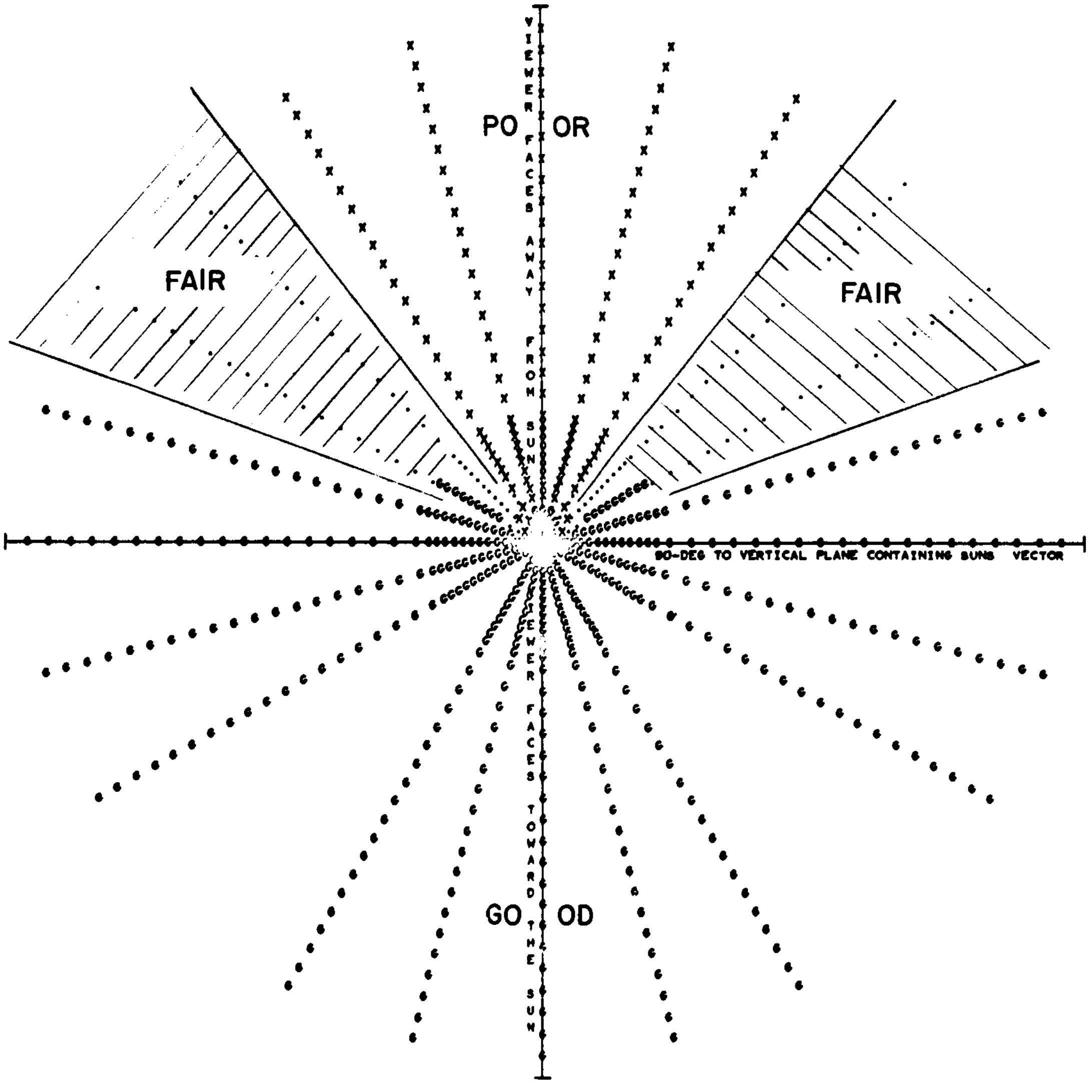
VIEWER FACES AWAY FROM SUN
POOR
FAIR
FAIR
90-DEG TO VERTICAL PLANE CONTAINING SUNS VECTOR
VIEWER FACES TOWARD THE SUN
GOOD

Figure IX-5. Visibility Contrast
15-Degree Sun Elevation Angle
View Out to 100 Meters
Observer's Height, 8 Feet

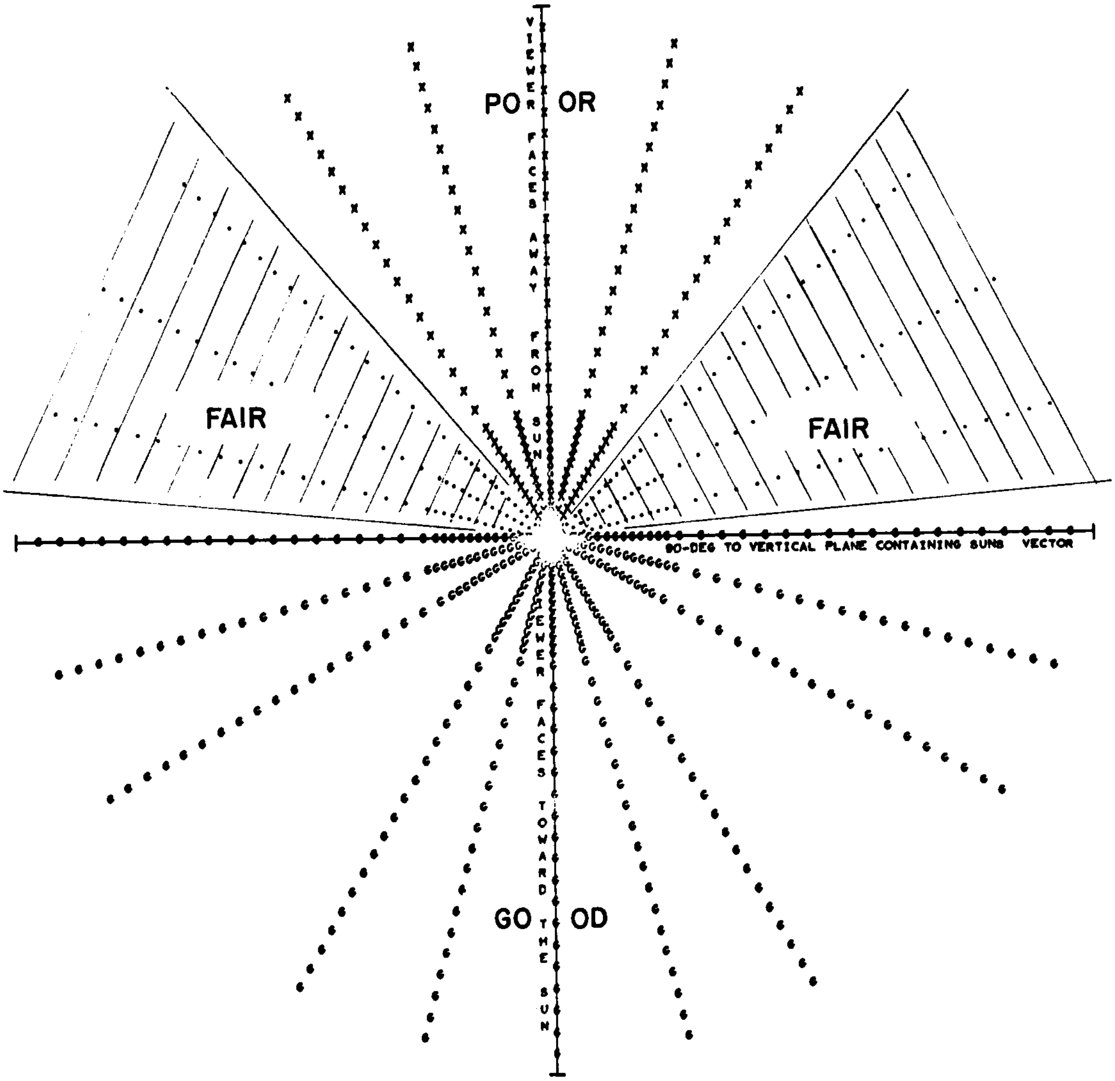

Figure IX-6. Visibility Contrast
30-Degree Sun Elevation Angle
View Out to 100 Meters
Observer's Height, 8 Feet

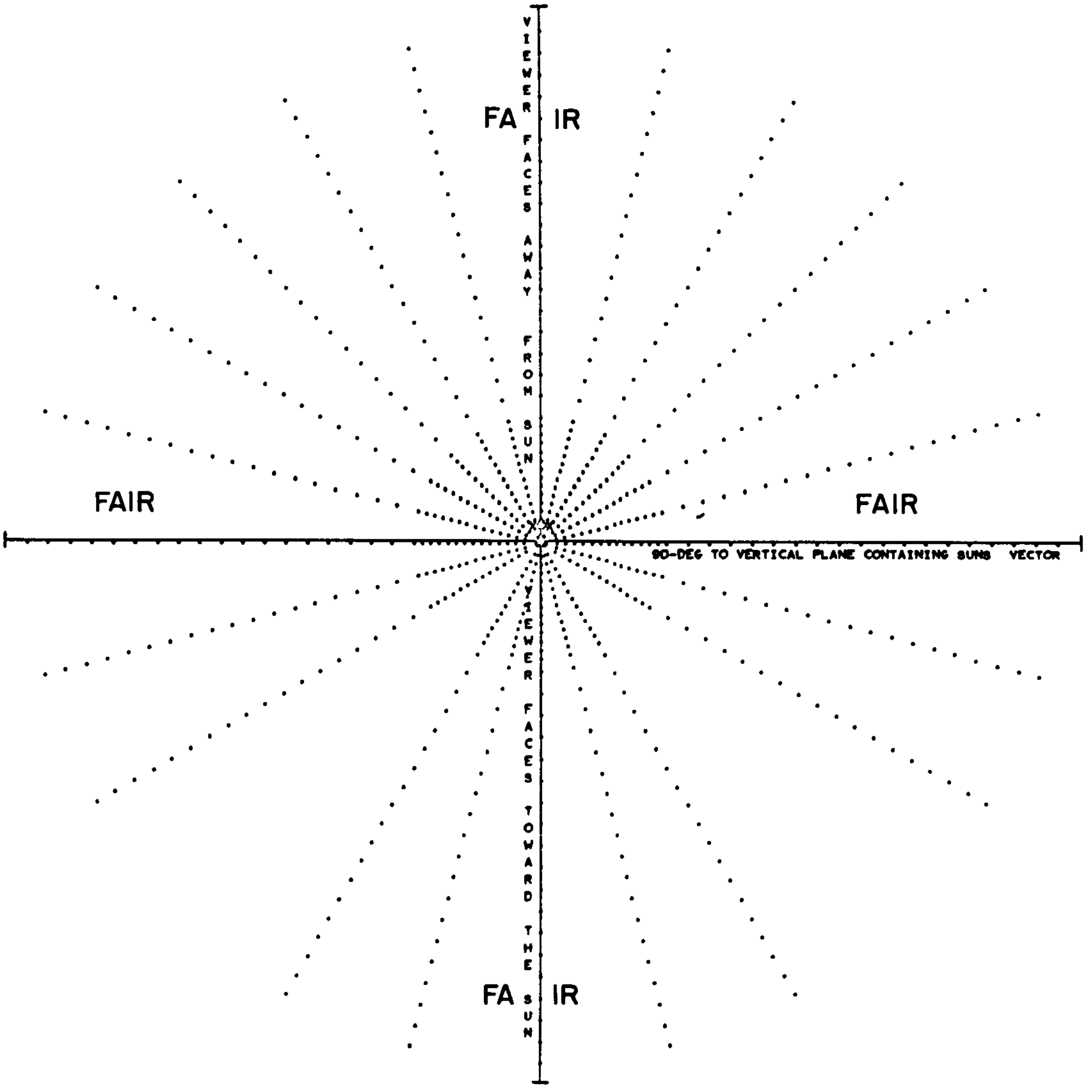
VIEWER FACES AWAY FROM SUN
FA IR
FAIR
FAIR
90-DEG TO VERTICAL PLANE CONTAINING SUNS VECTOR
VIEWER FACES TOWARD THE SUN
FA IR

Figure IX-7. Visibility Contrast
75-Degree Sun Elevation Angle
View Out to 100 Meters
Observer's Height, 8 Feet

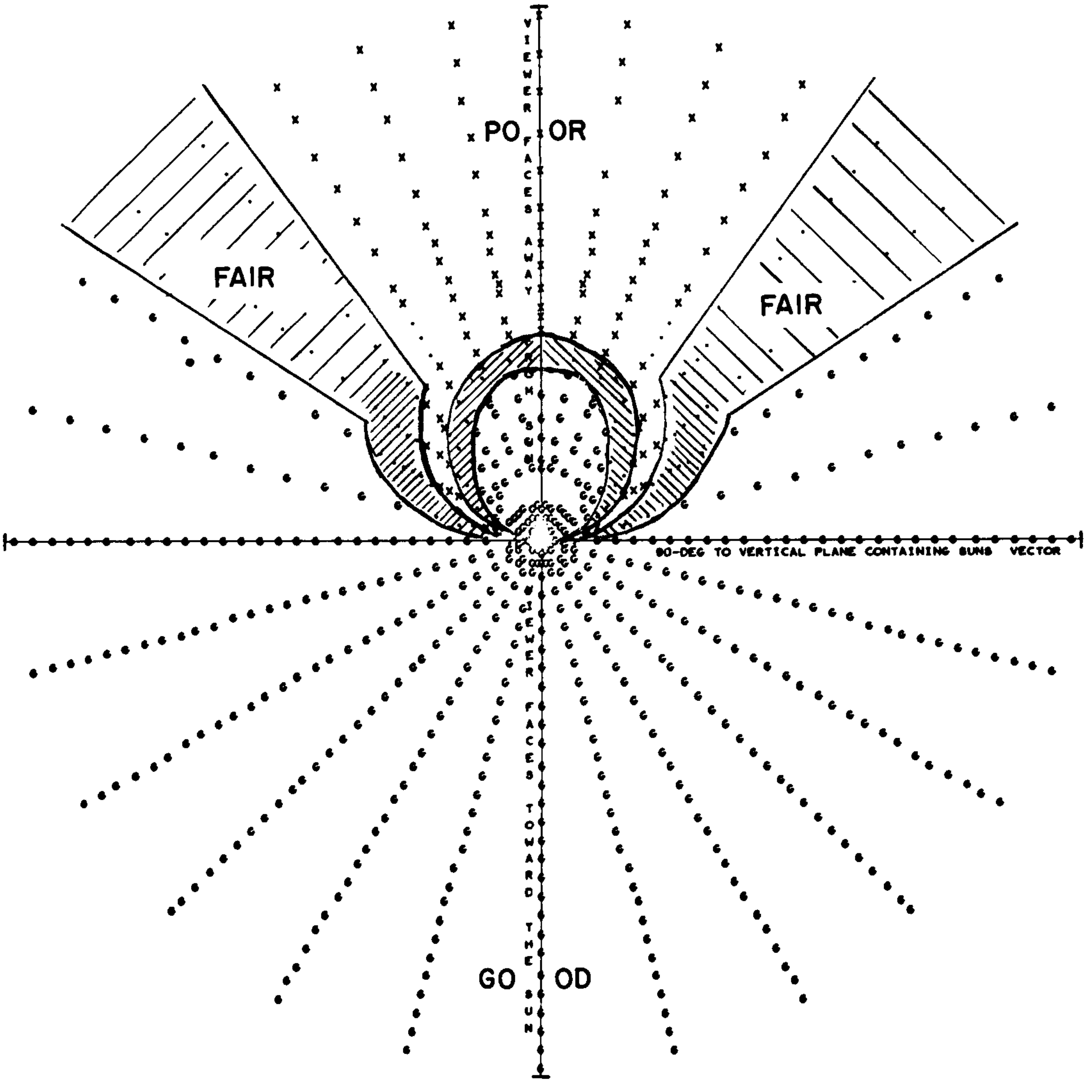

Figure IX-8. Visibility Contrast
15-Degree Sun Elevation Angle
View Out to 23 Meters
Observer's Height, 8 Feet

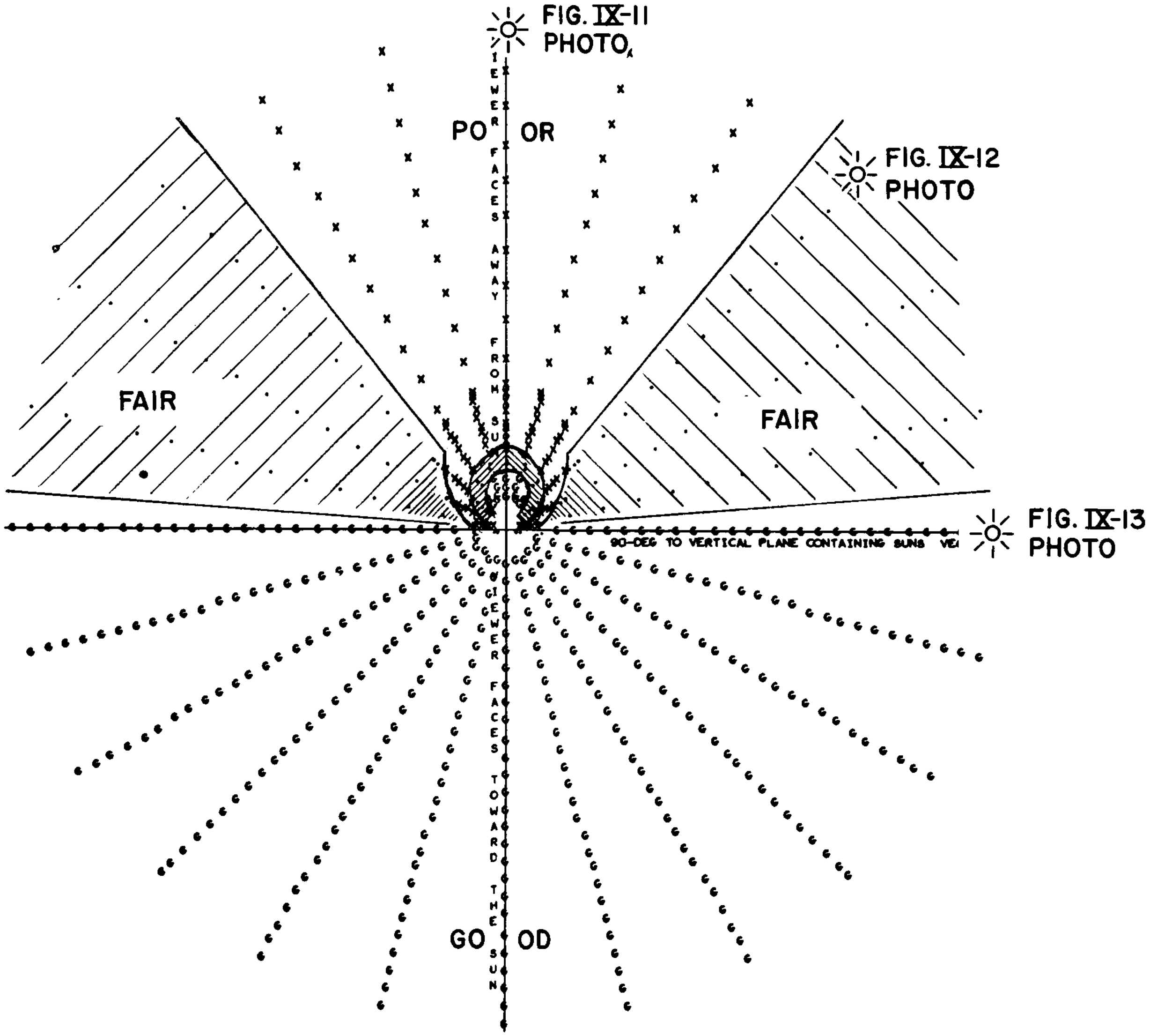
FIG. IX-11
PHOTO
IEWER FACES AWAY FROM SU
POOR
FIG. IX-12
PHOTO
FAIR
FAIR
FIG. IX-13
PHOTO
90-DEG TO VERTICAL PLANE CONTAINING SUNS VE
IEWER FACES TOWARD THE SUN
GOOD

Figure IX-9. Visibility Contrast
30-Degree Sun Elevation Angle
View Out to 23 Meters
Observer's Height, 8 Feet

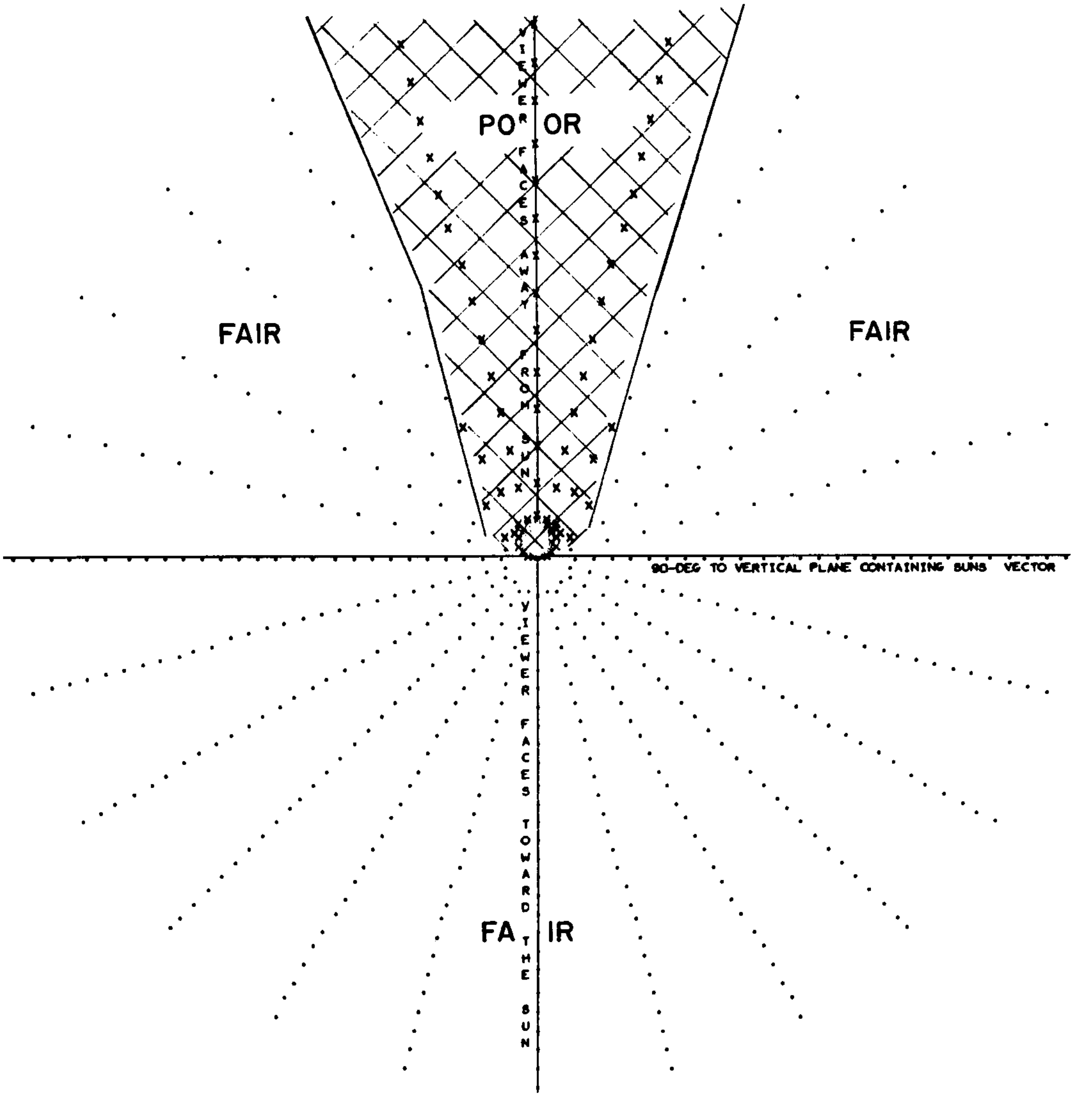
VIEWER FACES AWAY FROM SUN
POOR
FAIR
FAIR
90-DEG TO VERTICAL PLANE CONTAINING SUNS VECTOR
VIEWER FACES TOWARD THE SUN
FAIR

Figure IX-10. Visibility Contrast
65-Degree Sun Elevation Angle
View Out to 23 Meters
Observer's Height, 8 Feet

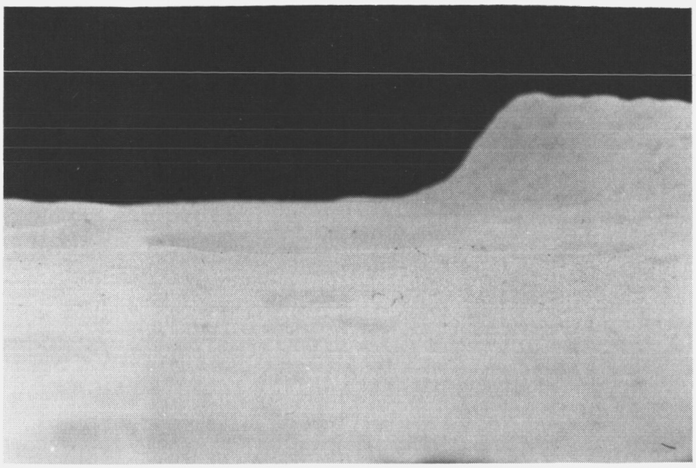

Figure IX-11. Viewing
Azimuth = 0 Degree

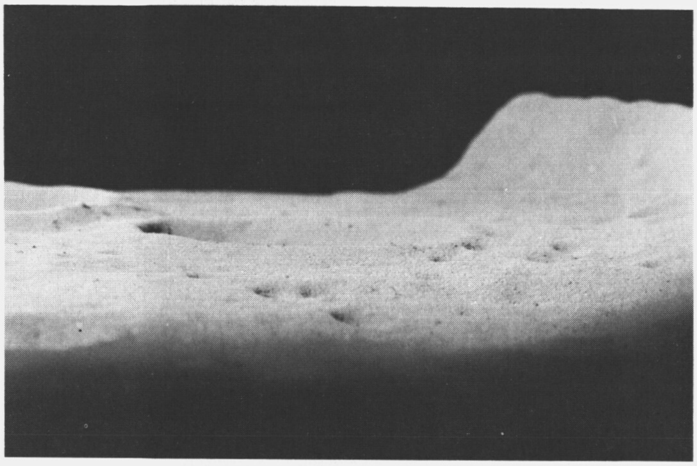

Figure IX-12. Viewing
Azimuth = 45 Degrees

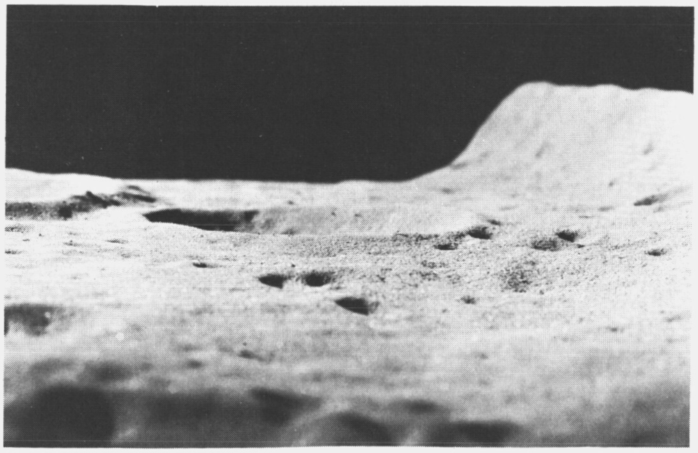

Figure IX-13. Viewing
Azimuth = 90 Degrees

Photographs of
Lunar Surface Model
30-Degree Sun Elevation Angle

Figures IX-8 and IX-9 show an anomaly close to the viewer. Along certain viewing azimuths in the sector 0 ± 90 degrees, the contrast conditions can vary over the full range of Good-Fair-Poor and all within a relatively short distance from the observer. This transition is more clearly apparent in the Figures IX-14 through IX-16 which plot the actual contrast values versus the distance from the observer along the lunar surface to the point being viewed. Along an azimuth less than 90 degrees, a sharp drop (or "null") in contrast is exhibited, its point of occurrence depending upon sun elevation angle. For the case of azimuth of 0 degrees which places the sun directly behind the viewer, the sharp drop from the Good to the null region occurs when the observer's line of sight and the sun's incidence vector coincide. This results in PHASE = 0 degrees which, as can be seen from the photometric function of Figure IX-2, in turn results in the same brightness independent of TAU. Thus, the contrast is zero for any slope relative to the background. For azimuths other than 0 degrees, it is obvious from Figure IX-3 that the line of sight and the sun's incidence vector cannot coincide, but nevertheless the Figures IX-14 through IX-16 show that a null point does exist. For these azimuths the null occurs when the normal to the background surface and the normal to the 10-degree sloping surface have projections which are coincident in the phase plane i.e., the two respective TAU angles are equal. To illustrate this point, the difference of the two TAU angles versus viewing angle is plotted on Figures IX-17 through IX-19, and on Figures IX-20 through IX-22, contrast is plotted also versus viewing angle. These show that the contrast null occurs at the same viewing angle that the zero TAU difference occurs. The surface normal projections are coincident when the plane formed by the two normals is perpendicular to the phase plane. Since, for the particular orientation of the 10-degree slope chosen for this study (Figure IX-3), the two surface normals and the observer's line of sight are all in the Y-Z plane, zero TAU difference always occurs for TAU equal zero. If this orientation were fixed at a different position, zero TAU difference would always occur at some other fixed value of TAU.

Since the computations are for the very specific conditions of a 10-degree sloping surface at a particular orientation (sloping toward the viewer), little significance can be attached to the particular location of contrast nulls on the data plots. In spite of this close-in anomoly, the general conclusion that contrast values are better along the azimuths where the viewer faces into the sun as compared to those where the viewer faces away from the sun is valid. In general, a low-contrast (or "washout") region exists in a sector centered along the 0-degree azimuth, and contrasts become progressively better as azimuth is increased to 180 degrees (viewer facing directly into sun).

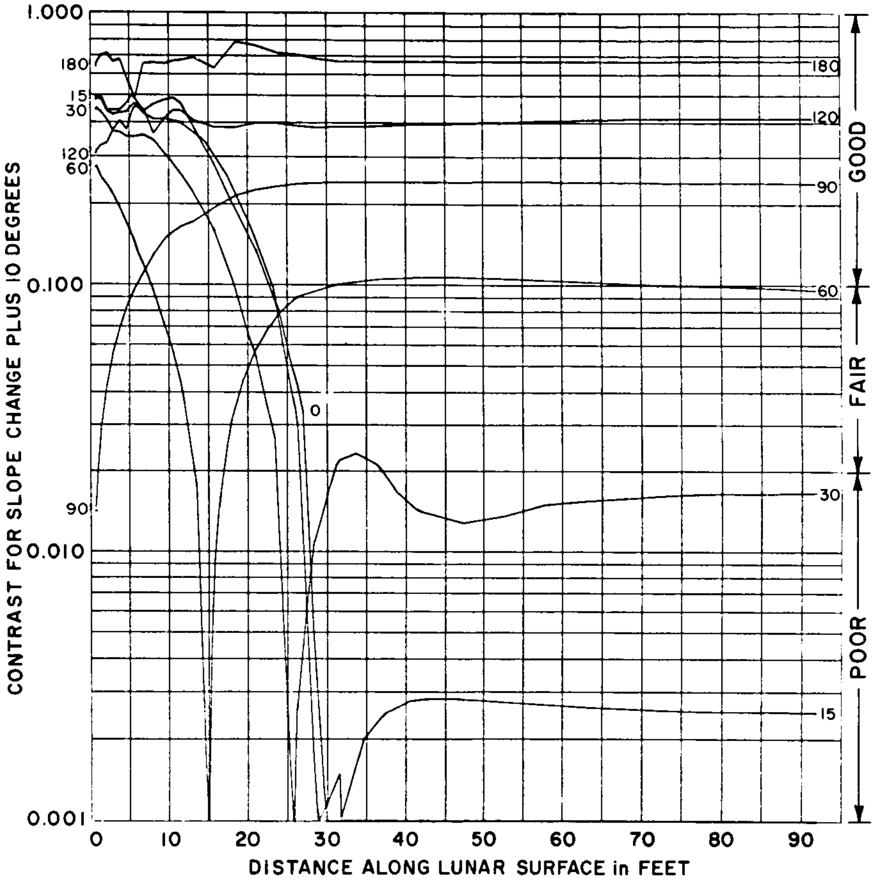

Figure IX-14. Visibility Contrast versus Distance
15-Degree Sun Elevation Angle
Observer's Height, 8 Feet

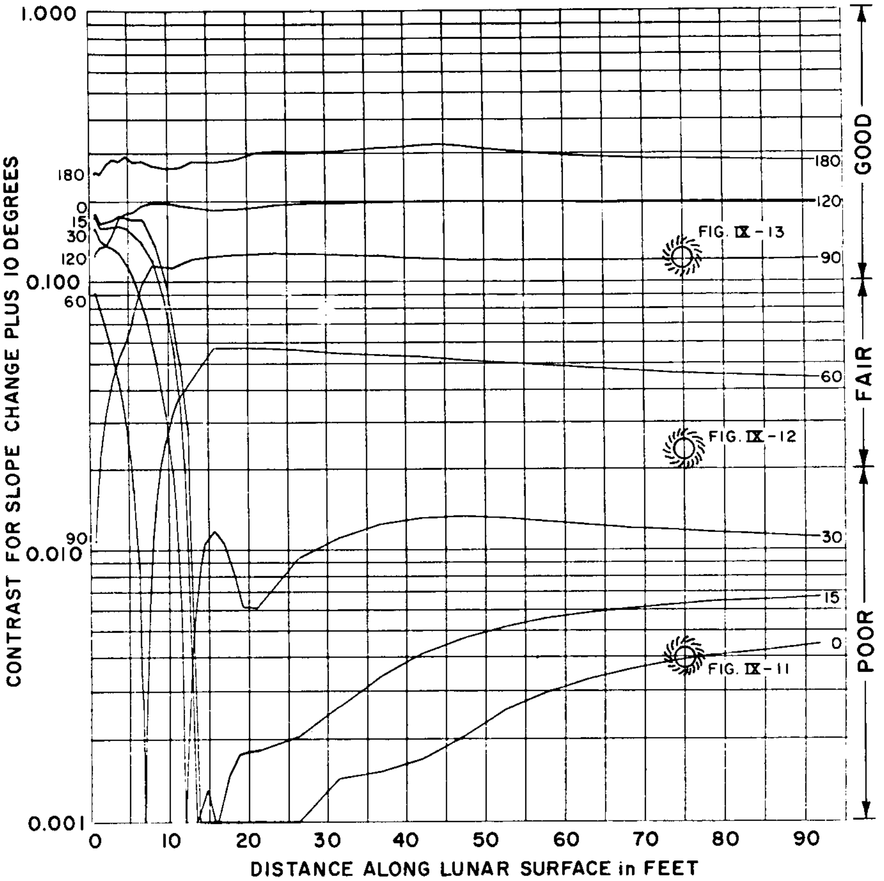

Figure IX-15. Visibility Contrast versus Distance
30-Degree Sun Elevation Angle
Observer's Height, 8 Feet

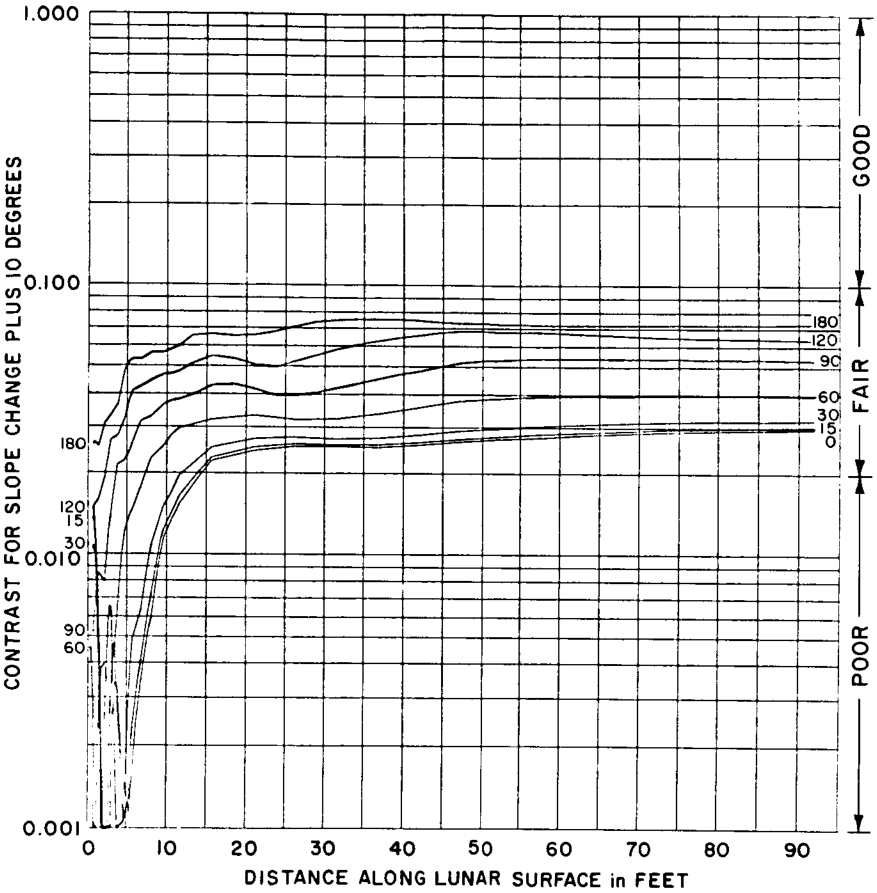

Figure IX-16. Visibility Contrast versus Distance
75-Degree Sun Elevation Angle
Observer's Height, 8 Feet

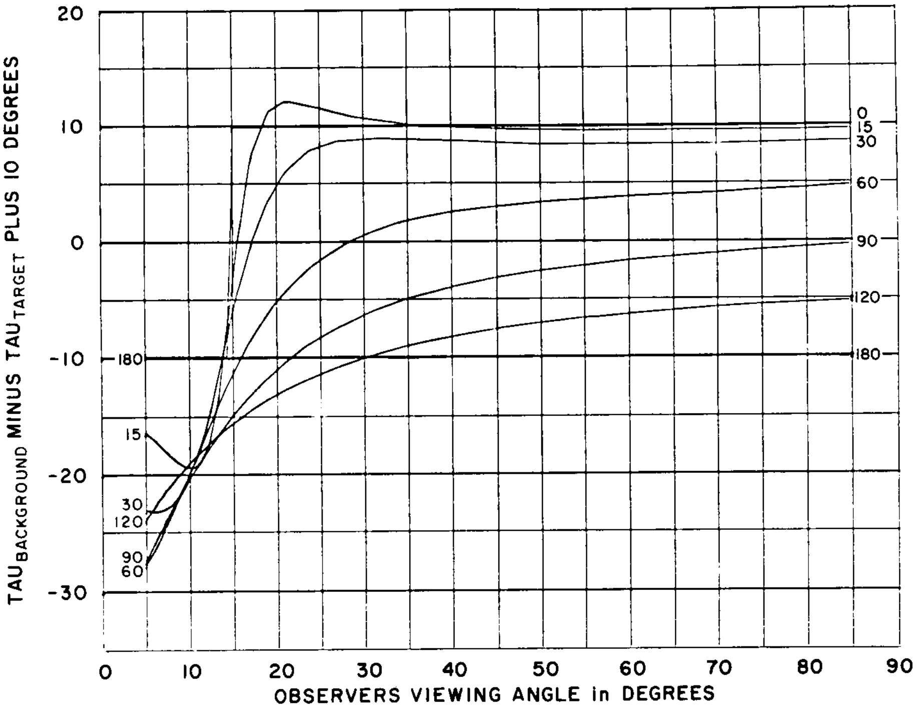

Figure IX-17. TAU Difference versus Observer's Viewing Angle 15-Degree Sun Elevation Angle

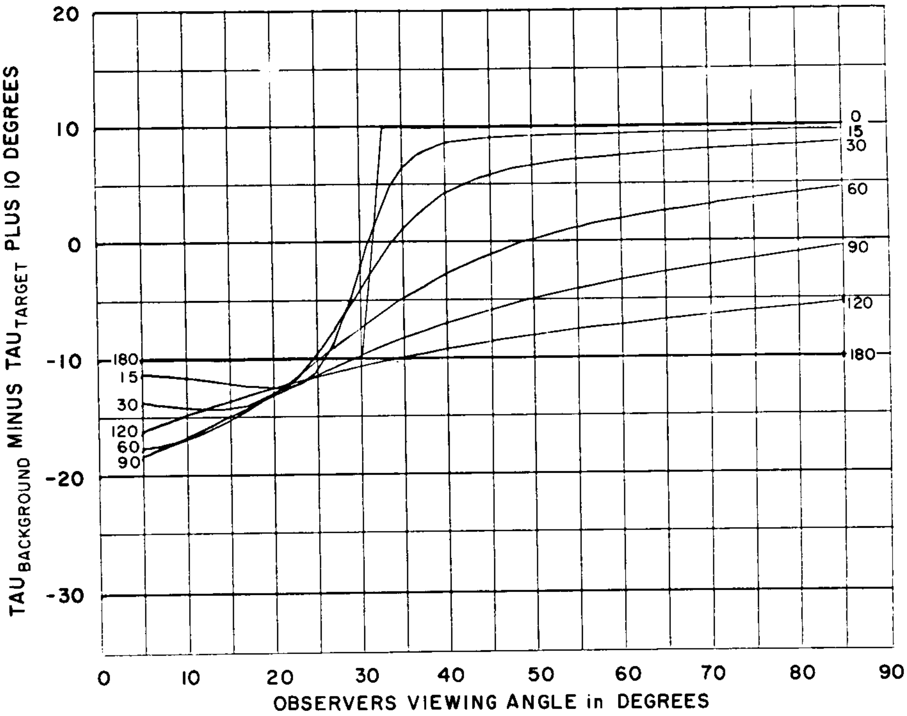

Figure IX-18. TAU Difference versus Observer's Viewing Angle 30-Degree Sun Elevation Angle

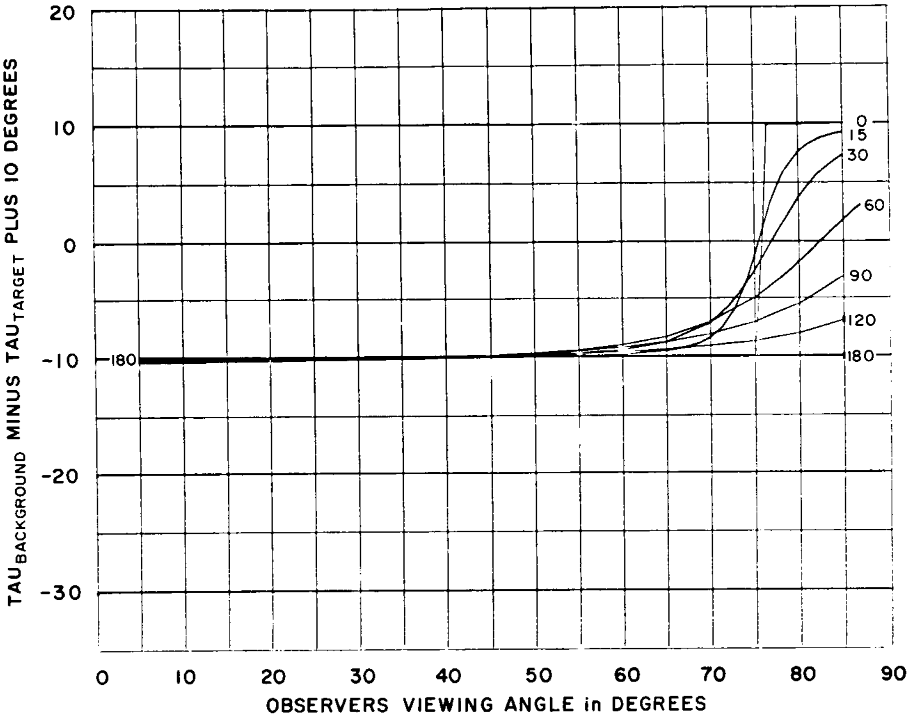

Figure IX-19. TAU Difference
versus Observer's Viewing Angle
75-Degree Sun Elevation Angle

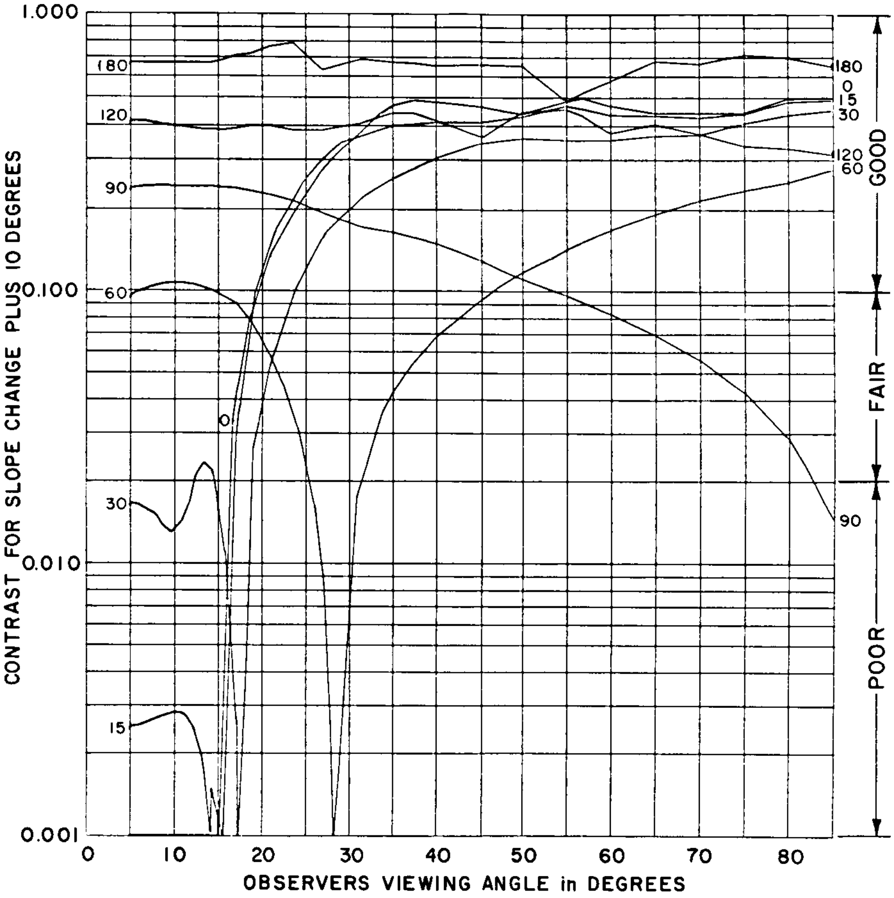

Figure IX-20. Visibility Contrast versus Observer's Viewing Angle 15-Degree Sun Elevation Angle

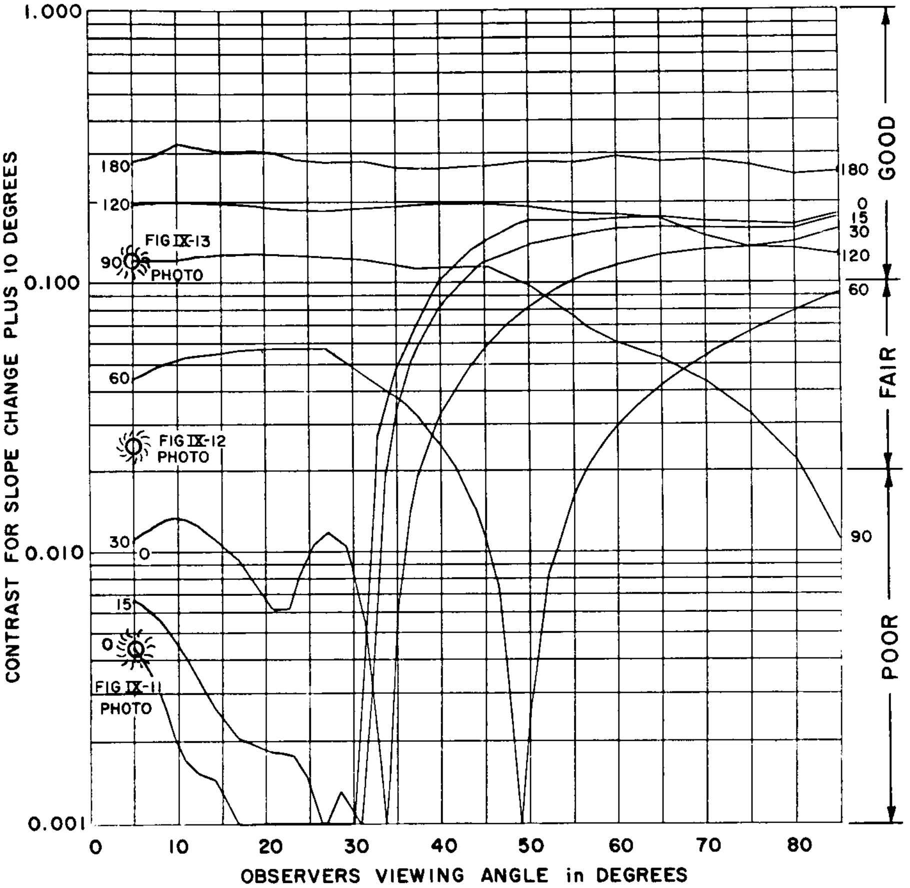

Figure IX-21. Visibility Contrast versus Observer's Viewing Angle 30-Degree Sun Elevation Angle

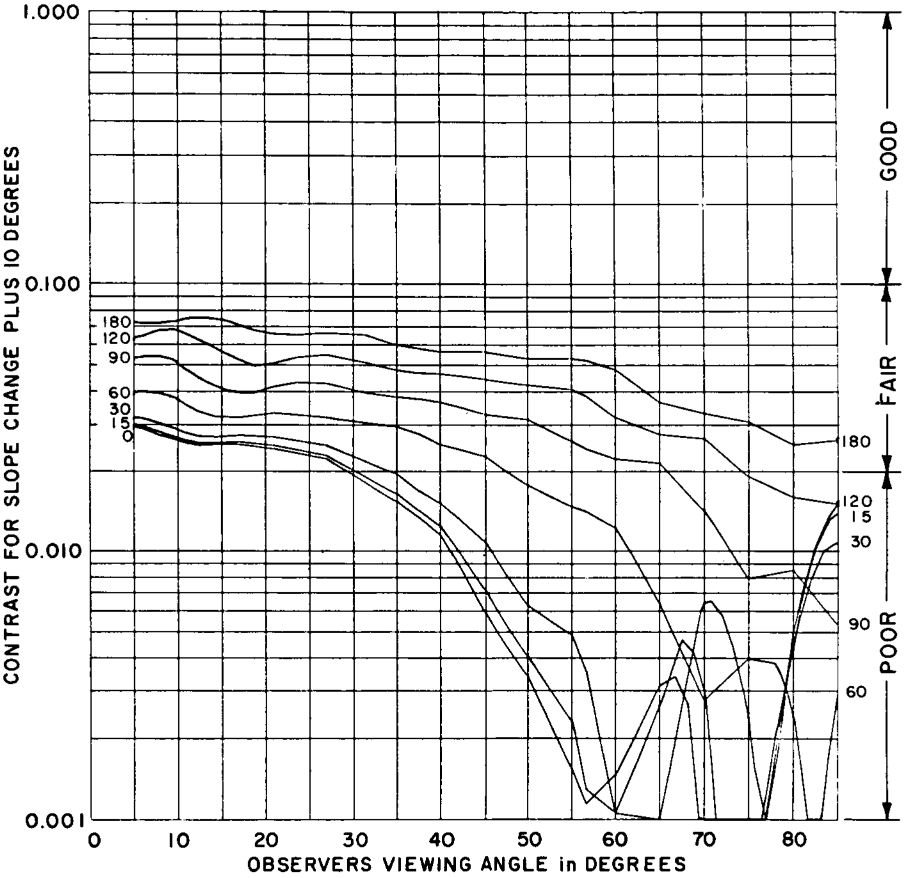

Figure IX-22. Visibility Contrast
versus Observer's Viewing Angle
75-Degree Sun Elevation Angle

The plots of TAU difference (Figures IX-17 through IX-19) point up a misconception which has appeared in the literature where a lunar-surface-slope-change is equivalenced directly to a TAU difference. But such equivalence is valid only for viewing azimuths of 0 and 180 degrees where, for example, the surface slope of 10 degrees results in a TAU difference of 10 degrees. However, Figure IX-17 shows that at azimuths of 60 to 90 degrees, the 10-degree slope may result in a TAU difference as high as 30 degrees.

The next series of computer plots in Figures IX-23 through IX-26 show the qualitative Good, Fair, and Poor gradations plotted on the computer-generated photometric function with viewing azimuth again as the parameter. A string of the visibility characters (G, ·, X) is shown for each azimuth with the particular azimuth identified along the τ = -40-degree line. The points are plotted at the TAU and PHASE angles corresponding to the background surface. These figures focus attention on the area of the photometric function actually used in determining contrast. This area is bounded by the 0- and 180-degree azimuth contours for each sun elevation angle, and a particular point within the area is uniquely determined from the positions of viewer and sun. However, the contrast at each point will be dependent upon surface slope which in this case is 10 degrees. The operating area decreases with increasing sun elevation angle, and with this angle at 90 degrees (Figure IX-26), operation is restricted along a single line. Since the photometric function has been derived from direct lunar photoelectric observation (see Reference 2), such figures could also serve to focus attention upon areas where additional physical measurements may be desirable to better determine the shape of this function.

Although for a given sun elevation angle, the positions of sun and viewer determine a unique position on the photometric function, the contrast calculated need not be the same at the same coordinate for different sun angles as is assumed in some of the literature on the subject. In other words, a single plot of the photometric function (Figure IX-2) when marked into Poor-Fair-Good regions (or equal contrast contours) is strictly valid only for a single sun elevation angle.

Figures IX-23 through IX-26 also point to the misconception mentioned earlier which equivalences a lunar-slope change directly to a TAU difference. In terms of the photometric function, this equivalence allows interpreting contrast in terms of the shape of the constant PHASE curves where a region of greater slope on the curve means a greater brightness difference over the assumed constant 10-degree TAU difference and, hence, is equivalent to a greater contrast. However, as noted earlier a 10-degree TAU difference cannot be assumed to result from a 10-degree lunar slope. These figures show, for example, that along the line of TAU equal to zero which intersects several constant PHASE curves (some having large slopes), contrast is Poor (in fact, zero) for any PHASE angle and any sun

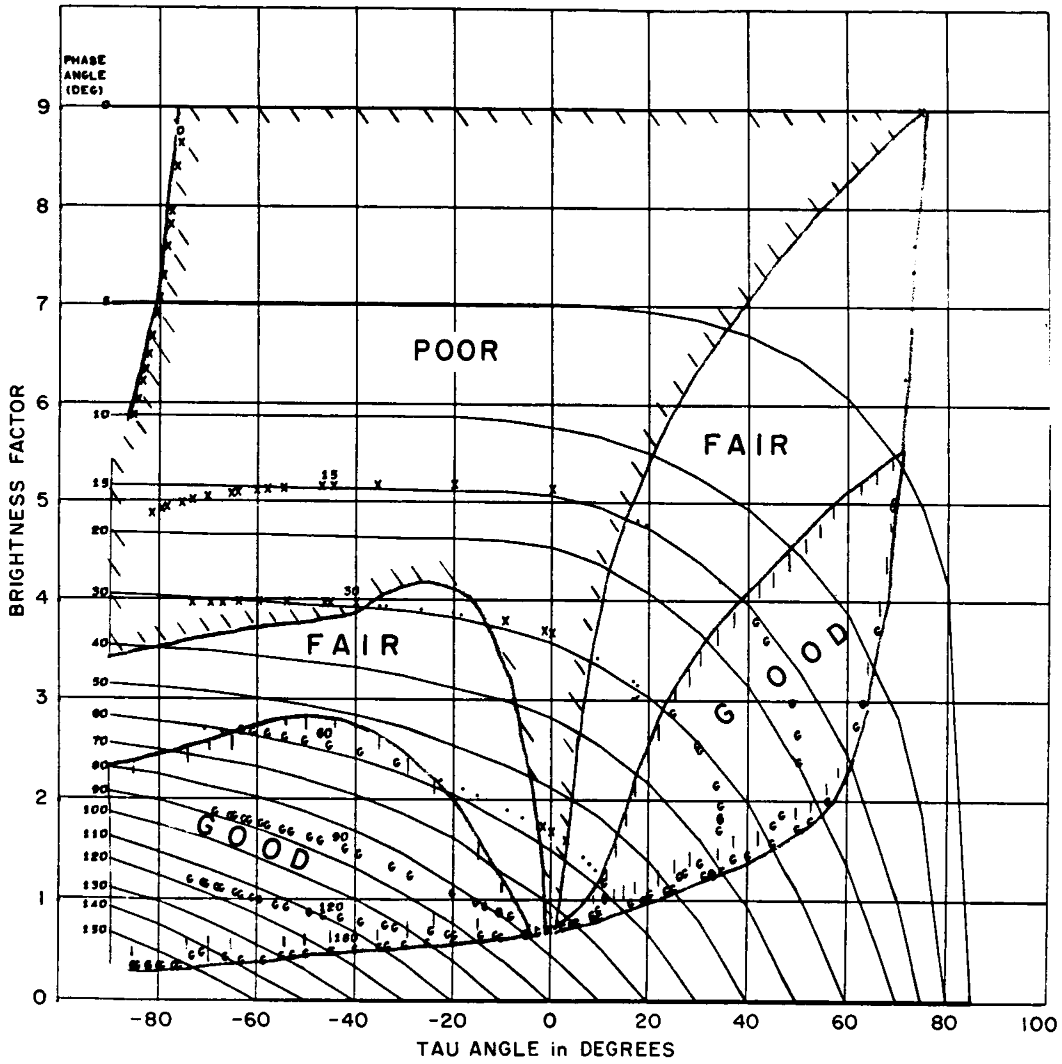

Figure IX-23. Contrast Plotted on Photometric Function
15-Degree Sun Elevation Angle
Plus 10-Degree Slope

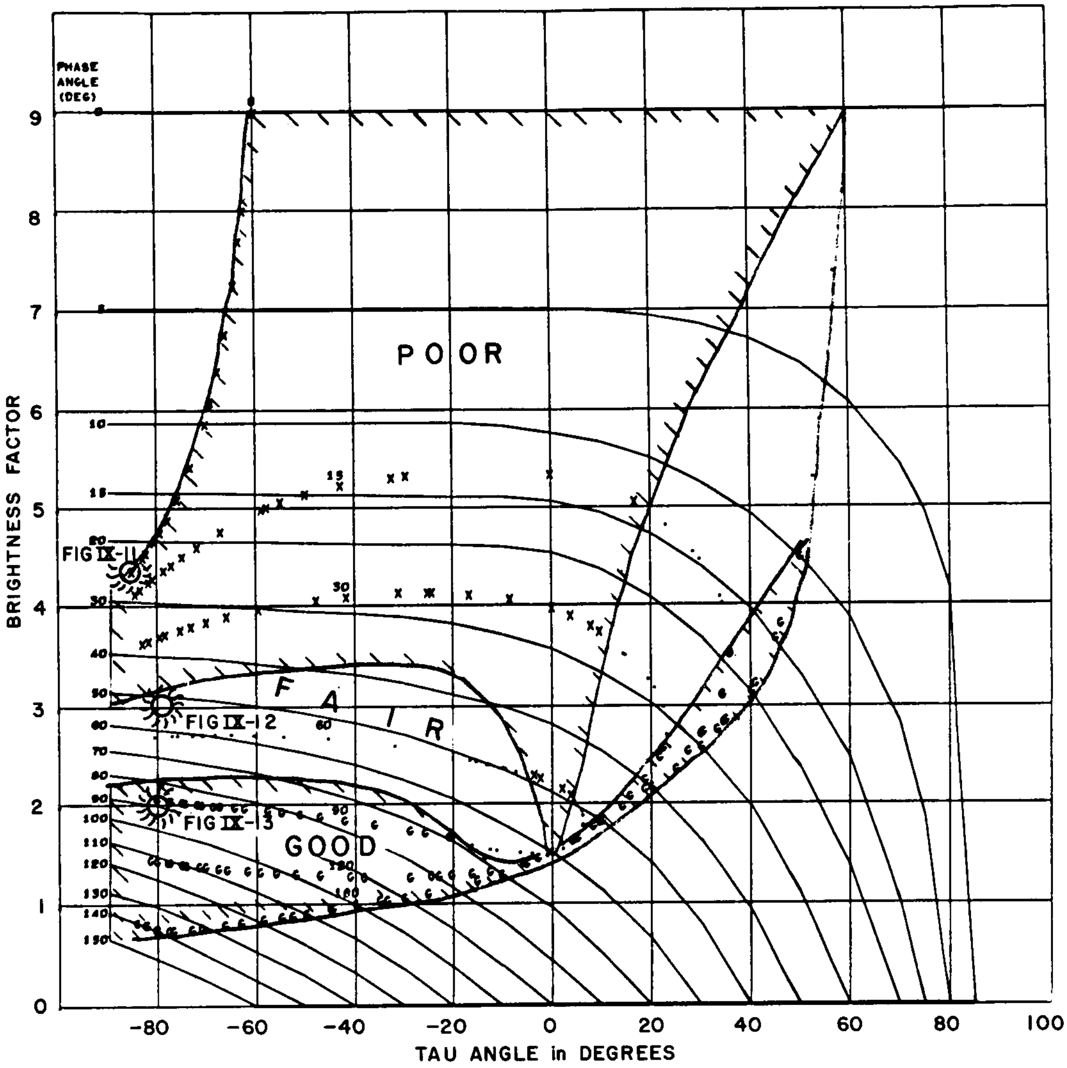

Figure IX-24. Contrast Plotted on Photometric Function
30-Degree Sun Elevation Angle
Plus 10-Degree Slope

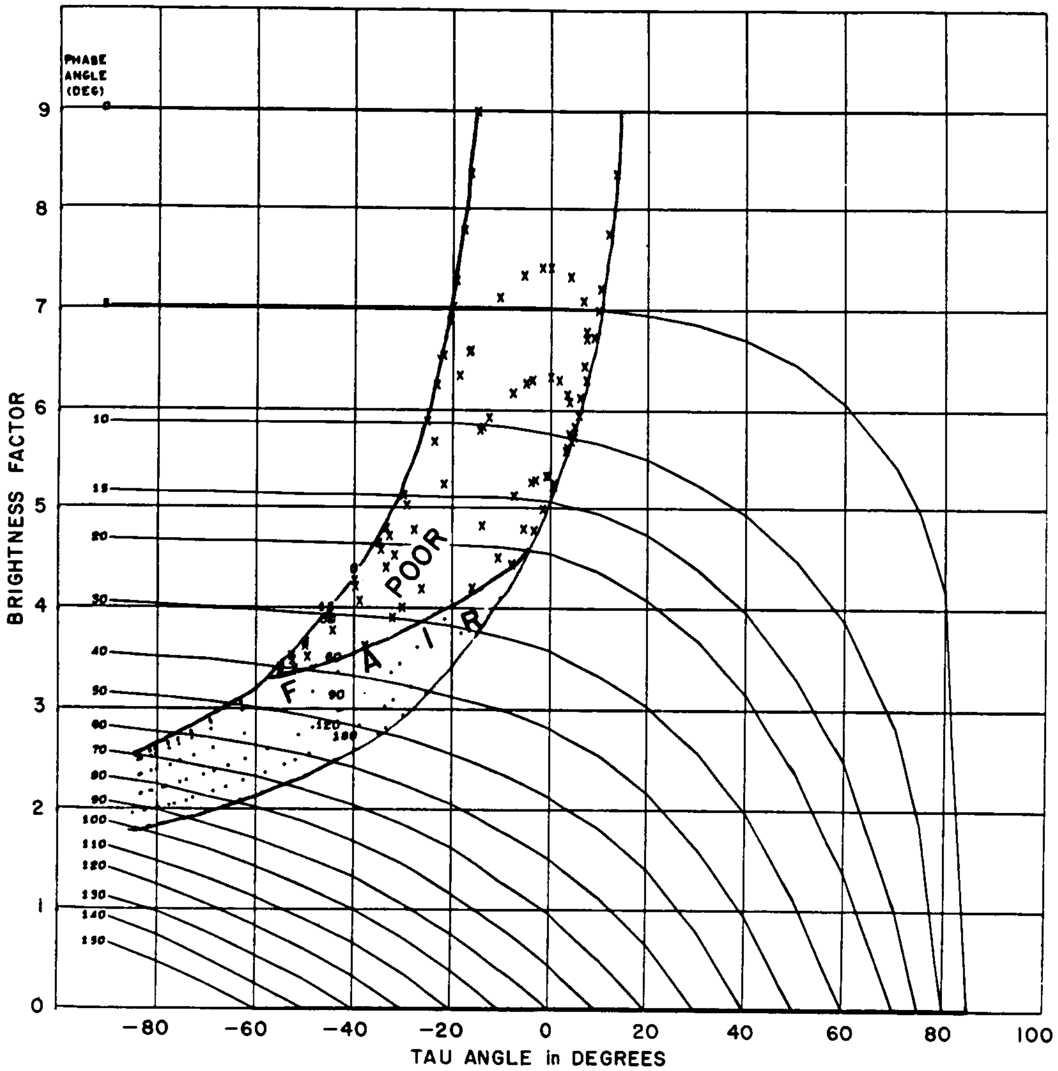

Figure IX-25. Contrast Plotted on Photometric Function
75-Degree Sun Elevation Angle
Plus 10-Degree Slope

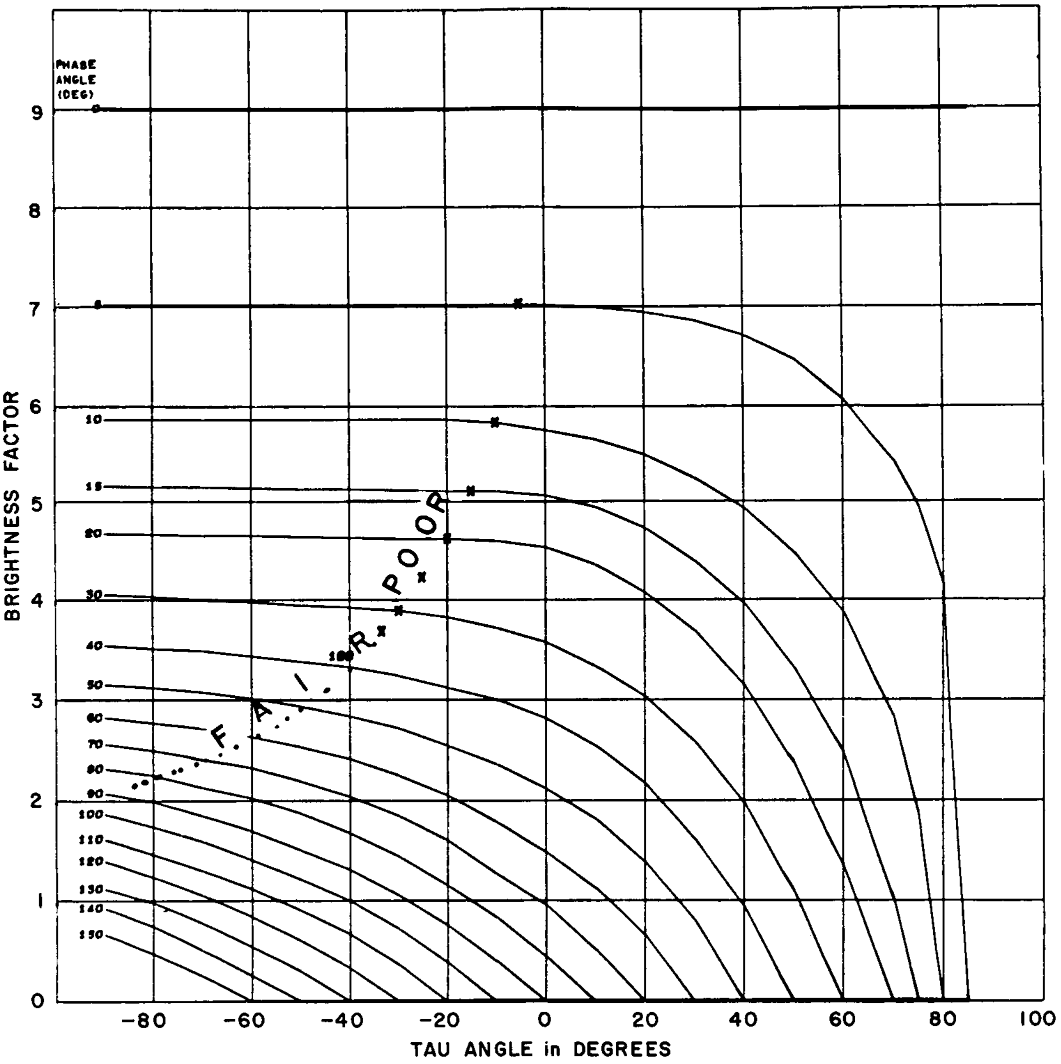

Figure IX-26. Contrast Plotted on Photometric Function
90-Degree Sun Elevation Angle
Plus 10-Degree Slope

elevation angle. As noted earlier, this zero-contrast condition results from the particular orientation of the 10-degree sloping surface chosen for this study. For a different orientation this zero-contrast contour is a function of PHASE and TAU.

The preceding calculations and data plots were repeated for the minus 10-degree slopes (i.e., the surface slope is away from the observer). For viewing angles below 10 degrees (corresponding to distance greater than 47 feet), the observer can no longer see the sloping surface; hence, contrast drops to zero. This is the greatest difference from the results shown for the plus 10-degree slopes. For the record, results obtained at the single sun elevation angle of 30 degrees are included in Figures IX-27 through IX-32. The qualitative contrast plot of Figure IX-27 for the 100-meter (328 feet) range is a striking example of the zero-cutoff point since only the small inner circle shows anything but Poor contrast. Out to the cutoff point, the expanded plot of Figure IX-28 shows the same general transition region as noted for the plus 10-degree slopes. The plot of contrast versus distance in Figure IX-29 shows the same type of transition of a null region as noted in Figures IX-14 through IX-16, and as previously noted the nulls occur at the exact same points. The character of the remaining plots (Figures IX-30 through IX-32) is in general also the same for both the plus and the minus slopes out to the cutoff point of the latter.

4. CONCLUSIONS

Based upon contrast calculations, it is concluded that an astronaut on the lunar surface will face visibility problems quite different from any encountered on the earth's surface. In general for far-out viewing at a fixed sun elevation, poorest contrast is experienced with 0 degrees viewing azimuth (sun directly at the viewer's back). As viewing azimuth is increased, the contrast is gradually improved until the best contrast is experienced when the viewer faces the sun at azimuth of 180 degrees. The difference between these two extremes in contrast is greatest at low sun elevation angle, and gradually decreases as sun elevation increases until it finally disappears at the condition of the sun directly overhead. With the sun at the viewer's back, there is a region of good contrast close-in and forward of the viewer (near his shadow) encircled by strips of poor visibility. These close-in poor regions are very dependent on, and move with, the orientation of the sloping surface. Craters and rocks are not restricted to the single sloping surface used here so the figures do not completely describe close-in hazard detection capability. But surfaces sloping toward the viewer, such as the front faces of rocks, raised crater rims, and the opposite walls of craters correspond to the model used.

With the range of contrast values categorized as Good, Fair, and Poor, visibility maps were generated on the computer and used as overlays in experiments which traversed typical lunar suface maps, also generated on the computer. These traverses showed that an astronaut will likely use a zig-zag tactic when his maneuvers about the lunar surface force him to proceed into a sector of Poor contrast.

REFERENCES

1. Ziedman, K. Lunar Surface Visibility, TRW Technical Report No. 05952-6011-R000, 3 August 1966.
2. Willingham, D. The Lunar Reflectivity Model for Ranger Block III Analysis, Jet Propulsion Laboratory Technical Report No. 32-664, November 2, 1964.
3. Anselmo, D. R. and Cavedo, P. A. "Evaluation of Lunar Lighting Constraint Based Upon Photometric Derived Scene Contrast, Case 310", Bellcomm, Inc., Tech. Memo 66-2013-1, April 29, 1966.
4. Taylor, J. H. "Use of Visual Performance Data in Visibility Prediction, Applied Optics, 3, No. 5, May 1964.
5. Taylor, J. H. "Visual Performance on the Moon," University of California, San Diego under NASA Grant NGR-05-009-059; S10 Ref. 67-3, January 1967.

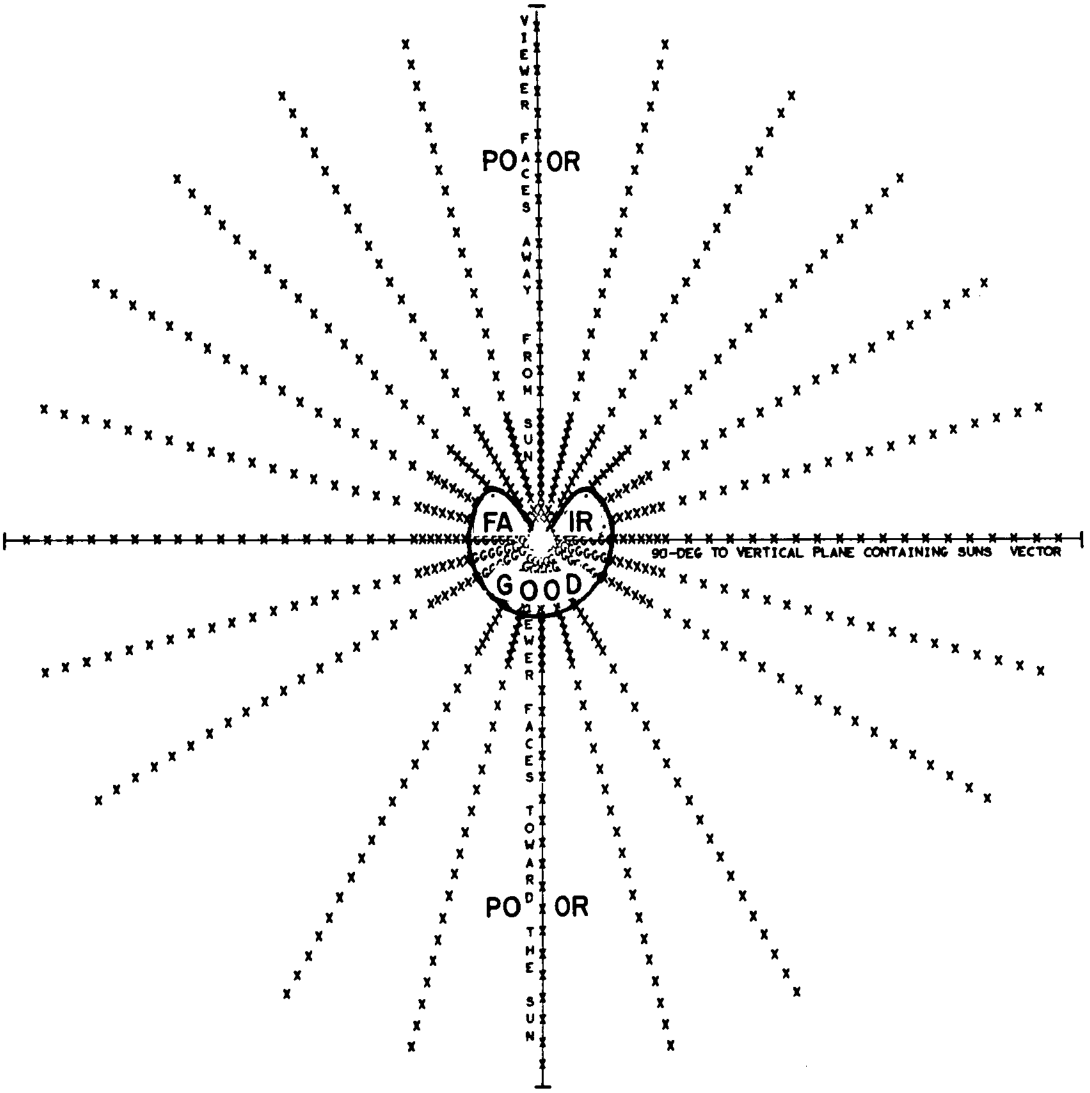
VIEWER FACES AWAY FROM SUN
POOR
FAIR
GOOD
90-DEG TO VERTICAL PLANE CONTAINING SUNS VECTOR
VIEWER FACES TOWARD THE SUN
POOR

Figure IX-27. Visibility Contrast
30-Degree Sun Elevation Angle
View Out to 100 Meters
Minus 10-Degree Slope
Observer's Height, 8 Feet

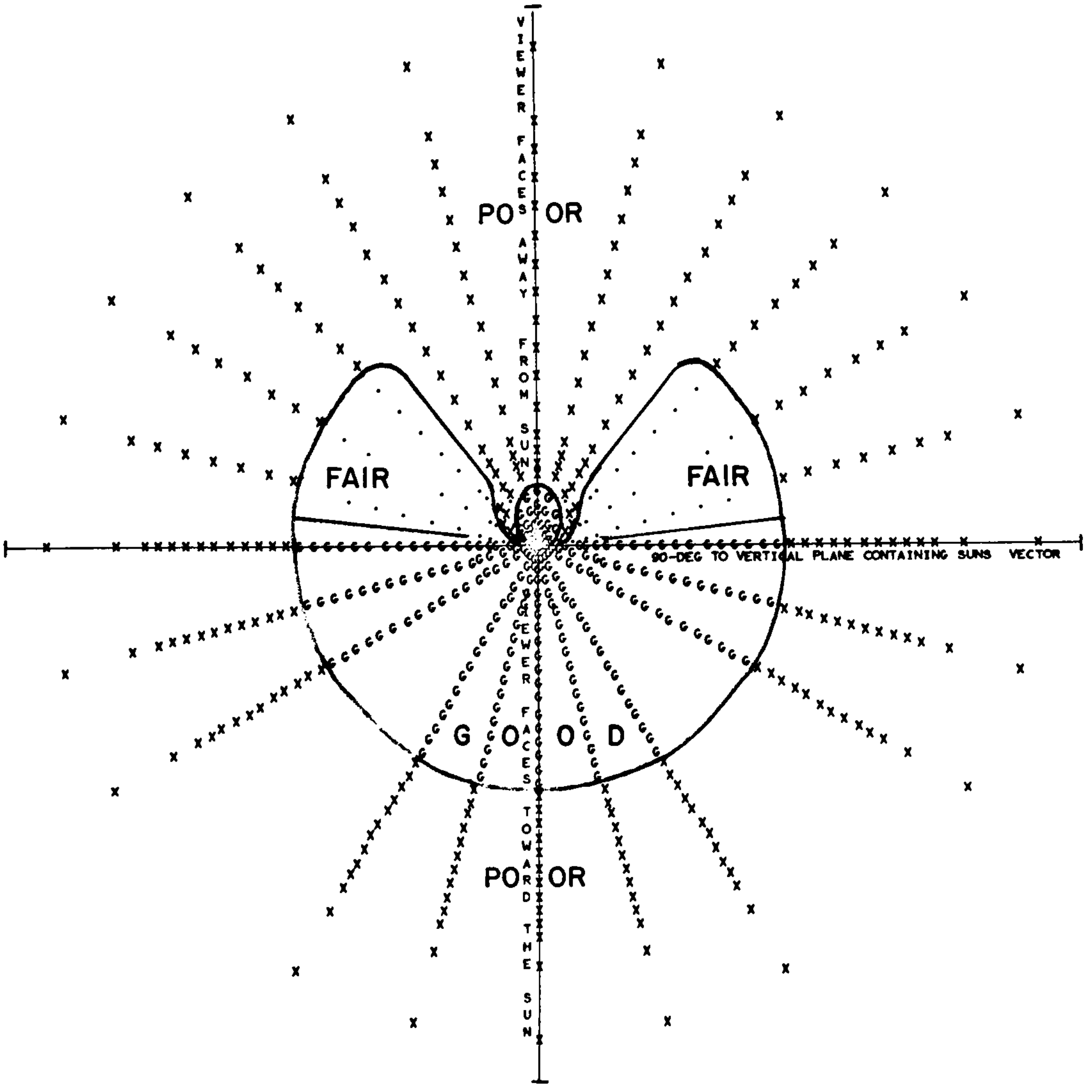

Figure IX-28. Visibility Contrast
30-Degree Sun Elevation Angle
View Out to 30 Meters
Minus 10-Degree Slope
Observer's Height, 8 Feet

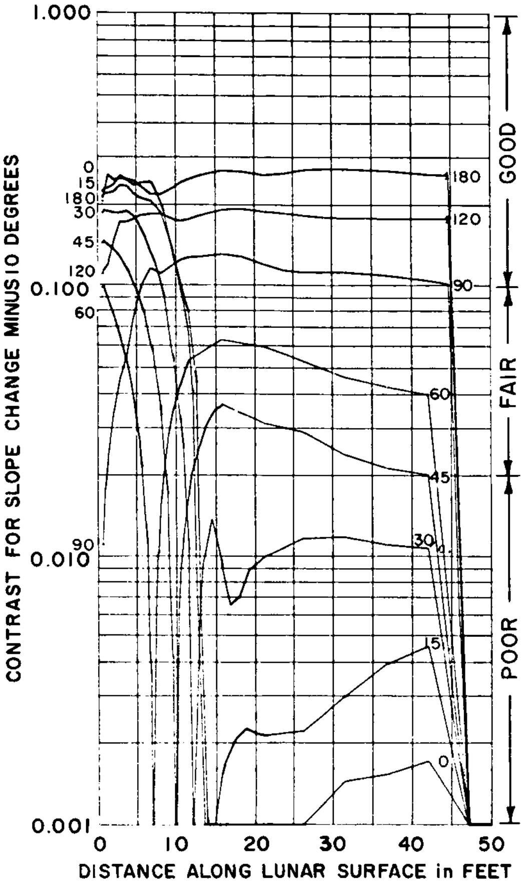

Figure IX-29. Visibility Contrast versus Distance
30-Degree Sun Elevation Angle
Observer's Height, 8 Feet

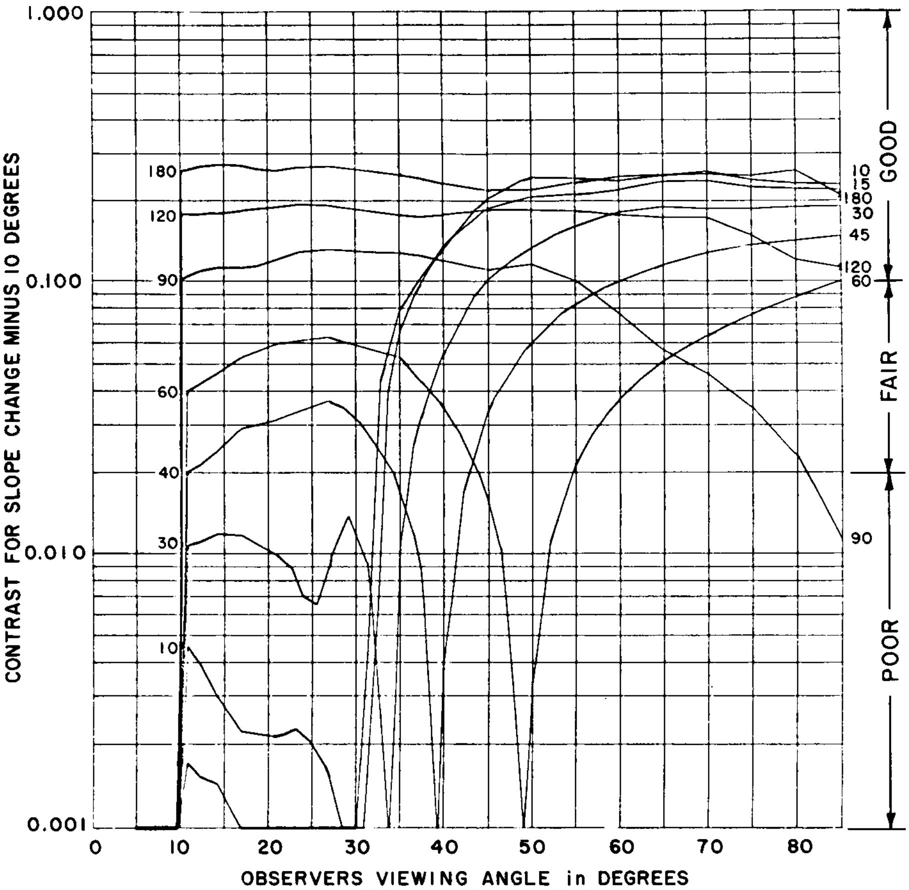

Figure IX-30. Visibility Contrast versus Observer's Viewing Angle 30-Degree Sun Elevation Angle

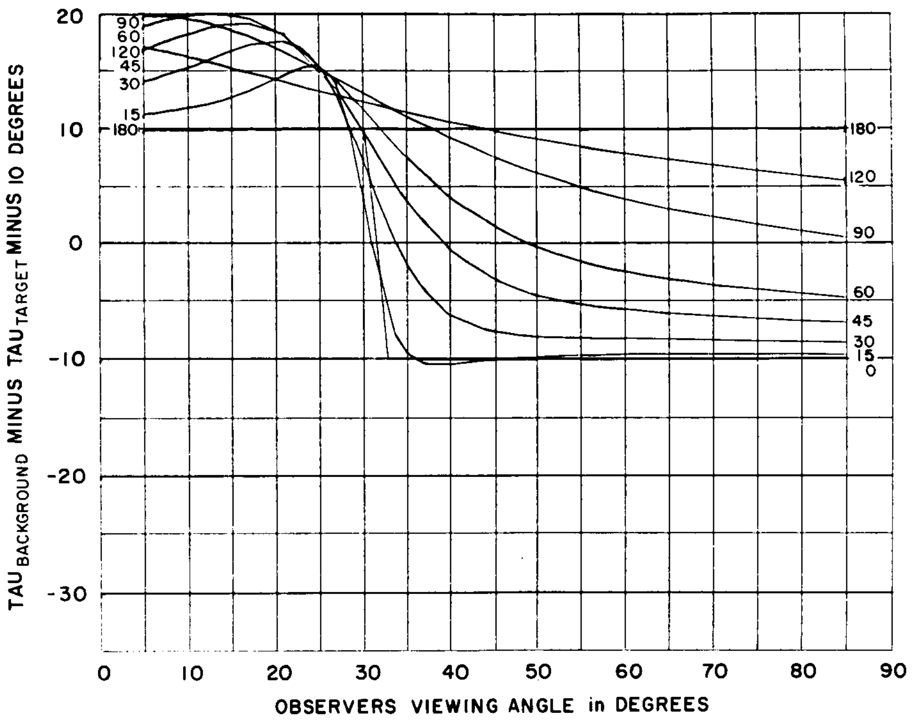

Figure IX-31. TAU Difference versus Observer's Viewing Angle 30-Degree Sun Elevation Angle

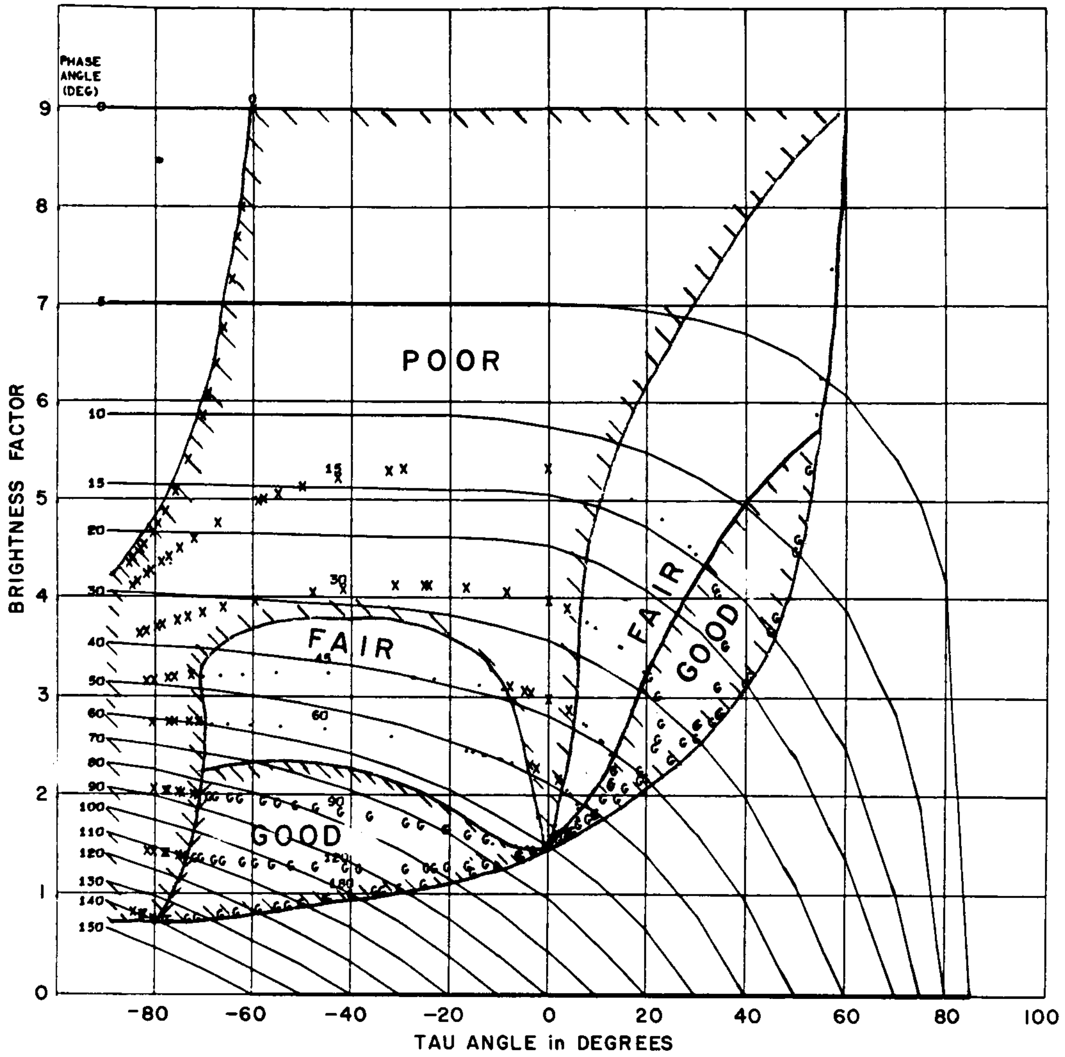

Figure IX-32. Contrast Plotted on Photometric Function
30-Degree Sun Elevation Angle
Minus 10-Degree Slope

X68-84340

SECTION X. A STUDY OF LUNAR CHARACTERISTICS TO BE CONSIDERED IN PLANNING EXTENDED MANNED LUNAR SURFACE MISSIONS INCLUDING A DIRECTORY OF LUNAR GEOLOGICAL FEATURES

by D. E. Morgan

1. INTRODUCTION AND SUMMARY

A survey of man's knowledge of the Moon was necessary as a foundation for mission planning. Since man's knowledge is increasing so rapidly, it is difficult to write a timely summary. This section includes only the survey made at the inception of the BTL study. During the study period, this information has been updated and expanded by consultation with N. W. Hinners and D. B. James at Bellcomm, by further reading of both the references noted here and other material, and by attendance at lunar science symposiums.

Until very recent times, man's knowledge of the Moon had been gained exclusively from observations by telescope and by radar. Space probes have vastly increased our knowledge of certain aspects. But man's knowledge of Earth's nearest neighbor is still largely based on visually observable surface phenomena and features; hence, a directory of lunar geological features drawn from the observations is also included in this section. In addition to general background material on lunar features, the location of general and certain specific features of interest is examined to determine if it is necessary for AAP to relax the Apollo accessibility constraints. Some interesting landing sites within the Apollo constraint are selected for AAP consideration.

In summary, the following conclusions have been drawn:

1. The number and nature of the features available within the Apollo constraints warrant AAP missions in this area.
2. Additional phenomena and features exist outside the constraints, information about which would add greatly to our overall knowledge of the Moon. These additional features appear to be of sufficient importance to recommend expanding the planned accessible area over that planned for Apollo, and relaxing the Apollo requirement on the flatness of the approach to the landing site.

The discussion in this section covers the following areas:

1. Scientific Considerations for AAP Surface Exploration
   a. Summary of scientific questions about the lunar surface
   b. General description of the expected constraints of the AAP for extended lunar exploration
   c. Discussion of the phenomena that can be investigated within the Apollo constraints
   d. Discussion of the significance of phenomena that cannot be investigated in the AAP without relaxing the constraints
2. Some Recommended Landing Sites
   a. Location
   b. Features of interest
3. Summary of some of the Geological Features of the Moon, including where practical:
   a. Name of the feature
   b. Description of the feature and its properties
   c. Discussion of some of the theories of origin
   d. Some occurrences of the feature, noted between 5°N and 5°S and between 45°E and 45°W (within Apollo constraints)
   e. Some examples of the feature found elsewhere on the side of the Moon facing the Earth (sub-Earth face)
   f. Samples and measurements to be made
   g. References for additional information about the feature
   h. Photograph of an example of the feature
   i. Diagram of a probable cross section of principal crater types

The references that are applicable to the areas covered are listed at the end of the section.

2. SCIENTIFIC CONSIDERATIONS FOR AAP SURFACE EXPLORATION

2.1 Aspects to Be Investigated

The National Academy of Sciences has formulated a list of questions about the moon. Its list, which follows, summarizes most of the important questions about the moon:

1. Is the internal structure of the Moon radially symmetrical like the Earth, and if so, is it differentiated? Specifically, does it have a core and does it have a crust?
2. (a) What is the geometric shape of the Moon? How does the shape depart from fluid equilibrium?

(b) Is there a fundamental difference in morphology and history between the sub-earth (toward the Earth) and averted faces of the Moon?

3. What is the present internal energy regime of the Moon? Specifically, (a) what is the present heat flow at the lunar surface and (b) what are the sources of this heat? (c) Is the Moon seismically active, and (d) is there active volcanism? (e) Does the Moon have an internally produced magnetic field?
4. What is the average composition of the rocks at the surface of the Moon and how does the composition vary from place to place? Are volcanic rocks present on the surface of the Moon?
5. What are the principal processes responsible for the present relief of the lunar surface?
6. What is the present tectonic pattern on the Moon and distribution of tectonic activity?
7. What are the dominant processes of erosion, transport, and deposition of material on the lunar surface?
8. What volatile substances are present on or near the surface of the Moon or in a transitory lunar atmosphere?
9. Is there evidence for organic or proto-organic materials on or near the lunar surface? Are living organisms present beneath the surface?
10. What is the age of the Moon? What is the range of age of the stratigraphic units on the lunar surface and what is the age of the oldest exposed material? Is a primordial surface exposed?
11. What is the history of dynamical interaction between the Earth and the Moon?
12. (a) What is the thermal history of the Moon?
    (b) What has been the distribution of tectonic and possible volcanic activity in time?
13. What has been the flux of solid objects striking the lunar surface in the past and how has it varied with time?
14. What has been the flux of cosmic radiation and high-energy solar radiation over the history of the Moon?
15. What past magnetic fields may be recorded in the rocks at the Moon's surface?

Some of these questions can be answered as easily by lunar orbiters or unmanned probes as by expensive manned surface missions. Most answers will require use of all three methods, however.

2.2 AAP Constraints

Under the Shelter/Taxi plan of AAP, a well-equipped, unmanned laboratory-shelter would be sent to the selected landing site on the moon. On a separate flight, the men to use the shelter would land a taxi adjacent to the shelter. This system can support up to fourteen days of exploration on the surface of the moon.

In choosing the landing site, however, several constraints on the system must be considered. Currently, Apollo plans are to limit exploration to the area between 5°N and 5°S latitude, and between 45°E and 45°W longitude. And, in an Apollo landing, the approach to the landing site must be relatively flat for several kilometers. These constraints could put severe limitations on the choice of landing sites.

One of the purposes of this study is to help determine whether, for AAP, it is necessary to enlarge the area of possible exploration described above. The scientific knowledge to be gained by exploring outside this area must be evaluated in the light of the increased cost and risk.

The Shelter/Taxi concept provides the opportunity of significantly increasing the payload to the moon. Plans are to include in this payload a scientific experiment package to be emplaced on the lunar surface, a hand-operated coring device (drive tube) capable of sampling the top layer of the lunar surface, a drill capable of extracting core samples from depths to three meters (rotary-percussive drill), and a Lunar Roving Vehicle.

The Lunar Roving Vehicle enables the astronaut to travel up to eight kilometers (five miles) from the shelter, perform several experiments, and return to the shelter. The equipment to perform sampling operations and other field experiments can be carried in this Lunar Roving Vehicle.

2.2.1 Lunar Features That Satisfy Apollo Constraints. Within the Apollo constraints, several types of features may be investigated quite readily. On the relatively flat maria, the astronauts can find wrinkle ridges, rilles, rays, domes, and several types of craters, including dark-haloed craters, impact craters, collapse depressions, secondary craters, and bowl craters. A few boundary areas between highlands and lowlands that satisfy the constraints are available: the western shore of Mare Tranquillitatis; the shores of Sinus Medii; south of Gambart; around Lansberg; around Encke; and northeast of Fra Mauro. Old craters such as Fra Mauro are of particular interest in regard to the erosion process. If the approach criterion were to be relaxed, the flat floors of some large craters such as Gambart and Reinhold would be available. In fact, if the restrictions could be relaxed enough, even Kunowsky with its flat floor and central peak would be fair game.

2.2.2 Lunar Features That Do Not Satisfy Apollo Constraints. Because of the current Apollo constraints, there are a few general types of interesting phenomena and many specific places of interest that cannot be investigated. How vital this information is to our knowledge of the moon will determine whether significant effort should be made to relax the constraints.

Areas and Types of Features Outside Apollo Constraints. There are no well-known, easily visible, major faults in the Apollo landing area. The famous Straight Wall is too far south, the Cauchy Fault is too far north. Seismic studies of such faults could give much information about the current level of activity. Stratigraphic analysis of a huge fault would disclose much about the history of the moon. Such investigations, however, would require some means of safely scaling fault walls.

Landing problems and surface transportation problems make it difficult to explore the highland areas. Such constraints could eliminate as much as two thirds of the visible lunar surface from consideration as possible landing sites. And, unfortunately, these constraints cannot be removed easily. The values to be gained may not be worth the increased costs and the much greater risks involved.

Until a way of communicating with a man on the surface of the far side of the moon is perfected, the exploration of this half of the moon is probably not worth the risks involved.

The possibility of unique phenomena occurring in permanently shadowed regions near the poles stimulates interest in these areas. However, the trajectory, landing, and surface mobility obstacles will probably preclude serious consideration of manned polar missions for AAP.

Nor will AAP astronauts be able to investigate craters on peaks; the dangers involved in ascending these peaks are too great.

Although craters with central eminences or peaks do occur inside the current Apollo permissible landing areas, the crater floors are not flat for a distance sufficient to allow landing. It is recommended that relaxation of this constraint be studied since a wealth of information is available for study within these craters. Rilles, several types of smaller craters, luminescence, and a central peak are but a few of the features within such a crater.

Specific Features Outside Apollo Constraints. The crater Alphonsus has two strikes against it from the beginning: first, it is slightly south of the Apollo landing area, and second, it has a central eminence which makes landing difficult. These constraints should be relaxed, if possible, for Alphonsus is one of the most interesting craters on the moon. Photographs of the floor of Alphonsus show fascinating rille structures, dark-haloed craters, maar craters, collapse depressions, bowl craters, impact craters, and even a possible fumarole. Parts of Alphonsus are covered from time to time with what appears to be a cloud of gas; this begs investigation. Some places on its central peak have a gentle incline, which could be easy to climb. Wall material and floor material of large saucer craters could be studied well on Alphonsus. Ranger IX has proved that the floor of Alphonsus is as fascinating and scientifically rewarding as it had appeared to man by telescopic observation.

The crater Aristarchus is of interest because of the red glow noted by several astronomers on its rim. Aristarchus, however, is far north of the permissible Apollo landing area, and the red glow (luminescence) occurs in its rough rim area, involving difficulties in landing and in surface exploration. It is true that a properly equipped Surveyor-type spacecraft could provide a great deal of information about the area and the atmosphere of Aristarchus, but a manned mission should probably not be risked, since much of the information could be found elsewhere. The red glow is a unique feature, but it is far more important that AAP study geological features and stratigraphy rather than curiosities such as the "red glow."

The two largest rills on the moon, Hyginus Rill and Ariadaeus Rill, are outside the permissible Apollo landing area. But studying them would not contribute much more to our knowledge of rills than, for instance, study of the Triesnecker Rill system, which is in the Apollo landing area. In fact, the Triesnecker Rill system could very probably turn out to be more interesting than either Hyginus or Ariadaeus.

Two of what appear to be the youngest craters on the lunar surface, Copernicus and Tycho, also outside the permissible landing area, have beckoned to would-be explorers for years. Since these two craters are young, clues to their origin should be readily available. A great deal about the formation and history of craters could probably be found, in these craters. Since Tycho has a very hot floor (Saari and Shorthill, 1965), it may have been formed quite recently; perhaps it is still in the formative stage. Tycho and Copernicus are not within the Apollo landing area, but their floors are flat enough over large distances to permit landings. If the technological problems could be overcome, a visit to either of these craters would be quite fruitful. However, suitably instrumented Surveyors sent to Tycho and to Copernicus could also provide a wealth of information about the origin of such craters.

3. SOME RECOMMENDED LANDING SITES

From the present knowledge of the lunar surface, it is possible to select certain areas that appear to be completely suitable sites on which manned flights might land. These sites satisfy all the existing constraints, and offer many interesting features to investigate.

Maps of seven recommended landing sites, together with a list of special features within the site to be studied, follow. Some features within a site cannot be seen on the map of the site because they are small, compared with the scale of the map. The radius of the circle that appears on each map represents a distance of 8 kilometers or 5 miles, the recommended distance that the astronauts would travel from the shelter to perform their experiments.

Of nine basic features (maria, craters, domes, rills, ridges, faults, rays, highlands, and rock fields), it was impossible to include two (highlands and faults) at the recommended sites — a reason for relaxing the expected landing constraints. It is interesting to note that the first site includes five of these general features (maria, craters, domes, rays, and probably rocks). The second site adds a ridge and the third site adds rills. Thus, the accessible basic features can be explored by a small number of missions. However, combinations and variations of the basic features may have to be explored to answer certain scientific questions. In addition, many scientific questions are not answered by single observations of features but require measurements from specific sites, coordinated measurements from several sites, and planned step-by-step studies where one answer provides enlightenment and, therefore, additional questions in several scientific areas.

So, while the sites are given as examples of suitable sites, it is not proposed that these particular sites will be the most promising when AAP missions are flown.

3.1 Landing Site 1

It is likely that the astronauts could land safely at 2°55'S, 14°W, a point southwest of Turner in Mare Nubium. The approach from the east to this site is relatively flat for several statute miles. Features of interest within the mare include:

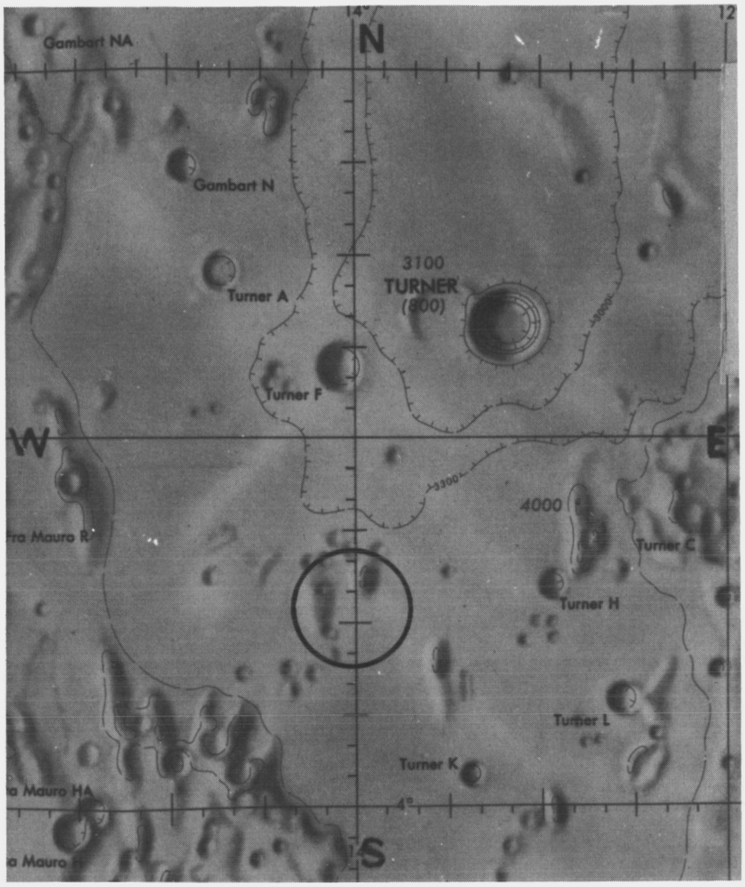
14°
12
N
Gambart NA
Gambart N
Turner A
3100
TURNER
(800)
3000
Turner F
W
E
3300
4000
Fra Mauro R
Turner C
Turner H
Turner L
Turner K
4°
a Mauro HA
a Mauro H
S

Figure X-1. Landing Site 1

- a large tear-shaped dome with a crater on top
- a peak with a crater at its summit
- three bowl-shaped craters, each about one mile across
- two consanguineous craters (a crater pair)
- ray material, apparently from Turner F
- mare surface
- boundary areas where the dome and the peak meet the mare surface.

3.2 Landing Site 2

In order to study "medium size" craters (about 5 statute miles in diameter), an excellent landing spot would be the flat area between Lansberg F and Lansberg D, i.e., at 2°35'S, 30°45'W. In addition to ease of landing due to the relatively flat terrain nearby, the site offers the following features of interest:

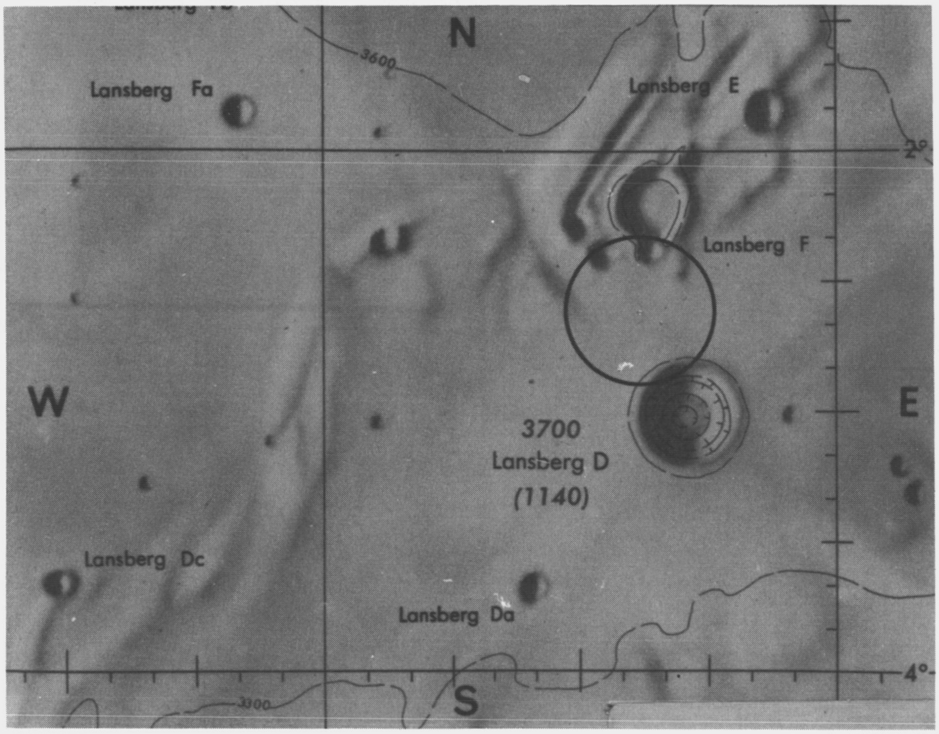
N
3600
Lansberg Fa
Lansberg E
2°
Lansberg F
W
E
3700
Lansberg D
(1140)
Lansberg Dc
Lansberg Da
S
3300
4°

Figure X-2. Landing Site 2

- a saucer crater (Lansberg F) with a bowl crater on its rim
- a wrinkle ridge with a small crater on it
- a deep bowl crater (Lansberg D)
- rays emanating from Lansberg D
- mare area between the two craters.

3.3 Landing Site 3

A fascinating part of the moon on which to land is the area east of the crater Triesnecker. If the astronauts landed at 4°20'N, 4°40'E, they could investigate:

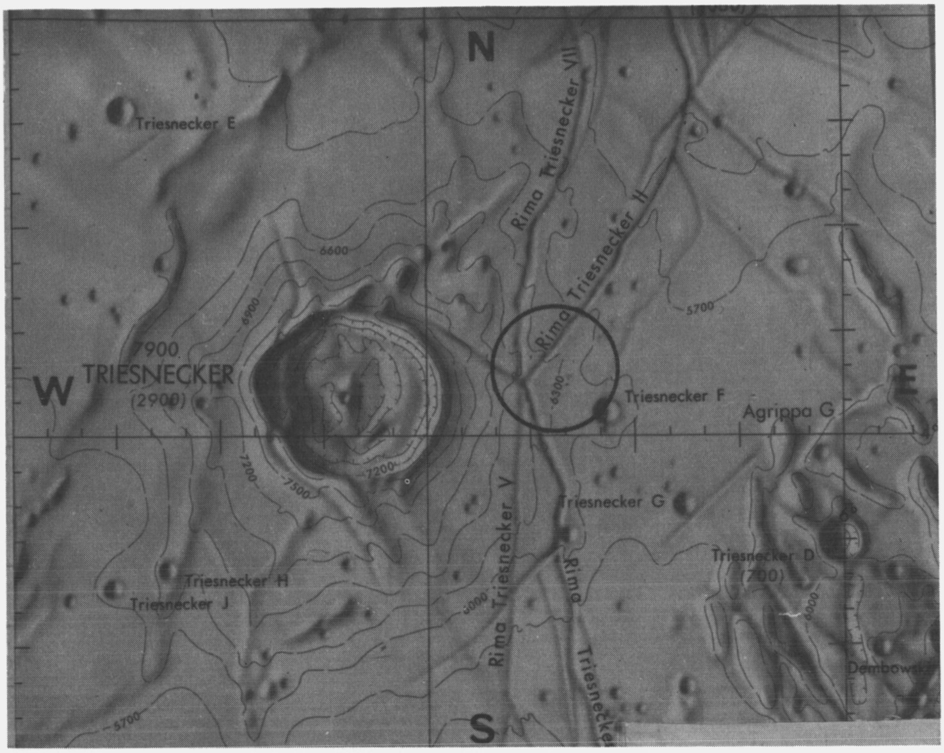
N
Triesnecker E
Rima Triesnecker VII
Rima Triesnecker II
6600
6900
5700
7900
TRIESNECKER
(2900)
W
6300
Triesnecker F
Agrippa G
E
7200
7500
7200
Triesnecker G
Triesnecker D
(700)
6000
Rima Triesnecker V
Rima Triesnecker
Triesnecker H
Triesnecker J
Dembowski
5700
S

Figure X-3. Landing Site 3

- bowl crater Triesnecker F
- outer edges of the rim of Triesnecker Crater (see Figure 13, arrow B)
- Triesnecker I, II, V, VII rills
- Sinus Medii
- the intersection of five rills
- a crater chain.

3.4 Landing Site 4

By landing at 4°45'N, 30°40'W, about two miles from Hortensius A, the astronauts could study:

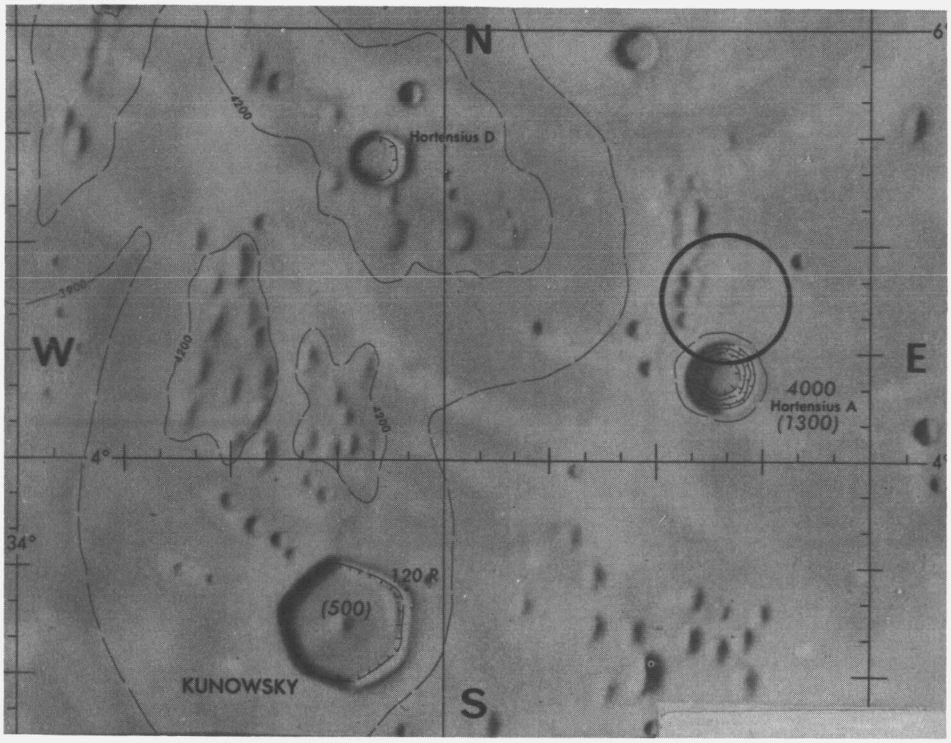
N
Hortensius D
4200
3900
W
4200
4200
E
4000
Hortensius A
(1300)
4°
34°
120 R
(500)
KUNOWSKY
S

Figure X-4. Landing Site 4

- the deep bowl crater Hortensius A
- a linear crater chain including three chain craters, each 2 miles in diameter
- Kepler and Copernicus ray material
- mare material.

3.5 Landing Site 5

If the astronauts land at 4°15'N, 39°5'W, the following features would be nearby for study:

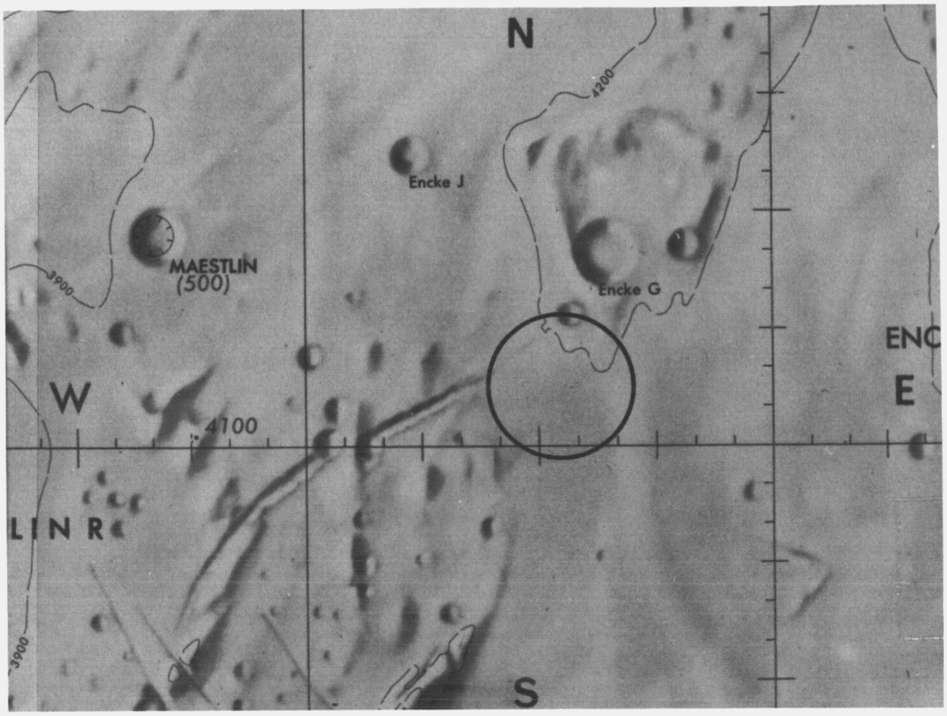
N
4200
Encke J
MAESTLIN
(500)
3900
Encke G
ENC
W
4100
E
LIN R
3900
S

Figure X-5. Landing Site 5

- Oceanus Procellarum
- a crater chain
- two domes, one with a crater on top
- a bowl crater 2 miles in diameter
- ray material, apparently from Kepler
- a wrinkle ridge.

3.6 Landing Site 6

If the landing took place at 1°30'N, 15°W, near Gambart, the astronauts could study:

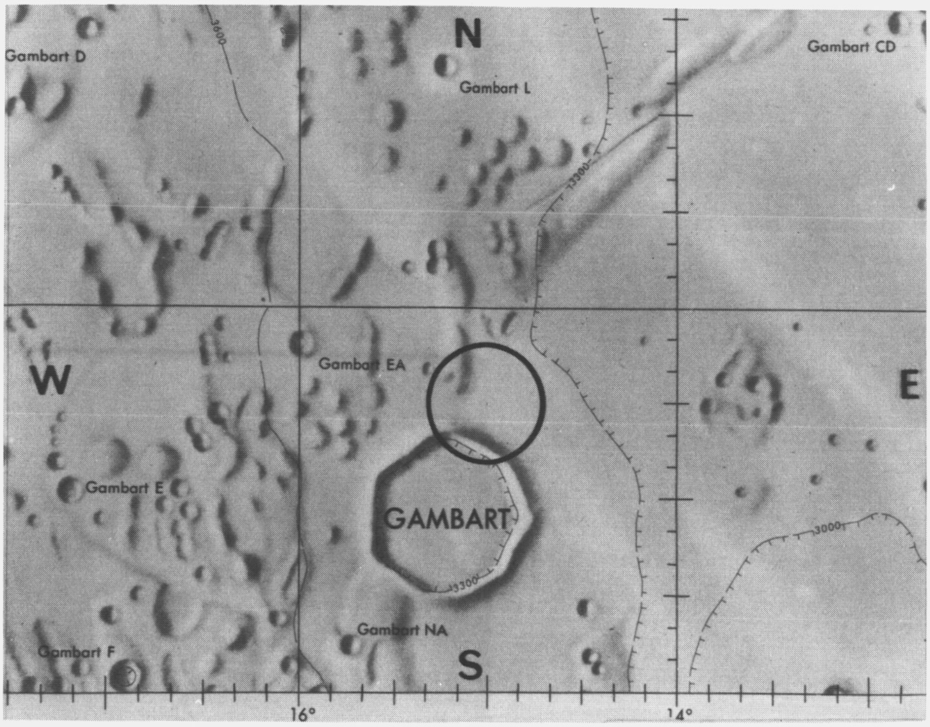
N
Gambart D
Gambart L
Gambart CD
3600
3300
W
Gambart EA
E
Gambart E
GAMBART
3000
3300
Gambart NA
Gambart F
S
16°
14°

Figure X-6. Landing Site 6

- the rim of the irregularly shaped saucer crater Gambart
- the bowl crater Gambart EA, 1 mile in diameter
- Sinus Aestuum
- Copernicus ray material
- a dome with craters on top.

3.7 Landing Site 7

By landing at 1°20'S, 0°25'W, the astronauts would land on the floor of an ancient crater that has a breached wall. Here, the astronauts could study:

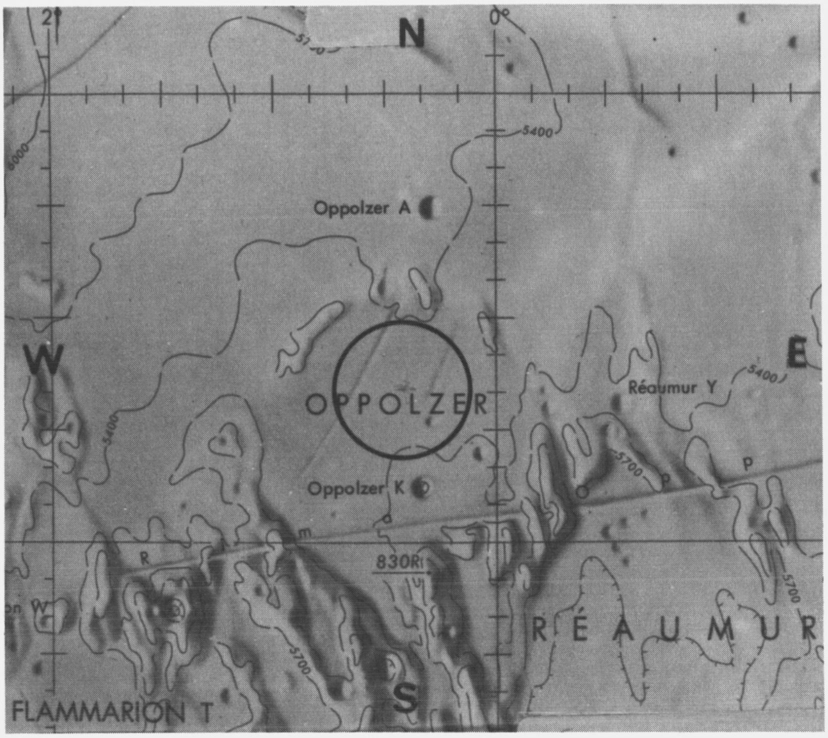
N
W
E
S
2
0°
5400
5700
6000
Oppolzer A
OPPOLZER
Oppolzer K
Réaumur Y
830R
P
R
m
RÉAUMUR
FLAMMARION T

Figure X-7. Landing Site 7

- the ancient crater
- the breached wall
- two parallel rills
- several bowl craters.

4. DIRECTORY OF LUNAR GEOLOGICAL FEATURES*

	Page
Bowl Craters	19
Saucer Craters	21
Craters With Central Ridges	23
Craters on Faults	25
Faults	27
Circular Collapse Depressions	29
Craters With Rays	30
Craters with Breached Walls	31
Polygonal or Irregularly Shaped Craters	32
Polygonal Collapse Depressions	33
Maar Craters	34
Dark-Haloed Craters	35
Secondary Craters	36
Impact Craters	37
Elliptical or Elongated Craters	38
Rill Craters	39
Chain Craters	40
Craters on Isolated Peaks	41
Craters on Domes	42
Craters on Wrinkle Ridges	43
Craters on Ringwalls	44
Consanguineous Craters	45
Domes	46
Maria	47
Rays	48
Rills	49
Rock Fields	50
Wrinkle Ridges	51

---

*Although this list may appear shorter than some in other sources, additional features included in other lists are subsets of the above features.

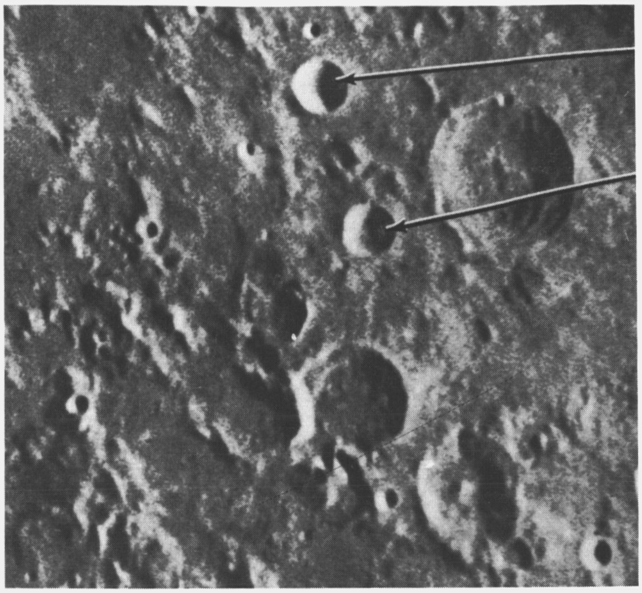

Figure X-8. Bowl Craters Theon Junior and Theon Senior

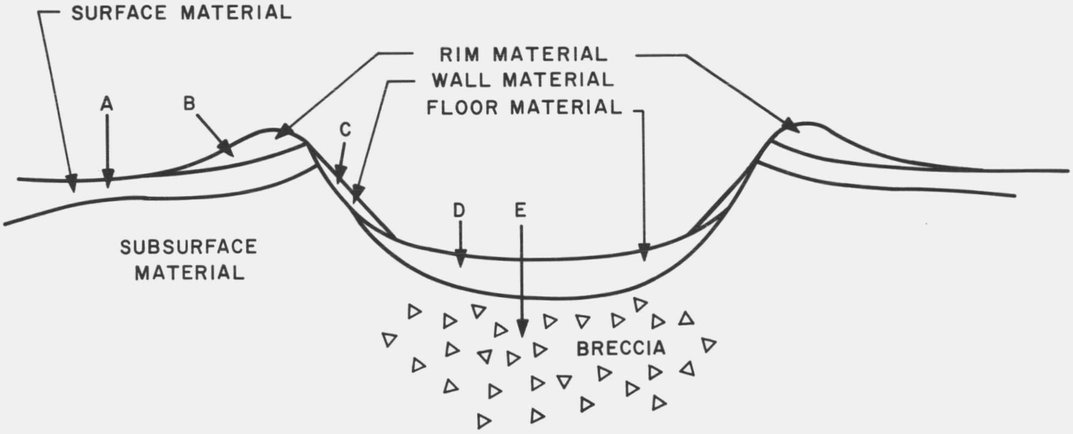
SURFACE MATERIAL
RIM MATERIAL
WALL MATERIAL
FLOOR MATERIAL
A
B
C
D
E
SUBSURFACE MATERIAL
BRECCIA

Figure X-9. Probable Cross Section of a Bowl Crater

4.1 Bowl Craters

Definition and Properties: A bowl crater is a deep, bowl-shaped depression, characterized by gentle outer slopes and steep inner slopes. It may be of conical shape.

Theories of Origin: Bowl craters are probably of impact origin.

Some Occurrences within ±5° Latitude and ±45° Longitude: Gambart A (1°N, 19°W), Gambart B (2°N, 12°W), Gambart C (3°N, 12°W), Theon Junior (2°20'S, 15°45'E), Theon Senior (0°45'S, 15°20'E). (Figure X-8).

Some Other Examples on the Sub-Earth Face: Hortensius (6°30'N, 28°W).

Information Needed (Samples, Measurements): Five major sections comprise a bowl crater, as illustrated in Figure X-9. Samples should be obtained from all five major sections of a bowl crater in order to provide scientists with sufficient information to determine the origin and the history of this type of crater. The drive tube should be used to obtain samples of the surface material of the area surrounding the crater (arrow A), the crater rim material (arrow B), the crater wall material (arrow C), and the crater floor material (arrow D). The drill must be used to sample material beneath the crater floor. Temperature and radiation measurements of the various sections should also be obtained, if possible. Photographs showing the natural orientation of the samples are essential.

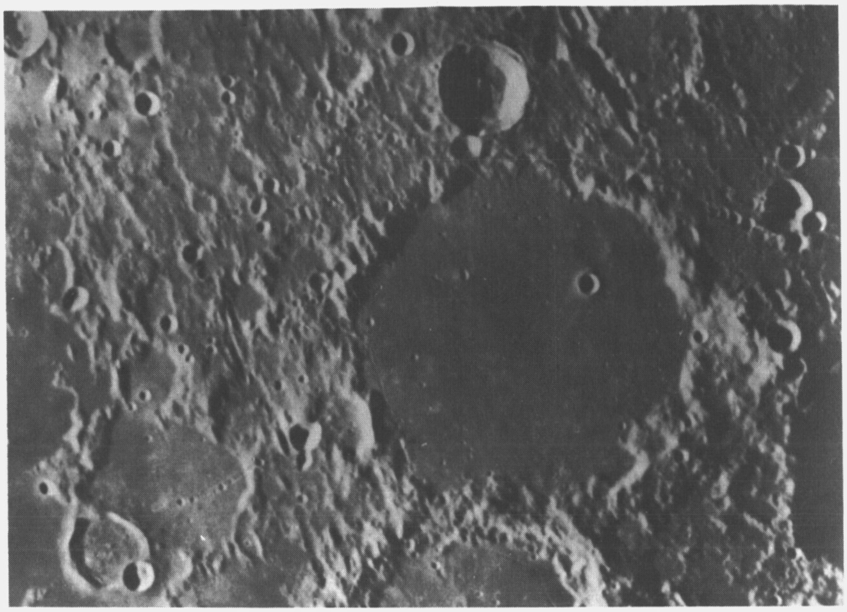

Figure X-10. Ptolemaeus Crater

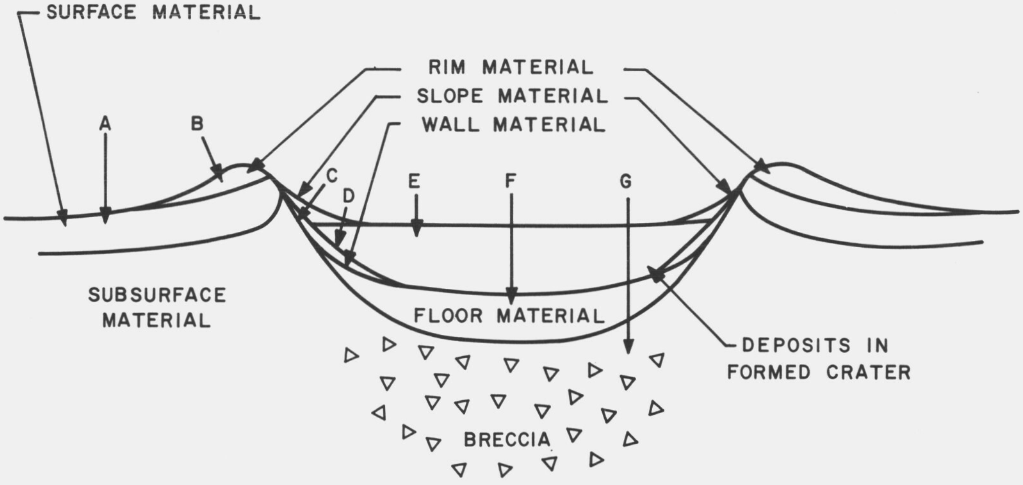
SURFACE MATERIAL
RIM MATERIAL
SLOPE MATERIAL
WALL MATERIAL
A
B
C
D
E
F
G
SUBSURFACE MATERIAL
FLOOR MATERIAL
DEPOSITS IN FORMED CRATER
BRECCIA

Figure X-11. Probable Cross Section of a Saucer Crater

4.2 Saucer Craters

Definition and Properties: Saucer craters are shallow, flat-floored craters. Both the inner and outer slopes are small.

Theories of Origin: These appear to be of impact origin, but may be of volcanic origin, since they are filled with lava.

Some Occurrences within ±5° Latitude and ±45 Longitude: Gambart (1°N, 15°W), Schmidt (1°N, 18°45'E), Réaumur A (4°15'S, 0°15'E), Kunowsky (3°10'N, 32°30'W).

Some Other Examples on the Sub-Earth Face: Hortensius E (5°15'N, 25°20'W), Parry (8°S, 16°W), Ptolemaeus (9°S, 2°W). (Figure X-10).

Information Needed (Samples, Measurements): Samples of the seven major types of material found in a saucer crater will help answer questions about their origin. Ranger, Surveyor, and telescopic photographs indicate that the astronaut will be able to differentiate visually between normal lunar surface material and saucer crater rim material.

The Figure X-11 shows the major sections of a saucer crater. Using his drive tube, the astronaut should obtain core samples of the endogenous surface material (arrow A), the crater rim material (arrow B), the crater slope material (arrow D), and the material deposited on the floor of the crater after the crater was formed (arrow E). Using a drill, the astronaut should obtain core samples of crater wall material (arrow C), crater floor material (arrow F), and the underlying breccia (arrow G). Photographs showing the orientation of these samples will aid researchers tremendously in their interpretations. Temperature and radiation measurements of the different sections of the craters should be made.

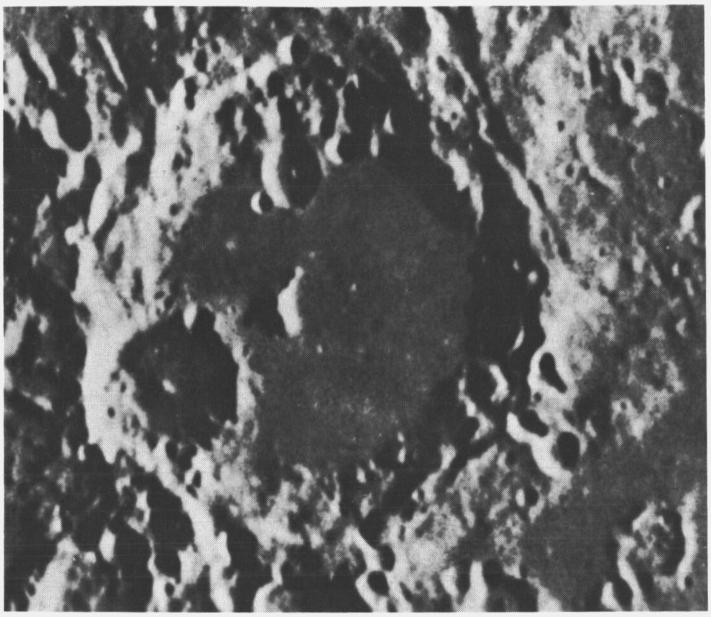

Figure X-12. Albategnius — a Large Crater with a Central Ridge

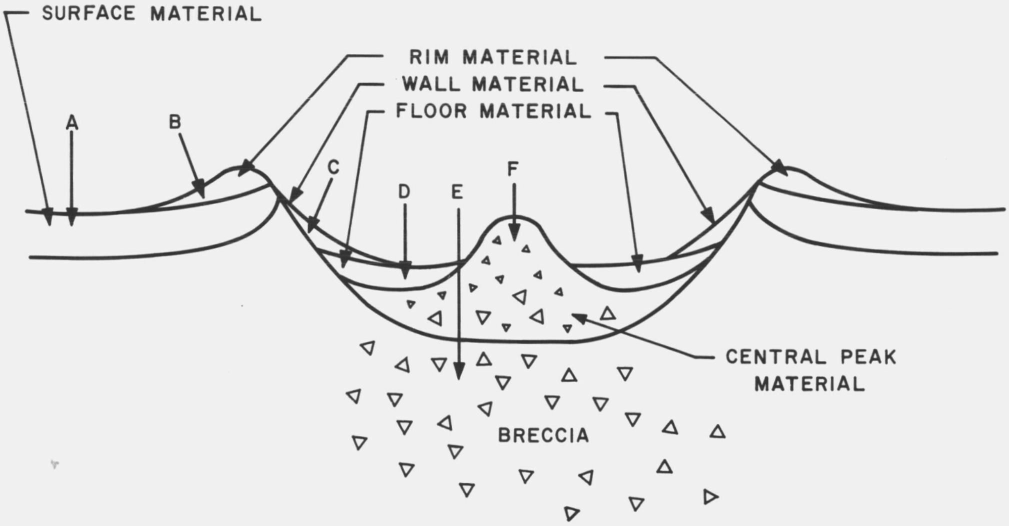
SURFACE MATERIAL
RIM MATERIAL
WALL MATERIAL
FLOOR MATERIAL
A
B
C
D
E
F
CENTRAL PEAK MATERIAL
BRECCIA

Figure X-13. Probable Cross Section of a Crater with a Central Ridge

4.3 Craters with Central Ridges

Definition and Properties: As the name implies, these are craters having ridges on the crater floor.

Theories of Origin: B. Warner attributes the production of central eminences to isostatic adjustments of the lunar surface (caused by gravity).

Some Occurrences within ±5°Latitude and ±45° Longitude: Lansberg, Reinhold, Rhaeticus A, Triesnecker, Mösting, Lalande, Horrocks, Rhaeticus, Lade S, Ritter, Agrippa, Sabine, Godin, Maskelyne, Delambre.

Some Other Examples on the Sub-Earth Face: Alphonsus, Eratosthenes, Arzachel.

Information Needed (Samples, Measurements): Samples of crater materials from a crater will help determine its origin. Visual differentiation between endogenous surface material and crater rim material should be possible.

The six major types of material in a crater having a central ridge or eminence are illustrated in Figure X-13. Using the drive tube, the astronaut should obtain core samples of the endogenous surface material (arrow A), crater rim material (arrow B), crater wall material (arrow C), crater floor material (arrow D), central ridge or eminence material (arrow F). A large drill is needed to obtain a core sample of the underlying breccia (arrow E). Photographs of the area from which the samples are taken are needed for orientation. Temperature and radiation measurements of the sections of the crater should also be made.

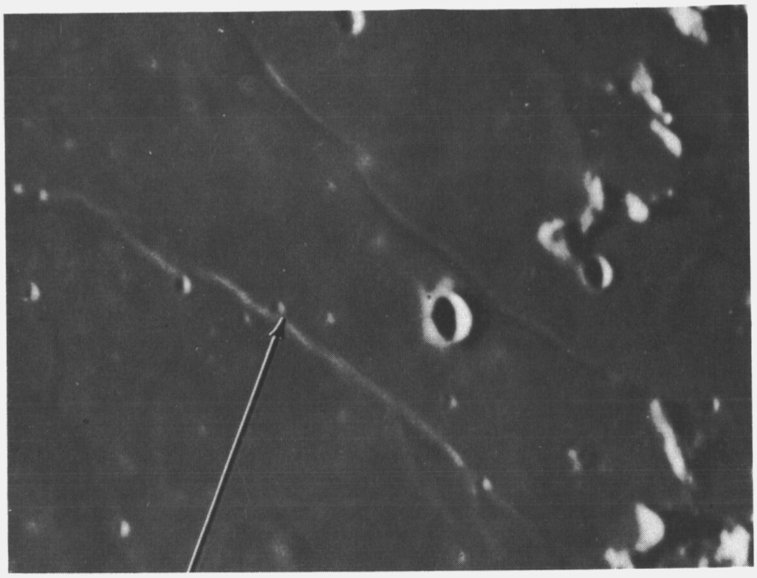

Figure X-14. Crater on Cauchy Fault I

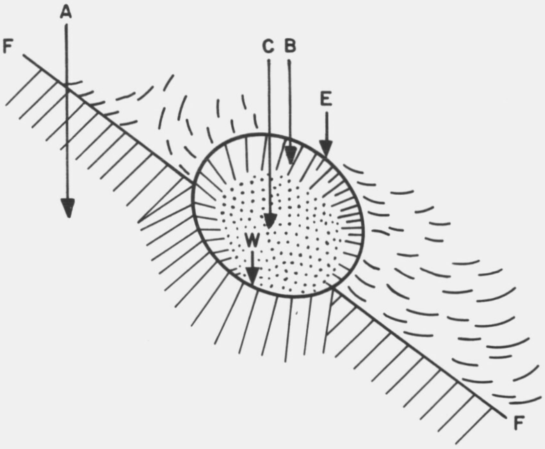

Figure X-15. Crater on a Fault

4.4 Craters on Faults

Definition and Properties: These peculiar formations have the form shown in Figure X-15 on the opposite page. The floor is enclosed by a wall that is higher at E than at W. The curvature of the crater is greater at E that it is at W. The fault FF follows wall W.

Theories of Origin: Fielder says that if the crater had originated after the fault, the fault would not bend around the crater, and if the crater were of explosive origin, the wall of the fault would have been blown off at W. If, however, the fault had been formed after the crater, the fault wall W would have been lower, and the fault would not have followed the curvature of the crater. Thus, apparently, the crater had a quiescent origin, and the crater and the fault occurred simultaneously.

Some Occurrences within ±5° Latitude and ±45° Longitude: None could be found in this region from earth observations.

Some Other Examples on the Sub-Earth Face: Cauchy Fault (9°15'N, 36°50'E). (Figure X-14).

Information Needed (Samples, Measurements): Eight samples are desired of a crater on a fault. Hand tool coring may be used to obtain samples of the fault floor material or surface material (arrow A), crater rim material or side of fault material (arrow W), crater wall material (arrow B), and crater floor material (arrow C). Deeper drilling will probably be necessary in order to obtain sufficient information about this weird formation. Thus, it is necessary to drill deeper in all four locations: fault floor, fault wall or crater rim, crater wall, and crater floor. Radiation and temperature measurements should be made, and seismic measurements would be of considerable interest here. Photographs are essential.

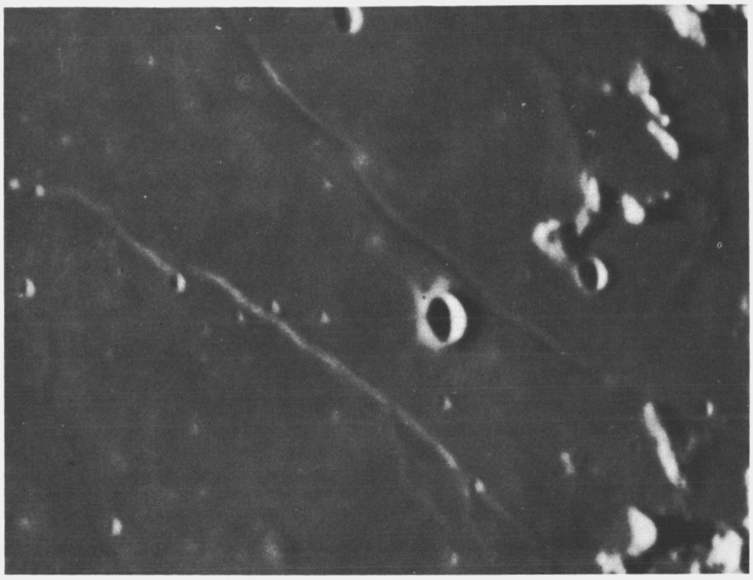

Figure X-16. Cauchy Fault I and Cauchy Fault II

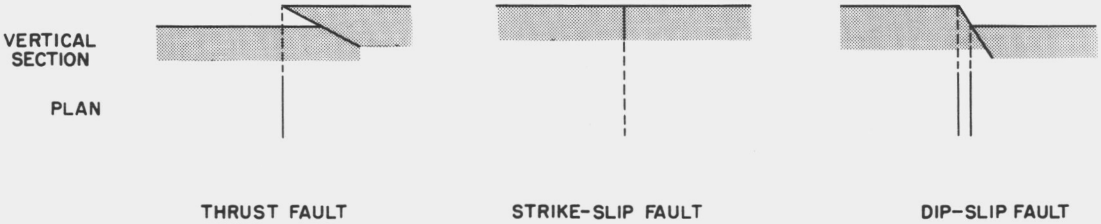
VERTICAL SECTION
PLAN
THRUST FAULT
STRIKE-SLIP FAULT
DIP-SLIP FAULT

Figure X-17. Three Kinds of Faults

4.5 Faults

Definition and Properties: Land slips or displacements of the lunar surface are known as faults.

Theories of Origin: Stresses acting on the interior of a planet will eventually cause the subsurface materials to change position. When this occurs, the surface layer will possibly break in order to relieve the stresses set up in it. Faults are the resulting cracks.

Some Occurrences within ±5° Latitude and ±45° Longitude: None were found in this region, although the area around Sinus Medii looks promising, e.g., Triesnecker Rill System (5°N, 5°E) and the area between Murchison and Pallas (5°N, 1°W).

Some Other Examples on the Sub-Earth Face: Straight Wall (22°S, 8°W), Cauchy Fault (9°N, 38°E), in Boscovich (10°N, 11°E,) Bürg Fault (45°N, 25°E). (Figure X-16).

Information Needed (Samples, Measurements): Obviously, seismic experiments should be set up to study such activity, if any is currently present. The exposed face of the fault should be sampled at various heights, as this would vividly illustrate the strata of the lunar surface. Studies should also be made to determine whether the feature is a thrust fault, a strike-slip fault, or a dip-slip fault (see Figure 17).

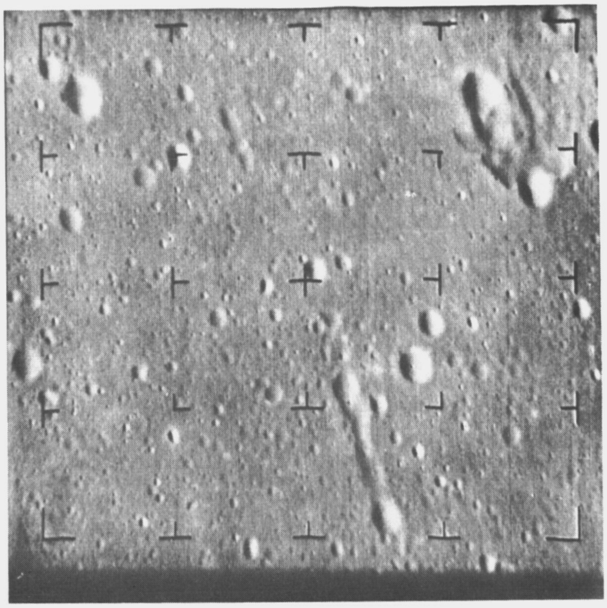

Figure X-18. Collapse Depressions on the Lunar Surface near Moltke Crater (Ranger VIII Photograph)

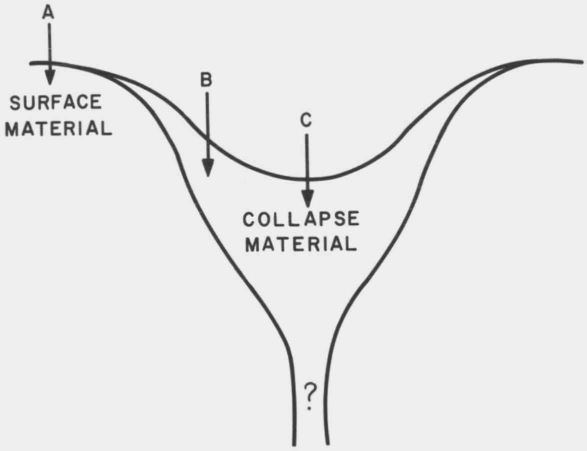
A
SURFACE MATERIAL
B
C
COLLAPSE MATERIAL
?

Figure X-19. Probable Cross Section of a Collapse Crater

4.6 Circular Collapse Depressions (Rimless Craters, Caldera, Dimple Craters)

Definition and Properties: As the names imply, this type of crater is characterized by having no rims, no ejecta rings, no rays.

Theories of Origin: Subsurface structural failures and/or internal activity apparently caused the collapse of the surface layer, thus forming the caldera.

Some Occurrences within ±5° Latitude and ±45° Longitude: Ranger VIII impact area (3°N, 24°E). (Figure X-18).

Information Needed (Samples, Measurements): Figure X-19 illustrates the two main types of material in a collapse depression: the surrounding surface material and the floor material of the collapse depression. The drive tube will be adequate for sampling the surrounding lunar terrain (arrow A) but both shallow coring with the drive tube (arrow B) and deep coring with the drill should be performed to sample the floor of the crater (arrow C). It will be necessary to drill deep into the center of the depression in order to obtain clues to the cause of its existence. Caution should be exercised when working on the floor of the depression, since it might not be sufficiently strong or stable to support the drilling and/or the additional weight. Temperature and radiation measurements should be made. Photographs are essential.

4.7 Craters with Rays

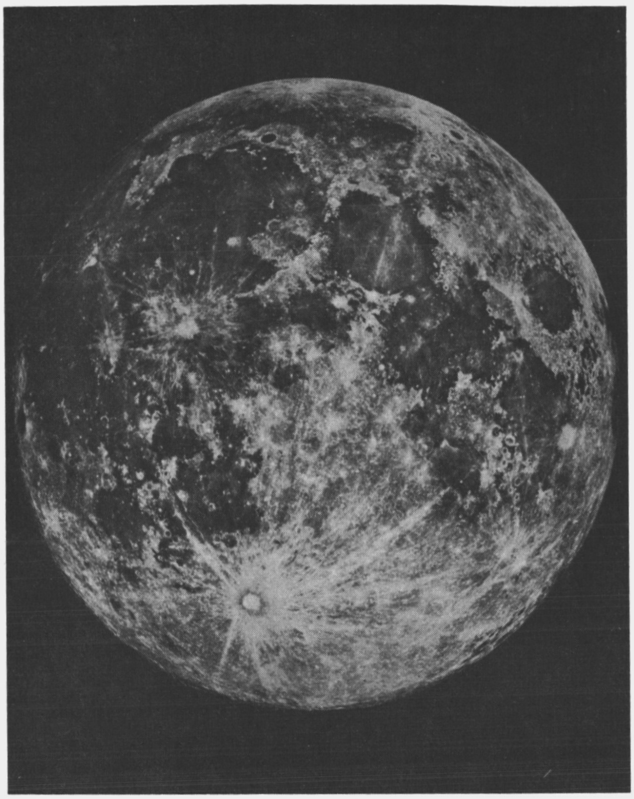

Figure X-20. Craters with Rays

Definition and Properties: Splash-like markings around certain craters are known as rays.

Theories of Origin: Ejecta from the explosion that formed the crater apparently splashed for miles. The craters themselves must have had an explosive beginning of some kind, possibly meteoric impact or volcanic eruption.

Some Occurrences within ±5° Latitude and ±45° Longitude: Hortensius A (4°20'N, 30°40'W), Chladni (4°N, 1°10'E), Triesnecker (4°10'N, 3°30'E), Agrippa (4°N, 10°30'E), Godin (2°N, 10°10'E), Dionysius (2°50'N, 17°20'E), Censorinus (0°40'S, 32°20'E), Mösting (0°40'S, 6°15'W), Lalande (4°30'S, 8°40'W), Encke B (2°20'N, 36°20'W), Turner F (1°35'S, 14°W), Gambart A (1°N, 18°40'W), Lansberg B (2°30'S, 28°10'W), Lansberg D (3°S, 30°30'W). (Figure X-20)

Some Other Examples on the Sub-Earth Face: Copernicus (10°N, 20°W), Tycho (43°S, 11°W), Kepler (8°N, 38°W).

Information Needed (Samples, Measurements): In addition to the appropriate measurements and samples for the particular type of crater, samples of the ray materials should be taken at various distances from the center of the crater. Some craters appear to have rays within the craters. Photographs are essential. Any evidence of erosion should be noted and samples of partially eroded and of healthy rays should be obtained.

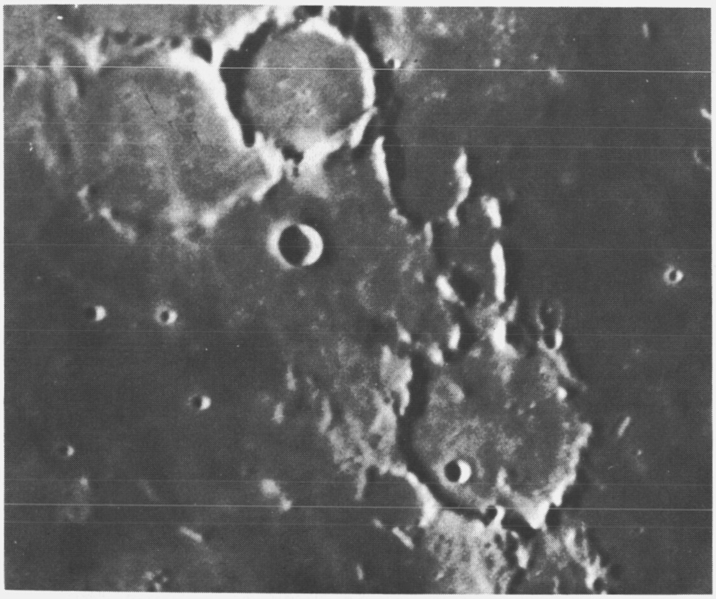

Figure X-21. Bonpland, Parry, Parry M, and Guericke Craters

4.8 Craters with Breached Walls

Definition and Properties: These are craters whose lava has breached their rims.

Theories of Origin: Apparently these craters are of volcanic origin. Their lava seems to have broken the crater walls and flowed into the surrounding terrain.

Some Occurrences within ±5° Latitude and ±45° Longitude: Fra Mauro (5°S, 16°W), Taylor A (4°30'S, 15°E), Réaumur (2°S, 1°E), Flammarion (2°S, 4°W), Flammarion T (2°30'S, 2°W), large crater enclosing Flamsteed (1°S, 44°W), Agrippa D (4°N, 6°30'E), Murchison (4°N, 0°), Schröter (2°N, 6°W), Sömmering (0°, 8°30'W).

Some Other Examples on the Sub-Earth Face: Taylor (6°S, 17°E), Bonpland (9°30'S, 17°W), Parry (8°S, 15°30'W), Davy Y (12°S, 7°W), Guericke (12°S, 14°W). (Figure X-21).

Information Needed (Samples, Measurements): Samples of the lava flow outside the crater and of the breached walls should be taken in addition to the tests made for saucer craters or bowl craters.

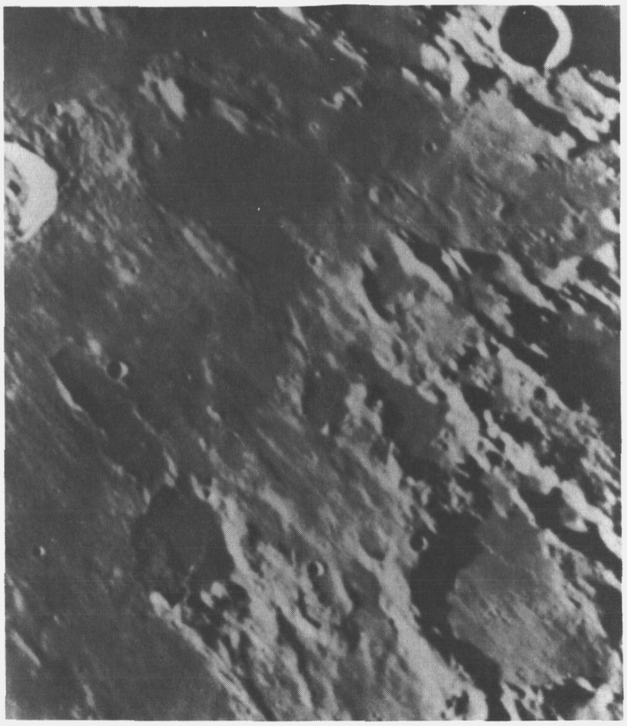

Figure X-22. Boscovich, Boscovich P, Julius Caesar, Julius Caesar P Craters

4.9 Polygonal or Irregularly Shaped Craters

Definition and Properties: Craters that have polygonal or irregular outlines are called polygonal or irregularly shaped craters.

Theories of Origin: The origin could be that of other craters but with the sides aligning with lunar grid systems.

Some Occurrences within ±5° Latitude and ±45° Longitude: Gambart (1°N, 15°W), Hypatia (4°S, 22°30'E), Alfraganus A (3°S, 20° 15'E).

Some Other Examples on the Sub-Earth Face: Davy Y (11°S, 7°W), Boscovich (10°N, 11°E), Boscovich P (12°N, 10°E), Julius Caesar P (11°N, 14°E). (Figure X-22)

Information Needed (Samples, Measurements): Except for their outlines, these craters fit into the other crater categories (bowl, saucer, etc.), and the information needed is the same as for the appropriate regularly shaped crater.

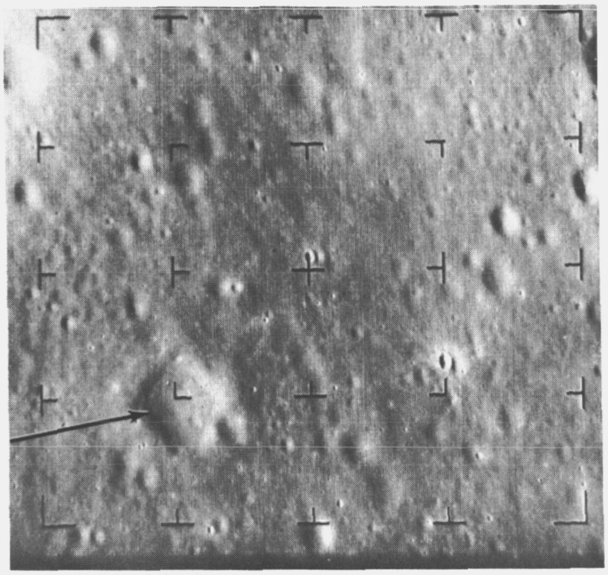

Figure X-23. Collapse Depression near
Moltke (Ranger VIII Photograph)

4.10 Polygonal Collapse Depressions

Definition and Properties: These are irregularly shaped, rimless depressions.

Theories of Origin: Internal structural failure or internal activity caused the surface to collapse.

Some Occurrences within ±5° Latitude and ±45° Longitude: Ranger VIII impact area (3°N, 24°E).

Information Needed (Samples, Measurement): See paragraph 4.6.

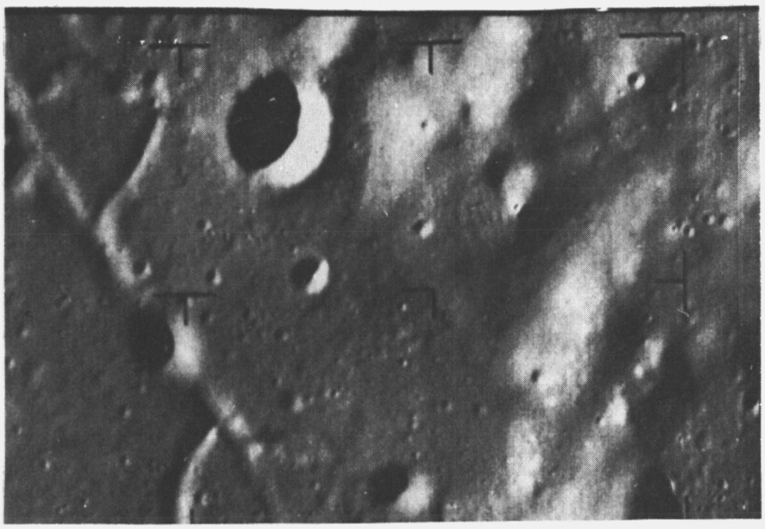

Figure X-24. Maar Craters near Eastern Wall on the Floor of the Crater Alphonsus

4.11 Maar Craters

Definition and Properties: A maar crater is a relatively shallow, flat-floored explosion crater. Usually the walls and surroundings are free from magmatic ejecta, but consist of loose fragments of native rock. Frequently, they have no built-up cones.

Theories of Origin: They are apparently caused by a single violent volcanic eruption.

Some Occurrences within ±5° Latitude and ±45° Longitude: None were found, but some probably exist here.

Some Other Examples on the Sub-Earth Face: Ross (12°N, 22°E), Maclear (11°N, 20°E), eastern floor of Alphonsus (13°S, 2°40'E). (Figure X-24)

Information Needed (Samples, Measurements): See paragraph 4.1.

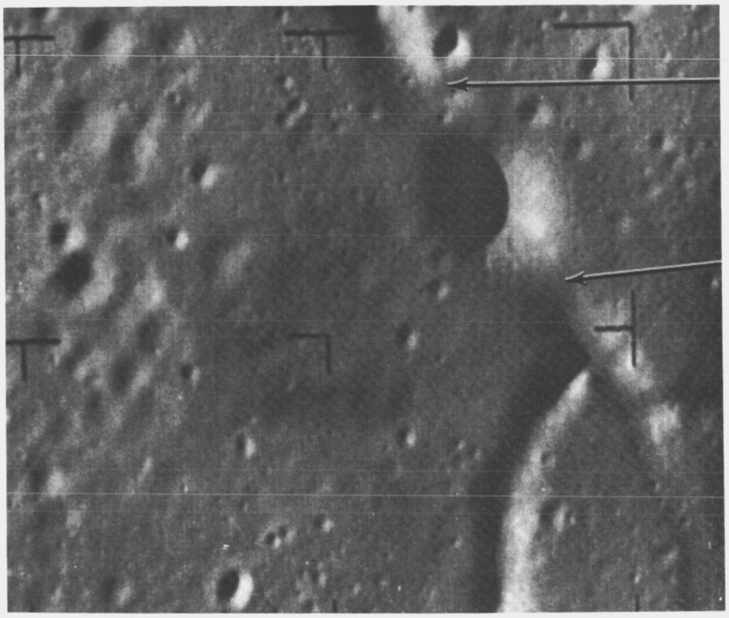

Figure X-25. Dark-Haloed Crater and Rill Structure on the Floor of Alphonsus Crater. The Arrows Point to the Two Places Where the Halo Cuts the Rill. (Ranger IX Photograph)

4.12 Dark-Haloed Craters

Definition and Properties: A dark-haloed crater is an explosion crater ringed by what appear to be magmatic ejecta. Usually dark-haloed craters have rays associated with them. They are characterized by the dark ring implied by the name.

Theories of Origin: Most scientists believe that dark-haloed craters are the results of volcanic eruptions.

Some Occurrences within ±5° Latitude and ±45° Longitude: Flamsteed F, (4°40'S, 41W), Maskelyne B (2°N, 29°E), Manners (4°30'N, 20°E).

Some Other Examples on the Sub-Earth Face: Floor of Alphonsus (Ranger IX photograph) (Figure X-25).

Information Needed (Samples, Measurements): See paragraphs 4.1 and 4.2.

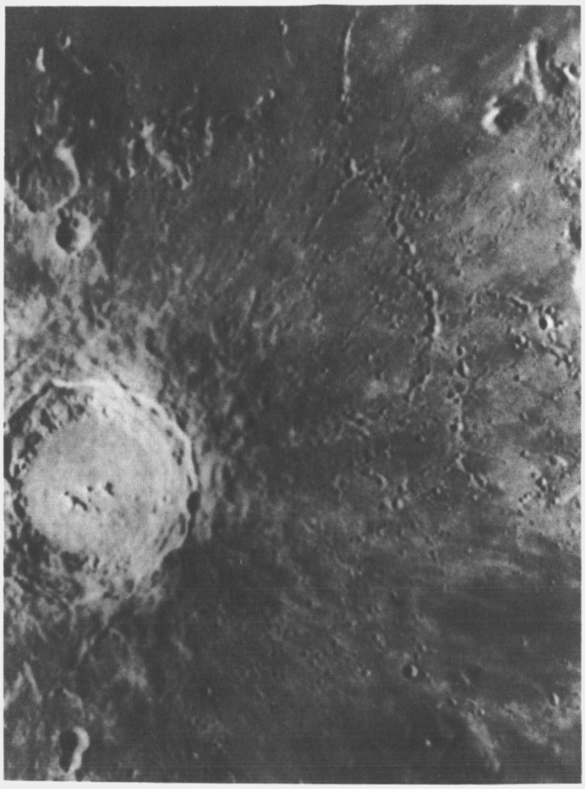

Figure X-26. Secondary Craters
East of Copernicus

4.13 Secondary Craters

Definition and Properties: Secondary craters are impact craters which appear to be caused by the explosion or impact of chunks of ejecta from another explosion.

Theories of Origin: Secondary craters apparently result from the explosion or impact of chunks of ejecta from another explosion.

Some Occurrences within ±5° Latitude and ±45° Longitude: Around Delambre, around Sabine, around Tempel, around Hipparchus, around Reinhold, south of Pallas, around Rhaeticus A.

Some Other Examples on the Sub-Earth Face: Around Copernicus (10°N, 20°W), around Eratosthenes (14°30'N, 11°30'W). (Figure X-26).

Information Needed (Samples, Measurements): See paragraph 4.1.

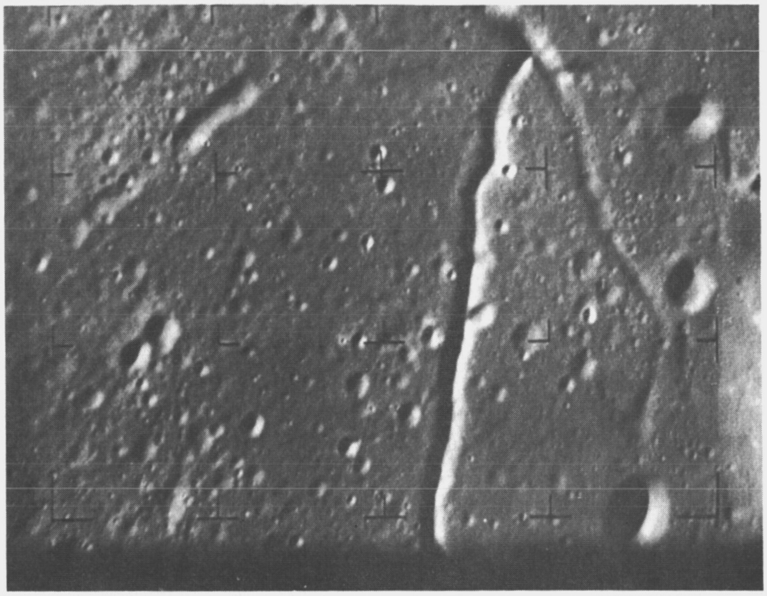

Figure X-27. Numerous Small Impact Craters on the Eastern Floor of Crater Alphonsus

4.14 Impact Craters

Definition and Properties: How to determine from earth-based photographs whether a crater is of impact origin or volcanic origin is the subject of much controversy among scientists. Frequently, impact craters are characterized by a built-up rim and by rays emanating from the rim. Usually these craters are bowl-shaped.

Theories of Origin: These craters are produced by the impact of some type of projectile.

Some Occurrences within ±5° Latitude and ±45° Longitude: Gambart A (1°N, 19°W), Gambart B (2°N, 12°W), Gambart C (3°N, 12°W), many south of Copernicus (10°N, 20°W).

Some Other Examples on the Sub-Earth Face: Copernicus (10°N, 20°W), eastern floor of Alphonsus (13°30'S, 3°W). (Figure X-27).

Information Needed (Samples, Measurements): See paragraph 4.1 or 4.2, whichever is appropriate.

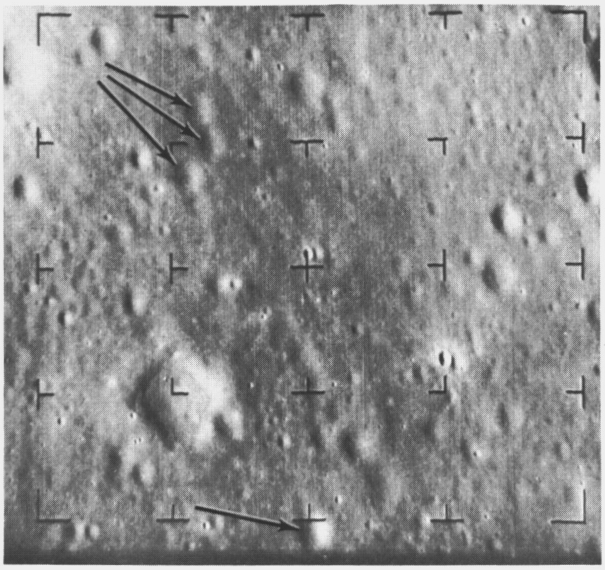

Figure X-28. Elliptical Craters near Moltke
in the Southern Part of Mare Tranquillitatis
(Ranger VIII Photograph)

4.15 Elliptical or Elongated Craters

Definition and Properties: Elliptical or elongated craters are those whose shapes approximate that of an ellipse. Frequently they occur in pairs.

Theories of Origin: B. Warner blames internal stresses for these structures, stating that ejected materials from a nearby explosion landed and produced a fracturing of the surface along stress lines. Baldwin suggested low-angle impact of ejected materials (ejectamenta) as the cause.

Some Occurrences within ±5° Latitude and ±45° Longitude: Several samples are found north and south of Maskelyne, in the southern part of Mare Tranquillitatis, north of Torricelli, around Copernicus.

Information Needed (Samples, Measurements): See paragraph 4.1.

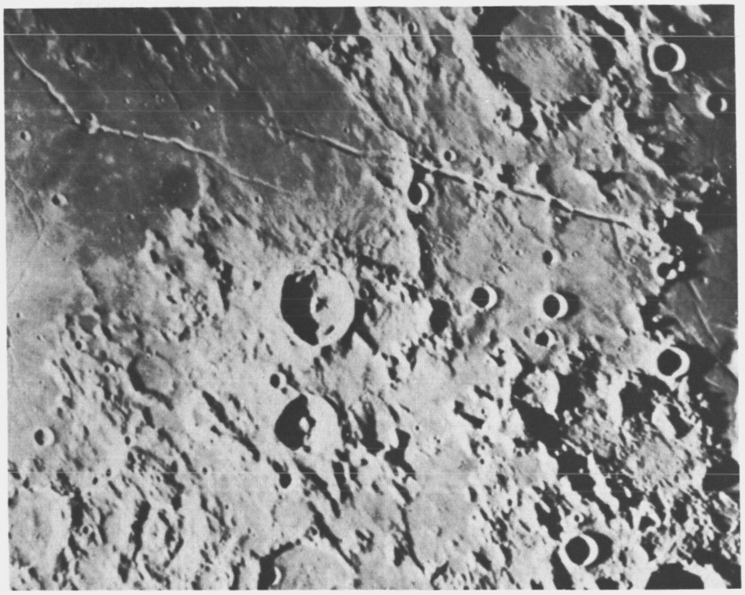

Figure X-29. Hyginus and Ariadaeus Rill Region

4.16 Rill Craters

Definition and Properties: A crater that occupies the whole width of a rill and is closely associated with it is called a rill crater. Rill craters apparently do not have raised rims. They frequently occur in chains.

Theories of Origin: These craters appear to be closely related to the formation of the associated rills. They apparently are caused by subsurface structural failures or by internal activity.

Some Occurrences within ±5° Latitude and ±45° Longitude. Near Fra Mauro (1°25'S, 17°W), Triesnecker VII Rill (3°15'N-6°N, 4°30'E), Rhaeticus I Rill (0°-2°45'N, 4°5'E-4°45'E), Schröter I Rill (1°N-2°30N; 6°30'W), near Reinhold (1°N, 23°W), near Gambart A (0°30'N and north, 19°W).

Some Other Examples on the Sub-Earth Face: Hyginus Rill, Birt Rill. (Figure X-29)

Information Needed (Samples, Measurements): See paragraph 4.6.

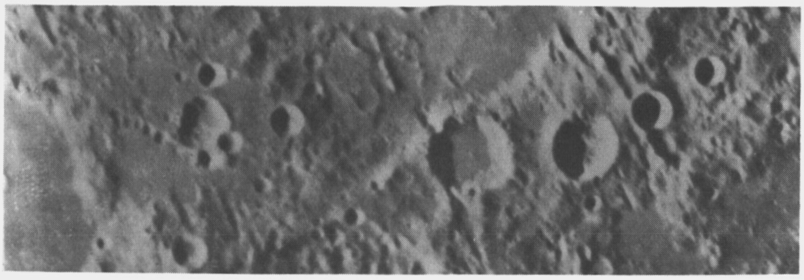

Figure X-30. Halley, Hind, Hipparchus C, Hipparchus L Craters

4.17 Chain Craters (Linear or Arcuated)

Definition and Properties: A chain crater is a rimless, circular depression that is one of several such depressions occurring in a straight or curved (arcuated) line (or chain). There are three types of chains of craters: (1) decremental chains, in which the craters decrease in size, (2) open chains, in which the craters of the chain are separated from each other, and (3) contiguous chains, in which the craters overlap.

Theories of Origin: According to the most popular theory, chain craters are subsidence phenomena, i.e., subsurface activity has caused the surface to collapse. Another theory states that the crater chains were formed by ejecta bouncing from another explosion.

Some Occurrences within ±5° Latitude and ±45° Longitude: Many south of Gambart, Gambart A (2°N, 19°W), Sömmering M (1°N, 6°W), Reinhold B (5°N, 21°W), Sabine area (1°N, 20°E).

Some Other Examples on the Sub-Earth Face: Decremental arcuated crater chain on rim of Hipparchus (8°S, 6°E), contiguous linear crater chain between Hipparchus and Ptolemaeus (8°S, 1°E), contiguous arcuated crater chain east of Copernicus (10°N, 16°W). (Figure X-30)

Information Needed (Samples, Measurements): See paragraph 4.6.

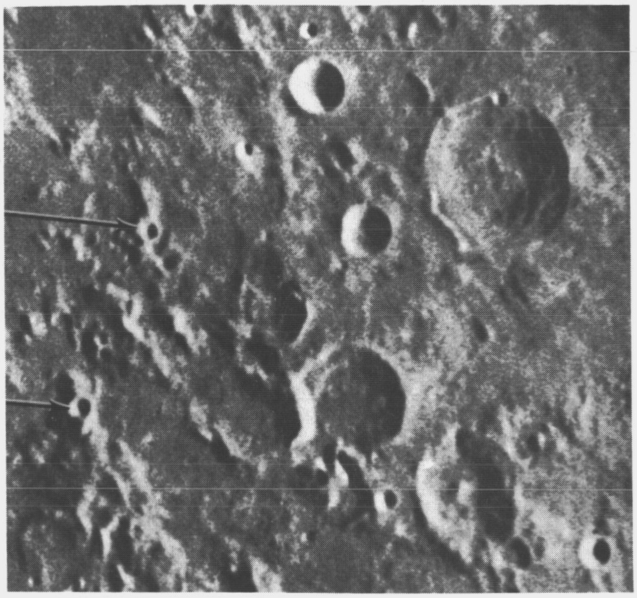

Figure X-31. Small Craters on Isolated Peaks near Theon Senior, Theon Junior

4.18 Craters on Isolated Peaks

Definition and Properties: Explosive craters found atop peaks that are not connected with any crater formations fall into this category.

Theories of Origin: Probably most are of volcanic origin, although some may be of impact origin or even possibly of collapse origin.

Some Occurrences within ±5° Latitude and ±45° Longitude: Reinhold (2°30'N, 20°45'W), Reinhold θ (3°30'N, 21°5'W), west northwest of Gambart EA (2°5'N, (16°40'W). (Figure X-31)

Some Other Examples on the Sub-Earth Face: Schneckenberg (9°20'N, 6°20'E).

Information Needed (Samples, Measurements): See appropriate paragraph on the specific crater type.

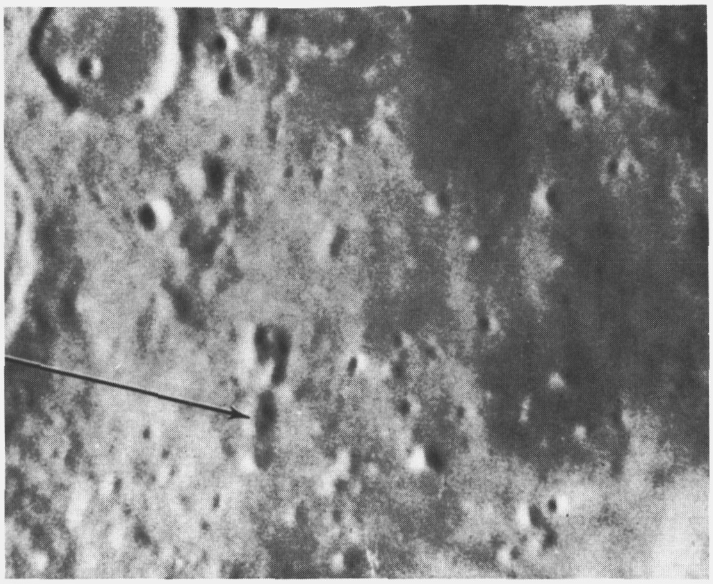

Figure X-32. Crater on Dome near
Reinhold and Reinhold B

4.19 Craters on Domes

Definition and Properties: Craters that are found atop domes fall under this heading. They do not appear to have raised rims, and they resemble caldera.

Theories of Origin: Most researchers agree that these formations are caused by stress, although some favor impact as the cause.

Some Occurrences within ±5° Latitude and ±45° Longitude: East of Fra Mauro (2°45'N, 14°15'W), Turner (4°N, 12°55'W), Reinhold (2°30'N, 25°50'W), south southeast of Gambart L (3°N, 15°W), Gambart (0°50'N, 19°40'W), east of Gambart (0°50'N, 13°50'W), east of Oppolzer (1°5'S, 1°5'E), southeast of Reinhold (1°20'N, 21°5'W). (Figure X-32)

Some Other Examples on the Sub-Earth Face: North of Hortensius (7°N, 28°W).

Information Needed (Samples, Measurements): See paragraph 4.6.

4.20 Craters on Wrinkle Ridges

Definition and Properties: As the name implies, these are craters that occur on wrinkle ridges.

Theories of Origin: Researchers have noted that on an area basis, craters occur more frequently on wrinkle ridges than on the surrounding lunar terrain. This has led to the theory that these craters are of volcanic origin.

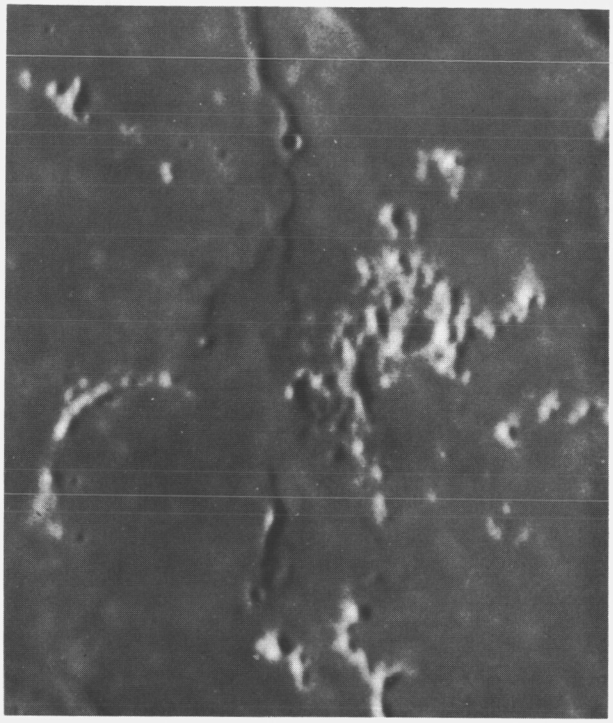

Figure X-33. Euclides F — a Crater on a Wrinkle Ridge in Mare Nubium near Letronne and Herigonius

Occurrences within ±5° Latitude and ±45° Longitude: Several in Mare Tranquillitatis (3°N, 22°E), between Oppolzer and Rhaeticus (0°15'S, 1°30'E), between Gambart L and Gambart C (2°40'N, 14°25'W), near Reinhold, Lansberg (1°45'N, 26°15'W), in Sinus Medii near Blagg (1°35'N, 1°20'E), near Triesnecker (4°40'N, 2°40'E), west of Riphaeus Mountains (0°-11°S, 34°W).

Some Other Examples on the Sub-Earth Face: Many such craters exist in Sinus Aestuum (12°N, 8°W), Mare Tranquillitatis (8°N, 28°E), Mare Nubium (20°N, 8°W); Euclides F (14°S, 34°W). (Figure X-33)

Information Needed (Samples, Measurements): See appropriate paragraph for the particular type of crater found on the ridge.

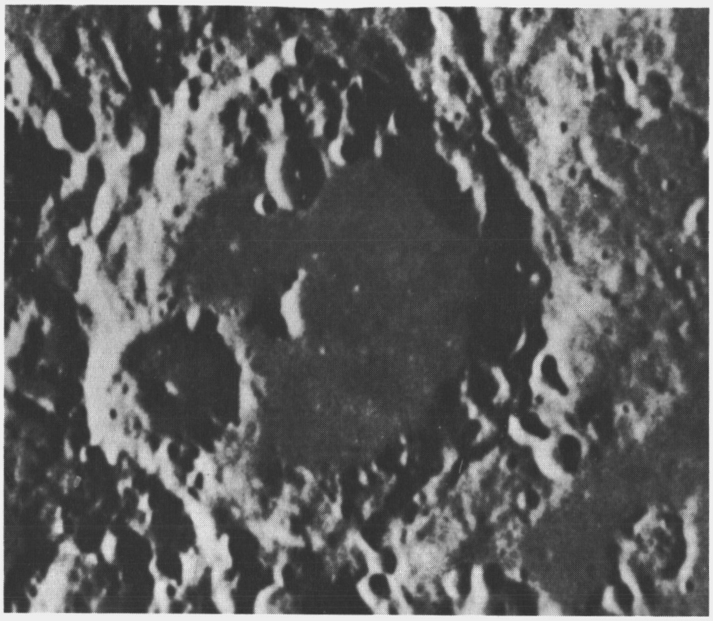

Figure X-34. Klein Crater on Albategnius

4.21 Craters on Ringwalls (Craters on Walls of Other Craters)

Definition and Properties: As the names imply, these are craters that have been formed on the walls of other craters.

Theories of Origin: These appear to be of impact origin.

Some Occurrences within ±5° Latitude and ±45° Longitude: Delambre D (1°5'S, 17°35'E), Agrippa H (4°45'N, 10°45'E), Ritter BA (3°5'N, 18°55'E), on rim of Whewell (4°5'N, 13°30'E), on rim of Gambart (0°45'N, 16°30'W), Ariadaeus A on Ariadaeus (4°40'N, 17°30'E).

Some Other Examples on the Sub-Earth Face: Davy (on Davy Y), Davy A (on Davy and Davy Y) (8°W, 12°S), Klein (on Albategnius) (12°S, 2°30'E). (Figure X-34)

Information Needed (Samples, Measurements): Each crater should be sampled and radiation and temperature measurements taken as though it were the only crater. The common wall should be sampled and measured separately, to note any differences in composition. For individual crater sampling and measuring recommendations, see appropriate paragraph for specific crater type.

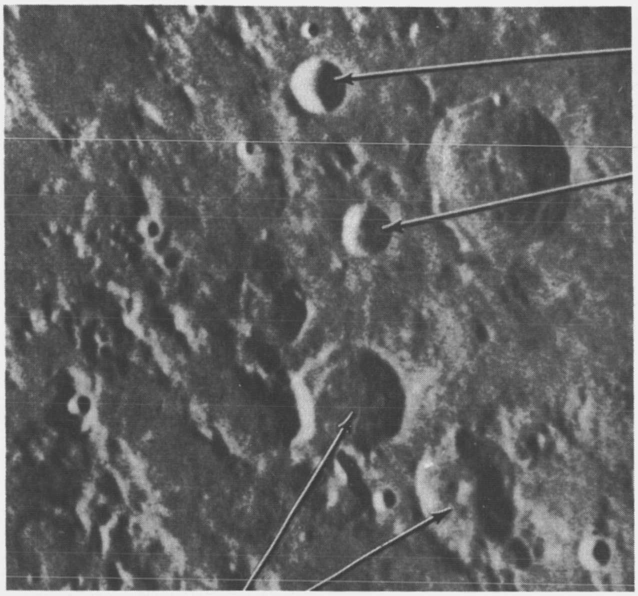

Figure X-35. Two Crater Pairs: Theon Junior and Theon Senior, Taylor and Taylor A Craters

4.22 Consanguineous Craters (Crater Pairs)

Definition and Properties: Pairs of very similar craters appearing close together are referred to as consanguineous craters.

Theories of Origin: There is little evidence to support a unique origin cause for this type of crater.

Some Occurrences within ±5° Latitude and ±45° Longitude: Sabine-Ritter (1°N-2°N, 19°E-20°E), Agrippa-Godin (2°N-4°N, 10°E), Theon Junior-Theon Senior (1°S-2°S, 15°E-16°E), Taylor-Taylor A (4°S-5°S, 15°E-16°E). (Figure X-35).

Some Other Examples on the Sub-Earth Face: Abulfeda-Almanon (14°S-17°S, 14°E-15°E), Aristoteles-Eudoxus (44°N-50°N, 16°E-17°E), Aristillus-Autolycus (31°N-34°N, 1°E), Helicon-Le Verrier (40°N, 21°W-23°W), Azophi-Abenezra (21°S-22°S, 12°E-13°E), Mercator-Campanus (28°S-29°S, 26°W-27°W).

Information Needed (Samples, Measurements): Samples should be taken and tests made in both members of the pair, if possible, so that similarities and differences can be compared. This could help prove or disprove the existence of any true kinship between them. The tests performed on the twins should be as described in the appropriate paragraph for that type of crater.

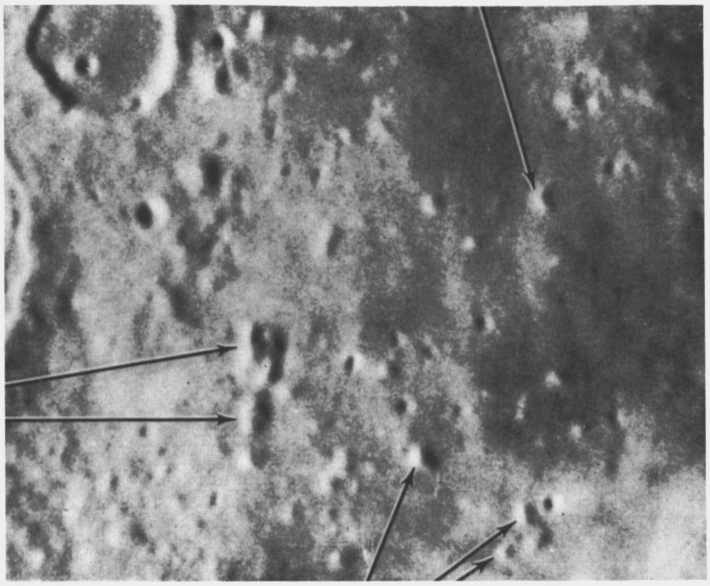

Figure X-36. Domes near Reinhold and Reinhold B

4.23 Domes

Definition and Properties: Domes are low, sometimes circular swellings resembling partially buried tennis balls. Their diameters may possibly range up to eight kilometers (five miles). Several have dome-top craters. As their slopes rarely exceed two to three degrees, they are difficult to detect from the earth.

Theories of Origin: Terrestrial domes are common igneous phenomena. Baldwin, however, thinks that lunar domes may be the surface results of deep explosions.

Some Occurrences within ±5° Latitude and ±45° Longitude: West of Reinhold (2°30'N, 26°W), north of Gambart (3°N, 15°W), south of Triesnecker (3°N, 3°E). (Figure X-36).

Some Other Examples on the Sub-Earth Face: Northeast of Milichius (11°30'N, 31°W) north and east of Hortensius (7°N, 28°W).

Information Needed (Samples, Measurements): Both the drive tube and the drill should be used to obtain samples. Rubble samples would be useful. Samples of the surrounding terrain, surface, and subsurface would help determine if this is merely raised surface material or deposited foreign material.

4.24 Maria [singular: mare (sinus, oceanus)]

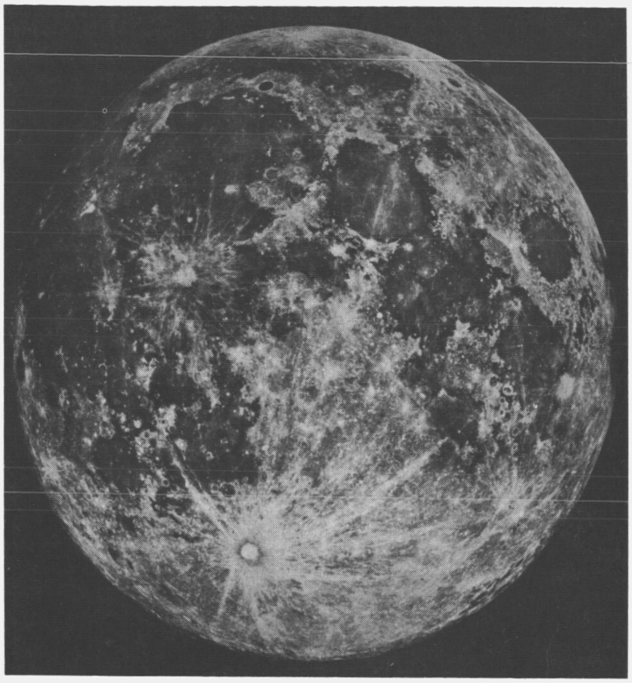

Figure X-37. Maria (Dark Areas)

Definition and Properties: A mare is a large, relatively flat, lowland area interrupted by occasional craters, rills, and wrinkle ridges and bordered by highland areas. Dark and light maria exist. A green luminescence has been noted in several maria.

Theories of Origin: Many experts believe that at some time vast amounts of magma flowed out from under the lunar surface, covering a huge area. In an attempt to attain isostatic equilibrium with the neighboring continents, the basic lava flows sank.

Some Occurrences within ±5° Latitude and ±45° Longitude: Sinus Medii (0°, 0°), Mare Tranquillitatis (2°N, 22°E), Sinus Aestuum (5°N, 10°W), Oceanus Procellarum (0°, 40°W). (Figure X-37)

Some Other Examples on the Sub-Earth Face: Mare Imbrium (31°N, 16°W), Mare Nubium (17°S, 18°W), Mare Humorum (24°S, 41°W), Mare Smythii (2°S, 84°E), Mare Serenitatis (26°N, 18°E). (Figure X-37)

Information Needed (Samples, Measurements): Using the drive tube and the drill, the astronaut should obtain several samples from widely separated areas. Samples of rubble should also be collected. Temperature and radiation measurements should be made at distant points. Photographs are essential.

4.25 Rays

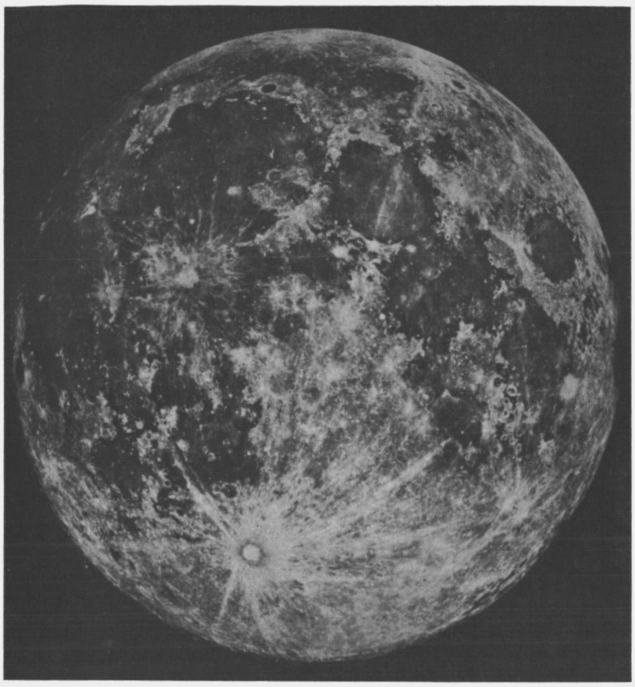

Figure X-38. Rays (Bright, Straight Lines)

Definition and Properties: Rays are roughly straight, permanent, bright streaks of material on the lunar surface. (Figure X-38) Associated with relatively young craters, rays usually diverge from within or from the rim of a crater. Some begin outside the crater walls; dark halos usually encircle such craters. Craters showing much erosion do not have rays. Rays cross over all other features, including mountains.

Theories of Origin: Rays are probably ejected materials from explosions. Still unanswered are questions about the cause of the explosion and its position relative to the surface, i.e., above, below, or at surface level.

Some Occurrences within ±5° Latitude and ±45° Longitude: Hortensius A (4°20'N, 30°40'W), Chladni (4°N, 1°10'E), Triesnecker (4°10'N, 3°30'E), Agrippa (4°N, 10°30'E), Godin (2°N, 10°10'E), Dionysius (2°50'N, 17°20'E), Censorinus (0°40'S, 32°20'E), Mösting (0°40'S, 6°15'W), Lalande (4°30'S, 8°40'W), Encke B (2°20'N, 36°20'W), Turner F (1°35'S, 14°W), Gambart A (1°N, 18°40'W), Lansberg B (2°30'S, 28°10'W), Lansberg D (3°S, 30°30'W).

Some Other Examples on the Sub-Earth Face: Kepler (emanating from 8°N, 38°W), Copernicus (emanating from 10°N, 20°W), Tycho (emanating from 43°S, 11°W).

Information Needed (Samples, Measurements): Photographs thus far have not had sufficient resolution to determine the depth of the rays. Since ray material is on the surface, core samples of the surface will be adequate. A landing site where rays from two craters intersect should be selected so that any differences in composition can be noted and relative ages of the two ray systems can be determined. Such a place would be in the area of intersection of ray systems of Kepler and Copernicus. Radiation measurements of samples of ray material and of the area from which they are taken will aid in determining the origin of the rays.

4.26 Rills (Rilles, Rimae)

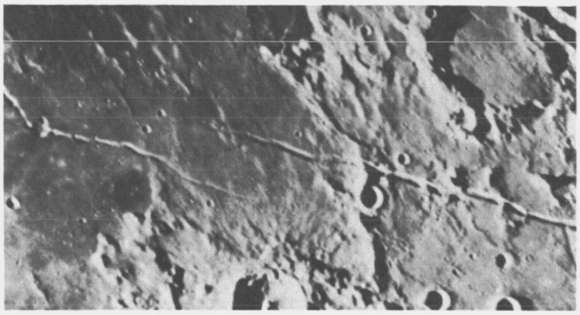

Figure X-39. Hyginus and Ariadaeus Rill Region

Definition and Properties: Rills are negative topographic features in the form of shallow trenches. Crater rills have crateriform banks (banks with craterlike shapes), while normal rills have gently sloping banks. Rills can be straight, arcuate, or sinuous. Straight and arcuate rills cut through or under other topographical features such as hills and crater walls; sinuous rills, however, tend to follow the periphery of positive topographical features. Sinuous rills are characterized by an enlargement at one end (the "head"), and a general narrowing toward the other end (the "tail").

Theories of Origin: Since certain rills become faults at one end, and since they frequently parallel known fault lines, the rills are probably closely associated with faults. The cross section of a rill strongly indicates collapse as a cause.

Some Occurrences within ±5° Latitude and ±45° Longitude: Straight rills: Réaumur (2°S-3°30'S, 1°30'E-3°30'E); arcuate rills: Oppolzer (2°W-3°30'E, 2°10'S-0°30'S); sinuous rills: none were apparent.

Some Other Examples on the Sub-Earth Face: Straight rills: Ariadaeus (5°N-8°N, 10°E-18°E), Hesiodus (29°S, 18°W), Sirsalis I (12°S, 58°W), Sirsalis II (13°S, 63°W), Sirsalis III (13°S, 59°W); arcuate rills: Oppolzer (2°10'S-0°30'S, 2°W-3°30'E); sinuous rills: Hadley (24°15'N-26°15'N, 2°10'E-3°15'E), Prinz (26°N, 44°W). (Figure X-39)

Information Needed (Samples, Measurements): Seismic measurements are a necessity. Shallow, surface samples of the surrounding terrain and of the rill floor and walls, coupled with deep samples from three meters (and more, if possible), are desired. Any evidence of earlier presence of fluid of any type would be of great interest. Heat flow and radiation experiments are always of interest. Detailed photographs are a must.

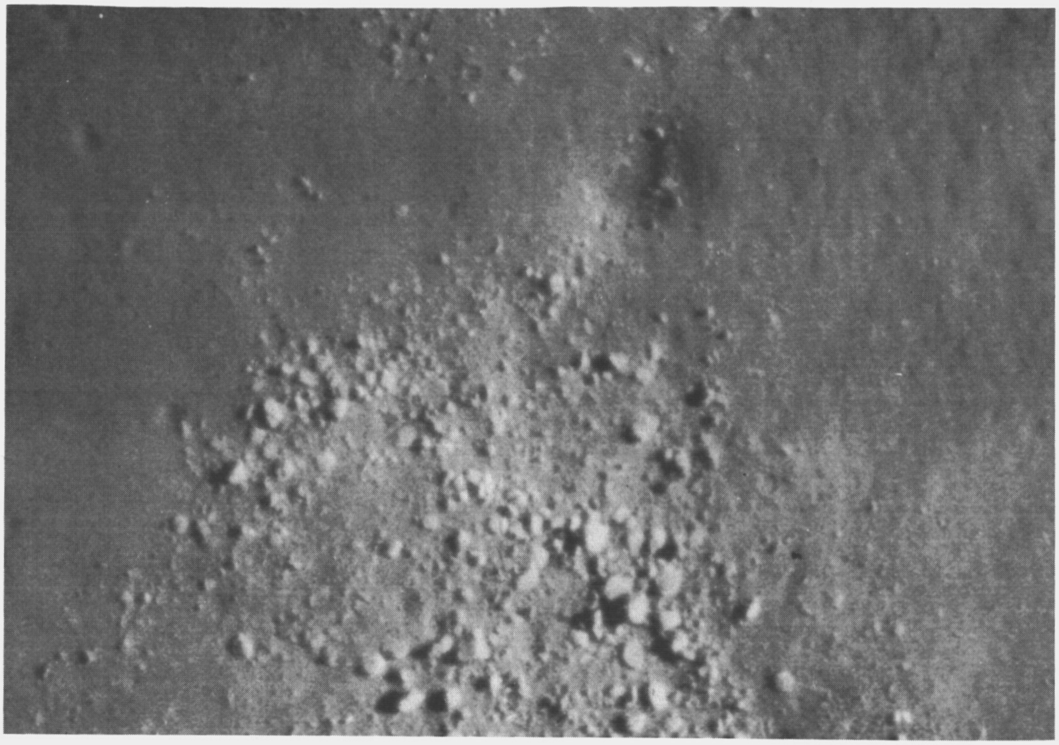

Figure X-40. A Rock-Strewn Area on the Moon in the Southeastern Part of Mare Tranquillitatis (Lunar Orbiter II Photograph)

4.27 Rock Fields

Definition and Properties: Rock fields are relatively flat areas strewn with many rather large rocks.

Theories of Origin: The rocks appear to be ejecta from nearby explosions. Not much is known about these fields, as they were discovered only recently by Lunar Orbiter II.

Some Occurrences within ±5° Latitude and ±45° Longitude: Lunar Orbiter II has discovered the presence of rock fields in Mare Tranquillitatis. (Figure X-40)

Some Other Examples on the Sub-Earth Face: Many examples must exist on the moon, especially in the maria.

Information Needed (Samples, Measurements): Samples of the various rocks and of the surrounding lunar terrain should be obtained. Comparisons of the composition of the rock samples and surrounding terrain should be made. Photographs of the rocks and their orientation would be quite useful in determining the origin of the field.

4.28 Wrinkle Ridges

Definition and Properties: Wrinkle ridges are positive topographic features occurring in lowland areas, having slopes of only a few degrees, and attaining altitudes of about 200 meters above the surrounding terrain. Wrinkle ridges generally occur near the centers of maria. At times, rills connect directly to wrinkle ridges.

Theories of Origin: Wrinkle ridges and faults seem to be related to stresses in the lunar surface. Extrusion seems to be the most frequently mentioned cause.

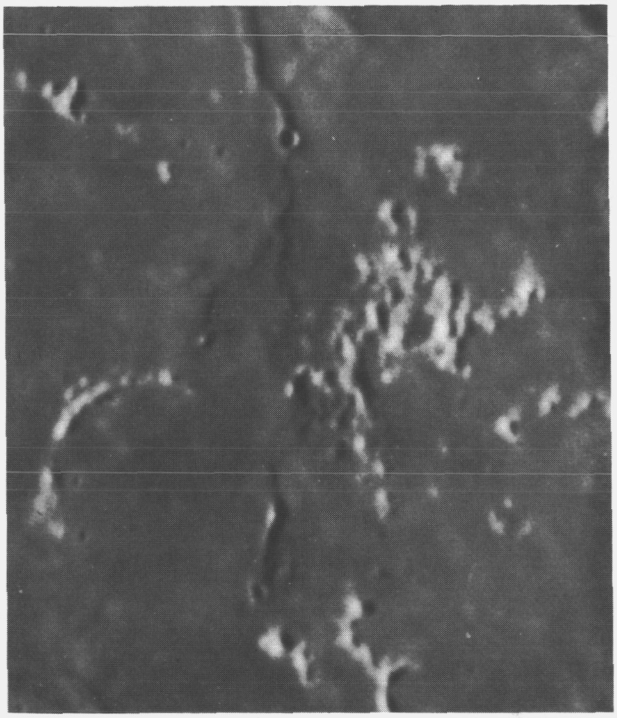

Figure X-41. Euclides F — a Crater on a Wrinkle Ridge near Letronne and Herigonius

Some Occurrences within ±5° Latitude and ±45° Longitude: Sinus Medii (2°S-15°N, 2°W-12°E), Oceanus Procellarum (5°S-5°N, 18°W-45°W), Mare Tranquillitatis (5°S-5°N, 18°E-42°E).

Some Other Examples on the Sub-Earth Face: Sinus Medii (5°N-8°N, 3°E-12°E), Mare Nubium (16°S, 17°W), Mare Nectaris (10°S-16°S, 30°E-39°E).

Information Needed (Samples, Measurements): Surface (drive tube) and subsurface (drill) samples from the surrounding terrain and from the top and sides of the ridge should be obtained. Photographs, as well as temperature and radiation measurements, are necessary.

REFERENCES

"Another Lunar Color Phenomenon," Sky and Telescope, January 1964, Vol. 27, p. 3.

Apollo Project, NASA Bibliography No. 1131, NASA Scientific and Technical Information Division, May 3, 1965.

"Are There Changes on the Moon?" Sky and Telescope, July 1964, Vol. 28, p. 3.

Astrogeologic Studies Annual Progress Report, August 25, 1961 to August 24, 1962, Part A: Lunar and Planetary Investigations, U.S. Geological Survey, 1963.

Astrogeologic Studies Annual Progress Report, August 25, 1961 to August 24, 1962, Part B: Crater Investigations, U.S. Geological Survey, 1963.

Astrogeologic Studies Annual Progress Report, July 1, 1964 to July 1, 1965, Part A: Lunar and Planetary Investigations, U.S. Geological Survey, 1965.

Astrogeologic Studies Annual Progress Report, July 1, 1964 to July 1, 1965, Summary, U.S. Geological Survey, 1965.

Astrogeologic Studies Semi-Annual Progress Report, February 26, 1961, U.S. Geological Survey, 1962.

Beller, William S., "Soviet View of Lunar Surface Reported," Missiles and Rockets, May 23, 1966, Vol. 18, pp. 14-15.

"Boeing Scientists Find Unexpected Abundance of 'Hot Spots' on the Moon," Missiles and Rockets, January 18, 1965, Vol. 16, p. 28.

Burns, Marvin, and Lester A. Gardner, "Rotary-Percussive System Favored for Moon Drilling," Technology Week, June 20, 1966, Vol. 18, pp. 33-36.

Cameron, A. G. W., "The Formation of the Sun and Planets," Icarus, May 1962, Vol. 1, pp. 13-69.

Clark, Sydney P., Jr., Some Calculations Pertaining to the Feasibility of Measuring Lunar Heat Flow, Yale University Press, New Haven, Connecticut, NASA Report N66-15434, September 1965, Final Report.

David, Heather M., "NASA Ponders Litton Hard Spacesuit," Technology Week, June 20, 1966, Vol. 18, pp. 29-30.

Eggleton, R. E., Geologic Map of the Riphaeus Mountains Region of the Moon, U.S. Geological Survey, 1965.

"Expert Believes Moon Is Crunchy," New York Times, June 12, 1966.

Fielder, Gilbert, Lunar Geology, Lutterworth Press, London, 1965.

———, Structure of the Moon's Surface, Pergamon Press, New York, 1961.

———, "Topography and Tectonics of the Lunar Straight Wall," Planet and Space Science, 1963, Vol. II, pp. 23-30.

Fleisig, Ross, ed., "Lunar Flight Programs," Advances in the Astronautical Sciences, American Astronautical Society, New York, 1964, Vol. 18.

Geological Problems in Lunar Research, Annals of the New York Academy of Sciences, July 15, 1965, Vol. 123, pp. 367-1257.

Gold, Theodore, "Ranger Moon Pictures: Implications," Science, September 4, 1964, Vol. 145, pp. 1046-48.

Greenacre, J. A., "Recent Observation of Lunar Color Phenomena," Sky and Telescope, December 1963, Vol. 26, pp. 316-317.

Hackman, Robert J., and Arnold C. Mason, Miscellaneous Geologic Investigations, Map I-351, U.S. Geological Survey, 1961.

Hawkins, Gerald S., H. W. Rack, and S. M. Saslow, Catalogue of Lunar Craters Cross Sections I - Craters with Peaks, Boston University, Boston, 1965.

Heacock, R. L., G. P. Kuiper, W. M. Shoemaker, H. C. Urey, and E. A. Whitaker, Ranger VIII and IX, Part II: Experimenters' Analyses and Interpretations, Jet Propulsion Laboratory, California Institute of Technology, Pasadena, N66-25046, March 15, 1966.

Hinners, N. W., "Lunar Mission Objectives and Rationale," Interim Report for AES Flight Mission Assignment Plan - Part V, Bellcomm TM 65-1011-4, January 29, 1965.

Jastrow, R. and A. G. W. Cameron, Origin of the Solar System, Academic Press, 1963.

Judge, J. F., "Bendix Simulating Lunar Magma in Laboratory Tests," Missiles and Rockets, March 23, 1964, Vol. 14, pp. 36-37.

Kopal, Zdenek, Luminescence of the Lunar Surface, Mathematical Note No. MN391, Mathematics Research Laboratory, Boeing Scientific Research Labs., D1-82-0410, AD615-260, February 1965.

———, and T. W. Rackham, "Lunar Luminescence and Solar Flares," Sky and Telescope, March 1964, Vol. 27, pp. 140-141.

Kuiper, Gerald P., and Barbara M. Middlehurst, eds., "The Moon, Meteorites, and Comets," University of Chicago Press, Chicago, 1963.

LeGalley, D. P., and J. W. McKee, Space Exploration, McGraw-Hill, New York, 1964.

———, and Alan Rosen, eds., Space Physics, Wiley, New York, 1964.

"Lively Moon," Scientific American, February 1964, Vol. 210, pp. 67-68.

Lucas, Wilmuth C., and Otha H. Vaughan, Jr., The Lunar Atmosphere, George C. Marshall Space Flight Center, Huntsville, Alabama, NASA TM-X53399; N66-22928, February 23, 1966.

Lunar Charts, (LAC) Aeronautical Chart and Information Center, U.S. Air Force, St. Louis, 1961—.

Lunar Roving Vehicles and Other Lunar Transporation, NASA Bibliography No. 1096, Literature Search, NASA Scientific and Technical Information Division, Washington, D. C., April 21, 1965.

Lunar Surface Studies - A Continuing Bibliography, NASA Scientific and Technical Information Division, NASA-SP-7003, Washington, D. C., June 1964—.

McIntosh, R. A., "Features of the Lunar Crater Aristarchus," The Journal of the British Astronomical Association, 1961, Vol. 71, pp. 380-88.

Middlehurst, B. M., "A Lunar Eruption in 1783 ?" Sky and Telescope, August 1964, Vol. 28, pp. 83-84.

NASA 1965 Summer Conference on Lunar Exploration and Science, Falmouth, Massachusetts, July 19-31, 1965, NASA Scientific and Technical Information Division, Washington, D. C., NASA SP-88, 1965.

Normyle, William J., "Lunar Survey Module Design Under Test," Aviation Week and Space Technology, July 18, 1966, pp. 97-101.

———, "NASA Given Lunar Surface Experiment Demonstration," Aviation Week and Space Technology, July 25, 1966, pp. 94-105.

Pay, Rex, "Surveyor Program Leapfrogs Ahead," Missiles and Rockets, June 6, 1966, Vol. 18, pp. 14-16.

"Project: Lunar Orbiter B," Press Kit, NASA Scientific and Technical Information Division, Release No. 66-286, November 4, 1966.

Report of August 1965 TYCHO Meeting, TYCHO Study Group, Electrical Engineering Department, University of Minnesota, N66-14001; NASA CR-8896.

Shoemaker, E. M., "The Geology of the Moon," Scientific American, December 1964, Vol. 211, pp. 38-47.

———,"Moon Close Up," National Geographic Magazine, November 1964, Vol. 126, pp. 690-707.

Strom, R. G., "Fault Mechanics of the Lunar Straight Wall and the Nature of the Mare Material," Space Sciences Laboratory Report, January 1963, Series No. 4, Issue No. 8, p. 13.

Surveyor I: A Preliminary Report, NASA Scientific and Technical Information Division, Washington, D. C., N66-29481; NASA-SP-126, June 1966.

Texas Instruments, Inc., Survey of Lunar Surface Measurements, Experiments, and Geologic Studies, Final Report, Contract No. NAE 9-2115, August 30, 1964, Texas Instruments, Inc., Science Services Division, Dallas, Texas, 1964.

Topographic Lunar Maps, Army Map Service, Corps of Engineers, U.S. Army, Washington, D. C., 1963.

Warner, Brian, "Some Problems of Lunar Orogeny," The Journal of the British Astronomical Association, 1962, Vol. 72, pp. 280-285.

———, "Stresses in the Surface of the Moon," The Journal of the British Astronomical Association, 1961, Vol. 71, pp. 288-395.

Watkins, H. D., "Ranger Photos Boost Confidence in Apollo," Aviation Week and Space Technology, August 10, 1964, Vol. 81, pp. 19-23.

X68-84341

SECTION XI. STRATEGY AND COST COMPARISONS FOR LUNAR SURFACE RENDEZVOUS OPERATIONS

by D. C. Swanay

1. INTRODUCTION

If Lunar Surface Rendezvous (LSR) is not accomplished, the Dual-Vehicle mission fails and either one or two complete systems are wasted, depending on the failure mode. There are two basic causes of failure to accomplish LSR-equipment failure of either of the two LM systems, and failure to launch the second system after the first system is launched. The probability of an equipment failure is determined by the LM reliability model, while the probability of failure to launch the second vehicle is determined by the number of launch opportunities provided and the launch probability for each attempt.

2. SELECTION OF PREFERRED OPERATIONAL STRATEGY

Several strategies for launch and LM delivery operations were considered in order to determine how LSR could best be accomplished. Each strategy has several failure modes associated with it, and each failure mode has a cost ($200 million if one complete system is wasted and $400 million if two complete systems are wasted). The expected loss per LSR mission is defined to be the product of failure mode probability and cost, summed over all the failure modes associated with the strategy used. The expected cost per LSR mission is defined to be the cost of two systems plus the expected loss per mission when the recommended strategy is used.

Four general operational strategies were evaluated in terms of expected loss. The first strategy attempts to minimize the degradation of LM reliability with time by launching and landing both systems as close together as possible. The second strategy embodies this principle, but, in addition, attempts to minimize the effects of launch failures by providing for a second series of launch attempts 1 month after the first. The third strategy trades off a month of time degradation of reliability to avoid launching the second LM before the first LM is landed and checked out. The fourth strategy avoids the lunar orbital waiting period necessary to provide acceptable launch probabilities in the first strategies. This is done by providing a single launch opportunity each month for 3 months after the unmanned LM landing, and accepting the time degradation of unmanned LM reliability. A more detailed definition of the four strategies follows.

2.1 Strategy 1

The unmanned LM system is launched first, with a preplanned lunar orbital waiting time of sufficient length to provide three launch opportunities for the second system. With an assumed 48-hour recycle time after a failure to launch, a 6-day waiting time would be required to provide three launch opportunities. Three opportunities are necessary to ensure a reasonably high launch probability in the presence of expected single-attempt launch probabilities. The unmanned LM delivery system will be free to return after the landing of its LM; hence, the additional requirements placed on CM life-support capability by the lunar orbital waiting time will be minimized by launching the unmanned system first.

The lunar orbits of the two systems are chosen so that both systems pass over the desired site with proper lighting conditions at the end of the preplanned orbital waiting time. The manned LM lands first, followed in a few hours by the unmanned LM.

2.2 Strategy 2

The unmanned LM system is launched first with a preplanned lunar orbital waiting time as in Strategy 1. The unmanned LM lands at the end of the preplanned waiting period, followed by the manned LM a few hours later if its launch is achieved. If the second system is not launched on the first three attempts, the capability exists to remotely deactivate the unmanned LM, check it out, and reactivate it 1 month later for a second series of three attempts. A lunar orbital waiting time must be provided so that the manned LM again has three launch opportunities.

Table XI-1

FAILURE MODES FOR STRATEGY 1

Manned LM		Unmanned	Probability	Loss per
Launch	LM Status	LM Status	of Failure*	Mission
Achieved	OK	Fails at or before landing	$P_{L3} R_2(0) \left[1-R_1(0)\right]$	2 AAP Systems
Achieved	Fails at or before landing	—	$P_{L3}\left[1-R_2(0)\right]$	2 AAP Systems
Not Achieved in Allotted 3 Attempts	—	—	$1-P_{L3}$	1 AAP System

*$R_1(t)$ = probability that unmanned LM capable of supporting remainder of mission at t days after touchdown.

$R_2(0)$ = probability that manned LM capable of supporting remainder of mission upon landing.

P_L = probability of achieving launch on single attempt.

$P_{L3} = 1 - (1-P_L)^3$ = probability of achieving launch in three attempts.

Table XI-2

FAILURE MODES FOR STRATEGY 2

Manned LM		Unmanned	Probability	Loss per
Launch	LM Status	LM Status	of Failure*	Mission
Achieved on 1st series of 3 Attempts.	–	Fails at or before landing	$P_{L3}\left[1-R_1(0)\right]$	2 AAP Systems
Achieved on 1st series of 3 attempts	Fails at or before landing	OK	$P_{L3}\left[R_1(0)\right]\left[1-R_2(0)\right]$	2 AAP Systems
Not Achieved on 1st series of 3 attempts	–	Fails at or before landing	$\left(1-P_{L3}\right)\left[1-R_1(0)\right]$	1 AAP System
Not Achieved on 1st series of 3 attempts	–	OK upon landing. Fails before 1st try of 2nd series.	$\left(1-P_{L3}\right)\left[R_1(0)\right] \cdot \left[R(0) - R(22)\right]$	1 AAP System
Not Achieved on 1st series. Achieved on 1st try of 2nd series	–	OK for 1st attempt in 2nd series. Fails before manned landing	$\left[\left(1-P_{L3}\right)P_L R_1(22)\right] \cdot \left[R_1(22)-R_1(30)\right]$	2 AAP Systems
Not Achieved on 1st series. Does not get off on 1st try of 2nd series.	–	OK at 1st try of 2nd series. Fails before 2nd try.	$\left(1-P_{L3}\right)\left(1-P_L\right)R_1(22) \cdot \left[R(22)-R(24)\right]$	1 AAP System
Not Achieved on 1st series. Achieved on 2nd try of 2nd series.	–	OK for 2nd try in 2nd series. Fails before manned landing.	$\left[\left(1-P_{L3}\right)\left(1-P_L\right)P_L\right] \cdot \left[R_1(24)\right] \cdot \left[R_1(24) - R_1(30)\right]$	2 AAP Systems
Not Achieved on 1st series. Does not get off on 1st or 2nd try of 2nd series.	–	OK for 2nd try of 2nd series. Fails before 3rd try.	$\left[\left(1-P_{L3}\right)\left(1-P_L\right)^2 R_1(24)\right] \cdot \left[R_1(24) - R_1(26)\right]$	1 AAP System
Not Achieved on 1st series. Launched on 3rd try of 2nd series.	–	OK for 3rd try in 2nd series. Fails before manned landing.	$\left[\left(1-P_{L3}\right)\left(1-P_L\right)^2 P_L\right] \cdot R_1(26)\left[R_1(26)-R_1(30)\right]$	2 AAP Systems
Not Achieved on 1st series of attempts. Achieved 1 month later.	Fails at or before landing	Still Ok 1 month after landing.	$R_1(30)\left[1-R_2(0)\right] \cdot \left[\left(1-P_{L3}\right)P_{L3}\right]$	2 AAP Systems
Not Achieved on 1st or 2nd series of attempts.	–	Still OK for final attempt	$R_1(26)\left[1-P_{L3}\right]^2$	1 AAP System

*$R_1(t)$ = probability that unmanned LM capable of supporting remainder of mission at t days after touchdown.

$R_2(0)$ = probability that manned LM capable of supporting remainder of mission upon landing.

P_L = probability of achieving launch on single attempt.

$P_{L3} = 1 - (1-P_L)^3$ = probability of achieving launch in three attempts.

2.3 Strategy 3

The unmanned LM system is launched first and, after landing, is checked out and deactivated. One month later, it is reactivated and checked out. If the unmanned system is judged capable of supporting the manned mission, the manned LM system launch is then initiated. A lunar orbital waiting time sufficient to allow three launch attempts is provided.

Table XI-3

FAILURE MODES FOR STRATEGY 3

Manned LM		Unmanned LM Status	Probability of Failure*	Loss per Mission
Launch	LM Status			
No attempt.	—	Fails at or before landing.	$1-R_1(0)$	1 AAP System
No attempt.	—	OK upon landing. Fails before 1st try.	$R_1(0)\left[R_1(0)-R_1(22)\right]$	1 AAP System
Achieved on 1st try.	—	OK for 1st try. Fails before manned landing.	$P_L R_1(22)\left[R_1(22) - R_1(30)\right]$	2 AAP Systems
Not Achieved on 1st try.	—	OK for 1st try. Fails before 2nd try.	$\left[(1-P_L)R_1(22)\right] \cdot \left[R_1(22)-R_1(24)\right]$	1 AAP System
Achieved on 2nd try.	—	OK for 2nd try. Fails before manned landing.	$\left[(1-P_L)P_L R_1(24)\right] \cdot \left[R_1(24)-R_1(30)\right]$	2 AAP Systems
Not Achieved on 2nd try.	—	OK for 2nd try. Fails before 3rd try.	$(1-P_L)^2 R_1(24) \cdot \left[R_1(24)-R_1(30)\right]$	1 AAP System
Achieved on 3rd try.	—	OK for 3rd try. Fails before manned landing.	$\left[(1-P_L)^2 P_L R_1(26)\right] \cdot \left[R_1(26)-R_1(30)\right]$	2 AAP Systems
Yes	Fails at or before landing.	Still OK 1 month after landing.	$R_1(28)\left[1-R_2(0)\right]P_{L3}$	2 AAP Systems
Not Achieved on 3 tries.	—	Still OK for 3rd try.	$R_1(26)\left(1-P_{L3}\right)$	1 AAP System

*$R_1(t)$ = probability that unmanned LM capable of supporting remainder of mission at t days after touchdown.

$R_2(0)$ = probability that manned LM capable of supporting remainder of mission upon landing.

P_L = probability of achieving launch on single attempt.

$P_{L3} = 1 - (1-P_L)^3$ = probability of achieving launch in three attempts.

2.4 Strategy 4

The unmanned LM system is launched, landed, and deactivated as in Strategy 3. One month later, it is reactivated and checked out. If the unmanned LM is capable of supporting the manned mission, a single attempt to launch the manned LM system is made. If this attempt fails, the unmanned LM is deactivated and the procedure is repeated a month later. Three launch attempts are provided for the manned LM system, so the unmanned LM must have the capability for a lunar storage period of up to 3 months with three activation and checkout cycles.

2.5 Evaluation of Strategies

Tables XI-1 through -4 summarize the failure modes for the four strategies just described. The tables also include the probability of each failure mode and the associated loss. To simplify the definition of the failure modes and the calculation of their probability of occurrence, the following two assumptions were made:

1. Since the requirements placed on LM operation by the LSR mission plan are considerably more severe than those placed on the CSM, it was assumed that the probability of CSM failure would be small relative to that of LM failure. Therefore, no failure modes involving CSM malfunctions were defined.
2. It was assumed that a safe unmanned LM landing can be achieved with high probability and that failures of additional equipment required by the unmanned landing system do not contribute significantly to the overall LM failure probability.

Figure XI-1 presents the expected loss as a function of single-attempt launch probability and LM reliability model for each of the four strategies. LM reliability model 1 is based on data in References 1 and 2.* Model 1 postulates an unmanned LM reliability of 0.903 at lunar touchdown with exponential degradation of reliability with time to a value of 0.755 at the end of a 3-month storage period, and a touchdown reliability of 0.922 for the manned LM. LM reliability model 2 is essentially an order-of-magnitude improvement of model 1, with a touchdown reliability of 0.99 for both LM's and a reliability of 0.975 at the end of the 3-month lunar storage period for the unmanned LM. Expected cost data used in Volume 1 of this report are based on LM reliability model 1 and a single-attempt launch probability of 0.67.

Strategy 4 is recommended for use if LM reliability model 1 applies. This operational strategy offers the minimum expected loss per mission for single-attempt launch probabilities above 0.85. The advantages in expected loss per

---

*References are listed at the end of the section.

Table XI-4

FAILURE MODES FOR STRATEGY 4

Manned LM		Unmanned LM Status	Probability of Failure*	Loss per Mission
Launch	LM Status			
No attempt.	—	Fails at or before landing.	$1-R_1(0)$	1 AAP System
No attempt.	—	OK upon landing. Fails before 1st launch attempt.	$R_1(0)\left[R_1(0)-R_1(26)\right]$	1 AAP System
Achieved on 1st try.	—	Still OK at manned LM launch. Fails before landing.	$P_L R_1(26)\left[R_1(26) - R_1(30)\right]$	2 AAP Systems
Does not get off on 1st try.	—	OK for 1st launch attempt. Fails before 2nd attempt.	$\left[(1-P_L)R_1(26)\right] \cdot \left[R_1(26)-R_1(56)\right]$	1 AAP System
Achieved on 2nd try.	—	Still OK at manned LM launch. Fails before landing.	$\left[P_L(1-P_L)R_1(56)\right] \cdot \left[R_1(56)-R_1(60)\right]$	2 AAP Systems
Does not get off on 2nd try.	—	OK for 2nd launch attempt. Fails before 3rd attempt.	$\left[(1-P_L)^2 R_1(56)\right] \cdot \left[R_1(56)-R_1(86)\right]$	1 AAP System
Achieved on 3rd try.	—	Still OK at manned LM launch. Fails before landing.	$\left[P_L(1-P_L)^2 R_1(86)\right] \cdot \left[R_1(86)-R_1(90)\right]$	2 AAP Systems
Launched on 1st try.	Fails at or before landing.	OK 1 month after landing.	$P_L R_1(30)\left[1-R_2(0)\right]$	2 AAP Systems
Launched on 2nd try.	Fails at or before landing.	OK 2 months after landing.	$\left[P_L(1-P_L)R_1(60)\right] \cdot \left[1-R_2(0)\right]$	2 AAP Systems
Launched on 3rd try.	Fails at or before landing.	OK 3 months after landing.	$\left[P_L(1-P_L)^2 R_1(90)\right] \cdot \left[1-R_2(0)\right]$	2 AAP Systems
Does not get off on 1st, 2nd or 3rd try.	—	Still OK for 3rd launch attempt.	$(1-P_L)^3 R_1(86)$	1 AAP System

*$R_1(t)$ = probability that unmanned LM capable of supporting remainder of mission at t days after touchdown.

$R_2(0)$ = probability that manned LM capable of supporting remainder of mission upon landing.

P_L = probability of achieving launch on single attempt.

$P_{L3} = 1 - (1-P_L)^3$ = probability of achieving launch in three attempts.

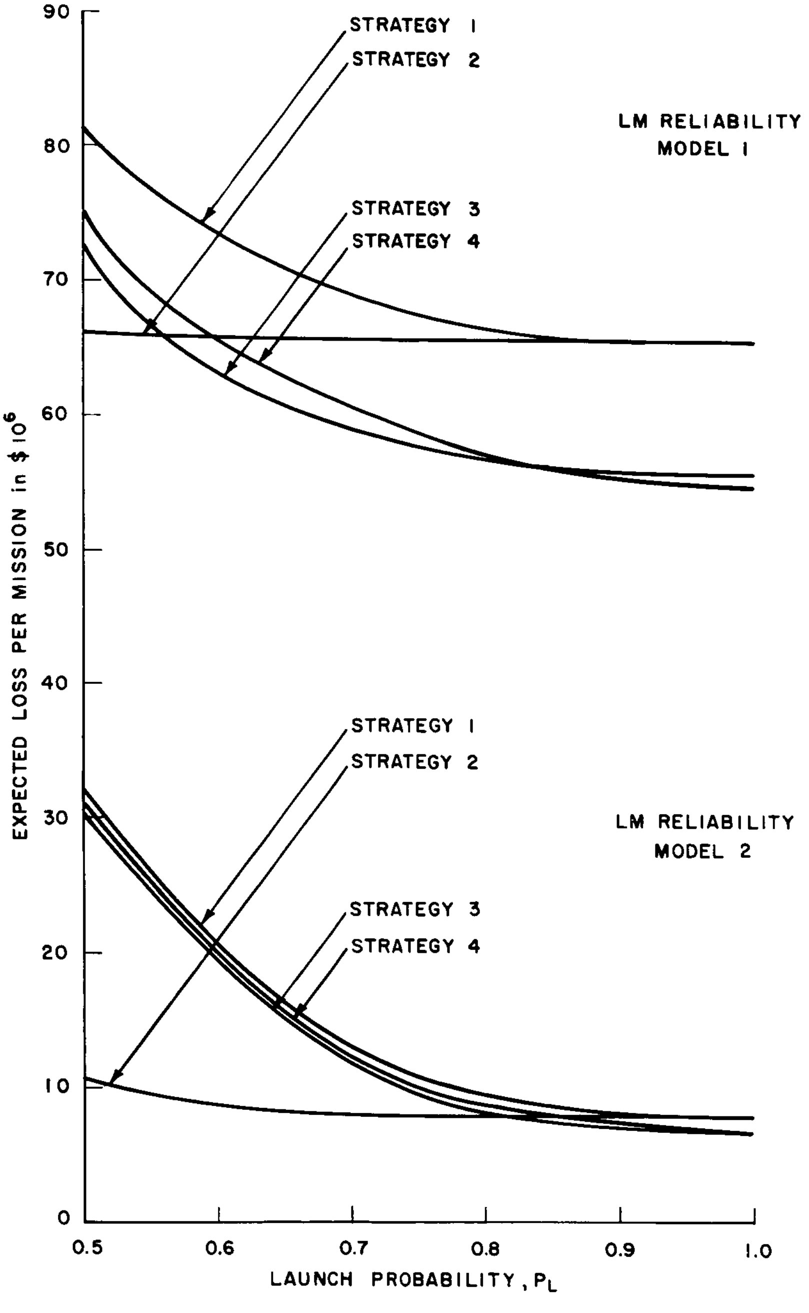

Figure XI-1. Expected Loss as a Function of Single-Attempt Launch Probability for Four Strategies

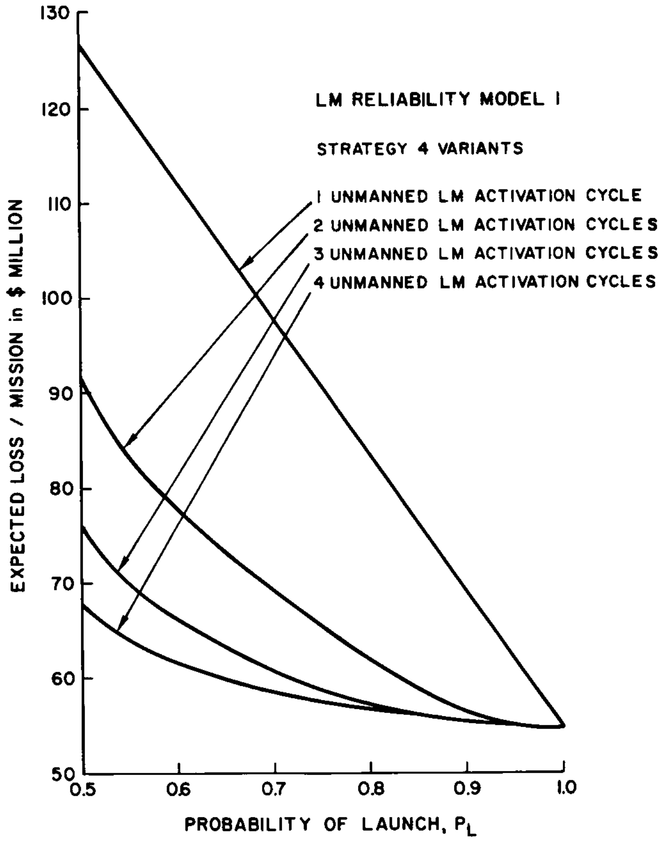

Figure XI-2. Effect of Varying Activation and Checkout Cycles in Strategy 4

mission offered by Strategies 2 and 3 at lower launch probabilities are not sufficient to warrant the operational complications of their required 6-day orbital waiting time.

Figure XI-2 evaluates the effect of varying the number of activation and checkout cycles required in Strategy 4. If it is assumed that 0.67 is a realistic estimate of single-attempt launch probability, then the three launch attempts offered by Strategy 4 lead to a reduction in expected loss per mission of $40 million over the single-attempt strategy and $10 million over the two-attempt strategy. There is not much further reduction in loss to be accrued by going to four attempts; therefore, only three attempts are recommended for Strategy 4.

3. EFFECT OF LM RELIABILITY ON MISSION COST

Comparison of expected loss for LM reliability models 1 and 2 indicates that an expected loss of $40 to 50 million per mission can be charged to the difference in LM reliability between the models. Thus, if an expenditure of a few million dollars could significantly upgrade LM reliability, the investment would be returned several times over in terms of reduced expected cost per mission.

REFERENCES

1. Apollo Extension System, Phase B Final Report, V, "Shelter Design Analysis Summary," Grumman Aircraft Engineering Corporation (CONFIDENTIAL).
2. Apollo Extension System, Phase B Final Report, VI, "Taxi Design Analysis Summary," Grumman Aircraft Engineering Corporation (CONFIDENTIAL).